Nanostructure Science and Technology
Series Editor: David J. Lockwood

Alexey A. Popov *Editor*

Endohedral Fullerenes: Electron Transfer and Spin

Springer

Nanostructure Science and Technology

Series editor

David J. Lockwood, FRSC
National Research Council of Canada
Ottawa, Ontario, Canada

More information about this series at http://www.springer.com/series/6331

Alexey A. Popov
Editor

Endohedral Fullerenes: Electron Transfer and Spin

Springer

Editor
Alexey A. Popov
Leibniz Institute for Solid State and
Materials Research
Dresden
Germany

ISSN 1571-5744 ISSN 2197-7976 (electronic)
Nanostructure Science and Technology
ISBN 978-3-319-47047-4 ISBN 978-3-319-47049-8 (eBook)
DOI 10.1007/978-3-319-47049-8

Library of Congress Control Number: 2017936031

Printed on acid-free paper

This Springer imprint is published by Springer Nature
The registered company is Springer International Publishing AG
The registered company address is: Gewerbestrasse 11, 6330 Cham, Switzerland

Preface

Over the last two decades, the research of endohedral fullerenes has made a dramatic progress. Many types of endohedral fullerenes have been discovered, their production and separation techniques have been substantially improved, and comprehensive studies of their chemical and physical properties became possible. Encapsulation into the interior space of the fullerene cage stabilizes unique metal clusters or single atoms which are not known to exist in the free form. However, this stabilization is only partially achieved by the shielding of the species from the surrounding. Another important factor is that the carbon cage is not "innocent". Namely, the electron transfer between the encapsulated species and the carbon cage plays crucial role in the structure and properties of endohedral metallofullerenes.

Unprecedented molecular and electronic structure of endohedral fullerenes leads to a plethora of phenomena at the interface between the endohedral atoms and π-system of the carbon cage. Charge transfer in endohedral metallofullerene (EMF) molecules can either leave encapsulated species intact (i.e., only carbon cage is active as in empty fullerene) or proceed across the metal–cage interface, and examples of both types are well documented nowadays. The latter case is especially interesting since it opens the way to tune charge states of endohedral species while keeping a fullerene as a protecting shell around the redox center. Good electron accepting properties of fullerenes made them attractive building blocks for organic electronics, and multiple studies of the EMF performance in this role have been carried out, from fundamental photophysical studies of the donor–acceptor dyads to the studies of the photoconversion efficiency in prototype bulk heterojunction solar cells. High thermal stability of endohedral metallofullerenes allows deposition of the molecules on various substrates in ultrahigh vacuum conditions and investigation of their electronic properties with high-resolution scanning probe and other surface science methods. Peculiar electronic states and dynamics of fullerene molecules and endohedral clusters could be investigated with the help of scanning tunneling microscopy.

Single-electron transfer is inevitably accompanied by the change of the spin state of the molecule, and here is another unique property of EMFs: the cage can either keep an unpaired spin itself, or it can transfer the spin to the endohedral cluster, and

hence both the cage and the cluster spin states can be altered. Furthermore, encapsulation of the species with unpaired electrons (e.g., nitrogen or phosphorus atoms or lanthanide-containing clusters) brings endohedral fullerenes to the fields of molecular magnetism and quantum computing. Electron spin resonance, nuclear magnetic resonance, magnetometry, and X-ray magnetic circular dichroism have been used extensively to analyze spin-related phenomena in endohedral fullerenes. Finally, well-defined spin state and long spin coherence make endohedral fullerenes with nitrogen atom, such as $N@C_{60}$, attractive for the field of quantum computing.

The aim of this book is a concise analysis of the behavior of the interface between encapsulated atoms and a carbon-based π-system under conditions of the electron transfer and description of the spin-based phenomena caused by the shielding of endohedral spins by the fullerene cage. In Chap. 1 we introduce the reader into the world of endohedral fullerenes by describing the basics of their synthesis, separation, and molecular structure elucidation. Chapter 2 gives an overview of electrochemical studies of EMFs supported by the molecular orbital analysis. Chapter 3 by Samoylova and Stevenson describes the development in the non-chromatographic separation techniques, which benefit from the difference of reduction and oxidation potentials of different types of EMFs and empty fullerenes. Chapter 4 by Boltalina reviews the studies of the ions of EMFs in the gas phase by various types of mass spectrometry and focuses on the ion molecular reactivity and determination of the electron affinities. In Chap. 5, Zhen, Liu, and Yang give an account on the photoexcitation behavior of EMF in molecular and supramolecular dyads with donors and acceptors and describe possible applications of EMFs in photovoltaics. Chapter 6 by Feng and Petek reviews the studies of the EMFs by low-temperature scanning tunneling microscopy with a focus on superatom electronic state and switching of the molecular geometry by tunneling currents. Chapters 7–9 are devoted to the studies of EMFs by electron spin resonance spectroscopy (ESR). In Chap. 7, Wang and Wang describe ESR studies of Sc and Y-based EMFs. Chapter 8 by Kato reviews ESR spectroscopy of lanthanide EMFs, including those with large spin moments exceeding 1/2. In Chap. 9, we describe EPR studies of ion radicals of EMFs in solution. Magnetic properties of EMFs with endohedral lanthanides are described in Chaps. 10 and 11. Chapter 10 reviews the studies by paramagnetic NMR in solution and describes the use of pNMR for the analysis of molecular structure and dynamics of EMFs as well as for the analysis of the magnetic anisotropy of lanthanide ions in nitride clusterfullerenes. Chapter 11 by Westerström and Greber provides extended introduction into the magnetism of EMF and in particular into single-molecule magnetism of EMFs in bulk and in molecular layers on surfaces. In Chap. 12, Lawler reviews nonmetal endohedral fullerenes with emphasis on dihydrogen-containing fullerenes, their molecular dynamics, and nuclear spin chemistry. Chapter 13 by Zhou and Porfyrakis gives a detailed account of the synthesis and separation of C_{60} with nitrogen atom in its center, $N@C_{60}$, its studies by ESR spectroscopy, and chemical derivatization for the use in quantum computing. In Chap. 14, Harneit describes general concepts of quantum information processing and shows how pnictide endohedral fullerenes, and especially $N@C_{60}$, can be used in this field. We hope that this collection of

chapters prepared by the scientists with diverse expertise and summarizing the vast development of our understanding of the charge transfer and spin-related properties of endohedral fullerenes will bring the information about the fascinating properties of these molecules to the broader audience and inspire further progress in this field.

Dresden, Germany Alexey A. Popov

Contents

Contributors

Olga V. Boltalina Department of Chemistry, Colorado State University, Fort Collins, CO, USA

Min Feng Department of Physics and Astronomy and Pittsburgh Quantum Institute, University of Pittsburgh, Pittsburgh, PA, USA; School of Physics and Technology, Wuhan University, Wuhan, Hubei, China

Thomas Greber Physik-Institut, University of Zürich, Zürich, Switzerland

Wolfgang Harneit Fachbereich Physik, Universität Osnabrück, Osnabrück, Germany

Tatsuhisa Kato Institute for Liberal Arts and Sciences, Kyoto University, Sakyoku, Kyoto, Japan

Ronald G. Lawler Department of Chemistry, Brown University, Providence, RI, USA

Qing Liu Hefei National Laboratory for Physical Science at Microscale, CAS Key Laboratory of Materials for Energy Conversion, Department of Materials Science and Engineering, University of Science and Technology of China (USTC), Hefei, China

Hrvoje Petek Department of Physics and Astronomy and Pittsburgh Quantum Institute, University of Pittsburgh, Pittsburgh, PA, USA

Alexey A. Popov Leibniz Institute for Solid State and Materials Research, Dresden, Germany

Kyriakos Porfyrakis Department of Materials Science, University of Oxford, Oxford, UK

Nataliya Samoylova Leibniz Institute for Solid State and Materials Research, Dresden, Germany

Steven Stevenson Department of Chemistry, Indiana-Purdue University Fort Wayne (IPFW), Fort Wayne, IN, USA

Chunru Wang Laboratory of Molecular Nanostructure and Nanotechnology, Institute of Chemistry, Chinese Academy of Sciences, Beijing, China

Taishan Wang Laboratory of Molecular Nanostructure and Nanotechnology, Institute of Chemistry, Chinese Academy of Sciences, Beijing, China

Rasmus Westerström Synchrotron Radiation Research, Department of Physics, Lund University, Lund, Sweden

Shangfeng Yang Hefei National Laboratory for Physical Science at Microscale, CAS Key Laboratory of Materials for Energy Conversion, Department of Materials Science and Engineering, University of Science and Technology of China (USTC), Hefei, China

Jieming Zhen Hefei National Laboratory for Physical Science at Microscale, CAS Key Laboratory of Materials for Energy Conversion, Department of Materials Science and Engineering, University of Science and Technology of China (USTC), Hefei, China

Shen Zhou Department of Materials Science, University of Oxford, Oxford, UK

Chapter 1
Synthesis and Molecular Structures of Endohedral Fullerenes

Alexey A. Popov

Abstract The chapter gives an introduction into the field of endohedral fullerenes and describes development in the synthesis and molecular structure determination of these compounds. An overview of elements capable of being encapsulated within the fullerene cage is given. Different types of endohedral metallofullerenes and clusterfullerenes as well as peculiarities in the carbon cage isomerism caused by encapsulated species are discussed.

1.1 Introduction

The ability of fullerenes to encapsulate foreign atoms within their inner space was first recognized in 1985, when stable species corresponding to LaC_{60} were detected by mass-spectrometry during laser ablation of graphite impregnated with La [1]. Since then the field has undergone a dramatic development over the last 30 years, and fullerenes encapsulating different atoms, ions, clusters, and even small molecules have been synthesized, some of them in decent amounts. Such fullerenes are termed as "endohedral" [2, 3] after a combination of Greek ἔνδον ("endon"—within) and ἕδρα ("hedra"—face of a geometrical figure). In the chemical formulae, endohedral species are written first followed by the symbol "@" and then by the carbon cage, e.g., $N@C_{60}$ denotes an endohedral fullerene molecule, in which nitrogen atom is encapsulated inside C_{60} cage.

Owing to the fundamental differences in their structural and electronic properties as well as synthetic approaches, endohedral fullerenes can be divided into two main classes: endohedral metallofullerenes (EMFs) and non-metal endohedral fullerenes (nMEFs). The class of EMFs includes fullerenes encapsulating one, two, or three metals atoms, as well as complex clusters comprising up to four metal atoms and up to three atoms of electronegative non-metals (N, O, C, S). NMEFs can comprise

A.A. Popov (✉)
Leibniz Institute for Solid State and Materials Research,
Helmholtzstraße 20, 01069 Dresden, Germany
e-mail: a.popov@ifw-dresden.de

A.A. Popov (ed.), *Endohedral Fullerenes: Electron Transfer and Spin*,
Nanostructure Science and Technology, DOI 10.1007/978-3-319-47049-8_1

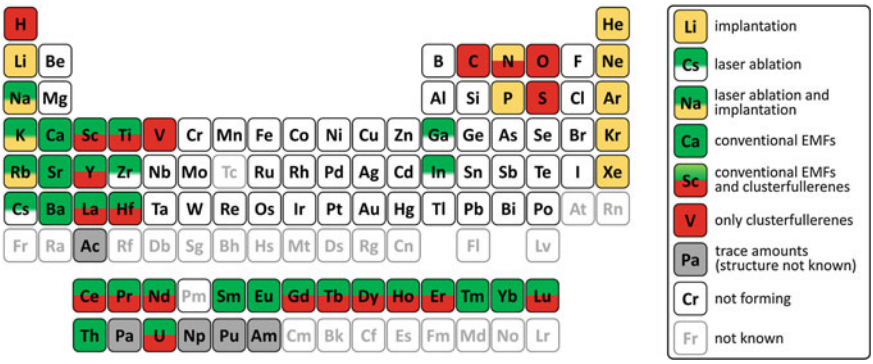

Fig. 1.1 Periodic table of endohedral elements describing the possibility to encapsulate different elements into carbon cages and suitable methods of synthesis for corresponding endohedral fullerenes (note that molecular surgery is not taken into account)

single atoms (noble gasses, nitrogen, and phosphorus) as well as simple molecules (H_2, H_2O, HF, etc.). Figure 1.1 shows the elements which have been successfully placed inside fullerenes.

Encapsulation of species inside the fullerene cage can be achieved in two conceptually different pathways: either species are "implanted" into empty fullerene molecules (which are synthesized beforehand), or encapsulation happens during the fullerene formation (Fig. 1.2). EMFs are usually obtained by the second procedure (only alkali-metal-based EMFs can be also obtained by direct implantation into C_{60}), whereas non-metal endohedral fullerenes (nMEFs) are synthesized by different implantation techniques.

1.2 Synthesis of Endohedral Metallofullerenes

The first EMFs were obtained in 1985 by laser ablation, but the real breakthrough in their synthesis was achieved by the discovery of the macroscopic fullerene production by arc-discharge synthesis in 1990 [4]. The use of metal-filled graphite targets or electrodes in the laser evaporation or arc-discharge synthesis resulted in formation of the appreciable amounts of EMFs along with much larger amounts of empty fullerenes [5–7]. Since then, the arc-discharge remains the main method for the EMF synthesis. Laser ablation coupled to mass-spectrometry detection of the formed species is now used mainly to study the mechanism of the fullerene formation [8, 9]. Ion bombardment of C_{60} is employed for the synthesis of alkali-metal EMFs, especially $Li@C_{60}$ [10, 11].

When metal-filled electrodes are evaporated in the inert atmosphere (usually He) by an arc-discharge method, mono- and dimetallofullerenes are formed. Rarely, trimetallofullerenes can be also obtained in small amounts. Besides, acetylide C_2

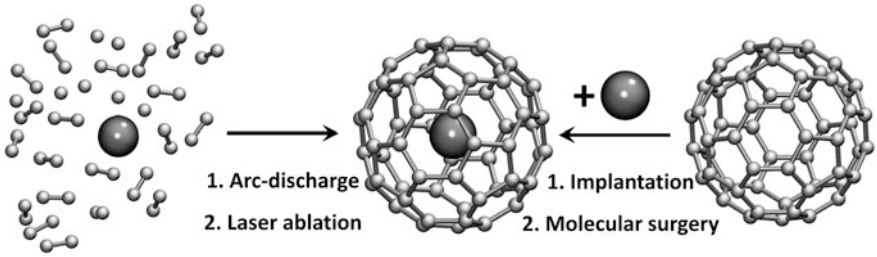

Fig. 1.2 Different approaches to synthesize endohedral fullerenes. (i) Encapsulation during the fullerene formation, such as in laser ablation or arc-discharge methods; main method for endohedral metallofullerenes. (ii) Encapsulation into already available empty fullerene; typical variants are implantation (through ion beam or high pressure-high temperature treatment) and molecular surgery (encapsulation is achieved in a series of chemical reactions "opening" and then "closing" the carbon cage); these approaches are applied for the synthesis of non-metal and alkali-metal endohedral fullerenes

units (which are the main species in the hot carbon plasma) can be also trapped inside the fullerene cages during the EMF formation, resulting in the so-called carbide clusterfullerenes. The first molecular structure of such EMF, $Sc_2C_2@C_{84}$, was elucidated in 2001 [12], when detailed structural characterization of EMF molecule became possible. Inability of mass-spectrometry to distinguish whether carbon atoms are encapsulated inside the fullerene cage or are a part of it resulted in a significant delay of the discovery of carbide clusterfullerenes. In fact, many carbide clusterfullerenes were available from the very first studies of EMFs, but were erroneously interpreted as di- and tri-EMFs.

In 1999 it was discovered that the presence of small amount of nitrogen gas in the arc-discharge generator afforded $Sc_3N@C_{80}$, a new type of EMFs with trimetal nitride clusters [13]. The use of NH_3 reactive gas instead of molecular nitrogen allowed much higher selectivity in the synthesis of nitride clusterfullerenes as the yield of empty fullerenes in such conditions was reduced dramatically [14]. Similar effect could be achieved by the use of solid organic sources of nitrogen (such as guanidium thiocyanate or melamine) [15–17]. Discovery of nitride clusterfullerenes triggered exhaustive studies of other clusterfullerenes. Modification of the EMF synthesis by using either reactive gas (NH_3, CH_4, SO_2, CO_2, H_2) or solid chemicals added to the graphite electrodes allowed the synthesis of new types of EMFs with endohedral sulfur, oxygen, CH, CN, and other units, whose structures are discussed below [18–27].

Usually, the arc-discharge synthesis produces simultaneously many different EMF structures as well as empty fullerenes, which are then extracted from the soot by organic solvents (EMFs as well as empty fullerene have reasonable solubility in CS_2, toluene, dichlorobenzene, other substituted benzenes, etc). The use of hydrogen-containing reactive gasses (NH_3, CH_4) or solid organic compounds dramatically reduces the yield of empty fullerenes, which substantially simplifies separation procedures; in certain cases, high selectivity for target EMFs can be

achieved [23, 28]. However, extended chromatographic procedures, such as high-performance liquid chromatography (HPLC) and recycling HPLC, are often required to separate EMFs from empty fullerenes and from each other to obtain them in compositionally and isomerically pure forms. Figure 1.3 demonstrates and example of such separation. Arc-discharge synthesis of mixed Lu–Sc system with NH_3 as a source of nitrogen produces mainly a mixture of $Lu_xSc_{3-x}N@C_{2n}$ nitride clusterfullerenes ($2n$ = 78–88) with small amounts of C_{60} and C_{70}; the most abundant are EMFs with C_{80}-I_h and C_{80}-D_{5h} carbon cages (Fig. 1.3a). The fraction eluting at 18.5–20 min (marked "A" in Fig. 1.3a) is a mixture of three EMFs with C_{68} cage: $Sc_3N@C_{68}$, $LuSc_2N@C_{68}$, and $Lu_2ScN@C_{68}$. This fraction is then subjected to recycling HPLC separation as shown in Fig. 1.3b, which eventually gives pure individual components as verified by mass-spectrometry (Fig. 1.3c).

The need for extended chromatographic separation is one of the main bottlenecks on the way to the broader availability of EMFs, and several non-chromatographic procedures based on the variation of redox and chemical properties of different EMFs were developed to circumvent this problem [29–35]. The methods based on redox properties of EMFs will be discussed in Chap. 3.

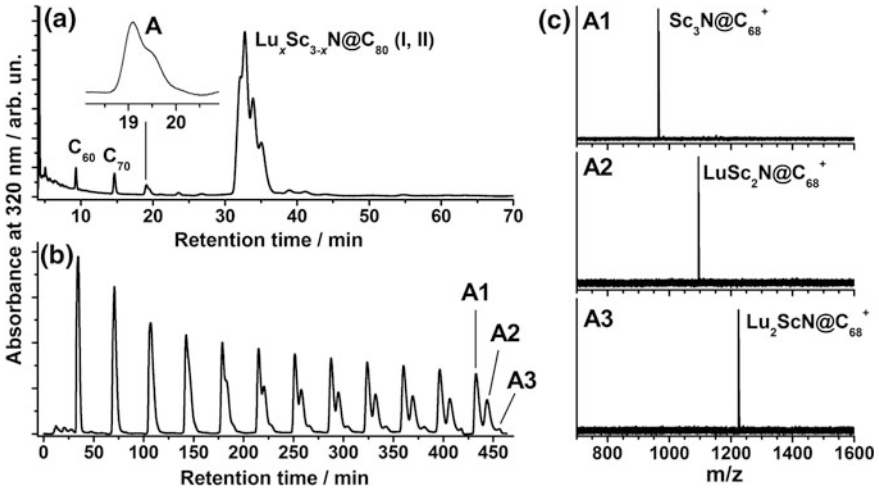

Fig. 1.3 An example of chromatographic separation of the mixed-metal nitride clusterfullerene mixture: **a** HLPC curve of the raw $Lu_xSc_{3-x}N@C_{2n}$ mixture (x = 0–3, $2n$ = 68–88) extracted from the soot, which was obtained by arc-discharge synthesis with NH_3 as reactive gas (note the small amount of C_{60} and C_{70} in comparison to EMFs). Fraction *A* collected at 18.5–20.5 min is then subjected to recycling HPLC separation shown in **b**. After 11 cycles, three components of the fraction can be separated. **c** Laser-desorption ionization mass spectrometry shows that *A1* is $Sc_3N@C_{68}$, *A2* is $LuSc_2N@C_{68}$, and *A3* is $Lu_2ScN@C_{68}$. Based on the data from [36]

1.3 Metals Forming Endohedral Metallofullerenes

Fullerenes are good electron acceptors, so metal atoms inside fullerenes transfer their valence electrons to the carbon cage forming thus non-dissociative "salts" such as $La^{3+}@C_{82}{}^{3-}$. Certainly, the ease of ionization of metal ions and stability of negatively charged carbon cages play important role in the EMF formation. Figure 1.1 shows the periodic table of elements and highlights the elements which are able to form EMFs.

Encapsulation of alkali metals within the carbon cage can be achieved either by the laser ablation [9] or by exposing thin films of fullerenes to the high-energy M^+-ion beams [10, 37]. Both methods produce mainly $M@C_{60}$, but the yield is rather low. Bulk amounts are obtained so far only for $Li@C_{60}$ [38], which can be stabilized in the form of cationic salts such as $[Li^+@C_{60}]SbCl_6^-$ [11]. Among the alkali earth metals, Be and Mg are not forming EMFs, whereas Ca, Sr, and Ba afford monometallofullerenes $M@C_{2n}$ in the arc-discharge synthesis with broad range of carbon cage sizes [39–41]. Divalent lanthanides (Sm, Eu, Tm, Yb) behave similarly to alkali earth in terms of the broad variety of the monometallofullerenes they form in the arc-discharge synthesis [42–45]. For Sm–EMFs, a series of dimetallofullerenes $Sm_2@C_{2n}$ [46, 47] and even a trimetallofullerene $Sm_3@C_{80}$ have been also characterized [48]. Neither alkali, nor alkali earth or divalent rare earth metals are known to form clusterfullerenes.

The group III elements Sc, Y, and La, as well as trivalent lanthanides are the most versatile metals in the EMF field as they afford a broad range of different types of EMFs, from mono- and dimetallofullerenes to a variety of clusterfullerenes [18–20]. Their structures will be discussed in more details further below.

In the group IV, formation of EMFs was achieved for Ti, Zr, and Hf. Laser ablation gives monometallofullerenes $M@C_{2n}$ ($2n$ = 26–46) with the most abundant species at $2n$ = 28 and 44 [49, 50]. Bulk amounts of these small-cage monometallofullerenes are not available. Arc-discharge synthesis of Ti-EMFs yields several structures with one and two Ti atoms within one cage, mainly $Ti@C_{88}$, $Ti@C_{90}$, Ti_2C_{80}, and Ti_2C_{84} [51, 52]. Ti_2C_{80} was found to be a carbide clusterfullerene $Ti_2C_2@C_{78}$ [53, 54], while molecular structures of other Ti–EMFs are not known yet. Ti has been also encapsulated in EMFs in the form of several types of clusterfullerenes, including aforementioned $Ti_2C_2@C_{78}$, sulfide $Ti_2S@C_{78}$ [55], mixed-metal nitride clusterfullerenes $TiM_2N@C_{80}$ (M = Sc and Y; Ti alone cannot form nitride clusterfullerenes) [56, 57], and two types of mixed-metal carbide clusterfullerenes, $TiM_2C@C_{80}$ and $TiM_2C_2@C_{80}$ (M = Sc, Y, Nd, Gd, Dy, Er, Lu) [23, 58, 59], which can be synthesized with high selectivity when methane is added to the arc-discharge reactor atmosphere. The information on the arc-discharge synthesis of Zr and Hf–EMFs is rather scarce. Both metals were found to form small amounts of EMFs [60]. $Hf@C_{84}$ and Hf_2C_{80} were isolated and studied spectroscopically, but their molecular structures were not elucidated [61].

Group V transition metals are not forming EMFs in laser ablation experiments [9]. The first successful synthesis of vanadium EMFs, mixed-metal nitride

clusterfullerenes $VSc_2N@I_h$-C_{80} and $V_2ScN@I_h$-C_{80}, was accomplished in 2015 [62]. It remains to be seen if nitride clusterfullerenes can be obtained with other group V transition metals. Inconclusive data on the possible formation of EMFs in the arc-discharge process are obtained on Nb [60] and Ge [63]. Laser ablation studies showed that Ga and In are forming monometallofullerenes with the structure distribution similar to that of alkali metals [9]. Other transition metals are not known to form EMFs.

Very limited availability of actinides precludes detailed studies of their EMFs. Formation of EMFs with Ac, Th, Pa, U, Np, and Am in the arc-discharge process was detected by radiochromatographic method [64–67]. By their retention behavior, the actinide-EMF were classified into two groups: Ac, U, Pu, Np, and Am are similar to the trivalent lanthanide analogs, whereas Th and Pa are substantially different. The amounts sufficient for spectroscopic characterization were obtained for $U@C_{82}$ and $Th@C_{84}$ [65]. In the laser ablation studies, uranium produces series of monometallofullerenes with the largest abundance of $U@C_{28}$ and $U_2@C_{60}$ [49], whereas Th gives a series of monometallofullerenes with the maxima at $Th@C_{36}$ and $Th@C_{44}$ [9].

1.4 Synthesis of Non-metal Endohedral Fullerenes

Synthesis of nMEFs starts with a corresponding empty fullerene (for this reason, nMEFs are mainly synthesized with the most abundant C_{60} and C_{70}). We will distinguish two approaches for the nMEF formation: implantation and molecular surgery. By "implantation" we imply all methods based on penetration of atoms through the wall of carbon cages under the impact of high-energy treatment. On the contrary, "molecular surgery" implies opening of the fullerene cage with a series of organic reaction, insertion of the species though the orifice, and then (optionally) closing the cage.

The first implantation of non-metal atoms within fullerene has been achieved in 1991 by high-energy ion-molecular collisions of C_{60}^+ or C_{70}^+ with He atoms [3, 68]. Ne [69, 70], and Ar [71] as well as alkali metals [72] have been also encapsulated in analogous experiments. Formation of nMEFs in these conditions was detected by mass-spectrometry. These experiments established the principal possibility of the implantation, but they were not suitable for the synthesis of bulk amounts of nMEFs.

In 1993 Saunders, Cross and their coworkers discovered that heating fullerene samples to 780–850 °C resulted in a release of small amounts of helium [73]. The authors hypothesized that He was trapped into fullerenes molecules during their formation in arc-discharge performed in He atmosphere. Based on the amount of released He, the degree of trapping was estimated as ca. one $He@C_{60}$ molecule for every 880,000 molecules of fullerene. More importantly, this work showed that He atoms can indeed penetrate through the wall of the carbon cage. In an attempt to reverse the process, the authors heated fullerene in several atmospheres of He, Ne,

Kr, or Xe and indeed found that these noble gasses can be encapsulated into C_{60}, although with quite a low yield [73, 74]. In a subsequent work, the pressure of helium was increased to 2500–3000 atm, which resulted in ca 0.1% yield of $He@C_{60}$ and $He@C_{70}$ [75]. This high pressure-high temperature conditions have been also applied for the synthesis of endohedral fullerenes with all other noble gasses. Although the yield was still rather modest, it was sufficient for unambiguous mass-spectroscopic characterization of such nMEFs as well the use of ^{3}He NMR spectroscopy for the study of He-containing fullerenes and their derivatives [76, 77]. Further enrichment of the samples was accomplished with the use of chromatographic approaches enabling spectroscopic and even structural studies of $Ar@C_{60}$ [78], $Kr@C_{60}$ [79, 80], and $Xe@C_{60}$ [81]. High pressure-high temperature method also resulted in smaller amounts of nMEFs with diatomic encapsulated species $He_2@C_{2n}$, $Ne_2@C_{2n,}$ $HeNe@C_{70}$, $N_2@C_{60,70}$, and $^{13}CO@C_{60}$ [82–85].

An original modification of high pressure-high temperature method for a synthesis of $He@C_{60}$ and $He_2@C_{60}$ with appreciable yields was proposed by Peng, Wang et al. [86]. C_{60} was placed into reaction vessel containing explosive cyclotetramethylenetetranitramine and 6 atm. of He; explosive was separated from C_{60}/He by a "flying" steel plate to reduce destruction of fullerenes. Detonation of explosive material pushed the flying plate to compress helium, which attained sufficient kinetic energy to penetrate the walls of C_{60} cage (with concomitant destruction of ca 60% of them). After the procedure, mass-spectrum of the soluble part showed the presence of $He@C_{60}$, whereas multistep HPLC separation allowed purification of $He_2@C_{60}$. Separation of $He@C_{60}$ from C_{60} by HPLC was proved impossible.

Another well-established method of synthesis of mono-atomic nMEFs is ion implantation. The method was first reported by Weidinger et al. for the synthesis of $N@C_{60}$: bombardment of C_{60} film with nitrogen ions from a plasma discharge ion source carried out in a vacuum of 10^{-5} mbar gave $N@C_{60}$ with the yield of 10^{-5} to 10^{-4}% [85, 87]. The procedure also results in the formation of $N_2@C_{60}$ [87]. Although the yield of $N@C_{60}$ is low, the concentration of $N@C_{60}$ is already sufficient for its detection by EPR spectroscopy [88]. Further enrichment of the samples by HPLC is then possible, although separation factors are rather small and hence many separation steps are necessary [87, 89, 90]. $N@C_{70}$, $N_2@C_{70}$, and $P@C_{60}$ were also synthesized by ion implantation method [91–93]. Synthesis and separation of $N@C_{60}$ are described in detail in Chap. 13.

Molecular surgery of fullerenes was developed as an alternative approach for the synthesis of nMEFs as opposed to high-energy impact methods. A series of controlled chemical reactions is applied to create an orifice in the fullerene cage, different molecular species are then enclosed inside such "opened" fullerene, and the orifice is then "closed" in another series of reactions. The full cycle of opening the cage, placing a molecule inside, and then closing a cage was first accomplished in 2005 by Komatsu et al. [94] in the synthesis of $H_2@C_{60}$. After that, syntheses of $He@C_{60,70}$ [95], $(H_2)_{1,2}@C_{70}$ [96], $H_2O@C_{60}$ [97], $(H_2O)_{1,2}@C_{70}$ [98], $H_2O@C_{59}N$, and $H_2@C_{59}N$ [99] were reported. Besides, numerous procedures for making an orifice in the fullerene cage were developed before 2005 and continued

to be developed afterwards [100–102]. A broad range of molecular species was encapsulated within such open-cage fullerenes, including H_2 [103], H_2O [104], HF [105], HCN [106], N_2 [107], CO [108], CO_2 [109], NH_3 [110], CH_4 [111], and CH_2O [106]. Encapsulation usually requires high pressure and is often reversible.

Combination of molecular surgery for encapsulation of He with ion bombardment for encapsulation of N was used in 2013 for the synthesis of $HeN@C_{60,70}$ and the study of the mutual influence of encapsulated atoms [112].

1.5 Molecular Structures of Endohedral Fullerenes

1.5.1 Molecular Structure Determination

Single-crystal X-ray diffraction. Molecular structure elucidation of endohedral fullerenes is not very straightforward. One should be able to determine the carbon cage isomer, the structure of the internal species (when it is more complex than a single atom or ion), and location of the endohedral species with respect to the fullerene cage (center or off-center position, coordination to a particular cage fragment, etc). Theoretically, single-crystal X-ray diffraction should be able to address all these issues. However, the method meets sever difficulties in the studies of fullerenes because of the rotational disorder of the fullerene molecules in their crystals, which usually precludes direct determination of the carbon cage structures. Furthermore, endohedral species often have several possible positions inside the carbon cage, which makes disorder problem even more complicated for EMFs. It is not then surprising that the progress in the crystallographic studies of EMFs during the first decade (between 1990 and 2000) was very modest. In 2000s, the strategies were developed to circumvent the disorder problem, which are either based on co-crystallization (particularly successful and commonly used co-crystallizing agents are Ni- or Co-octaethylporphyrines [113, 114], Ni · OEP and Co · OEP hereafter) or include exohedral chemical derivatization of the EMF [115, 116]. Both approaches hinder rotation of EMF molecules in their crystals and often (but not always) reduce disorder in the positions of endohedral species thus enabling determination of atomic coordinates. With the use of these approaches, molecular structures of dozens of EMFs were elucidated by single-crystal X-ray diffraction. X-ray structure elucidation is especially important for clusterfullerenes, since alternative approaches such as NMR spectroscopy are not able to determine geometry of the endohedral cluster. Figure 1.4 shows two examples of EMFs co-crystallized with Ni · OEP: clusterfullerene $CeLu_2N@C_{80}$-I_h [117] and monometallofullerenes $Sm@C_{90}$-C_{2v}(46) [118]. For the former, the study successfully determined pyramidal structure of the $CeLu_2N$ cluster despite residual disorder (Fig. 1.4a). The structure of $Sm@C_{90}$ (Fig. 1.4b, c) with multiple Sm positions illustrates that the problem of disorder remains for many EMFs (especially

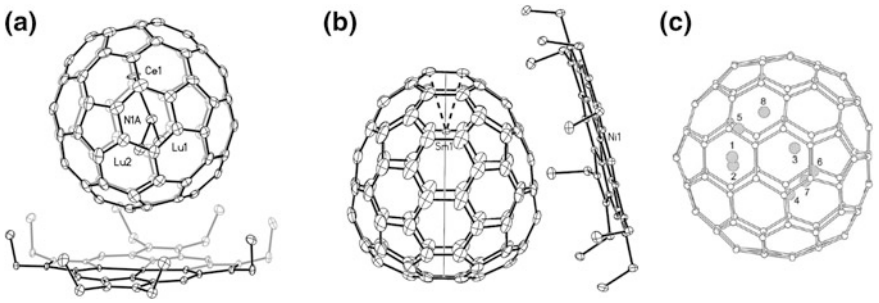

Fig. 1.4 Single-crystal X-ray diffraction studies of endohedral metallofullerenes. **a** $CeLu_2N@C_{80} \cdot Ni(OEP) \cdot 2C_7H_8$ with 50% thermal ellipsoids; solvent molecules and hydrogens are omitted, only major location of $CeLu_2$ with 0.65 fractional occupancy is shown; the cluster is pyramidal with nitrogen positions above and below the $CeLu_2$ plane (only one nitrogen is shown). Reproduced with permission from [117]. **b** $Sm@C_{90}$-$C_{2v}(46) \cdot Ni(OEP) \cdot 2C_7H_8$ with 30% thermal ellipsoids, solvent molecules are omitted, only the major sites for the fullerene at 0.88 fractional occupancy and the samarium atom with 0.58 fractional occupancy are shown. **c** Location of eight partially occupied sites for the samarium atom in $Sm@C_{90}$-$C_{2v}(46)$ (fractional occupancies are 0.58, 0.11, 0.08, 0.09, 0.06, 0.03, 0.03, and 0.02). **b** and **c** are reproduced with permission from [118]

monometallofullerenes) and such disorder usually indicates that metal atoms circulate inside the carbon cage.

Crystallographic studies of non-metal endohedral fullerenes are not as abundant as those for EMFs. One of the reasons is that the carbon cage in nMEFs is usually well known, hence the molecular structure is less ambiguous even when not determined by single-crystal X-ray diffraction. Another reason was low yield of nMEFs obtained by implantation techniques and difficulties of their separation. The first successful single-crystal study of nMEF was performed with the sample containing 9% of $Kr@C_{60}$ and showed that the Kr atom resides in the center of C_{60} [80]. With the development of molecular surgery approach after 2005 [94], pure nMEFs became available in sufficient amounts, and their crystallographic studies became possible [97, 98, 112]. Figure 1.5 shows molecular structures of $He@C_{60}$ and $H_2O@C_{70}$ determined for their co-crystals with Ni · OEP. Note that in both molecules endohedral species are located in the center of the fullerene cage as opposed to the off-center positions of metal atoms in EMFs.

Nuclear Magnetic Resonance. Nuclear magnetic resonance is another popular method in the structural studies of endohedral fullerenes. In particular, ^{13}C NMR is often applied to address the structure of the fullerene cage. Figure 1.6 shows an illustrative example of the structure elucidation of EMF by ^{13}C NMR. As many other carbide clusterfullerenes, $Sc_2C_2@C_{82}$ was first believed to be dimetallofullerene $Sc_2@C_{84}$. However, ^{13}C NMR study of the molecule showed that the fullerene cage signals correspond to 82 carbons, and their intensity ratio points to C_{3v} symmetry [119]. Furthermore, a signal corresponding to two more carbon atoms (assigned to the endohedral acetylide unit) was been detected at much lower

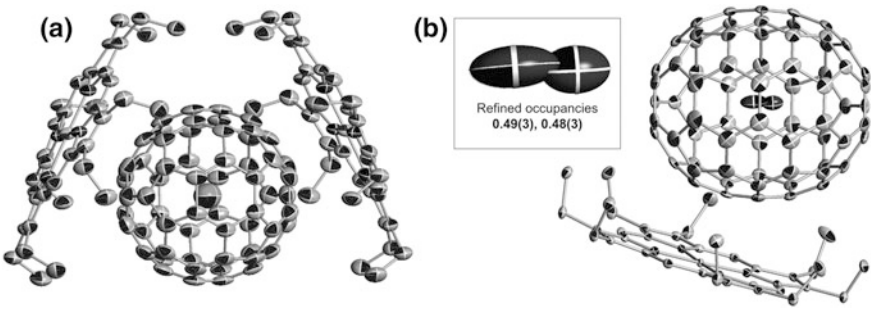

Fig. 1.5 Single-crystal X-ray diffraction studies of non-metal endohedral fullerenes. **a** $He@C_{60} \cdot 2Ni \cdot OEP$ with 50% thermal ellipsoids, hydrogen atoms are omitted for clarity; reproduced with permission from [112]. **b** $H_2O@C_{70} \cdot Ni \cdot OEP$ with 50% thermal ellipsoids, hydrogen atoms and solvent molecules are omitted; encapsulated H_2O molecule is disordered between two positions with refined occupancies of 0.49(3) and 0.48(3). Reproduced with permission from [98]

field (253.3 ppm) than the signals of cage carbons. Finally, connectivity pattern determined in INADEQUATE NMR study provided compelling evidence of the C_{82}-C_{3v}(8) isomer [120]. Such exhaustive ^{13}C NMR studies of EMFs are still rather rare and require appreciable amounts of ^{13}C-enriched samples and long acquisition times. So, only few INADEQUATE NMR studies of EMFs have been reported to date. Elucidation of the carbon cage symmetry by 1D ^{13}C NMR is much more common. For highly symmetric cages (such as icosahedral C_{80}-I_h with only two carbon signals) this information can be sufficient for an unambiguous structure elucidation. For low-symmetric cages, many isomers of given symmetry may exist, and additional data (such as provided by quantum-chemical calculations or by other spectroscopic techniques) is necessary to sort out the isomers.

^{13}C NMR studies of those paramagnetic EMFs, whose paramagnetism is caused by the odd number of electron transferred to the carbon cage, can be studied in their ionic forms obtained by electrolysis. For example, C_{2v} symmetry of the carbon cage in paramagnetic $La@C_{82}$ was first determined by the study of its diamagnetic anion [121, 122]. Paramagnetic ^{13}C NMR studies of lanthanide-based (especially Ce) EMFs were found to be useful for the determination of the position of metal atoms and their dynamics [123–125], as will be discussed in Chap. 10.

The structure of the endohedral species cannot be directly elucidated from NMR data. Still, multinuclear NMR techniques, such as ^{3}Li [11], ^{89}Y [126], ^{14}N [127, 128], ^{139}La [129, 130], and especially ^{45}Sc [130–134], can provide a detailed information on the dynamics of the clusters. For instance, detection of two distinct signals in ^{45}Sc NMR spectra of $Sc_3NC@C_{80}$ and $Sc_4O_2@C_{80}$ proves that the clusters are not symmetric and rather rigid (the averaging of signals is not happening).

NMR spectroscopy is also an important tool for nMEFs. Although carbon cage isomerism for these molecules is not in question, ^{13}C NMR studies still provide

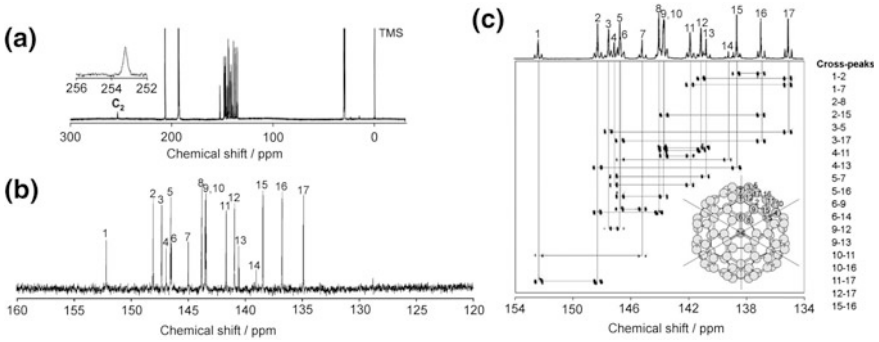

Fig. 1.6 ^{13}C NMR spectroscopic study of $Sc_2C_2@C_{82}$-$C_{3v}(8)$. **a** overall spectrum of ^{13}C-enriched sample, note the peak at 253.2 ppm due to the endohedral C_2 unit, which is reliable detected only for ^{13}C-enriched sample; **b** ^{13}C NMR spectrum in the range of fullerene cage carbons (intensity distribution $\{1 \times 1,\ 5 \times 3,\ 11 \times 6\}$ corresponds to the C_{82}-$C_{3v}(8)$ cage isomer); **c** INADEQUATE NMR spectrum of ^{13}C-enriched sample, all 19 cross-correlation peaks expected for C_{82}-$C_{3v}(8)$ cage are observed. **a** and **c** are reproduced with permission from [120], **b** is reproduced with permission from [119]

information on the interaction between the internal species and the fullerene. Encapsulated species in nMEFs often include magnetic nuclei (^{1}H, ^{3}He, ^{129}Xe), and hence the studies of magnetic resonance on these nuclei may give a valuable information about nMEFs. ^{3}He NMR spectroscopy has been especially common because chemical shift of ^{3}He strongly depends on the fullerene cage (Fig. 1.7) and is very sensitive to the chemical modification of the latter.

Optical spectroscopic studies. Optical spectroscopic techniques, such as UV-Vis-NIR, FTIR, or Raman spectroscopy, can also help in the structure elucidation of endohedral fullerenes. Although these methods do not provide structural information directly, similarity of the spectral patterns of different EMFs may indicate that these molecules have the same carbon cage isomer in the same formal charge state. For example, Fig. 1.8a shows that Vis-NIR absorption spectra of a series of Sc-EMFs with C_{82} cage ($Sc_2@C_{82}$, $Sc_2C_2@C_{82}$, and $Sc_2S@C_{82}$) are virtually identical. Since absorption spectra in this energy range are dominated by π–π^* excitations of the fullerene, one can conclude that all these molecules share the same C_{82}-$C_{3v}(8)$ cage isomer. Likewise, very similar spectra are also measured for $Lu_2@C_{82}$, $Er_2@C_{82}$, and $Er_2S@C_{82}$ (Fig. 1.8b). On the other hand, the spectra of $Lu_2@C_{82}$, $Er_2@C_{82}$, and $Er_2S@C_{82}$ with $C_s(6)$ cage shown in Fig. 1.8c are again very similar within the group, but are very different from the spectra of EMFs with C_{82}-$C_{3v}(8)$ cage. Thus, absorption spectra do not depend on the encapsulated species but are determined solely by the cage isomer. Therefore, it is sufficient to know the structure for only one of the compounds in the series to make reliable conclusions on the carbon cage structure of the other compounds in the series with similar spectra. Vibrational IR and Raman spectra also exhibit similar sensitivity to the molecular structure of fullerenes [136]. In certain cases, combination of IR

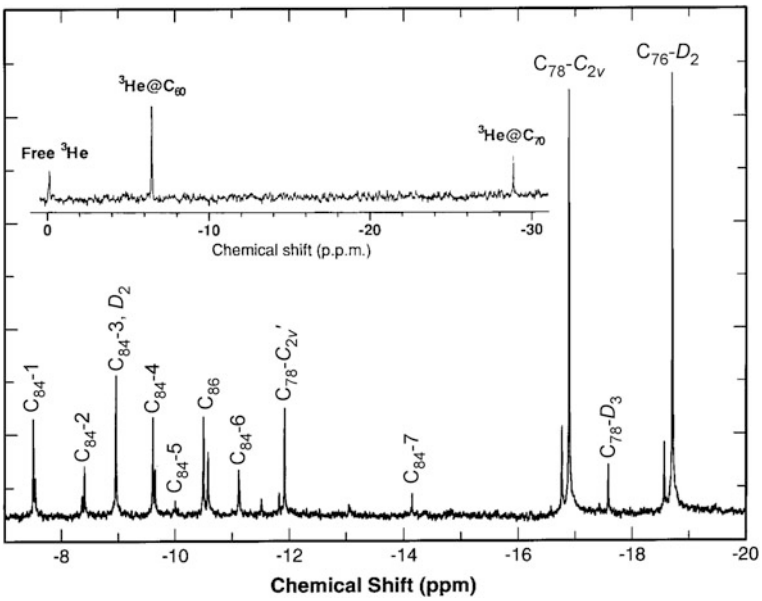

Fig. 1.7 ^{3}He NMR spectrum of the higher fullerene mixture (C_{76}, three isomer of C_{78}, and seven isomers of C_{84}, C_{86}) subjected to helium encapsulation; satellites are molecules with two encapsulated He atoms. Reproduced with permission from [135]. *Inset* shows ^{3}He NMR of C_{60}/C_{70} mixture with encapsulated He; reproduced with permission from [75]

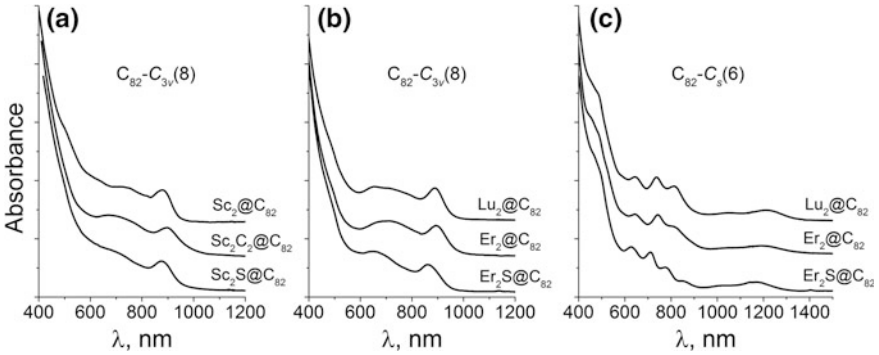

Fig. 1.8 UV-Vis-NIR absorption spectra of selected EMFs with C_{82} cage. **a** Three types of Sc-EMFs: dimetallofullerene, carbide clusterfullerene, and sulfide clusterfullerene, all with C_{82}-C_{3v}(8) cage; **b** lanthanide (Lu, Er) di-EMFs and sulfide clusterfullerenes with C_{82}-C_{3v}(8) cage; **c** same as (**b**), but with C_{82}-C_s(6) cage. Note close similarity of all spectra within the series with the same carbon cage in (**a**) and (**b**), and strong difference between the spectra of cage isomers in (**b**) and (**c**)

spectroscopy and DFT calculations of molecular structures and vibrational spectra allowed reliable structure elucidation of EMFs [137, 138].

1.5.2 Types of Endohedral Metallofullerenes

Table 1.1 lists different classes of EMFs and metals which form them, formal charges of endohedral species, and the most abundant and typical fullerene cages for each class of EMFs. Representative examples of EMF molecules are shown in Figs. 1.9, 1.10 and 1.11. Cage isomers of fullerene are labeled by their symmetry and the number of the isomer in accordance with the spiral algorithm [139]. Usually, a short form of numbering system is used, in which only the isomers following the isolated pentagon rule (IPR) are numbered. However, a large number of the non-IPR isomers found for EMFs require the use of the extended notation, which includes all possible isomers for a given number of carbon atoms. In this chapter, we use a two-fold numbering system which is de facto employed in many publications: the short notation is retained for all IPR isomers (i.e., their numbers are usually below 1000), while the full notation is adopted for the non-IPR isomers [19, 136].

Mono-, di-, and trimetallofullerenes. Although La@C_{60} was the first EMF ever detected, the isolation of EMFs with C_{60} cage was proved to be difficult due to the low kinetic stability. The first attempts of the bulk synthesis showed that for trivalent metals (Sc, Y, and many lanthanides) the most abundant isolable monometallofullerenes have C_{82} cage. Its isomeric structure, C_{2v}(9), was proposed in the synchrotron X-ray diffraction studies of powder samples [140] and confirmed by ^{13}C NMR spectroscopic study of the La@C_{82} anion [141]. Position of the metal atom inside the carbon cage was a matter of numerous studies in 1990s when endohedral structure was still questioned by some researchers. The first unambiguous proof of the endohedral position of metal atoms was obtained in the synchrotron X-ray diffraction study of the Y@C_{82} powder samples [142]. Electron density distribution of Y@C_{82} determined from the diffraction data showed the maximum of the density at the interior of the C_{82} cage. Importantly, Y atom was found close to the wall of the fullerene cage rather than in its center. Non-central position of metal atoms is typical for all EMFs and is caused by strong bonding interaction between the metal ion and the carbon cage. More precise positon of metal atom inside the C_{82}-C_{2v}(9) cage shown in Fig. 1.9 was determined by single-crystal X-ray diffraction studies of M@C_{82} EMFs [143, 144]. M^{III}@C_{82} EMFs also have another, less abundant isomer with C_s(6) cage [121]. Akasaka and coworkers also found that many La@C_{2n} EMFs remain in the carbon soot during the standard extraction procedure. However, the use of 1,2,4-trichlorobenzene as extraction solvent promoted reaction with insoluble EMFs with formation of soluble La@C_{2n}($C_6H_3Cl_2$) monoadducts. Structural characterization of such adducts by single-crystal X-ray diffraction proved formation of La@C_{72}-C_2(10612), La@C_{74}-D_{3h}(1), La@C_{80}-C_{2v}(3), and La@C_{82}-C_{3v}(7) [145].

Table 1.1 Families of EMFs with their cluster composition, formal charge, most abundant carbon cages, and typical metals

Cluster	Formal charge	Main cage(s)	Other cages	Metals
M^{I}	1+	C_{60}-I_h(1)	C_{70}-D_{5h}(1)	Li
M^{II}	2+	C_{82}-C_2(5), C_{82}-C_s(6), C_{82}-C_{2v}(9)	C_{60}-I_h(1), C_{74}-D_{3h}(1), C_{80}-C_{2v}(3), C_{84}, C_{90}, C_{92}, C_{94}-C_{3v}(134), etc.	Ca, Sr, Ba, Sm, Eu, Tm, Yb
MCN	2+	C_{82}-C_2(5), C_{82}-C_s(6), C_{82}-C_{2v}(9)	C_{76}-C_{2v}(19138)	Y, Tb
M^{III}	3+	C_{82}-C_{2v}(9)	C_{82}-C_s(6), C_{60}-I_h(1), C_{72}-C_2(10612), C_{74}-D_{3h}(1), C_{80}-C_{2v}(3), C_{82}-C_{3v}(7)	Sc, Y, La, Ce, Pr, Nd, Gd, Tb, Dy, Ho, Er, Lu
M_2	4+	C_{82}-C_{3v}(8), C_{82}-C_s(6)	C_{76}-T_d(1), C_{82}-C_{2v}(9), C_{88}-D_2(35), C_{90}-C_1(21), C_{92}-D_3(85), C_{104}-D_{3d}(822)	Sc, Y, Er Lu, Tm, Sm
M_2C_2	4+	C_{82}-C_{3v}(8), C_{82}-C_s(6)	C_{82}-C_{2v}(9), C_{72}-C_s(10528), C_{80}-C_{2v}(5), C_{84}-D_{2d}(23), C_{84}-C_1(51383), C_{86}-C_{2v}(9), C_{92}-D_3(85), C_{100}-D_5(450), C_{102}-C_s(574), C_{104}-C_2(816)	Sc, Y, La, Gd, Tb, Dy, Er, Lu
M_2S	4+	C_{82}-C_{3v}(8), C_{82}-C_s(6)	C_{70}-C_s(7892), C_{72}-C_s(10528)	Sc, Y, Dy, Er
M_2O	4+	C_{82}-C_{3v}(8), C_{82}-C_s(6)	C_{70}-C_2(7892), C_{76}-T_d(1), C_{80}-C_{2v}(5)	Sc
M_2	5+	$C_{79}N$-[I_h]		Y, Gd, Tb
M_2	6+	C_{80}-I_h(7)	C_{66}-C_{2v}(4059), C_{80}-D_{5h}(7), C_{72}-D_2(10611), C_{76}-C_s(17490), C_{78}-D_{3h}(5), C_{80}-D_{5h}(6), C_{100}-D_5(450)	Sc, La, Ce, Pr
M_3	6+	C_{80}-I_h(7)	C_{74}-C_1(13771)	Sm, Y, Tb, Er
M_3N	6+	C_{80}-I_h(7)	C_{68}-D_3(6138), C_{70}-C_{2v}(7854), C_{78}-D_{3h}(5), C_{80}-D_{5h}(6), C_{82}-C_{2v}(9)	Sc
M_3N	6+	C_{80}-I_h(7)	C_{76}-C_s(17490), C_{78}-C_2(22010), C_{80}-D_{5h}(6), C_{80}-C_s(hept), C_{82}-C_s(39663), C_{84}-C_s(51365), C_{86}-D_3(19), C_{88}-D_2(35)	Sc-mixed, Y, La, Ce, Pr, Nd, Gd, Tb, Dy, Ho, Er, Tm, Lu
M_2TiN	6+	C_{80}-I_h(7)		Sc, Y
M_2TiC	6+	C_{80}-I_h(7)	C_{80}-D_{5h}(7)	Sc, Y, Nd, Gd, Dy, Er, Lu
M_2TiC_2	6+	C_{80}-I_h(7)	C_{80}-D_{5h}(7)	Sc, Y, Nd, Gd, Dy, Er, Lu
M_3CH	6+	C_{80}-I_h(7)		Sc
M_3C_2	6+	C_{80}-I_h(7)	C_{88}-D_2(35)	Sc, Lu
M_4C_2	6+	C_{80}-I_h(7)		Sc
M_4O_2	6+	C_{80}-I_h(7)		Sc
M_4O_3	6+	C_{80}-I_h(7)		Sc
M_3CN	6+	C_{80}-I_h(7)	C_{78}-C_2(22010)	Sc
M_3C_2CN	6+	C_{80}-I_h(7)		Sc

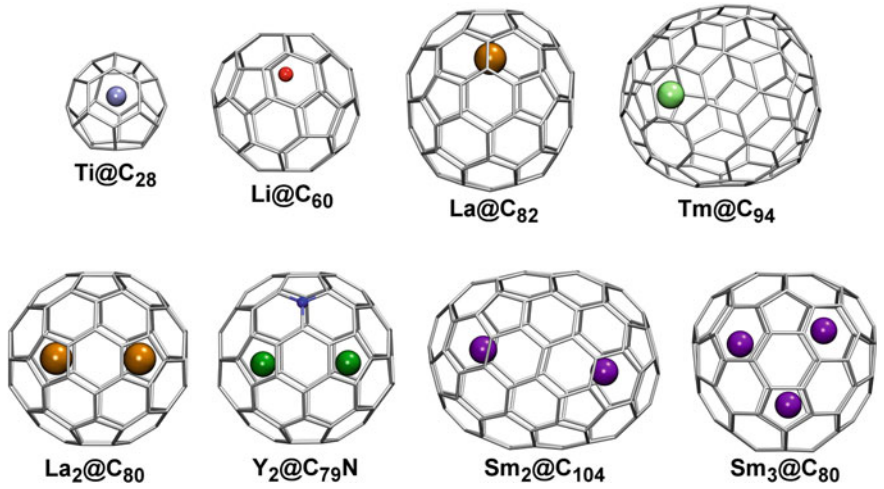

Fig. 1.9 Molecular structures of conventional endohedral metallofullerenes: monometallofullerenes (*upper row*) and di- and trimetallofullerenes (*bottom row*). Note that $Tm@C_{94}$ (and also $Sm@C_{94}$) and $Sm_2@C_{104}$ are the largest mono- and dimetallofullerenes characterized so far by single-crystal X-ray diffraction. Carbon cages are shown in *gray color*, metal atoms are colored, nitrogen atom in $Y_2@C_{79}N$ is *blue*

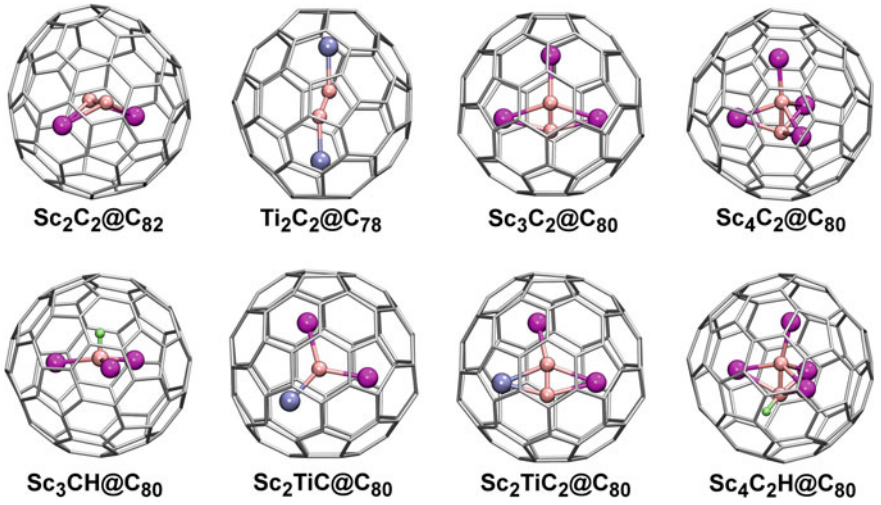

Fig. 1.10 Molecular structure of representative carbide clusterfullerenes. Carbon cages are shown in *gray*, Sc atoms are *magenta*, Ti atoms are *ice-blue*, internal carbons are *pink*, hydrogen is *light green*. The most typical are carbide clusterfullerenes with acetylide unit and two metal atoms ($M_2C_2@C_{2n}$, such as $Sc_2C_2@C_{82}$, with 2n from 72 to 104 and metals including Sc, Ti, Y, and lanthanides). $Sc_4C_2@C_{80}$, $Sc_3CH@C_{80}$, and $Sc_4C_2H@C_{80}$ are known only for Sc and for the C_{80} cage. $M_2TiC@C_{80}$ and $M_2TiC_2@C_{80}$ are available for Sc, Y, and medium-sized lanthanides. See Table 1.1 for further details

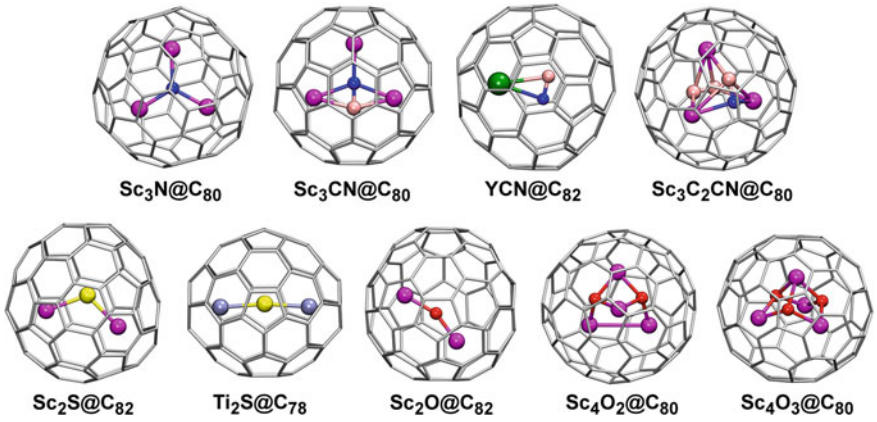

Fig. 1.11 Molecular structures of representative clusterfullerenes with endohedral heteroatoms (N, O, S). Nitride clusterfullerenes (represented here by $Sc_3N@C_{80}$) are the most versatile EMFs in terms of possible metals (Sc, Y, and lanthanides) and cage sizes (from C_{68} to C_{96} and even larger). $Sc_3C_2CN@C_{80}$, $Sc_4O_2@C_{80}$, and $Sc_4O_3@C_{80}$ are unique members in each class described so far only for Sc and for the C_{80} cage. See Table 1.1 for further details

Mono-EMFs with divalent metals are also dominated by $M^{II}@C_{82}$ species, but here four isomers with $C_2(5)$, $C_s(6)$, $C_{3v}(7)$, and $C_{2v}(9)$ are usually obtained in comparable yield [43, 146, 147]. Detailed studies were also reported for $M^{II}@C_{74}$ structures Isolated for Ca, Ba, Eu, Sm, and Yb [42, 148, 149]. ^{13}C NMR showed the fluxional motion of metal atoms between several equivalent positions within the symmetric C_{74}-$D_{3h}(1)$ carbon cage [150, 151]. Many $Yb@C_{2n}$ and especially $Sm@C_{2n}$ mono-EMFs with $2n = 74$, 80, 82 (4 isomers), 84 (3 isomers), 90 (4 isomers), 92 (2 isomers), and 94 (4 isomers) were isolated and partially structurally characterized [44, 118, 149, 152–158]. The largest characterized mono-EMF is $M@C_{94}$-$C_{3v}(134)$ with M = Ca, Tm, or Sm [155, 159]. Position of metal atom inside the fullerene cage in M^{II}-mono-EMFs is often not well defined, resulting in large disorder in X-ray determined structures (Fig. 1.4b).

Formation of dimetallofullerenes (di-EMFs) was discovered along with mono-EMFs in early 1990s, when $La_2@C_{80}$ and $Y_2@C_{82}$ were obtained [6, 160]. $La_2@C_{80}$ was shown to have icosahedral $I_h(7)$ cage with freely rotating La_2 cluster [129, 161]. Analogs di-EMFs structures were later described for Ce and Pr. In addition to $M_2@C_{80}$-$I_h(7)$, the family of di-EMFs based on early lanthanides (M = La, Ce, Pr) is represented by a number of cages, including C_{72}-$D_2(10611)$, C_{76}-$C_s(17490)$, C_{78}-$D_{3h}(5)$, and C_{80}-$D_{5h}(6)$ [123–125, 129, 162–164]. The largest structurally characterized M^{III}-di-EMF known so far is $La_2@C_{100}$-$D_5(450)$, while mass-spectrometry showed that di-EMFs up to $La_2@C_{138}$ were formed [165].

Sc, Y, and "late" lanthanides (Er, Lu) also form di-EMF, but with rather unusual bonding situation. Although these metals prefer a trivalent state in mono-EMFs, in di-EMFs they adopt a formal 2+ charge state with the metal-metal bond in the M_2 cluster [166]. The most abundant di-EMFs of this type are $M_2@C_{82}$-$C_{3v}(8)$

and $M_2@C_{82}$-C_s(6) [167–171]. Also known are $Er_2@C_{82}$-C_{2v}(9) [172] and $Lu_2@C_{76}$-T_d(1) [173]. At the same time, in $Sc_2@C_{66}$-C_{2v}(4059), the smallest isolated di-EMF, Sc is trivalent [174]. Among the truly divalent metals, di-EMFs are described so far for only for Sm (a series of di-EMFs, including $Sm_2@C_{88}$-D_2(35), $Sm_2@C_{90}$-C_2(21), $Sm_2@C_{92}$-D_3(85), and $Sm_2@C_{104}$-D_{3d}(822)) [46, 47, 175].

A special group of di-EMFs to be mentioned are paramagnetic azafullerenes $M_2@C_{79}N$ (M = Y, Tb, Gd) described first by Dorn a coworkers [176, 177]. The carbon cage in these EMFs is quasi C_{80}-I_h(7) with one of the carbon atoms substituted by nitrogen. Two metal atoms form a single-electron bond and both have large spin population.

Genuine trimetallofullerenes are very rare. Possible formation of $M_3@C_{80}$ species for Er, Tb, and Y was shown by mass-spectrometry without further structure elucidation. The only unambiguously characterized trimetallofullerene is $Sm_3@C_{80}$-I_h(7), whose structure was elucidated by single-crystal X-ray diffraction [48].

Although EMFs can comprise up to four metal atoms, the large number of metal atoms can be achieved only in the form of the clusters with non-metals described below. Endohedral metal atoms transfer their valence electrons to the carbon cage and bear significant positive charges, which results in strong Coulomb repulsion when two or more metals are encapsulated inside one carbon cage. The large number of metal atoms in EMFs can be easier achieved in clusters with electronegative with non-metals: the latter bear a negative charge (the formal charge of nitrogen in nitride clusterfullerenes is −3; oxygen, sulfur, and acetylide unit C_2 all have a formal charge of −2) and hence partially compensate Coulomb repulsion between the metal atoms.

Clusterfullerenes with endohedral carbon. The clusterfullerenes with carbon atoms in the endohedral clusters is the most versatile family in terms of possible cluster compositions (Fig. 1.10) [178, 179]. In addition to its obvious role of forming the fullerene cage, carbon is also found in the core of several types of endohedral clusters.

Carbon vapor in conditions of the fullerene synthesis mainly consists of C_2 species, and formation of carbide clusterfullerenes with acetylide unit is believed to be a result of the C_2 trapping. The inability of conventional mass spectrometry to distinguish if C_2 unit is endohedral or is a part of the carbon cage bluffed the EMF researchers for two decades and still remains a problem when new EMF compositions are detected in mass spectra. The most common endohedral carbide clusters have M_2C_2 composition, where M is a trivalent metal (Sc, Y, lanthanides La, Gd, Tb, Dy, Ho, Er, Lu), and acetylide unit has a formal charge 2−, so that the total charge of the cluster is 4+. A special case is $Ti_2C_2@C_{78}$, in which Ti atoms are in the four-valent state and the charge of the cluster is 6+ [53]. The shape of the M_2C_2 cluster depends on the size of the carbon cage: in smaller cages, C_2 unit is perpendicular to the M···M axis, whereas in large cages more linear arrangement is possible [180–182]. Fullerene cages in structurally characterized $M_2C_2@C_{2n}$ molecules range from C_{72}-C_s(10528) [183] in $Sc_2C_2@C_{72}$ to C_{92}-D_3(85) [184] in $Gd_2C_2@C_{92}$ to C_{104}-C_2(816) in $La_2C_2@C_{104}$ [185].

The number of metal atoms in carbide clusterfullerenes with endohedral acetylide unit can be also three or four. Encapsulation of M_3C_2 clusters (two examples known so far, $Sc_3C_2@C_{80}$ [186] and $Lu_3C_2@C_{88}$ [187]) result in paramagnetic but rather stable EMF molecules. "Substitution" of one of the trivalent metals by Ti gives closed-shell structures, and $M_2TiC_2@C_{80}$ EMFs were described for Sc and medium-size lanthanides [23, 58].

The only acetylide clusterfullerene with four metal atoms known so far is $Sc_4C_2@C_{80}$ [188]. In Sc_4C_2, Sc atoms form a tetrahedron with one carbon atom in the center and one above the Sc_3 face; the C_2 unit in $Sc_4C_2@C_{80}$ adopts a formal charge of −6 [189]. Wang et al. [24] showed that endohedral C_2 unit can also bear a bonded hydrogen atom forming a paramagnetic $Sc_4C_2H@C_{80}$.

A single carbon atom can be a central atom in two types of endohedral clusters. In $Sc_3CH@C_{80}$, the central carbon atom is bonded by a hydrogen [22, 190], whereas in the $TiM_2C@C_{80}$ family (M = Sc, Y, Nd, Gd, Dy, Er, Lu) [23, 58, 59], the μ_3-carbido ligand forms a double bond with Ti atom. Small amounts of other cage sizes have been also reported (C_{78} for Sc_2TiC cluster and C_{82}-C_{88} for larger metals). Both types of clusterfullerenes with single carbon atoms exhibit a certain analogy to nitride clusterfullerenes $M_3N@C_{80}$. The difference in the valence of carbon and nitrogen is compensated here either by an additional hydrogen atom (C–H vs. N), or via encapsulation of the tetravalent metal and double bond formation (C=Ti vs. N–Sc). An EMF with presumable composition $Sc_4C@C_{80}$ was detected by mass-spectrometry and studied computationally [191], but it is still awaiting for a detailed structural characterization.

Nitride clusterfullerenes. In 1999 the molecular structure of the first isolated nitride clusterfullerene, $Sc_3N@C_{80}$-I_h(7), was determined by single-crystal X-ray diffraction and ^{13}C NMR spectroscopy [13]. The Sc atoms were found to form an equilateral triangle with nitrogen atom in the center of the planar cluster (Fig. 1.11). Eventually, nitride clusterfullerenes (NCFs) turned to be the most abundantly produced EMFs [192, 193], and $Sc_3N@C_{80}$-I_h(7) is the third most abundantly produced fullerene (after C_{60} and C_{70}). $Sc_3N@C_{80}$ also has another, less abundant isomer with D_{5h}(6) cage, whose structure was determined by ^{13}C NMR spectroscopy [194] and single-crystal X-ray study [195]. In addition to $Sc_3N@C_{80}$, the family of Sc-based NCFs includes less abundant $Sc_3N@C_{68}$, $Sc_3N@C_{70}$, $Sc_3N@C_{78}$, and $Sc_3N@C_{82}$. The non-IPR cage structure with D_3(6140) symmetry and three pairs of adjacent pentagons was first proposed for $Sc_3N@C_{68}$ in 2000 based on the ^{13}C NMR and computational data [196] and then confirmed in 2003 by single-crystal X-ray diffraction study [197]. $Sc_3N@C_{78}$-D_{3h}(5) was first isolated in 2001 and characterized by ^{13}C NMR and single-crystal X-ray diffraction [198]. The yield of $Sc_3N@C_{70}$ is almost 50 times lower than that of $Sc_3N@C_{68}$, and this NCF with the non-IPR C_{70}-C_{2v}(7854) cage was first isolated in 2007 and characterized by vibrational spectroscopy and DFT computations [138]. Due to its low kinetic stability, structural characterization of elusive $Sc_3N@C_{82}$-C_{2v}(9) was accomplished only in 2015 [199].

With the increase of the ionic radii of metals, the cage size distribution of $M_3N@C_{2n}$ clusterfullerenes is shifting to larger fullerenes. Yttrium and the

elements from the second half of the lanthanide row (Gd–Lu except for Yb) form isolable $M_3N@C_{2n}$ NCFs with $2n$ = 78–88 [126, 187, 200–206]. $M_3N@C_{80}$-I_h(7) is still the most abundant NCF for these metals. Other structurally characterized cage isomers are C_{78}-C_2(22010) [137, 207], C_{82}-C_s(39663) [208], C_{84}-C_s(51365) [203], C_{86}-D_3(19) [205], and C_{88}-D_2(35) [205].

For the first half of the lanthanide row (La, Ce, Pr, Nd), the distribution of the fullerene size shifts further to larger cages with the highest yield for $M_3N@C_{88}$ [209–211]. The relative yield of $M_3N@C_{96}$ is also gradually increasing with the increase of the ionic radius from Nd to La, so that the yield of $La_3N@C_{96}$ equals that of $La_3N@C_{88}$. Neither ^{13}C NMR spectroscopic nor crystallographic studies have been performed so far for any $M_3N@C_{2n}$ with $2n > 88$. C_{92}-T(86) and C_{96}-D_2(186) cage isomers were tentatively assigned based on computational studies [212–214].

Mixing "small" Sc and "larger" lanthanide metals in the M_3N cluster enables the tuning of the cluster size (from small Sc_3N via MSc_2N and M_2ScN to larger M_3N) and opens a possibility for carbon cages to adopt the cluster of the most suitable size [215]. Whereas the carbon cages smaller than C_{78} are not accessible for non-Sc NCFs, mixing Sc with lanthanide makes it possible: for instance $LuSc_2N@C_{68}$ and $Lu_2ScN@C_{68}$ can be formed in the mixed Lu–Sc system [36]. A drawback of the mixed-metal NCFs is that the separation of individual compounds often becomes more complicated as illustrated in Fig. 1.3 for a $Lu_xSc_{3-x}N@C_{68}$ mixture.

Cyano clusterfullerenes. Carbon and nitrogen at once can be encapsulated in the form of cyanide fragment coordinated either to three metal atoms ($Sc_3NC@C_{80}$ [134] and $Sc_3NC@C_{78}$ [216]) or to only one metal atom ($YNC@C_{82}$ [217], $TbNC@C_{82}$ [218, 219]). The formal charge of the Sc_3NC cluster is 6+ (hence formal charge of CN fragment is 3−), whereas YNC or TbNC are only twofold charged (the formal charge of CN is 1−). A combination of both acetylide and cyanide fragments in one EMF molecule, $Sc_3C_2CN@C_{80}$, was also described [220].

Oxide clusterfullerenes. Oxygen-containing endohedral clusterfullerenes were discovered in 2008. Arc-discharge synthesis in the presence of air and $Cu(NO_3)_2$ afforded formation of $Sc_4O_2@C_{80}$-I_h(7) and $Sc_4O_3@C_{80}$-I_h(7) [221]. Both molecules have Sc_4 tetrahedron, with two or three oxygen atoms located above the Sc_3 faces in the μ_3-fashion [221, 222] (Fig. 1.11). In $Sc_4O_2@C_{80}$ two Sc atoms are in the formal divalent state with the Sc–Sc bond, whereas in $Sc_4O_3@C_{80}$ all Sc atoms are in the 3+ oxidation state [133, 223]. The formal charge of both Sc_4O_2 and Sc_4O_3 clusters is 6+. Stevenson et al. also discovered $Sc_2O@C_{82}$-C_s(6) with bended Sc–O–Sc cluster [224]. Addition of CO_2 to the arc-discharge reactor atmosphere afforded the whole family of $Sc_2O@C_{2n}$ oxide clusterfullerenes ($2n$ = 70–94) [25]. From this family, $Sc_2O@C_{70}$-C_2(7892), $Sc_2O@C_{76}$-T_d(1), $Sc_2O@C_{80}$-C_{2v}(5), and $Sc_2O@C_{82}$-C_{3v}(8) were isolated and characterized by X-ray diffraction [225–228]. Stevenson et al. [229] also reported that the use of Y or Lu instead of Sc in the oxide clusterfullerene synthesis resulted in formation of $Y_2O@C_{2n}$ and $Lu_2O@C_{2n}$ structures ($2n$ = 80–92). Formation of $M_4O_2@C_{2n}$ or $M_4O_3@C_{2n}$ clusterfullerenes with large metals was not detected.

Sulfide clusterfullerenes. Sulfide clusterfullerenes were discovered in 2010 in the form of $M_2S@C_{82}$ molecules (M = Sc, Y, Dy, Lu) when guanidinium thiocyanate $C(NH_2)_3{\cdot}SCN$ was used for the synthesis of nitride clusterfullerenes. Their absorption spectra closely resembled those of $M_2C_2@C_{82}$-$C_{3v}(8)$ which indicated that isolated $M_2S@C_{82}$ molecules also had $C_{3v}(8)$ cage isomer. With the use of SO_2 as a reactive gas, Echegoyen et al. [26] synthesized a family of $Sc_2S@C_{2n}$ clusterfullerenes ($2n$ = 70–100) and $Ti_2S@C_{78}$-$D_{3h}(5)$ [55]. The structures of two isomers of $Sc_2S@C_{82}$ with $C_s(6)$ and $C_{3v}(8)$ cages as well as that of $Sc_2S@C_{72}$-$C_s(10528)$ were elucidated by single-crystal X-ray diffraction [230, 231]. The Sc_2S cluster in these molecules has bent structure with the Sc–S–Sc angles in the 97°–114°. Isolation and spectroscopic and electrochemical characterization was also reported for $Sc_2S@C_{70}$-$C_2(7892)$ [231]. The use of CH_4 as a reactive gas and metal sulfide as a source of metal and sulfur afforded selective synthesis of $C_{3v}(8)$ and $C_s(6)$ isomers of $Dy_2S@C_{82}$.

1.5.3 Carbon Cage Isomerism of EMFs

Overview of the most abundant fullerene cages in EMFs (Table 1.1) shows that few cages are repeatedly preferred for different types of clusterfullerenes. For instance, C_{82}-$C_{2v}(9)$ is preferred for M^{III} monometallofullerenes, some dimetallofullerenes and EMFs with M_2C_2, M_2S, and M_2O clusters are usually formed with the C_{82}-$C_{3v}(8)$ and C_{82}-$C_s(6)$ cages, whereas many other clusterfullerenes are predominantly obtained with the C_{80}-$I_h(7)$ cage. Computational studies showed that the cage isomerism of EMFs is largely determined by the formal charge of the fullerene, and that the lowest energy isomers for the same fullerene size are usually different in different charge states, e.g., whereas the most stable isomer of hollow C_{80} is $D_2(2)$, the most stable isomer of C_{80}^{6-} is $I_h(7)$ [232]; furthermore, C_{80}^{6-}-$I_h(7)$ has enhanced stability in comparison to many other cage sizes due to the very uniform spatial distribution of the pentagons [212, 233]. Thus, this cage is preferred for sixfold charged clusters such as $(M^{3+})_2$, $(M^{3+})_3N^{3-}$, $(Sc^{3+})_4(C_2)^{6-}$, etc. Likewise, C_{82}-$C_{3v}(8)$ is the most suitable cage for the fourfold charged clusters such as $(M^{2+})_2$, $(M^{3+})_2S^{2-}$, or $(M^{3+})_2(C_2)^{2-}$ [234]. Thus, the most suitable carbon cage isomers of EMFs can be reliably predicted by a broad search of empty fullerene isomers in a proper charge state [212].

Another important factor in determination of the cage isomerism of EMFs is commensurable size and shape of the endohedral cluster and the fullerene cage (the factor is described as "cage form factor"). A clear illustration to the importance of this factor is the evolution of the fullerene cage distribution for nitride clusterfullerenes with the increase of the metal size from Sc (Shannon ionic radius R^{3+} = 0.745 Å) to Y, Gd–Lu (R^{3+} = 0.86–0.94 Å) and further to La–Nd (R^{3+} = 0.98–1.03 Å). The increase of the M_3N cluster size increases the strain in $M_3N@C_{2n}$ molecules when larger and larger clusters are encapsulated in the given cage and hence shifts the distribution toward the larger cage sizes. The strain

experienced by the M_3N cluster can lead to the significant changes in its geometry: whereas nitride clusters are usually planar, the Gd_3N cluster is pyramidalized in the $Gd_3N@C_{80}$ molecule because of the limited space [235]. In larger cages (such as $Gd_3N@C_{86}$), the strain is reduced and the Gd_3N cluster is also planar [236]. Another illustrative example of the cluster size factor is isomerism of $M_3N@C_{78}$: whereas Sc_3N cluster is encapsulated in the C_{78}-D_{3h}(5) cage isomer, lanthanides form $M_3N@C_{78}$ molecule with the non-IPR C_{78}-C_2(22010) cage [137]. The reason is that the latter cage has a flattened shape and can easier accommodate large M_3N clusters, whereas the C_{78}-D_{3h}(5) isomer is more suitable for clusters of smaller size such as Sc_3N. Likewise, the absence of nitride clusterfullerenes and availability of dimetallofullerenes with C_{72} cage is also explained by this factor. The most stable C_{72}^{6-} isomer, D_2(10611), has elongated shape with two pentagon pairs on the poles. The cage of such a shape perfectly suits dimetallofullerenes, such as $La_2@C_{72}$, but cannot accommodate triangular M_3N cluster without dramatic distortion of the latter.

1.5.4 Endohedral Metallofullerenes with Non-conventional Fullerene Cages

Large formal charge and strong metal-cage interaction lead to a specific structural feature of EMFs, a violation of the isolated pentagon rule (IPR). According to IPR, in stable fullerenes isomers all pentagons should be surrounded by hexagons, while adjacency of pentagons is strongly destabilizing. This rule imposes a strict limitation on the possible isomers of empty fullerenes, but is often violated in EMFs (Fig. 1.12). In fact, experimental evidence of dozens of structurally characterized non-IPR EMFs shows that the isolated pentagon rule is not applicable for metallofullerenes, and all isomers should be considered on an equal basis. The possibility of the non-IPR EMFs was first anticipated by Kobayashi et al. [237] in computational studies of $Ca@C_{72}$ isomers, and the first experimental evidence was provided in 2000 by the synthesis of $Sc_2@C_{66}$ [238] and $Sc_3N@C_{68}$ [196]. Neither C_{66} nor C_{68} have IPR cage isomers, and therefore both EMFs are inevitably non-IPR ones. The most common non-IPR motif in EMFs is the adjacent pentagon pair (APP, also known as pentalene unit). Non-IPR EMFs known so far have from one to three APPs, depending on the number of metal atoms and the formal charge of the cage. Since pentalene units are stabilized by coordinating metal atoms, the number of APPs in a given non-IPR EMF molecule usually does not exceed the number of metal atoms. Metal atoms coordinate to the carbon cage near adjacent pentagons and hence stabilize otherwise destabilizing pentalene units (Fig. 1.12a). Furthermore, the number of APPs is usually decreasing with the increase of the cage size. For instance, among the non-IPR nitride clusterfullerenes, $Sc_3N@C_{68}$-D_3(6140) and $Sc_3N@C_{70}$-C_{2v}(7854) have 3 APPs, $DySc_2N@C_{76}$-C_s(17490) and $M_3N@C_{78}$-C_2(22010) have two APPs (M = Y, Dy, Gd), and $M_3N@C_{82}$-C_s(39663) and $M_3N@C_{84}$-C_s(51365) have one APP (M = Gd).

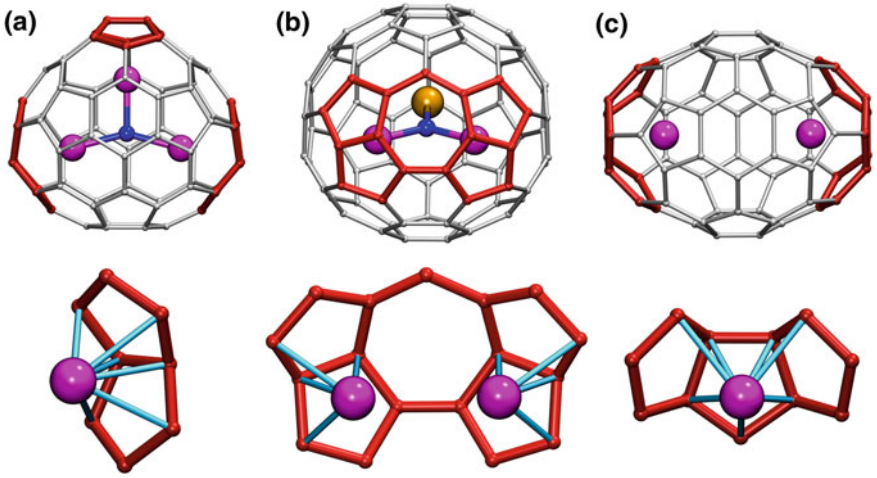

Fig. 1.12 Representative EMFs with non-conventional fullerene cages: **a** $Sc_3N@C_{70}$-C_{2v}(7854) with three pairs of adjacent *pentagons*; **b** $LaSc_2N@C_{80}$-C_s(hept) with one heptagon fused to two pairs of adjacent *pentagons*; **c** $Sc_2@C_{66}$-C_{2v}(4059) with two linear triquinanes (three fused pentagons). Carbon cages are shown in *gray* except for unconventional cage fragments shown in *red*; Sc atoms are *magenta*, La is *orange*, nitrogen is *blue*. The *bottom row* emphasizes how metal atoms are coordinated to unconventional cage fragments, *light blue lines* denote the shortest metal–carbon distances

Two other violations of the IPR in EMFs are presented by only few examples. The structure of $Sc_2@C_{66}$, one of the first non-IPR EMFs, was unambiguously elucidated only in 2014 and was found to have a C_{66}-C_{2v}(4059) cage with two unsaturated linear triquinanes (Fig. 1.12c), i.e., triply fused pentagons [174]. $LaSc_2N@C_{80}$-C_s(hept), the first EMF with one heptagon and 13 pentagons, was characterized in 2015 [239]. Its carbon cage has two pentalene units which are fused to the heptagon ring (Fig. 1.12b). Stabilization of the C_{80}-C_s(hept) cage by the $LaSc_2N$ cluster is another example of the effect of the cage form factor. DFT calculations showed that this isomer is rather unstable for C_{80}^{6-} and $Sc_3N@C_{80}$ (171/83 and 92/25 kJ/mol less stable than the most abundant $I_h(7)/D_{5h}(6)$ isomers, respectively), but with the increase of the cluster size the heptagon-containing isomer increases its relative stability and becomes 35–40 kJ/mol more stable than the $D_{5h}(6)$ isomer when Y_3N or $LaSc_2N$ clusters are encapsulated [239]. Similar stabilization of heptagon-containing isomers with large or non-symmetric clusters was also found for fullerenes of other sizes [240]. Recently, the second EMF with heptagon in the carbon cage, carbide clusterfullerene $Sc_2C_2@C_{88}$-C_s(hept), was reported by Echegoyen et al. [241].

1.6 Concluding Remarks

Since their discovery in 1985, endohedral fullerenes have come a long way from few molecules detectable only in mass spectra to a well-established class of compounds with a variety of well-defined molecular structures. The methods were developed to encapsulate various species within the carbon cage, from single atoms to complex hybrid clusters. Such variability enables the synthesis of molecules with distinct and sometimes unique electronic and magnetic properties, as will be described in the remaining chapters of this book.

References

1. Heath JR, O'Brien SC, Zhang Q et al (1985) Lanthanum complexes of spheroidal carbon shells. J Am Chem Soc 107(25):7779–7780
2. Cioslowski J, Fleischmann ED (1991) Endohedral complexes—atoms and ions inside the C_{60} Cage. J Chem Phys 94(5):3730–3734
3. Weiske T, Bohme DK, Hrusak J et al (1991) Endohedral cluster compounds—inclusion of helium within C_{60}^{+} and C_{70}^{+} through collision experiments. Angew Chem-Int Edit Engl 30 (7):884–886
4. Kratschmer W, Lamb LD, Fostiropoulos K et al (1990) Solid C_{60}—a new form of carbon. Nature 347(6291):354–358
5. Chai Y, Guo T, Jin CM et al (1991) Fullerenes with metals inside. J Phys Chem 95 (20):7564–7568
6. Alvarez MM, Gillan EG, Holczer K et al (1991) La_2C_{80}—a soluble dimetallofullerene. J Phys Chem 95(26):10561–10563
7. Johnson RD, Devries MS, Salem J et al (1992) Electron-paramagnetic resonance studies of lanthanum-containing C_{82}. Nature 355(6357):239–240
8. Dunk PW, Kaiser NK, Hendrickson CL et al (2012) Closed network growth of fullerenes. Nat Commun 3:855
9. Dunk PW, Mulet-Gas M, Nakanishi Y et al (2014) Bottom-up formation of endohedral mono-metallofullerenes is directed by charge transfer. Nat Commun 5:5844
10. Tellgmann R, Krawez N, Lin SH et al (1996) Endohedral fullerene production. Nature 382 (6590):407–408
11. Aoyagi S, Nishibori E, Sawa H et al (2010) A layered ionic crystal of polar $Li@C_{60}$ superatoms. Nat Chem 2(8):678–683
12. Wang CR, Kai T, Tomiyama T et al (2001) A scandium carbide endohedral metallofullerene: $(Sc_2C_2)@C_{84}$. Angew Chem-Int Edit 40(2):397–399
13. Stevenson S, Rice G, Glass T et al (1999) Small-bandgap endohedral metallofullerenes in high yield and purity. Nature 401(6748):55–57
14. Dunsch L, Krause M, Noack J et al (2004) Endohedral nitride cluster fullerenes - Formation and spectroscopic analysis of $L_{3-x}M_xN@C_{2n}$ ($0 \leq x \leq 3$; n = 39,40). J Phys Chem Solids 65(2–3):309–315
15. Liu F, Guan J, Wei T et al (2013) A series of inorganic solid nitrogen sources for the synthesis of metal nitride clusterfullerenes: the dependence of production yield on the oxidation state of nitrogen and counter ion. Inorg Chem 52(7):3814–3822
16. Yang S, Zhang L, Zhang W et al (2010) A facile route to metal nitride clusterfullerenes by using guanidinium salts: a selective organic solid as the nitrogen source. Chem-Eur J 16 (41):12398–12405

17. Svitova A, Braun K, Popov AA et al (2012) A platform for specific delivery of lanthanide-scandium mixed-metal cluster fullerenes into target cells. Chem Open 1(5):207–210
18. Yang S, Liu F, Chen C et al (2011) Fullerenes encaging metal clusters-clusterfullerenes. Chem Commun 47(43):11822–11839
19. Popov AA, Yang S, Dunsch L (2013) Endohedral fullerenes. Chem Rev 113(8):5989–6113
20. Lu X, Feng L, Akasaka T et al (2012) Current status and future developments of endohedral metallofullerenes. Chem Soc Rev 41(23):7723–7760
21. Stevenson S, Thompson MC, Coumbe HL et al (2007) Chemically adjusting plasma temperature, energy, and reactivity (CAPTEAR) method using NO_x and combustion for selective synthesis of $Sc_3N@C_{80}$ metallic nitride fullerenes. J Am Chem Soc 129(51): 16257–16262
22. Junghans K, Rosenkranz M, Popov AA (2016) $Sc_3CH@C_{80}$: selective ^{13}C enrichment of the central carbon atom. Chem Commun 52:6561–6564
23. Junghans K, Schlesier C, Kostanyan A et al (2015) Methane as a selectivity booster in the arc-discharge synthesis of endohedral fullerenes: selective synthesis of the single-molecule magnet $Dy_2TiC@C_{80}$ and its congener $Dy_2TiC_2@C_{80}$. Angew Chem-Int Edit Engl 54 (45):13411–13415
24. Feng Y, Wang T, Wu J et al (2014) Electron-spin excitation by implanting hydrogen into metallofullerene: the synthesis and spectroscopic characterization of $Sc_4C_2H@I_h$-C_{80}. Chem Commun 50(81):12166–12168
25. Zhang M, Hao Y, Li X et al (2014) Facile synthesis of an extensive family of $Sc_2O@C_{2n}$ (n = 35-47) and chemical insight into the smallest member of $Sc_2O@C_2(7892)$-C_{70}. J Phys Chem C 118(49):28883–28889
26. Chen N, Chaur MN, Moore C et al (2010) Synthesis of a new endohedral fullerene family, $Sc_2S@C_{2n}$ (n = 40-50) by the introduction of SO_2. Chem Commun 46(26):4818–4820
27. Dunsch L, Yang S, Zhang L et al (2010) Metal sulfide in a C_{82} fullerene cage: a new form of endohedral clusterfullerenes. J Am Chem Soc 132(15):5413–5421
28. Yang SF, Kalbac M, Popov A et al (2006) A facile route to the non-IPR fullerene $Sc_3N@C_{68}$: synthesis, spectroscopic characterization, and density functional theory computations (IPR = isolated pentagon rule). Chem-Eur J 12(30):7856–7863
29. Bolskar RD, Alford JM (2003) Chemical oxidation of endohedral metallofullerenes: identification and separation of distinct classes. Chem Commun 11:1292–1293
30. Tsuchiya T, Wakahara T, Shirakura S et al (2004) Reduction of endohedral metallofullerenes: a convenient method for isolation. Chem Mat 16(22):4343–4346
31. Ge ZX, Duchamp JC, Cai T et al (2005) Purification of endohedral trimetallic nitride fullerenes in a single, facile step. J Am Chem Soc 127(46):16292–16298
32. Stevenson S, Harich K, Yu H et al (2006) Nonchromatographic "stir and filter approach" (SAFA) for isolating $Sc_3N@C_{80}$ metallofullerenes. J Am Chem Soc 128(27):8829–8835
33. Stevenson S, Mackey MA, Pickens JE et al (2009) Selective complexation and reactivity of metallic nitride and oxometallic fullerenes with lewis acids and use as an effective purification method. Inorg Chem 48(24):11685–11690
34. Akiyama K, Hamano T, Nakanishi Y et al (2012) Non-HPLC rapid separation of metallofullerenes and empty cages with $TiCl_4$ lewis acid. J Am Chem Soc 134(23):9762–9767
35. Cerón MR, Li F-F, Echegoyen L (2013) An efficient method to separate $Sc_3N@C_{80}$ I_h and D_{5h} isomers and $Sc_3N@C_{78}$ by selective oxidation with acetylferrocenium $[Fe(COCH_3C_5H_4)Cp]^+$. Chem-Eur J 19(23):7410–7415
36. Yang SF, Popov AA, Dunsch L (2008) Large mixed metal nitride clusters encapsulated in a small cage: the confinement of the C_{68}-based clusterfullerenes. Chem Commun 2885–2887
37. Campbell EEB, Tellgmann R, Krawez N et al (1997) Production and LDMS characterisation of endohedral alkali-fullerene films. J Phys Chem Solids 58(11):1763–1769
38. Gromov A, Kratschmer W, Krawez N et al (1997) Extraction and HPLC purification of $Li@C_{60/70}$. Chem Commun 20:2003–2004
39. Kubozono Y, Ohta T, Hayashibara T et al (1995) Preparation and extraction of $Ca@C_{60}$. Chem Lett 6:457–458

40. Xu ZD, Nakane T, Shinohara H (1996) Production and isolation of Ca@C82 (I-IV) and Ca@C84 (I, II) metallofullerenes. J Am Chem Soc 118(45):11309–11310
41. John T, Dennis S, Shinohara H (1998) Production, isolation, and characterization of group-2 metal-containing endohedral metallofullerenes. Appl Phys A-Mater Sci Process 66(3): 243–247
42. Kuran P, Krause M, Bartl A et al (1998) Preparation, isolation and characterisation of Eu@C_{74}: the first isolated europium endohedral fullerene. Chem Phys Lett 292(4–6): 580–586
43. Kirbach U, Dunsch L (1996) The existence of stable Tm@C_{82} isomers. Angew Chem-Int Edit Engl 35(20):2380–2383
44. Xu JX, Lu X, Zhou XH et al (2004) Synthesis, isolation, and spectroscopic characterization of ytterbium-containing metallofullerenes. Chem Mat 16(15):2959–2964
45. Okazaki T, Lian YF, Gu ZN et al (2000) Isolation and spectroscopic characterization of Sm-containing metallofullerenes. Chem Phys Lett 320(5–6):435–440
46. Yang H, Jin H, Hong B et al (2011) Large endohedral fullerenes containing two metal ions, $Sm_2@D_2(35)$-C_{88}, $Sm_2@C_1(21)$-C_{90}, and $Sm_2@D_3(85)$-C_{92}, and their relationship to endohedral fullerenes containing two gadolinium ions. J Am Chem Soc 133(42):16911–16919
47. Mercado BQ, Jiang A, Yang H et al (2009) Isolation and structural characterization of the molecular nanocapsule $Sm_2@D_{3d}(822)$-C_{104}. Angew Chem-Int Edit Engl 48(48):9114–9116
48. Xu W, Feng L, Calvaresi M et al (2013) An experimentally observed trimetallofullerene $Sm_3@I_h$-C_{80}: Encapsulation of three metal atoms in a cage without a nonmetallic mediator. J Am Chem Soc 135(11):4187–4190
49. Guo T, Diener MD, Chai Y et al (1992) Uranium stabilization of C_{28}—a tetravalent fullerene. Science 257(5077):1661–1664
50. Dunk PW, Kaiser NK, Mulet-Gas M et al (2012) The smallest stable fullerene, M@C_{28} (M = Ti, Zr, U): stabilization and growth from carbon vapor. J Am Chem Soc 134(22): 9380–9389
51. Cao BP, Hasegawa M, Okada K et al (2001) EELS and ^{13}C NMR characterization of pure $Ti_2@C_{80}$ metallofullerene. J Am Chem Soc 123(39):9679–9680
52. Cao BP, Suenaga K, Okazaki T et al (2002) Production, isolation, and EELS characterization of $Ti_2@C_{84}$ dititanium metallofullerenes. J Phys Chem B 106(36):9295–9298
53. Tan K, Lu X (2005) Ti_2C_{80} is more likely a titanium carbide endohedral metallofullerene (Ti_2C_2)@C_{78}. Chem Commun 35:4444–4446
54. Sato Y, Yumura T, Suenaga K et al (2006) Direct imaging of intracage structure in titanium-carbide endohedral metallofullerene. Phys Rev B 73(19):193401
55. Li F-F, Chen N, Mulet-Gas M et al (2013) $Ti_2S@D_{3h}(24109)$-C_{78}: a sulfide cluster metallofullerene containing only transition metals inside the cage. Chem Sci 4(9):3404–3410
56. Yang S, Chen C, Popov A et al (2009) An endohedral titanium(III) in a clusterfullerene: putting a non-group-III metal nitride into the C_{80}-I_h fullerene cage. Chem Commun 6391–6393
57. Chen C, Liu F, Li S et al (2012) Titanium/yttrium mixed metal nitride clusterfullerene $TiY_2N@C_{80}$: synthesis, isolation, and effect of the group-III metal. Inorg Chem 51(5): 3039–3045
58. Junghans K, Ghiassi KB, Samoylova NA et al (2016) Synthesis and isolation of the titanium-scandium endohedral fullerenes—$Sc_2TiC@I_h$-C_{80}, $Sc_2TiC@D_{5h}$-C_{80}, and $Sc_2TiC_2@I_h$-C_{80}: metal size tuning of the Ti^{IV}/Ti^{III} redox potentials. Chem-Eur J 22(37): 13098–13107
59. Svitova AL, Ghiassi K, Schlesier C et al (2014) Endohedral fullerene with μ_3-carbido ligand and titanium-carbon double bond stabilized inside a carbon cage. Nat Commun 5 3568
60. Sueki K, Kikuchi K, Akiyama K et al (1999) Formation of metallofullerenes with higher group elements. Chem Phys Lett 300(1–2):140–144
61. Akiyama K, Sueki K, Kodama T et al (2000) New fullerenes of a group IV element: Hf metallofullerenes. Chem Phys Lett 317(3–5):490–496

62. Wei T, Wang S, Lu X et al (2016) Entrapping a group-VB transition metal, vanadium, within an endohedral metallofullerene: $V_xSc_{3-x}N@I_h$-C_{80} (x = 1, 2). J Am Chem Soc 138(1): 207–214
63. Roy D, Tripathi NK, Ram K et al (2009) Synthesis of germanium encapsulated fullerene. Solid State Commun 149(31–32):1244–1247
64. Akiyama K, Zhao YL, Sueki K et al (2001) Isolation and characterization of light actinide metallofullerenes. J Am Chem Soc 123(1):181–182
65. Akiyama K, Sueki K, Tsukada K et al (2002) Study of metallofullerenes encapsulating actinides. J Nucl Radiochem Sci 3(1):151–154
66. Akiyama K, Sueki K, Haba H et al (2003) Production and characterization of actinide metallofullerenes. J Radioanal Nucl Chem 255(1):155–158
67. Akiyama K, Haba H, Tsukada K et al (2009) A metallofullerene that encapsulates ^{225}Ac. J Radioanal Nucl Chem 280(2):329–331
68. Ross MM, Callahan JH (1991) Formation and characterization of $C_{60}He^+$. J Phys Chem 95(15):5720–5723
69. Caldwell KA, Giblin DE, Gross ML (1992) High-energy collisions of fullerene radical cations with target gases—capture of the target gas and charge stripping of C-60(.+), C-70(.+), and C-84(.+). J Am Chem Soc 114(10):3743–3756
70. Wan Z, Christian JF, Anderson SL (1992) Ne^++C_{60}: Collision energy and impact parameter dependence for endohedral complex formation, fragmentation, and charge transfer. J Chem Phys 96(4):3344–3347
71. Mosely J, Cooper H, Gallagher R et al (1995) Letter: target capture of argon by fullerene radical cations in high-energy collisions. Eur J Mass Spectrom 1(5):501–502
72. Wan ZM, Christian JF, Anderson SL (1992) Collision of Li^+ and Na^+ with C_{60}^- insertion, fragmentation, and thermionic emission. Phys Rev Lett 69(9):1352–1355
73. Saunders M, Jiménez-Vázquez HA, Cross RJ et al (1993) Stable compounds of helium and neon—He@C_{60} and Ne@C_{60}. Science 259(5100):1428–1430
74. Saunders M, Jiménez-Vázquez HA, Cross RJ et al (1994) Incorporation of helium, neon, argon, krypton, and xenon into fullerenes using high-pressure. J Am Chem Soc 116(5):2193–2194
75. Saunders M, Jiménez-Vázquez HA, Cross RJ et al (1994) Probing the interior of fullerenes by ^{3}He NMR-spectroscopy of endohedral ^{3}He@C_{60} and ^{3}He@C_{70}. Nature 367(6460): 256–258
76. Saunders M, Cross RJ, Jiménez-Vázquez HA et al (1996) Noble gas atoms inside fullerenes. Science 271(5256):1693–1697
77. Saunders M, Jiménez-Vázquez HA, Cross RJ et al (1995) Analysis of isomers of the higher fullerenes by ^{3}He NMR-spectroscopy. J Am Chem Soc 117(36):9305–9308
78. DiCamillo BA, Hettich RL, Guiochon G et al (1996) Enrichment and characterization of a noble gas fullerene: Ar@C_{60}. J Phys Chem 100(22):9197–9201
79. Yamamoto K, Saunders M, Khong A et al (1999) Isolation and spectral properties of Kr@C-60, a stable van der Waals molecule. J Am Chem Soc 121(7):1591–1596
80. Lee HM, Olmstead MM, Suetsuna T et al (2002) Crystallographic characterization of Kr@C_{60} in (0.09Kr@C_{60}/0.91C_{60})·{Ni^{II}(OEP)}·2C_6H_6. Chem Commun 13:1352–1353
81. Syamala MS, Cross RJ, Saunders M (2002) Xe-129 NMR spectrum of xenon inside C-60. J Am Chem Soc 124(21):6216–6219
82. Khong A, Jimenez-Vazquez HA, Saunders M et al (1998) An NMR study of He_2 inside C_{70}. J Am Chem Soc 120(25):6380–6383
83. Sternfeld T, Hoffman RE, Saunders M et al (2002) Two helium atoms inside fullerenes: probing the internal magnetic field in C_{60}^{6-} and C_{70}^{6-}. J Am Chem Soc 124(30):8786–8787
84. Laskin J, Peres T, Lifshitz C et al (1998) An artificial molecule of Ne_2 inside C_{70}. Chem Phys Lett 285(1–2):7–9
85. Peres T, Cao B, Cui W et al (2001) Some new diatomic molecule containing endohedral fullerenes. Int J Mass Spectrom 210–211:241–247

86. Peng RF, Chu SJ, Huang YM et al (2009) Preparation of $He@C_{60}$ and $He_2@C_{60}$ by an explosive method. J Mater Chem 19:3602–3605
87. Suetsuna T, Dragoe N, Harneit W et al (2002) Separation of $N_2@C_{60}$ and $N@C_{60}$. Chem-Eur J 8(22):5079–5083
88. Murphy TA, Pawlik T, Weidinger A et al (1996) Observation of atomlike nitrogen in nitrogen-implanted solid C-60. Phys Rev Lett 77(6):1075–1078
89. Weidinger A, Waiblinger M, Pietzak B et al (1998) Atomic nitrogen in C_{60}: $N@C_{60}$. Appl Phys A-Mater Sci Process 66(3):287–292
90. Jakes P, Dinse KP, Meyer C et al (2003) Purification and optical spectroscopy of $N@C_{60}$. Phys Chem Chem Phys 5(19):4080–4083
91. Dietel E, Hirsch A, Pietzak B et al (1999) Atomic nitrogen encapsulated in fullerenes: effects of cage variations. J Am Chem Soc 121(11):2432–2437
92. Knapp C, Weiden N, Kass K et al (1998) Electron paramagnetic resonance study of atomic phosphorus encapsulated in [60]fullerene. Mol Phys 95(5):999–1004
93. Ito S, Shimotani H, Takagi H et al (2008) On the synthesis conditions of N and N_2 endohedral fullerenes. Fullerenes Nanotubes Carbon Nanostruct 16(3):206–213
94. Komatsu K, Murata M, Murata Y (2005) Encapsulation of molecular hydrogen in fullerene C60 by organic synthesis. Science 307(5707):238–240
95. Morinaka Y, Tanabe F, Murata M et al (2010) Rational synthesis, enrichment, and ^{13}C NMR spectra of endohedral C_{60} and C_{70} encapsulating a helium atom. Chem Commun 46(25): 4532–4534
96. Murata M, Maeda S, Morinaka Y et al (2008) Synthesis and reaction of fullerene C_{70} encapsulating two molecules of H_2. J Am Chem Soc 130(47):15800–15801
97. Kurotobi K, Murata Y (2011) A single molecule of water encapsulated in fullerene C_{60}. Science 333(6042):613–616
98. Zhang R, Murata M, Aharen T et al (2016) Synthesis of a distinct water dimer inside fullerene C_{70}. Nat Chem 8(5):435–441
99. Hashikawa Y, Murata M, Wakamiya A et al (2016) Synthesis and properties of endohedral Aza[60]fullerenes: $H_2O@C_{59}N$ and $H_2@C_{59}N$ as their dimers and monomers. J Am Chem Soc 138(12):4096–4104
100. Vougioukalakis GC, Roubelakis MM, Orfanopoulos M (2010) Open-cage fullerenes: towards the construction of nanosized molecular containers. Chem Soc Rev 39(2):817–844
101. Gan LB, Yang DZ, Zhang QY et al (2010) Preparation of open-cage fullerenes and incorporation of small molecules through their orifices. Adv Mater 22(13):1498–1507
102. Murata M, Murata Y, Komatsu K (2008) Surgery of fullerenes. Chem Commun 46:6083–6094
103. Rubin Y, Jarrosson T, Wang GW et al (2001) Insertion of helium and molecular hydrogen through the orifice of an open fullerene. Angew Chem-Int Edit 40(8):1543
104. Iwamatsu S, Uozaki T, Kobayashi K et al (2004) A bowl-shaped fullerene encapsulates a water into the cage. J Am Chem Soc 126(9):2668–2669
105. Krachmalnicoff A, Bounds R, Mamone S et al (2015) Synthesis and characterisation of an open-cage fullerene encapsulating hydrogen fluoride. Chem Commun 51(24):4993–4996
106. Chen C-S, Kuo T-S, Yeh W-Y (2016) Encapsulation of formaldehyde and hydrogen cyanide in an open-cage fullerene. Chem-Eur J 22(26):8773–8776
107. Stanisky CM, Cross RJ, Saunders M (2009) Putting atoms and molecules into chemically opened fullerenes. J Am Chem Soc 131(9):3392–3395
108. Iwamatsu S, Stanisky CM, Cross RJ et al (2006) Carbon monoxide inside an open-cage fullerene. Angew Chem-Int Edit 45(32):5337–5340
109. Futagoishi T, Murata M, Wakamiya A et al (2015) Trapping N_2 and CO_2 on the sub-nano scale in the confined internal spaces of open-cage C60 derivatives: isolation and structural characterization of the host-guest complexes. Angew Chem-Int Edit Engl 54(49):14791–14794
110. Whitener KE, Frunzi M, S-i Iwamatsu et al (2008) Putting ammonia into a chemically opened fullerene. J Am Chem Soc 130(42):13996–13999

111. Whitener KE, Cross RJ, Saunders M et al (2009) Methane in an open-cage [60] fullerene. J Am Chem Soc 131(18):6338–6339
112. Morinaka Y, Sato S, Wakamiya A et al (2013) X-ray observation of a helium atom and placing a nitrogen atom inside He@C_{60} and He@C_{70}. Nat Commun 4:1554
113. Olmstead MM, Costa DA, Maitra K et al (1999) Interaction of curved and flat molecular surfaces. The structures of crystalline compounds composed of fullerene (C_{60}, $C_{60}O$, C_{70}, and $C_{120}O$) and metal octaethylporphyrin units. J Am Chem Soc 121(30):7090–7097
114. Rodriguez-Fortea A, Balch AL, Poblet JM (2011) Endohedral metallofullerenes: a unique host-guest association. Chem Soc Rev 40:3551–3563
115. Yamada M, Akasaka T, Nagase S (2010) Endohedral metal atoms in pristine and functionalized fullerene cages. Acc Chem Res 43(1):92–102
116. Lu X, Akasaka T, Nagase S (2011) Chemistry of endohedral metallofullerenes: the role of metals. Chem Commun 47(21):5942–5957
117. Stevenson S, Thompson HR, Arvola KD et al (2015) Isolation of $CeLu_2N@I_h$-C_{80} through a non-chromatographic, two-step chemical process and crystallographic characterization of the pyramidalized $CeLu_2N$ within the icosahedral cage. Chem-Eur J 21(29):10362–10368
118. Yang H, Jin H, Zhen H et al (2011) Isolation and crystallographic identification of four isomers of Sm@C_{90}. J Am Chem Soc 133(16):6299–6306
119. Iiduka Y, Wakahara T, Nakajima K et al (2006) ^{13}C NMR spectroscopic study of scandium dimetallofullerene, $Sc_2@C_{84}$ *vs*. $Sc_2C_2@C_{82}$. Chem Commun 19:2057–2059
120. Yamazaki Y, Nakajima K, Wakahara T et al (2008) Observation of ^{13}C NMR chemical shifts of metal carbides encapsulated in fullerenes: $Sc_2C_2@C_{82}$, $Sc_2C_2@C_{82}$, and $Sc_3C_2@C_{80}$. Angew Chem-Int Edit Engl 47:7905–7908
121. Akasaka T, Wakahara T, Nagase S et al (2001) Structural determination of the La@C_{82} isomer. J Phys Chem B 105(15):2971–2974
122. Tsuchiya T, Wakahara T, Maeda Y et al (2005) 2D NMR characterization of the La@C_{82} anion. Angew Chem-Int Edit 44(21):3282–3285
123. Yamada M, Wakahara T, Tsuchiya T et al (2008) Location of the metal atoms in $Ce_2@C_{78}$ and its bis-silylated derivative. Chem Commun 558–560
124. Yamada M, Wakahara T, Tsuchiya T et al (2008) Spectroscopic and theoretical study of endohedral dimetallofullerene having a non-IPR fullerene cage: $Ce_2@C_{72}$. J Phys Chem A 112:7627–7631
125. Yamada M, Mizorogi N, Tsuchiya T et al (2009) Synthesis and characterization of the D_{5h} isomer of the endohedral dimetallofullerene $Ce_2@C_{80}$: two-dimensional circulation of encapsulated metal atoms inside a fullerene cage. Chem-Eur J 15:9486–9493
126. Fu W, Xu L, Azurmendi H et al (2009) ^{89}Y and ^{13}C NMR cluster and carbon cage studies of an yttrium metallofullerene family, $Y_3N@C_{2n}$ (n = 40-43). J Am Chem Soc 131(33):11762–11769
127. Fu W, Wang X, Azuremendi H et al (2011) ^{14}N and ^{45}Sc NMR study of trimetallic nitride cluster $(M_3N)^{6+}$ dynamics inside a icosahedral C_{80} cage. Chem Commun 47(13):3858–3860
128. Popov AA, Schiemenz S, Avdoshenko SM et al (2011) The state of asymmetric nitride clusters in endohedral fullerenes as studied by ^{14}N NMR spectroscopy: experiment and theory. J Phys Chem C 115(31):15257–15265
129. Akasaka T, Nagase S, Kobayashi K et al (1997) ^{13}C and ^{139}La NMR studies of $La_2@C_{80}$: first evidence for circular motion of metal atoms in endohedral dimetallofullerenes. Angew Chem-Int Edit Engl 36(15):1643–1645
130. Suzuki M, Mizorogi N, Yang T et al (2013) $La_2@C_s$(17 490)-C76: a new non-IPR dimetallic metallofullerene featuring unexpectedly weak metal-pentalene interactions. Chem-Eur J 19 (50):17125–17130
131. Kurihara H, Lu X, Iiduka Y et al (2011) $Sc_2C_2@C_{80}$ rather than $Sc_2@C_{82}$: templated formation of unexpected C_{2v}(5)-C_{80} and temperature-dependent dynamic motion of internal Sc_2C_2 cluster. J Am Chem Soc 133(8):2382–2385
132. Feng Y, Wang T, Xiang J et al (2015) Tuneable dynamics of a scandium nitride cluster inside an I_h-C_{80} cage. Dalton Trans 44:2057–2061

133. Popov AA, Chen N, Pinzón JR et al (2012) Redox-active scandium oxide cluster inside a fullerene cage: spectroscopic, voltammetric, electron spin resonance spectroelectrochemical, and extended density functional theory study of $Sc_4O_2@C_{80}$ and its ion radicals. J Am Chem Soc 134(48):19607–19618
134. Wang T-S, Feng L, Wu J-Y et al (2010) Planar quinary cluster inside a fullerene cage: synthesis and structural characterizations of $Sc_3NC@C_{80}$-I_h. J Am Chem Soc 132 (46):16362–16364
135. Wang GW, Saunders M, Khong A et al (2000) A new method for separating the isomeric C_{84} fullerenes. J Am Chem Soc 122(13):3216–3217
136. Popov AA (2009) Metal-cage bonding, molecular structures and vibrational spectra of endohedral fullerenes: bridging experiment and theory. J Comput Theor Nanosci 6(2): 292–317
137. Popov AA, Krause M, Yang SF et al (2007) C_{78} cage isomerism defined by trimetallic nitride cluster size: a computational and vibrational spectroscopic study. J Phys Chem B 111(13):3363–3369
138. Yang SF, Popov AA, Dunsch L (2007) Violating the isolated pentagon rule (IPR): the endohedral non-IPR cage of $Sc_3N@C_{70}$. Angew Chem-Int Edit 46(8):1256–1259
139. Fowler P, Manolopoulos DE (1995) An atlas of fullerenes. Clarendon Press, Oxford
140. Takata M, Nishibori E, Sakata M et al (2003) Synchrotron radiation for structural chemistry —endohedral natures of metallofullerenes found by synchrotron radiation powder method. Struct Chem 14(1):23–38
141. Akasaka T, Wakahara T, Nagase S et al (2000) $La@C_{82}$ anion. An unusually stable metallofullerene. J Am Chem Soc 122(38):9316–9317
142. Takata M, Umeda B, Nishibori E et al (1995) Confirmation by X-ray-diffraction of the endohedral nature of the metallofullerene $Y@C_{82}$. Nature 377(6544):46–49
143. Sato S, Nikawa H, Seki S et al (2012) A co-crystal composed of the paramagnetic endohedral metallofullerene $La@C_{82}$ and a nickel porphyrin with high electron mobility. Angew Chem-Int Edit Engl 51(7):1589–1591
144. Suzuki M, Lu X, Sato S et al (2012) Where does the metal cation stay in $Gd@C_{2v}(9)$-C_{82}? A single-crystal X-ray diffraction study. Inorg Chem 51(9):5270–5273
145. Akasaka T, Lu X (2012) Structural and electronic properties of endohedral metallofullerenes. Chem Rec 12(2):256–269
146. Kodama T, Ozawa N, Miyake Y et al (2002) Structural study of three isomers of $Tm@C_{82}$ by ^{13}C NMR spectroscopy. J Am Chem Soc 124(7):1452–1455
147. Kodama T, Fujii R, Miyake Y et al (2003) Structural study of four $Ca@C_{82}$ isomers by ^{13}C NMR spectroscopy. Chem Phys Lett 377(1–2):197–200
148. Reich A, Panthofer M, Modrow H et al (2004) The structure of $Ba@C_{74}$. J Am Chem Soc 126(44):14428–14434
149. Xu W, Hao Y, Uhlik F et al (2013) Structural and electrochemical studies of $Sm@D_{3h}$-C_{74} reveal a weak metal-cage interaction and a small band gap species. Nanoscale 5(21):10409–10413
150. Kodama T, Fujii R, Miyake Y et al (2004) ^{13}C NMR study of $Ca@C_{74}$: the cage structure and the site-hopping motion of a Ca atom inside the cage. Chem Phys Lett 399(1–3):94–97
151. Xu JX, Tsuchiya T, Hao C et al (2006) Structure determination of a missing-caged metallofullerene: $Yb@C_{74}$ (II) and the dynamic motion of the encaged ytterbium ion. Chem Phys Lett 419(1–3):44–47
152. Lu X, Slanina Z, Akasaka T et al (2010) $Yb@C_{2n}$ (n = 40, 41, 42): new fullerene allotropes with unexplored electrochemical properties. J Am Chem Soc 132(16):5896–5905
153. Yang H, Wang Z, Jin H et al (2013) Isolation and crystallographic characterization of $Sm@C_{2v}(3)$-C_{80} through cocrystal formation with Ni^{II}(octaethylporphyrin) or bis(ethylenedithio)tetrathiafulvalene. Inorg Chem 52(3):1275–1284
154. Yang H, Yu M, Jin H et al (2012) The isolation of three isomers of $Sm@C_{84}$ and the X-ray crystallographic characterization of $Sm@D_{3d}(19)$-C_{84} and $Sm@C_2(13)$-C_{84}. J Am Chem Soc 134(11):5331–5338

155. Jin H, Yang H, Yu M et al (2012) Single samarium atoms in large fullerene cages. characterization of two isomers of Sm@C_{92} and four isomers of Sm@C_{94} with the X-ray crystallographic identification of Sm@C_1(42)-C_{92}, Sm@C_s(24)-C_{92}, and Sm@C_{3v}(134)-C_{94}. J Am Chem Soc 134(26):10933–10941
156. Xu W, Niu B, Feng L et al (2012) Access to an unexplored chiral C_{82} Cage by encaging a divalent metal: structural elucidation and electrochemical studies of Sm@C_2(5)-C_{82}. Chem-Eur J 18(45):14246–14249
157. Yang H, Jin H, Wang X et al (2012) X-ray crystallographic characterization of new soluble endohedral fullerenes utilizing the popular C_{82} bucky cage. isolation and structural characterization of Sm@C_{3v}(7)-C_{82}, Sm@C_s(6)-C_{82}, and Sm@C_2(5)-C_{82}. J Am Chem Soc 134(34):14127–14136
158. Xu W, Niu B, Shi Z et al (2012) Sm@C_{2v}(3)-C_{80}: site-hopping motion of endohedral Sm atom and metal-induced effect on redox profile. Nanoscale 4:6876–6879
159. Che Y, Yang H, Wang Z et al (2009) Isolation and structural characterization of two very large, and largely empty, endohedral fullerenes: Tm@C_{3v}-C_{94} and Ca@C_{3v}-C_{94}. Inorg Chem 48(13):6004–6010
160. Shinohara H, Sato H, Saito Y et al (1992) Mass spectroscopic and ESR characterization of soluble yttrium-containing metallofullerenes YC_{82} and Y_2C_{82}. J Phys Chem 96(9): 3571–3573
161. Nishibori E, Takata M, Sakata M et al (2001) Pentagonal-dodecahedral La_2 charge density in [80-I_h]fullerene: La_2@C_{80}. Angew Chem-Int Edit 40(16):2998–2999
162. Kato H, Taninaka A, Sugai T et al (2003) Structure of a missing-caged metallofullerene: La_2@C_{72}. J Am Chem Soc 125(26):7782–7783
163. Cao BP, Wakahara T, Tsuchiya T et al (2004) Isolation, characterization, and theoretical study of La_2@C_{78}. J Am Chem Soc 126(30):9164–9165
164. Yamada M, Nakahodo T, Wakahara T et al (2005) Positional control of encapsulated atoms inside a fullerene cage by exohedral addition. J Am Chem Soc 127(42):14570–14571
165. Beavers CM, Jin H, Yang H et al (2011) very large, soluble endohedral fullerenes in the series La_2C_{90} to La_2C_{138}: isolation and crystallographic characterization of La_2@D_5(450)-C_{100}. J Am Chem Soc 133(39):15338–15341
166. Popov AA, Avdoshenko SM, Pendás AM et al (2012) Bonding between strongly repulsive metal atoms: an oxymoron made real in a confined space of endohedral metallofullerenes. Chem Commun 48:8031–8050
167. Kurihara H, Lu X, Iiduka Y et al (2012) Sc_2@C_{3v}(8)-C_{82} *vs.* Sc_2C_2@C_{3v}(8)-C_{82}: drastic effect of C_2 capture on the redox properties of scandium metallofullerenes. Chem Commun 48:1290–1292
168. Inoue T, Tomiyama T, Sugai T et al (2004) Trapping a C_2 radical in endohedral metallofullerenes: synthesis and structures of (Y_2C_2)@C_{82} (isomers I, II, and III). J Phys Chem B 108(23):7573–7579
169. Olmstead MM, de Bettencourt-Dias A, Stevenson S et al (2002) Crystallographic characterization of the structure of the endohedral fullerene Er_2@C_{82} Isomer I with C_s cage symmetry and multiple sites for erbium along a band of ten contiguous hexagons. J Am Chem Soc 124(16):4172–4173
170. Olmstead MM, Lee HM, Stevenson S et al (2002) Crystallographic characterization of Isomer 2 of Er_2@C_{82} and comparison with Isomer 1 of Er_2@C_{82}. Chem Commun 22: 2688–2689
171. Ito Y, Okazaki T, Okubo S et al (2007) Enhanced 1520 nm photoluminescence from Er^{3+} ions in di-erbium-carbide metallofullerenes (Er_2C_2)@C_{82} (isomers I, II, and III). ACS Nano 1(5):456–462
172. Plant SR, Dantelle G, Ito Y et al (2009) Acuminated fluorescence of Er^{3+} centres in endohedral fullerenes through the incarceration of a carbide cluster. Chem Phys Lett 476:41–45
173. Umemoto H, Ohashi K, Inoue T et al (2010) Synthesis and UHV-STM observation of the Td-symmetric Lu metallofullerene: Lu_2@C_{76}(T_d). Chem Commun 46(31):5653–5655

174. Yamada M, Kurihara H, Suzuki M et al (2014) $Sc_2@C_{66}$ Revisited: an endohedral fullerene with scandium ions nestled within two unsaturated linear triquinanes. J Am Chem Soc 136(21):7611–7614
175. Kikuchi K, Akiyama K, Sakaguchi K et al (2000) Production and isolation of the isomers of dimetallofulerenes, $HoTm@C_{82}$ and $Tm_2@C_{82}$. Chem Phys Lett 319(5–6):472–476
176. Zuo T, Xu L, Beavers CM et al (2008) $M_2@C_{79}N$ (M = Y, Tb): isolation and characterization of stable endohedral metallofullerenes exhibiting M…M bonding interactions inside Aza [80] fullerene cages. J Am Chem Soc 130(39):12992–12997
177. Fu W, Zhang J, Fuhrer T et al (2011) $Gd_2@C_{79}N$: isolation, characterization, and monoadduct formation of a very stable heterofullerene with a magnetic spin state of S = 15/2. J Am Chem Soc 133:9741–9750
178. Lu X, Akasaka T, Nagase S (2013) Carbide cluster metallofullerenes: structure, properties, and possible origin. Acc Chem Res 46(7):1627–1635
179. Jin P, Tang C, Chen Z (2014) Carbon atoms trapped in cages: metal carbide clusterfullerenes. Coord Chem Rev 270–271:89–111
180. Kurihara H, Lu X, Iiduka Y et al (2012) X-ray structures of $Sc_2C_2@C_{2n}$ (n = 40-42): in-depth understanding of the core-shell interplay in carbide cluster metallofullerenes. Inorg Chem 51(1):746–750
181. Zhang J, Fuhrer T, Fu W et al (2012) Nanoscale fullerene compression of a yttrium carbide cluster. J Am Chem Soc 134(20):8487–8493
182. Deng Q, Popov AA (2014) Clusters encapsulated in endohedral metallofullerenes: how strained are they? J Am Chem Soc 136(11):4257–4264
183. Feng Y, Wang T, Wu J et al (2013) Structural and electronic studies of metal carbide clusterfullerene $Sc_2C_2@C_s$-C_{72}. Nanoscale 5(15):6704–6707
184. Yang H, Lu C, Liu Z et al (2008) Detection of a family of gadolinium-containing endohedral fullerenes and the isolation and crystallographic characterization of one member as a metal-carbide encapsulated inside a large fullerene cage. J Am Chem Soc 130(51):17296–17300
185. Cai W, Li F-F, Bao L et al (2016) Isolation and crystallographic characterization of $La_2C_2@C_s$(574)-C_{102} and $La_2C_2@C_2$(816)-C_{104}: evidences for the top-down formation mechanism of fullerenes. J Am Chem Soc 138(20):6670–6675
186. Iiduka Y, Wakahara T, Nakahodo T et al (2005) Structural determination of metallofuIlerene Sc_3C_{82} revisited: a surprising finding. J Am Chem Soc 127(36):12500–12501
187. Xu W, Wang T-S, Wu J-Y et al (2011) Entrapped planar trimetallic carbide in a fullerene cage: synthesis, isolation, and spectroscopic studies of $Lu_3C_2@C_{88}$. J Phys Chem C 115 (2):402–405
188. Wang T-S, Chen N, Xiang J-F et al (2009) Russian-doll-type metal carbide endofullerene: synthesis, isolation, and characterization of $Sc_4C_2@C_{80}$. J Am Chem Soc 131(46): 16646–16647
189. Tan K, Lu X, Wang CR (2006) Unprecedented μ_4-C_2^{6-} anion in $Sc_4C_2@C_{80}$. J Phys Chem B 110(23):11098–11102
190. Krause M, Ziegs F, Popov AA et al (2007) Entrapped bonded hydrogen in a fullerene: the five-atom cluster Sc_3CH in C_{80}. ChemPhysChem 8(4):537–540
191. Deng Q, Junghans K, Popov AA (2015) Carbide clusterfullerenes with odd number of carbon atoms: molecular and electronic structures of $Sc_4C@C_{80}$, $Sc_4C@C_{82}$, and $Sc_4C_3@C_{80}$. Theor Chem Acc 134(2):10
192. Dunsch L, Yang S (2007) Metal nitride cluster fullerenes: their current state and future prospects. Small 3(8):1298–1320
193. Zhang J, Stevenson S, Dorn HC (2013) Trimetallic nitride template endohedral metallofullerenes: discovery, structural characterization, reactivity, and applications. Acc Chem Res 46(7):1548–1557
194. Duchamp JC, Demortier A, Fletcher KR et al (2003) An isomer of the endohedral metallofullerene $Sc_3N@C_{80}$ with D_{5h} symmetry. Chem Phys Lett 375(5–6):655–659

195. Cai T, Xu LS, Anderson MR et al (2006) Structure and enhanced reactivity rates of the D_{5h} $Sc_3N@C_{80}$ and $Lu_3N@C_{80}$ metallofullerene isomers: the importance of the pyracylene motif. J Am Chem Soc 128(26):8581–8589
196. Stevenson S, Fowler PW, Heine T et al (2000) Materials science—a stable non-classical metallofullerene family. Nature 408(6811):427–428
197. Olmstead MM, Lee HM, Duchamp JC et al (2003) $Sc_3N@C_{68}$: folded pentalene coordination in an endohedral fullerene that does not obey the isolated pentagon rule. Angew Chem-Int Edit 42(8):900–903
198. Olmstead MM, de Bettencourt-Dias A, Duchamp JC et al (2001) Isolation and structural characterization of the endohedral fullerene $Sc_3N@C_{78}$. Angew Chem-Int Edit 40(7): 1223–1225
199. Wei T, Wang S, Liu F et al (2015) Capturing the long-sought small-bandgap endohedral fullerene $Sc_3N@C_{82}$ with low kinetic stability. J Am Chem Soc 137(8):3119–3123
200. Krause M, Dunsch L (2005) Gadolinium nitride Gd_3N in carbon cages: the influence of cluster size and bond strength. Angew Chem-Int Edit 44(10):1557–1560
201. Yang SF, Dunsch L (2005) A large family of dysprosium-based trimetallic nitride endohedral fullerenes: $Dy_3N@C_{2n}$ ($39 \leq n \leq 44$). J Phys Chem B 109(25):12320–12328
202. Krause M, Wong J, Dunsch L (2005) Expanding the world of endohedral fullerenes—the $Tm_3N@C_{2n}$ ($39 \leq n \leq 43$) clusterfullerene family. Chem-Eur J 11(2):706–711
203. Beavers CM, Zuo TM, Duchamp JC et al (2006) $Tb_3N@C_{84}$: an improbable, egg-shaped endohedral fullerene that violates the isolated pentagon rule. J Am Chem Soc 128(35):11352–11353
204. Chaur MN, Melin F, Elliott B et al (2007) $Gd_3N@C_{2n}$ (n = 40, 42, and 44): remarkably low HOMO-LUMO gap and unusual electrochemical reversibility of $Gd_3N@C_{88}$. J Am Chem Soc 129(47):14826–14829
205. Zuo TM, Beavers CM, Duchamp JC et al (2007) Isolation and structural characterization of a family of endohedral fullerenes including the large, chiral cage fullerenes $Tb_3N@C_{88}$ and $Tb_3N@C_{86}$ as well as the I_h and D_{5h} isomers of $Tb_3N@C_{80}$. J Am Chem Soc 129(7):2035–2043
206. Fu W, Zhang J, Champion H et al (2011) Electronic properties and ^{13}C NMR structural study of $Y_3N@C_{88}$. Inorg Chem 50(10):4256–4259
207. Beavers CM, Chaur MN, Olmstead MM et al (2009) Large metal ions in a relatively small fullerene cage: the structure of $Gd_3N@C_2$(22010)-C_{78} departs from the isolated pentagon rule. J Am Chem Soc 131(32):11519–11524
208. Mercado BQ, Beavers CM, Olmstead MM et al (2008) Is the isolated pentagon rule merely a suggestion for endohedral fullerenes? The structure of a second egg-shaped endohedral fullerene—$Gd_3N@C_s$(39663)-C_{82}. J Am Chem Soc 130(25):7854–7855
209. Melin F, Chaur MN, Engmann S et al (2007) The large $Nd_3N@C_{2n}$ ($40 \leq 2n \leq 49$) cluster fullerene family: preferential templating of a C_{88} Cage by a trimetallic nitride cluster. Angew Chem-Int Edit 46(47):9032–9035
210. Chaur MN, Melin F, Elliott B et al (2008) New $M_3N@C_{2n}$ endohedral metallofullerene families (M = Nd, Pr, Ce; n = 40-53): expanding the preferential templating of the C_{88} cage and approaching the C_{96} cage. Chem-Eur J 14(15):4594–4599
211. Chaur MN, Melin F, Ashby J et al (2008) Lanthanum nitride endohedral fullerenes $La_3N@C_{2n}$ ($43 < n < 55$): preferential formation of $La_3N@C_{96}$. Chem-Eur J 14(27): 8213–8219
212. Popov AA, Dunsch L (2007) Structure, stability, and cluster-cage interactions in nitride clusterfullerenes $M_3N@C_{2n}$ (M = Sc, Y; 2n = 68-98): a density functional theory study. J Am Chem Soc 129(38):11835–11849
213. Valencia R, Rodriguez-Fortea A, Clotet A et al (2009) Electronic structure and redox properties of metal nitride endohedral fullerenes $M_3N@C_{2n}$ (M = Sc, Y, La, and Gd; 2n = 80, 84, 88, 92, 96). Chem-Eur J 15(41):10997–11009
214. Chaur MN, Valencia R, Rodriguez-Fortea A et al (2009) Trimetallic nitride endohedral fullerenes: experimental and theoretical evidence for the $M_3N^{6+}@C_{2n}^{6-}$ model. Angew Chem-Int Edit 48(8):1425–1428

215. Svitova AL, Popov AA, Dunsch L (2013) Gd/Sc-based mixed metal nitride cluster fullerenes: the mutual influence of the cage and cluster size and the role of Sc in the electronic structure. Inorg Chem 52(6):3368–3380
216. Wu J, Wang T, Ma Y et al (2011) Synthesis, isolation, characterization, and theoretical studies of $Sc_3NC@C_{78}$-C_2. J Phys Chem C 115(48):23755–23759
217. Yang S, Chen C, Liu F et al (2013) An improbable monometallic cluster entrapped in a popular fullerene cage: YCN@C_s(6)-C_{82}. Sci Rep 3:1487
218. Liu F, Wang S, Guan J et al (2014) Putting a terbium-monometallic cyanide cluster into the C_{82} fullerene cage: TbCN@C_2(5)-C_{82}. Inorg Chem 53(10):5201–5205
219. Liu F, Gao C-L, Deng Q et al (2016) Triangular monometallic cyanide cluster entrapped in carbon cage with geometry-dependent molecular magnetism. J Am Chem Soc 138(44):14764–14771
220. Wang T, Wu J, Feng Y (2014) Scandium carbide/cyanide alloyed cluster inside fullerene cage: synthesis and structural studies of $Sc_3(\mu_3\text{-}C_2)(\mu_3\text{-}CN)@I_h\text{-}C_{80}$. Dalton Trans 43:16270–16274
221. Stevenson S, Mackey MA, Stuart MA et al (2008) A distorted tetrahedral metal oxide cluster inside an icosahedral carbon cage. synthesis, isolation, and structural characterization of $Sc_4(\mu_3\text{-}O)_2@I_h\text{-}C_{80}$. J Am Chem Soc 130(36):11844–11845
222. Mercado BQ, Olmstead MM, Beavers CM et al (2010) A seven atom cluster in a carbon cage, the crystallographically determined structure of $Sc_4(\mu_3\text{-}O)_3@I_h\text{-}C_{80}$. Chem Commun 46:279–281
223. Valencia R, Rodriguez-Fortea A, Stevenson S et al (2009) Electronic structures of scandium oxide endohedral metallofullerenes, $Sc_4(\mu_3\text{-}O)_n@I_h\text{-}C_{80}$ (n = 2, 3). Inorg Chem 48: 5957–5961
224. Mercado BQ, Stuart MA, Mackey MA et al (2010) $Sc_2(\mu_2\text{-}O)$ trapped in a fullerene cage: the isolation and structural characterization of $Sc_2(\mu_2\text{-}O)@C_s$(6)-C_{82} and the relevance of the thermal and entropic effects in fullerene isomer selection. J Am Chem Soc 132:12098–12105
225. Tang Q, Abella L, Hao Y et al (2016) $Sc_2O@C_{3v}$(8)-C_{82}: a missing isomer of $Sc_2O@C_{82}$. Inorg Chem 55(4):1926–1933
226. Feng L, Zhang M, Hao Y et al (2016) Endohedrally stabilized C_{70} isomer with fused pentagons characterized by crystallography. Dalton Trans 45:8142–8148
227. Yang T, Hao Y, Abella L et al (2015) $Sc_2O@T_d$(19151)-C_{76}: hindered cluster motion inside a tetrahedral carbon cage probed by crystallographic and computational studies. Chem-Eur J 21(31):11110–11117
228. Tang Q, Abella L, Hao Y et al (2015) $Sc_2O@C_{2v}$(5)-C_{80}: dimetallic oxide cluster inside a C_{80} fullerene cage. Inorg Chem 54(20):9845–9852
229. Stevenson S (2014) Metal Oxide Clusterfullerenes. In: Yang S, Wang C-R (eds) Endohedral fullerenes. From fundamentals to applications. World Scientific, Singapore, pp 179–210
230. Mercado BQ, Chen N, Rodriguez-Fortea A et al (2011) The shape of the $Sc_2(\mu_2\text{-}S)$ unit trapped in C_{82}: crystallographic, computational, and electrochemical studies of the isomers, $Sc_2(\mu_2\text{-}S)@C_s$(6)-C_{82} and $Sc_2(\mu_2\text{-}S)@C_{3v}$(8)-$C_{82}$. J Am Chem Soc 133(17):6752–6760
231. Chen N, Mulet-Gas M, Li Y-Y et al (2013) $Sc_2S@C_2$(7892)-C_{70}: a metallic sulfide cluster inside a non-IPR C_{70} cage. Chem Sci 4(1):180–186
232. Nakao K, Kurita N, Fujita M (1994) Ab-initio molecular-orbital calculation for C_{70} and seven isomers of C_{80}. Phys Rev B 49(16):11415–11420
233. Rodriguez-Fortea A, Alegret N, Balch AL et al (2010) The maximum pentagon separation rule provides a guideline for the structures of endohedral metallofullerenes. Nat Chem 2(11):955–961
234. Valencia R, Rodríguez-Fortea A, Poblet JM (2008) Understanding the stabilization of metal carbide endohedral fullerenes $M_2C_2@C_{82}$ and related systems. J Phys ChemA 112(20):4550–4555
235. Stevenson S, Phillips JP, Reid JE et al (2004) Pyramidalization of Gd_3N inside a C_{80} cage. the synthesis and structure of $Gd_3N@C_{80}$. Chem Commun 24:2814–2815

236. Chaur MN, Aparicio-Angles X, Mercado BQ et al (2010) Structural and electrochemical property correlations of metallic nitride endohedral metallofullerenes. J Phys Chem C 114(30):13003–13009
237. Kobayashi K, Nagase S, Yoshida M et al (1997) Endohedral metallofullerenes. Are the isolated pentagon rule and fullerene structures always satisfied? J Am Chem Soc 119(51):12693–12694
238. Wang CR, Kai T, Tomiyama T et al (2000) C_{66} fullerene encaging a scandium dimer. Nature 408:426–427
239. Zhang Y, Ghiassi KB, Deng Q et al (2015) Synthesis and structure of $LaSc_2N@C_s$(hept)-C_{80} with one heptagon and thirteen pentagons. Angew Chem-Int Edit Engl 52(2):495–499
240. Gan L-H, Lei D, Fowler PW (2016) Structural interconnections and the role of heptagonal rings in endohedral trimetallic nitride template fullerenes. J Comput Chem 37(20): 1907–1913
241. Chen C-H, Abella L, Cerón MR et al (2016) Zigzag Sc_2C_2 carbide cluster inside a [88] fullerene cage with one heptagon, $Sc_2C_2@C_s$(hept)-C_{88}: a kinetically trapped fullerene formed by C_2 insertion? J Am Chem Soc 138(39):13030–13037

Chapter 2
Electrochemistry and Frontier Molecular Orbitals of Endohedral Metallofullerenes

Alexey A. Popov

Abstract Fullerenes exhibit rich redox activity and are able to accommodate up to 6 surplus electrons or give away 1–2 electrons in solution. EMFs inherit this property from empty fullerenes, and also add a new dimension to the redox behavior because endohedral clusters can exhibit their own redox activity despite their shielding by the carbon cage. This chapter provides a systematic overview of electrochemical properties of different classes of endohedral metallofullerenes. In particular, the balance between fullerene- and cluster-based redox activity in complex endohedral metallofullerenes is discussed using frontier molecular orbitals as a guide.

2.1 Introduction

Electrochemical properties of endohedral metallofullerenes (EMFs) were in focus of the research since mid-1990s, when the first isomerically pure samples became available [1–5]. Since that time, virtually any newly isolated EMF and many of their derivatives were characterized electrochemically, in particular by cyclic voltammetry or pulse voltammetric techniques (differential pulse voltammetry, DPV, and squarewave voltammetry, SWV). Redox potentials, especially those of the first oxidation and reduction steps ($E_{1/2}$(+/0) and $E_{1/2}$(0/−), hereafter), provide information on the electronic properties of fullerenes and enable straightforward estimation of the HOMO-LUMO gap. Electrochemical gap (gap_{EC}), defined as the difference between $E_{1/2}$(+/0) and $E_{1/2}$(0/−) values, can be used, along with the optical gap, as a measure of kinetic stability of fullerenes. Redox potentials discussed in this chapter are measured in *o*-dichlorobenzene and referred versus the $Fe(Cp)_2^{+/0}$ couple. We will not distinguish the values obtained by cyclic voltammetry (half-wave potentials, $E_{1/2}$, for reversible processes, and peak potentials for irre-

A.A. Popov (✉)
Leibniz Institute for Solid State and Materials Research,
Helmholtzstraße 20, 01069 Dresden, Germany
e-mail: a.popov@ifw-dresden.de

A.A. Popov (ed.), *Endohedral Fullerenes: Electron Transfer and Spin*,
Nanostructure Science and Technology, DOI 10.1007/978-3-319-47049-8_2

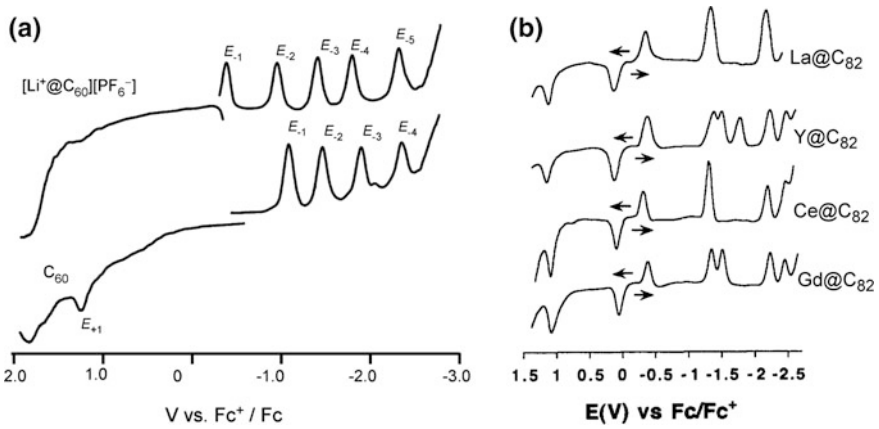

Fig. 2.1 **a** Squarewave voltammetry of the $[Li^+@C_{60}][PF_6^-]$ salt compared to that of fullerene C_{60}; Reproduced with permission from [16]. **b** Squarewave voltammetry of monometallofullerenes $M^{III}@C_{82}$-C_{2v}(9) with trivalent lanthanides measured in *o*-dichlorobenzene. Reproduced with permission from [3]

versible processes) and those determined by pulse method (SWV, DPV). Deviations between such values are usually less than few tens mV, which is not substantial for an overview of electrochemical properties of EMFs.

Fullerenes are known as good electron acceptors and undergo multiple electrochemically reversible single-electron redox processes in solution. Electrochemical studies of C_{60} showed that it is able to accept up to 6 electrons under optimized conditions at reduced temperature [6], whereas three–four reversible reductions steps are usually accessible at room temperature in *o*-dichlorobenzene (*o*-DCB, the most common solvent for electrochemical studies of fullerenes; Fig. 2.1). Similar cathodic behavior is exhibited by higher fullerenes [7–10]. Oxidation of C_{60} and C_{70} fullerenes occurs at relatively high potentials, making it difficult to achieve the reversible process in standard electrochemical studies [11–14]. However, oxidation of many other higher fullerenes (C_{76}, C_{78}, C_{82}, C_{84} etc.) occurs at less positive potentials and usually one or even two oxidation steps can be accessed [8, 9, 15].

Encapsulation of metal atoms and clusters in EMFs can result in more complex redox behavior than that of empty fullerenes. The carbon cage in the EMF molecule can be considered as a special type of π-ligand, similar to those in organometallic complexes (e.g., as in ferrocene). In terms of organometallic electrochemistry, the ligand can be "non-innocent," when it exhibits its own redox activity, or "innocent," when it does not take part in the redox process. In a similar fashion, both the fullerene cage and the endohedral species can exhibit redox activity in EMFs. Figure 2.2 shows two extremes of such redox behavior. In the first case, only the carbon cage is redox-active, meaning that the valence and spin state endohedral species remains intact during electrochemical processes (i.e., fullerene behaves as

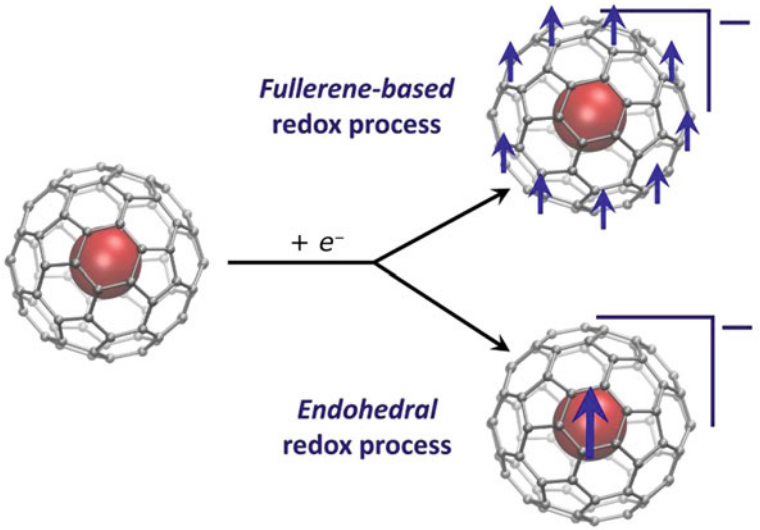

Fig. 2.2 Schematic description of the fullerene-based and endohedral redox processes. In the former, with the surplus charge and spin density are delocalized over the fullerene cage, whereas in the latter the spin state of the endohedral cluster is altered, whereas the fullerene remains intact. Reproduced with permission from [18]

"non-innocent" ligand). In the second case, the endohedral cluster is the redox-active species, whereas the carbon cage merely acts as an inert container, transparent to electrons. In terms of organometallic electrochemistry, here the fullerene cage behaves as an innocent ligand, even though the electron transfer occurs across the metal/π-system interface. This type of electron transfer is described as an endohedral (or *in cavea*) electron transfer process [17, 18]. An obvious, but not always necessary, prerequisite for endohedral redox activity is a suitable energy of the metal-based molecular orbitals (MOs), which should be the frontier MOs (HOMO or LUMO) of the EMF molecule. Experimentally, the endohedral redox processes can be revealed via unexpected redox behavior (e.g., shifted potential when compared to analogous molecules) and/or with the use of spectroelectrochemical methods (such as electron spin resonance or nuclear magnetic resonance spectroelectrochemistry). In EPR spectra of ion-radicals, EMFs with endohedral redox activity often exhibit rich hyperfine structure with large coupling constants, as will be discussed in Chap. 9.

2.2 Monometallofullerenes

In monometallofullerenes (mono-EMFs), metal atoms transfer all valence electrons to the cage. The energies of metal-based electronic states are far from the frontier MOs, and hence HOMO and LUMO are completely localized on the fullerene cage, and redox activity of mono-EMFs is thus determined exclusively by the fullerene cage. As a result, redox properties are not strongly dependent on a particular metal, but are only determined by its valence state (i.e., the number of electrons transferred to the fullerene). Mono-EMFs usually exhibit electrochemically reversible reduction and oxidations.

$Li@C_{60}$ is the only $M^{I}@C_{60}$ EMF produced in sufficient amounts to be studied electrochemically. In a neutral state $Li@C_{60}$ is paramagnetic, and its stable form is the cation $Li^{+}@C_{60}$. Figure 2.1 shows that reduction behavior of $Li^{+}@C_{60}$ is similar to that of pristine C_{60} but with a cathodic shift of all reduction steps by ca 0.6 V [19]. Such a shift can be rationalized taking into account Coulomb interaction of electrons delocalized over the fullerene with the positive charge located in the center of the fullerene. Note that the data in Fig. 2.1 can be also described as that of $Li@C_{60}$. That is, the first reduction potential of $Li^{+}@C_{60}$ is the same as the first oxidation potential of $Li@C_{60}$. If considered this way, $Li@C_{60}$ appears to be easy to oxidize (−0.38 V) and easy to reduce (−0.95 V) due to an unpaired electron delocalized over the cage. The small gap_{EC} of $Li@C_{60}$, 0.47 V, is a common feature for paramagnetic mono-EMFs.

$M^{II}@C_{2n}$ mono-EMFs (M^{II} = Ca, Sm, Eu, Tm, Yb; $2n$ = 74–94) are diamagnetic molecules with closed-shell electronic structure. Their redox properties are comparable to those of higher empty fullerenes in that they are reasonably good

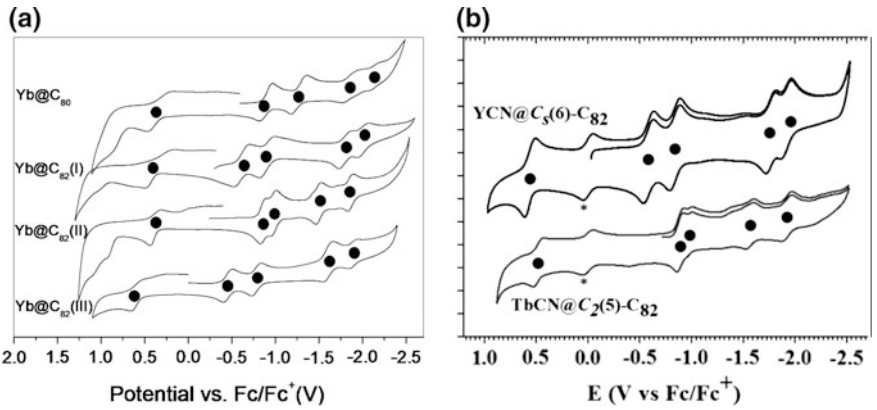

Fig. 2.3 **a** Cyclic voltammetry curves of $Yb@C_{80}$ and three isomers of $Yb@C_{82}$ (isomer I is $C_s(6)$, isomer II is $C_2(5)$, isomer III is $C_{2v}(9)$); reproduced with permission from [21]; **b** Cyclic voltammetry of $YbCN@C_{82}$-$C_s(6)$ and $TbCN@C_{82}$-$C_2(5)$; reproduced with permission from [29]. *Asterisk* denotes oxidation of ferrocene, *dots* denote EMF redox processes. Note similar redox potentials of $Yb@C_{82}$ and $(Tb,Y)CN@C_{82}$ EMFs with the same carbon cage isomers

electron acceptors (the first reduction potentials are more positive than −1 V), but at the same time their oxidation potentials are usually within the reach of standard conditions [20–28]. EC gaps of $M^{II}@C_{2n}$ EMFs typically exceed 1 V (Fig. 2.3b). Comparison of redox potentials of several Yb and Sm mono-EMFs with C_{82} cages (Table 2.1) shows that variation of redox potential due to the carbon cage isomerism can exceed 0.5 V. At the same time, variation of the metal has a minor influence (typically less than 0.05 V).

The redox behavior of $M^{III}@C_{2n}$ mono-EMFs (M^{III} is Sc, Y, La, Ce, Pr, Nd, Gd–Er, Lu) is substantially different from that of empty fullerenes and $M^{II}@C_{2n}$ EMFs because $M^{III}@C_{2n}$ molecules are radicals with an unpaired electron delocalized over the fullerene cage. As a result, their gap_{EC} values are usually close to

Table 2.1 Redox potentials of monometallofullerenes, their derivatives, and cyano-clusterfullerenes

EMF	Ox-II	Ox-I	Red-I	Red-II	Red-III	Gap_{ec}	References
C_{60}-I_h(1)		1.21	−1.12	−1.50	−1.95	2.33	[3]
C_{82}-C_2(3)		0.72	−0.69	−1.04	−1.58	1.41	[9]
$Li^+@C_{60}$-I_h(1)			−0.39	−0.98	−1.44		[19]
Yb@C_{82}-C_2(5)	0.90	0.38	−0.86	−0.98		1.24	[21]
Sm@C_{82}-C_2(5)		0.42	−0.84	−1.01	−1.51	1.26	[27]
Yb@C_{82}-C_s(6)		0.34	−0.62	−0.92	−1.81	0.96	[21]
Sm@C_{82}-C_{3v}(7)		0.56	−0.94	−1.25	−1.79	1.50	[26]
Yb@C_{82}-C_{2v}(9)		0.61	−0.46	−0.78		1.07	[21]
Sm@C_{82}-C_{2v}(9)		0.52	−0.42	−0.77	−1.60	0.94	[26]
TbCN@C_{82}-C_2(5)		0.50	−0.88	−0.97	−1.55	1.38	[29]
YCN@C_{82}-C_s(6)		0.56	−0.59	−0.84	−1.76	1.15	[30]
TbCN@C_{82}-C_s(6)		0.55	−0.59	−0.84	−1.77	1.14	[31]
TbCN@C_{82}-C_{2v}(9)		0.55	−0.46	−0.81	−1.78	1.01	[31]
La@C_{82}-C_s(6)	1.08	−0.07	−0.47	−1.40	−2.01	0.40	[5]
La@C_{82}-C_{2v}(9)	1.07	0.07	−0.42	−1.37	−1.53	0.49	[1]
Ce@C_{82}-C_{2v}(9)	1.08	0.08	−0.41	−1.41	−1.53	0.49	[3]
Gd@C_{82}-C_{2v}(9)	1.08	0.09	−0.39	−1.38	−2.22	0.48	[3]
Lu@C_{82}-C_{2v}(9)		0.11	−0.38	−1.17	−1.54	0.49	[32]
La@C_{82}-cycloadducts							
La@$C_{82}(Mes_2Si)_2CH_2$		−0.07	−0.50	−1.71	−1.75	0.43	[33]
La@C_{82}Ad	1.01	−0.07	−0.50	−1.71	−1.75	0.43	[34]
La@$C_{82}[C(COOEt)_2]$		0.08	−0.28	−1.19	–	0.36	[35]
La@C_{82}-R							
La@$C_{82}(C_6H_5CH_2)$-a		0.25	−0.68	−1.02	−1.21	0.93	[36]
La@$C_{82}(C_6H_5CH_2)$-d		0.15	−1.05	−1.15	−1.81	1.20	[36]
La@$C_{82}[CBr(COOEt)_2]$-A	0.85	0.38	−0.66	−1.31	−1.47	1.04	[35]

All values are measured in *o*-dichlorobenzene solution and are referred versus $Fe(Cp)_2^{+/0}$ pair

0.5 V, and such EMFs are normally easier to reduce or oxidize than empty fullerenes (Fig. 2.1, Table 2.1) [1, 3, 32, 37, 38]. The most studied are $M^{III}@C_{82}$ EMFs with $C_{2v}(9)$ cage isomer. Comparison of the redox potentials of such EMF with several different metals (Table 2.1) shows the values remain almost constant within the whole lanthanide row. Isomerism of the cage again has stronger influence: for instance, $C_s(6)$ isomer of $La@C_{82}$ is easier to oxidize than $C_{2v}(9)$ isomer by 0.14 V [5]. Interestingly, $M^{II}@C_{82}$-$C_{2v}(9)$ and $M^{III}@C_{82}$-$C_{2v}(9)$ have very similar reduction potentials, but oxidation potentials of $M^{III}@C_{82}$-$C_{2v}(9)$ are ca 0.4 V less positive.

Chemical derivatization of EMFs can significantly modify their redox potentials. Comparison of the redox properties of several derivatives of $La@C_{82}$-$C_{2v}(9)$ (Table 2.1) shows that derivatives can be divided into two groups. Cycloaddition (Diels–Alder, Bingel–Hirsch, bis-sylilation) does not change the paramagnetic state of the molecule, and hence the small gap_{EC} remains in the derivatives [33–35]. Redox potentials can be either positively or negatively shifted versus those of the parent $La@C_{82}$, depending on the addition site and the nature of the addend. On the other hand, when $La@C_{82}$ is functionalized by the groups forming single bond to the carbon cage (such as benzyl $C_6H_5CH_2$ or malonate $CBr(COOEt)_2$), the number of added groups is odd, and the carbon cage of the derivative becomes diamagnetic [35, 36]. Transformation of the open-shell structure of $La@C_{82}$ molecule to the closed-shell structure of the derivative strongly affects redox potentials. Oxidation potentials are shifted positively, whereas reduction potentials are shifted in the negative direction, and resulting gap_{EC} values usually exceed 1 V. Position of the group(s) on the cage may have strong influence on the exact values, as can be seen from comparison of the two isomer of $La@C_{82}(C_6H_5CH_2)$ with the difference of $E_{1/2}(0/-)$ values of 0.37 V [36].

2.3 Dimetallofullerenes

Whereas mono-EMFs show only cage-based redox properties, the encapsulation of two normally trivalent metal atoms (such as Sc, Y, La, and some lanthanides) within an EMF results in dimetallofullerenes (di-EMFs) with endohedral redox activity. The reason for the metal-based redox activity of $M_2@C_{2n}$ is the metal–metal bonding orbital (Figs. 2.4 and 2.5), which has a comparable energy to the frontier MOs of the carbon cage and can be either the HOMO or the LUMO of the di-EMF molecule.

Whether the M–M bonding MO in a given di-EMF involves the HOMO or the LUMO depends on the relative energies of the cage frontier MO and the energy of the metal–metal bonding orbital. It was shown that the energy of the M–M bonding MO in EMFs is similar to the lowest energy valence MO of the free metal dimer, which usually has $(ns)\sigma_g^2$ character [39]. The energy of the $(ns)\sigma_g^2$ orbital in the M_2 dimer correlates with the $ns^2(n-1)d^1 \rightarrow ns^1(n-1)d^2$ excitation energy of the free metal atom, and therefore this excitation energy to a large extent determines the

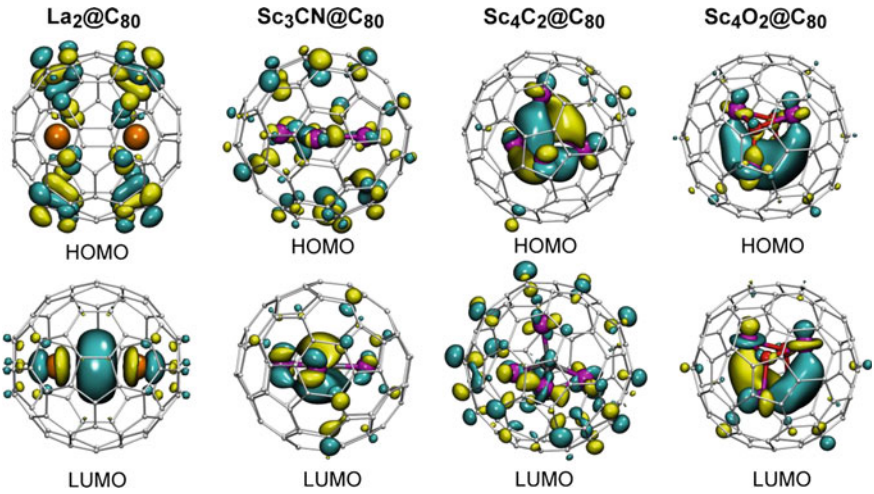

Fig. 2.4 DFT-computed frontier molecular orbitals (HOMO and LUMO) of several endohedral metallofullerenes with C_{80}-$I_h(7)$ carbon cage (formal charge of the cage −6): $La_2@C_{80}$, $Sc_3CN@C_{80}$, $Sc_4C_2@C_{80}$, and $Sc_4O_2@C_{80}$. Metals atoms are *orange* (La) or *magenta* (Sc)

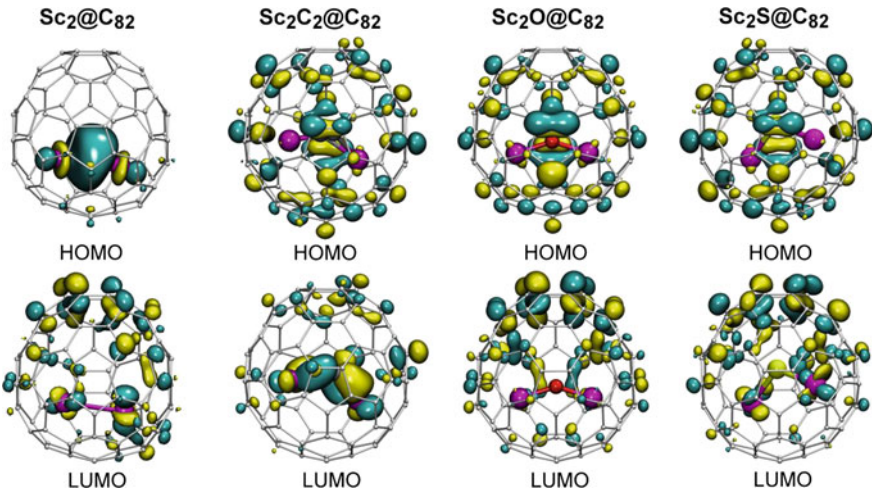

Fig. 2.5 DFT-computed frontier molecular orbitals (HOMO and LUMO) of several endohedral metallofullerenes with C_{82}-$C_{3v}(8)$ carbon cage (formal charge of the cage −4): $Sc_2@C_{82}$, $Sc_2C_2@C_{82}$, $Sc_2O@C_{82}$, and $Sc_2S@C_{82}$. Scandium atoms are *magenta*, oxygen is *red*, sulfur is *yellow*

valence state of metal atoms in di-EMFs. For instance, $ns^2(n-1)d^1 \rightarrow ns^1(n-1)d^2$ excitation energies increase in the row La–Sc/Y–Lu as 0.33–1.43/1.36–2.34 eV, respectively, and the $(ns)\sigma_g^2$ MO in corresponding M_2 dimers are stabilized in the row La_2–Sc_2/Y_2–Lu_2. As a result, in di-EMFs, La is always trivalent (the La–La

bonding MO is the LUMO in $(La^{3+})_2@C_{2n}^{6-}$), Lu tends to adopt a divalent state (the Lu–Lu bonding MO is the HOMO or even below the HOMO level in $(Lu^{2+})_2@C_{2n}^{4-}$), whereas the valence state of Sc, Y, and other lanthanides is more sensitive to the energy of the carbon cage MOs [39]. Figures 2.4 and 2.5 show frontier MOs of $La_2@C_{80}$-I_h(7) and $Sc_2@C_{82}$-C_{3v}(8) with M–M bonding LUMO and HOMO, respectively.

Since the La–La bonding MO is the LUMO in La-based di-EMFs (Fig. 2.4), reduction of a $La_2@C_{2n}$ molecules should be an endohedral redox process, whereas oxidation is expected to be fullerene-based. Electrochemical studies of $La_2@C_{2n}$ ($2n$ = 72, 78, 80) showed that these EMFs exhibit 2–3 reversible single-electron reduction steps and are relatively easy to reduce (Fig. 2.6). For instance, the first reduction of $La_2@C_{80}$-I_h occurs at −0.31 V [4]. Likewise, the first reductions of $La_2@C_{72}$ (−0.68) [40], $La_2@C_{78}$ (−0.40 V) [41], and $La_2@C_{80}$-D_{5h} (−0.36 V) [42] are also significantly more positive than for EMFs with fullerene-based reduction (Table 2.2). The first reduction potentials of analogous Ce di-EMFs are systematically more negative by up to 0.13 V (see Table 2.2) [42–45].

Metal-based reduction of $La_2@C_{80}$ is proved EPR spectroscopy. The M–M bonding orbitals in di-EMFs have hybrid *spd* character with large *s*-contribution. When such orbital is populated by a single electron, a hyperfine structure with large metal-based hyperfine constants can be expected in EPR spectra of corresponding anion-radicals. The EPR spectrum of the $[La_2@C_{80}$-$I_h]^{-}$ radical-anion exhibits a huge ^{139}La coupling constant of 364 G, which proves predominant localization of the spin density on the metals (see Chap. 8 for more details on EPR spectroscopy of $La_2@C_{80}$ anion and derivatives) [48]. Another indication of the endohedral reduction in La and Ce di-EMFs is the difference between the first and the second reduction potentials. For a cage-based redox process, the difference between the first and second reduction (or oxidation) steps is usually within 0.4–0.5 V range if the process is based on the same cage MO (see Table 2.1 for reduction potentials of C_{60}, C_{82} etc.). An endohedral redox process results in a much larger potential difference for the consequent redox steps, since these steps are either based on the

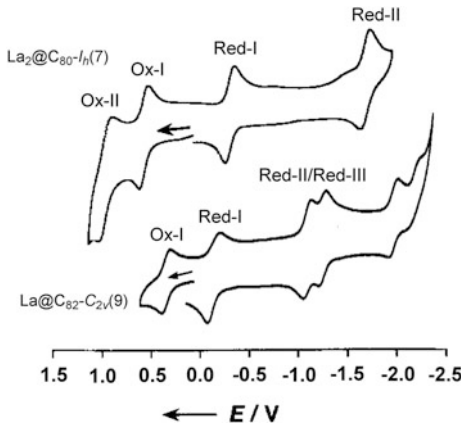

Fig. 2.6 Cyclic voltammetry of $La_2@C_{80}$-I_h(7) compared to that of $La@C_{82}$-C_{2v}(9); scan rate 20 mV/s, *o*-dichlorobenzene solution. Reproduced with permission from [4] and [1]

Table 2.2 Redox potentials of representative di-EMFs

EMF	Ox-II	Ox-I	Red-I	Red-II	Red-III	Gap_{EC}	References
$La_2@C_{72}$-D_2(10611)	0.75	0.24	−0.68	−1.92	–	0.92	[40]
$Ce_2@C_{72}$-D_2(10611)	0.82	0.18	−0.81	−1.86		0.99	[43]
$La_2@C_{76}$-C_s(17490)	0.65	0.21	−0.63	−1.83	−2.40	0.84	[46]
$La_2@C_{78}$-D_{3h}(5)	0.62	0.26	−0.40	−1.84	−2.28	0.66	[41]
$Ce_2@C_{78}$-D_{3h}(5)	0.79	0.25	−0.52	−1.86	−2.23	0.77	[44]
$La_2@C_{80}$-D_{5h}(6)	0.78	0.22	−0.36	−1.72		0.58	[42]
$Ce_2@C_{80}$-D_{5h}(6)	0.66	0.20	−0.40	−1.76	−2.16	0.60	[42]
$La_2@C_{80}$-I_h(7)	0.95	0.56	−0.31	−1.72		0.87	[4]
$Ce_2@C_{80}$-I_h(7)	0.95	0.57	−0.39	−1.71	–	0.96	[45]
			–	–	–		
$Gd_2@C_{79}N$-I_h(7)		0.51	−0.96	−1.98	–	1.45	[47]

cluster MO (which has a much higher on-site Coulomb interaction than in the fullerene cage) or affect different MOs (one on the cluster and one on the carbon cage). The difference between the first and the second reduction potentials in all $La_2@C_{2n}$ and $Ce_2@C_{2n}$ di-EMFs is in the range of 1.23–1.44 V (Table 2.2), which is much larger than for consequent cage-based reductions.

Substituting one carbon atom for a nitrogen atom in $M_2@C_{80}$-I_h results in paramagnetic azafullerenes $M_2@C_{79}N$ (M = Y, Tb, Gd) [47, 49]. The SOMO of these molecules is an M–M bonding MO similar to the anion radicals of $La_2@C_{80}$. In line with this MO analysis, the ESR study of $Y_2@C_{79}N$ revealed an enhanced ^{89}Y hfc constant of 81.2 G (see Chap. 7 for more details on EPR spectra of $Y_2@C_{79}N$) [49]. An electrochemical study of $Gd_2@C_{79}N$ showed that its first reduction potential, −0.96 V, is not as positive as that of $La_2@C_{80}$-I_h. However, the second reduction of $Gd_2@C_{79}N$ is found at −1.98 V, i.e., the difference between the first and second reduction potentials is as large as 1.02 V. Based on redox potentials and DFT calculations, which predict a Gd_2-localized LUMO, the first reduction of $Gd_2@C_{79}N$ can be tentatively assigned to an endohedral reduction. Interestingly, the M–M bonding SOMO in $M_2@C_{79}N$ is "buried" below the cage-based MOs, and hence oxidation of $M_2@C_{79}N$ should be a cage-based process [47, 49]. Indeed, the oxidation potential of $Gd_2@C_{79}N$ is +0.51 V, which is close to the value of $La_2@C_{80}$-I_h (+0.56) with cage-based oxidation.

Metal-based oxidation and fullerene-based reduction can be expected for di-EMFs with metal-based HOMO, such as $M_2@C_{82}$ di-EMFs (M = Sc, Lu, Y etc.). The information on electrochemical behavior of such di-EMFs is rather limited, and the proof of the metal-based oxidation is not as straightforward as for La-based di-EMFs. The most illustrative in such situation is comparison with redox behavior of other EMFs, with the same carbon cage in the same formal charge state. Figure 2.5 compares frontier MOs of $Sc_2@C_{82}$, $Sc_2C_2@C_{82}$, $Sc_2O@C_{82}$, and $Sc_2S@C_{82}$, all with the C_{82}-C_{3v}(8) cage isomer in the formal charge of −4. It can be seen that in the whole series, the HOMO of $Sc_2@C_{82}$ is localized on the endohedral

scandium dimer, whereas the HOMO of other clusterfullerenes is mainly fullerene based. At the same time, the LUMO of $Sc_2@C_{82}$ as well as that of $Sc_2O@C_{82}$ and $Sc_2S@C_{82}$ is localized on the fullerene cage. Based on the MO analysis, similar reduction potentials can be expected for $Sc_2@C_{82}$ and clusterfullerenes due to the same nature of electron-accepting orbital, whereas oxidation potential of $Sc_2@C_{82}$ should be more negative than in other clusterfullerenes because of the higher energy of the Sc–Sc bonding MO than that of the cage MO. Indeed, oxidation potential of $Sc_2@C_{82}$-C_{3v}(8), +0.05 V [50], is considerably less positive than that of $Sc_2C_2@C_{82}$ (+0.47 V) [51], $Sc_2O@C_{82}$ (+0.54 V) [52], or $Sc_2S@C_{82}$ (+0.52 V) [53], whereas their reduction potentials are more similar (Table 2.3). Definitive proof of the Sc-based oxidation of $Sc_2@C_{82}$ is provided by EPR spectrum of its radical-cation with a huge ^{45}(Sc) hfc constant of 199 G (see Chap. 9).

Since the energy of the $(ns)\sigma_g^2$ orbital in the M_2 dimer and hence the energy of the M–M bonding orbital in di-EMFs correlates with the $ns^2(n-1)d^1 \rightarrow ns^1(n-1)d^2$ excitation energy of the free metal atom, the oxidation potentials of di-EMFs with M–M bonding HOMO can be expected to vary with the metal. In

Table 2.3 Redox potentials of representative EMFs with 4-fold charged cluster (oxide, sulfide, and carbide clusterfullerenes and dimetallofullerenes)

EMF	Ox-II	Ox-I	Red-I	Red-II	Red-III	Gap_{ec}	References
$Sc_2O@C_{70}$-C_2(7892)	0.55	0.10	−1.36	−1.80	−	1.46	[54]
$Sc_2S@C_{70}$-C_2(7892)	0.65	0.14	−1.44	−1.87	−1.99	1.58	[55]
$Sc_2C_2@C_{72}$-C_S(10528)		0.41	−1.19	−1.54	−1.75	1.60	[56]
$Sc_2S@C_{72}$-C_S(10528)	1.21	0.64	−1.14	−1.53	−2.24	1.78	[57]
$Sc_2O@C_{76}$-T_d(1)		0.32	−0.91	−1.40	−1.65	1.23	[58]
$Sc_2C_2@C_{80}$-C_{2v}(5)		0.41	−0.74	−1.33	−	1.15	[59]
$Sc_2O@C_{80}$-C_{2v}(5)	0.56	0.24	−0.89	−1.48	−1.75	1.13	[60]
$Er_2@C_{82}$-C_s(6)	0.65	0.02	−1.01	−1.31	−	1.03	[61]
$Lu_2@C_{82}$-C_s(6)	0.74	0.34	−1.00	−1.32	−1.77	1.34	[61]
$Sc_2C_2@C_{82}$-C_s(6)	0.64	0.42	−0.93	−1.30	−	1.35	[62]
$Sc_2O@C_{82}$-C_s(6)	0.72	0.35	−0.96	−1.28	−1.74	1.31	[53]
$Sc_2S@C_{82}$-C_s(6)	0.65	0.39	−0.98	−1.12	−1.73	1.37	[53]
$Er_2S@C_{82}$-C_s(6)		0.39	−1.01	−1.85	−2.21	1.40	[61]
$Sc_2@C_{82}$-C_{3v}(8)		0.05	−1.10	−		1.15	[50]
$Er_2@C_{82}$-C_{3v}(8)		0.13	−1.14	−1.41	−1.83	1.27	[61]
$Lu_2@C_{82}$-C_{3v}(8)	0.95	0.50	−1.16	−1.46	−1.77	1.66	[61]
$Sc_2C_2@C_{82}$-C_{3v}(8)	0.93	0.47	−0.94	−1.15	−1.60	1.41	[51]
$Sc_2O@C_{82}$-C_{3v}(8)	1.09	0.54	−1.17	−1.44	−1.55	1.71	[52]
$Sc_2S@C_{82}$-C_{3v}(8)	0.96	0.52	−1.04	−1.19	−1.63	1.56	[53]
$Er_2S@C_{82}$-C_{3v}(8)	0.88	0.51	−0.98	−1.21	−1.70	1.49	[61]
$Sc_2C_2@C_{82}$-C_{2v}(9)	0.67	0.25	−0.74	−0.96		0.99	[63]
$Sc_2C_2@C_{86}$-C_{2v}(9)		0.47	−0.84	−1.11	−1.63	1.31	[64]

All values are measured in *o*-dichlorobenzene solution and are referred versus $Fe(Cp)_2^{+/0}$ pair

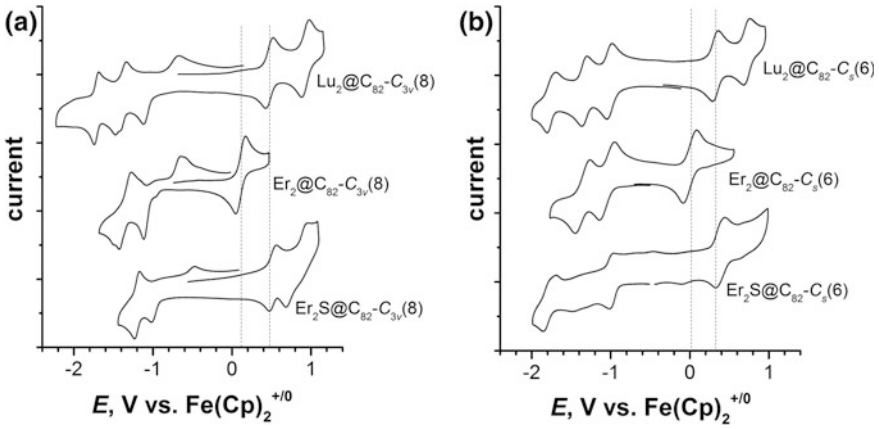

Fig. 2.7 **a** Cyclic voltammetry of a series of $Lu_2@C_{82}$, $Er_2@C_{82}$, and $Er_2S@C_{82}$, all with C_{82}-C_{3v}(8) cage isomer; **b** isomeric EMFs with C_{82}-C_s(6) cage. Scan rate 100 mV/s, *o*-dichlorobenzene solution

particular, Lu with the lowest energy of this MO should have the highest oxidation potential. Indeed, whereas reduction potentials of $Er_2@C_{82}$ and $Lu_2@C_{82}$ are close to each other and to that of $Er_2S@C_{82}$, their oxidation potentials are substantially different: $Er_2@C_{82}$ is easier to oxidize than $Lu_2@C_{82}$ by 0.36 V (see Fig. 2.7 and Table 2.3 for comparison of cyclic voltammetry curves and redox potentials). Furthermore, the first oxidation potential of $Lu_2@C_{82}$ is close to that of $Er_2S@C_{82}$, which has fullerene-based oxidation. Similar redox properties are observed for C_{82}-C_s(6) cage isomers of these EMFs (Table 2.3). Thus, due to the metal-based redox process, oxidation potentials of di-EMFs are subject to significant variation in dependence on the encapsulated metal.

2.4 Clusterfullerenes

Electrochemical properties of clusterfullerenes (CFs), i.e., endohedral metallofullerenes whose endohedral species comprise metal and nonmetal atoms, may vary significantly in dependence on the formal charges and spatial localization of frontier MOs. Typical formal charges of endohedral cluster are +2 (cyano-clusterfullerenes with single metal, such as $YCN@C_{82}$ and $TbCN@C_{82}$), +4 (carbide CFs $M_2C_2@C_{2n}$, sulfide CFs $M_2S@C_{2n}$, oxide CFs $M_2O@C_{2n}$), or +6 (nitride CFs $M_3N@C_{2n}$, methano-CF $Sc_3CH@C_{80}$, μ^3-carbido CF $M_2TiC@C_{80}$, oxide CF $Sc_4O_2@C_{80}$, and many other EMFs, see Chap. 1 for a complete list).

Clusterfullerenes with formal charge +2. Redox potentials of $MCN@C_{82}$ are similar to those of corresponding cage isomers of mono-EMFs with divalent metals, $M^{II}@C_{82}$ with corresponding cage isomers (Refs. [29–31], see Table 2.1). This

close similarity indicates that the fullerene cage has the dominant contribution to HOMO and LUMO of these clusterfullerenes. Reduction and oxidation steps are usually reversible, similar to those of mono-EMFs (Fig. 2.3).

Oxide, carbide, and sulfide clusterfullerenes with fourfold charged clusters. For clusterfullerenes with +4 charge, the most typical cages are C_{82}-$C_{3v}(8)$ and C_{82}-$C_s(6)$. Figure 2.5 compares frontier MOs of the carbide CF $Sc_2C_2@C_{82}$, oxide CF $Sc_2O@C_{82}$, and sulfide CF $Sc_2S@C_{82}$, all with the C_{82}-$C_{3v}(8)$ cage isomers. In these molecules, the HOMOs are predominantly localized on the carbon cage, which results in close values of their oxidation potentials at 0.47–0.54 V (Table 2.3), significantly more positive that the first oxidation potential of the di-EMF $Sc_2@C_{82}$ with the same carbon cage isomer but metal-based HOMO. The LUMO distributions of these CFs show a subtle balance between the fullerene and the cluster: the LUMO of $Sc_2O@C_{82}$ is localized on the fullerene, the LUMO of $Sc_2S@C_{82}$ is also largely fullerene-based but with noticeable metal contributions, whereas the LUMO of $Sc_2C_2@C_{82}$ is predominantly localized on the carbide cluster. The first reduction potentials follow the order of the cage contribution to the LUMOs: the most negative value is reported for $Sc_2O@C_{82}$ (−1.17 V) [52] followed by $Sc_2S@C_{82}$ (−1.04 V) [53] and then by $Sc_2C_2@C_{82}$ (−0.94 V) [51]. Similar correlations between redox potential and endohedral cluster can be revealed for analogous CFs with C_{82}-$C_s(6)$ cages (Table 2.3). Remarkably, CFs with C_{82}-$C_{3v}(8)$ and $C_s(6)$ cages exhibit different electrochemical behavior in terms of reversibility: whereas EMFs with $C_s(6)$ cage have reversible reductions, those of EMFs with $C_{3v}(8)$ cage are electrochemically irreversible (Fig. 2.7). In fact, low electrochemical reversibility of reduction and oxidation steps is rather common for CFs, and we will return to this point below, in the discussion of nitride CFs.

Information on electrochemical properties of carbide, sulfide, or oxide CFs with other cage sizes is rather limited. All data available at the moment of mid 2016 are compiled in Table 2.3. Typically, compounds exhibit reasonably high gap_{EC} (exceeding 1 V) and irreversible reduction behavior. When different clusters are available within the same fullerene cage, redox potential are usually rather similar.

Nitride Clusterfullerenes. Figure 2.8 shows frontier MOs of nitride clusterfullerenes $Sc_3N@C_{80}$-I_h and $Y_3N@C_{80}$-I_h. $Y_3N@C_{80}$ with fullerene-based HOMO and LUMO represents a typical situation for a majority of nitride CFs. On the contrary, high electronegativity of Sc results in rather unique situation for $Sc_3N@C_{80}$, whose LUMO has large cluster contribution. Furthermore, there is a structural flexibility caused by rotation of the M_3N cluster inside the cage, which also affects spatial localization of the LUMO. Computational studies showed that in the neutral state, $Sc_3N@C_{80}$ and $Y_3N@C_{80}$ both have C_3-symmetric configuration, in which metal atoms are facing hexagons in quasi-η^6 manner (albeit somewhat shifted from the center of hexagons to pentagon/hexagon edges) [65]. In the anionic state, C_{3v}-symmetric configuration with metals η^2-coordinating centers of pentagon/hexagon edges is preferred for $Sc_3N@C_{80}$. Importantly, rotation of the cluster in $Sc_3N@C_{80}$ results in dramatic redistributing of the LUMO: in the C_3-conformer, the orbitals is equally shared between the cage and the cluster, whereas in the C_{3v}-conormer the cluster has dominant contribution to the LUMO

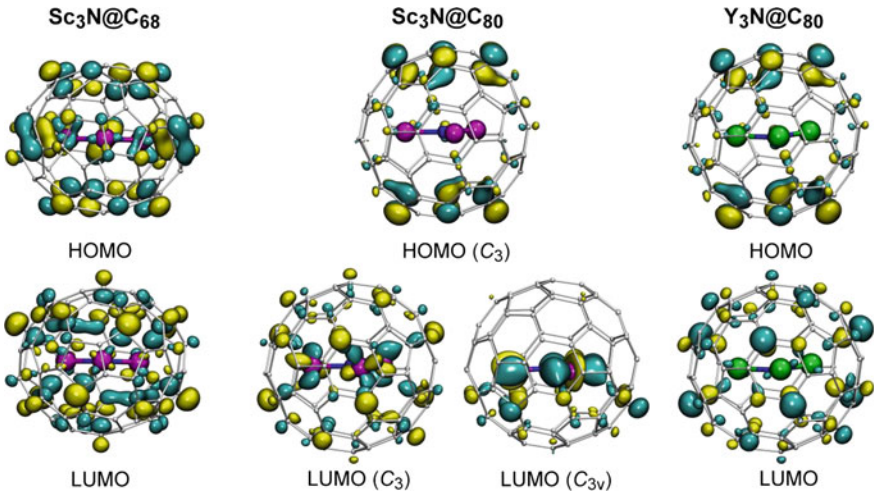

Fig. 2.8 Frontier molecular orbitals (HOMO and LUMO) of $Sc_3N@C_{68}$-D_3(6140), $Sc_3N@C_{80}$-I_h(7), and $Y_3N@C_{80}$-I_h(7). The LUMO of $Sc_3N@C_{80}$ is show for two conformers: C_3-conformer is the lowest energy for the neutral state, whereas C_{3v}-conformer is the lowest energy for the anion. For $Y_3N@C_{80}$, C_3-conformer has the lowest energy in both neutral and anionic states

(Fig. 2.8). For $Y_3N@C_{80}$, C_{3v}-conformer is much higher in energy due to the larger size of the cluster, and the C_3-conformer with dominant cage contribution to the LUMO remains the ground state for both neutral and anionic forms.

Based on the spatial distribution of frontier orbitals, one can expect similar anodic and different cathodic behavior of $Sc_3N@C_{80}$ and $Y_3N@C_{80}$. Indeed, both EMFs have similar oxidation potential near 0.6 V, but noticeably different reduction potentials, −1.26 V for $Sc_3N@C_{80}$ and −1.41 for $Y_3N@C_{80}$. $Sc_3N@C_{80}$ is reduced mainly at its endohedral cluster, as was also proved by the EPR spectrum of its anion radical [66]. $Y_3N@C_{80}$ is reduced predominantly at its fullerene cage, and its reduction potential can be considered as a reference point for cage-based reduction in EMFs with C_{80}-I_h cage. Not only reduction potential of the two nitride CFs is different, they also have a different reversibility of the process. At modest voltammetric scan rates both EMFs exhibit electrochemically irreversible but chemically reversible reduction. That is, reduction is followed by a chemical reaction, which can be reversed at positive potentials so that pristine EMF is restored. However, in $Sc_3N@C_{80}$ electrochemical reversibility of the first reduction can be achieved at scan rates of several V/s (Fig. 2.9), whereas in $Y_3N@C_{80}$ and many other nitride CFs the first reduction remains electrochemically irreversible up to the scan rates of at least 70 V/s [67, 68].

The nature of the follow-up reaction in reduction of nitride CFs was debated for quite a long time. Reaction with solvent or decomposition of nitride CFs upon reduction can be excluded by chemical reversibility of the reduction. Hypothesis of dimerization of anion-radicals was proposed in 2008 based on ESR

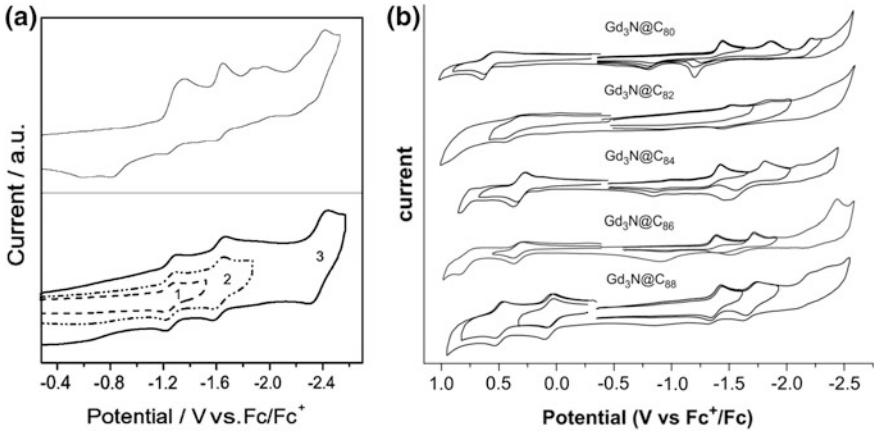

Fig. 2.9 **a** Cyclic voltammograms of $Sc_3N@C_{80}$-I_h(7) in *o*-dichlorobenzene at scan rates of 100 mV/s in the upper panel, and 6 V/s (1), 10 V/s (2), and 20 V/s (3) in the lower panel. The different scan rates for each reduction reflect the scan rate necessary to achieve full electrochemical reversibility. Reproduced with permission from [69]; **b** cyclic voltammograms of the $Gd_3N@C_{2n}$ family measured in *o*-dichlorobenzene at 100 mV/s. Reproduced from Ref. [70]

spectroelectrochemical studies of $Sc_3N@C_{68}$ [71]. Although radical-anion and radical-cation could be detected by ESR upon reduction and oxidation, respectively, integral intensity of the radical-anion was an order of magnitude lower in the same experimental conditions. This fact indicated that the main product of the reduction was diamagnetic, and reversible formation of the single-bonded $(Sc_3N@C_{68}^{-})_2$ dimer was proposed. DFT computations showed that dimerization of anion radicals of nitride CFs is more energetically favorable than that of empty fullerenes [72]. Recently, a strong argument in favor of dimerization hypothesis was provided by an observation of $(Sc_3N@C_{80}^{-})_2$ dimers in the single-crystal X-ray diffraction study of the anion-radical $Sc_3N@C_{80}^{-}$ crystallized with cryptand [2,2,2] (Na^+) cation [73].

Electrochemical properties of nitride CFs were studied in a lot of details, with many cage sizes and different metals in nitride clusters (Table 2.4). For Sc-based nitride CFs, available cages are C_{68}, C_{78}, two isomers of C_{80}, and C_{82}. Remarkably, $Sc_3N@C_{80}$-I_h has the highest oxidation potential among the series, whereas the first oxidation potential of another isomer, $Sc_3N@C_{80}$-D_{5h}, is 0.25 V more negative. The difference in oxidation potentials of the two isomers was used by Echegoyen et al. for their facile separation [69]. Redox behavior of $Sc_3N@C_{68}$ was studied especially carefully, and cage-based reduction and oxidation were confirmed by EPR spectroelectrochemistry in agreement with DFT-predicted localization of HOMO and LUMO on the carbon cage (Fig. 2.8) [71].

For medium size nitride clusters, such as exemplified by Gd_3N in Table 2.4 and Fig. 2.9, cages from C_{78} to C_{88} were studied electrochemically (note that C_{78} and C_{82} cage isomers for Sc_3N and Gd_3N are different). Even larger cages, up to C_{96}, were studied for large lanthanides such as La or Ce. Redox properties of all these

Table 2.4 Redox potentials of representative nitride clusterfullerenes

EMF	Ox-II	Ox-I	Red-I	Red-II	Red-III	Gap_{ec}	References
$Sc_3N@C_{68}$-D_3(6140)	0.85	0.33	−1.45	−2.05		1.78	[74]
$Sc_3N@C_{78}$-D_{3h}(5)	0.68	0.21	−1.56	−1.91		1.77	[75]
$Sc_3N@C_{80}$-D_{5h}(6)		0.34	−1.33			1.68	[76]
$Sc_3N@C_{80}$-I_h(7)	1.09	0.59	−1.26	−1.62	−2.37	1.85	[69]
$Sc_3N@C_{82}$-C_{2v}(9)	0.37	0.00	−1.35	−1.52	−1.78	1.35	[77]
$Gd_3N@C_{78}$-C_2(22010)	1.00	0.47	−1.53	−1.89		2.00	[78]
$Gd_3N@C_{80}$-I_h(7)		0.58	−1.44	−1.86	−2.13	2.02	[79]
$Gd_3N@C_{82}$-C_s(39663)		0.38	−1.53	−1.87		1.91	[70]
$Gd_3N@C_{84}$-C_s(51365)		0.32	−1.37	−1.76		1.69	[79]
$Gd_3N@C_{86}$-D_3(17)		0.33	−1.39	−1.72		1.82	[70]
$Gd_3N@C_{88}$-D_2(35)	0.45	0.05	−1.39	−1.71		1.49	[80]
$Ce_3N@C_{88}$-D_2(35)	0.63	0.08	−1.30	−1.57		1.38	[81]
$Ce_3N@C_{92}$-T(92)		0.32	−1.48	−1.64		1.80	[82]
$Ce_3N@C_{96}$-D_2(186)	0.67	0.18	−1.50	−1.84		1.68	[83]

All values are measured in *o*-dichlorobenzene solution and are referred versus $Fe(Cp)_2^{+/0}$ pair

NCFs are to some extent similar to the properties of $M_3N@C_{80}$-I_h(7). The first (and sometimes also the second) oxidation step is usually reversible, while reduction steps are electrochemically irreversible. Variation of redox potentials of different NCFs with the same carbon cage hardly exceeds 0.1 V and is usually smaller (except for Sc). With variation of the carbon cages, reduction potentials also do not show significant changes, whereas oxidation potentials seem to shift cathodically with the increase of the cage size, so that the electrochemical gap tends to be smaller for larger cages, from 2.0 V for $M_3N@C_{78}$-C_2(22010) to ca 1.7 V for $M_3N@C_{96}$. Redox properties of $M_3N@C_{88}$-D_2(35) NCFs fall apart from the others in that it is the only group of NCFs which exhibits electrochemically reversible reductions and the most cathodically shifted oxidation near +0.05 V.

Derivatives of $Sc_3N@C_{80}$. Chemical derivatization (such as cycloaddition or radical addition) and its influence on electrochemical properties of nitride CFs has been studied very extensively, especially for $Sc_3N@C_{80}$-I_h. Table 2.5 compares redox potentials of several derivatives of the latter. There are at least two factors which determine how redox potentials are changed in the derivative when compared to the pristine EMFs. First, topology of the π-system of the fullerene is changed in its derivatives, which substantially influence the energies of frontier MOs. Second, the energies of the frontier MOs can be influenced by an electron-donating or electron-withdrawing nature of the addends.

Highly symmetrical C_{80}-I_h fullerene has only two types of bonds at which cycloaddition can occur: pentagon/hexagon edge (denoted as [5,6]) and hexagon/hexagon edge (denoted as [6,6]). Besides, the sigma-bond at the functionalized edge can remain intact (then the cycloadduct is "closed") or it can be broken (then the cycloadduct is "open"). Thus, four types of cycloadducts can be

Table 2.5 Redox potentials of $Sc_3N@C_{80}$-I_h derivatives

$Sc_3N@C_{80}$ derivative	Ox-II	Ox-I	Red-I	Red-II	Red-III	Gap_{EC}	References
$Sc_3N@C_{80}$-I_h(7)	1.09	0.59	−1.26	−1.62	−2.37	1.85	[69]
[5,6]-closed $Sc_3N@C_{80}$-pyrrolidine (N-ethyl)		0.62	−1.18	−1.57	−2.29	1.80	[84]
[5,6]-closed $Sc_3N@C_{80}$-Diels–Alder		0.62	−1.16	−1.54	−2.26	1.78	[84]
[5,6]-closed $Sc_3N@C_{80}(C_6H_4)$	0.92	0.34	−1.11	−1.50	−2.21	1.45	[85]
[6,6]-closed $Sc_3N@C_{80}(C_6H_4)$	0.83	0.42	−1.08	−1.29	−2.23	1.50	[85]
[6,6]-open $Sc_3N@C_{80}$-methano-$C(CO_2Et)_2$	1.08	0.56	−1.34	−1.90	−2.22	1.90	[86]
[6,6]-open $Sc_3N@C_{80}$-methano-(CHPh)	1.08	0.50	−1.48	−2.01	−2.40	1.98	[87]
[6,6]-open $Sc_3N@C_{80}$-PCBM	1.15	0.52	−1.33	−1.91	–	1.85	[88]
1,4-$Sc_3N@C_{80}(Mes_2Si)_2CH_2$		0.08	−1.45	–	–	1.53	[89]
1,4-$Sc_3N@C_{80}(CF_3)$	1.66	0.43	−1.16	−1.65	−2.14	1.59	[90]
$Sc_3N@C_{80}(CF_3)_4$		0.55	−1.06	−1.55	−2.03	1.61	[91]
$Sc_3N@C_{80}(CF_3)_{10}$		0.86	−0.84	−1.32	−2.11	1.70	[91]
$Sc_3N@C_{80}(CF_3)_{12}$		0.95	−0.95	−1.38	−1.98	1.90	[91]

All values are measured in *o*-dichlorobenzene solution and are referred versus $Fe(Cp)_2^{+/0}$ pair

expected for $Sc_3N@C_{80}$-I_h: [5,6]-open, [5,6]-closed, [6,6]-open, and [6,6]-closed. Electrochemical data is available for three of them, whereas [5,6]-open cycloadducts (which are very rare) have not been studied by electrochemistry so far. [5,6]-closed adducts are the most abundant products of cycloaddition to $Sc_3N@C_{80}$ in Prato or Diels–Alder reactions. Remarkably, they exhibit reversible reductions (as opposed to electrochemically irreversible reductions of pristine $Sc_3N@C_{80}$) [84, 85]. In all three [5,6]-closed adducts listed in Table 2.5, the first reduction is more positive than that of $Sc_3N@C_{80}$. Oxidation potential is virtually not affected by the addend. [6,6]-closed adducts also exhibit reversible reduction behavior, and their reduction potentials are slightly more positive than in analogous [5,6]-closed adducts, as can be concluded from the comparison of two isomers of $Sc_3N@C_{80}(C_6H_4)$ benzoadducts [85]. [6,6]-open adducts (such as those obtained in Bingel–Hirsch reaction or PCBM-like-derivatives of $Sc_3N@C_{80}$) exhibit distinctly different electrochemical behavior: their reductions are irreversible and occur at more negative potentials than in $Sc_3N@C_{80}$.

Reaction of $Sc_3N@C_{80}$ with two bulky radical groups (such CF_3 or benzyl) or its bis-silylation result in 1,4-addition to one of the fullerene hexagons. Comparison of two derivatives with 1,4-addition pattern, $Sc_3N@C_{80}(CF_3)_2$ and $Sc_3N@C_{80}(Mes_2Si)_2CH_2$ (Mes = mesityl), shows how the electronic properties of the addends can affect redox potentials [89, 90]. Strongly electron-donating $(Mes_2Si)_2CH_2$ shifts reduction and oxidation potentials negatively with respect to the $Sc_3N@C_{80}$ values, whereas electron-withdrawing CF_3 groups move redox

potentials positively [89, 90]. As a result, the difference of the first reduction potentials of the two derivatives (which is solely due to the electron-donating/withdrawing effects) is as large as 0.29 V. Note that both derivatives exhibit reversible reduction steps. Interestingly, multiple CF_3 addition shifts the first reduction potential further in the positive direction up to $Sc_3N@C_{80}(CF_3)_{10}$ ($E_{1/2}(0/-) = -0.84$ V), whereas for $Sc_3N@C_{80}(CF_3)_{12}$ the effect is reversed ($E_{1/2}(0/-) = -0.95$ V), presumably because saturation of the π-system outweighs the electron-withdrawing effect of CF_3 groups [91].

Mixed-metal nitride clusterfullerenes with electroactive metals. Nitride clusterfullerenes provide a convenient platform for creating redox-active endohedral cluster via formation of the mixed-metal clusters with redox-active metals. Three such metals were incorporated in nitride CFs so far: cerium, titan, and vanadium.

Ce is different from all other lanthanides in that its Ce^{IV} valence state is accessible and known for a plethora of inorganic and organometallic compounds, and redox potential of the Ce^{IV}/Ce^{III} couple can vary in a broad range [92]. However, redox behavior of Ce-based mono- and di-EMFs as well as Ce_3N-nitride CFs was found to be very similar to that of La-counterparts, suggesting that Ce^{III} in EMFs is electrochemically inert. The first indication that endohedral Ce can be redox active was obtained in 2010 with isolation of $CeLu_2N@C_{80}$-I_h [93]. Its first oxidation potential at 0.01 V was ca 0.6 V more negative than expected for a fullerene-based oxidation in $M_3N@C_{80}$-I_h nitride CF, which was interpreted as an oxidation of endohedral Ce^{III}. DFT computational study also showed that removal of the $4f^1$ electron from Ce is more energetically favorable (i.e., gives lower ionization potential) than removal of an electron from the fullerene cage.

In a follow-up study, Sc and Y were chosen to vary the size of the endohedral cluster in the $CeM_2N@C_{80}$ series (Shannon's radii of Sc^{3+}, Lu^{3+}, and Y^{3+} ions are 0.745, 0.86, and 0.90 Å, respectively) [94]. Figure 2.10a shows cyclic voltammograms of three $CeM_2N@C_{80}$-I_h NCFs compared to $PrSc_2N@C_{80}$-I_h (the latter was chosen as a reference because of the close ionic radii of Ce^{3+}, 1.01 Å, and Pr^{3+}, 0.99 Å). Whereas cathodic behavior with the first reduction near −1.36 V is similar for all four EMFs, their anodic behavior is quite different (Table 2.6). $CeM_2N@C_{80}$ compounds exhibit one reversible oxidation step whose potential varies from –0.07 V for $CeY_2M@C_{80}$ to +0.33 V for $CeSc_2N@C_{80}$. The latter is still 0.31 V more negative than the oxidation potential of $PrSc_2N@C_{80}$, hence indicating a Ce-based redox process. Compelling evidence of the endohedral oxidation of Ce^{III} in $CeM_2N@C_{80}$-I_h NCFs was provided by NMR spectroscopy of the $CeM_2N@C_{80}^+$ cations obtained by chemical oxidation (Fig. 2.10b). The NMR study showed that cations are diamagnetic, which is possible only in case of endohedral $Ce^{III} \rightarrow Ce^{IV}$ oxidation (cage-based oxidation would produce radicals with non-detectable NMR signals). The metal dependence of the oxidation potential can be explained by a buildup of an inner strain in the $CeM_2N@C_{80}$ row with increasing the cluster size from $CeSc_2N$ to CeY_2N. The strained is caused by the limited interior space inside the C_{80}-I_h cage, and the increase of the ionic radius of M^{3+} in the Sc → Lu → Y series makes the corresponding $CeM_2N@C_{80}$ more

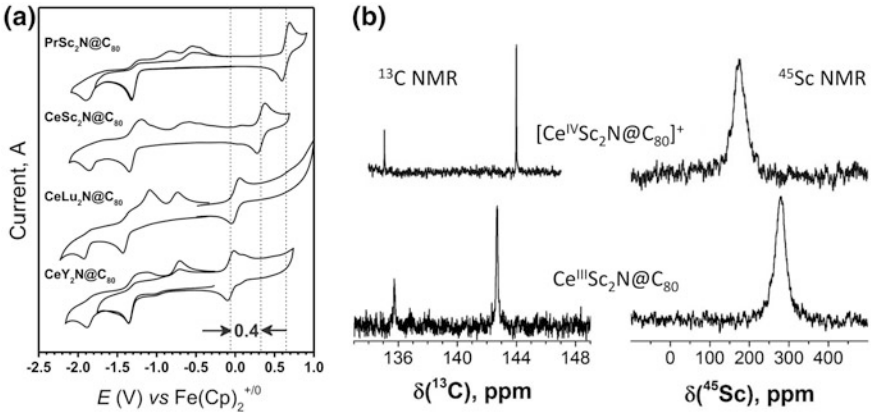

Fig. 2.10 **a** Cyclic voltammetry $PrSc_2N@C_{80}$-I_h(7) and $CeM_2N@C_{80}$-I_h(7) (M = Sc, Lu, and Y) (scan rate 100 mV/s, *o*-dichlorobenzene solution). Strong negative shift of the oxidation potential on coming from $PrSc_2N@C_{80}$ (fullerene-based oxidation) to $CeSc_2N@C_{80}$ (Ce-based oxidation) is observed. Further negative shift in the $CeM_2N@C_{80}$ series is caused by the increased *inner strain* with the increase of the metal size. **b** ^{13}C and ^{45}Sc NMR spectra of pristine and oxidized $CeSc_2N@C_{80}$ in *o*-dichlorobenzene solution. Based on the data from [94]

prone to oxidation as a way to release the strain (ionic radius of Ce^{4+}, 0.87 Å, is considerably smaller than that of Ce^{3+}). Therefore, the oxidation potential of $CeM_2N@C_{80}$-I_h shifts to more negative values for larger M^{3+} ions.

The concept of the strain-driven Ce^{IV}/Ce^{III} endohedral redox couple was further developed in the study of $Ce_xM_{3-x}N@C_{2n}$ nitride CFs with different cages and cluster compositions (x = 1, 2; M = Sc or Y; $2n$ = 78, 84, 86, 88) [95]. Redox potentials were determined for 12 Ce-containing NCFs and compared to the non-Ce analogs. On the basis of the shift of the oxidation potential and an increased difference between the first and second oxidation potentials, an endohedral $Ce^{III} \rightarrow Ce^{IV}$ redox process at the first oxidation step was proven for $CeSc_2N@C_{78}$, $CeY_2N@C_{84}$, and $Ce_2YN@C_{86}$. Less confidently, an endohedral oxidation of Ce was also proposed for $Ce_2ScN@C_{86}$, $CeY_2N@C_{86}$, and $Ce_3N@C_{88}$. For cages larger than C_{80}, the cluster-induced strain is weaker than for the C_{80}-I_h cage, whereas cage oxidation potentials are below those for $M_3N@C_{80}$-I_h. Thus, the preference of an endohedral Ce or a fullerene-based oxidation at the first anodic step depends on whether the inner strain is high enough to render a Ce-based oxidation below the oxidation potential of the fullerene cage. It is thus possible that varying the cluster composition can switch the oxidation mechanism.

Titanium and vanadium do not form nitride CFs on their own, but can be incorporated into the nitride CF by a mixed-metal approach. In particular, titan was encapsulated as $TiSc_2N@C_{80}$ and $TiY_2N@C_{80}$, whereas vanadium formed $VSc_2N@C_{80}$ and $V_2ScN@C_{80}$ [96–98]. Comparison of the redox potentials of Ti- and V-containing nitride CFs to those of $Y_3N@C_{80}$ (Table 2.6) shows that their electrochemical properties are largely determined by the transition metals. These

Table 2.6 Redox potentials of selected endohedral metallofullerenes with C_{80}-I_h cage

EMF	Ox-II	Ox-I	Red-I	Red-II	Red-III	Gap_{EC}	References
$Y_3N@C_{80}$-I_h(7)		0.64	−1.41	−1.83		2.05	[84]
$La_2@C_{80}$-I_h(7)	0.95	0.56	−0.31	−1.72	−2.13	0.87	[4]
$Sm_3@C_{80}$-I_h(7)	0.78	0.30	−0.83	−1.88		1.13	[108]
$Sc_3N@C_{80}$-I_h(7)	1.09	0.59	−1.26	−1.62	−2.37	1.85	[69]
$Sc_3CH@C_{80}$-I_h(7)		0.67	−1.21	−1.53	−2.28	1.88	[100]
$Sc_3CN@C_{80}$-I_h(7)		0.60	−1.05	−1.68		1.65	[102]
$Sc_3C_2@C_{80}$-I_h(7)		−0.03	−0.50	−1.64	−1.84	0.47	[109]
$Sc_2TiC@C_{80}$-I_h(7)		0.66	−0.67	−1.51	−1.66	1.33	[106]
$Lu_2TiC@C_{80}$-I_h(7)	1.10	0.63	−0.87	−1.53		1.50	[105]
$Dy_2TiC@C_{80}$-I_h(7)		0.61	−0.97	−1.62	−1.87	1.58	[107]
$Sc_2TiC_2@C_{80}$-I_h(7)		0.53	−0.76	−1.01	−1.96	1.26	[106]
$Dy_2TiC_2@C_{80}$-I_h(7)		0.47	−1.14	−1.58	−2.29	1.61	[107]
$TiSc_2N@C_{80}$-I_h(7)		0.16	−0.94	−1.58		1.10	[99]
$TiY_2N@C_{80}$-I_h(7)		0.00	−1.11	−1.79		1.11	[96]
$VSc_2N@C_{80}$-I_h(7)		0.44	−0.42	−0.66	−1.33	0.86	[98]
$V_2ScN@C_{80}$-I_h(7)		0.60	−0.77	−2.38	–	1.37	[98]
$CeY_2N@C_{80}$-I_h(7)		−0.07	−1.36	−1.88		1.30	[94]
$CeLu_2N@C_{80}$-I_h(7)		0.01	−1.39	−1.88		1.40	[110]
$CeSc_2N@C_{80}$-I_h(7)		0.33	−1.31	−1.83		1.64	[94]
$Sc_4O_2@C_{80}$-I_h(7)	0.79	0.00	−1.10	−1.73		1.10	[101]
$Sc_4C_2@C_{80}$-I_h(7)		0.01	−1.53	−1.97		1.54	[103]
$Sc_4C_2H@C_{80}$-I_h(7)		0.20	−0.87	−1.68	−1.95	1.07	[103]

All values are measured in *o*-dichlorobenzene solution and are referred versus $Fe(Cp)_2^{+/0}$ pair

nitride CFs are paramagnetic and have Ti or V in the formal oxidation state 3+, which is subject to reduction and oxidation within the window of potentials defined by the oxidation and reduction of the fullerene cage. Oxidation of $V_2ScN@C_{80}$ at +0.60 V is the only process which cannot be reliably assigned to the cage or transition metal. Remarkably, Ti- and V-based redox processes in nitride CFs are electrochemically reversible (Fig. 2.11).

Other clusterfullerenes with 6-fold charged cage. For many clusterfullerenes with sixfold charged cluster, C_{80}-I_h cage isomer is the most abundant, or even the only cage isolated in sufficient amounts for electrochemical studies. Comparison of redox potentials of these EMFs to the first oxidation and reduction potentials of $Y_3N@C_{80}$-I_h (Table 2.6) shows that the cluster-based reduction is typical for all of them. All $E_{1/2}(0/-)$ values in Table 2.6 are substantially more positive than −1.41 V reported for $Y_3N@C_{80}$-I_h and span rather broad range, from −1.21 V for $Sc_3CH@C_{80}$ [100] to −0.31 V in the aforementioned $La_2@C_{80}$-I_h [4]. At the same time, the first oxidation potentials for a majority of clusterfullerenes listed in Table 2.6 is close to +0.6 V, which is an indication of the fullerene-based process. Several exception exist though, in which oxidation is also a cluster-based process:

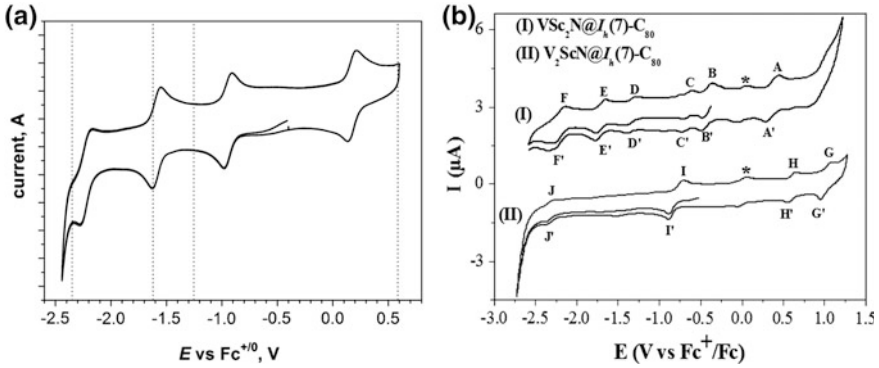

Fig. 2.11 **a** Cyclic voltammogram of Ti-nitride cluster fullerene $TiSc_2N@C_{80}$-I_h(7) (scan rate 20 mV/s, *o*-dichlorobenzene solution), vertical bars denote redox potentials of $Sc_3N@C_{80}$-I_h(7); reproduced with permission from [99]. **b** Cyclic voltammetry of V-nitride clusterfullerenes $VSc_2N@C_{80}$-I_h(7) and $V_2ScN@C_{80}$-I_h(7) (scan rate 100 mV/s, *o*-dichlorobenzene solution); *asterisks* denote redox potential of ferrocene, *block letters* marks redox processes of EMFs. Reproduced with permission from [98]

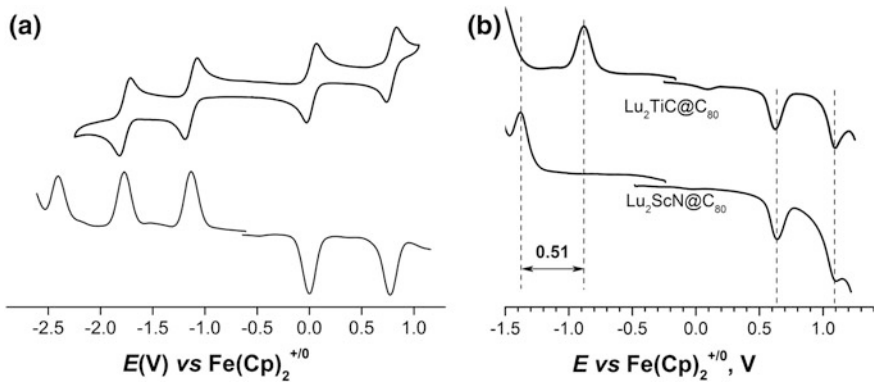

Fig. 2.12 **a** Cyclic voltammetry (*upper trace*) and squarewave voltammetry (*lower trace*) of $Sc_4O_2@C_{80}$-I_h(7) (scan rate 20 mV/s, *o*-dichlorobenzene solution); reproduced with permission from [104]; **b** comparison of the squarewave voltammograms of isoelectronic $Lu_2TiC@C_{80}$-I_h(7) and $Lu_2ScN@C_{80}$-I_h(7) in *o*-dichlorobenzene solution. Note almost identical oxidation potentials and a 0.51 V difference for the reduction potentials

Typical examples are $Sc_4C_2@C_{80}$, $Sc_4O_2@C_{80}$, $M_2TiC_2@C_{80}$ (M = Sc, Dy). Low oxidation potentials are also reported for paramagnetic clusterfullerenes ($Sm_3@C_{80}$, $Sc_3C_2@C_{80}$, or $Sc_4C_2H@C_{80}$), but in this case deviation from a typical values cannot serve as an indication of the cluster-based redox process. Importantly, cluster-based reductions are usually electrochemically reversible.

An overview of the frontier MOs of representative clusterfullerenes with C_{80}-I_h cage, including $La_2@C_{80}$, $Sc_3CN@C_{80}$, $Sc_4C_2@C_{80}$, and $Sc_4O_2@C_{80}$, is given in

Fig. 2.4; frontier MOs of nitride CFs $Sc_3N@C_{80}$-I_h and $Y_3N@C_{80}$-I_h are shown in Fig. 2.8 as discussed above. Spatial localization of the HOMOs and LUMOs in these compounds can again serve as a guide to the experimentally measured redox potentials. For instance, both HOMO and LUMO of $Sc_4O_2@C_{80}$ are predominantly localized on the Sc_4O_2 cluster. Experimentally, $Sc_4O_2@C_{80}$ exhibits reversible reduction and oxidation at 0.00 and −1.10 V (Fig. 2.12), respectively, which is far from the values expected for the fullerene-based redox processes [101]. Indeed, EPR spectroelectrochemistry proved localization of the spin density on the cluster in radical-anion and radical-cation of $Sc_4O_2@C_{80}$ [101]. In $Sc_3CN@C_{80}$, the LUMO is localized on the cluster, and its first reduction potential at −1.05 V is much more positive than the reference cage value of ca −1.4 V. On the contrary, HOMO is largely localized on the cage, and the first oxidation potential of $Sc_3CN@C_{80}$, 0.60 V, is in the range of the values for cage-based oxidation [102]. On the contrary, $Sc_4C_2@C_{80}$ has its HOMO localized on the Sc_4C_2 cluster, and its first oxidation potential is 0.01 V, whereas the LUMO has large cage component, and the first reduction of $Sc_4C_2@C_{80}$ occurs at quite rather negative potential of −1.53 V [103]. Note that in some cases frontier MOs have mixed character with equally considerable contributions from the cluster and the cage (HOMO of $Sc_3NC@C_{80}$, LUMO of $Sc_4C_2@C_{80}$). It can be understood so that the cage and the cluster MOs have equal energies, and hence they are efficiently "hybridized". In such cases, redox potentials of EMFs are usually close to those for EMFs with fullerene-based redox processes.

A special case of *in cavea* electrochemistry is a found in a series of Ti-based carbide CFs with the formulae $M_2TiC@C_{80}$-I_h, where M is Sc, Y, or lanthanides

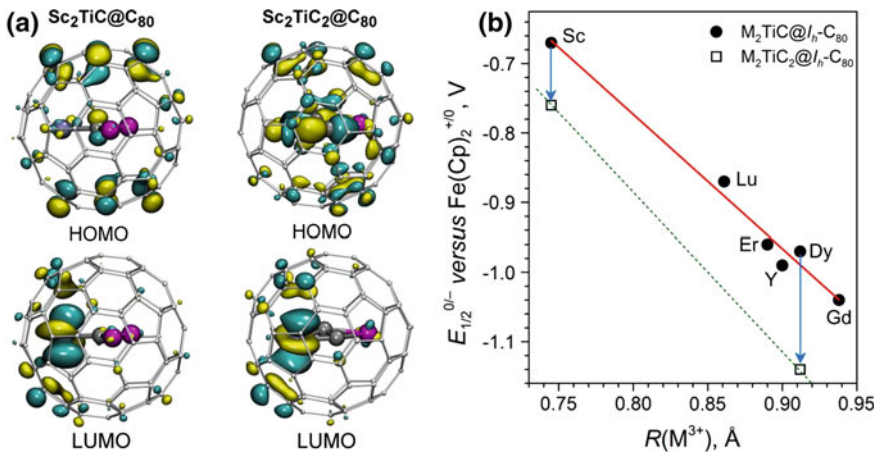

Fig. 2.13 **a** Frontier molecular orbitals of $Sc_2TiC@C_{80}$-I_h(7) and $Sc_2TiC_2@C_{80}$-I_h(7). **b** Dependence of the first reduction potentials in $M_2TiC@C_{80}$-I_h(7) and $M_2TiC_2@C_{80}$-I_h(7) molecules on the ionic radius of M^{3+}. Vertical *blue arrows* mark the shift of the reduction potentials caused by replacement of single central carbon atom by a C_2 unit. Reproduced with permission from [106]

from Gd to Lu [105–107]. $M_2TiC@C_{80}$ carbide CF is isostructural and isoelectronic to $M_2ScN@C_{80}$ nitride CF, and certain similarity in their electronic properties can be expected. Indeed, the HOMO of $M_2TiC@C_{80}$ is essentially a fullerene-based orbital, and hence oxidation potential of all $M_2TiC@C_{80}$ EMFs is close to 0.6 V similar to those of $M_2ScN@C_{80}$ nitride CFs. However, the LUMO of $M_2TiC@C_{80}$ is localized predominantly on the Ti atom (Fig. 2.13a), and the first reduction of $M_2TiC@C_{80}$ EMFs can be thus described as an endohedral Ti^{IV}/Ti^{III}-redox couple with considerably more positive reduction potential than that of $M_2ScN@C_{80}$ (Fig. 2.12b). Interestingly, reduction potentials in the $M_2TiC@C_{80}$ series vary systematically with the ionic radius of M^{3+} (Fig. 2.13b), although these metals are not involved in the electron transfer. The most negative value of −1.04 V is found for $Gd_2TiC@C_{80}$-I_h, whereas the most positive reduction potential of −0.67 V is reported for $Sc_2TiC@C_{80}$-I_h. The reason for such a variation of the Ti^{IV}/Ti^{III}-redox potential in different $M_2TiC@C_{80}$ EMFs is rooted in the inner strain, similar to the situation discussed above for Ce-based nitride CFs. Ionic radius of Ti^{III}, 0.67 Å, is much larger than that of Ti^{IV}, 0.61 Å, and hence the size of the cluster is increased in the reduced state. When the cluster is already rather large (Gd_2TiC), further increase of its size builds up a significant strain caused by the limited inner space in the fullerene cage. Thus, a higher energy (and more negative potential) is needed to add an electron to $Gd_2TiC@C_{80}$ when compared to $Sc_2TiC@C_{80}$ with much smaller cluster. The same reasoning can explain reduction potentials of $M_2TiC_2@C_{80}$. Here LUMO is also Ti-based (Fig. 2.13a), but reduction potentials are more negative than in $M_2TiC@C_{80}$ analogs. Obviously, C_2 unit occupies more space than a single carbon atom, and hence size-driven strain is stronger in $M_2TiC_2@C_{80}$.

2.5 Concluding Remarks

Interaction between metals atoms and clusters with carbon-based π-system in endohedral fullerenes result in fascinating diversity of the electronic structures of EMFs, which also reflects in the electrochemical properties of these molecules. Whereas monometallofullerenes exhibit only fullerene-based redox activity, starting from dimetallofullerenes and to more complex clusters, the frontier orbitals can be partially or completely localized on the endohedral species. As a result, the latter undergo electron transfer reactions independently on the carbon cage. Endohedral electrochemistry thus opens the way to unusual bonding and spin states in charged endohedral metallofullerenes.

References

1. Suzuki T, Maruyama Y, Kato T et al (1993) Electrochemical properties of La@C_{82}. J Am Chem Soc 115(23):11006–11007
2. Suzuki T, Maruyama Y, Kato T et al (1995) Electrochemical properties of fullerenolanthanides. Synth Met 70(1–3):1443–1446
3. Suzuki T, Kikuchi K, Oguri F et al (1996) Electrochemical properties of fullerenolanthanides. Tetrahedron 52(14):4973–4982
4. Suzuki T, Maruyama Y, Kato T et al (1995) Electrochemistry and Ab-Initio study of the dimetallofullerene La_2@C_{80}. Angew Chem-Int Edit Engl 34(10):1094–1096
5. Kikuchi K, Nakao Y, Suzuki S et al (1994) Characterization of the isolated Y@C_{82}. J Am Chem Soc 116(20):9367–9368
6. Xie QS, Perezcordero E, Echegoyen L (1992) Electrochemical detection of C_{60}^{6-} and C_{70}^{6-}—enhanced stability of fullerides in solution. J Am Chem Soc 114(10):3978–3980
7. Reed CA, Bolskar RD (2000) Discrete fulleride anions and fullerenium cations. Chem Rev 100(3):1075–1119
8. Zalibera M, Rapta P, Popov AA et al (2009) Charged states of four isomers of C_{84} fullerene: In Situ ESR and Vis-'NIR Spectroelectrochemistry and DFT Calculations. J Phys Chem C 113(13):5141–5149
9. Zalibera M, Popov AA, Kalbac M et al (2008) The extended view on the empty $C_2(3)$-C_{82} fullerene: isolation, spectroscopic, electrochemical, and spectroelectrochemical characterization and DFT calculations. Chem-Eur J 14(32):9960–9967
10. Gao XA, Van Caemelbecke E, Kadish KM (1998) Visible and near-infrared absorption spectra of singly and doubly reduced C_{76} fullerene anions. Electrochem Solid State Lett 1 (5):222–223
11. Xie QS, Arias F, Echegoyen L (1993) Electrochemically-reversible, single-electron oxidation of C_{60} and C_{70}. J Am Chem Soc 115(21):9818–9819
12. Dubois D, Kadish KM, Flanagan S et al (1991) Electrochemical detection of fulleronium and highly reduced fulleride C_{60}^{5-} Ions in solution. J Am Chem Soc 113(20):7773–7774
13. Bruno C, Doubitski I, Marcaccio M et al (2003) Electrochemical generation of C_{60}^{2+} and C_{60}^{3+}. J Am Chem Soc 125(51):15738–15739
14. Webster RD, Heath GA (2001) Voltammetric, EPR and UV-VIS-NIR spectroscopic studies associated with the one-electron oxidation of C_{60} and C_{70} in 1,1′,2,2′-tetrachloroethane containing trifluoromethanesulfonic acid. Phys Chem Chem Phys 3(13):2588–2594
15. Yang YF, Arias F, Echegoyen L et al (1995) Reversible fullerene electrochemistry—correlation with the Homo-Lumo energy difference for C_{60}, C_{70}, C_{76}, C_{78}, and C_{84}. J Am Chem Soc 117(29):7801–7804
16. Okada H, Komuro T, Sakai T et al (2012) Preparation of endohedral fullerene containing lithium (Li@C_{60}) and isolation as pure hexafluorophosphate salt ([Li^+@C_{60}][PF_6^-]). RSC Adv 2(28):10624–10631
17. Popov AA, Dunsch L (2011) Electrochemistry in Cavea: endohedral redox reactions of encaged species in fullerenes. J Phys Chem Lett 2(7):786–794
18. Zhang Y, Popov AA (2014) Transition-metal and rare-earth-metal redox couples inside carbon cages: fullerenes acting as innocent ligands. Organometallics 33(18):4537–4549
19. Aoyagi S, Nishibori E, Sawa H et al (2010) A layered ionic crystal of polar Li@C_{60} superatoms. Nat Chem 2(8):678–683
20. Liu J, Shi Z, Gu Z (2009) The cage and metal effect: spectroscopy and electrochemical survey of a series of Sm-containing high metallofullerenes. Chem-Asian J 4(11):1703–1711
21. Lu X, Slanina Z, Akasaka T et al (2010) Yb@C_{2n} (n = 40, 41, 42): new fullerene allotropes with unexplored electrochemical properties. J Am Chem Soc 132(16):5896–5905
22. Xu JX, Li MX, Shi ZJ et al (2005) Electrochemical survey: the effect of the cage size and structure on the electronic structures of a series of ytterbium metallofullerenes. Chem-Eur J 12(2):562–567

23. Zhang Y, Xu JX, Hao C et al (2006) Synthesis, isolation, spectroscopic and electrochemical characterization of some calcium-containing metallofullerenes. Carbon 44(3):475–479
24. Sun BY, Li MX, Luo HX et al (2002) Electrochemical properties of metallofullerenes and their anions. Electrochim Acta 47(21):3545–3549
25. Kuran P, Krause M, Bartl A et al (1998) Preparation, isolation and characterisation of Eu@C_{74}: the first isolated europium endohedral fullerene. Chem Phys Lett 292(4–6):580–586
26. Hu Z, Hao Y, Slanina Z et al (2015) Popular C_{82} fullerene cage encapsulating a divalent metal ion Sm^{2+}: structure and electrochemistry. Inorg Chem 54(5):2103–2108
27. Xu W, Niu B, Feng L et al (2012) Access to an unexplored chiral C_{82} cage by encaging a divalent metal: structural elucidation and electrochemical studies of Sm@C_2(5)-C_{82}. Chem-Eur J 18(45):14246–14249
28. Hao Y, Feng L, Xu W et al (2015) Sm@C_{2v}(19138)-C_{76}: a non-IPR cage stabilized by a divalent metal ion. Inorg Chem 54(9):4243–4248
29. Liu F, Wang S, Guan J et al (2014) Putting a terbium-monometallic cyanide cluster into the C_{82} fullerene cage: TbCN@C_2(5)-C_{82}. Inorg Chem 53(10):5201–5205
30. Yang S, Chen C, Liu F et al (2013) An improbable monometallic cluster entrapped in a popular fullerene cage: YCN@C_s(6)-C_{82}. Sci Rep 3:1487
31. Liu F, Gao C-L, Deng Q et al (2016) Triangular monometallic cyanide cluster entrapped in carbon cage with geometry-dependent molecular magnetism. J Am Chem Soc 138 (44):14764–14771
32. Wang W, Ding J, Yang S et al (1997) Electrochemical properties of 4f-block metallofullerenes. In: Kadish KM, Ruoff RS (eds) Fullerenes. Recent advances in the chemistry and physics of fullerenes and related materials, vol 4. Electrochemical society, Pennington, pp 417–428
33. Yamada M, Feng L, Wakahara T et al (2005) Synthesis and characterization of exohedrally silylated M@C_{82} (M = Y and La). J Phys Chem B 109(13):6049–6051
34. Maeda Y, Matsunaga Y, Wakahara T et al (2004) Isolation and characterization of a carbene derivative of La@C_{82}. J Am Chem Soc 126(22):6858–6859
35. Feng L, Wakahara T, Nakahodo T et al (2006) The bingel monoadducts of La@C_{82}: synthesis, characterization, and electrochemistry. Chem-Eur J 12(21):5578–5586
36. Takano Y, Yomogida A, Nikawa H et al (2008) Radical coupling reaction of paramagnetic endohedral metallofullerene La@C_{82}. J Am Chem Soc 130(48):16224–16230
37. Popov AA, Yang S, Dunsch L (2013) Endohedral fullerenes. Chem Rev 113(8):5989–6113
38. Yamamoto K (1999) Electrochemical study on electronic structure of mono-lanthanofullerenes of La@C_n (n = 82, 86, and 90). In: Kamat PV, Guldi D, Kadish KM (eds) Fullerenes. Recent advances in the chemistry and physics of fullerenes and related materials, vol 7. Electrochemical Society, Pennington, pp 761–770
39. Popov AA, Avdoshenko SM, Pendás AM et al (2012) Bonding between strongly repulsive metal atoms: an oxymoron made real in a confined space of endohedral metallofullerenes. Chem Commun 48:8031–8050
40. Lu X, Nikawa H, Nakahodo T et al (2008) Chemical understanding of a Non-IPR metallofullerene: stabilization of encaged metals on fused-pentagon bonds in La_2@C_{72}. J Am Chem Soc 130:9129–9136
41. Cao BP, Wakahara T, Tsuchiya T et al (2004) Isolation, characterization, and theoretical study of La_2@C_{78}. J Am Chem Soc 126(30):9164–9165
42. Yamada M, Mizorogi N, Tsuchiya T et al (2009) Synthesis and characterization of the D_{5h} isomer of the endohedral dimetallofullerene Ce_2@C_{80}: two-dimensional circulation of encapsulated metal atoms inside a fullerene cage. Chem-Eur J 15:9486–9493
43. Yamada M, Wakahara T, Tsuchiya T et al (2008) Spectroscopic and theoretical study of endohedral dimetallofullerene having a Non-IPR fullerene cage: Ce_2@C_{72}. J Phys Chem A 112:7627–7631
44. Yamada M, Wakahara T, Tsuchiya T et al (2008) Location of the metal atoms in Ce_2@C_{78} and its bis-silylated derivative. Chem Commun 558–560

45. Yamada M, Nakahodo T, Wakahara T et al (2005) Positional control of encapsulated atoms inside a fullerene cage by exohedral addition. J Am Chem Soc 127(42):14570–14571
46. Suzuki M, Mizorogi N, Yang T et al (2013) $La_2@C_s$(17490)-C_{76}: a new non-IPR dimetallic metallofullerene featuring unexpectedly weak metal-pentalene interactions. Chem-Eur J 19 (50):17125–17130
47. Fu W, Zhang J, Fuhrer T et al (2011) $Gd_2@C_{79}N$: isolation, characterization, and monoadduct formation of a very stable heterofullerene with a magnetic spin state of S = 15/2. J Am Chem Soc 133:9741–9750
48. Kato T (2007) Metal dimer and trimer within spherical carbon cage. J Mol Struct 838(1–3):84–88
49. Zuo T, Xu L, Beavers CM et al (2008) $M_2@C_{79}N$ (M = Y, Tb): isolation and characterization of stable endohedral metallofullerenes exhibiting M…M bonding interactions inside Aza[80]fullerene cages. J Am Chem Soc 130(39):12992–12997
50. Kurihara H, Lu X, Iiduka Y et al (2012) $Sc_2@C_{3v}(8)$-C_{82} *vs.* $Sc_2C_2@C_{3v}(8)$-C_{82}: drastic effect of C_2 capture on the redox properties of scandium metallofullerenes. Chem Commun 48:1290–1292
51. Iiduka Y, Wakahara T, Nakajima K et al (2007) Experimental and theoretical studies of the scandium carbide endohedral metallofullerene $Sc_2C_2@C_{82}$ and its carbene derivative. Angew Chem-Int Edit 46(29):5562–5564
52. Tang Q, Abella L, Hao Y et al (2016) $Sc_2O@C_{3v}(8)$-C_{82}: a missing isomer of $Sc_2O@C_{82}$. Inorg Chem 55(4):1926–1933
53. Mercado BQ, Chen N, Rodriguez-Fortea A et al (2011) The shape of the $Sc_2(\mu_2\text{-S})$ unit trapped in C_{82}: crystallographic, computational, and electrochemical studies of the isomers, $Sc_2(\mu_2\text{-S})@C_s(6)$-$C_{82}$ and $Sc_2(\mu_2\text{-S})@C_{3v}(8)$-$C_{82}$. J Am Chem Soc 133(17):6752–6760
54. Zhang M, Hao Y, Li X et al (2014) Facile synthesis of an extensive family of $Sc_2O@C_{2n}$ (n = 35-47) and chemical insight into the smallest member of $Sc_2O@C_2$(7892)-C_{70}. J Phys Chem C 118(49):28883–28889
55. Chen N, Mulet-Gas M, Li Y-Y et al (2013) $Sc_2S@C_2$(7892)-C_{70}: a metallic sulfide cluster inside a non-IPR C_{70} cage. Chem Sci 4(1):180–186
56. Feng Y, Wang T, Wu J et al (2013) Structural and electronic studies of metal carbide clusterfullerene $Sc_2C_2@C_s$-C_{72}. Nanoscale 5(15):6704–6707
57. Chen N, Beavers CM, Mulet-Gas M et al (2012) $Sc_2S@C_s$(10528)-C_{72}: a dimetallic sulfide endohedral fullerene with a Non-IPR cage. J Am Chem Soc 134(18):7851–7860
58. Yang T, Hao Y, Abella L et al (2015) $Sc_2O@T_d$(19151)-C_{76}: hindered cluster motion inside a tetrahedral carbon cage probed by crystallographic and computational studies. Chem-Eur J 21(31):11110–11117
59. Kurihara H, Lu X, Iiduka Y et al (2011) $Sc_2C_2@C_{80}$ rather than $Sc_2@C_{82}$: templated formation of unexpected $C_{2v}(5)$-C_{80} and temperature-dependent dynamic motion of internal Sc_2C_2 cluster. J Am Chem Soc 133(8):2382–2385
60. Tang Q, Abella L, Hao Y et al (2015) $Sc_2O@C_{2v}(5)$-C_{80}: dimetallic oxide cluster inside a C_{80} fullerene cage. Inorg Chem 54(20):9845–9852
61. Samoylova NA, Avdoshenko SM, Krylov DS et al (2017) Confining the spin between two metal atoms within the carbon cage: Redox-active metal-metal bonds in dimetallofullerenes and their stable cation radicals. Nanoscale doi: 10.1039/C7NR02288C
62. Lu X, Nakajima K, Iiduka Y et al (2011) Structural elucidation and regioselective functionalization of an unexplored carbide cluster metallofullerene $Sc_2C_2@C_s(6)$-C_{82}. J Am Chem Soc 133(48):19553–19558
63. Lu X, Nakajima K, Iiduka Y et al (2012) The long-believed $Sc_2@C_{2v}(17)$-C_{84} is actually $Sc_2C_2@C_{2v}(9)$-C_{82}: unambiguous structure assignment and chemical functionalization. Angew Chem-Int Edit Engl 51(24):5889–5892
64. Chen C-H, Ghiassi KB, Cerón MR et al (2015) Beyond the butterfly: $Sc_2C_2@C_{2v}(9)$-C_{86}, an endohedral fullerene containing a planar, twisted Sc_2C_2 unit with remarkable crystalline order in an unprecedented carbon cage. J Am Chem Soc 137(32):10116–10119

65. Popov AA, Dunsch L (2008) Hindered cluster rotation and ^{45}Sc hyperfine splitting constant in distonoid anion radical $Sc_3N@C_{80}$, and spatial spin charge separation as a general principle for anions of endohedral fullerenes with metal-localized lowest unoccupied molecular orbitals. J Am Chem Soc 130(52):17726–17742
66. Jakes P, Dinse KP (2001) Chemically induced spin transfer to an encased molecular cluster: an EPR study of $Sc_3N@C_{80}$ radical anions. J Am Chem Soc 123(36):8854–8855
67. Yang SF, Zalibera M, Rapta P et al (2006) Charge-induced reversible rearrangement of endohedral fullerenes: electrochemistry of tridysprosium nitride clusterfullerenes $Dy_3N@C_{2n}$ (2n = 78, 80). Chem-Eur J 12(30):7848–7855
68. Tarabek J, Yang S, Dunsch L (2009) Redox properties of mixed lutetium/yttrium nitride clusterfullerenes: endohedral $Lu_xY_{3-x}N@C_{80}$(I) (x = 0-3) compounds. Chem Phys Chem 10 (7):1037–1043
69. Elliott B, Yu L, Echegoyen L (2005) A simple isomeric separation of D_{5h} and I_h $Sc_3N@C_{80}$ by selective chemical oxidation. J Am Chem Soc 127(31):10885–10888
70. Chaur MN, Athans AJ, Echegoyen L (2008) Metallic nitride endohedral fullerenes: synthesis and electrochemical properties. Tetrahedron 64(50):11387–11393
71. Rapta P, Popov AA, Yang SF et al (2008) The charged states of $Sc_3N@C_{68}$: an in situ spectroelectrochemical study of the radical cation and radical anion of a Non-IPR fullerene. J Phys Chem A 112:5858–5865
72. Popov AA, Avdoshenko SM, Cuniberti G et al (2011) Dimerization of radical-anions: nitride clusterfullerenes versus empty fullerenes. J Phys Chem Lett 1592–1600
73. Konarev DV, Zorina LV, Khasanov SS et al (2016) A crystalline anionic complex of scandium nitride endometallofullerene: experimental observation of single-bonded $(Sc_3N@I_h\text{-}C_{80}^-)_2$ dimers. Chem Commun 52:10763–10766
74. Yang SF, Rapta P, Dunsch L (2007) The spin state of a charged non-IPR fullerene: the stable radical cation of $Sc_3N@C_{68}$. Chem Commun 2:189–191
75. Chaur MN, Aparicio-Angles X, Mercado BQ et al (2010) Structural and electrochemical property correlations of metallic nitride endohedral metallofullerenes. J Phys Chem C 114 (30):13003–13009
76. Cai T, Xu LS, Anderson MR et al (2006) Structure and enhanced reactivity rates of the D_{5h} $Sc_3N@C_{80}$ and $Lu_3N@C_{80}$ metallofullerene isomers: the importance of the pyracylene motif. J Am Chem Soc 128(26):8581–8589
77. Wei T, Wang S, Liu F et al (2015) Capturing the long-sought small-bandgap endohedral fullerene $Sc_3N@C_{82}$ with low kinetic stability. J Am Chem Soc 137(8):3119–3123
78. Beavers CM, Chaur MN, Olmstead MM et al (2009) Large metal ions in a relatively small fullerene cage: the structure of $Gd_3N@C_2$(22010)-C_{78} departs from the isolated pentagon rule. J Am Chem Soc 131(32):11519–11524
79. Chaur MN, Melin F, Elliott B et al (2007) $Gd_3N@C_{2n}$ (n = 40, 42, and 44): remarkably low HOMO-LUMO gap and unusual electrochemical reversibility of $Gd_3N@C_{88}$. J Am Chem Soc 129(47):14826–14829
80. Fu W, Zhang J, Champion H et al (2011) Electronic properties and ^{13}C NMR structural study of $Y_3N@C_{88}$. Inorg Chem 50(10):4256–4259
81. Chaur MN, Melin F, Elliott B et al (2008) New $M_3N@C_{2n}$ endohedral metallofullerene families (M = Nd, Pr, Ce; n = 40-53): expanding the preferential templating of the C_{88} cage and approaching the C_{96} cage. Chem-Eur J 14(15):4594–4599
82. Chaur MN, Valencia R, Rodriguez-Fortea A et al (2009) Trimetallic nitride endohedral fullerenes: experimental and theoretical evidence for the $M_3N^{6+}@C_{2n}^{6-}$ model. Angew Chem-Int Edit 48(8):1425–1428
83. Chaur MN, Melin F, Ashby J et al (2008) Lanthanum nitride endohedral fullerenes $La_3N@C_{2n}$ (43 < n < 55): preferential formation of $La_3N@C_{96}$. Chem-Eur J 14(27):8213–8219
84. Cardona CM, Elliott B, Echegoyen L (2006) Unexpected chemical and electrochemical properties of $M_3N@C_{80}$ (M = Sc, Y, Er). J Am Chem Soc 128(19):6480–6485

85. Li F-F, Pinzon JR, Mercado BQ et al (2011) [2 + 2] cycloaddition reaction to $Sc_3N@I_h$-C_{80}. The formation of very stable [5,6]- and [6,6]-adducts. J Am Chem Soc 133(5):1563–1571
86. Pinzon JR, Zuo TM, Echegoyen L (2010) Synthesis and electrochemical studies of bingel-hirsch derivatives of $M_3N@I_h$-C_{80} (M = Sc, Lu). Chem-Eur J 16(16):4864–4869
87. Li F-F, Rodríguez-Fortea A, Peng P et al (2012) Electrosynthesis of a $Sc_3N@I_h$-C_{80} methano derivative from trianionic $Sc_3N@I_h$-C_{80}. J Am Chem Soc 134(17):7480–7487
88. Feng L, Gayathri Radhakrishnan S, Mizorogi N et al (2011) Synthesis and charge-transfer chemistry of $La_2@I_h$-C_{80}/$Sc_3N@I_h$-C_{80}-Zinc porphyrin conjugates: impact of endohedral cluster. J Am Chem Soc 133(19):7608–7618
89. Wakahara T, Iiduka Y, Ikenaga O et al (2006) Characterization of the bis-silylated endofullerene $Sc_3N@C_{80}$. J Am Chem Soc 128(30):9919–9925
90. Popov AA, Shustova NB, Svitova AL et al (2010) Redox-tuning endohedral fullerene spin states: from the dication to the trianion radical of $Sc_3N@C_{80}(CF_3)_2$ in five reversible single-electron steps. Chem-Eur J 16(16):4721–4724
91. Shustova NB, Peryshkov DV, Kuvychko IV et al (2011) Poly(perfluoroalkylation) of metallic nitride fullerenes reveals addition-pattern guidelines: synthesis and characterization of a family of $Sc_3N@C_{80}(CF_3)_n$ (n = 2-16) and their radical anions. J Am Chem Soc 133 (8):2672–2690
92. Piro NA, Robinson JR, Schelter EJ (2014) The electrochemical behavior of cerium(III/IV) complexes: thermodynamics, kinetics and applications in synthesis. Coord Chem Rev 260:21–36
93. Vargová A, Popov A, Rapta P et al (2010) Electrochemical tuning of spin states of the endohedral metallofullerene $Y@C_{82}$ as probed by ESR spectroelectrochemistry. Chem Phys Chem 11(8):1650–1653
94. Zhang Y, Schiemenz S, Popov AA et al (2013) Strain-driven endohedral redox couple Ce^{IV}/Ce^{III} in nitride clusterfullerenes $CeM_2N@C_{80}$ (M = Sc, Y, Lu). J Phys Chem Lett 4:2404–2409
95. Zhang Y, Popov AA, Dunsch L (2014) Endohedral metal or a fullerene cage based oxidation? Redox duality of nitride clusterfullerenes $Ce_xM_{3-x}N@C_{78-88}$ (x = 1, 2; M = Sc and Y) dictated by the encaged metals and the carbon cage size. Nanoscale 6:1038–1048
96. Chen C, Liu F, Li S et al (2012) Titanium/yttrium mixed metal nitride clusterfullerene $TiY_2N@C_{80}$: synthesis, isolation, and effect of the group-III metal. Inorg Chem 51(5):3039–3045
97. Yang S, Chen C, Popov A et al (2009) An endohedral titanium(III) in a clusterfullerene: putting a non-group-III metal nitride into the C_{80}-I_h fullerene cage. Chem Commun 6391–6393
98. Wei T, Wang S, Lu X et al (2016) Entrapping a group-VB transition metal, vanadium, within an endohedral metallofullerene: $V_xSc_{3-x}N@I_h$-C_{80} (x = 1, 2). J Am Chem Soc 138 (1):207–214
99. Popov AA, Chen C, Yang S et al (2010) Spin-flow vibrational spectroscopy of molecules with flexible spin density: electrochemistry, ESR, cluster and spin dynamics, and bonding in $TiSc_2N@C_{80}$. ACS Nano 4(8):4857–4871
100. Junghans K, Rosenkranz M, Popov AA (2016) $Sc_3CH@C_{80}$: selective ^{13}C enrichment of the central carbon atom. Chem Commun 52:6561–6564
101. Popov AA, Chen N, Pinzón JR et al (2012) Redox-active scandium oxide cluster inside a fullerene cage: spectroscopic, voltammetric, electron spin resonance spectroelectrochemical, and extended density functional theory study of $Sc_4O_2@C_{80}$ and its ion radicals. J Am Chem Soc 134(48):19607–19618
102. Wang T-S, Feng L, Wu J-Y et al (2010) Planar quinary cluster inside a fullerene cage: synthesis and structural characterizations of $Sc_3NC@C_{80}$-I_h. J Am Chem Soc 132 (46):16362–16364
103. Feng Y, Wang T, Wu J et al (2014) Electron-spin excitation by implanting hydrogen into metallofullerene: the synthesis and spectroscopic characterization of $Sc_4C_2H@I_h$-C_{80}. Chem Commun 50(81):12166–12168

104. Elliott B, Pykhova AD, Rivera J et al (2013) Spin density and cluster dynamics in $Sc_3N@C_{80}^-$ upon [5,6] exohedral functionalization: an ESR and DFT study. J Phys Chem C 117(5):2344–2348
105. Svitova AL, Ghiassi K, Schlesier C et al (2014) Endohedral fullerene with μ_3-carbido ligand and titanium-carbon double bond stabilized inside a carbon cage. Nat Commun 5:3568. doi:3510.1038/ncomms4568
106. Junghans K, Ghiassi KB, Samoylova NA et al (2016) Synthesis and isolation of the titanium-scandium endohedral fullerenes—$Sc_2TiC@I_h$-C_{80}, $Sc_2TiC@D_{5h}$-C_{80}, and $Sc_2TiC_2@I_h$-C_{80}: metal size tuning of the Ti^{IV}/Ti^{III} redox potentials. Chem-Eur J 22 (37):13098–13107
107. Junghans K, Schlesier C, Kostanyan A et al (2015) Methane as a selectivity booster in the arc-discharge synthesis of endohedral fullerenes: selective synthesis of the single-molecule magnet $Dy_2TiC@C_{80}$ and its congener $Dy_2TiC_2@C_{80}$. Angew Chem-Int Edit Engl 54 (45):13411–13415
108. Xu W, Feng L, Calvaresi M et al (2013) An experimentally observed trimetallofullerene $Sm_3@I_h$-C_{80}: encapsulation of three metal atoms in a cage without a nonmetallic mediator. J Am Chem Soc 135(11):4187–4190
109. Wakahara T, Sakuraba A, Iiduka Y et al (2004) Chemical reactivity and redox property of $Sc_3@C_{82}$. Chem Phys Lett 398:553–556
110. Zhang L, Popov AA, Yang S et al (2010) An endohedral redox system in a fullerene cage: the Ce based mixed cluster fullerene $Lu_2CeN@C_{80}$. Phys Chem Chem Phys 12:7840–7847

Chapter 3
Non-Chromatographic Separation of Endohedral Metallofullerenes by Utilizing Their Redox Properties

Nataliya Samoylova and Steven Stevenson

Abstract Development of non-chromatographic separation for endohedral metallofullerenes has been put forward by many research groups with the goal of more straightforward and less expensive alternatives to HPLC. This chapter describes the progress in non-chromatographic separation approaches utilizing redox properties of EMFs, including electrolysis-assisted separation, separation with the use of redox-active solvents and redox reagents, or the use of complexation of fullerenes with Lewis acids.

3.1 Introduction

The synthesis of endohedral metallofullerenes (EMFs) from the arc-discharge method often produces complex extracts containing dozens of different EMFs and empty fullerenes. These mixtures require some purification technique for isolation of individual fullerenes. Traditionally, chromatography (i.e., high pressure liquid chromatography (HPLC), and recycling HPLC) remains the main separation method of fullerenes. However, HPLC separation is both time and labor intensive, not mentioning the cost of the chromatographic equipment, which can be very high. Therefore, development of non-chromatographic separation approaches has been put forward by many research groups with the goal of more straightforward and less expensive alternatives to HPLC.

Several strategies have been proposed to employ the difference in physicochemical and chemical properties of EMFs and empty fullerenes for their separation. EMFs usually have higher sublimation enthalpies (ΔH_{sub}) than empty

N. Samoylova
Leibniz Institute for Solid State and Materials Research,
Helmholtzstraße 20, 01069 Dresden, Germany

S. Stevenson (✉)
Department of Chemistry, Indiana-Purdue University Fort Wayne (IPFW),
2101 E. Coliseum Blvd, Fort Wayne, IN 46805, USA
e-mail: stevenss@ipfw.edu

A.A. Popov (ed.), *Endohedral Fullerenes: Electron Transfer and Spin*,
Nanostructure Science and Technology, DOI 10.1007/978-3-319-47049-8_3

fullerenes [1]. Their enthalpy differences can be the basis for separation by means of fractional sublimation [2–6]. Dramatic developments in the studies of the chemical properties of EMFs during the last decade revealed strong differences in their chemical reactivity in comparison of empty fullerenes to EMFs [7, 8]. Various reaction types were shown to be useful for fullerene separation. Dorn et al. [9, 10] showed substantial differences in the fullerene reactivity with respect to a Diels–Alder cycloaddition, which was used to develop a scalable chromatography separation using self-packed columns with cyclopentadienyl functionalized resins. Wang [11] demonstrated that dipolar cycloaddition with subsequent retro-reaction and removal of the pyrrolidine group simplified the separation of nitride clusterfullerenes.

Different reactivity with respect to immobilized amines was the basis for the "stir and filter approach," SAFA, developed by Stevenson et al. [12–14]. In this method, fullerene extracts reacted with amine-functionalized silica, which trapped the more reactive fullerenes. The less reactive fullerenes and EMFs remained in solution and upon filtration, remained in the filtrate. Immobilized fullerenes could subsequently be recovered from the spent silica via addition of CS_2 [13]. Variation of the reaction time enabled separation of different types of fullerenes and even their isomers [15].

In this chapter, we focus on non-chromatographic separation procedures by strategically manipulating the redox properties of EMFs. In Sect. 3.2, we review the use of electrolysis at suitable potentials to separate EMFs from empty fullerenes. Section 3.3 describes the use of redox-active solvents and chemical redox reagents. Section 3.4 is devoted to the use of arrays of Lewis acids, whose reactivity with fullerenes and EMFs depends on their oxidation potentials.

3.2 Electrolysis-Assisted Separation

The electrochemical behavior of EMFs can be significantly different from that of empty fullerenes. Therefore selective reduction or oxidation processes can be manipulated to isolate EMFs from fullerene mixtures.

The first electrolysis-based approach of the EMF separation was proposed in 1998 by Diener and Alford [16]. The authors synthesized Gd-EMFs by arc-discharge and used a sublimation technique to separate fullerenes from the carbon soot, followed by dissolution of the sublimate in *o*-xylene. However, a significant part of the sublimate did not dissolve (approximately 20% of Gd-EMF sublimate and 10% of the empty fullerene sublimate). Mass-spectrometric analysis of the initial sublimate indicated the presence of a number of fullerene species which were not detected in the *o*-xylene extract. Thus, some empty fullerenes (the most prominent is C_{74}) and many mono-metallofullerenes (e.g., Gd@C_{60} and Gd@C_{74}) were not soluble, presumably because of their low-band gap facilitating their polymerization.

Electrolysis of the insoluble part suspended in benzonitrile at −1.0 V (vs. $Ag/AgNO_3$ reference) resulted in dissolution of 98% of the particles, and a mass

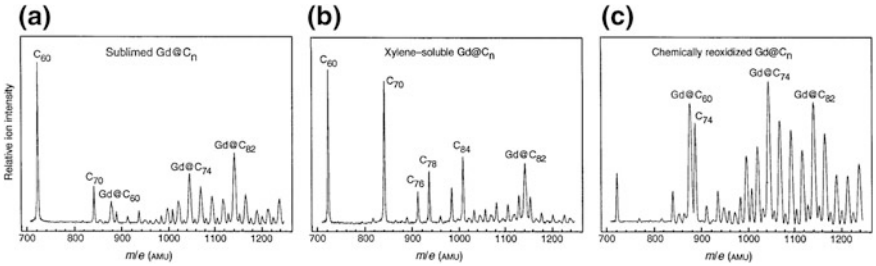

Fig. 3.1 Laser-desorption mass spectra of Gd-metallofullerenes at different process stages. **a** Gd-metallofullerenes sublimed at 750 °C from soot. Elemental analysis indicates that 6–10% of the fullerenes contain Gd. **b** The xylene-soluble portion of the sublimate. Only 4% of the Gd-metallofullerenes are soluble $Gd@C_{82}$. **c** Precipitate obtained by chemical re-oxidation of the solubilized anions with (ferrocenium) PF_6. Reproduced with permission from Ref. [16], © Nature

spectrum of the solution showed the presence of the "missing" empty and metallofullerenes, including C_{74}, $Gd@C_{60}$, and $Gd@C_{74}$. Upon reoxidation at +0.4 V, the insoluble small-band gap empty fullerenes and Gd-EMFs polymerized on the Pt working electrode and were thus separated from the large-band gap fullerenes, which remained in benzonitrile solution. The electrochemical process is reversible, as the film on the electrode can be dissolved in a fresh portion of benzonitrile. Reoxidation of the anions via ferrocenium salt $[Fe(Cp)_2]PF_6$ gave a precipitate containing mainly Gd-EMFs (Fig. 3.1). Importantly, this approach also gives fullerenes which are otherwise not accessible with standard extraction techniques.

In 2004, Akasaka and coworkers developed an effective separation technique based on the electrochemical reduction of fullerene extract in *o*-DCB at the potential of 0.00 V versus saturated calomel electrode (*ca.* −0.60 V vs. $Fe(Cp)_2^{+/0}$ pair) [17]. At this potential, mono- and dimetallofullerenes (such as $La@C_{82}$ and $La_2@C_{80}$) are reduced, whereas empty fullerenes with more negative reduction potentials remain uncharged (Fig. 3.2a). After electrolysis, the solvent was evaporated. Residual fullerenes were treated with a polar acetone/CS_2 mixture (4:1), in which neutral empty fullerenes remained insoluble, while anionic EMFs were dissolved. The filtrate was then reoxidized in acetone/CS_2 solution by the weak acid $CHCl_2COOH$, resulting in precipitation of neutral EMFs.

3.3 Separation with the Use of Redox-Active Solvents and Redox Reagents

Selective reduction or oxidation of EMFs can also be achieved with the help of redox reagents or even the solvent used for the fullerene extraction. Since the early studies of EMFs, extraction with *N*-containing solvents (e.g., *N,N*-dimethylformamide [19–22], pyridine [23–27], and aniline [28, 29]) has been shown to be a

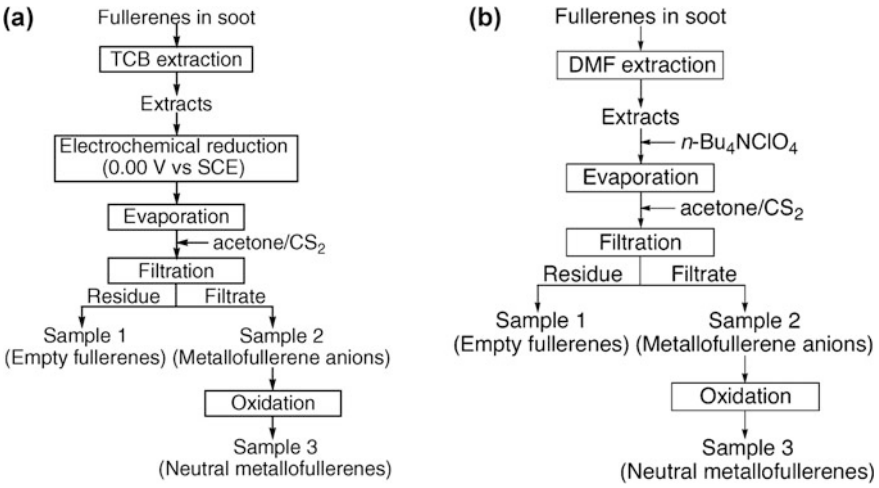

Fig. 3.2 **a** Scheme of Akasaka's electrolysis-based separation method. Fullerenes are extracted from the soot with 1,2,4-trichlorobenzene (TCB), the solvent is then removed and residual fullerenes are dissolved in o-DCB. After electrolysis, o-DCB is removed, charged EMFs are dissolved in acetone/CS_2 and then reoxidized to the neutral form by $CHCl_2COOH$. Reproduced with permission from Akasaka et al. [17]. **b** Scheme of the separation of EMFs from empty fullerenes based on selective extraction with *N,N*-dimethylformamide (DMF) developed in the same group. DMF reduces mono- and dimetallofullerenes during extraction, making this stage similar to the electrolysis-based process described in (**a**). Reproduced with permission from Ref. [18]

powerful method for EMF enrichment of extracts (Fig. 3.3) [27]. The mechanism of the special action from these donor solvents is based on the charge-transfer to EMFs, which are present in solution in an anionic state [30, 31]. Non-charged fullerenes are only poorly soluble in *N,N*-dimethylformamide (DMF), whereas solubility of the anions is quite high. Due to this behavior, an improved extraction of EMFs can be achieved. Furthermore, this method permits the extraction of EMFs which are not extractable with standard solvents. For example, $M@C_{60}$ compounds are efficiently extracted with aniline [28].

A scheme of the La-EMF separation from empty fullerenes using DMF extraction is shown in Fig. 3.2b [18]. DMF extracts empty fullerenes in their neutral form and La-EMFs as anions. Addition of *n*-Bu_4NClO_4 salt to DMF solution before evaporation of the solvent ensures that EMFs remain in the anionic state in the residual (in the absence of counter-ions, evaporation of DMF results in the uncharged EMFs). Anionic EMFs can be then dissolved in acetone/CS_2 mixture and processed in a similar way to the electrolysis-assisted separation described in Fig. 3.2a.

An efficient separation procedure based on the selective oxidation of EMFs with an array of oxidants was developed by Bolskar et al. [3, 32] and successfully applied to Gd- and Tm-EMFs. Their approach is based on different oxidation

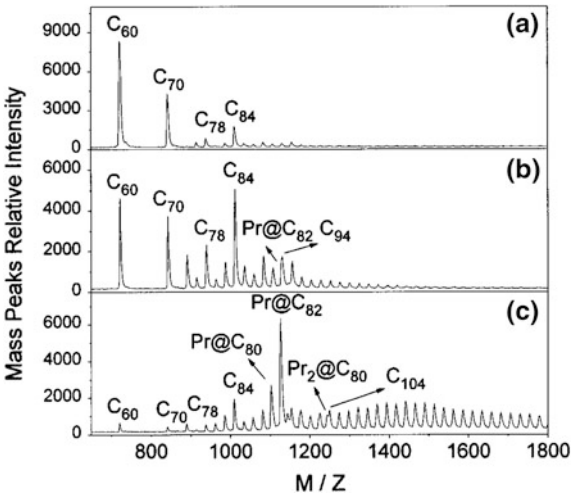

Fig. 3.3 Laser desorption ionization mass spectra of extracts obtained from soot produced by the arc-burning of carbon rods containing the rare-earth oxide Pr_6O_{11}: **a** soxhlet extract with toluene at its boiling point, **b** toluene extract at high temperature, high pressure, **c** pyridine extract at high temperature, high pressure. Reproduced with permission from Ref. [27]

potentials and different solubility of oxidized and neutral states of EMFs and empty fullerenes in polar solvents. The separation scheme is outlined in Fig. 3.4. First, the arc sublimate was separated into two parts, which were soluble and nonsoluble species in *o*-dichlorobenzene. The nonsoluble part was treated with oxidants of increasing strength such as medium oxidants $AgSbF_6$ (E° +0.65 V vs $Fe(Cp)_2^{+/0}$) or $(BrC_6H_4)_3NSbCl_6$ (tris(4-bromophenyl) aminium hexachloroantimonate, also known as "magic blue", E° +0.70 V), and strong oxidants $AlCl_3$ (E° = +1.1 V) or $NOSbF_6$ (E° = +1.0 V). In *o*-DCB, medium-strength oxidants preferentially oxidized $Gd@C_{2n}$ ($2n > 72$), whose cationic forms become soluble. The use of stronger oxidants afforded a solution enriched with $Gd@C_{60}^+$. The part of the sublimate soluble in *o*-DCB was then dried and dispersed in CH_2Cl_2, in which the solubility of neutral fullerenes is rather low. Treatment of the dispersion with $AgSbF_6$ formed soluble $Gd@C_{2n}^+$ cations (predominantly $Gd@C_{82}^+$), whereas fullerenes with higher oxidation potentials remained in the solid phase. EMFs from the $Gd@C_{82}^+$ enriched fraction were thereafter reduced to a neutral state by reaction with decamethylferrocene $Fe(Cp^*)_2$. Finally pure $Gd@C_{82}$ and $Gd@C_{76}$ were chromatographically separated from this fraction in one step.

Selective oxidation of an EMF was also developed by Shinohara et al. to separate $Li@C_{60}$, which was obtained via irradiation of C_{60} by energetic Li ions, from unreacted fullerene [33, 34]. The oxidation potential of $Li@C_{60}$ is −0.39 V, and therefore the compound can be easily oxidized by tris(4-bromophenyl) ammoniumyl hexachloroantimonate, leaving empty C_{60} intact ($E^{+/0}$ = 1.21 V). In spite of a very low concentration of $Li@C_{60}$ (less than 1%) in the final irradiation product, it was demonstrated that stirring an *o*-DCB/acetonitrile solution with $(BrC_6H_4)_3NSbCl_6$ at 100 °C for 23 h and subsequent addition of hexane excess resulted in precipitation of pure $[Li@C_{60}]^+(SbCl_6)^-$. Recrystallization of this salt

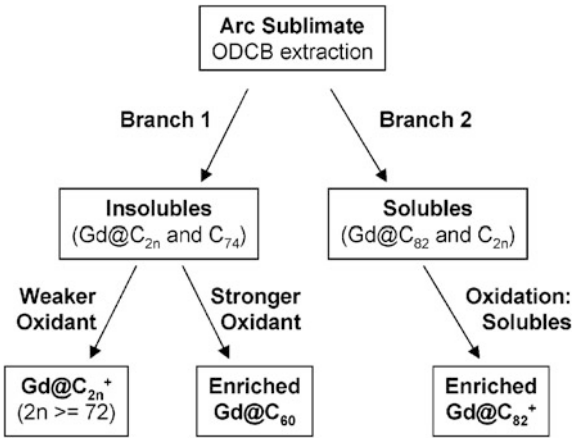

Fig. 3.4 Scheme of the selective oxidation based separation method developed by Bolskar et al. Fullerenes are extracted from the soot with o-DCB. Insoluble material (Branch 1) is then treated by weaker oxidants $AgSbF_6$ or $(BrC_6H_4)_3NSbCl_6$ in o-DCB to dissolve the minor fraction of $Gd@C_{2n}^{+}$ ($2n > 72$) fullerenes, or by stronger oxidants $AlCl_3$ or $NOSbF_6$ to dissolve the mixture of $Gd@C_{60}^{+}$ with $Gd@C_{2n}^{+}$ ($2n > 72$). Soluble extract (Branch 2) is dried and then dispersed in CH_2Cl_2 with $AgSbF_6$, herewith oxidized $Gd@C_{82}^{+}$ becomes soluble in a polar solvent. Reproduced with permission from Ref. [3]

afforded crystals suitable for single-crystal X-ray diffraction study, which enabled the authors to determine the molecular structure of $Li@C_{60}$ for the first time.

The separation of EMF cage isomers by redox reagents was first achieved by Echegoyen et al. [35]. They found that the oxidation potential of the minor isomer of $Sc_3N@C_{80}$ with D_{5h} cage symmetry is 0.27 V less positive than that of the major I_h isomer and proposed that selective oxidation of the D_{5h} isomer with a suitable redox reagent can be used for an isomeric separation. Indeed, reaction of a $Sc_3N@C_{80}$ isomeric mixture with $(BrC_6H_4)_3NSbCl_6$ resulted in precipitation of the oxidized D_{5h} isomer, leaving the neutral I_h isomer in solution. However, the reduction potential of $(BrC_6H_4)_3NSbCl_6$ is more positive than the oxidation potential of the I_h isomer. Moreover, fullerenes were not recovered from the precipitate. This separation procedure was further improved in 2013 [36]. This time, acetylferrocenium tetrakis (pentafluorophenyl) boride $[Fe(COCH_3C_5H_4)Cp]$ [TFAB] was used as a milder oxidation agent, and the fullerene mixture to be separated contained $Sc_3N@C_{68}$, $Sc_3N@C_{78}$, I_h and D_{5h} isomers of $Sc_3N@C_{80}$, and some empty fullerenes. With the reduction potential of $E^{+/0} = 0.27$ V, the excess of $[Fe(COCH_3C_5H_4)Cp]^+$ cation was able to oxidize all $Sc_3N@C_{2n}$ EMFs, except for the I_h isomer of $Sc_3N@C_{80}$.

Their separation scheme is outlined in Fig. 3.5. First, the fullerene extract was dissolved in CS_2 and sonicated for 90 min with excess of $[Fe(COCH_3C_5H_4)Cp]$ [TFAB]. The mixture was deposited onto a silica gel column. Neutral $Sc_3N@C_{80}$-I_h

with some impurities of empty fullerenes was eluted by nonpolar CS_2 (fraction O1, Fig. 3.5), whereas oxidized $Sc_3N@C_{2n}$ EMFs adhered to the silica gel. This oxidized fraction was later reduced by CH_3SNa in methanol and then eluted by CS_2 (fraction R1, Fig. 3.5, containing $Sc_3N@C_{68}$, $Sc_3N@C_{78}$, $Sc_3N@C_{80}$-D_{5h}, and some amount of $Sc_3N@C_{80}$-I_h). Such a procedure was repeated three times with different fullerene/salt ratios. At the second cycle, the fraction R1 was divided into oxidized $Sc_3N@C_{68}$, $Sc_3N@C_{78}$, and $Sc_3N@C_{80}$-D_{5h} (fraction R2) and the unoxidized rest of $Sc_3N@C_{80}$-I_h (fraction O2). For the third cycle, fraction R2 was divided into oxidized $Sc_3N@C_{78}$ (fraction R3) and a mixture of unoxidized $Sc_3N@C_{68}$ and $Sc_3N@C_{80}$-D_{5h} (fraction O3). Further separation of the latter two EMFs by this method is not possible, because they possess almost identical oxidation potentials. This three-step procedure, described by Echegoyen et al., resulted in the isolation of pure $Sc_3N@C_{80}$-I_h, $Sc_3N@C_{78}$, and a mixture of $Sc_3N@D_{5h}$-C_{80} and $Sc_3N@C_{68}$.

3.4 Lewis Acids to Separate Fullerenes and Endohedrals

3.4.1 Empty-Cage Fullerenes

The reaction of Lewis acids with fullerenes began in 1991 with the work of Olah et al. [37]. Those initial experiments involved empty-cage fullerenes (e.g., either pure C_{60} or a mixture of C_{60}/C_{70}) in benzene with a large molar excess of $AlCl_3$ to produce polyarenefullerenes (Scheme 3.1). The reaction proceeded only with relatively strong Lewis acids. The weaker $SnCl_4$ and $TiCl_4$ were not successful at catalyzing the reaction. The authors noted that single electron transfer (SET) could also be operative in redox processes for Lewis acid halides that are more easily reducible [37].

In 1992, Olah et al. [38] discovered that polychlorinated empty-cage fullerenes underwent Friedel–Crafts reactions to produce aromatic derivatives (Scheme 3.2). Switching to brominated C_{60} also resulted in the Friedel–Crafts type fullerylation of benzene [38]. The authors have later published a review of Friedel–Crafts reactions with empty-cage fullerenes [39].

A key outcome of Olah's work [37–39] with Lewis acids was their discovery of a reactivity difference between C_{60} and C_{70}. In 1994, Bucsi et al. [40] manipulated their chemical reactivity differences into a separation method. When empty-cage fullerene extract was dissolved in CS_2 and $AlCl_3$ added, the more reactive C_{70} species precipitated. The more inert C_{60} remained in solution. Upon filtration, the filtrate was purified C_{60} (>99.8%), and the method possessed a good recovery (73%). The authors also noted that recovery of the fullerenes (e.g., C_{70}) which had complexed with $AlCl_3$ could be achieved [40].

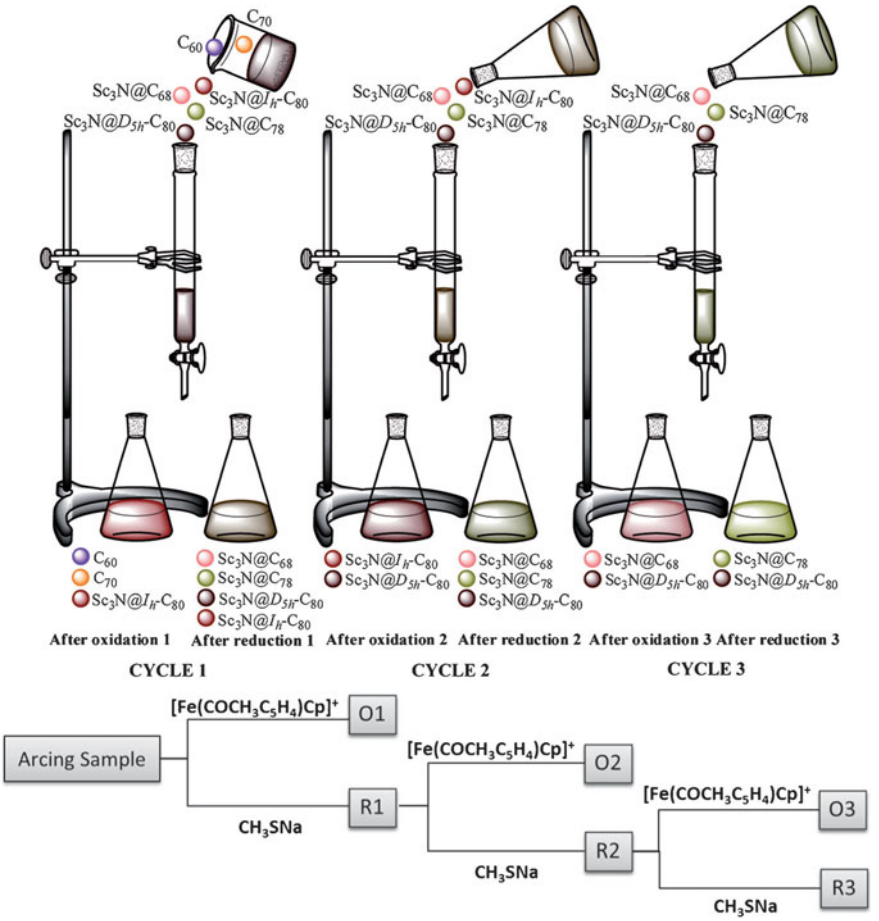

Fig. 3.5 Scheme of the separation of $Sc_3N@C_{2n}$ EMFs based on their selective oxidation by [Fe($COCH_3C_5H_4$)Cp] [TFAB] with subsequent reduction by CH_3SNa. O1 contains $Sc_3N@C_{80}$-I_h and empty fullerenes, R1 is a mixture of $Sc_3N@C_{68}$, $Sc_3N@C_{78}$, $Sc_3N@C_{80}$-D_{5h} and a fraction of $Sc_3N@C_{80}$-I_h; O2 is $Sc_3N@C_{80}$-I_h, R2 is a mixture of $Sc_3N@C_{68}$, $Sc_3N@C_{78}$ and $Sc_3N@C_{80}$-D_{5h}; O3 is a mixture of $Sc_3N@C_{68}$ and $Sc_3N@C_{80}$-D_{5h}, R3 is $Sc_3N@C_{78}$. Reproduced with permission from Ref. [36]

Scheme 3.1 Acid-catalyzed fullerenation of aromatics using $AlCl_3$ [37]

$$C_{60} \xrightarrow[AlCl_3]{\text{H-Ar (excess)}} C_{60}(\text{H-Ar})_n$$

Scheme 3.2 Friedel–Crafts fullerylation of aromatics [38]

$$C_{60}Cl_n \xrightarrow[AlCl_3]{\text{Benzene}} C_{60}(\text{Ph})_n$$

3.4.2 Metallofullerenes

In 2009, Stevenson et al. [41] addressed the curiosity of how EMFs would behave when exposed to Lewis acids. With a focus on metallic nitride (Sc_3N) and metallic oxide (Sc_4O_2) metallofullerenes, it was determined that these endohedrals were much more reactive than C_{60} and C_{70}. This large reactivity difference between empty-cage fullerenes and endohedrals permitted the isolation of $Sc_3N@I_h$-C_{80} [41]. As a non-chromatographic method, this purification approach using a Lewis acid was advantageous as it required no specialty columns and no HPLC fraction collection. By adjusting reaction time and varying the Lewis acid, it was possible to fractionate a metallofullerene extract (e.g., Sc) into an array of different types of endohedrals.

As shown in Fig. 3.6, $Sc_4O_2@I_h$-C_{80} can be enriched in Step 1 using $AlCl_3$ with a short reaction time. The D_{5h} isomer of $Sc_3N@C_{80}$, $Sc_3N@C_{68}$, and $Sc_3N@C_{78}$ are enriched in Step 2. By stopping the reaction in Step 2 when $Sc_3N@I_h$-C_{80} is the only metallofullerene in solution, it is then possible to precipitate this species in Step 3 to achieve its purification. A reactivity order of $Sc_4O_2@I_h$-C_{80} > $Sc_3N@C_{78}$ > $Sc_3N@C_{68}$ > $Sc_3N@D_{5h}$-C_{80} > $Sc_3N@I_h$-C_{80} has also been established for $AlCl_3$ [41].

In 2012, the Shinohara group [42] investigated the response of Lewis acids to other types of metallofullerenes. With a focus on pure metallic (e.g., $M_x@C_n$, x = 1, 2, n > 70) and carbide ($M_yC_2@C_{n-2}$; y = 2, 3, 4; $n - 2 > 68$) endohedrals, the authors reported that $TiCl_4$ was an excellent Lewis acid for quickly and selectively reacting with metallofullerenes [42]. In only 10 min, endohedrals can complex, precipitate, and be separated from unreacted, lower empty-cage fullerenes (e.g., C_{60}, C_{70}). Excellent recovery of precipitated metallofullerenes was also possible

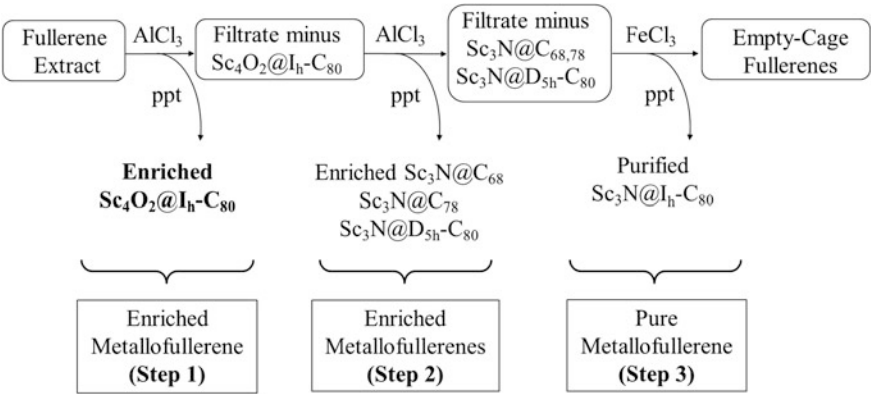

Fig. 3.6 Isolation of $Sc_3N@I_h$-C_{80} via selective complexation with $AlCl_3$ and $FeCl_3$. Reproduced with permission from Ref. [41]

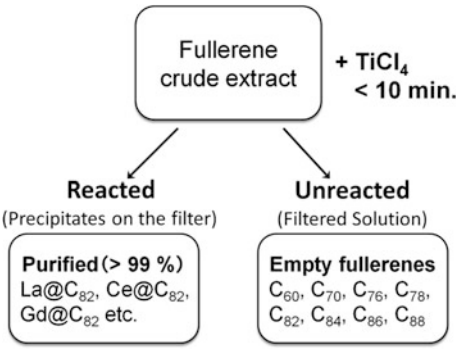

Fig. 3.7 Isolation of C_{82} endohedrals (e.g., Ce@C_{82}, La@C_{82}, Gd@C_{82}) with $TiCl_4$. Reproduced with permission from Ref. [42]

with $TiCl_4$. Several types of C_{82} endohedrals (e.g., Gd@C_{82}) were isolated from the separation scheme shown in Fig. 3.7 [42].

Also in 2012, Wang et al. [43] reported the mechanism for metallofullerene reactions with $TiCl_4$. Their findings correlated the reactivity of fullerenes and endohedrals to $TiCl_4$ as a function of their 1st oxidation potential, as shown in Fig. 3.8. They estimated a precipitation threshold of 0.62–0.72 V (vs. Fc/Fc^+) for fullerene reaction with $TiCl_4$ [43]. Formation of the metallofullerene-Lewis acid complex involved an electron transfer from the endohedral to $TiCl_4$. Although a detailed description of the redox state of $TiCl_4$ in the complex was not clear, the Shinohara group [43] was able to use elemental analysis to estimate a molar ratio of $TiCl_4$ to metallofullerene of approximately 18:1. The Nd@C_{82}-$TiCl_4$ complex was described as $[Nd@C_{82}]^+[TiCl_4]^-_m$, $m \approx 18$ [43].

In 2013, Wang et al. [44] have subsequently demonstrated that $TiCl_4$ is useful for isolating CF_3 derivatives of highly reactive, small band gap endohedrals. Such species, as M@C_{72} and M@C_{74}, would otherwise form insoluble polymerized solids in soot. As an example, the Shinohara group [44] has shown the purification of Y@$C_{2n}(CF_3)_m$ derivatives by selectively complexing these functionalized

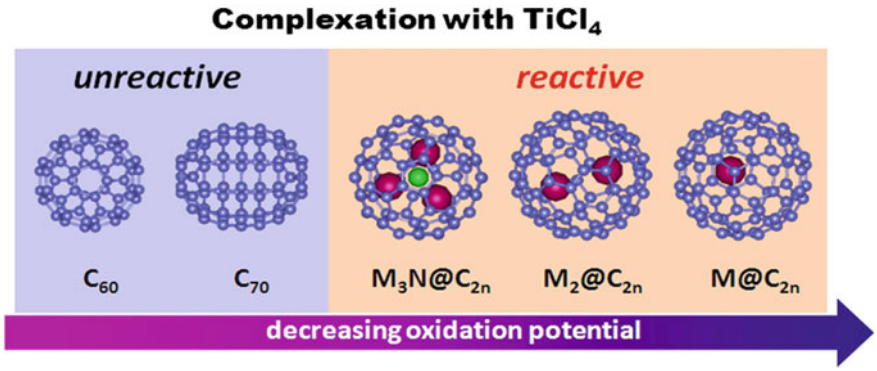

Fig. 3.8 Correlation of fullerene reactivity with 1st oxidation potential. Reproduced with permission from Ref. [43]

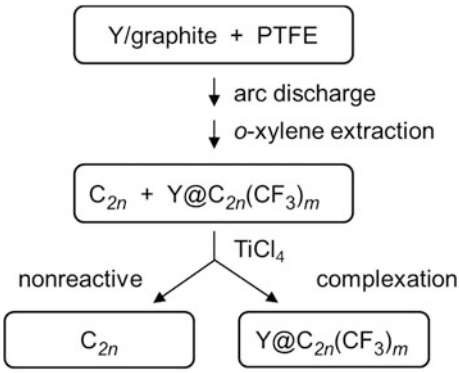

Fig. 3.9 Isolating CF_3 derivatives of *Y* endohedrals. Reproduced with permission from Ref. [44]

species with $TiCl_4$. As shown in Fig. 3.9, $Y@C_{72}(CF_3)$ and several isomers of $Y@C_{74}(CF_3)_3$ have been produced and isolated from soot extract using $TiCl_4$ [44].

In 2009 Stevenson et al. [45] reported $CuCl_2$ as a weaker Lewis acid than $AlCl_3$ or $TiCl_4$, which tended to strongly react and precipitate the bulk of the metallofullerene family. The advantage of $CuCl_2$ was its ability to lower the precipitation threshold from 0.62 V to a much lower value of approximately 0.19 V. Preferential precipitation of those endohedrals having a first oxidation potential less than 0.19 V permitted a separation of highly reactive (i.e., <0.19 V) metallofullerenes from the less reactive (i.e., >0.19 V) endohedrals [45]. $CuCl_2$ could also separate different classes of endohedrals. For example, $Sc_4O_2@C_{80}$ can be separated from other metallic oxide endohedrals and metallic nitride fullerenes. $Sc_3N@C_{78}$ (0.12 V [46]) was easily separated from $Sc_3N@C_{68}$ (0.33 V [47]) and from both D_{5h} (0.34 V [48]) and I_h (0.62 V [49]) isomers of $Sc_3N@C_{80}$ [45]. For scandium carbide endohedrals, $Sc_3C_2@C_{80}$ (−0.04 V [50]/−0.03 V [51]) was the dominant species isolated from soot extract. $CuCl_2$ also separated structural isomers of $Er_2@C_{82}$ [45]. An overview of the $CuCl_2$ separation approach is shown in Fig. 3.10.

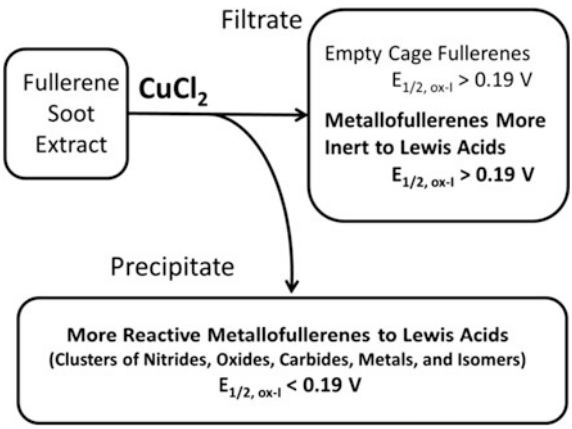

Fig. 3.10 Overview of the weaker $CuCl_2$ Lewis acid for the separation of different types of metallofullerenes. Reproduced with permission from Ref. [45]

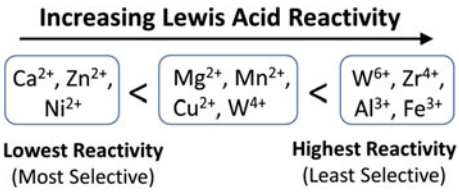

Fig. 3.11 Summary of the selectivity and reactivity of Gd-based metallofullerenes with a variety of Lewis acid strengths. Reproduced with permission from Ref. [63]

Further Lewis acid experiments have been performed on Gd endohedrals, which are of interest as MRI contrast agents [52–62]. In 2014, Stevenson et al. [63] evaluated their reactivity with a diverse array of 11 Lewis acids (Fig. 3.11). The goal was to determine a range of precipitation thresholds such that a targeted Gd endohedral could be matched with a Lewis acid of a strategic strength to just permit selective precipitation.

As an example, the authors found that $CaCl_2$ and $ZnCl_2$ had the lowest precipitation thresholds of the 11 tested Lewis acids [63]. Matching these weak Lewis acids with the very low first oxidation potential of $Gd_3N@C_{88}$ (i.e., only 0.06 V [64]) allowed the facile precipitation of $Gd_3N@C_{88}$ from Gd soot extract. As shown in Fig. 3.12, reaction of extract with $ZnCl_2$ for 4 h permitted a precipitate, that upon decomplexation with water, yielded a sample containing $Gd_3N@C_{88}$ as the dominant endohedral [63]. Additional reaction for 7 days with a larger molar excess of $ZnCl_2$ resulted in a sample containing $Gd_3N@C_{84}$ (0.32 V, [64] first oxidation potential) as the dominant metallofullerene (Fig. 3.12b). Remaining in solution are lower empty-cage fullerenes (e.g., C_{60}–C_{84}), $Gd_3N@C_{86}$ (0.35 V [65]) and $Gd_3N@C_{80}$ (0.58 V [64]) as the dominant endohedral (Fig. 3.12c) [63].

The weaker Lewis acids selectively fractionate Gd-metallofullerenes from extract because their precipitation thresholds are between the lowest and highest first oxidation potentials. Figure 3.13 describes this approach to isolate $Gd_3N@C_{88}$, which can be the dominant species precipitated if the weaker (e.g., $CaCl_2$, $ZnCl_2$, $NiCl_2$) Lewis acids are used. This is true because the weaker Lewis acids are selective for only those endohedrals with very low 1st oxidation potentials (e.g., $Gd_3N@C_{88}$). In other words, only the most reactive metallofullerenes would be allowed to precipitate under this "weak Lewis acid" approach.

In 2015, Stevenson et al. [66] developed a dual approach to chemically isolate a mixed-metal nitride endohedral, $CeLu_2N@I_h$-C_{80}. This integrated separation approach is described in Fig. 3.14. In Stage 1, a weak Lewis acid, $MgCl_2$, selectively precipitates only those endohedrals in soot extract (Fig. 3.15a) that possess very low first oxidation potentials (e.g., $Ce_2LuN@I_h$-C_{80} and $CeLu_2N@I_h$-C_{80}). By virtue of its low potential (+0.1 V), $CeLu_2N@I_h$-C_{80} is a dominant endohedral precipitated with the Lewis acid approach (Fig. 3.15b). Note that most endohedrals and empty-cage fullerenes remain in solution [66].

Because traces of co-precipitating endohedrals remain in the Lewis acid-enriched $CeLu_2N@I_h$-C_{80} sample, a second stage of separation (Stage 2) with amine chemistry was implemented [66]. Addition of dried aminosilica to the enriched $CeLu_2N@I_h$-C_{80} sample immobilized and removed the trace amounts of endohedral

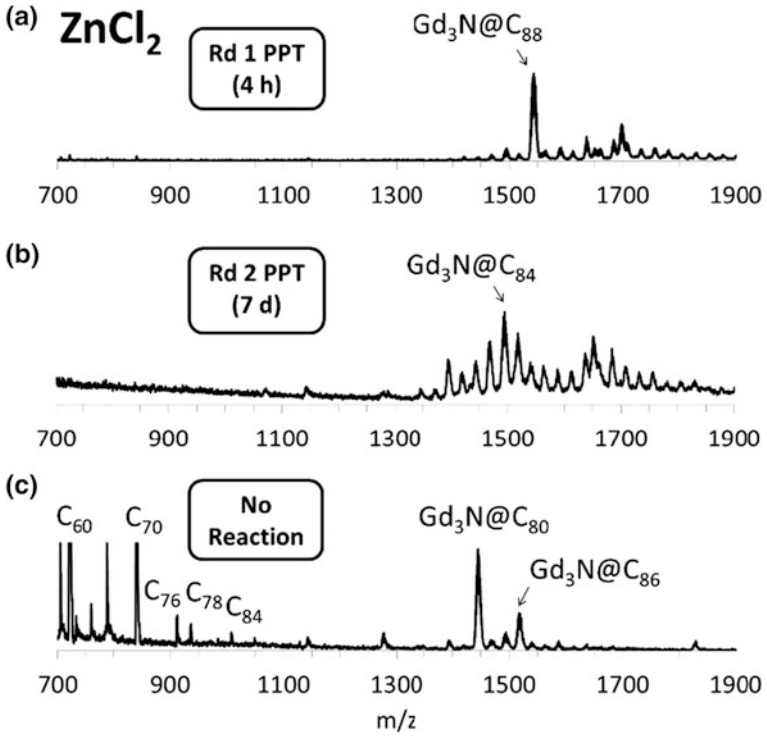

Fig. 3.12 MALDI mass spectra of **a** recovered endohedrals from precipitated material obtained after 4 h of reaction with $ZnCl_2$, Round 1, **b** recovered endohedrals from additional precipitate, Round 2, obtained after 7 days of further $ZnCl_2$ reaction, and **c** fullerenes remaining in solution after 7 days. Reproduced with permission from Ref. [63]

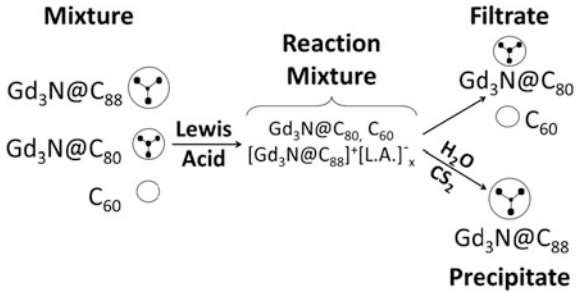

Fig. 3.13 Isolating $Gd_3N@C_{88}$ with the "weak Lewis acid" approach. Reproduced with permission from Ref. [63]

and empty-cage fullerene contaminants. Upon filtering the reaction slurry, this SAFA filtrate contained the unreacted $CeLu_2N@I_h$-C_{80}. From 500 mg of Ce/Lu soot extract, 4 mg of purified $CeLu_2N@I_h$-C_{80} was obtained (Fig. 3.15c, d) [66]. In a similar fashion, reaction with $ZnCl_2$ and subsequent SAFA separation of fullerenes

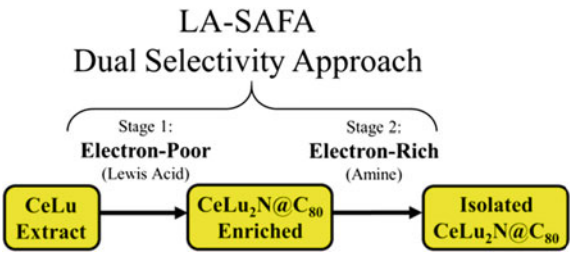

Fig. 3.14 Manipulation of endohedral reactivity differences with Lewis acids (LA) and amines (Stir and Filter Approach, SAFA) to non-chromatographically isolate $CeLu_2N@I_h$-C_{80}. Reproduced with permission from Ref. [66]

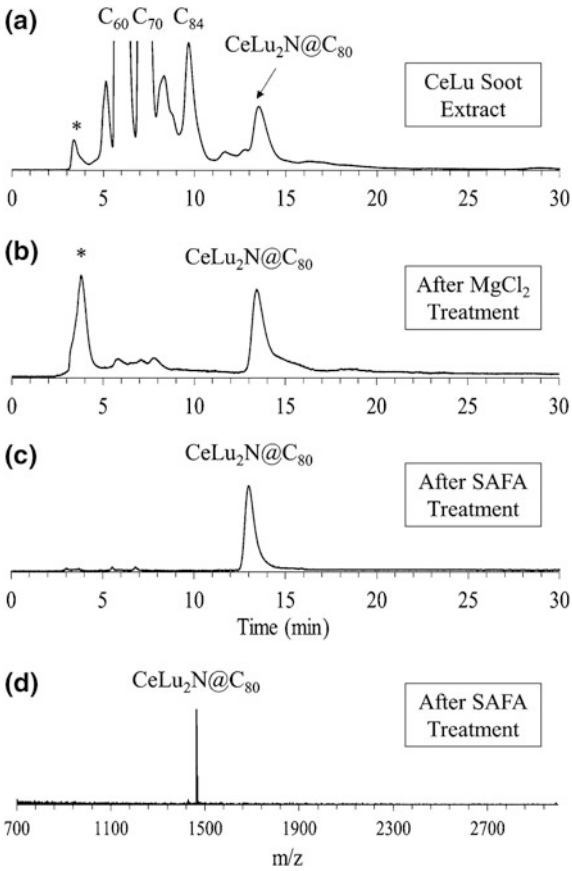

Fig. 3.15 HPLC of **a** Ce/Lu soot extract, **b** enriched $CeLu_2N@I_h$-C_{80} after Lewis acid treatment with $MgCl_2$, Stage 1 **c** isolated sample of $CeLu_2N@I_h$-C_{80} after reaction with aminosilica with the SAFA method, Stage 2, and **d** corresponding MALDI of purified $CeLu_2N@I_h$-C_{80}. Reproduced with permission from Ref. [66]

recovered from precipitate enabled non-chromatographic separation of pure $Gd_3N@C_{88}$ [67].

Acknowledgements SS thanks the National Science Foundation for funding (Grants CHE-1151668 and CHE-1465173).

References

1. Stibor A, Schefzyk H, Fortagh J (2010) Sublimation of the endohedral fullerene $Er_3N@C_{80}$. Phys Chem Chem Phys 12(40):13076–13081
2. Chai Y, Guo T, Jin CM et al (1991) Fullerenes with metals inside. J Phys Chem 95(20): 7564–7568
3. Raebiger JW, Bolskar RD (2008) Improved production and separation processes for gadolinium metallofullerenes. J Phys Chem C 112(17):6605–6612
4. Diener MD, Smith CA, Veirs DK (1997) Anaerobic preparation and solvent-free separation of uranium endohedral metallofullerenes. Chem Mat 9(8):1773–1777
5. Yeretzian C, Wiley JB, Holczer K et al (1993) Partial separation of fullerenes by gradient sublimation. J Phys Chem 97(39):10097–10101
6. Ogawa T, Sugai T, Shinohara H (2000) Isolation and characterization of $Er@C_{60}$. J Am Chem Soc 122(14):3538–3539
7. Lu X, Bao L, Akasaka T et al (2014) Recent progresses in the chemistry of endohedral metallofullerenes. Chem Commun 50:14701–14715
8. Lu X, Akasaka T, Nagase S (2011) Chemistry of endohedral metallofullerenes: the role of metals. Chem Commun 47(21):5942–5957
9. Song FY, Zhang S, Bonifazi D et al (2005) Self-assembly of [60]fullerene-thiol derivatives on mercury surfaces. Langmuir 21(20):9246–9250
10. Angeli CD, Cai T, Duchamp JC et al (2008) Purification of trimetallic nitride templated endohedral metallofullerenes by a chemical reaction of congeners with eutectic 9-methylanthracene. Chem Mat 20(15):4993–4997
11. Wu B, Wang T, Zhang Z et al (2013) An effective retro-cycloaddition of $M_3N@C_{80}$ (M = Sc, Lu, Ho) metallofulleropyrrolidines. Chem Commun 49(89):10489–10491
12. Stevenson S, Rose CB, Robson AA et al (2014) Effect of water and solvent selection on the SAFA purification times for metallic nitride fullerenes. Fullerenes, Nanotubes, Carbon Nanostruct 22(1–3):182–189
13. Stevenson S, Rottinger KA, Field JS (2014) Fractionation of rare-earth metallofullerenes via reversible uptake and release from reactive silica. Dalton Trans 43(20):7435–7441
14. Stevenson S, Harich K, Yu H et al (2006) Nonchromatographic "stir and filter approach" (SAFA) for isolating $Sc_3N@C_{80}$ metallofullerenes. J Am Chem Soc 128(27):8829–8835
15. Stevenson S, Mackey MA, Coumbe CE et al (2007) Rapid Removal of D_{5h} isomer using the "stir and filter approach" and isolation of large quantities of isomerically pure $Sc_3N@C_{80}$ metallic nitride fullerenes. J Am Chem Soc 129(19):6072–6073
16. Diener MD, Alford JM (1998) Isolation and properties of small-bandgap fullerenes. Nature 393(6686):668–671
17. Tsuchiya T, Wakahara T, Shirakura S et al (2004) Reduction of endohedral metallofullerenes: a convenient method for isolation. Chem Mat 16(22):4343–4346
18. Tsuchiya T, Wakahara T, Lian YF et al (2006) Selective extraction and purification of endohedral metallofullerene from carbon soot. J Phys Chem B 110(45):22517–22520
19. Fuchs D, Rietschel H, Michel RH et al (1996) Extraction and chromatographic elution behavior of endohedral metallofullerenes: inferences regarding effective dipole moments. J Phys Chem 100(2):725–729
20. Laukhina EE, Bubnov VP, Estrin YI et al (1998) Novel proficient method for isolation of endometallofullerenes from fullerene-containing soots by two-step o-xylene-N. *N*-dimethyl-formamide extraction. J Mater Chem 8(4):893–895
21. Ding JQ, Yang SH (1996) Efficient N, N-dimethylformamide extraction of endohedral metallofullerenes for HPLC purification. Chem Mat 8(12):2824–2827
22. Yamamoto K, Funasaka H, Takahashi T et al (1994) Isolation of an ESR-active metallofullerene of $La@C_{82}$. J Phys Chem 98(8):2008–2011
23. Kubozono Y, Ohta T, Hayashibara T et al (1995) Preparation and extraction of $Ca@C_{60}$. Chem Lett 6:457–458

24. Xiao J, Savina MR, Martin GB et al (1994) Efficient HPLC purification of endohedral metallofullerenes on a porphyrin-silica stationary phase. J Am Chem Soc 116(20):9341–9342
25. Anderson MR, Dorn HC, Stevenson SA (2000) Making connections between metallofullerenes and fullerenes: electrochemical investigations. Carbon 38(11–12):1663–1670
26. Liu BB, Zou GT, Yang HB et al (1997) Synthesis, extraction and electronic structure of $Ce@C_{2n}$. J Phys Chem Solids 58(11):1873–1876
27. Sun DY, Liu ZY, Guo XH et al (1997) High-yield extraction of endohedral rare-earth fullerenes. J Phys Chem B 101(20):3927–3930
28. Kubozono Y, Maeda H, Takabayashi Y et al (1996) Extractions of $Y@C_{60}$, $Ba@C_{60}$, $La@C_{60}$, $Ce@C_{60}$, $Pr@C_{60}$, $Nd@C_{60}$ and $Gd@C_{60}$ with aniline. J Am Chem Soc 118 (29):6998–6999
29. Lian YF, Shi ZJ, Zhou XH et al (2004) Different extraction behaviors between divalent and trivalent endohedral metallofullerenes. Chem Mat 16(9):1704–1714
30. Solodovnikov SP, Tumanskii BL, Bashilov VV et al (2001) Spectral study of reactions of La@C-82 and Y@C-82 with amino-containing solvents. Russ Chem Bull 50(11):2242–2244
31. Kareev IE, Bubnov VP, Laukhina EE et al (2004) Experimental evidence in support of the formation of anionic endohedral metallofullerenes during their extraction with N. *N*-dimethylformamide. Fuller Nanotub Carbon Nanostruct 12(1–2):65–69
32. Bolskar RD, Alford JM (2003) Chemical oxidation of endohedral metallofullerenes: identification and separation of distinct classes. Chem Commun 11:1292–1293
33. Aoyagi S, Nishibori E, Sawa H et al (2010) A layered ionic crystal of polar $Li@C_{60}$ superatoms. Nat Chem 2(8):678–683
34. Okada H, Komuro T, Sakai T et al (2012) Preparation of endohedral fullerene containing lithium ($Li@C_{60}$) and isolation as pure hexafluorophosphate salt ($[Li^+@C_{60}][PF_6^-]$). RSC Adv 2(28):10624–10631
35. Elliott B, Yu L, Echegoyen L (2005) A Simple Isomeric Separation of D_{5h} and I_h $Sc_3N@C_{80}$ by Selective Chemical Oxidation. J Am Chem Soc 127(31):10885–10888
36. Cerón MR, Li F-F, Echegoyen L (2013) An efficient method to separate $Sc_3N@C_{80}$ I_h and D_{5h} isomers and $Sc_3N@C_{78}$ by selective oxidation with acetylferrocenium $[Fe(COCH_3C_5H_4)Cp]^+$. Chem-Eur J 19(23):7410–7415
37. Olah GA, Bucsi I, Lambert C et al (1991) Considered polycarbon supercage chemistry. 3. Polyarenefullerenes, C_{60}(H–Ar)N, obtained by acid-catalyzed fullerenation of aromatics. J Am Chem Soc 113(24):9387–9388
38. Olah GA, Bucsi I, Aniszfeld R et al (1992) Chemical-reactivity and functionalization of C_{60} and C_{70} fullerenes. Carbon 30(8):1203–1211
39. Olah GA, Bucsi I, Ha DS et al (1997) Friedel-crafts reactions of buckminsterfullerene. Fullerene Sci Technol 5(2):389–405
40. Bucsi I, Aniszfeld R, Shamma T et al (1994) Convenient separation of high-purity C_{60} from crude fullerene extract by selective complexation with $AlCl_3$. Proc Natl Acad Sci U S A 91 (19):9019–9021
41. Stevenson S, Mackey MA, Pickens JE et al (2009) Selective complexation and reactivity of metallic nitride and oxometallic fullerenes with lewis acids and use as an effective purification method. Inorg Chem 48(24):11685–11690
42. Akiyama K, Hamano T, Nakanishi Y et al (2012) Non-HPLC rapid separation of metallofullerenes and empty cages with $TiCl_4$ lewis acid. J Am Chem Soc 134(23): 9762–9767
43. Wang Z, Nakanishi Y, Noda S et al (2012) The origin and mechanism of non-HPLC purification of metallofullerenes with $TiCl_4$. J Phys Chem C 116(48):25563–25567
44. Wang Z, Nakanishi Y, Noda S et al (2013) Missing small-bandgap metallofullerenes: their isolation and electronic properties. Angew Chem-Int Edit Engl 52(45):11770–11774
45. Stevenson S, Rottinger KA (2013) $CuCl_2$ for the isolation of a broad array of endohedral fullerenes containing metallic, metallic carbide, metallic nitride, and metallic oxide clusters, and separation of their structural isomers. Inorg Chem 52(16):9606–9612

46. Cai T, Xu L, Shu C et al (2008) Selective formation of a symmetric $Sc_3N@C_{78}$ bisadduct: adduct docking controlled by an internal trimetallic nitride cluster. J Am Chem Soc 130 (7):2136–2137
47. Yang SF, Rapta P, Dunsch L (2007) The spin state of a charged non-IPR fullerene: the stable radical cation of $Sc_3N@C_{68}$. Chem Commun 2:189–191
48. Cai T, Xu LS, Anderson MR et al (2006) Structure and enhanced reactivity rates of the D_{5h} $Sc_3N@C_{80}$ and $Lu_3N@C_{80}$ metallofullerene isomers: the importance of the pyracylene motif. J Am Chem Soc 128(26):8581–8589
49. Krause M, Dunsch L (2004) Isolation and characterisation of two $Sc_3N@C_{80}$ isomers. Chem Phys Chem 5(9):1445–1449
50. Anderson MR, Dorn HC, Stevenson S et al (1997) The voltammetry of $Sc_3@C_{82}$. J Am Chem Soc 119(2):437–438
51. Wakahara T, Sakuraba A, Iiduka Y et al (2004) Chemical reactivity and redox property of $Sc_3@C_{82}$. Chem Phys Lett 398:553–556
52. Ghiassi KB, Olmstead M, Balch AL (2014) Gadolinium-containing endohedral fullerenes: structures and function as magnetic resonance imaging (MRI) agents. Dalton Trans 43: 7346–7358
53. Zhang JF, Fatouros PP, Shu CY et al (2010) High relaxivity trimetallic nitride (Gd_3N) metallofullerene MRI contrast agents with optimized functionality. Bioconjugate Chem 21 (4):610–615
54. Zhang J, Ye Y, Chen Y et al (2014) $Gd_3N@C_{84}(OH)_x$: a new egg-shaped metallofullerene magnetic resonance imaging contrast agent. J Am Chem Soc 136(6):2630–2636
55. Shu CY, Gan LH, Wang CR et al (2006) Synthesis and characterization of a new water-soluble endohedral metallofullerene for MRI contrast agents. Carbon 44(3):496–500
56. Toth E, Bolskar RD, Borel A et al (2005) Water-soluble gadofullerenes: toward high-relaxivity, pH-responsive MRI contrast agents. J Am Chem Soc 127(2):799–805
57. Sitharaman B, Bolskar RD, Rusakova I et al (2004) $Gd@C_{60}[C(COOH)_2]_{10}$ and $Gd@C_{60}(OH)_x$: nanoscale aggregation studies of two metallofullerene MRI contrast agents in aqueous solution. Nano Lett 4(12):2373–2378
58. Kato H, Kanazawa Y, Okumura M et al (2003) Lanthanoid endohedral metallofullerenols for MRI contrast agents. J Am Chem Soc 125(14):4391–4397
59. Bolskar RD, Benedetto AF, Husebo LO et al (2003) First soluble $M@C_{60}$ derivatives provide enhanced access to metallofullerenes and permit in vivo evaluation of $Gd@C_{60}[C(COOH)_2]_{10}$ as a MRI contrast agent. J Am Chem Soc 125(18):5471–5478
60. Fatouros PP, Shultz MD (2013) Metallofullerenes: a new class of MRI agents and more? Nanomedicine 8(11):1853–1864
61. Okumura M, Mikawa M, Yokawa T et al (2002) Evaluation of water-soluble metallofullerenes as MRI contrast agents. Academic Radiology 9:S495–S497
62. Mikawa M, Kato H, Okumura M et al (2001) Paramagnetic water-soluble metallofullerenes having the highest relaxivity for MRI contrast agents. Bioconjugate Chem 12(4):510–514
63. Stevenson S, Rottinger KA, Fahim M et al (2014) Tuning the selectivity of Gd_3N cluster endohedral metallofullerene reactions with lewis acids. Inorg Chem 53(24):12939–12946
64. Chaur MN, Melin F, Elliott B et al (2007) $Gd_3N@C_{2n}$ (n = 40, 42, and 44): remarkably low HOMO-LUMO gap and unusual electrochemical reversibility of $Gd_3N@C_{88}$. J Am Chem Soc 129(47):14826–14829
65. Chaur MN, Athans AJ, Echegoyen L (2008) Metallic nitride endohedral fullerenes: synthesis and electrochemical properties. Tetrahedron 64(50):11387–11393
66. Stevenson S, Thompson HR, Arvola KD et al. (2015) Isolation of $CeLu_2N@I_h$-C_{80} through a non-chromatographic, two-step chemical process and crystallographic characterization of the pyramidalized $CeLu_2N$ within the icosahedral cage. Chemistry (Weinheim an der Bergstrasse, Germany) 21 (29):10362–10368
67. Stevenson S, Arvola KD, Fahim M et al (2016) Isolation and crystallographic characterization of $Gd_3N@D_2(35)$-C_{88} through non-chromatographic methods. Inorg Chem 55(1):62–67

Chapter 4
Ions of Endometallofullerenes in the Gas Phase

Olga V. Boltalina

Abstract This chapter describes the studies of the endometallofullerene (EMF) ions in the gas phase by various mass spectrometric methods. Historically, mass spectrometry was the first method to indicate the possible existence of EMFs, which happened several years before the discovery of their bulk arc-discharge synthesis. The studies of the ions of EMFs in the gas phase often preceded studies by other techniques that require substantial quantities of EMFs and provided a lot of information on their electronic properties and reactivity. In this chapter, particular attention is devoted to the gas-phase reactions of EMF ions with small molecules, and to the studies of the electron affinity of EMFs.

4.1 Introduction

A short communication in the Journal of the American Chemical Society published in 1985 by the group of scientists from Rice University, USA and University of Sussex, UK consists of only six paragraphs and one figure (see Fig. 4.1) [1]. This figure contains the very first experimental evidence of the existence of metallofullerenes, i.e., complexes of carbon cluster with a metal. This group had just had their paper on the discovery of buckminsterfullerene accepted in Nature, in which they reported that laser vaporization of graphite in a supersonic nozzle resulted in the formation of remarkably stable all-carbon spherical molecule C_{60} [2]. In the experiment that is described in their second paper, the 1985 JACS communication mentioned above [1], a small modification was made to an original fullerene generation method, i.e., a low-density graphite disk was soaked in $LaCl_3$ and then subjected to laser vaporization in a supersonic nozzle.

Figure 4.1 shows a positive-ion time-of-flight (TOF) mass spectrum of the carbon-La cluster beam, which contains two ions due to C_{60} and C_{70} clusters, whereas other species constitute ionized complexes C_nLa^+ (per original notation of

O.V. Boltalina (✉)
Department of Chemistry, Colorado State University, Fort Collins, CO 80523, USA
e-mail: olga.boltalina@colostate.edu

A.A. Popov (ed.), *Endohedral Fullerenes: Electron Transfer and Spin*,
Nanostructure Science and Technology, DOI 10.1007/978-3-319-47049-8_4

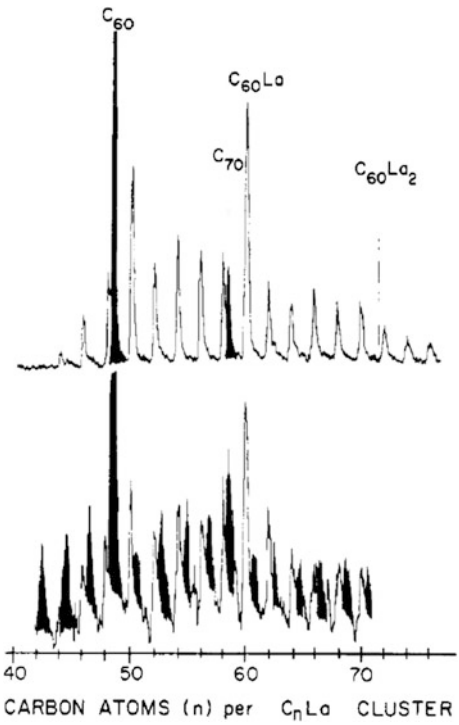

Fig. 4.1 Positive-ion time-of-flight mass spectrum of the products of laser vaporization of $LaCl_3$-doped graphite in a pulsed supersonic nozzle. Top spectrum was recorded at higher ArF laser fluence of 1–2 mJ cm^{-2}; bottom spectrum was recorded at lower laser fluence (<0.01 mJ cm^{-2}). Peaks colored in *solid black* are due to bare carbon clusters C_n. Reproduced with permission from [1]

the authors) where n = 44–76. The most prominent ion among the latter was $C_{60}La^+$, and no dimetallic clusters were observed. Based on this mass spectrum alone, the authors bravely hypothesized "…C_nLa complexes are also highly stable —particularly C_{60}La—just as would be expected if these C_n species surround the metal atom much as an egg (shell) surrounds its yoke." They concluded by suggesting that such "egg shell" complexes might be stable in normal chemical environment. This report has since been cited 883 times, as it has pronounced the birth of endometallofullerenes (EMFs). This report exemplifies the courage and remarkable collective scientific intuition that led this group of researchers beyond the concrete technical results from a mass spectrometry observation of the-gas phase ionic species, and opened the new path toward EMF research for many others who followed the challenge.

This chapter describes some of the significant studies of endofullerene ions in the gas phase. Due to unprecedented interest that the field of endofullerene research has inspired since the first report postulating their existence [1], the body of research is vast, with many hundreds of publications that appeared since 1985. Therefore, it would be unreasonable and overly ambitious to attempt to present a comprehensive review of these studies. Some topics in gas-phase science of endofullerene ions have been thoroughly reviewed over the years, and the author refers the reader to excellent reviews by Campbell and Rohmund [3], and Liu and Sun [4].

There are several reasons why gas-phase studies of EMF ions thrived in the past three decades. First, EMFs can be readily transferred into the gas phase via sublimation at high temperatures without degradation, and therefore they can be studied spectroscopically providing data on their fundamental molecular properties that are not obscured by solvation effects or solid-state interactions. Such properties include ionization characteristics, such as ionization energy and electron affinity, chemical bonding, and intramolecular charge transfer.

Second, material requirements for such studies are typically much lower than for any condensed phase studies. Just as a reminder, the first EMF was observed as a positive ion inside the mass spectrometer and not as a bulk material. Therefore, a wider range of EMF species can be studied in the gas phase, as long as appropriate ionization techniques are used to produce intense beams of charged EMF species.

By its virtue, mass spectrometry has been the method of choice for initial screenings of EMF-containing bulk materials. Compared to other fullerenes and their exohedral derivatives, EMFs and other endofullerenes remain the most challenging materials to prepare in large quantities. Synthesis of EMFs typically yields complex mixtures of compounds. Reliable initial identification of the EMF products, evaluation of their relative abundances in the product are crucial steps that determine further success with the reaction condition optimization and subsequent isolation of purified EMF compounds. Therefore, mass spectrometry that rapidly and efficiently detects ionizable species in the gas phase and provides their molecular compositions continues to be a crucial method in the EMF chemistry development. At the same time, correct interpretation of the mass spectral data critically depend on the knowledge of ionization characteristics of EMFs, their fragmentation patterns and chemical reactivity in the gas phase. This chapter will give an overview of the current knowledge of these properties of EMFs, both from the experiment and theory.

4.2 Generation and Detection of Endometallofullerene Ions in the Gas Phase

The mass spectrum in Fig. 4.1 depicts EMF cations generated by laser vaporization of graphite doped with $LaCl_3$, which is the first direct observation of EMF species in the gas phase [1]. For ionization of evaporated neutral species, an ArF excimer laser irradiation at 6.4 eV was employed. When higher laser fluence was used, $C_{60}La^+$ cation was prominent, and bare carbon cluster cations C_{60}^+ and C_{70}^+ were predominant among the bare fullerenes (top spectrum on Fig. 4.1). Under milder ionization conditions (lowering laser fluence from 1 to 0.01 mJ cm^{-2}), the distribution of positively charged ions changed significantly, leading to relative decrease of the La-containing clusters, this result was interpreted in favor of the enhanced stability of La-containing clusters toward multiphoton-induced fragmentation (bottom spectrum on Fig. 4.1). This led the authors to suggest that La atoms may be

protected by the shell of the carbon cluster, i.e., that metal atom is actually inside the C_{60} cluster. This hypothesis has later been proven correct by many researchers.

Can one assume, based on these mass spectra, that the concentrations of neutral species $C_{60}La$ in this experiment might be as high as some bare fullerenes? This would be a desirable supposition, especially from the point of view of synthetic opportunities, but the same group addressed this question in a later report concerning studies of Ca-containing EMFs [5]. In this work, they compared the positive-ion mass spectra with the negative-ion spectra of the toluene-soluble Ca-EMFs sample. Positive-ion mass spectrometry analysis on a FT-ICR instrument with ArF excimer laser ionization (6.4 eV photon energy) showed considerable amounts of $Ca@C_n^+$ (n = 60, 70, 84) species in the toluene-extracted product, the most abundant EMF was $Ca@C_{60}^+$ ion, it constituted nearly 40% of C_{60}^+ ion (Fig. 4.2, left). Interestingly, the negative-ion mass spectrum of the same sample showed that $Ca@C_{60}^-$ signal was only 5% of that of C_{60}^-. Such a difference, and particularly, over-representation of $Ca@C_{60}^+$ was explained by the lower ionization energy of $Ca@C_{60}$ compared to that of C_{60}, (i.e., <6.4 eV) and hence, the latter required two-photon process for ionization, while the former was formed in a one-photon process. Subsequent studies and especially efforts on bulk synthesis of EMFs have proven that content of the latter in the crude solvent-extracted products constitutes lower single digits, if not lower. For example, similar approach was used in the interpretation of the mass spectral data for Er-EMF samples produced using carbon arc method (Fig. 4.2, right) [6]. The authors noted an unexpectedly high ion abundance of $Er_2@C_{82}$ species in the positive ion mass spectra, which was higher than those of empty higher fullerenes and 20 times higher than any other Er-EMF in the sample. Taking into account differences in ionization energies of empty fullerenes and EMFs the authors proposed that actual content of Er-EMFs was similar to that of C_{84}. No negative-ion mass spectral data were obtained to confirm this conclusion.

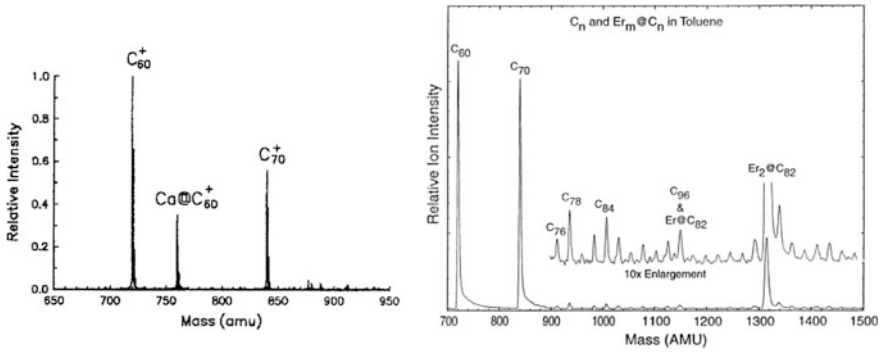

Fig. 4.2 *Left* Positive-ion mass spectrum of a Ca-containing fullerene film dried from toluene solution, reproduced with permission from [5]. *Right* LD-TOF mass spectrum of the toluene extract of the Er-containing fullerene soot, reproduced with permission from [6]

A comparative study of metallofullerene ions produced by laser-vaporization cluster beam technique was reported for three metals, Y, Sc and Ca [7]. Composite rods with optimal metal/carbon atomic ratios were used and the mass spectra of positive and negative ions generated by direct laser vaporization were mass analyzed using a reflectron TOF mass spectrometer. Intensities of EMF negative ions were very low, and most of the analysis was done using positive ion spectra. Figure 4.3 compares positive ion intensity distributions of MC_n^+ for three metals. The most likely onsets for fullerene-type clusters were identified as $n = 44$ for CaC_n^+, whereas YC_n^+ and ScC_n^+ have two onsets, at $n = 36$ and $n = 44$. The proposed structure of the smallest EMF is shown in Fig. 4.3. For dimetallic clusters, such onset was determined at $n = 62$ for M = Y, and $n = 52$ for M = Sc. Interestingly, only in the case of CaC_n^+, the peak due to $CaC_{60}{}^+$ exhibits prominently, whereas, for M = Y and Sc, species with $n = 44$ and 50 are more abundant among the MC_n^+ species. The authors also noted unusually intense ions with odd n values in the range of $29 < n < 59$ for $Y_2C_n^+$, and $29 < n < 49$ for $Sc_2C_n^+$, which were hypothesized to represent networked metallofullerene structures. Such species can be formed by incorporation of one of

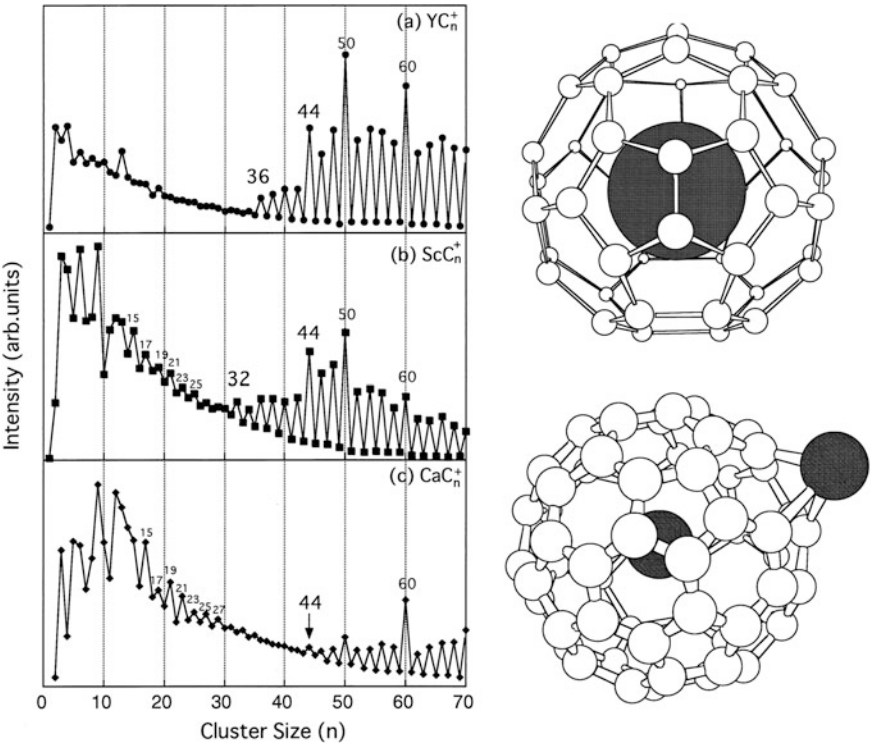

Fig. 4.3 *Left* Relative abundances of $M@C_n^+$ where M = Y, Sc and Ca. *Right* Hypothetical structures of $M@C_{44}$ and networked dimetallic EMF $M_2@C_{29}$, reproduced with permission from [7]

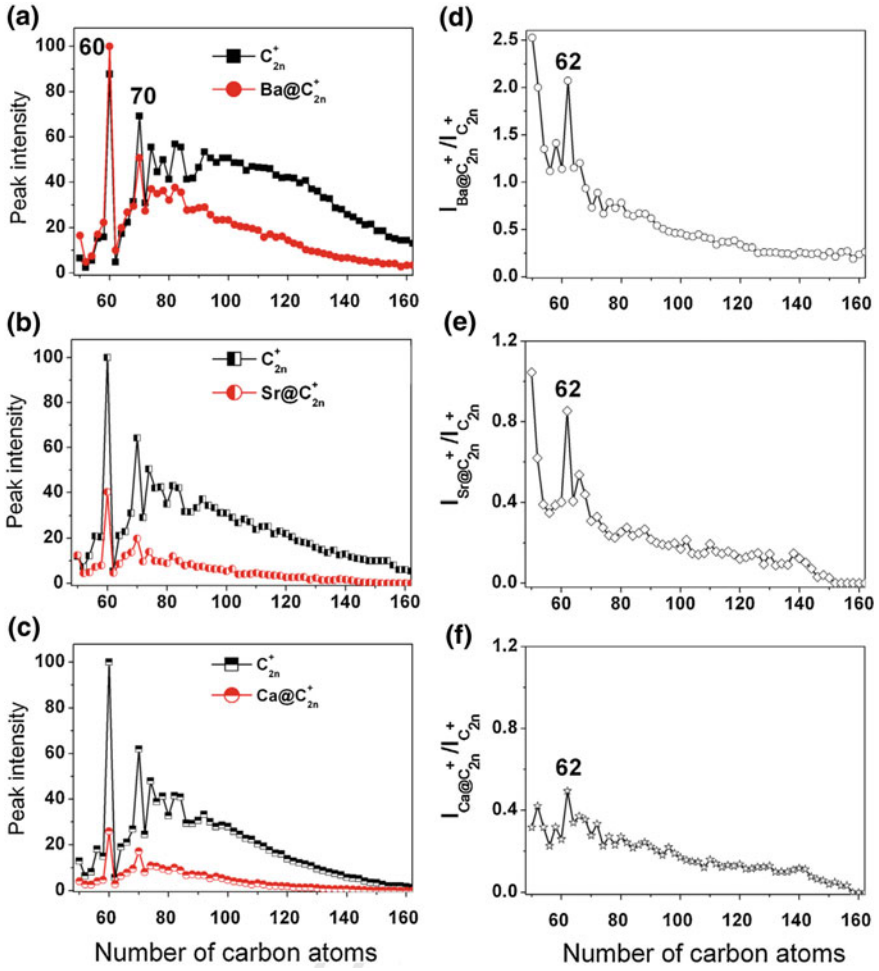

Fig. 4.4 *Left* Intensity distributions of $M@C^+_{2n}$: **a** M = Ba; **b** M = Sr; **c** M = Ca. *Right* Relative intensities of $M@C^+_{2n}/C^+_{2n}$. Reproduced with permission from [8]

the metals in the carbon network, whereas the second metal is encapsulated, as shown on hypothetical structure in Fig. 4.3, bottom right [7].

In the more recent study of laser ablation of graphene doped with alkaline earth metal salts, the authors compared metal cluster behavior of MC^+_n where M = Ba, Sr and Ca [8]. Figure 4.4 shows absolute abundances of positive ions formed in these systems, (Fig. 4.4, left) and relative intensities of MC^+_n versus C^+_n (Fig. 4.4, right). The MALDI FT-ICR mass spectrometer used in the study has a capability to study collisionally activated dissociation (CAD) of ions of interest by applying on-resonance excitation. Such experiments were carried out for several MC^+_n monoisotopic peaks in order to ascertain that ions in the selected mass range indeed

represent endohedral metallofullerenes and not exohedral metal complexes. If a metal is encapsulated inside the cage, the characteristic fragmentation pattern is known to occur via C_2 loss, and not a loss of a metal. Using such approach, the authors confirmed earlier suggestions that $Ca@C_{44}^+$ ion is indeed an endometallofullerene. In the MC_n^+ series, relative abundances of EMFs decrease in going from Ba to Sr and Ca. Experiments with MgC_n^+ did not produce any EMF ions at all, an increasing size of the metal was viewed as possible explanation of such a trend.

Similar series of studies were carried out for alkali metal carbon clusters generated by laser ablation of graphene doped with alkali metal salts. Figure 4.5 shows relative abundances of metal cluster ions in the range of MC_n^+, $60 < n < 200$.

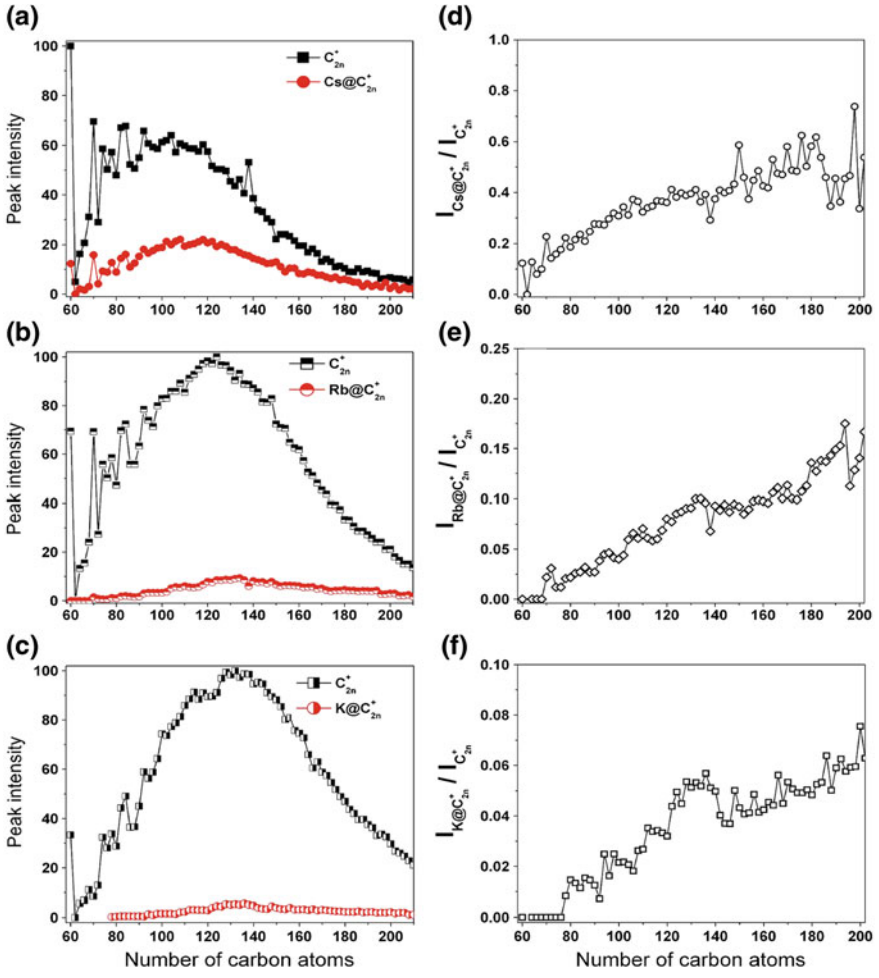

Fig. 4.5 *Left* Intensity distributions of $M@C_{2n}^+$ and C_{2n}^+: **a** M = Cs, **b** M = Rb, **c** M = K. *Right* Relative intensities of $M@C_{2n}^+/C_{2n}^+$. Reproduced with permission from Ref. [9]

The on-resonance excitation CAD method was used to distinguish whether metal-containing clusters were endohedral fullerenes or exohedral complexes. Under the applied experimental conditions, no metallofullerene ions were observed in the case of LiCl-doped graphene, either in the positive or in the negative ion modes of ionization. For other alkali metals, $M@C_n^+$ ions with n = 70–220 were observed as proven by the CAD method. No dimetallofullerene ions were detected for any of the alkali metals. Productivity of EMF formation decreases with the metal size, in agreement with findings for alkaline earth metal clusters [8]. However, the general trend of increasing productivity of EMFs relative to empty cage clusters with the cage size increase that was found for alkali metals, is opposite in the case of alkaline earth metals (compare graphs on Fig. 4.4, right, and Fig. 4.5, right).

4.3 Gas-Phase Reactivity of Endometallofullerene Ions

Studies of the gas-phase reactivity of fullerenes and their ions have been an active research area, with many dozens of chemical reactions explored [10, 11]. Mostly, positive-ion reactivity of the most abundant fullerene C_{60} was studied [10, 12]. Much less is known about the gas-phase reactions of higher fullerenes or exohedral fullerene derivatives, and even less work was done for EMFs. The focus of the gas-phase chemistry of EMFs was directed toward identifying chemical reagents that would have distinctly different behavior toward exohedral metal complexes and endometallofullerenes. Once such reagents were identified they became valuable analytical tools for determination of the nature of MC_n species in the gas phase. This section describes several examples of chemical reactions of EMFs and their cations carried out in the mass spectrometer.

4.3.1 Reactions with Oxygen

Chemical reactivity of the gas-phase EMF positive ions toward ethylene oxide was studied [13]. The choice of the reagent was based on the fact that exohedral metal fullerene complexes can readily react with ethylene oxide breaking oxygen–carbon bond and forming metal oxides. Such reactions are exothermic. In contrast, EMF cations do not react with ethylene oxide at thermal energies, just like bare (i.e., without encapsulated metal) fullerene cations. However, when EMF cations, $Sr@C_{60}^+$, were excited to enable energetic collisions with ethylene oxide in an experiment involving sustained off-resonance irradiation (SORI), the oxidation reaction was observed. Figure 4.6 shows the positive-ion mass spectra with the increasing collision energy. Only at the collision energy of 10 eV, the oxide $Sr@C_{58}O^+$ was detected as the most abundant ion. No oxidized molecular cation $Sr@C_{60}O^+$ was observed, however, leading the authors to the conclusion that it was a more reactive fragment ion $Sr@C_{58}^+$ formed by C_2 elimination that reacted with

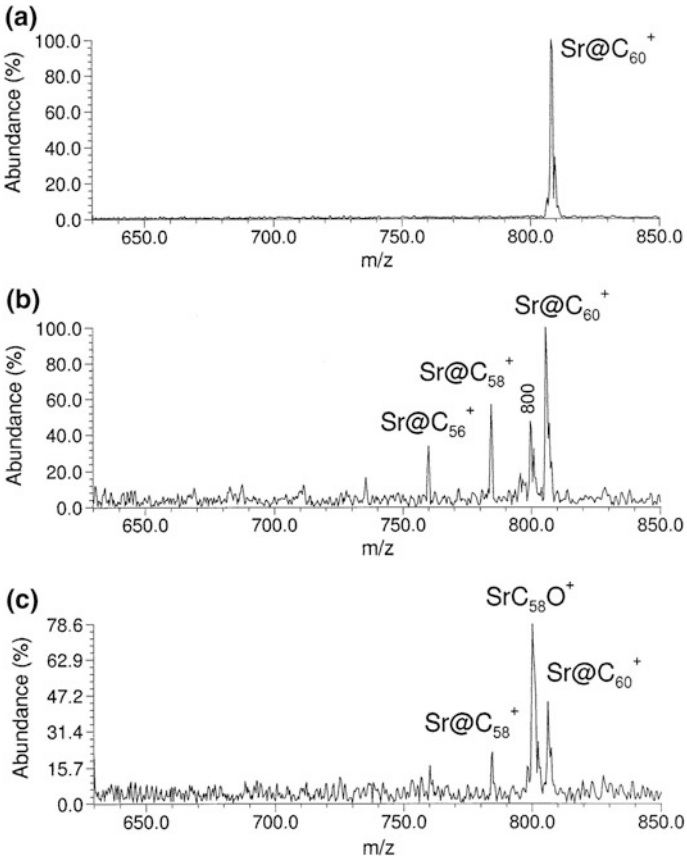

Fig. 4.6 Mass spectra of the products of endothermic reaction (SORI) of $Sr@C_{60}^+$ with ethylene oxide at **a** E_{com} = 0 eV; **b** E_{com} = 6 eV; and **c** E_{com} = 10 eV; reproduced with permission from [13]

ethylene oxide. Notably, no deeper fragmentation via subsequent C_2 eliminations was observed, and neither Sr oxide species were detected in that experiment. Interestingly, when degradation of the sample of $Sr@C_{60}$ exposed to open air for 60 days was monitored, the resultant mass spectrum of the degraded product showed drastic decrease in the intensity of $Sr@C_{60}^+$, and appearance of small-mass ions that were assigned to SrO^+, $Sr_2O_2^+$ and $SrCO_3^+$ species (Fig. 4.7). These two results provide a significant proof that possible route of EMF degradation in the presence of oxygen can be via formation of oxides followed by cage rupture and cage opening, leading to escaping of the metal from the cage, as clearly demonstrated in Fig. 4.7. Similar observations, with $La@C_{82}$ purified samples exposed to ambient environment were made by other researchers, using a MALDI mass spectrometer for the detection of oxidized products [14].

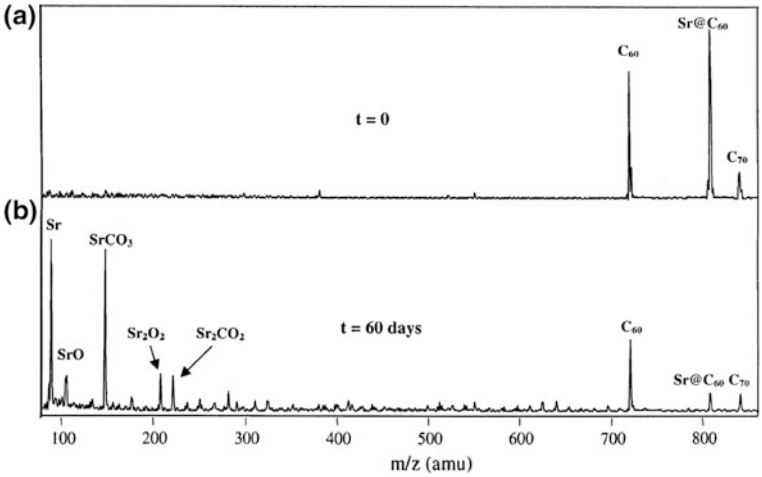

Fig. 4.7 Positive-ion mass spectrum of Sr@C_n sample at **a** 0 days (the same day as sample preparation); **b** 60 days; reproduced with permission from [13]

4.3.2 Reactions with Small Organic Molecules

Reactivity of the gas-phase EMFs toward several small organic ionic species was studied using the following method [15, 16]. EMF samples were dissolved in pyridine and solutions were used to deposit a thin film on the filament of the desorption chemical ionization (DCI) probe of the triple quadrupole mass spectrometer. Organic reagents were introduced via reference gas inlet. The filament was heated and EMFs desorbed. For ionization, electrons with 100 eV energy were used. The choice of the first reagent, vinyl acetate, was based on the prior data obtained in the studies of its reactions with C_{60} under similar conditions, which produced a positively charged adduct $[C_{60}\text{-}C_2H_3O]^+$ with high yield. Using collision-induced dissociation experimental data and theoretical calculations, the authors concluded that the most likely structure of the observed adduct was [2 + 3] cycloadduct. When a sample containing Nd@C_n (along with empty fullerenes) was reacted with vinyl acetate under identical conditions, the mass spectrum showed that the reactions occurred not only with empty fullerenes C_{60} and C_{70} as expected, but the adducts of Nd@C_n with the C_2H_3O moiety were even more prominent (Fig. 4.8). The authors reported that the ratio adduct/parent cations increased in the series: C_{60}, C_{70}, Nd@C_{82}, Nd@C_{80} as follows: 46, 64, 75 and 83%, respectively.

The proposed structures and reaction mechanism are shown in Fig. 4.9. Similar results were obtained in the reactions of Tb@C_n species with vinyl acetate. Improved gas-phase reactivity of EMFs toward [2 + 3] cycloadditions with reactive cation $C_2H_3O^+$ was rationalized as follows.

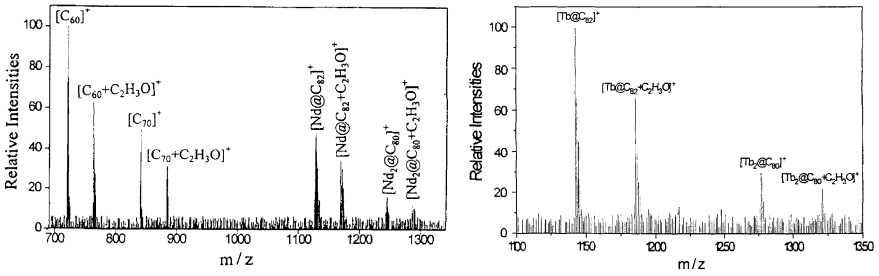

Fig. 4.8 *Left* Positive-ion mass spectrum of the products of reaction between vinyl acetate and Nd@C_n. *Right* Positive-ion mass spectrum of the products of reaction between vinyl acetate and Tb@C_n [16]

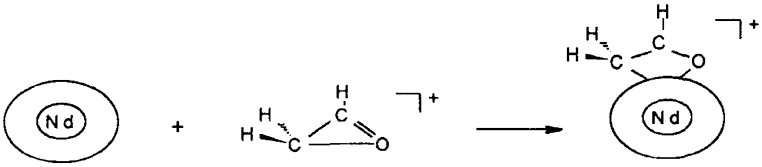

Fig. 4.9 Proposed reaction mechanism and the structure of the adduct between vinyl acetate and Nd@C_n; reproduced with permission from [16]

Donation of electrons from encapsulated metal to the cage increases electron cloud density on the cage double bonds which greatly facilitates cycloaddition chemistry of endometallofullerenes with the organic cation compared to the empty fullerene.

In contrast, reactions of Nd@C_n with benzene ions in the gas phase resulted in much lower yields of the adducts compared to reactions of C_{60} with benzene ions. Only a low-intensity signal due to Nd@$C_{82}(C_6H_6)^+$ was observed, as shown in Fig. 4.10, the suggested structure of the adduct is a π-π conjugated complex, by analogy with that of $C_{60}(C_6H_6)^+$. Reactivity of EMFs toward acetone in the gas phase was also explored. Reactions of empty fullerenes with acetone typically result in acetylation and formation of the new σ C–C bonds. In contrast, a very low conversion of Nd@C_{82} into the product in similar reaction with acetone was observed which prevented the authors from comparing its reactivity with that of C_{60} or from making conclusions about the possible structure of the observed adduct Nd@$C_{82}(COCH_3)^+$.

To summarize, data on reactivity of EMFs in the gas phase is surprisingly scarce, considering that it is technically relatively easy to accomplish using commercial mass spectrometers with gas inlet units and CID capability for structural studies of the EMF adducts. Additional advantage to utilize gas-phase reactivity research is that one does not need high-purity samples in large quantities for such experiments. Many opportunities are open in this area for future research regarding availability of the diverse types of EMFs, wide range of reagents, and available rich data on the gas-phase reactions of empty fullerenes, their singly and doubly charged cations. Gas-phase reactivity of anionic EMFs has barely been explored up to date, despite

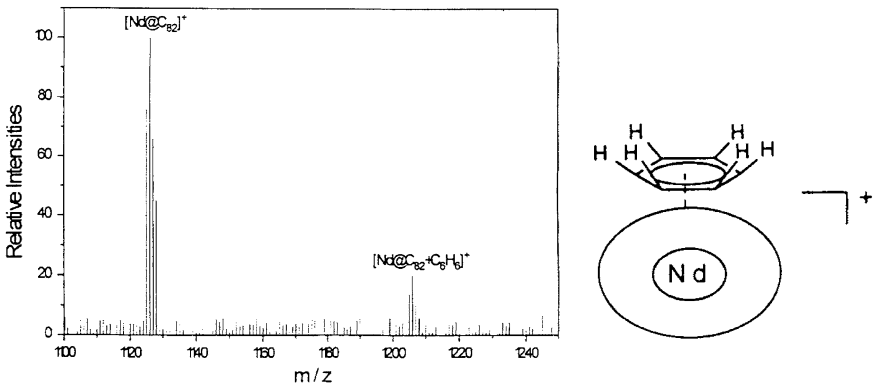

Fig. 4.10 Positive-ion mass spectrum of the products of reaction between benzene and Nd@C_n. *Right* Proposed structure of adduct between benzene and Nd@C_n. Reproduced with permission from [16]

the fact that generation of the anions from the high-electron affinity EMFs is relatively easy to achieve.

4.4 Electron Affinity Measurements of Endometallofullerenes

Electron affinity (EA) of a molecule A in the gas phase is defined as the energy released upon the attachment of an electron to A to form a molecular anion, A^-, via the reaction:

$$\begin{aligned} &A + e = A^-, \\ &EA = -H_0^0 \end{aligned} \tag{4.1}$$

This fundamental characteristic provides a quantitative measure of an intrinsic ability of a gas-phase species to attach an electron. If the EA value is positive, the anion formation is thermodynamically favorable process. If the neutral species possesses high positive value, i.e., EA > 2.5 eV, it is generally regarded as a strong electron acceptor. Two most electronegative atoms Cl and F have EA values of 3.60 and 3.39 eV, respectively. The fullerenes C_{60} and C_{70} have EA values of 2.683(8) eV [17], and 2.765(10) respectively [18], whereas the highest EA among closed-shell fullerene derivatives was determined for a fluorofullerene, $C_{60}F_{48}$ (4.1(3) eV) [19]. In the latter, the presence of many electron-withdrawing fluorine atoms causes drastic increase in the electron acceptor ability of the fullerene.

How do electronic properties change after a metal(s) is placed inside the carbon cage? Will charge transfer between the metal and the cage result in lowering its

electron affinity? Does an EA value of an EMF depend on the nature of the metal? Is an EA value of an EMF affected by the size and isomerism of the carbon cage? All these questions are important to address not only because the answers help basic understanding of the relationships between the structures of EMFs and their electronic properties, but also because this knowledge may be useful for designing EMF-containing materials for practical electronic applications. Relatively inexpensive DFT calculations are widely used for predictions of ionic properties of EMFs, however, currently, a typical under- (or over-)estimation of the DFT-calculated EA values of the fullerene- size molecules reaches a few hundred meV, and large discrepancies between different authors (DFT functional and basis sets they use) are common. To further improve computational approaches, accurate experimental data on EAs of EMFs are necessary.

The range of applications of strong acceptor molecules such as fullerenes and related compounds includes organic photovoltaics, organic transistors, or *p*-dopants. Even though currently commercial viability of endometallofullerenes may appear as remote possibility due to lower yields and difficulty of purification compared to exohedral derivatives, one can envision the demand for these materials will grow in the future due to the unique combination of their electronic and magnetic properties. In this section, a compilation of the experimental data on the EAs of endometallofullerenes is presented.

4.4.1 Photoelectron Spectroscopy

The first measurement of the electron photodetachment from an EMF anion was reported in 1993 [5]. An EMF-containing sample was prepared using laser vaporization/high temperature furnace method, in which the composite CaO/graphite rods were used to generate $Ca@C_n$ compounds. The photoelectron spectrum of the mass-selected ion $Ca@C_{60}^-$ was recorded using TOF mass spectrometer supplied with the laser vaporization ion source with "a waiting room" for cooling ions, and a magnetic bottle electron energy analyzer. The PES spectra of $Ca@C_{60}^-$ and, for comparison, C_{60}^-, are shown in Fig. 4.11.

Whereas the general qualitative features of the two spectra are similar (Fig. 4.11), the EA value for $Ca@C_{60}$ was found to be higher by 0.35 eV than that of C_{60} (2.65 eV, measured by the same authors earlier [20]).

In the past two decades, the photoelectron spectroscopy technique has undergone drastic improvements: (i) more efficient methods of ionization were introduced that cause less fragmentation, e.g., electrospray ionization; (ii) higher sensitivity was achieved thus smaller samples can be analyzed; (iii) more effective cooling of the excited ions become possible so that adiabatic EAs can be measured with high precision and accuracy. These instrumental advances are becoming increasingly valuable for accumulating reliable data on the ionic properties of fullerenes and their derivatives. For example, since the first report on EA of C_{60} (2.65 eV) [20], its absolute value has been corrected several times, and the

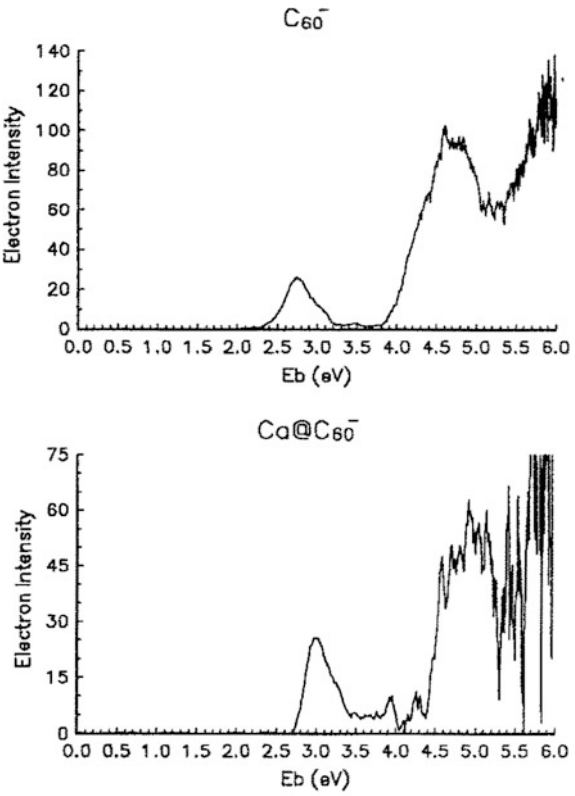

Fig. 4.11 Photoelectron spectra of C_{60}^- (*top*) and $Ca@C_{60}^-$ (*bottom*). Reproduced with copyright Permission from Ref. [5]

uncertainty decreased by several orders of magnitude (2.6835(6) eV) [21]. So far, EMFs have not received sufficient attention in these studies, probably due to the relative scarcity of samples for such studies. At the same time, knowledge of electron affinities of larger groups and different families of EMFs would be beneficial for understanding their electronic properties, for revealing effects of structural differences, such as carbon cage isomerism and size, metal nature, type of encapsulated moieties, and charge transfer to the cage. These new studies would also assist in validating the EA data that are available currently in the literature, both from the experimental works, and from theoretical calculations.

A particular advantage that the current state-of-the-art low-temperature PES technique offers is the improved sensitivity and the possibility to study single-isomer EMF samples with the well-characterized structures, even if they are available in sub-milligram amounts. With the kind permission of Dr. Popov (IFW, Dresden, Germany) and Dr. X.-B. Wang (Pacific Northwest National Laboratory, USA), the unpublished PES spectra of two trimetallic nitride cluster EMFs recorded using such a modern PES instrument, are shown in Fig. 4.12.

When the first measurement of the EA value for $Sc_3N@C_{80}$ was reported [22], it was met with surprise, as all EMFs studied before had a higher EA than the parent fullerenes. The EA value obtained for $Sc_3N@C_{80}$ in the Knudsen cell mass

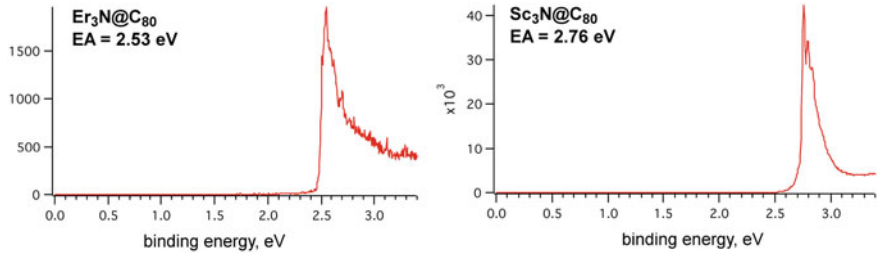

Fig. 4.12 *Left* Photoelectron spectrum of $Sc_3N@C_{80}^-$. *Right* Photoelectron spectrum of $Er_3N@C_{80}^-$. Excitation wavelength 355 nm

spectrometry experiment was lower than that of the bare cage C_{80}, and only 100 meV higher than that of the smallest IPR fullerene, C_{60}. The new and more precise EA data for $Sc_3N@C_{80}$ (2.76 eV; Fig. 4.12, right) confirm the earlier result. Furthermore, the PES data obtained for $Er_3N@C_{80}$ demonstrate, for the first time, that EMF molecule can have EA even lower than that of C_{60} (Fig. 4.12, left). Possible reasons of the lower acceptor ability of $M_3N@C_{80}$ are discussed below, in the following section.

4.4.2 *Ion-Molecular Equilibria by Knudsen Cell Mass Spectrometry (KCMS-IME)*

Application of the Knudsen cell mass spectrometry (KCMS) method to the studies of ion-molecular equilibria (IME) with EMFs yielded so far the largest body of data on their electron affinities (Table 4.1). In a typical KCMS-IME experiment, a sample containing a mixture of EMFs and potassium fluoride is placed into a platinum Knudsen effusion cell and heated to the temperatures that enable measurable signals of negative ions and their positive counterparts. Potassium fluoride is used as a solid with the low work function to increase concentrations of fullerene and metallofullerene anions in the gas phase which are generated via thermal surface ionization process. In some experiments, potassium fluoride polycrystalline powder was placed in the cell separately, without mixing with EMFs, and the results concerning concentrations of negative ions did not differ significantly, in agreement with the proposed role of KF as inner work function lowering material. The neutral components of the effusive beam evaporating from the cell are analyzed and quantified via converting them into positive ions by electron ionization (with the energy of 75 eV) and mass analyzed in the magnetic sector mass spectrometer. Thermally generated negatively charged ions are simply pulled out of the effusion cell by a weak electric field (2 kV) which is followed by mass analysis.

In the first KCMS-IME experiment, electron affinity of $Gd@C_{60}$ was determined as 2.9 eV [23]. In this and following studies, crude EMF-containing fullerene samples were used that were prepared by the arc vaporization of the corresponding

Table 4.1 Electron affinities and ionization energies of EMFs

EMF	Cage charge	I.E.$_{theor}$ eV	Ref.	EA$_{exp}$ eV	Ref.	EA$_{theor}$ eV	Ref.
Li@C_{60}	1−	6.06 6.5[a]	[35] [36]	–		2.97	[35]
Ca@C_{60}	2−	6.14	[35]	3.0(1)	[5]	3.02	[35]
La@C_{60}	3−	6.17	[35]			3.03	[35]
La@C_{74}	3−			2.9	[38]		
La@$C_{60,70\text{-}84}$	3−			2.7 < EA < 3.3	[37]		
La@$C_{60,74\text{-}82}$	3−	6.2–6.4[b]	[37]				
La@C_{80}	3−			3.32	[38]		
La@C_{82}	3−	6.19	[27]			3.22	[27]
Gd@C_{60}	3−			2.9(2)	[23]		
Gd@C_{74}	3−			3.3	[38]		
Gd@C_{76}	3−			3.2(1)	[38]		
Gd@C_{78}	3−			3.3	[38]		
Gd@C_{80}	3−			3.3(1)	[38]		
Gd@C_{82}	3−	6.25	[27]	3.3(1)	[38]	3.20	[27]
Sc_2@C_{80}	4−			3.20(4)	[22]		
Sc_2@C_{82}	4−			3.21(4)	[22]		
Sc_2@C_{84}	4−			3.10(4)	[22]		
Sc_3N@C_{80}	6−	6.88	[39]	2.81(5)	[22]	2.99	[39]
				2.76(1)	[40]		
Sc_2ErN@C_{80}	6−			2.76(5)	[22]		
$ScEr_2N$@C_{80}	6−			2.73(5)	[22]		
Er_3N@C_{80}	6−			2.53(1)	[40]		
C_{60}	0	7.78 7.6[c]	[27] [41]	2.6835 (6)	[21]	2.69	[27]

[a]Experimental estimate from photoionization study by UV laser in TOF MS [36]; [b]experimental value from charge exchange reactions using FTMS [37]; [c]experimental value from appearance potential measurements by mass spectrometry [41]

M_2O_3-graphite rods (M = Gd or La) with the subsequent in situ extraction of the fullerenes and metallofullerenes by sublimation. Such sample preparation method typically results in different distribution of EMFs than in the sample from the liquid extraction with the use of organic solvents, i.e., in the latter method the most soluble EMF species are isolated predominantly.

Equilibrium constants of the electron exchange reactions between the gadolinium metallofullerene Gd@C_n and C_{74} neutral molecules and their anions were studied:

$$\mathrm{Gd@C}_n{}^- + \mathrm{C}_{74} = \mathrm{Gd@C}_n + \mathrm{C}_{74}{}^- \tag{4.2}$$

When La-EMF sample was studied, positive ions due to neutral La@C_{74} molecule were not detected, therefore only lower limit to the EA value of La@C_{74}

was estimated from the instrument detection limit using equilibrium constant for the reaction with C_{76}:

$$La@C_n^- + C_{76} = La@C_n + C_{76}^- \quad (4.3)$$

Several assumptions were used to derive EA values from the equilibrium constants of reactions (4.2) and (4.3). First, the ratio between the positive-ion ionization cross sections of C_m and $M@C_n$ molecules was taken as the ratio between the number of carbon atoms in their fullerene cages; this has been found a good approximation for the empty fullerenes C_{60} and C_{70} [24]. Second, it was suggested that differences in the entropy and enthalpy between the fullerene molecules and their anions and between the metallofullerene molecules and their anions were nearly equal. Third, the fragmentation under electron impact conditions was assumed negligible. Finally, it is important to take into account that since only crude EMF mixtures were used in these studies, the presence of different molecules with the same m/z ratio (e.g., different cage isomers, or even different molecular structures, such as $M_2C_2@C_n$ vs. $M_2@C_{n+2}$) cannot be ruled out. Table 4.1 lists EA values obtained in those experiments. It appears that the presence of the Gd atom inside the fullerene cage results in an increase in its electron affinity compared to the EAs of the empty fullerene of the same cage size.

Another interesting observation is that no strong dependence of the EA values on cage size n for $Gd@C_n$ (n = 74–82) was found, as all values lie within a narrow range of 3.2–3.3 eV. At the same time, for empty fullerenes C_n a clear trend of increasing EA with the cage size was determined [24].

This observation might imply that the electronic structure of the parent carbon cluster does not have a significant effect on the EA of EMF, whereas the metal ion has a stronger effect. Similar conclusions were made in the studies of the electrochemical properties of EMFs in solution. It was shown, for example, that the linear dependence exists between the third ionization potentials of the lanthanide metal atoms and the first reduction potentials of EMFs in solution [25]. Similar correlation between the ionic radii of the M^{3+} ions and the first reduction potentials of EMFs was rationalized as follows. In the EMF anion, the highest electron density on SOMO (single-occupied molecular orbital, responsible for the electron attachment) is found on the nearest to the metal atom cage carbon atoms. This may have an effect on the dependence between the electron attachment energy and the distance between the metal atom and the cage, which is the function of the ionic radii of the encaged metal ions [26].

In another KCMS-IME study, three samples of trimetallic nitride endohedral fullerenes with different relative content of EMFs were used to generate anionic species in the gas phase [22]. One sample contained only Sc-EMFs, whereas two other samples contained mixed (Sc, Er)-EMFs and empty fullerenes. Typical positive and negative ion mass spectra of the first sample and one of the (Sc, Er)-EMF samples are shown in Fig. 4.12. Besides triscandium nitride EMFs, discandium derivatives of C_{80}, C_{82} and C_{84} were observed. The EA values were determined via

studying ion-molecular equilibria as described above, and the reference compound was C_{84}:

$$A@C_n^- + C_{84} = C_{84}^- + A@C_n \quad (4.4)$$

The positive and negative ion mass spectra of (Sc, Er)-EMF sample are presented in Fig. 4.13, right. Noticeably, a lower abundance of Er-containing anionic species is indicative of the lower EA.

Table 4.1 lists the EA values obtained in these experiments. The effective charges on the fullerene cage predicted by theoretical calculations [27] or established experimentally [28] [29] are given in the second column. The electron affinity of the discandium EMFs is very close to EA of the corresponding hollow fullerenes while EA ($Sc_3N@C_{80}$) is about 0.38 eV lower than previously measured EA (C_{80}). However, such comparison may be incorrect because of the different isomerism of the empty fullerene cages and carbon cages of the corresponding EMFs. Therefore, the authors calculated adiabatic electron affinity of different C_{80} isomers with PBE exchange-correlation functional [30]. It was found that the electron affinity of the I_h-C_{80} may be even 0.4 eV greater than that for the D_2 isomer, which is typically found in the fullerene extracts. As for C_{84}, the EA values for D_{2d} and D_2 isomers are predicted to be almost equal [31].

It was concluded that the decrease in the EA values in going from discandium fullerenes to $Sc_3N@C_{80}$ and other triscandium nitride molecules is governed by the increase in the charge transfer to the carbon cage. This conclusion can be extended to monogadolinium fullerenes, which have charge 2−, according to the DFT calculations, [32]) or 3− (from the ultraviolet photoelectron spectroscopy (UPS) study [33]. Mono-Gd-EMFs with a single metal atom inside have consistently higher EA values than di-Sc-EMFs with two metal atoms. Surprisingly, replacement of scandium by erbium in $M_3N@C_{80}$ species had little effect on their EA values, despite large differences in the first, second and third ionization potentials between scandium and erbium atoms (0.4, 0.9, and 2.0 eV respectively [34]). The observed correlation between the EAs of EMFs and the charge of the carbon cage, i.e., molecules with higher cage charge have lower EAs, need further investigations with larger series of molecules and with the use of the method that gives higher precision in the measured EAs than had been used previously (Fig. 4.13).

4.4.3 *Fourier Transform Mass Spectrometry*

In the Fourier transform ion cyclotron mass spectrometry (FTMS) experiment, electron exchange was studied between EMF anions and organic molecules with different electron affinities. EMF anions were generated by slow electron attachment, then ions of interest were directed in the ICR cell and were trapped there for several seconds, allowing them to react with the reference organic molecules, which EA values are well known. For example, when $La@C_n^-$ was brought in contact with

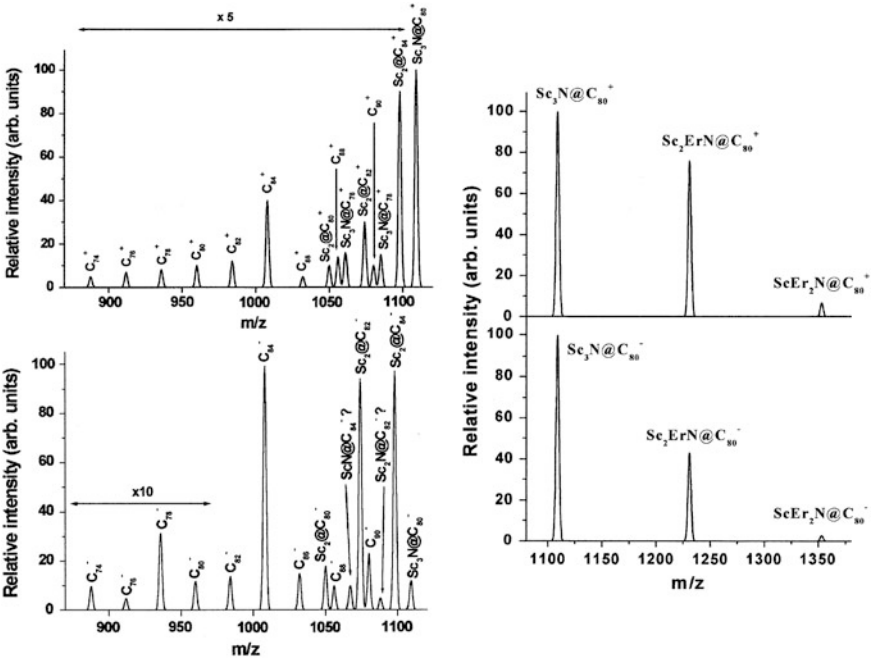

Fig. 4.13 *Left* Positive (*top*) and negative (*bottom*) ion mass spectra of Sc-EMF sample. *Right* Positive (*top*) and negative (*bottom*) ion mass spectra of (Sc, Er)-EMF sample. Reproduced from Ref. [22]

fluoranil (EA = 2.7 eV), this did not lead to the appearance of the fluoranil anion and disappearance of the $La@C_n^-$ anions, indicating that electron exchange did not occur due to higher EA of $La@C_n$ as shown in the reaction (4.5). The literature value of EA of fluoranil was thus taken as a lower bracket for EA($La@C_n$). The absence of electron transfer between $La@C_n$ ions and fluoranil was observed for several $La@C_n$, with n = 60, 70–84.Then a gas-phase species with the higher EA of 3.3 eV, tetracyanoquinodimethane TCNQ, was used in the similar experiment, and the electron exchange with $La@C_n^-$ was observed, pointing to the weaker electron acceptor ability of $La@C_n$. Thus, the value of EA(TCNQ) = 3.3 eV was taken as a higher bracketing estimate, yielding 2.7 < EA($La@C_n$) < 3.3 eV.

$$La@C_n + B^- = B + La@C_n^- \tag{4.5}$$

These brackets for EA($La@C_n$) fall within the values obtained for La-and Gd-EMFs using KCMS-IME method, and they also agree with the earlier measurement by PES for $Ca@C_{60}$.

4.5 Conclusions and Outlook

Endometallofullerenes continue to fascinate and inspire scientists from different disciplines. The role of gas-phase studies of EMFs has been paramount in the discovery of EMFs, and will continue to be an important integral part of multi-disciplinary research of the known and new classes of EMFs. Primary analysis of the EMF-containing products in the gas phase provides crucial initial data on molecular compositions. As has been shown in this chapter, qualitative identification of the charged EMFs can be readily achieved using high-resolution mass spectrometers, in many cases assisted by multi-isotopic patterns of the metal atoms. As far as quantitative analysis is concerned, which can be based on the relative EMF peak intensities, no satisfactory mass spectrometry techniques exist at the present time that provide reliable relative (let alone absolute) abundances of EMFs in the mixtures. Several examples are given in this chapter that demonstrate significant discrepancies between the data on the relative ionic distributions in the positive and negative ion modes, and between different ionization methods. More work needs to be done including judicious choice of ionization method, consideration of differences in ionization efficiency of EMFs of different structures, compositions, and comparison of their behavior with that of the empty fullerenes. Many gaps exist in the data on ionization energies and electron affinities of EMFs. Table 4.1 contains the compilation of the published data on IE and EA values of EMFs. The majority of these values have large errors, which precludes meaningful comparisons across groups of the compounds. For example, EA data for La@C_n and Gd@C_n molecules were determined for different cage sizes, from $n = 60$ to $n = 82$, however, due to low precision, one cannot deduce whether the cage size has any effect on EA. Furthermore, with the few exceptions ($Sc_3N@C_{80}$ and $Er_3N@C_{80}$), the IE and EA measurements were done using crude mixtures of EMFs, and presence of different isomers has not been taken into account in these studies. Furthermore, one has to take into account the possibility that the structural assignments based entirely on the m/z ratio for dimetallic EMFs can be complicated due to the possibility of the presence of metal dicarbide clusters: for example, an ion with formula $Sc_2@C_{84}$ can be assigned to dimetallic EMF with C_{84} cage or, alternatively, to $Sc_2C_2@C_{82}$.

Several interesting approaches have been proposed in the literature regarding chemical reactivity of EMFs in the gas phase. Besides the obvious value of such studies for fundamental research they can be useful for analytical purposes, i.e., identification whether metallofullerene species has an exohedral metal attached from outside the cage or metal encapsulated inside the cage. Fundamental studies of chemical reactivity of various EMFs in the gas phase, either as neutral or charged species are still at the very early stage of development, especially when compared to the analogous studies of empty fullerenes. No work has been published on the gas-phase chemical reactions with exohedrally derivatized EMFs. Such studies might provide valuable information on the chemical bonding in EMF derivatives, their relative stabilities and ionic properties.

Acknowledgement The author is grateful for partial support from the National Science Foundation (grants NSF/CHE 1362302, and CHE-1012468).

References

1. Heath JR, Obrien SC, Zhang Q et al (1985) Lanthanum complexes of spherodal carbon shells. J Am Chem Soc 107(25):7779–7780
2. Kroto HW, Heath JR, Obrien SC et al (1985) C_{60} - Buckminsterfullerene. Nature 318(6042):162–163
3. Campbell EEB, Rohmund F (2000) Fullerene reactions. Rep Prog Phys 63(7):1061–1109
4. Liu SY, Sun SQ (2000) Recent progress in the studies of endohedral metallofullerenes. J Organomet Chem 599(1):74–86
5. Wang LS, Alford JM, Chai Y et al (1993) Photoelectron-spectroscopy and electronic-structure of $Ca@C_{60}$. Z Phys D-Atoms Mol Clusters 26:S297–S299
6. Hoffman K, Norris B, Merle R et al (1998) Near infrared Er^{3+} photoluminescence from erbium metallofullerenes. Chem Phys Lett 284(3):171–176
7. Kimura T, Sugai T, Shinohara H (1999) Production and mass spectroscopic characterization of metallocarbon clusters incorporating Sc, Y, and Ca atoms. Int J Mass Spectrom 188(3):225–232
8. Kong XL, Bao XD (2014) Generation of $M@C_{2n}^{+}$ (M = Ca, Sr, Ba, 2n = 50-230) by laser ablation of graphene. Int J Mass Spectrom 372:1–7
9. Bao XD, Kong XL (2015) Generation of $M@C_{2n}^{+}$ (M = K, Rb, Cs, 2n = 80-220) by laser ablation of graphene. Rapid Commun Mass Spectrom 29(19):1774–1778
10. Javahery G, Petrie S, Wang J et al (1993) Gas-phase reactions of fullerene monocations, dications, and trications with nitriles. J Am Chem Soc 115(21):9701–9707
11. Bohme DK, Boltalina OV, Hvelplund P (2000) Fullerenes and fullerene ions in the gas phase. Fullerenes: Chem Phys Technol 481
12. Böhme DK (1999) 1998 JC Polanyi Award Lecture fullerene ions in the gas phase: chemistry as a function of charge state. Can J Chem 77(9):1453–1464
13. Hettich R, Lahamer A, Zhou L et al (1999) Investigation of the fragmentation and oxygen reactivity of endohedral metallofullerenes $M@C_{60}$. Int J Mass Spectrom 182:335–348
14. Lassesson A, Gromov A, Jonsson M et al (2003) Oxygen reactivity of $La@C_{82}$ investigated with laser desorption mass spectrometry. Int J Mass Spectrom 228(2–3):913–920
15. Hao CY, Liu ZY, Guo XH et al (1997) Gas phase derivatization of endohedral metallofullerenes $R@C_{82}$ and $R_2@C_{80}$ (R = Nd, Ce). Rapid Commun Mass Spectrom 11(15):1677–1680
16. Sun D, Liu Z, Liu Z et al (1997) Gas phase derivations of endohedral metallofullerenes by ion-molecular reactions. Fullerenes Nanotubes Carbon Nanostruct 5(7):1461–1477
17. Wang XB, Woo HK, Wang LS (2005) Vibrational cooling in a cold ion trap: Vibrationally resolved photoelectron spectroscopy of cold C_{60}^{-} anions. J Chem Phys 123:051106/051101
18. Wang X-B, Woo H-K, Huang X et al (2006) Direct experimental probe of the on-site coulomb repulsion in the doubly charged fullerene anion C_{70}^{2-}. Phys Rev Lett 96(14):143002
19. Jin C, Hettich RL, Compton RN et al (1994) Attachment of two electrons of $C_{60}F_{48}$: Coulomb barriers in doubly charged anions. Phys Rev Lett 73(21):2821–2824
20. Wang LS, Conceicao J, Jin CM et al (1991) Threshold photodetachment of cold C_{60}. Chem Phys Lett 182(1):5–11
21. Huang D-L, Dau PD, Liu H-T et al (2014) High-resolution photoelectron imaging of cold C_{60}^{-} anions and accurate determination of the electron affinity of C_{60}. J Chem Phys 140(22):224315
22. Ioffe I, Ievlev A, Boltalina O et al (2002) Electron affinity of some trimetallic nitride and conventional metallofullerenes. Int J Mass Spectrom 213(2):183–189

23. Boltalina OV, Markov VY, Lukonin AY et al (eds) (1995) Mass spectrometric measurements of the equilibrium constants of ion-molecular reactions of fullerenes, fluorine derivatives and endohedrals. Electron and fluorine affinity estimates, vol 95–100. Recent advances in the chemistry and physics of fullerenes and related materials. The Electrochemical Society, Inc., Pennington
24. Boltalina OV, Dashkova EV, Sidorov LN (1996) Gibbs energies of gas-phase electron transfer reactions involving the larger fullerene anions. Chem Phys Lett 256(3):253–260
25. Wang W, Ding J, Yang S et al (1997) Electrochem Soc Proc 97-14:186
26. Suzuki T, Kikuchi K, Oguri F et al (1996) Electrochemical properties of fullerenolanthanides. Tetrahedron 52(14):4973–4982
27. Nagase S, Kobayashi K, Akasaka T (1996) Endohedral metallofullerenes: new spherical cage molecules with interesting properties. Bull Chem Soc Japan 69(8):2131–2142
28. Stevenson S, Rice G, Glass T et al (1999) Small-bandgap endohedral metallofullerenes in high yield and purity. Nature 401(6748):55–57
29. Takata M, Nishibori E, Umeda B et al (1997) Structure of endohedral dimetallofullerene $Sc_2@C_{84}$. Phys Rev Lett 78(17):3330
30. Perdew JP, Burke K, Ernzerhof M (1996) Generalized gradient approximation made simple. Phys Rev Lett 77(18):3865
31. Compton R, Tuinman A, Klots C et al (1997) Electron attachment to a negative ion: $e + C_{84}^{-} \rightleftharpoons C_{84}^{-2}$. Phys Rev Lett 78(23):4367
32. Kobayashi K, Nagase S (1998) Chem Phys Lett 282:325
33. Hino S, Umishita K, Iwasaki K et al (1997) Photoelectron spectra of metallofullerenes, GdC_{82} and La_2C_{80}: electron transfer from the metal to the cage. Chem Phys Lett 281(1):115–122
34. Lide DR (2004) CRC handbook of chemistry and physics, vol 85. CRC Press, New York
35. Broclawik E, Eilmes A (1998) Density functional study of endohedral complexes $M@C_{60}$ (M = Li, Na, K, Be, Mg, Ca, La, B, Al): electronic properties, ionization potentials, and electron affinities. J Chem Phys 108(9):3498–3503
36. Rohmund F, Bulgakov A, Hedén M et al (2000) Photoionisation and photofragmentation of $Li@C_{60}$. Chem Phys Lett 323(1):173–179
37. Hettich R, Ying Z, Compton R (1995) Recent advances in the chemistry and physics of fullerenes and related materials. In: Kadish, KM, Ruoff RS (eds). The Electrochemical Society, Inc., Pennington
38. Boltalina OV, Ioffe IN, Sorokin ID et al (1997) Electron affinity of some endohedral lanthanide fullerenes. J Phys Chem A 101(50):9561–9563
39. Campanera JM, Bo C, Olmstead MM et al (2002) Bonding within the endohedral fullerenes $Sc_3N@C_{78}$ and $Sc_3N@C_{80}$ as determined by density functional calculations and reexamination of the crystal structure of $\{Sc_3N@C_{78}\}\cdot Co(OEP)\cdot 1.5(C_6H_6)\cdot 0.3(CHCl_3)$. J Phys Chem A 106(51):12356–12364
40. Popov AA, Wang X-B (2016) Unpublished results
41. Scheier P, Dünser B, Wörgötter R et al (1994) Appearance and ionization energies of singly, doubly and triply charged C_{60} and its fragment ions produced by electron impact ionization. Int J Mass Spectrom Ion Processes 138:77–93

Chapter 5
Photoexcitation in Donor–Acceptor Dyads Based on Endohedral Fullerenes and Their Applications in Organic Photovoltaics

Jieming Zhen, Qing Liu and Shangfeng Yang

Abstract Fullerenes are popular electron acceptors for their high electron affinity and low reorganization energy. Photoexcitation in endohedral fullerenes (EMFs)-based donor–acceptor dyads have been comprehensively studied in the past decade. Different donor moieties such as ferrocene, exTTF, zinc tetraphenylporphyrine, triphenylamine were successfully used to construct EMF-based donor–acceptor dyads, and the charge/energy transfer mechanisms between versatile donors and EMF acceptors were extensively investigated. Besides, the charge carrier mobility of solid EMFs and applications of EMFs in organic photovoltaics (OPVs) and photoelectrochemical (PEC) cells were also reviewed.

5.1 Introduction

During the past 2 decades, photoactive electron donor–acceptor dyads have drawn great attention of researchers, especially in the field of organic photovoltaics (OPVs) [1]. In particular, fullerenes like C_{60} and C_{70} and their derivatives have been widely used as electron acceptors in OPVs, due to their low reorganization energies and high electron affinity [1]. So far hundreds of fullerene derivatives including donor–acceptor dyads have been designed and synthesized in order to understand the nature of photoexcitation within the dyad molecules and to develop new OPV materials.

Endohedral fullerenes (or termed as endohedral metallofullerenes, EMFs) have special properties in comparison with empty fullerenes, due to the encapsulation of atom, ion or cluster inside the carbon cages, which results in electron transfer from the encapsulated species to the outer carbon cage and consequently influence the

J. Zhen · Q. Liu · S. Yang (✉)
Hefei National Laboratory for Physical Science at Microscale, CAS Key Laboratory of Materials for Energy Conversion, Department of Materials Science and Engineering, University of Science and Technology of China (USTC), Hefei 230026, China
e-mail: sfyang@ustc.edu.cn

A.A. Popov (ed.), *Endohedral Fullerenes: Electron Transfer and Spin*, Nanostructure Science and Technology, DOI 10.1007/978-3-319-47049-8_5

electronic structures and physical/chemical properties of the entire EMF molecule [2]. Therefore, the properties of EMFs can be readily modulated by tuning the encapsulated species [2]. In particular, since the chemical properties of EMFs are quite different to those of empty fullerenes, the formation of donor–acceptor dyads and/or their OPV performance change dramatically.

In this chapter, the photoexcited charge transfer in donor–acceptor dyads based on EMFs are reviewed, including EMF-based molecular donor–acceptor dyads, host–guest supramolecular complexes and EMF–polymer blends. In addition, the applications of EMFs in OPVs and photoelectrochemical (PEC) cells as electron acceptors will be also presented.

5.2 Photoexcited Charge Transfer in EMF-Based Donor–Acceptor Dyads

5.2.1 Molecular Donor–Acceptor Dyads

5.2.1.1 Ferrocene–EMF Dyad

The first EMF-based donor–acceptor dyad was constructed via conjugating an EMF with ferrocene by Pinzón et al. [3]. The $Sc_3N@C_{80}$-ferrocene dyad, *N*-methyl-2-ferrocenyl-[5,6]-$Sc_3N@C_{80}$-pyrrolidine dyad, was synthesized via a Prato reaction of $Sc_3N@C_{80}$, sarcosine and ferrocene carboxaldehyde as illustrated in Fig. 5.1. Formation of the [5,6]-regioisomer of $Sc_3N@C_{80}$-ferrocene dyad was confirmed by NMR spectroscopy and electrochemistry. The optical bandgap of the dyad was determined to be 1.3 eV by absorption spectroscopy [3]. Photophysical study of the $Sc_3N@C_{80}$-ferrocene dyad was carried out by time-resolved transient absorption spectroscopy. Upon excited at 388 nm, the singlet excited state of the dyad decayed rapidly into a charge-separated state with a lifetime of only 5 ps, which was about 10 times faster than that detected for the pristine $Sc_3N@C_{80}$ reference system (lifetime: 48 ps). The radical ion pair state is metastable as it decays with a lifetime of 128 ps in carbon disulfide (CS_2) and 84 ps in *o*-dichlorobenzene (*o*-DCB) [3], and is more stable than that of the similar C_{60}-ferrocene dyad reported by Guldi and co-workers, for which the lifetime is 46, 49 and 27 ps in CS_2, THF and benzonitrile, respectively [4].

Later on, using the similar approach, the same groups reported the synthesis of new donor–acceptor dyad based on $Y_3N@C_{80}$–ferrocene. It was found that the $Y_3N@C_{80}$–ferrocene dyad took a retrocycloaddition reaction upon heated at 150 °C. However, the photophysical study of the $Y_3N@C_{80}$–ferrocene dyad was not reported [5].

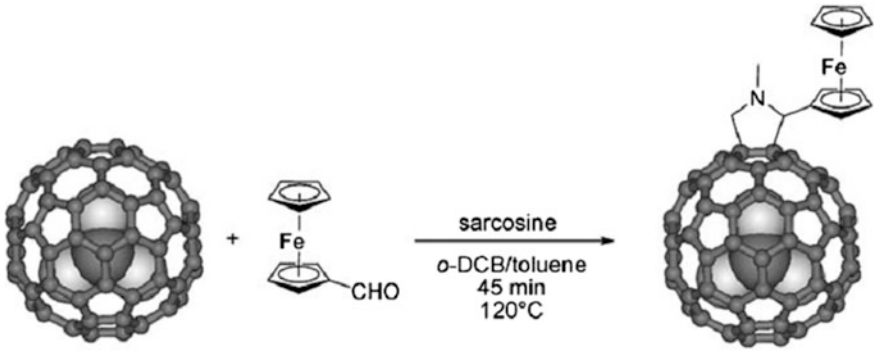

Fig. 5.1 Prato reaction of $Sc_3N@C_{80}$ with ferrocene carboxaldehyde and sarcosine. Reproduced with permission from Ref. [3]. Copyright 2008 Wiley-VCH Verlag GmbH&Co. KGaA

5.2.1.2 π-Extended Tetrathiafulvalene-EMF Dyad

Linking the π-extended tetrathiafulvalene (exTTF) groups to EMFs can enhance the physical and photoactive functionality of the donor–acceptor dyads [6]. In 2009, Echegoyen et al. [5] synthesized several donor–acceptor dyads based on $Sc_3N@C_{80}$ or $Y_3N@C_{80}$ and exTTF via Bingel–Hirsch reaction, but their photophysical properties were not reported. One year later, Martin, Guldi, Akasaka et al. reported the photophysical studies of donor–acceptor dyads of $La_2@I_h$-C_{80} and exTTF, $La_2@I_h$-C_{80}-exTTF, which was synthesized by highly regioselective 1,3-dipolar cycloadditions of exTTF-containing azomethineylide to $La_2@I_h$-C_{80} (Fig. 5.2). A [5,6] metallofulleropyrrolidine structure was confirmed by NMR, UV-Vis-NIR spectra and electrochemical measurement. When excited at 430 nm, no quenching of exTTF fluorescence was observed. According to the transient absorption measurement, both $La_2@C_{80}$ and exTTF were excited to their singlet states upon photoexcitation at 387 nm, and then decayed into charge-separated state within about 20 ps. The authors supposed that the ground state was characterized by weak interactions between the photo- and redox-active constituents, while the excited state was subject to sizable interactions between the electron acceptor and the electron donor [6].

In 2012, the same group reported photophysical studies of an analogue dyads based on $La@C_{82}$ and exTTF. Both $La@C_{82}$ and exTTF moieties were excited upon photoexcitation at 387 nm, and evolved rapidly into radical ion pair state within few picoseconds. The charge recombination in this pair was remarkably slow with values of 2.4 ± 0.5 ns in THF and 1.1 ± 0.3 ns in cyclohexylisonitrile [7].

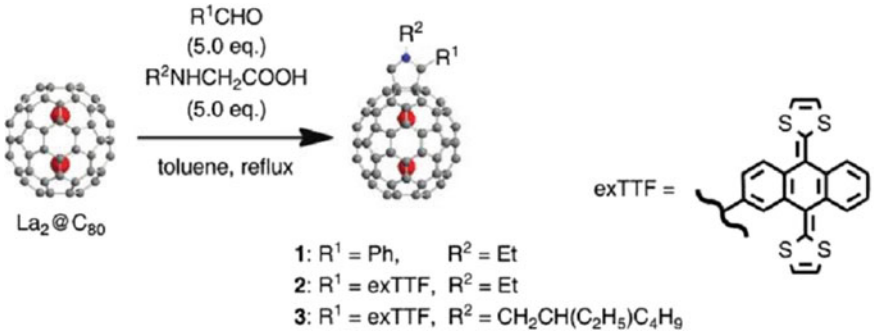

Fig. 5.2 The synthetic route of $La_2@I_h$-C_{80}-exTTF conjugate molecules. Reproduced with permission from Ref. [6]. Copyright 2010 American Chemical Society

5.2.1.3 Zinc Tetraphenylporphyrine-EMF Dyad

Zinc tetraphenylporphyrine (ZnP) was first used as electron donor conjugated with an acceptor of $Ce_2@I_h$-C_{80} by Guldi and Akasaka et al. in 2010 [8]. The dyad named $Ce_2@I_h$-C_{80}-ZnP (Fig. 5.3a) was synthesized via a typical diazo precursor with a [6,6]-phenyl-C_{61}-butyric acid methyl ester (PCBM)-like 2-oxyethyl butyrate as a bridge. Upon photoexcited at 387 nm, the fluorescence of ZnP in $Ce_2@I_h$-C_{80}-ZnP dyad effectively quenched in polar solvents like DMF and benzonitrile, or in nonpolar ones such as toluene and THF. The result revealed remarkably strong interactions between $Ce_2@I_h$-C_{80} and ZnP. However, unprecedented difference was observed in the transient absorption spectra measured in polar and nonpolar solvents: while a reductive charge transfer leading to the formation of $(Ce_2@I_h\text{-}C_{80})^{\bullet-}$-$(ZnP)^{\bullet+}$) was observed in nonpolar solvent (i.e., toluene/THF), the formation of $(Ce_2@I_h\text{-}C_{80})^{\bullet+}$-$(ZnP)^{\bullet-}$) as a result of an oxidative charge transfer dominated in polar media (i.e., benzonitrile/DMF). This phenomena was explained by the comparison of the transient spectra and absorption spectra of electrochemically generated $ZnP^{\bullet-}$, $(Ce_2@I_h\text{-}C_{80}\text{-}ZnP)^{\bullet-}$ and $(Ce_2@I_h\text{-}C_{80}\text{-}ZnP)^{\bullet+}$. The authors concluded that the different strength in electronic coupling, $[Ce_2]^{6+}$/ZnP versus C_{80}^{6-}/ZnP, affected the charge transfer kinetics and the charge transfer mechanism, leading to the formation of different ion pairs [8].

In 2011 Martin, Echegoyen, Guldi et al. reported the long-range charge transfer within a ZnP–EMF dyad comprised of $Sc_3N@C_{80}$ and ZnP [9]. Two $Sc_3N@C_{80}$-ZnP dyads were constructed via long chain linkers, with center-to-center donor-acceptor distances were 32.7 and 45.9 Å, respectively (Fig. 5.3b). Measurement of the fluorescence of the $Sc_3N@C_{80}$-ZnP dyads excited at 420 nm, which was near the Soret band of ZnP at 428 nm, showed notably quenching in comparison to the fluorescence of pristine ZnP molecule. The fluorescence lifetime of the ZnP singlet excited state in dyads was, respectively, 0.5 and 1.6 ns for $Sc_3N@C_{80}$-ZnP dyads with shorter and longer center-to-center distances, which were shorter than that for free ZnP (2.1 ns) [9]. The result of transient absorption

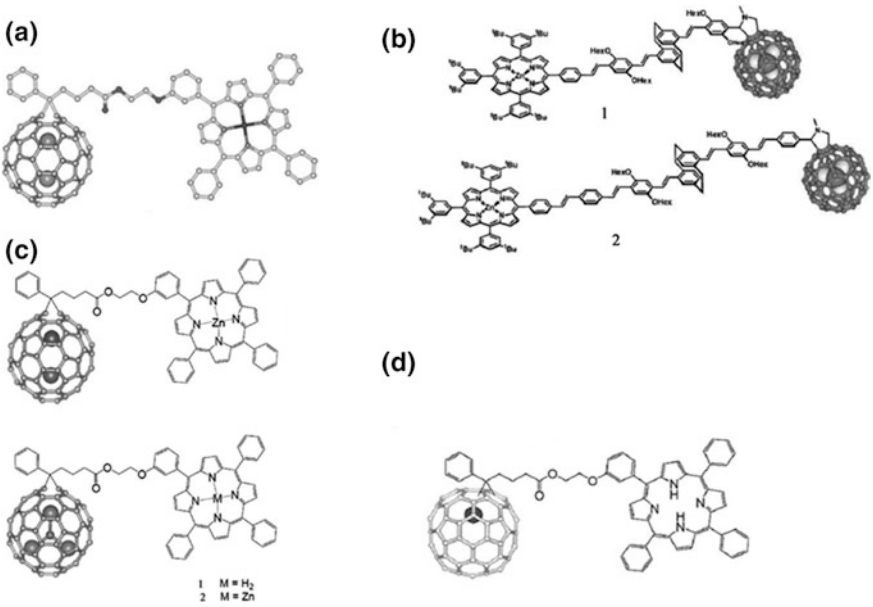

Fig. 5.3 The molecular structures of $Ce_2@I_h$-C_{80}-ZnP (**a**, Reproduced with permission from Ref. [8]. Copyright 2010 American Chemical Society), two $Sc_3N@C_{80}$-ZnP dyads with different center-to-center donor-acceptor distances of 32.7 Å (*1*) and 45.9 Å (*2*) (**b**, Reproduced with permission from Ref. [9]. Copyright 2011 The Royal Society of Chemistry), $Sc_3N@I_h$-C_{80}-ZnP and $La_2@I_h$-C_{80}-PCBE-ZnP dyads (**c**, Reproduced with permission from Ref. [10]. Copyright 2011 American Chemical Society) and $La@C_{82}$-TPP dyad (**d**, Reproduced with permission from Ref. [11]. Copyright 2011 Wiley-VCH Verlag GmbH&Co. KGaA)

spectroscopic studies proved that the singlet excited state of ZnP in dyads decayed via $(Sc_3N@C_{80})^{\bullet-}$-$(ZnP)^{\bullet+}$ charge-separated states with long lifetimes of 1.0 and 1.2 ns for $Sc_3N@C_{80}$-ZnP dyads with shorter and longer center-to-center distances, respectively [9].

The solvent-dependent photophysical property of ZnP–EMF dyad discussed above was also found in an analogous dyad consisting of $La_2@I_h$-C_{80} and ZnP (Fig. 5.3c) [10]. Two EMFs, $Sc_3N@I_h$-C_{80} and $La_2@I_h$-C_{80}, were conjugated to ZnP via [1 + 2] cycloaddition, which were featured by a (6,6)-open addition pattern (Fig. 5.3c). The absorption spectra of these two dyads revealed a redistribution of electron density between EMF and ZnP molecules. The singlet excited state lifetime of $La_2@I_h$-C_{80}-ZnP dyad measured at 387 nm excitation was 30 ps, which was nearly a hundred times faster than that of the C_{60} analogue. Interestingly, it was found that the fast charge separation of radical ion pair of $La_2@I_h$-C_{80}-ZnP including $(La_2@I_h\text{-}C_{80})^{\bullet-}$-$(ZnP)^{\bullet+}$ versus $(La_2@I_h\text{-}C_{80})^{\bullet+}$-$(ZnP)^{\bullet-}$, varied with solvent polarity. However, although the singlet excited state lifetime of $Sc_3N@I_h$-C_{80}-ZnP dyad (48 ps) was comparable to that of $La_2@I_h$-C_{80}-ZnP one, $Sc_3N@I_h$-C_{80}-ZnP dyad did not show the dependence of radical ion pair formation on solvent

polarity because the formation of $(Sc_3N@I_h\text{-}C_{80})^{\bullet+}$-$(ZnP)^{\bullet-}$ radical ion pair was difficult due to the thermodynamically uphill processes [10].

Metal-free porphyrine was also used to construct dyads with EMFs. In 2011 Akasaka et al. reported the synthesis of tetraphenylporphyrine (H_2Por)-La@C_{82} dyad (Fig. 5.3d) following the method used for the synthesis of PCBM [11]. Steady-state fluorescence spectroscopic study of the La@C_{82}-H_2Por dyad revealed strong intramolecular interactions between the excited state of La@C_{82} and the H_2Por group, which was interpreted by a hypothesis of an energy transduction evolving from photoexcited H_2Por to La@C_{82} [11]. The energy level of the first doublet excited state of La@C_{82} was about 0.88 eV, while the value of the radical ion pair state, $(La@C_{82})^{\bullet-}$-$(H_2Por)^{\bullet+}$, was 1.05 eV, and this made electron transfer thermodynamically less favored [11].

5.2.1.4 Triphenylamine-EMF Dyad

Photophysical properties of triphenylamine (TPA)–EMF dyads were studied by Echegoyen et al. in 2009 [12]. TPA was linked to $Sc_3N@C_{80}$ via Prato reaction to form two isomers of [5,6]-prrolidine-$Sc_3N@C_{80}$-TPA dyads (Fig. 5.4) with difference on the location of TPA group which was connected either to the nitrogen or the carbon atom of the ring, and the latter one had a shorter distance between $Sc_3N@C_{80}$ and TPA. The nitrogen-linked dyad showed a better thermal stability than that of the carbon-linked one. Based on the differential absorption measurement, the nitrogen-linked dyad showed a longer lifetime of the photoinduced charge-separated state, compared to the carbon-linked one. The former one had a lifetime of 3 ns in benzonitrile, while the lifetime of the latter one was 2.2 ns [12]. For the charge recombination processes, the $Sc_3N@C_{80}$–TPA dyads had considerably larger rate constants than the C_{60}–TPA analogues, indicating the EMF-based dyads had longer lived photoinduced charge-separated states [12].

5.2.1.5 Dyads Based on Other Donors

A perylene dye, namely 1,6,7,12-tetrachloro-3,4,9,10-perylenediimide (PDI), has advantages of outstanding light harvesting and electron-accepting properties, thus was used as an electron acceptor linked to $Lu_3N@C_{80}$ EMF by Akasaka and Guldi et al. in 2012 (Fig. 5.5a) [13]. $Lu_3N@C_{80}$-PDI dyad was synthesized via [1 + 2]-cycloaddition reaction of $Lu_3N@C_{80}$ and PDI diazo compounds, yielding a [6,6]-open product. According to the transient photophysics study of the dyad excited at 530 nm, electron transfer evolved from the ground state of $Lu_3N@C_{80}$ to the PDI singlet excited state to form radical ion pair of $(Lu_3N@C_{80})^{\bullet+}$-$(PDI)^{\bullet-}$, whose lifetime was 120 ± 10 ps in toluene, 100 ± 10 ps in chlorobenzene, and 45 ± 5 ps in benzonitrile. However, only $Lu_3N@C_{80}$-based triplet state was observed when the dyad was excited at 387 nm [13]. This result was quite contrary

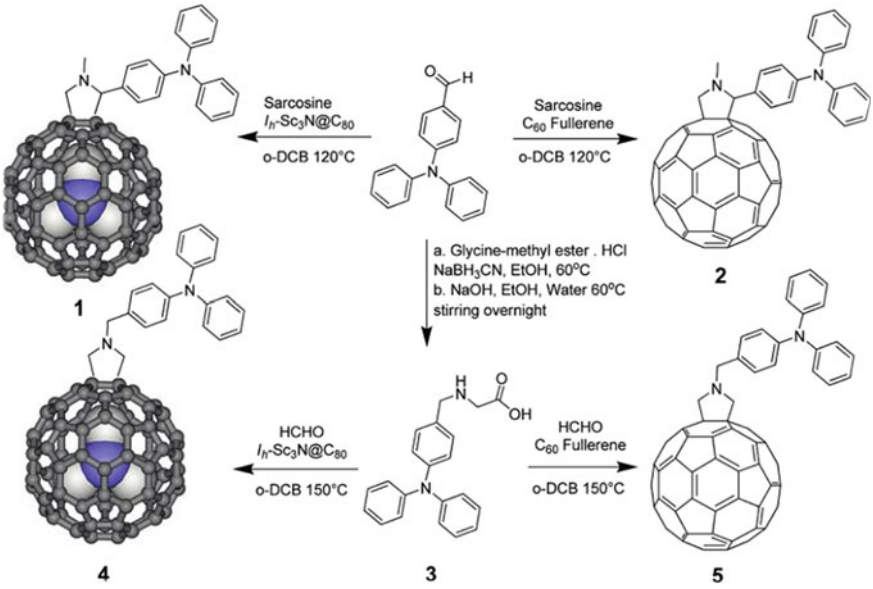

Fig. 5.4 Synthesis of triphenylaime $Sc_3N@C_{80}$ or C_{60} donor-acceptor conjugates. Reproduced with permission from Ref. [12]. Copyright 2009 American Chemical Society

to the excited state deactivation of an analogue C_{60}-PDI dyad, in which the presence of two electron acceptors precluded any electron transfer (Fig. 5.5b) [13].

A similar concept to construct EMF–acceptor dyad was also applied by using another acceptor, namely 11,11,12,12-tetracyano-9,10-anthra-*p*-quinodimethane (TCAQ) [14]. The TCAQ moiety was linked to $La_2@C_{80}$ via a Prato reaction by Guldi, Martin, Akasaka et al. (Figure 5.6). Time-resolved transient absorption study of the $La_2@C_{80}$-TCAQ dyad revealed in the formation of radical ion pair of $(La_2@C_{80})^{\bullet+}$- $(TCAQ)^{\bullet+}$, which had various lifetime dependent on the polarity of the solvent: 230 ± 15 ps in THF, which was larger than those measured in less polar solvents (80 ± 30 ps in cyclohexanecarbonitrile, 110 ± 10 ps in toluene, and 130 ± 15 ps in carbon disulfide) [14].

Very recently, Guldi et al. [15] synthesized an EMF-based donor-acceptor dyad via a 1,3-dipolar cycloaddition reaction of a corrole-based precursor with $Sc_3N@C_{80}$. The structure was confirmed by mass spectrometry, NMR spectroscopy and electrochemical investigation, which suggested that the addition of the corrole moiety took place at the [5,6]-junction of $Sc_3N@C_{80}$. According to the photophysical studies of the $Sc_3N@C_{80}$-corrole conjugate, when excited at 387 nm, the radical ion pair of $[Sc_3N@C_{80}]^{\bullet-}$-$[corrole]^{\bullet+}$ was formed with different charge recombination lifetime of 21 ± 4, 19 ± 4, and 16 ± 5 ps in toluene, THF, and benzonitrile, respectively. The result was well in accord with the dynamics in the inverted region of the Marcus parabola [15].

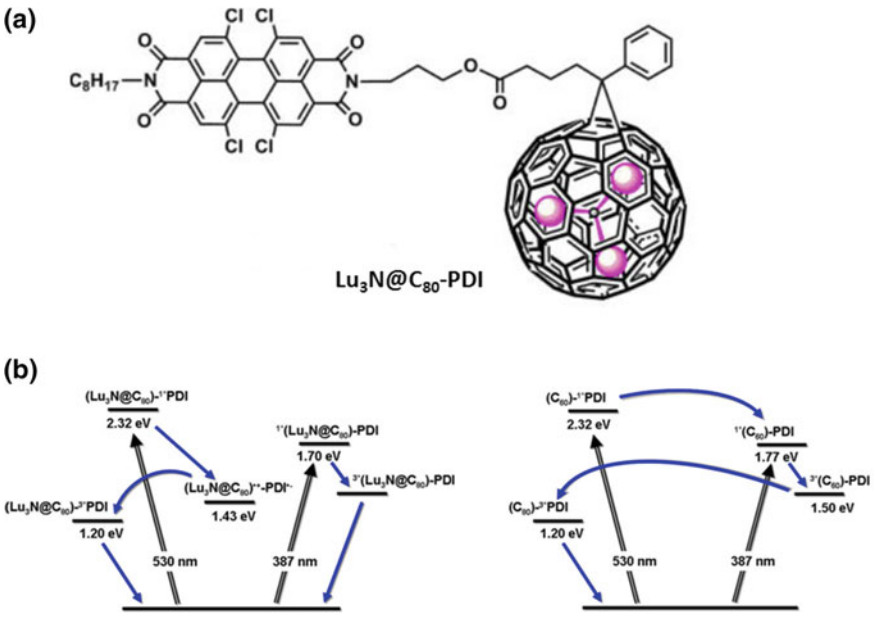

Fig. 5.5 Molecule structure (**a**) and energy level diagram (**b**) of $Lu_3N@C_{80}$-PDI dyad in comparison with that of C_{60}-PDI. Reproduced with permission from Ref. [13]. Copyright 2012 American Chemical Society

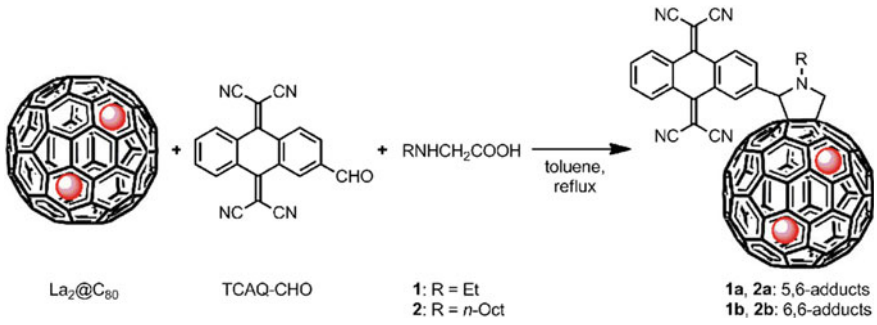

Fig. 5.6 Synthesis scheme of $La_2@C_{80}$-TCAQ dyad. Reproduced with permission from Ref. [14]. Copyright 2012 American Chemical Society

In another work reported by Guldi, Akasaka et al. in 2015, novel $La_2@C_{80}$ and subphthalocyanines (SubPcs)-based donor–acceptor dyads $La_2@C_{80}$-SubPc were synthesized via a Prato reaction. NMR spectrum and DFT calculations revealed that the $La_2@C_{80}$-SubPc had two conformers with a ratio of 3:1. The electrochemical and steady-state absorption studies suggested that there was no electronic interactions between $La_2@C_{80}$ and SubPc in the ground state, while in the excited state,

intramolecular electron transfer evolves from $La_2@C_{80}$ to SubPc to form $(La_2@C_{80})^{\bullet+}$-$(F_{12}SubPc)^{\bullet-}$ or $(La_2@C_{80})^{\bullet+}$-$((SO_2C_5H_{11})_6SubPc)^{\bullet-}$. On the contrary, the C_{60} analogues with SubPcs showed a singlet-singlet energy transfer from SubPc to C_{60}. Therefore, replacing C_{60} by $La_2@C_{80}$ can be an efficient way to tune energy transfer versus electron transfer [16].

5.2.2 Host–Guest Supramolecular Complexes

The spherical shape and large π system of EMF molecule makes it suitable to form host-guest supramolecular complexes with versatile host molecules comprising of π systems. In 2003 Yang and co-workers mixed $Dy@C_{82}$ EMF with different metallophtalocyanines (MPc, M = Cu, Zn) and prepared the Langmuir-Blodgett (LB) films of the $Dy@C_{82}$-MPc mixture [17]. The authors found that the packing of $Dy@C_{82}$-MPc supramolecular complex was dependent on the substituents and the central metal ion of MPc, resulting in different relative orientations of the MPc's macrocyclic ring plane and the EMF ball in the Langmuir films. Steady anodic photocurrent responses was observed for the $Dy@C_{82}$-MPc mixture LB films with enhanced quantum yields compared to the pure forms of both MPc and $Dy@C_{82}$, and the highest photocurrent quantum yield of $Dy@C_{82}$/MPc (M = Cu, Zn) LB films reached up to 7–8% under applying the appropriate voltage and light intensity, which was higher than that obtained for the analogues C_{60} films [17]. The same group also prepared host–guest supramolecular complex of $Dy@C_{82}$ EMF and *p*-tertbutylcalix[8]arene (C8A) (1:1), and studied its LB film formation behavior [18].

In 2011, supramolecular complexes of EMFs with bisporphyrins hosts were reported by two groups independently. Complexes of $Sc_3N@C_{80}$ and $Lu_3N@C_{80}$ guests with bisporphyrins host were prepared by Guldi, Boyd et al. [19]. $Sc_3N@C_{80}$ and $Lu_3N@C_{80}$ EMFs had a stronger binding constant with bisporphyrinand zinic derivative, which was about two orders of magnitude of that for C_{60}. According to the transient absorption spectroscopic measurements, the characteristic near-infrared absorption bands appeared upon the formation of bisporphyrin–EMF complex. It was attributed to charge transfer with the formation of the cationic states of EMFs and anionic bisporphyrins [19]. The binding constant of $Sc_3N@C_{80}$ and bisporphyrins complexes determined by UV-Vis and fluorescence titration was at the order of 10^{-5} M^{-1} [19]. In another report, Echegoyen, Ballesteret al. investigated the complexes of $Sc_3N@C_{80}$ with cyclic Zn–porphyrin receptors bearing aryl groups in all meso positions and flexible hexyldioxo spacers [20], and found that the steady-state fluorescence of Zn–porphyrin was efficiently quenched upon its complex with $Sc_3N@C_{80}$. This phenomenon was explained by photoinduced electron transfer between the receptor and EMF. At micromolar concentration, the Zn–porphyrin receptor formed only a 1:1 complex with the $Sc_3N@C_{80}$ EMF with stability constant of $2.6 \pm 0.3 \times 10^5$ M^{-1} [20].

In 2013 Akasaka and Guldi et al. synthesized the coordination complexes of Zinc tetraphenylporphyrin (ZnP) and $La@C_{82}$ and $La_2@C_{80}$ derivatives (Fig. 5.7)

having pyridyl groups as linkers ($La@C_{82}Py$, $La_2@C_{80}Py$) [21]. The binding constants of the EMF–ZnP complexes determined by absorption spectroscopic study were about 10^4. The photophysical studies by transient absorption spectrum photoexcited at 420 nm revealed deactivation in the excited state of the complexes, which was attributed to electron transfer with the formation of $(ZnP)^{\bullet+}$ and radical anion of EMF [21]. The fastest charge separation was observed in $La@C_{82}Py$ due to the lowest reduction potential/largest driving force for charge separation, while $La_2@C_{80}Py$ exhibited the slowest charge recombination owing to the localization of singly occupied molecular orbital (SOMO) between the encapsulated La atoms [21].

Photoinduced electron transfer between $Li^+@C_{60}$ and different donors in Benzonitrile (PhCN) solution was studied by Fukuzumiet al [22]. The rate constant of the inter system crossing from the singlet excited state of $Li^+@C_{60}$ to the triplet excited state measured by femtosecond laser flash photolysis of $Li^+@C_{60}$ was $8.9 \times 10^8\ s^{-1}$. The reactivity of the electron transfer reduction of $^3(Li^+@C_{60})^*$ is much higher than that of $^3C_{60}^*$, which was attributed to higher one-electron reduction potential of $Li^+@C_{60}$ than that of C_{60}. The reorganization energy of electron transfer of $Li^+@C_{60}$ was determined from the driving force dependence of electron transfer rate as 1.1 eV, which was 0.28 eV lager than that of C_{60} probably due to the change in electrostatic interaction of the encapsulated Li^+ during the electron transfer [22]. Later on, the same group studied the photoinduced electron transfer between two EMFs by nanosecond laser flash photolysis, in which $Sc_3N@C_{80}$ played a role of electron donor and the triplet excited state of $Li^+@C_{60}$ worked as electron acceptor in PhCN and *o*-dichlorobenzene [23]. The constant rate of electron transfer from $Sc_3N@C_{80}$ to [3] $(Li^+@C_{60})^*$ and back from $Li^+@C_{60}^{\bullet-}$ to $Sc_3N@C_{80}^{\bullet+}$ were both at the order of $10^9\ M^{-1}\ s^{-1}$ [23]. Very recently, the same group successfully prepared a charge transfer complex between corannulene ($C_{20}H_{10}$) and $Li^+@C_{60}$ via concave–convex π–π charge transfer interaction, which had a binding constant of $1.9 \times 10\ M^{-1}$ [24]. The absorption spectra of the complex revealed that the lifetime of the singlet charge-separated state of the

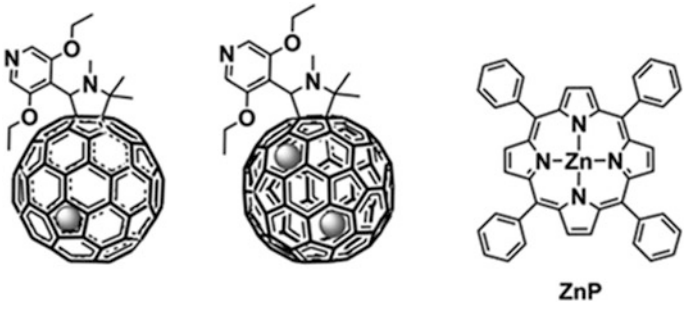

Fig. 5.7 Structures of $La@C_{82}Py$ and $La_2@C_{80}Py$ that were used to complex zincporphyrin (ZnP). Reproduced with permission from Ref. [21]. Copyright 2013 Wiley-VCH Verlag GmbH&Co. KGaA

$C_{20}H_{10}/Li^+@C_{60}$ complex was 1.4 ns, while the triplet excited state formed by the electron transfer from $C_{20}H_{10}$ to $^3(Li^+@C_{60})^*$ showed a remarkable long lifetime of 240 μs, which was attributed to the small electronic coupling term ($V = 0.0080\ cm^{-1}$) and the spin forbidden back electron transfer process [24]. In another recent work, Fukuzumi et al. extended the studies of $Li^+@C_{60}$-based complex to the inclusion complexes between crown ether fused tetrathiafulvalenes and $Li^+@C_{60}$. The result showed that the complexes had large binding constants, which suggested that $Li^+@C_{60}$ can be a better alternative than the pristine fullerene to combine with TTFs for practical application in energy conversion [25].

In 2013 Taherpour et al. studied theoretically the electron transfer in a series of complexes of $Gd_3N@C_n$ (n = 80, 82, 84, 86 and 88) EMFs and thiocrown ethers derivatives ([X-UT-Y]). The authors calculated the first and second free energies of electron transfer and kinetic rate constants of the electron transfers for [X-UT-Y]-$Gd_3N@C_{80}$-R, which was in accordance with the Marcus theory [26].

5.2.3 EMF–Polymer Blends

OPVs especially polymer solar cells (PSCs) have been receiving great attention in recent years, because it has many advantages compared to the traditional inorganic solar cells, including light weight, flexibility, and low manufacturing cost by the large area roll-to-roll production process [1]. Fullerenes specifically C_{60} and C_{70} have been extensively applied as electron acceptors in OPVs, while there are only quite few reports on the application of EMFs in OPVs. In 2009 Drees and co-workers reported the first application of EMF as electron acceptors in OPVs [27]. The authors first synthesized a series of [6,6]-PCBM-like derivatives of $Lu_3N@C_{80}$, namely $Lu_3N@C_{80}$-PCBX (X = Methyl, Butyl, Hexyl, Octyl), which only differs in the terminal alkyl groups in the ether fragment. $Lu_3N@C_{80}$-PCBH was then mixed with poly(3-hexyl)thiophene (P3HT) to form a donor/acceptor active layer in the OPV devices. Differential absorption spectra of a P3HT/$Lu_3N@C_{80}$-PCBH film showed that the singlet excited state lifetime of P3HT was only 0.55 ps, and it rapidly decayed to charge-separated state with the P3HT-localized radical cation and $Lu_3N@C_{80}$-PCBH radical anion [27]. Such a radical ion pair states exhibited remarkable stability in films with lifetimes exceeding 1.0 ms. Upon incorporating $Lu_3N@C_{80}$-PCBH as electron acceptor in OPV devices, the power conversion efficiency (PCE) of the P3HT/$Lu_3N@C_{80}$-PCBH OPV device was 4.2%, about 20% higher than the P3HT/C_{60}-PCBM one [27]. The main factor responsible for such an increase was the dramatic increase of the open circuit voltage (V_{oc}) by 260 mV (890 and 630 mV for $Lu_3N@C_{80}$-PCBH and C_{60}-PCBM-based device, respectively), which was resulted from the negative shift of the first reduction potential of $Lu_3N@C_{80}$-PCBH by 0.28 V compared to that of C_{60}-PCBM [27]. Later on, the same authors optimized the blending ratio of P3HT:$Lu_3N@C_{80}$-PCBH, and revealed that $Lu_3N@C_{80}$-PCBH promoted phase

segregation of P3HT similar to C_{60}-PCBM, and increased interlayer interactions in the P3HT matrix [28].

In 2011 Liedtke studied the effects of other factors, including morphology of the film and donor/acceptor ratio on the short circuit current (J_{sc}) of the P3HT/$Lu_3N@C_{80}$-PCBEH (EH = 2-ethyl-hexyl) OPV device [29]. The results revealed that the photoluminescence quenching of P3HT in P3HT/$Lu_3N@C_{80}$-PCBEH blend was two times weaker than that in P3HT/C_{60}-PCBM one, and consequently smaller J_{sc} in P3HT/$Lu_3N@C_{80}$-PCBEH OPV device was observed. Besides, the authors proposed that triplet excitons formed on the P3HT polymer chain in the P3HT/$Lu_3N@C_{80}$-PCBEH blend, which were however absent in P3HT/C_{60}-PCBM one. The reason for the lower photocurrent in P3HT/$Lu_3N@C_{80}$-PCBEH OPV device was that electrons transferred to the triplet state and exciton dissociation was lower [29].

PEC cells based on EMF-polymer blend were also studied. In 2004 Yang et al. reported the application of Dy@C_{82}-P3HT blend LB films in PEC cells, and found that the power conversion efficiency and photocurrent quantum yield of PEC cell based on Dy@C_{82}-P3HT blend films exhibited dramatic enhancement compared to that based on pure P3HT [30]. However, the clear mechanism of the electron transfer was still unknown without transient spectroscopic study [30].

5.3 Applications of EMFs in Organic Photovoltaic (OPV)

5.3.1 Charge Carrier Mobility of Solid EMFs

Conductivity and charge carrier mobility are intrinsic properties of solid EMFs, which play important role in practical application in electronic devices such as photovoltaics. So far, charge carrier mobilities of several kinds of EMFs have been studied, The dielectric activity of La@C_{82} solids was first studied by Iwasa et al. in 2002, and the dipole dynamics in La@C_{82} showed complicated temperature dependence [31]. In 2003 Kubozono et al. studied transport properties of Dy@C_{82}, and semiconducting behavior was observed in the Dy@C_{82} crystals from 170 to 350 K [32]. In 2003, Kareev et al. [33] studied the transport properties of the extracts of La@C_{82} and Y@C_{82}. They found that oxygen and heat treatments affected the conductivity of the EMFs, and the conductivity of these EMFs increased from 10^{-5} to 10^{-2} Ω^{-1} cm^{-1} after heat treatment [33]. During 2003-2005, charge carrier mobilities of Dy@C_{82}, Ce@C_{82}, Pr@C_{82} and $La_2@C_{80}$ were measured in the form of sublimed film via field effect transistor (FET) mode [34]. The measurements were carried out on the sublimed film of EMFs, and the results showed that the electron mobilities of EMFs were in the order of $\sim 1\times10^{-4}$ cm^2V^{-1} s^{-1}. Such a low electron mobility was mainly attributed to the low crystallinity of the samples [34]. In 2008, electrical properties of sublimed film of La@C_{82} and Li@C_{60} were studied by

Popok et al. Resistivity of La@C_{82} was measured to be about 21 kΩ cm, which was two orders of magnitude lower than that of Li@C_{60} [35].

Recently, time-resolved microwave conductivity (TRMC) method has been used to measure electron mobilities of EMFs, including La@C_{82} derivative, Sc_3N@C_{80} and Sc_3C_2@C_{80} [36]. The adamantylidene (Ad) derivative of La@C_{82}, La@C_{82}Ad, was first prepared [36]a, and the electron mobility of La@C_{82}Ad single crystal along the c axis crystal direction was measured to be as high as 10 ± 5 cm^2 V^{-1} s^{-1} under normal temperature and pressure in the atmosphere, which represents the largest mobility for organic semiconductors measured via TMRC [36]a. However, the mobility showed significant anisotropy, and the values along other crystal directions reduced more than an order of magnitude (Fig. 5.8a) [36]a. In addition, drop-casted polycrystalline films of La@C_{82}Ad were also studied by TMRC in the same work. The drop-casted film of La@C_{82}Ad from carbon disulfide exhibited a mobility of $(7 \pm 3) \times 10^{-2}$ cm^2 V^{-1} s^{-1}, which was similar to the drift mobilities of the films of La@C_{82}Ad and La@C_{82} obtained by time-of-flight technique (TOF), but smaller than that of La@C_{82}Ad single crystal (Fig. 5.8b) [36]a. These results proved that the crystallinity of samples eventually affected the carrier mobility. Moreover, according to density functional theory (DFT) calculations, La@C_{82}Ad has a small band gap of 0.005 eV, thus La@C_{82}Ad can be regarded as a semimetal [36]a.

In another work by Akasaka et al., co-crystal of La@C_{82} with nickel porphyrin [Ni^{II}(OEP)] (OEP = octaethylporphyrin) was studied in the single crystalline state, which was the first characterization of pristine La@C_{82} by single-crystal X-ray diffraction analysis [37]. The result revealed that the electron mobility of La@C_{82}·Ni^{II}(OEP) co-crystal was anisotropic, varying from 0.1 to 0.9 cm^2 V^{-1} s^{-1} in different crystal directions [37]. DFT result indicated that some bands of the crystal crossed the Fermi level, thus the sample had a metallic character and good electrical conduction.

The mobilities of paramagnetic EMFs including La_2@C_{80}, Sc_3N@C_{80} and Sc_3C_2@C_{80} in the form of drop-casted films were also studied by TMRC [36]b. Thin film of Sc_3C_2@C_{80} exhibits a high electron mobility of 0.13 cm^2 V^{-1} s^{-1}, while the value of La_2@C_{80} or Sc_3N@C_{80} was 2 times smaller [36]b. The electrical transport properties of Er_3N@C_{80} in the form of nanocrystal were also studied by measuring temperature-dependent conductivity and current–voltage characteristics [38].

5.3.2 *EMF-Based Polymer Solar Cells (PSCs)*

EMF was first applied as a novel photovoltaic acceptor in polymer solar cells (PSCs) in 2009 [27]. Drees et al. first synthesized several Lu_3N@C_{80} methano derivatives and integrated them into PSC devices as photovoltaic acceptors blended with the donor, poly(3-hexyl)thiophene (P3HT) (Fig. 5.9). Their results revealed that the offset of the molecular orbitals of Lu_3N@C_{80} to P3HT were reduced,

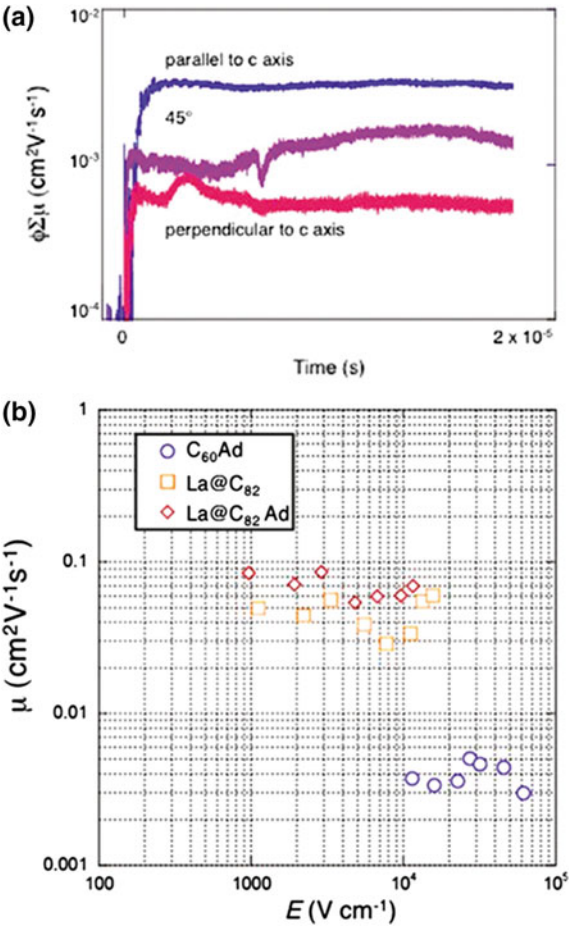

Fig. 5.8 **a** Transient conductivity for single-crystal La@C_{82}Ad. Excitation was conducted at 532 nm: 10 mJ/cm^2; **b** dependence of mobility upon electronic field strength in negative bias mode observed for La@C_{82}, La@C_{82}Ad, and C_{60}Ad. Reproduced with permission from Ref. [36]a. Copyright 2011 American Chemical Society

compared with [6,6]-phenyl-C_{61}-butyric methylester (C_{60}-PCBM) acceptor. The open circuit voltage (V_{oc}) reached 890 mV by using 1-(3-hexoxycarbonyl) propyl-1-phenyl-[6,6]-$Lu_3N@C_{81}$($Lu_3N@C_{80}$–PCBH) as photovoltaic acceptor, which was 260 mV higher than the reference devices based on C_{60}-PCBM acceptor [27]. Thus, by using $Lu_3N@C_{80}$–PCBH acceptor, power conversion efficiency (PCE) reached 4.2% with open circuit voltage (V_{oc}), short circuit current density (J_{sc}) and fill factor (FF) being 0.81 V, 8.64 mA/cm^3 and 0.61, respectively, under the illumination of AM1.5, 100 mW/cm^2. Comparatively, PCE of the reference device based on P3HT/PC_{61}BM was only 3.4% with a V_{oc} of 0.63 V, a J_{sc} of 8.9 mA/cm^2 and a FF of 0.61 under the same experimental conditions [28]. The main factor responsible for the significant increase of V_{oc} was the negative shift of the first reduction potential of $Lu_3N@C_{80}$-PCBH by 0.28 V compared to that of C_{60}-PCBM [27].

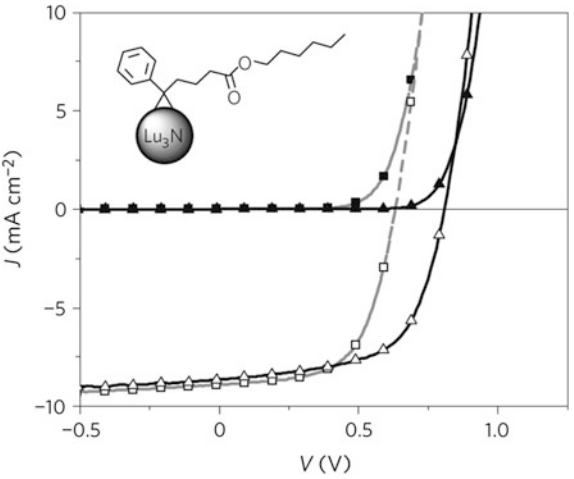

Fig. 5.9 J–V curves of P3HT/$Lu_3N@C_{80}$-PCBH (*triangles*) and P3HT/C_{60}-PCBM (*squares and dashed lines*) *filled symbols* show the *dark curves* and *open symbols* show devices under simulated Air Mass 1.5 (100 $mWcm^{-2}$). *Inset* the structures of $Lu_3N@C_{80}$ methano derivative $Lu_3N@C_{80}$-PCBH. Reproduced with permission from Ref. [27]. Copyright 2009 Nature Publishing Group

Later on, the same authors studied the influence of the blending ratio of P3HT donor and $Lu_3N@C_{80}$–PCBH acceptor on the active layer morphology and the performance of PSC devices by using absorption and photocurrent spectroscopies, grazing incident X-ray diffraction (GIXRD) [28]. The results revealed that the optimal blend ratio of P3HT:$Lu_3N@C_{80}$–PCBH was 50wt%, which was different from that for the typical P3HT:C_{60}-PCBM system (44 wt%). This difference was attributed to the increased molecular size of the $Lu_3N@C_{80}$ methano derivatives. For this reason, effectively reducing the amount of fullerene was needed for efficient charge transport to occur [28]. Furthermore, $Lu_3N@C_{80}$–PCBH promoted phase segregation of P3HT similar to C_{60}-PCBM, and increased interlayer interactions in the P3HT matrix according to the GIXRD results [28].

5.3.3 EMF-Based Photoelectrochemical (PEC) Cells

PEC cells with semiconductor/electrolyte junction have attracted great attention in the field of solar energy conversion [39]. When irradiated, semiconductor material will generate a pair of electron and hole per absorbed photon if the energy of the photon is higher than the bandgap of the semiconductor. Then an electric potential difference will be set up between the semiconductor/electrolyte interface. When using a suitable redox electrolyte, the semiconductor electrode and a metal counter electrode immersed in it can become a simple PEC cell. PEC is an option for solar energy conversion methods, since it provides routes to device with high energy conversion efficiencies. PEC is a way to understand the nature of the electrode–solution interface. Moreover, the subject of PEC processing has also attracted great interests in the field of photocatalysis, electro-optics and electronics [40].

By far, studies on fullerene-based PEC are still at the stage of fundamental issues instead of practical applications. Only a small number of PEC studies based on C_{60} and its derivatives were reported, and the results indicated that the efficiency of C_{60} derivatives is comparable to the PV's solid-solid junction [41]. PEC studies based on EMFs are even rarer and only few studies about the pristine metallofullerenes Dy@C_{82} were reported by Yang et al. [17, 30, 42]. Compared to the empty fullerene C_{60}, the photoinduced electron transfer process of Dy@C_{82} is interestingly different. Monolayer and multilayer Langmuir-Blodgett (LB) films of Dy@C_{82} EMF mixed with arachidic acid (Dy@C_{82}/AA) were firstly deposited onto ITO substrates from the N_2/water interface by Yang et al. in 2001 [42]a. PEC response of the Dy@C_{82}/AA LB films on ITO was investigated and a stable anodic photocurrent was observed [42]a. Later on, the same authors reported PCE studies of LB films of Dy@C_{82} mixed with several different metallophthalocyanines (MPcs) fabricated from the N_2/water interface at a molar ratio of 1:1 [17]. In this study, Dy@C_{82}/MPc mixture films exhibited steady anodic photocurrent responses with enhanced quantum yields compared to the pure forms of both MPc and Dy@C_{82}, and the quantum yields reached up to 7–8% under appropriate conditions [17].

In addition, based on the p-type semiconductor character and excellent PV performance of Dy@C_{82} as well as its good film formation property, Yang et al. constructed PEC cells based on LB films of Dy@C_{82} doped with P3HT [42]b. The authors proposed that the Dy@C_{82} molecules were partially inserting into the chain matrix of P3HT with the polymer backbones taking an edge-on arrangement [42]b. A dramatic enhancement of the stable cathodic photocurrent was obtained for the PEC cells prepared by dispersing Dy@C_{82} into the LB films of P3HT at an optimum ratio of 20:1 (P3HT:Dy@C_{82}), and the PEC cells exhibited 16-fold power conversion efficiency and ninefold quantum yield, respectively, compared to cells made of pure P3HT.

Very recently, Yang et al. studied the photocurrent response of metal nitride clusterfullerene $Sc_3N@C_{80}$ [43]. Micron-sized hexagonal single-crystalline $Sc_3N@C_{80}$ was prepared by a liquid–liquid interfacial precipitation (LLIP) method (Fig. 5.10a). $Sc_3N@C_{80}$ rods-modified ITO electrode prepared by electrophoretic deposition demonstrated a higher photocurrent response than the one obtained by the $Sc_3N@C_{80}$ drop-coated films (Fig. 5.10b).

5.4 Conclusion and Outlook

During the past decade, with the construction of versatile types of EMF-based donor–acceptor dyads, photoexcitation followed by electron transfer between EMFs and many kinds of donor materials was revealed. Up to now, the reported EMF-based donor–acceptor dyads include molecular donor–acceptor dyads containing donors like ferrocene, exTTF, zinc tetraphenylporphyrine, triphenylamine, etc., host-guest supramolecular complexes and EMF-polymer blend. The synthetic strategy, characterization and photophysical study of EMF-based donor–acceptor

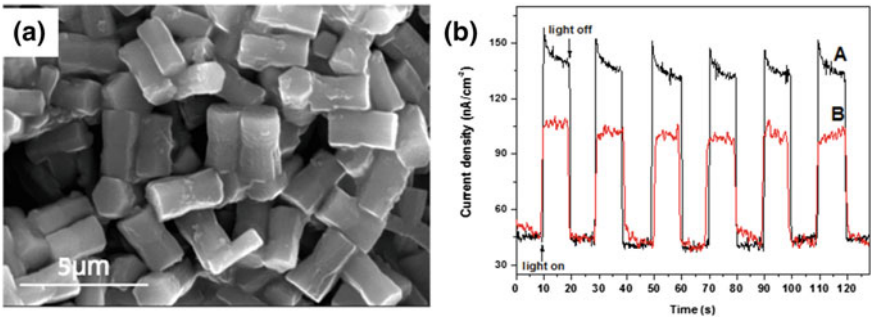

Fig. 5.10 **a** SEM images of micron-sized hexagonal $Sc_3N@C_{80}$ rods prepared by LLIP method; **b** Representative photocurrent trace versus time obtained from Sc3 N@C80 rods-modified ITO prepared by electrophoretic deposition (*A*) or by drop-coating Sc3 N@C80 solution in toluene onto ITO (*B*). The *arrows* mark the light on-off cycles (0.2 V bias voltage, 0.1 M KCl electrolyte solution, 500 W white light illumination). Reproduced with permission from Ref. [43]. Copyright 2014 The Royal Chemical Society

dyad are elaborately reviewed here, providing a better understanding of the nature of electron transfer between EMFs and different donor materials.

We also reviewed the studies of charge carrier mobility of solid EMFs and applications of EMFs in OPV. Despite that quite rare studies on applications of EMFs in OPV have been reported so far, which may be account for the low yield of EMFs, the application of $Lu_3N@C_{80}$–polymer blends as photovoltaic acceptor in PSCs showed outstanding photovoltaic performance with dramatically higher V_{oc} than that obtained for devices based on C_{60}–PCBM acceptor, suggesting the promising potential of EMFs in OPV. In addition, application of EMF in PEC cells was also discussed on the basis of LB films of $Dy@C_{82}$ EMF blended with different molecules such as MPc or P3HT donors, revealing steady photocurrent responses with enhanced quantum yields compared to the pure forms of both $Dy@C_{82}$ and donor.

Although various types of donor moieties have been successfully used to construct EMF-based donor–acceptor dyads, there are still many kinds of donor molecules can be explored, such as benzodithiophene which has been frequently used as a building block of small molecular donors for OPV. On the other hand, given that the photovoltaic performances of EMF-based acceptors such as $Lu_3N@C_{80}$–PCBH can surpass their empty fullerene-based analogues, the next imperative challenge is to develop novel acceptors based on a variety of other EMFs, thus widening the applications of EMFs.

Acknowledgements The research work was partially supported by National Basic Research Program of China (2011CB921400) and National Natural Science Foundation of China (21132007, 21371164).

References

1. He Y, Li Y (2011) Fullerene derivative acceptors for high performance polymer solar cells. Phys Chem Chem Phys 13:1970–1983
2. (a) Popov AA, Yang S, Dunsch L (2013) Endohedral fullerenes. Chem Rev 113:5989–6113; (b) Lu X, Feng L, Akasaka T et al (2012) Current status and future developments of endohedral metallofullerenes. Chem Soc Rev 41:7723–7760
3. Pinzón JR, Plonska-Brzezinska ME, Cardona CM et al (2008) $Sc_3N@C_{80}$-ferrocene electron-donor/acceptor conjugates as promising materials for photovoltaic applications. Angew Chem Int Ed Engl 47:4173–4176
4. Guldi DM, Maggini M, Scorrano G et al (1997) Intramolecular electron transfer in fullerene/ferrocene based donor–bridge–acceptor dyads. J Am Chem Soc 119:974–980
5. Pinzón JR, Cardona CM, Herranz MA et al (2009) Metal nitride cluster fullerene $M_3N@C_{80}$ (M = Y, Sc) based dyads: synthesis, and electrochemical, theoretical and photophysical studies. Chem Eur J 15:864–877
6. Takano Y, Herranz MA, Martin N et al (2010) Donor-acceptor conjugates of lanthanum endohedral metallofullerene and pi-extended tetrathiafulvalene. J Am Chem Soc 132:8048–8055
7. Takano Y, Obuchi S, Mizorogi N et al (2012) Stabilizing ion and radical ion pair states in a paramagnetic endohedral metallofullerene/pi-extended tetrathiafulvalene conjugate. J Am Chem Soc 134:16103–16106
8. Guldi DM, Feng L, Radhakrishnan SG et al (2010) A molecular $Ce_2@I(h)$-C_{80} switch–unprecedented oxidative pathway in photoinduced charge transfer reactivity. J Am Chem Soc 132:9078–9086
9. Wolfrum S, Pinzon JR, Molina-Ontoria A et al (2011) Utilization of $Sc_3N@C_{80}$ in long-range charge transfer reactions. Chem Commun 47:2270–2272
10. Feng L, Radhakrishnan SG, Mizorogi N et al (2011) Synthesis and charge-transfer chemistry of $La_2@I(h)$-C_{80}/$Sc_3N@I(h)$-C_{80}-zinc porphyrin conjugates: impact of endohedral cluster. J Am Chem Soc 133:7608–7618
11. Feng L, Slanina Z, Sato S et al (2011) Covalently linked porphyrin-$La@C_{82}$ hybrids: structural elucidation and investigation of intramolecular interactions. Angew Chem Int Ed Engl 50:5909–5912
12. Pinzón JR, Gasca DC, Sankaranarayanan SG et al (2009) Photoinduced charge transfer and electrochemical properties of triphenylamineIh-$Sc_3N@C_{80}$ donor–acceptor conjugates. J Am Chem Soc 131:7727–7734
13. Feng L, Rudolf M, Wolfrum S et al (2012) A paradigmatic change: linking fullerenes to electron acceptors. J Am Chem Soc 134:12190–12197
14. Takano Y, Obuchi S, Mizorogi N et al (2012) An endohedral metallofullerene as a pure electron donor: intramolecular electron transfer in donor–acceptor conjugates of $La_2@C_{80}$ and 11,11,12,12-tetracyano-9,10-anthra-p-quinodimethane (TCAQ). J Am Chem Soc 134:19401–19408
15. Liu B, Fang H, Li X et al (2015) Synthesis and photophysical properties of a $Sc_3N@C_{80}$-Corrole electron donor–acceptor conjugate. Chem Eur J 21:746–752
16. Feng L, Rudolf M, Trukhina O (2015) Tuning intramolecular electron and energy transfer processes in novel conjugates of $La_2@C_{80}$ and electron accepting subphthalocyanines. Chem Comm 51:330–333
17. Yang S, Fan L, Yang S (2003) Preparation, characterization, and photoelectrochemistry of Langmuir–Blodgett films of the endohedral metallofullerene $Dy@C_{82}$ mixed with metallophthalocyanines. J Phys Chem B 107:8403–8411
18. Yang S, Yang S (2002) Preparation and film formation behavior of the supramolecular complex of the endohedral metallofullerene $Dy@C_{82}$ with Calix[8]arene. Langmuir 18:8488–8495

19. Grimm B, Schornbaum J, Cardona CM et al (2011) Enhanced binding strengths of acyclic porphyrin hosts with endohedral metallofullerenes. Chem Sci 2:1530–1537
20. Hernandez-Eguia LP, Escudero-Adan EC, Pinzon JR et al (2011) Complexation of $Sc_3N@C_{80}$ endohedral fullerene with cyclic Zn-bisporphyrins: solid state and solution studies. J Org Chem 76:3258–3265
21. Tsuchiya T, Rudolf M, Wolfrum S et al (2013) Coordinative interactions between porphyrins and C_{60}, $La@C_{82}$, and $La_2@C_{80}$. Chem Eur J 19:558–565
22. Kawashima Y, Ohkubo K, Fukuzumi S (2012) Enhanced photoinduced electron-transfer reduction of $Li^+@C_{60}$ in comparison with C_{60}. J Phys Chem A 116:8942–8948
23. Kawashima Y, Ohkubo K, Fukuzumi S (2013) Small reorganization energies of photoinduced electron transfer between spherical fullerenes. J Phys Chem A 117:6737–6743
24. Yamada M, Ohkubo K, Shionoya M et al (2014) Photoinduced electron transfer in a charge-transfer complex formed between corannulene and $Li^+@C_{60}$ by concave–convex π–π interactions. J Am Chem Soc 136:13240–13248
25. Supur M, Kawashima Y, Larsen KR et al (2014) Robust Inclusion Complexes of crown ether fused tetrathiafulvalenes with $Li^+@C_{60}$ to afford efficient photodriven charge separation. Chem Eur J 20:13976–13983
26. Taherpour A, Maleki-Noureini M (2013) Free energies of electron transfer, electron transfer kinetic theoretical and quantitative structural relationships and electrochemical properties studies of gadolinium nitride cluster fullerenes $Gd_3N@C_n$ in $[X–UT–Y][Gd_3N@C_n]$(n = 80, 82, 84, 86 and 88) Supramolecular Complexes. Fuller Nanotub Carbon Nanostruct 21: 485–502
27. Ross RB, Cardona CM, Guldi DM et al (2009) Endohedral fullerenes for organic photovoltaic devices. Nat Mater 8:208–212
28. Ross RB, Cardona CM, Swain FB et al (2009) Tuning conversion efficiency in metallo endohedral fullerene-based organic photovoltaic devices. Adv Funct Mater 19:2332–2337
29. Liedtke M, Sperlich A, Kraus H et al (2011) Triplet exciton generation in bulk-heterojunction solar cells based on endohedral fullerenes. J Am Chem Soc 133:9088–9094
30. Yang S, Fan L, Yang S (2004) Langmuir–Blodgett Films of Poly(3-hexylthiophene) Doped with the endohedral metallofullerene $Dy@C_{82}$: preparation, characterization, and application in photoelectrochemical cells. J Phys Chem B 108:4394–4404
31. Nuttall CJ, Hayashi Y, Yamazaki K et al (2002) Dipole dynamics in the endohedral metallofullerene $La@C_{82}$. Adv Mater 14:293–296
32. Kubozono Y, Takabayashi Y, Shibata K et al (2003) Crystal structure and electronic transport of $Dy@C_{82}$. Phys Rev B 67
33. Kareev IE, Bubnov VP, Laukhina EE et al (2003) Endohedral metallofullerenes $M@C_{82}$ (M = La, Y): synthesis and transport properties. Carbon 41:1375–1380
34. (a) Kanbara T, Shibata K, Fujiki S et al (2003) N-channel field effect transistors with fullerene thin films and their application to a logic gate circuit. Chem Phys Lett 379:223–229; (b) Rikiishi Y, Kubozono Y, Hosokawa T et al (2004) Structural and electronic characterizations of two isomers of $Ce@C_{82}$. J Phys Chem B 108:7580–7585; (c) Nagano T, Kuwahara E, Takayanagi T et al (2005) Fabrication and characterization of field-effect transistor device with C_{2v} isomer of $Pr@C_{82}$. Chem Phys Lett 409:187–191; (d) Kobayashi S, Mori S, Iida S et al (2003) Conductivity and field effect transistor of $La_2@C_{80}$ metallofullerene. J Am Chem Soc 125:8116–8117
35. Popok VN, Gromov AV, Jönsson M et al (2008) Electronic properties of thin films sublimed from $La@C_{82}$ and Li@C60. NANO 03:155–160
36. (a) Sato S, Seki S, Honsho Y et al (2011) Semi-metallic single-component crystal of soluble $La@C_{82}$ derivative with high electron mobility. J Am Chem Soc 133:2766–2771; (b) Sato S, Seki S, Luo G et al (2012) Tunable charge-transport properties of I(h)-C_{80} endohedral metallofullerenes: investigation of $La_2@C_{80}$, $Sc_3N@C_{80}$, and $Sc_3C_2@C_{80}$. J Am Chem Soc 134:11681–11686

37. Sato S, Nikawa H, Seki S et al (2012) A co-crystal composed of the paramagnetic endohedral metallofullerene La@C_{82} and a nickel porphyrin with high electron mobility. Angew Chem Int Ed Engl 51:1589–1591
38. Sun Y, Maeda Y, Sezaimaru H et al (2014) Carrier transport properties of nanocrystalline Er_3N@C_{80}. J Appl Phys 116:034301
39. Li Z, Luo W, Zhang M et al (2013) Photoelectrochemical cells for solar hydrogenproduction: current state of promising photoelectrodes, methods to improve their properties, and outlook. Energy Environ Sci 6:347–370
40. Bard AJ, Stratmann M, Licht S (eds) (2002) Encyclopedia of electrochemistry. In: Semiconductor Electrodes and Photoelectrochemistry, vol 6. Wiley-VCH, Weinheim
41. (a) Miller B, Rosamilia JM, Dabbagh G et al (1991) Photoelectrochemical behavior of C_{60} films. J Am Chem Soc 113:6291–6293; (b) Licht S, Khaselev O, Ramakrishnan PA et al (1998) Fullerene photoelectrochemical solar cells. Sol Energ Mat Sol C 51:9–19; (c) Wei T, Shi Y, Zhai J et al (2000) Synthesis, monolayer fabrication and photoelectric conversion property of two pyrrolidinofullerene carboxylic acid derivatives. Chem Phys Lett 319:7–12
42. (a) Yang S, Yang S (2001) Photoelectrochemistry of Langmuir–Blodgett films of the endohedral metallofullerene Dy@C_{82} on ITO electrodes. J Phys Chem B 105:9406–9412; (b) Yang S, Fan L, Yang S (2004) Significantly enhanced photocurrent efficiency of a poly (3-hexylthiophene) photoelectrochemical device by doping with the endohedral metallofullerene Dy@C_{82}. Chem Phys Lett 388:253–258
43. Xu Y, Guo J, Wei T et al (2013) Micron-sized hexagonal single-crystalline rods of metal nitride clusterfullerene: preparation, characterization, and photoelectrochemical application. Nanoscale 5:1993–2001

Chapter 6
Scrutinizing the Endohedral Space: Superatom States and Molecular Machines

Min Feng and Hrvoje Petek

Abstract In this chapter, we discuss two topics concerning the inner space of hollow molecules such as fullerenes, nanotubes, and even potentially materials like metal-organic frameworks. The first topic describes the special properties of electronic states, whose orbitals are not bound to specific atoms, but rather confined to vacuum region within the hollow molecules or materials. The second topic describes the dynamics of endohedral clusters within hollow molecules, whose motion can be manipulated by inelastic electron scattering, in order to realize a single-molecule switch.

6.1 Superatom States of Hollow Molecules

6.1.1 Introduction

Charge transport through carbon-based molecular materials can be highly anisotropic. It occurs efficiently through π-conjugated orbital networks, but is tentative between such networks in molecular solids that interact though weak van der Waals forces [1, 2]. Buckminsterfullerene (C_{60}) molecular crystal is a typical strongly correlated Mott–Hubbard solid with a high effective mass and low mobility for electron conduction [3]. This is because for the highest occupied molecule orbital (HOMO) with π-bonding character and lowest unoccupied molecule orbital (LUMO) with π^*-antibonding character the on-site repulsion energy U is much larger than the intermolecular hopping integral t. The conductivity of C_{60} could be greatly improved if the overlap between the frontier orbitals, and therefore t could

M. Feng · H. Petek (✉)
Department of Physics and Astronomy and Pittsburgh Quantum Institute,
University of Pittsburgh, Pittsburgh, PA 15260, USA
e-mail: petek@pitt.edu

M. Feng
School of Physics and Technology, Wuhan University,
Wuhan, Hubei 430072, China

A.A. Popov (ed.), *Endohedral Fullerenes: Electron Transfer and Spin*,
Nanostructure Science and Technology, DOI 10.1007/978-3-319-47049-8_6

be enhanced. C_{60} in fact possesses another set of molecular orbitals, which have far superior intermolecular overlap that makes them attractive for the molecular electronic applications. These are the superatom molecular orbitals (SAMOs), which we discovered in a low-temperature scanning tunneling microscopy (LT-STM) study of C_{60} on Cu substrates. Spectroscopic imaging by LT-STM demonstrated that SAMOs form nearly free-electron (NFE) bands in one (1D) and two dimensional (2D) C_{60} nanostructures, but at energies that are several eV above the LUMO [4]. The NFE properties of the C_{60} assemblies originate from the distinctive diffuse properties of SAMOs, which impart superior wave function overlap compared with the commonly encountered intermolecular interactions between the σ and π molecular orbitals. These interactions are distinct from the extrinsic NFE bands of molecules on metals, which originate in perturbation of surface states of the substrates [4–6].

The particular diffuse nature of SAMOs can be traced back to the diffuse orbitals of the component C atoms. Instead of hybridizing from the 2*s* and 2*p* atomic orbitals like the valence σ and π molecular orbitals, the SAMOs arise from the 3*s* and higher unoccupied orbitals within an atomic basis set. A more intuitive and universal way to explain the origin of SAMOs, however, is the universal long-range exchange-correlation potential, which gives rise to the image potential (IP) states at vacuum interfaces [7–10]. Placing an external charge in front of a polarizable medium triggers the screening response of its bound and free electrons. The interaction between the external charge and its screening charge is described by the universal image potential, which supports the associated IP states. The IP states are generally unoccupied, and form a Rydberg-like series, which converges to the vacuum level; their density in the vacuum increases with the principal quantum number *n*. Parallel to molecular planes the IP states have free-electron like dispersion [7–9] and for high parallel momentum they can even exist above the vacuum level, E_v, because the kinetic energy associated with parallel motion cannot be used to overcome the vacuum potential in absence of momentum scattering [11].

The origin of the diffuse properties of SAMOs is the image potential of graphene [4–6, 12]. As will be described in the next section, the associated IP states of a 2D molecular material such as graphene exists on both sides of the molecular sheet (Fig. 6.1), and form a dual series of symmetric and antisymmetric states [4, 6, 13]. Creating a curvature in graphene breaks the symmetry and stabilizes the IP states on the concave surface with respect to the convex surface. Therefore, rolling or wrapping graphene into a nanotube or fullerene transforms the lowest energy IP states into diffuse orbitals that preserve some of the IP-state character. Specifically, such hollow molecules posses a central, nonnuclear potential that is created by the topological transformation of the molecular sheet. Like the image potential, this potential is universal as it arises from the exchange–correlation interaction. In addition, the curvature creates a weak dipole potential [4]. Solutions to the Schrödinger equation for the effective potential, which includes the exchange–correlation and describes the familiar σ and π states, also include atom-like orbitals that are bound primarily to hollow molecular cores. This atom-like character is evident in the LT-STM images of C_{60}, hence the name superatom molecular

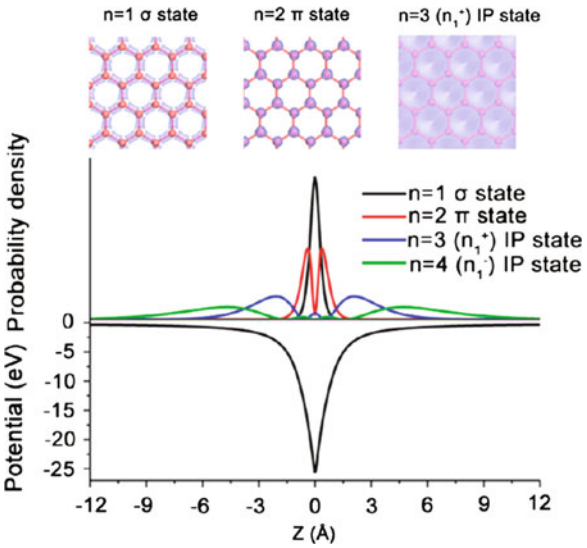

Fig. 6.1 The effective potential and the calculated surface-normal probability densities of n = 1–4 states of a graphene sheet at z = 0 Å. *Top views* of n = 1–3 state probability densities at the Γ- point are also shown. Reprinted with permission from *Acc. Chem. Res.* **44**, 360–368 (2011). Copyright 2011 American Chemical Society

orbitals [4]. Like the excitonic states of semiconductors, and plasmonic resonances of metallic nanoparticles, SAMOs of fullerenes at the van der Waals distance can combine to form diatomic-like molecular orbitals of C_{60} dimers, and for larger 1D to 3D aggregates, they hybridize as would atoms in a metal into NFE bands of super-atomic quantum structures and solids [14].

Whereas the electronic properties of molecular solids are traditionally viewed from the perspective of interaction between the frontier valence HOMO and LUMO orbitals [15], the hybridization of SAMO wave functions provides a completely different paradigm for band formation. The properties of SAMOs and their interactions can be tuned by external perturbations, topological distortions, intercalation, etc. Therefore, the realization that hollow molecules and molecular structures have NFE molecular states provide new insights into design of molecular materials with potentially superior properties as compared with the conventional molecular electronics.

6.1.2 *Diffuse States of Molecular Sheets and Their Derivatives*

In this section, we describe the IP states of graphene as the primary manifestation of the universal exchange-correlation potential of a molecular sheet, and the NFE properties of materials derived from graphene, namely graphite, fullerenes, and nanotubes. We first describe the IP states of graphene as the physical origin of the superatom states. Next, we show how the IP states hybridize into the interlayer states of graphite, and investigate by experiment and theory how the IP states of

graphene evolve through topological transformations into atom-like orbitals of graphitic hollow molecules. We show that these atom-like states, in turn, hybridize into NFE bands of fullerene and nanotube quantum structures or solids. Finally, we speculate on the prospects of exploiting the NFE states of hollow molecules in molecular electronics. Specifically, we study the novel properties of SAMOs of C_{60} and related materials through LT-STM, time-resolved two-photon photoemission spectroscopy (TR-2PP), and density functional theory (DFT) calculations.

6.1.2.1 Image Potential States of Graphene

To understand the origin of SAMOs, we begin by considering the electronic structure of graphene. The effective 1D electronic potential of graphene for the surface-normal direction in Fig. 6.1 is constructed by joining the short range screened Coulomb potential of C atom cores from DFT to the long-range V_{xc} potential, which has the asymptotic *1/4z* form far from the surface and is not correctly described by DFT. The potentials are spliced at a distance Z_i above and below the graphene plane, as has been done by Chulkov et al. to describe the IP sates of metals [12, 16]. The splicing is performed so that the first and second derivatives of the effective potential are continuous.

Thus calculated potential as well as the probability densities for the n = 1–4 states averaged in the graphene plane are plotted in Fig. 6.1. According to the number of nodes with respect to the molecular plane, the σ and π orbitals are the n = 1 and 2 solutions of the Schrödinger equation for the effective potential. The IP states with NFE properties are the $n \geq 3$ solutions with even and odd symmetry; they are the IP states [the n = 3 and n = 4 solutions are the first even (n_1^+) and odd (n_1^-) IP states, respectively], which form a double Rydberg series converging to E_v. Like their semi-infinite counterparts on metals, the bilateral IP states of molecular sheets have small density on the graphene sheet and pronounced n-dependent nonnuclear density on both sides of the molecular plane, as seen in Fig. 6.1 [12]. The predicted bilateral IP states of graphene have not yet been observed for suspended molecular sheets; perturbed IP states have only been observed for supported graphene films on metal and semiconductor surfaces, where the substrate breaks the even-odd symmetry [17]. The IP states of graphene are the origin of the NFE states we consider in related materials in the rest of this section.

6.1.2.2 Interlayer States of Graphite

The IP states of graphene can give rise to novel electronic states through various transformations such as stacking, rolling, wrapping, and doping. Graphite is a van der Waals solid formed by stacking graphene sheets. It is informative to consider how the n = 3 states appear in the interlayer electronic structure of graphite [12, 18–20]. Most of the electronic bands of graphite disperse parallel to the graphene sheets, but are nondispersive in the perpendicular Γ-A direction. Posternak et al.

were first to describe theoretically the interlayer band of graphite, which has a strong dispersion in the Γ-A direction starting at 4 eV above the Fermi level, E_F, and related nonnuclear probability density maxima that are a consequence of the interlayer hybridization [19, 21]. In Fig. 6.2, we demonstrate the origin of the interlayer band in the IP states of graphene.

Figure 6.2a–c illustrates the formation of the interlayer state (IS) through hybridization of IP states when two graphene sheets are brought together. The IS probability density is calculated by solving the 1D Schrödinger equation for a potential that is the sum of the individual graphene potentials in Fig. 6.1 for two graphene sheets at several interlayer distances, d. The interlayer density of IS between the basal planes depends strongly on d, as it is reduced from 10 to 3.35 Å (Fig. 6.2a–c). The IS density is maximized for $d \sim 7$ Å. The IS spatial distribution is affected by the competing effects of hybridization and confinement (Fig. 6.2b). For $d < 7$ Å, the increasing wave function confinement expels the probability density of IS from the interlayer region to the vacuum interface giving it distinct IP character (Fig. 6.2c). The IS band formation is demonstrated in Fig. 6.3e for a ten-layer graphite slab with the corresponding sheet separation of 3.35 Å. The calculated probability density again has the dual IP and IS character, respectively, on the surface and in the bulk of the slab. IS attains strong dispersion normal to the basal planes through the overlap of the constituent IP states, while retaining the NFE dispersion parallel to the planes [5, 12, 19]. The IP and IS states derive from

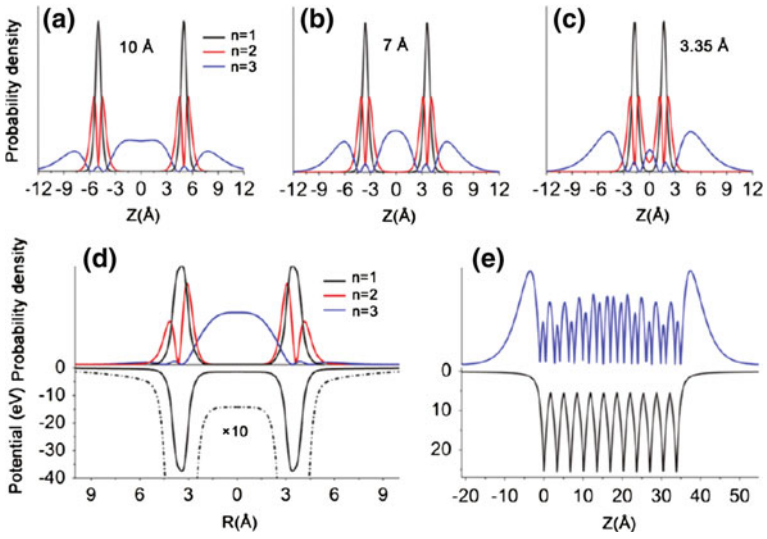

Fig. 6.2 **a–c** The calculated hybridization of the $n = 1$–3 states of bilayer graphene for separations of 10.0, 7.0, and 3.35 Å. **d** The effective potential and calculated radial distributions of the $n = 1$–3 states of C_{60} molecule. **e** The effective potential and calculated hybridization of the n_1^+ IP state of graphene into the interlayer state for a 10-layer graphite slab. The mixed IP and IS character is evident. Reprinted with permission from *Acc. Chem. Res.* **44**, 360–368 (2011). Copyright 2011 American Chemical Society

the V_{ex} potential and thus are a universal property of molecular sheets and their layered quasi-2D solids; because these materials have been under intense experimental and theoretical scrutiny, it is likely that their IP and IS states contribute to their optical and electronic properties [22, 23].

The IS of the intrinsic and Li intercalated graphite has been characterized by inverse photoemission spectroscopy (IPS) and theory [18, 19, 24]. More recently, they have also been observed as intermediate states in two- and three-photon photoemission spectroscopy on graphite and graphene terminated Pt(111) surfaces [25–27]. The IS has been implicated in multi-photon photoemission spectroscopy of graphite, where it acts as a reservoir of hot electrons [28]. IPS measurements found that the intercalation of Li stabilizes IS by $\sim$3 eV. As we will show in the case of endohedral fullerenes, the stabilization can be explained by the hybridization between the SAMOs of fullerenes and 2*s* states of Li atoms. In the case of graphite, stabilization of IS below E_F has been implicated in superconductivity of intercalated compounds such as C_6Ca [29]. Although IP states of graphene are bound by $\sim$1 eV with respect to E_v, through doping with metal atoms, and other stratagems, the IS can be stabilized to below E_F [29].

6.1.2.3 Superatom States of Hollow Molecules

Here we examine how superatom states arise from topological transformations of graphene into fullerenes and nanotubes [4, 13]. The curvature-induced symmetry breaking mixes the bilateral even n^+ and odd n^- IP states of graphene [30], and thereby lowers/raises the energy of IP states on the concave/convex side of a distorted molecular sheet. DFT calculations predict that the internal $n = 3$, $l = 0$ NFE states (parallel momentum $k_{||}$ of graphene transforms into orbital angular momentum l of fullerene or nanotube), formed by wrapping or rolling graphene into nanotubes or fullerenes, is stabilized with respect to the parent IP state [4, 31]. Figure 6.2d shows that calculated probability densities of the n = 1–3 states of C_{60}

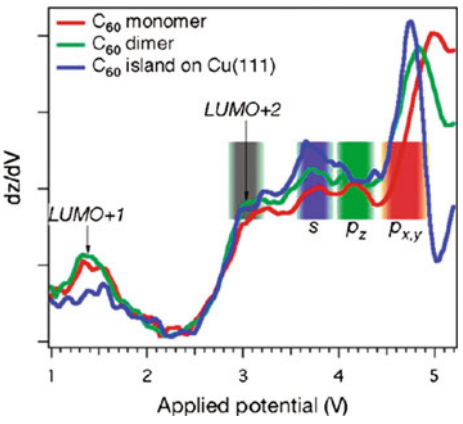

Fig. 6.3 The *dz/dV* spectra identifying specific tunneling resonances of an isolated C_{60} molecule and C_{60} dimer on the Cu domains of the Cu (110)-(2 × 1)-O surface, as well as a quantum well on Cu(111) surface. Reprinted with permission from *Science* **320**, 359–362 (2008). Copyright 2008 American Association for the Advancement of Science

with a diameter of 7 Å. The calculated internal probability density of the $n = 3$ state within DFT is significantly larger than for the graphene bilayer with comparable sheet separation in Fig. 6.2b. This is because for a concave surface the polarizable sheet is closer to the external charge, which favors stronger interaction. Moreover, the curvature causes hybridization of the σ and π orbitals, which creates a net positive charge on the concave surface due to stronger electron confinement. The relative stabilization of the internal NFE states has been assessed for various diameter carbon and BN nanotubes (BNNT), which are formed in a broad range of sizes. Within DFT For these materials the maximum stabilization of the $n = 3$, $l = 0$ NFE state occurs for a diameter of 10 Å [32, 33].

Although SAMO-like molecular orbitals were found as a subset of solutions in model theoretical calculations that treated C_{60} as a conductive sphere [34, 35], their existence was first established experimentally in a joint LT-STM and theoretical study of C_{60} molecules on copper surfaces [4]. The electronic structure of the lower lying LUMO states with π^*-orbital character of C_{60} molecules has been extensively studied by LT-STM and theory [36–40]. The energy resolved local density of states (LDOS) maps of LUMO–LUMO + 2 orbitals show features corresponding to the π^*- molecular orbitals on individual pentagons and hexagons comprising C_{60} molecules [36, 38]. We explored the high-lying electronic structure of C_{60} molecules by *z-V* spectroscopy (Fig. 6.3), where the distance–voltage relationship above single molecule is measured at a constant current by the STM tip; on single C_{60} molecules on bare Cu domains of Cu(110)-(2 × 1)-O surface, we identified several new tunneling resonances for bias voltages above 3.5 eV by differentiating the *z-V* signal [4]. Rather than exhibiting the π^*-orbital character, the intramolecular LDOS of all resonances above 3.5 eV cannot be resolved. Instead, as can be seen in Fig. 6.4, the LDOS takes on appearance of atom-like *s*, *p*, and *d* orbitals that are centered on C_{60} molecules.

In DFT calculations with a plane-wave basis set, we found that in addition to the π^*-orbitals, there exists another set of orbitals, which are diffuse and their probability density is not associated with individual atoms or bonds, but rather is organized by the central potential of the hollow molecular sphere (Fig. 6.5). Due to the anisotropy of the Cu(110)-(2 × 1)-O surface we could image all three components of the *p*-SAMOs (Fig. 6.4c–e), which would degenerate in an isotropic medium. The spatial distributions of these wave functions with respect to the C atom shell identifies them as the $n = 3$ solutions of the Schrödinger equation for a hollow polarizable sphere. Model calculations, such as in Fig. 6.2, show that the $n = 3$ states of C_{60} molecules correspond to the internal IP state of graphene that is obtained by wrapping it into a sphere [5].

Because the accurate description of SAMOs requires a complete basis set, such as plane-waves, they have largely escaped scrutiny by theory. An early study by Martins et al. on the photoemission and inverse photoemission of C_{60} solid employed a plane-wave basis set and classified the states obtained for a self-consistent central potential of a hollow spherical shell according to their n and l [41]. Subsequently, Yannouleas et al. found the $n = 3$ solutions in a calculation that treated C_{60} as a jellium shell [35]. After the experimental discovery of SAMOs,

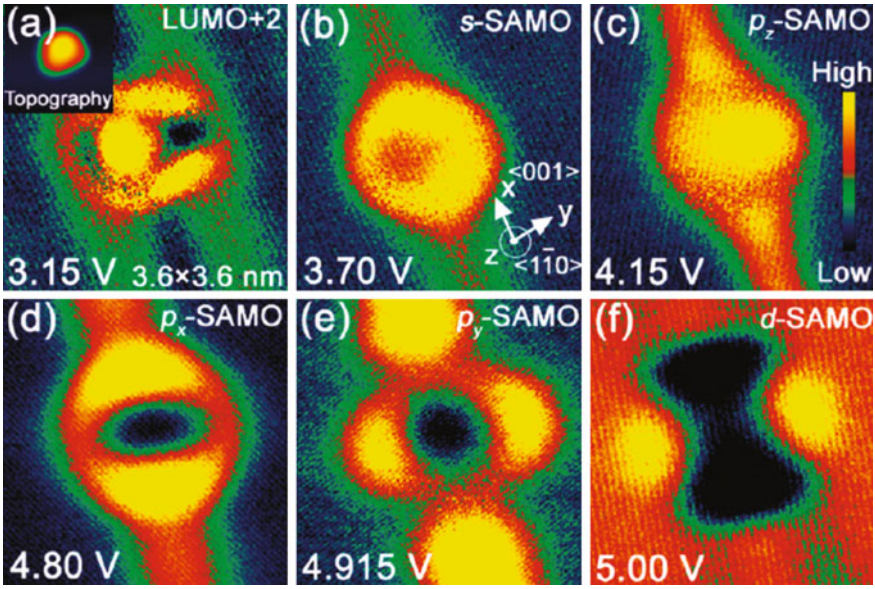

Fig. 6.4 **a–f** The *dI/dV* images of LUMO + 2 and *s*-, *p*-, and *d*-SAMOs for a C_{60} molecule on Cu (110)-(2 × 1)-O surface. Reprinted with permission from *Science* **320**, 359–362 (2008). Copyright 2008 American Association for the Advancement of Science

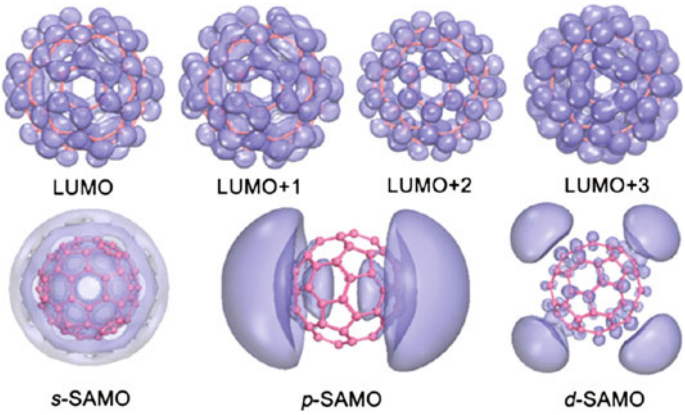

Fig. 6.5 The unoccupied LUMO-LUMO + 3, and *s*-, *p*-, and *d*-SAMOs of isolated C_{60} molecule from a plane- wave DFT calculation. Reprinted with permission from *Acc. Chem. Res.* **44**, 360–368 (2011). Copyright 2011 American Chemical Society

we found the corresponding orbitals in DFT calculations with a plane-wave basis set [4]. Later, Pavlyukh et al. described the electronic structure of spherical molecules in terms of angular electronic bands, where SAMOs emerge as a consequence of a radial potential and symmetry [42]. Most recently, Jordan,

Cederbaum, and coworkers applied high level, beyond Hartree–Fock theory to describe correlation bound resonances of free C_{60} and larger fullerenes; they found that only the lowest energy s-SAMO is bound by $\sim$0.1 eV, and 90% of the wave function is external to the fullerene shell [43–45]. Surprisingly, the calculations at the DFT level appear to be in better agreement with experiment on metal surfaces both in terms of the binding energy and wave function distribution than the high level calculations for isolated molecules. This may be because DFT tends to overbind such states, and the metal substrate may substantially contribute to the binding.

The theoretical description of SAMOs and their experimental LDOS imaging confirms them as the modes of the exchange-correlation potential of hollow spherical shell. Viewed as a consequence of the universal surface screening and dipole potentials, SAMOs emerge as a general feature of hollow molecules and molecular structures. Indeed, Johansson et al. found SAMO-like orbitals in neutral C_{60} and C_{70} by angular-resolved photoelectron spectroscopy. SAMO-like orbitals can also be expected in planar molecules, because IP-like orbitals of graphene should exist in planar structures. Our subsequent joint STM-theory studies revealed that the σ^* symmetry LUMO of C_6F_6 also has SAMO-like character, which enables NFE band formation in C_6F_6 quantum structures [46]. Other groups have reported SAMO-like states in rubrene and corannulene [47, 48]. Thus, the existence of SAMO-like orbitals in fullerenes and cyclical molecules composed of single or multiple rings is now well established by experiment and theory.

6.1.3 Formation of SAMO-Derived NFE Bands

Because SAMOs are more diffuse than the valence σ and π orbitals, the molecular bands derived from their interactions impart enhanced charge delocalization, which could be useful in molecular electronics. The experimentally observed hybridization of $n = 3$ states into NFE bands for single-molecule wide C_{60} quantum wires [49], and quantum wells provide examples where the intrinsic intermolecular interactions give rise to metal-like electron delocalization in a molecular solid [4, 6, 14].

LT-STM LDOS images can directly reveal intermolecular interactions that are mediated by SAMOs. We present the STM imaging of how SAMOs hybridize into NFE bands of 1D and 2D quantum structures on noble metals. The fundamental interactions leading to band formation are observed in *dI/dV* LDOS images of C_{60} and endohedral fullerene dimers, assembled on the bare Cu domains of the Cu (110)-(2 $\times$ 1)-O surface (Fig. 6.6) [49, 50]. The intermolecular spacing between molecules comprising the dimers is 1.07 $\pm$ 0.02 nm, corresponding to three unit cells with 0.36 nm size of the Cu(110) substrate; this is $\sim$7% larger that the Van der Waals diameter of C_{60}. From Fig. 6.6, it is evident that intermolecular hybridization of SAMOs transforms the LDOS of the interacting orbitals so profoundly that the individual molecular contrast and orbital character is lost.

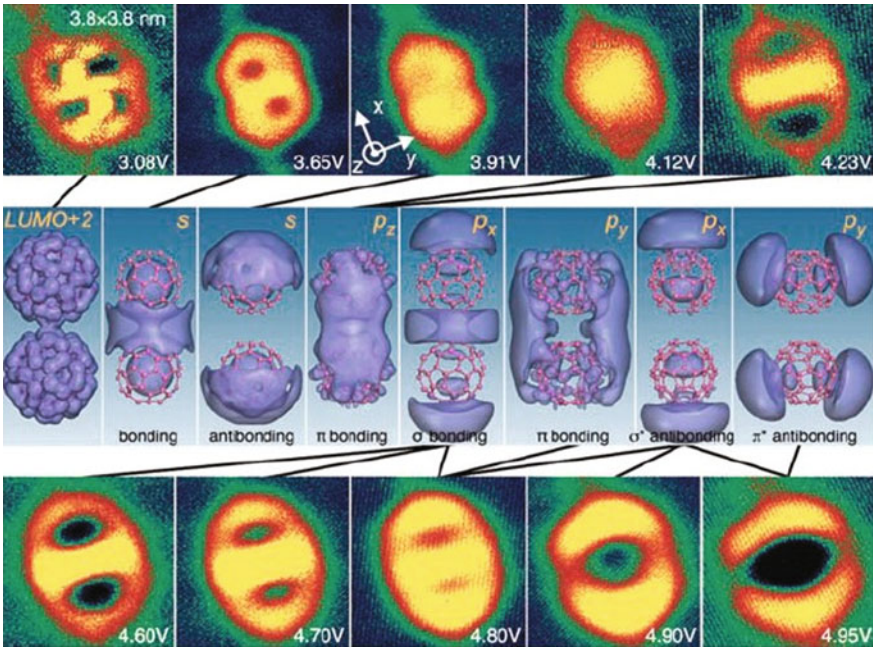

Fig. 6.6 STM *dI/dV* imaging and calculated hybridization of the SAMOs of individual C_{60} into the corresponding molecular orbitals of C_{60} dimers. Reprinted with permission from *Science* **320**, 359–362 (2008). Copyright 2008 American Association for the Advancement of Science

This is not the case for the π*-orbitals of the dimer (Fig. 6.6a), where the LDOS of the LUMO + 2 is largely retained from the monomer (Fig. 6.4a). By contrast, the energy dependent images of the LDOS of SAMOs can be understood in analogy with hybridization of atomic *s* and *p* orbitals into the bonding and antibonding orbitals of a homonuclear diatomic molecule [15]. The bonding and antibonding interactions appear in the LDOS as characteristic anti-nodes and nodes between the two molecules, which can be correlated with the calculated probability densities in Fig. 6.6. Similar intermolecular hybridization also occurs for the SAMOs of endohedral fullerenes [50].

Next, we examine the SAMO-derived electronic bands of C_{60} molecule quantum structures. Figure 6.7 shows a topographic and the corresponding *dI/dV* images of a self-assembled chain of nine C_{60} molecules on Cu domains of the Cu(110)-(2 × 1)-O surface. The self-assembly occurs by preferential adsorption of C_{60} molecules in one-atom-wide Cu domains that form on nearly completely oxidized Cu(110)-(2 × 1)-O surface [51]. From the loss of molecular contrast in the *dI/dV* images, it is evident that SAMOs hybridize into delocalized 1D bands. The LDOS corresponding to individual bands in Fig. 6.7 can be assigned to particular orbitals and their hybridization into bands by comparison with the calculated SAMO orbital distributions for a C_{60} molecule chain [5]. The energy-momentum dispersions

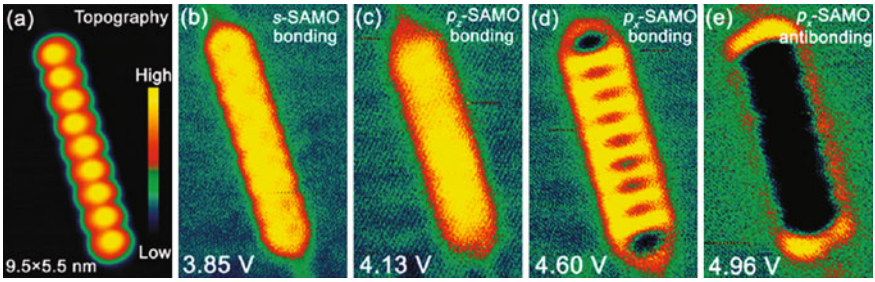

Fig. 6.7 **a–e** The topography and *dI/dV* images of a linear chain of C_{60} molecules on Cu(110)-(2 × 1)-O surface showing the LDOS delocalization through the 1D σ- and π-band formation. Reprinted with permission from *Acc. Chem. Res.* **44**, 360–368 (2011). Copyright 2011 American Chemical Society

calculated from DFT gives m_{eff} of $1.0m_e$, $1.0m_e$, and $-0.2m_e$ (m_e is the free-electron mass) for the s-σ, p-π, and p_x-σ^* bands, respectively. Thus, the STM imaging and DFT calculations demonstrate that SAMOs hybridize into NFE bands, which resemble those of alkali atoms chains [15].

Similar band formation via SAMO hybridization is expected for 2D and 3D aggregates of C_{60} molecules. Figure 6.8 shows LT-STM topographic and LDOS images of a C_{60} island on Cu(111) surface where C_{60} forms 2D islands with a hexagonal 4 × 4 structure and 1.02 nm intermolecule distance defined by the 0.255 nm surface unit cell. Again, LDOS images show evidence of SAMO hybridization into NFE bands of a quantum well. The LDOS at 3.74 V shows complete loss of molecular contrast on account of the 2D hybridization of s-SAMO into an NFE band [5]. Such wave function delocalization is evident in imaging of the $n = 1$ IP state at 4.2 V where similar flat contrast is found on the complementary bare-metal region (Fig. 6.8d); like the intrinsic free-electron-like IP state of the Cu(111) surface, the LDOS of s-SAMO within the quantum well is featureless. By contrast to s-SAMO, the band formed by p_x, p_y-SAMO has a node seen as darker contrast above each molecule, which reflects its negative mass and antibonding character at the Γ point [5].

The NFE band formation evident in two-photon photoemission (2PP) spectroscopy of monolayer (ML) and multilayer C_{60} molecule films on the Cu(111), Ag(111), and Au(111) surfaces [52–56]. As shown in Fig. 6.9, the main feature attributed to SAMOs is the 3.7 eV band in 2PP spectra of C_{60}/Au(111) surface. This band appears at the comparable energy as the s-SAMO in the STM *dz/dV* spectra of C_{60} on copper surfaces. Zhu et al. found this band to disperse with both parallel and perpendicular momenta for monolayer to multilayer films. The NFE like character could account for both the parallel dispersion, and the splitting of the state with increasing film thickness above 2 ML. The splitting with increasing films thickness is an electronic signature of a transition from a 2D quantum well to a 3D molecular solid. A tight binding model described both the parallel dispersions and interlayer energy splitting with a hopping integral $t = -33 \pm 3$ meV, giving a

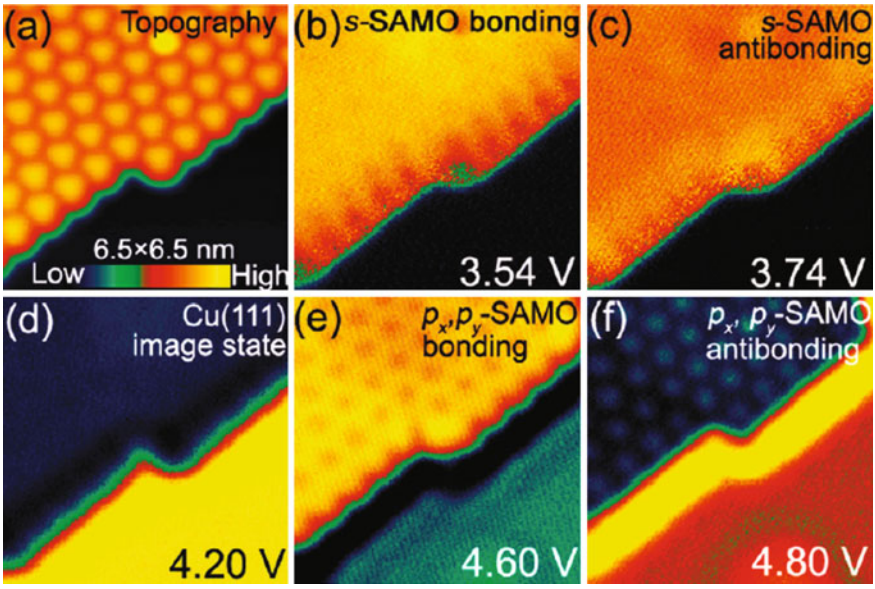

Fig. 6.8 **a–f** The topography and *dI/dV* images of a C_{60} island on Cu(111) showing the 2D *s*-, p_x, p_y- SAMO ($m = 0$ and $m = \pm 1$) bands, and the IP state of Cu(111) surface. Reprinted with permission from *Acc. Chem. Res.* **44**, 360–368 (2011). Copyright 2011 American Chemical Society

bandwidth of $12t = 400$ meV [5, 52]. The NFE character of the *s*-SAMO band stands in strong contrast to the more weakly interacting LUMO bands of C_{60} on Ag (111) surface, which appear, in accordance with theory, to have effectively no dispersion, and therefore a large band mass [5, 53]. Subsequent reexamination of 2PP spectra of the C_{60}/Au(111) surface confirmed that the dispersive band is due to the *s*-SAMO [57]. Thus, both the 2PP and LT-STM measurements establish that SAMOs mediated interactions give rise to bands with a lower band mass than the π^* character LUMO states, and therefore, SAMO mediated transport could be of interest in molecular electronics.

6.1.4 Tuning SAMOs in Endohedral Fullerenes

Despite the attractive prospect of utilizing the NFE bands of fullerenes for charge transport, their energy (>3 eV above the LUMO in the case of C_{60} [52, 57, 58]) precludes such applications, because of electronic relaxation on the femtosecond time scale to the conduction band minimum (CBM), which has the π^*-LUMO character [4]. For SAMOs to be useful in charge transport, they should be stabilized to below the unoccupied π^* states so that they form the CBM. We have therefore explored different strategies to stabilize the SAMOs relative to the LUMOs.

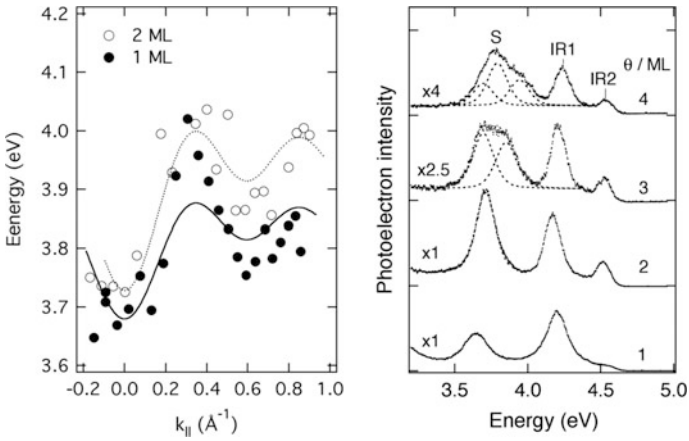

Fig. 6.9 *Right* 2PP spectra taken with a photon energy of 4.593 eV for C_{60} covered Au(111) surfaces for film thicknesses of 1–4 ML. IR1 & IR2 are assigned to IP resonances of the C_{60} overlayer, and S to the *s*-SAMO band. The *dashed curves* show peak deconvolution for multilayer films that are split by the interlayer interaction. *Left* Parallel dispersions of the *s*-SAMO band for 1 and 2 ML thick films. The *solid* and *dashed curves* are fits to a tight binding model. Reprinted with permission from *Phys. Rev. B* **74**, 241401 (2006). Copyright 2006 American Physical Society

6.1.4.1 Theoretical Studies on Tuning of C_{60} SAMOs

We explored different strategies to stabilize SAMOs by DFT electronic structure calculations. The potential for tuning the energy of SAMOs relative to LUMOs depends on their propensity to respond more strongly to electronic perturbations, such as endohedral and exohedral doping, or applying an external electric field [5]. The endohedral doping of metal atoms into the fullerene cage has emerged as the most effective approach to stabilize SAMOs. This approach relies on the hybridization between *s*-SAMO and valence states of the doping atoms with the same *s*-symmetry [4–6].

The different charge density distributions of the unoccupied states of fullerenes affect their susceptibility to electronic perturbations. The π^* states are localized on the carbon cage, whereas SAMOs are diffuse. An endohedral atom (EA) introduces an additional potential that supports the third type of state, namely the EA-states [59]. The EA-states are derived from the atomic orbitals of the endohedral atom; they mix with both the cage states and SAMOs of the appropriate symmetry. Because fullerenes have a high electron affinity, an EA experiences some charge transfer that depends on its ionization potential [60–66]. For low ionization potential EA, one or more electrons are fully transferred to the LUMO of the cage, such that the E_F of the combined system is lifted to lie within the LUMO [4]. The charge transfer and the consequent Coulomb interaction between the included cation and the negatively charged cage cause EA to adsorb on the inner wall of the cage, provided that ionic radius of the atom is less than the effective inner radius of

the cage that is defined by the Pauli repulsion. For EAs with a high ionization potential, such as rare gas atoms [67, 68], there is essentially no charge transfer, and the LUMO remains empty; the neutral interactions are much weaker and dominated by the Pauli exclusion and van der Waals interaction, which favor the EA to reside at the cage center. In either case, the EA lowers all energy levels of the fullerene due to the Coulomb or dispersion interactions.

In contrast to the π^* states, the presence and location of the EA within the cage strongly affects SAMOs [5]. Because SAMOs occupy the inner space they experience simultaneously the potentials of the hollow fullerene core as well as the EA. The effect of EA on SAMOs depends strongly on their symmetry and spatial distribution. The *s*-SAMO of the interacting system is strongly stabilized with respect to that of the empty cage because it hybridizes with the *s*-orbital of the atom, which is at a lower energy. For C_{60} molecules endohedrally doped with alkali, alkaline earth, noble, and rare earth metal atoms there is a nearly linear relation between the energy of *s*-SAMO of the combined system with respect to E_F and the ionization potential of the free metal atoms (representing the binding energy of the valence *s*-symmetry state) [5]. Therefore, the strength of the endohedral atomic potential determines the stabilization of the *s*-SAMO state. Figure 6.10 shows the anticorrelation of the *s*-SAMO energy for different EAs placed at the center of C_{60} molecule with the first ionization potential of the free atom. Further analysis shows that upon hybridizing, the *s*-SAMO mainly has the character of the *s*- orbital of the EA, i.e, it is more localized than *s*-SAMO of the empty cage because of the EA atomic potential is stronger than the central potential of the empty cage; nevertheless, the SAMO admixture imparts some diffuse character to the hybridized state.

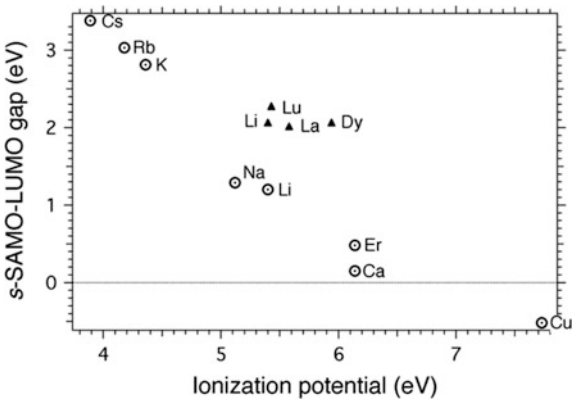

Fig. 6.10 The anticorrelation between the *s*-SAMO energies calculated by DFT for M@C_{60} molecules with different metal atoms, M, placed at the center of fullerene *versus* the first ionization potential of M. The data points for La, Dy, and Lu represent the energies from spectroscopic STM measurements, which have been assigned to *s*-SAMO. For the experimental data the metal atoms are displaced from the center to the cage wall. Reprinted with permission from *Phys. Rev. B* **88**, 075417 (2013). Copyright 2013 American Physical Society

These general features are illustrated by Li@C_{60}, [4] where the Li atom with a relatively small ionization potential donates one electron to C_{60}; this shifts E_F into the π^* states. Placing Li at the center of C_{60}, stabilizes *s*-SAMO from 3.5 eV above LUMO for the empty C_{60} to 1.2 eV above E_F through the hybridization with the unoccupied 2*s*-orbital of the Li ion. At equilibrium, however, the relatively small Li atom is displaced from the center of C_{60} to the cage wall, and consequently, the *s*-SAMO energy is raised by 0.85 eV from its minimum value at the center. The coupling of charge and nuclear motion of Li atom in C_{60} cage via the charge-transfer excitation from the ionic ground state to the neutral *s*-SAMO has been proposed as a mechanism for actuating an endohedral fullerene-based molecular switch [69].

6.1.4.2 SAMOs of La@C_{82}

STM imaging of endohedral fullerene, La@C_{82}, provides experimental evidence for the hybridization between *s*-SAMO and *s*-orbital of a metal ion within an endohedral metallofullerene that was predicted by theory [14, 70]. The La@C_{82} molecule among endohedral metallofullerenes is readily available and extensively studied [71, 72].

STM experiments combined with DFT electronic structure calculations confirm that the endohedral La stabilizes *s*-SAMO in La@C_{82} by ~2 eV compared with the empty C_{82} molecule. Figure 6.11 shows the *dI/dV* spectra of single La@C_{82} and C_{60} molecules deposited on a C_{60} monolayer on Cu(111) surface [73]. The pre-deposited C_{60} monolayer acts as a buffer to minimize the electronic perturbation of La@C_{82} molecule by the metal substrate. The analysis of *dI/dV* spectra and LDOS images shows that La@C_{82} has a much lower energy *s*-SAMO (1.85 eV above E_F)

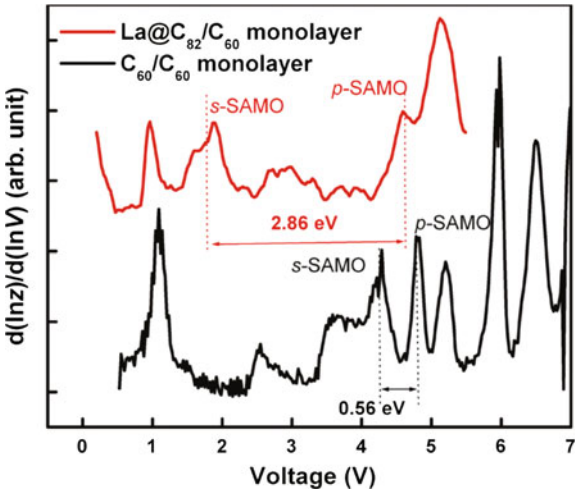

Fig. 6.11 The energy splitting between the *s*- and *p*-SAMOs of isolated La@C_{82} and C_{60} molecules on a C_{60} buffer layer. For the La@C_{82} molecule the splitting is 2.86 eV as compared with 0.56 eV for C_{60}. Reprinted with permission from *Phys. Rev. B* **88**, 075417 (2013). Copyright 2013 American Physical Society

and the energy difference between *s*- and *p*-SAMOs is much larger than in C_{60}. The *s*-*p* energy gaps of 2.86 eV in La@C_{82} and of 0.56 eV in C_{60} are consistent with the DFT calculations on La@C_{82} and C_{82}.

Furthermore, the STM experiments show that the *s*-SAMO is the second unoccupied state of La@C_{82} (LUMO + 1) when the molecule is adsorbed on Cu (111) surface, with the LUMO being derived from the La 4*f* state (the π^* symmetry LUMO, of isolated La@C_{82} molecule is half-filled because of charge transfer from the La atom. The π^* symmetry LUMO + 1 is 1.01 eV above E_F. Both states couple strongly with metal substrates and broaden into resonances when adsorbed onto Cu surface) [70]. Because the 4*f* state of La is very compact and the *f*-SAMO is very diffuse, the energy separation between the hybridized states is large and their mixing is small. Therefore, the La 4*f* state-derived LUMO is not expected to have significant SAMO character. This analysis suggests that for an EA with a fully occupied 4*f* state the *s*-SAMO may be stabilized sufficiently to become the LUMO at the metal/molecule interface. This is expected for Lu@C_{82}, where the Lu atom with the electronic configuration [Xe] $6s^2 4f^{14} 5d^1$ can donate approximately three electrons to the cage, leaving the Lu^{3+} ion with a closed shell $4f^{14}$ configuration [74, 75]. If the charge transfer from the substrate to Lu@C_{82} led to full occupation of the LUMO of the free molecule, then the *s*-SAMO would become the LUMO of the chemisorbed Lu@C_{82}/substrate system. This is to be expected for EAs with closed shell configurations, which donate their valence electrons to the fullerene cage.

6.1.4.3 SAMOs in Fullerenes with Endohedral Clusters

The family of endohedral fullerenes containing M_3N clusters, where M stands for a transition or rare earth metal atom, has been of interest because they are predicted to enhance electron transmission through single-molecule junctions, can have interesting magnetic properties, and exhibit M dependent cluster rotation at room temperature [71, 76–78]. LT-STM and DFT studies of Sc_3N@C_{80} molecules were performed (1) to verify the universality of the SAMOs; (2) to explore how the internal doping affects the energy, spatial distribution, and intermolecular hybridization of the SAMOs; and (3) to explore their properties as molecular switches [50]. The combination of the Sc_3N cluster structure, its orientation within the C_{80} cage on a substrate, and the interaction Sc_3N@C_{80} molecules with the anisotropic Cu(110)-O substrate causes the SAMOs of single-Sc_3N@C_{80} molecules to have nonspherical shapes in *dI/dV* images, which differ from molecule-to-molecule. By contrast to the Sc_3N@C_{80} monomers, the SAMOs of dimers and trimmers have nearly identical spatial distributions for many samples due to strong intermolecular hybridization among the interacting molecules. The images of Sc_3N@C_{80} trimers are determined by the spatial distribution of Sc_3N@C_{80} molecules and the hybridization of SAMOs among them rather than the internal cluster

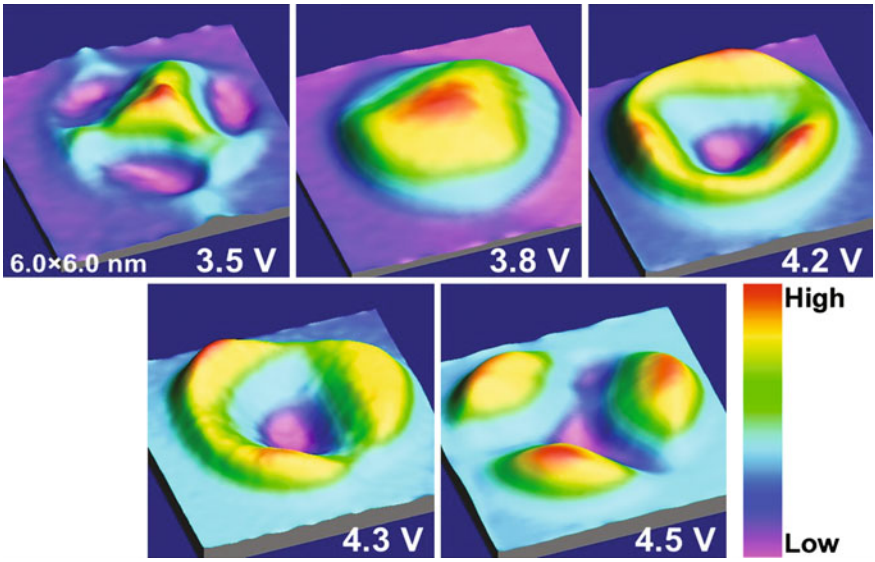

Fig. 6.12 STM *dI/dV* mappings (**a**–**e**) of the SAMOs in a $Sc_3N@C_{80}$ trimer. SAMOs show typical bonding and antibonding characters originating from the strong hybridization of the SAMOs between molecules. Reprinted with permission from *Phys. Rev. B* **81**, 085434 (2010). Copyright 2013 American Physical Society

structure or their interaction with the substrate (Fig. 6.12) [50]. The strong intermolecular hybridization can also be inferred from pronounced changes in *dz/dV* spectra as the $Sc_3N@C_{80}$ aggregation increases from monomers to trimers.

The effective hybridization of $Sc_3N@C_{80}$ aggregates can be attributed to the electronegative N atom in the center. Because of the Pauli exclusion, the central N pushes more of the SAMO density to the exterior of the fullerene cage, which enables larger wave function overlap among the adjacent molecules. For the same reason, the central N atom destabilizes SAMOs such that their energy is higher for $Sc_3N@C_{80}$ than for C_{60} [50]. In the related molecule $Y_3@C_{80}$, which is missing the central N atom, the HOMO orbital resembles the bonding orbital of the missing N atom [79]. Thus, the bonding of the Y_3 cluster is through a nonnuclear pseudoatomic orbital that has *s*-SAMO character. Apparently, the Y atoms contribute to strengthening of the central potential so that charge is transferred from Y atoms to the central nonnuclear region in a manner that contributes to the molecular bonding and stabilizes the cluster structure. This is another example of how SAMOs can be stabilized by endohedral atoms and clusters; in this case, the *s*- SAMO orbital is occupied.

6.2 A Single-Molecular Switch Based on an Endohedral Fullerene

6.2.1 Introduction

As elements of logic gates and electronic memories, single-molecule switching devices represent the smallest molecular electronic components [80–82]. A typical molecular switching device consists of a junction where a single-molecule element is in contact with two electrodes. External stimuli, such as electron charge [83, 84], electric field [85], electron spin, light [86], chemical force [87], heat [88], magnetic field [89], and others could trigger reversible molecular configuration change, and thus control the current flowing through the junction. Because of the ability to apply an electric field and/or inject electron charge locally at the atomic scale [90, 91], STM has been employed in construction of single-molecule switches where single molecules form the active element in the tunneling junction formed by the STM tip and the supporting substrate [92, 93].

Molecular level switching was first demonstrated for a Xe atom sandwiched between a nickel substrate and an STM tungsten tip [87]. By applying voltage pulses of the opposite polarity, single-Xe atoms could be reversibly transferred between the tip and the substrate thereby changing the junction conductivity. Because the conductivity is modulated through interaction of electrodes with the atomic/molecular element rather than being a property of the molecule itself, such a device is considered to be extrinsic [94]. Intrinsic single-molecular switches, by contrast, rely on specific switching behavior of the molecule itself. Intrinsic switching behavior is available from molecular materials based on conformational change [95–97], charging [92, 93], spin, and magnetic [88, 98] mechanisms. Because the switching mechanism can be tailored by chemical synthesis, the conformational switching among isomers has been widely studied [49, 95, 96, 99–105]. A disadvantage of switches based on a large structural change within single molecules is that it is difficult to track the large amplitude motion with an STM tip in order to actuate and record the switching behavior over multiple switching cycles, as might be required for a molecular device operation. Other switches, based on the hydrogen atom tautomerization [103] or the mechanical oscillation [105] of small functional groups, minimize the overall structural change but can be vulnerable to external chemical perturbations. The development of molecular switches that function with minimal structural change, are stable with respect to spurious switching, and are adamant to environmental perturbations, therefore, remains an important goal toward achieving practical single-molecular switches.

In this section, we describe a molecular switch based on a single endohedral cluster fullerene as a prototype for a new class of single-molecule devices [50, 106], where the switching is based on current-induced internal cluster rotational motion. Fullerenes constitute one particularly promising family of molecular devices with invariant external morphology and high chemical stability. Molecular transistors [107] and rectifiers [108], which have been demonstrated for single fullerene

molecules, work on well-established principles. These actuation mechanism include mechanical oscillation of single C_{60} molecule within a junction [107, 109], reversible dimerization [110], and cage rotation [111, 112]. Endohedral doping of fullerenes by atoms or clusters introduces additional conformational, chemical, electrical, spin, and magnetic degrees-of-freedom that can confer particular functions to a single-molecular device [113]. Soon after the discovery of fullerenes, it was proposed that the endohedral fullerenes could serve as switching devices if motion of the encapsulated moiety within the cage could be stimulated in a controlled manner [60]. The previously mentioned light or electron actuated $Li@C_{60}$ molecule switch is one embodiment of such device, where one might actuate and image single-molecule femtochemistry [69, 114]. Fulfilling the long-anticipated endohedral fullerene switch based on the actuation of motion of the included moiety, we describe here controllable switching of tunneling current by triggering the encapsulated cluster rotation [106, 115].

6.2.2 $Sc_3N@C_{80}$ Molecule Spectroscopy and Microscopy

$Sc_3N@C_{80}$ is the most abundant endohedral fullerene produced in electrical discharge synthesis among metallonitride cluster fullerenes [71]. It is produced as a mixture of dominant I_h and minority D_{5h} isomers (the symmetry refers to the fullerene cage), which can be separated by chemical means [116–118]. Molecular switching has been investigated for the I_h isomer. The Sc_3N cluster and the icosahedral C_{80} cage are mutually stabilized by both the electron transfer of $6e^-$ from the nitride cluster to the cage and covalent cluster–cage bonding [119, 120]. Both experimental and theoretical studies show that at room temperature the Sc_3N cluster performs almost free three-dimensional rotation within the C_{80} cage [79, 116, 121]. The thermally activated internal rotation of the Sc_3N enables single-molecular switching at cryogenic temperatures, where the cluster rotation can be stimulated by electrical or optical means. In fact, in $ErSc_2N@C_{80}$, a fullerene with very similar molecular structure to $Sc_3N@C_{80}$, the optical-switching of the $ErSc_2N$ rotor between two stable configurations was observed at 20 K [122]. Here we describe a single-molecule switch based on the tunneling electron stimulated internal cluster motion within $Sc_3N@C_{80}$ molecule in a junction of an atomically ordered Cu(110)-O substrate and atomically sharp tungsten LT- STM tip. The experiments are performed at 4.7 K [123, 124].

A free $Sc_3N@C_{80}$ molecule has a 40-fold degenerate ground state. The C_{80} cage of I_h symmetry has 10 equivalent C_3 rotational symmetry axes passing through opposing pairs of C atoms at junctions of three hexagons and the N atom of Sc_3N cluster; for each C_3 axis, the Sc_3N cluster has four energetically equivalent azimuths (Fig. 6.13) [116, 125]. The elementary rotations of the Sc_3N cluster interconverting these equivalent structures can be classified into two types: in-plane rotation by 37°

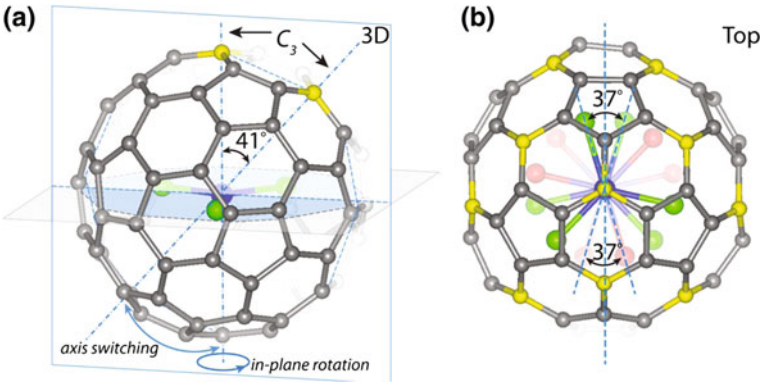

Fig. 6.13 Molecular structure of $Sc_3N@C_{80}$ molecule. **a** A perspective view of one of the 40 degenerate minima occupied by the Sc_3N cluster in a free $Sc_3N@C_{80}$ molecule. The C_3 symmetry axis of C_{80} cage coincides with the axis for the cluster in-plane hindered rotation; it passes through the N atom and opposing C_{666} atoms at junctions of three hexagons (indicated in *yellow*). Two neighboring C_3 axes (*blue dashed lines*) with a mutual angle of 41° define a reflection plane of C_{80} (σ_{001} as indicated by the *blue square*), which is a chiral plane with respect to Sc_3N. The *curved arrows* indicate the elementary motions of the Sc_3N cluster, the in-plane rotation and the axis-switching. **b** The *top view* of $Sc_3N@C_{80}$ looking down onto the Sc_3N cluster. The *blue solid line* indicates the chiral plane. For each C_3 axis the Sc_3N can adopt four equivalent orientations corresponding to two chiral pairs (indicated with *green* and *red*) in which an Sc-N bond is rotated by $\Phi = \pm 18.5°$ from a chiral plane. Enantiomers are interconverted by Sc_3N in-plane rotation of 37°. Reprinted with permission from *Chem. Phys. Lett.* **552**, 1–12 (2012). Copyright 2012 Elsevier

around the C_3 axis, and axis-switching rotation by 41° between two C_3 axes on the opposite side of a carbon hexagon; their calculated barriers are 74 and 100 meV, respectively [125]. Experimental barriers from NMR measurements in different solvents are 75 and 122 meV [126]. At room temperature, the cluster continuously interconverts among these structures. At 4.7 K, the isomerization thermally quenched. The highly anisotropic Cu(110)-O substrate immobilizes $Sc_3N@C_{80}$ molecules, and its anisotropy is useful for the symmetry analysis of the switching behavior [106, 115]. Despite $Sc_3N@C_{80}$ molecules being chemisorbed on the Cu(110)-O surface, ab initio DFT calculations on both the free and adsorbed $Sc_3N@C_{80}$ molecules show almost the same electronic properties, including the width of the HOMO-LUMO gap, the distribution of the electronic states, and the potential barrier for the in-plane rotation; this shows that the fullerene cage protects the endohedral clusters from strong perturbations by the substrate. Whereas $Sc_3N@C_{80}$ molecules adsorb in several shell and cluster orientations, the STM experiments focus only on one subset of molecules, which exhibit consistent hierarchical multi-level switching behavior among six stationary states with characteristic symmetry. For this subset, we observe consistent switching behavior for multiple molecules [123, 124].

6.2.3 STM Observations of the Switch Actuation in $Sc_3N@C_{80}$ Molecules

Controllable switching of Sc_3N cluster within single $Sc_3N@C_{80}$ molecules can be detected by topographic images of each molecule before and after switching, and by recording the current *versus* time (*I-t*) trends at specific locations above a molecule [123, 124]. Figure 6.14 shows the tunneling current-induced switching between two equivalent structures. Figure 6.14a is a topographic image of single $Sc_3N@C_{80}$ molecule under 50 mV bias where the molecular topography is stable. The STM image shows apparent distortion from the nearly spherical structure of the C_{80} cage, implying that the image is affected by the particular orientation of the Sc_3N cluster. Even though we refer to these images as topographic, the apparent structure includes distortions caused by the cluster orientation dependent tunneling current, rather than actual distortion of the C_{80} cage.

Applying a voltage pulse of 100 mV at molecule in Fig. 6.14a switches the topography in Fig. 6.14a into its mirror image in Fig. 6.14b. The absolute value of the difference between the enantiomeric topographies in Fig. 6.14a and b (Fig. 6.14c) has a mirror symmetry plane σ_{001} parallel to the $\langle 001 \rangle$ crystallographic direction of the substrate; this is expected for enantiomeric structures. The switching between the two enantiomers is furthered characterized by imaging the same molecule at a bias of 100 mV (Fig. 6.14d) as well as recording an *I-t* trend (Fig. 6.14g). The enantiomeric topographs under 50 mV bias, blend into a symmetric and nearly spherical topograph 100 mV. Furthermore, the image is superimposed by high-frequency noise associated with the switching. The *I-t* trend shows that the switching between two stationary states causes the noise in the tunneling current. Therefore, the STM topography in Fig. 6.14d is a superposition of two enantiomeric images (Fig. 6.14a, b), which stochastically interconvert during scanning of the image. Processing Fig. 6.14d with a high-pass filter removes the topographic information and maps the spatial distribution of the switching amplitude between the low and high current states (Fig. 6.14f). This switching pattern (SP) is a fingerprint of a particular switching process. The SP is related to and resembles the contrast in the difference image in Fig. 6.14c, confirming that Fig. 6.14d comes from switching between enantiomeric structures in Fig. 6.14a, b.

SPs such as in Fig. 6.14f are distinguishing characteristics indicative of the rotational and azimuthal orientation of both the cage with respect to the substrate and the cluster with respect the cage. It is a diagnostic that enables us to identify a particular subset of molecules capable of characteristic switching processes. For the selected subset of $Sc_3N@C_{80}$ molecules, six stable configurations grouped into three enantiomeric pairs are found (Fig. 6.15). Each SP has a node in the switching amplitude at the bisecting σ_{001} mirror plane, as expected for the interconversion of enantiomers. The evolution of SPs with increasing bias voltage from 100 to 1200 mV traces reproducible hierarchical switching pattern common to all $Sc_3N@C_{80}$ molecules within this subset. Based on a comparison between the experimental SPs and theoretically calculated ones, assignments can be made for

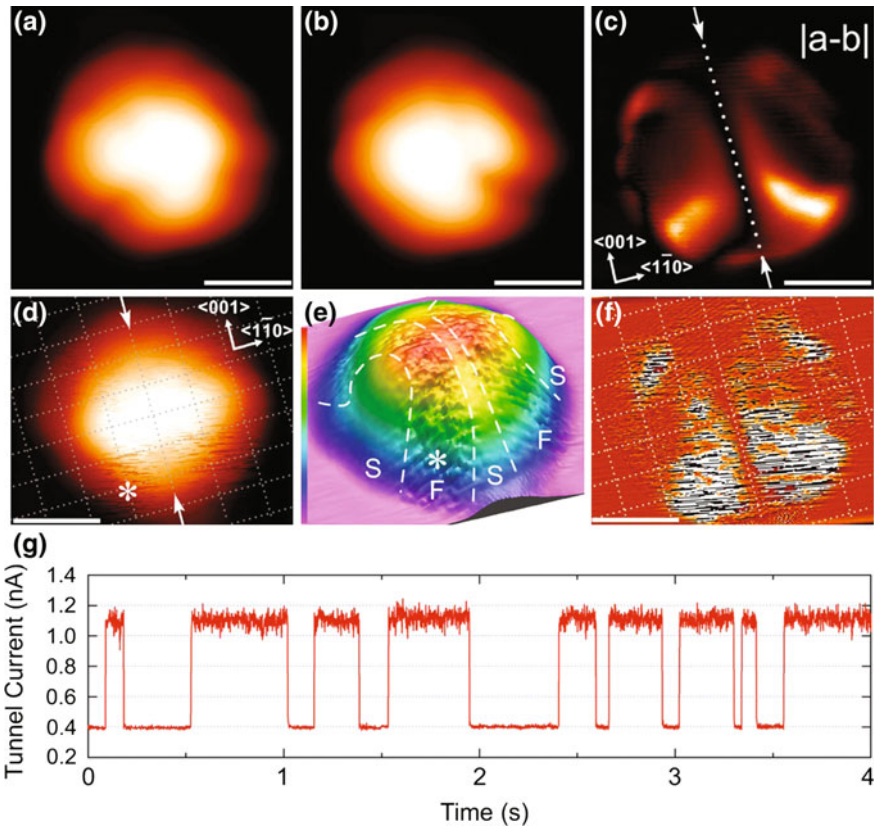

Fig. 6.14 Tunneling electron stimulated enantiomerization of $Sc_3N@C_{80}$. **a** Topographic STM image of a single $Sc_3N@C_{80}$ molecule. The *white* scale bars correspond to 1 nm in all images. **b** Image of the same molecule after isomerization by applying a pulse of 100 meV. The tunneling conditions are V_{bias} = 50 mV and $I_{setpoint}$ = 0.1 nA for both (**a**) and (**b**). **c** The difference pattern obtained by subtracting (**a**) from (**b**) and taking the absolute value. **d** The image of the same molecule as in (**a**) and (**b**) recorded at V_{bias} = 100 mV and $I_{setpoint}$ = 0.4 nA becomes symmetric, because of fast isomerization during the imaging process. The *arrows* in **c** and **d** indicate the σ_{001} mirror plane, and the *dotted line* meshes in (**d**) represent the substrate lattice. **e** Three-dimensional pseudo color plot of (**d**). The superposed *dashed curves* delineate regions characterized by stable (S) and fluctuating (F) tunneling current. **f** The switching pattern obtained by high-pass filtering of (**d**). **g** *I-t* trace taken with V_{bias} = 100 mV by fixing the tip at the *asterisk* in (**d**) and (**e**) showing the telegraph noise associated with stochastic switching between two enantiomers. Reprinted with permission from *Nano Lett* **11**, 5327–5332 (2011). Copyright 2011 American Chemical Society

SP_I to C_3 axis-switching, SP_{II} to rotation about a C_3 axis perpendicular to the substrate, and SP_{III} to rotation about a C_3 axis canted with respect to the substrate (Fig. 6.15). The switching processes interconverting a pair of enantiomers into another pair occur at higher energies than for interconversion between the enantiomers. Specifically, the (II*)–(III*) process is an achiral axis-switching, and the

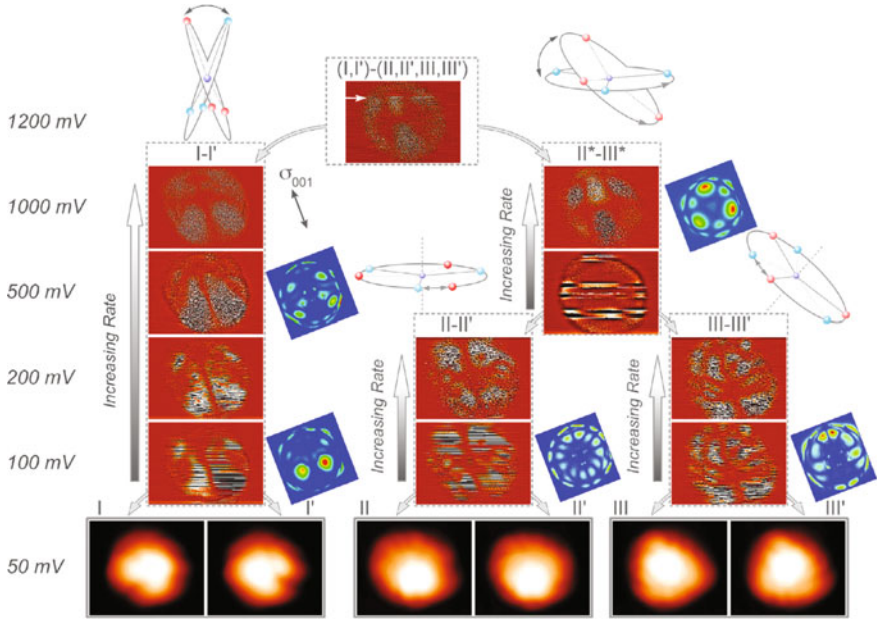

Fig. 6.15 Hierarchical switching in $Sc_3N@C_{80}$ and the identification of the associated Sc_3N motions (*bottom*). STM images of six stable configurations taken at 50 mV bias. Increasing the bias (*vertical direction*) actuates the switching with characteristic SPs recorded at different bias voltages on the same $Sc_3N@C_{80}$ molecule. The *curved arrows* at specific voltages indicate onsets of switching between different configurations. The *vertical arrows* convey the increasing rate of specific switching processes at higher voltages. The SPs reveal the evolution with increasing bias voltage of the switching from enantiomeric configurations, with a node of the switching amplitude in the σ_{001} mirror plane, to nonenantiomeric ones without a node. The *blue* objects are the calculated switching patterns from DFT, which form the basis for the assignments. Reprinted with permission from *Chem. Phys. Lett.* **552**, 1–12 (2012). Copyright 2012 Elsevier

switching from (I, I′) to either (II, II′) or (III, III′) involves two successive axis-switching steps between the next-nearest neighbor C_3 axes. Consequently, the SPs for these processes lack the node in the σ_{001} mirror plane.

6.2.4 Switching Mechanisms and Dynamics

Detailed analysis of the *I-t* trends at different voltages and initial conformations identifies the mechanism for actuating the cluster rotations. First, by monitoring the tunneling current at a particular voltage above a single $Sc_3N@C_{80}$ molecule, the number of interconverting cluster configurations and the switching rate among them is determined. From Fig. 6.5 in Ref. [106, 115], it is evident that for three primary switching processes (I-I′, II-II′, III-III′), only two stationary enantiomeric

configurations are active. In addition, at the same bias voltage, the III-III′ switching occurs at a markedly higher rate than I-I′ and II-II′ processes, implying a higher switching quantum yield. The *I-t* trend for the II-III switching shows that the molecule access multiple quasi-stationary states, implying that the switching process evolves through metastable configurations. A statistical analysis of the residence times of molecules in the high-conductance state directly gives the switching quantum yields [127]. For Poisson statistics with respect to the tunneling current, the residence times should be distributed exponentially with a characteristic time *t*. Figure 6.16 shows an *I-t* trace and the corresponding distribution of residence times for the I-I′ process.

The residence times are described by an exponential distribution $N = A\ exp(-t/\tau)$, where N is the number of switching events, t is the residence time, and τ is the time constant. The switching quantum yield, i.e., number of switching events per tunneling electron, is given by $Y = e/(I*\tau)$, where e is the electron charge and I the tunneling current [127]. *I-t* trends recorded at various bias voltages give the action spectrum [128], i.e., the quantum yield for switching as a function of bias voltage [129]. Figure 6.17a shows the action spectra for processes I-I′, II-II′, and III-III′ for positive and negative bias voltages. The action spectra show that the three elementary switching processes depend on the magnitude, but not the polarity of the bias voltage; the quantum yields rise in an interval between |50| and |100| mV. Moreover, the III-III′ process has a qualitatively different action spectrum

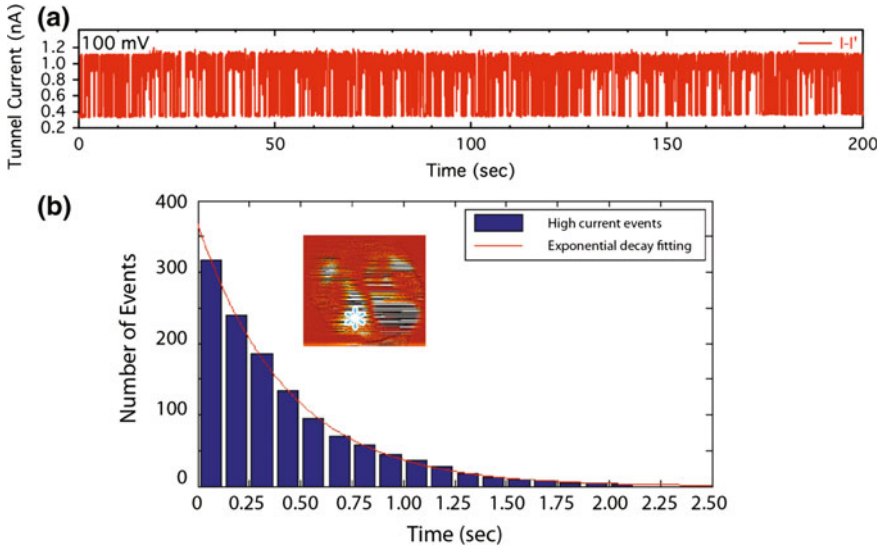

Fig. 6.16 Extracting the switching quantum yields (*Y*) from the I-t trends. **a** 200 s *I-t* trend corresponding to 315 events for I-I′ switching recorded at V_{bias} = 100 mV. **b** A histogram of residence times in the high-conductance state for the *I-t* trend in A with a time bin width of 0.125 s. Fitting the data with an exponential function gives the time constant τ = 0.436 s. Reprinted with permission from *Chem. Phys. Lett.* **552**, 1–12 (2012). Copyright 2012 Elsevier

profile and its quantum yields are about two orders-of-magnitude higher than those of I-I′ and II-II′.

The polarity independent yields and low thresholds imply a vibrational excitation mechanism for the switching, where inelastic scattering of tunneling electrons energizes the cluster rotation by exciting one or more molecular vibrational modes [87, 127, 128, 130–134]. The vibrational modes of the Sc_3N cluster from Raman and infrared spectroscopy, as well as quantum-chemical calculations, give the Sc-N symmetric (v_s) and antisymmetric (v_{as}) stretching frequencies of 51 (52) and 74 (79) meV, respectively [135]. These are the highest frequency modes of the Sc_3N cluster making them candidates for the acceptor modes; the reaction coordinate (RC) vibrations, however, must the frustrated in-plane, R_z, and out-of-plane (i.e., axis-switching), R_x and R_y, rotations of Sc_3N cluster, with much lower frequencies of 10 (13) and 6 (9) meV, respectively [135]. Because elementary rotation processes have energy barriers in excess of 70 meV between equivalent conformations

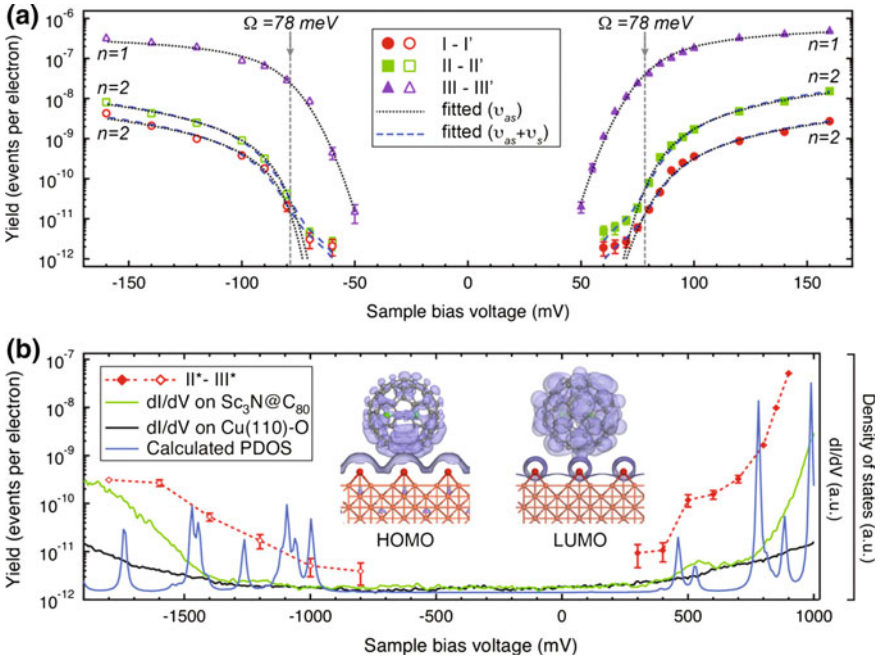

Fig. 6.17 Tunneling bias voltage-dependent switching quantum yields. **a** Experimental yields as a function of bias voltage for the switching processes I-I′ (*circles*), II-II′ (*squares*), and III-III′ (*triangles*). *Dotted curves* are the best fits to the data including only the antisymmetric stretching mode (v_{as}). *Dashed curves* are the simulated data assuming coexcitation of the symmetric stretching mode (v_s), which reproduces the low-energy onsets. Best-fit vibrational energies (Ω) and reaction orders (n) are indicated. **b** Yields as a function of voltage for the switching process (II*)-(III*). Experimental *dI/dV* spectra of $Sc_3N@C_{80}$ (*green*) and the substrate (*black*), along with the calculated PDOS of $Sc_3N@C_{80}$ (*blue*) are shown for comparison. Reprinted with permission from *Nano Lett* **11**, 5327–5332 (2011). Copyright 2011 American Chemical Society

of Sc_3N cluster, the switching between them requires excitation of multiple quanta of the RC modes; this is unlikely to occur directly by inelastic scattering of single-electrons [136]. The activation most likely proceeds by excitation of a high-frequency mode, such as the Sc-N stretching vibration, which acts as energy acceptor; from there intramolecular vibrational redistribution excites multiple quanta of the RC modes, thereby enabling the cluster to overcome the barrier to rotation. The anharmonic coupling may be particularly efficient if the energy is localized within the cluster, because coupling between the cluster and the cage may be weak [131–133].

The action spectra provide quantitative information on the tunneling electron induced dynamics that can test models for the switching mechanism. We adopt the model of Motobayashi et al. for describing the chemistry induced by inelastic tunneling electrons via intermediate vibrational-energy acceptor states [127, 136] to model the vibrational dynamics that actuate the switching process. Ueba et al. have shown that the reaction rate depends on the applied voltage *R(V)* as

$$R(V) = k\left(\frac{I_{\text{in}}(V)}{e}\right)^n \tag{1}$$

where I_{in} is the inelastic tunneling current, $k = \tau_v/\tau_{v,RC}$ is a rate constant given by the ratio of the transition rate $1/\tau_{v,RC}$ describing the excitation of the RC mode via anharmonic mode coupling from the acceptor v mode, and $1/\tau_v$ is the decay rate of the v mode into the electron-hole pair excitation in substrate [87]. The inelastic current I_{in} vanishes when the energy of tunneling electron, eV, is below that of the v mode, Ω, whereas I_{in} increases linearly with the inelastic conductance, σ_{in}, when $eV \geq \Omega$. The second derivative of I_{in} with respect to the voltage, d^2I_{in}/dV^2, directly reflects the vibrational density of states (DOS), $\rho(\Omega)$ [137]. The intrinsic vibrational damping and thermal excitation causes broadening of the $\rho(\Omega)$ and consequently the gradual increase of the slope from 0 to σ_{in} near the threshold energy Ω in $I_{\text{in}}(V)$. The main approximation of the model is to simulate the *effective* vibrational DOS with a Gaussian function (GF), which includes the instrumental, thermal, and lifetime broadening. The $I_{\text{in}}(V)$ can therefore be expressed as

$$I_{in}(V) = \sigma_{\text{in}} f(V, \Omega, \gamma) \tag{2}$$

where $f(V, \Omega, \gamma)$ is the double integration of the GF with respect to V, and γ is the full width at half maximum of the GF. Substituting Eq. (2) into (1), and noticing that $Y(V) = eR(V)/I_{\text{total}}(V)$ allows the reaction yield to be expressed as

$$Y(V)_{\text{tot}} = \sum_i K_i \frac{f(V, \Omega_i, \gamma_i)^{n_i}}{V} \tag{3}$$

where K represents the energy transfer efficiency from the v to the RC mode. This model has been successful in interpreting action spectra for a variety of STM

tunneling current-induced chemical phenomena [128, 138]. The excitation model for $Sc_3@C_{80}$ switching is tested and confirmed by fitting the action spectra in Fig. 6.17a by Eq. (3). The fitting gives the acceptor vibrational mode energies (Ω) as well as reaction orders (n) for different switching processes. The action spectra for three elementary switching processes are reproduced with $\Omega = 78 \pm 1$ meV, consistent with ν_{as} being the acceptor mode; the reaction orders are $n = 1$ for III-III′ process and $n = 2$ for I-I′ and II-II′, explaining the difference in the quantum yields. The reaction orders imply that the barrier for III-III′ is comparable or lower than 78 meV, whereas for I-I′ and II-II′ they are between 78 and 156 meV. In the latter cases, excitation of two quanta of the acceptor mode is necessary to overcome the reaction barrier [139]. The model can be further refined to match the gradual onset of switching below $\sim$70 meV for processes I-I′ and II-II′, by supposing that the lower frequency ν_s mode also contributes through the $n = 2$ process.

In contrast to the three elementary switching processes, the higher energy II*-III* switching requires electronic excitation of the frontier orbitals. Figure 6.17b shows that the action spectra for the II*-III* switching have significantly higher threshold voltages than the elementary processes, and their onsets and slopes depend on the bias polarity. Comparing the action spectra, the spectroscopic *dI/dV* curves, and the calculated molecular LDOS shows that the thresholds for switching coincide with the frontier orbitals of the $Sc_3N@C_{80}$ molecule. Because the thresholds are higher than the energies of any of the fundamental vibrational modes of $Sc_3N@C_{80}$ molecule, the actuation of the (II*)-(III*) switching process must be activated by electronic excitations [140]. Evidently the switching occurs through a nonadiabatic process where the electronic excitation is transferred to vibrational modes of $Sc_3N@C_{80}$ molecule [134, 141].

The surface-supported multi-level hierarchical conductance switch based on single endohedral fullerene molecule enantiomerization described in this chapter has multiple advantages over other single-molecule switches: (i) the switching preserves the external molecular shape simplifying the connection to the external electrodes; (ii) the carbon shell acts as a molecular and electrical shield protecting the functional element from external perturbations; (iii) the spherical shape and small volume of the active element favor high density integration; (iv) the device performance can be optimized by the choice of the internal cluster and carbon shell; and (v) other functions can be incorporated based on spin, or magnetic properties of the metal cluster. For example, substituting Sc by a larger metal ion will increase the barrier to the hindered rotation [125]. Therefore, the concept of molecular switching based on stimulation on internal cluster motion within a hollow shell is general and can be extended to a broad range of endohedral fullerenes by independent choice of the external cage, internal cluster, and external molecular leads, the charge and spin state, and the barriers to internal motions among multiple potential minima actuated by charge, spin, applied electric or magnetic field, and optical stimulation [106, 115].

6.3 Conclusions

The goal of this chapter was to present the rich physics of the inner space of fullerenes and other hollow molecules. In the first part, we have demonstrated that the inner space of hollow molecules has particular electronic structure that is associated with the atomic or molecular constituents of the cage only through their screening properties. The nonnuclear electronic structure exemplified by the SAMO orbitals of fullerenes can be extended to other molecular nanoconstructs, such as nanotubes, molecular sheet-nanotube composites, metal-organic frameworks, and superatom solids [142–145], to create materials that enable nonnuclear charge transport with potentially superior properties than conventional solids. In the second part, we further demonstrated that the fullerene cage can shield cluster contents from environmental influences such that only the tunneling electrons, or other selective stimuli, can alter the internal structure and thereby the molecular properties with respect to charge conduction [146]. We hope that these ideas will stimulate further research on harnessing the inner space of molecular materials.

Acknowledgments The authors thank J. Zhao, T. Huang, A. Popov, S. Yang, and L. Dunsch for their contributions to the research described herein. The authors acknowledge support from the W. M. Keck Foundation and the Division of Chemical Sciences, Geosciences, and Biosciences, Office of Basic Energy Sciences of the U.S. Department of Energy through Grant DE-FG02-09ER16056. We also thank support from NSFC 11574364 of China.

References

1. Coropceanu V, Cornil J, da Silva Filho DA, Olivier Y, Silbey R, Brédas J-L (2007) Charge transport in organic semiconductors. Chem Rev 107:926–952
2. Tautz FS (2007) Structure and bonding of large aromatic molecules on noble metal surfaces: the example of PTCDA. Prog Surf Sci 82:479–520
3. Gunnarsson O (1997) Superconductivity in fullerides. Rev Mod Phys 69:575–606
4. Feng M, Zhao J, Petek H (2008) Atomlike, hollow-core-bound molecular orbitals of C_{60}. Science 320:359–362
5. Zhao J, Feng M, Yang JL, Petek H (2009) The Superatom states of fullerenes and their hybridization into the nearly free electron bands of fullerites. ACS Nano 3:853–864
6. Feng M, Zhao J, Huang T, Zhu X, Petek H (2011) The electronic properties of superatom states of hollow molecules. Acc Chem Res 44:360–368
7. Echenique PM, Pendry JB (1978) The existence and detection of Rydberg states at surface. J Phys C: Solid State Phys 11:2065
8. Inkson JC (1971) The electron-electron interaction near an interface. Surf Sci 28:69–76
9. Inkson JC (1973) The effective exchange and correlation potential for metal surface. J Phys F: Met Phys 3:2143
10. Horowitz CM, Proetto CR, Pitarke JM (2010) Localized versus extended systems in density functional theory: some lessons from the Kohn-Sham exact exchange potential. Phys Rev B 81:121106
11. Bisio F, Nývlt M, Franta J, Petek H, Kirschner J (2006) Mechanisms of high-order perturbative photoemission from Cu(001). Phys Rev Lett 96:087601

12. Silkin VM, Zhao J, Guinea F, Chulkov EV, Echenique PM, Petek H (2009) Image potential states in graphene. Phys Rev B 80:121404–121408
13. Hu S, Zhao J, Jin Y, Yang J, Petek H, Hou JG (2010) Nearly free electron superatom states of carbon and boron nitride nanotubes. Nano Lett 10:4830–4838
14. Zhao J, Feng M, Yang J, Petek H (2009) The superatom states of fullerenes and their hybridization into the nearly free electron bands of fullerites. ACS Nano 3:853–864
15. Hoffmann R (1988) A chemical and theoretical way to look at bonding on surfaces. Rev Mod Phys 60:601–628
16. Chulkov EV, Silkin VM, Echenique PM (1999) Image potential states on metal surfaces: binding energies and wave functions. Surf Sci 437:330–352
17. Bose S, Silkin VM, Ohmann R, Brihuega I, Vitali L, Michaelis CH, Mallet P, Veuillen JY, Schneider MA, Chulkov EV, Echenique PM, Kern K (2010) Image potential states as a quantum probe of graphene interfaces. New J Phys 12:023028
18. Strocov VN, Blaha P, Starnberg HI, Rohlfing M, Claessen R, Debever JM, Themlin JM (2000) Three-dimensional unoccupied band structure of graphite: very-low-energy electron diffraction and band calculations. Phys Rev B 61:4994–5001
19. Posternak M, Baldereschi A, Freeman AJ, Wimmer E, Weinert M (1983) Prediction of electronic interlayer states in graphite and reinterpretation of alkali bands in graphite intercalation compounds. Phys Rev Lett 50:761–764
20. Holzwarth NAW, Louie SG, Rabii S (1982) X-ray form factors and the electronic structure of graphite. Phys Rev B 26:5382–5390
21. Fauster T, Himpsel FJ, Fischer JE, Plummer EW (1983) Three-dimensional energy band in graphite and lithium-intercalated graphite. Phys Rev Lett 51:430–433
22. Brus L (2014) Size, dimensionality, and strong electron correlation in nanoscience. Acc Chem Res 47:2951–2959
23. Lv R, Robinson JA, Schaak RE, Sun D, Sun Y, Mallouk TE, Terrones M (2015) Transition metal dichalcogenides and beyond: synthesis, properties, and applications of single- and few-layer nanosheets. Acc Chem Res 48:56–64
24. Fauster T, Himpsel FJ, Fischer JE, Plummer EW (1983) Three-dimensional energy band in graphite and lithium-intercalated graphite. Phys Rev Lett 51:430–433
25. Kinoshita I, Ino D, Nagata K, Watanabe K, Takagi N, Matsumoto Y (2002) Anomalous quenching of electronic states of nanographene on Pt(111) by deuterium edge termination. Phys Rev B 65:241402(R)
26. Lehmann J, Merschdorf M, Thon A, Voll S, Pfeiffer W (1999) Properties and dynamics of the image potential states on graphite investigated by multiphoton photoemission spectroscopy. Phys Rev B 60:17037–17045
27. Takahashi K, Azuma J, Kamada M (2012) Two-dimensional band dispersion and momentum-resolved lifetime of the image-potential state on graphite studied by angle-resolved multiphoton photoemission spectroscopy. Phys Rev B 85:075325
28. Tan S, Argondizzo A, Wang C, Cui X, Petek H (2017) Ultrafast multiphoton thermionic photoemission from graphite. Phys Rev X 7: 011004
29. Csányi G, Littlewood PB, Nevidomskyy AH, Pickard CJ, Simons BD (2005) The role of the interlayer state in the electronic structure of superconducting graphite intercalated compounds. Nat Phys 1:42–45
30. Meyer JC, Geim AK, Katsnelson MI, Novoselov KS, Booth TJ, Roth S (2007) The structure of suspended graphene sheets. Nature 446:60–63
31. Hu SL, Zhao J, Jin YD, Yang JL, Petek H, Hou JG (2010) Nearly free electron superatom states of carbon and boron nitride nanotubes. Nano Lett 10:4830–4838
32. Blase X, Rubio A, Louie SG, Cohen ML (1995) Quasi-particle band-structure of bulk hexagonal boron-nitride and related systems. Phys Rev B 51:6868–6875
33. Margine ER, Crespi VH (2006) Universal behavior of nearly free electron states in carbon nanotubes. Phys Rev Lett 96:196803–196804
34. Martins JL, Troullier N, Weaver JH (1991) Analysis of occupied and empty electronic states of C_{60}. Chem Phys Lett 180:457–460

35. Yannouleas C, Landman U (1994) Stabilized-jellium description of neutral and multiply charged fullerenes $C_{60}^{x\pm}$. Chem Phys Lett 217:175–185
36. Lu XH, Grobis M, Khoo KH, Louie SG, Crommie MF (2004) Charge transfer and screening in individual C_{60} molecules on metal substrates: a scanning tunneling spectroscopy and theoretical study. Phys Rev B 70:115418
37. Menech DD, Saalmann U, Garcia ME (2006) Energy-resolved STM mapping of C_{60} on metal surfaces: a theoretical study. Phys Rev B 155407
38. Fernandez-Torrente I, Franke KJ, Pascual JI (2008) Spectroscopy of C_{60} single molecules: the role of screening on energy level alignment. J Phys: Condens Matter 20:184002–184011
39. Hashizume T, Motai K, Wang XD, Shinohara H, Saito Y, Maruyama Y, Ohno K, Kawazoe Y, Nishina Y, Pickering HW, Kuk Y, Sakurai T (1993) Intramolecular structures of C_{60} molecules adsorbed on the Cu(111)-(1x1) surface. Phys Rev Lett 71:2959–2962
40. Hou JG, Yang JL, Wang H, Li Q, Zeng CG, Lin H, Wang B, Chen DM, Zhu Q (1999) Identifying molecular orientation of individual C_{60} on a Si(111)-(7x7) surface. Phys Rev Lett 83:3001–3004
41. Martins JL, Troullier N, Weaver JH (1991) Analysis of occupied and empty electronic stats of C_{60}. Chem Phys Lett 180:457–460
42. Pavlyukh Y, Berakadar J (2009) Angular electronic "band structure" of molecules. Chem Phys Lett 468:313–318
43. Voora VK, Cederbaum LS, Jordan KD (2013) Existence of a correlation bound s-type anion state of C_{60}. J Phys Chem Lett 4:849–853
44. Voora VK, Jordan KD (2014) Nonvalence correlation-bound anion states of spherical fullerenes. Nano Lett 14:4602–4606
45. Klaiman S, Gromov EV, Cederbaum LS (2013) Extreme correlation effects in the elusive bound spectrum of C_{60}. J Phys Chem Lett 4:3319–3324
46. Dougherty DB, Feng M, Petek H, Yates JT, Zhao J (2012) Band formation in a molecular quantum well via 2D superatom orbital interactions. Phys Rev Lett 109:266802
47. Ueba T, Terawaki R, Morikawa T, Kitagawa Y, Okumura M, Yamada T, Kato HS, Munakata T (2013) Diffuse unoccupied molecular orbital of rubrene causing image-potential state mediated excitation. J Phys Chem C 117:20098–20103
48. Zoppi L, Martin-Samos L, Baldridge KK (2015) Buckybowl superatom states: a unique route for electron transport? Phys Chem Chem Phys 17:6114–6121
49. Feng M, Lee J, Zhao J, Yates JT, Petek H (2007) Nanoscale templating of close-packed C_{60} nanowires. J Am Chem Soc 129:12394–12395
50. Huang T, Zhao J, Feng M, Petek H, Yang SF, Dunsch L (2010) Superatom orbitals of $Sc_3N@C_{80}$ and their intermolecular hybridization on Cu(110)-(2 x 1)-O surface. Phys Rev B 81:085434
51. Feng M, Lee J, Zhao J, Yates JT, Petek H (2007) Nanoscale templating of close- packed C_{60} nanowires. J Am Chem Soc 129:12394–12395
52. Zhu XY, Dutton G, Quinn DP, Lindstrom CD, Schultz NE, Truhlar DG (2006) Molecular quantum well at the C_{60}/Au(111) interface. Phys Rev B 74:241401
53. Shipman ST, Garrett-Roe S, Szymanski P, Yang A, Strader ML, Harris CB (2006) Determination of band curvatures by angle-resolved two-photon photoemission in thin films of C_{60} on Ag(111). J Phys Chem B 110:10002–10010
54. Dutton G, Zhu XY (2001) Electronic band formation at organic-metal interfaces: role of adsorbate-surface interaction. J Phys Chem B 105:10912–10917
55. Dutton G, Zhu XY (2002) Unoccupied states in C_{60} thin films probed by two-photon photoemission. J Phys Chem B 106:5975–5981
56. Dutton G, Zhu XY (2004) Distance-dependent electronic coupling at molecule-metal interfaces: C_{60}/Cu(111). J Phys Chem B 108:7788–7793
57. Chan W, Tritsch J, Dolocan A, Ligges M, Miaja-Avila L, Zhu X (2011) Communication: momentum-resolved quantum interference in optically excited surface states. J Chem Phys 135:031101–031104

58. Zamkov M, Woody N, Bing S, Chakraborty HS, Chang Z, Thumm U, Richard P (2004) Time-resolved photoimaging of image-potential states in carbon nanotubes. Phys Rev Lett 93:156803
59. Wang KD, Zhao J, Yang SF, Chen L, Li QX, Wang B, Yang SH, Yang JL, Hou JG, Zhu QS (2003) Unveiling metal-cage hybrid states in a single endohedral metallofullerene. Phys Rev Lett 91:185504
60. Shinohara H (2000) Endohedral metallofullerenes. Rep Prog Phys 63:843–892
61. Nagase S, Kobayashi K, Kato T, Achiba Y (1993) A theoretical approach to C_{82} to La@C_{82}. Chem Phys Lett 201:475–480
62. Laasonen K, Andreoni W, Parrinello M (1992) Structural and electronic-properties of La@C_{82}. Science 258:1916–1918
63. Poirier DM, Knupfer M, Weaver JH, Andreoni W, Laasonen K, Parrinello M, Bethune DS, Kikuchi K, Achiba Y (1994) Electronic and geometric structure of La@C_{82} and C_{82}: theory and experiment. Phys Rev B 49:17403–17412
64. Hino S, Takahashi H, Iwasaki K, Matsumoto K, Miyazaki T, Hasegawa S, Kikuchi K, Achiba Y (1993) Electronic-structure of metallofullerene LaC_{82} - electron transfer from lanthanum to C_{82}. Phys Rev Lett 71:4261–4263
65. Kessler B, Bringer A, Cramm S, Schlebusch C, Eberhardt W, Suzuki S, Achiba Y, Esch F, Barnaba M, Cocco D (1997) Evidence for incomplete charge transfer and La-derived states in the valence bands of endohedrally doped La@C_{82}. Phys Rev Lett 79:2289–2292
66. Bennig PJ, Martins JL, Weaver JH, Chibante LPF, Smalley RE (1991) Electronic states of K_xC_{60}: insulating, metallic, and superconducting character. Science 252:1417–1419
67. Syamala MS, Cross RJ, Saunders M (2002) ^{129}Xe NMR spectrum of xenon inside C_{60}. J Am Chem Soc 124:6216–6219
68. Gromov EV, Klaiman S, Cederbaum LS (2015) Influence of caged noble-gas atom on the superatomic and valence states of C_{60}. Mol Phys 1–6
69. Jorn R, Zhao J, Petek H, Seideman T (2011) Current-driven dynamics in molecular junctions: endohedral fullerenes. ACS Nano 5:7858–7865
70. Feng M, Shi YL, Lin CW, Zhao J, Liu FP, Yang SF, Petek H (2013) Energy stabilization of the s-symmetry superatom molecular orbital by endohedral doping of C_{82} fullerene with a lanthanum atom. Phys Rev B 88:075417
71. Popov AA, Yang S, Dunsch L (2013) Endohedral fullerenes. Chem Rev 113:5989–6113
72. Shinohara H (2000) Endohedral metallofullerenes. Rep Prog Phys 63:843
73. Feng M, Shi Y, Lin C, Zhao J, Liu F, Yang S, Petek H (2013) Energy stabilization of the s-symmetry superatom molecular orbital by endohedral doping of C_{82} fullerene with a lanthanum atom. Phys Rev B 88:075417
74. Iwamoto M, Ogawa D, Yasutake Y, Azuma Y, Umemoto H, Ohashi K, Izumi N, Shinohara H, Majima Y (2010) Molecular orientation of individual Lu@C_{82} molecules demonstrated by scanning tunneling microscopy. J Phys Chem C 114:14704–14709
75. Huang HJ, Yang SH (2000) Preparation and characterization of the endohedral metallofullerene Lu@C_{82}. J Phys Chem Solids 61:1105–1110
76. Svitova AL, Krupskaya Y, Samoylova N, Kraus R, Geck J, Dunsch L, Popov AA (2014) Magnetic moments and exchange coupling in nitride clusterfullerenes $Gd_xSc_{3-x}N@C_{80}$ (x = 1-3). Dalton Trans 43:7387–7390
77. Hermanns CF, Bernien M, Krüger A, Schmidt C, Waßerroth ST, Ahmadi G, Heinrich BW, Schneider M, Brouwer PW, Franke KJ, Weschke E, Kuch W (2013) Magnetic coupling of $Gd_3N@_{80}$ endohedral fullerenes to a substrate. Phys Rev Lett 111:167203
78. Popov AA, Dunsch L (2008) Hindered cluster rotation and ^{45}Sc hyperfine splitting constant in distonoid anion radical $Sc_3N@C_{80}$, and spatial spin − charge separation as a general principle for anions of endohedral fullerenes with metal-localized lowest unoccupied molecular orbitals. J Am Chem Soc 130:17726–17742
79. Popov AA, Zhang L, Dunsch L (2010) A pseudoatom in a cage: trimetallofullerene $Y_3@C_{80}$ mimics $Y_3N@C_{80}$ with nitrogen substituted by a pseudoatom. ACS Nano 4:795–802

80. Aviram A (1988) Molecules for memory, logic, and amplification. J Am Chem Soc 110:5687–5692
81. Hopfield JJ, Onuchic JN, Beratan DN (1988) A molecular shift register based on electron-transfer. Science 241:817–820
82. Zhang JL, Zhong JQ, Lin JD, Hu WP, Wu K, Xu GQ, Wee ATS, Chen W (2015) Towards single molecule switches. Chem Soc Rev 44:2998–3022
83. Kaun CC, Seideman T (2005) Current-driven oscillations and time-dependent transport in nanojunctions. Phys Rev Lett 94:226801
84. Lee J, Tallarida N, Rios L, Perdue SM, Apkarian VA (2014) Single electron bipolar conductance switch driven by the molecular Aharonov-Bohm effect. ACS Nano 8:6382–6389
85. Blum AS, Kushmerick JG, Long DP, Patterson CH, Yang JC, Henderson JC, Yao YX, Tour JM, Shashidhar R, Ratna BR (2005) Molecularly inherent voltage-controlled conductance switching. Nat Mater 4:167–172
86. Dulic D, van der Molen SJ, Kudernac T, Jonkman HT, de Jong JJD, Bowden TN, van Esch J, Feringa BL, van Wees BJ (2003) One-way optoelectronic switching of photochromic molecules on gold. Phys Rev Lett 91:207402
87. Eigler DM, Lutz CP, Rudge WE (1991) An atomic switch realized with the scanning tunneling microscope. Nature 352:600–603
88. Osorio EA, Moth-Poulsen K, van der Zant HSJ, Paaske J, Hedegård P, Flensberg K, Bendix J, Bjørnholm T (2010) Electrical manipulation of spin states in a single electrostatically gated transition-metal complex. Nano Lett 10:105–110
89. Khajetoorians AA, Wiebe J, Chilian B, Wiesendanger R (2011) Realizing all-spin-based logic operations atom by atom. Science 332:1062–1064
90. Eigler DM, Schweizer EK (1990) Positioning single atoms with a scanning tunneling microscope. Nature 344:524–526
91. Crommie MF, Lutz CP, Eigler DM (1993) Confinement of electrons to quantum corrals on a metal surface. Science 262:218–220
92. Repp J, Meyer G, Olsson FE, Persson M (2004) Controlling the charge state of individual gold adatoms. Science 305:493–495
93. Wu SW, Ogawa N, Nazin GV, Ho W (2008) Conductance hysteresis and switching in a single-molecule junction. J Phys Chem C 112:5241–5244
94. Jan van der Molen S, Liljeroth P (2010) Charge transport through molecular switches. J Phys Condens Matter 22 133001
95. Collier CP, Mattersteig G, Wong EW, Luo Y, Beverly K, Sampaio J, Raymo FM, Stoddart JF, Heath JR (2000) A [2]catenane-based solid state electronically reconfigurable switch. Science 289:1172–1175
96. Morgenstern K (2009) Isomerization reactions on single adsorbed molecules. Acc Chem Res 42:213–223
97. Feng M, Gao L, Deng ZT, Ji W, Guo XF, Du SX, Shi DX, Zhang DQ, Zhu DB, Gao HJ (2007) Reversible, erasable, and rewritable nanorecording on an H_2 rotaxane thin film. J Am Chem Soc 129:2204–2205
98. Gauyacq JP, Lorente N, Novaes FD (2012) Excitation of local magnetic moments by tunneling electrons. Prog Surf Sci 87:63–107
99. Collier CP, Wong EW, Belohradsky M, Raymo FM, Stoddart JF, Kuekes PJ, Williams RS, Heath JR (1999) Electronically configurable molecular-based logic gates. Science 285:391–394
100. Choi BY, Kahng SJ, Kim S, Kim H, Kim HW, Song YJ, Ihm J, Kuk Y (2006) Conformational molecular switch of the azobenzene molecule: a scanning tunneling microscopy study. Phys Rev Lett 96:156106
101. Iancu V, Hla SW (2006) Realization of a four-step molecular switch in scanning tunneling microscope manipulation of single chlorophyll-a molecules. P Natl Acad Sci USA 103:13718–13721

102. Comstock MJ, Levy N, Kirakosian A, Cho J, Lauterwasser F, Harvey JH, Strubbe DA, Frechet JMJ, Trauner D, Louie SG, Crommie MF (2007) Reversible photomechanical switching of individual engineered molecules at a metallic surface. Phys Rev Lett 99:038301
103. Liljeroth P, Repp J, Meyer G (2007) Current-induced hydrogen tautomerization and conductance switching of naphthalocyanine molecules. Science 317:1203–1206
104. Hagen S, Kate P, Leyssner F, Nandi D, Wolf M, Tegeder P (2008) Excitation mechanism in the photoisomerization of a surface-bound azobenzene derivative: role of the metallic substrate. J Chem Phys 129
105. Pan SA, Fu Q, Huang T, Zhao AD, Wang B, Luo Y, Yang JL, Hou JG (2009) Design and control of electron transport properties of single molecules. Proc Natl Acad Sci USA 106:15259–15263
106. Huang T, Zhao J, Feng M, Popov AA, Yang SF, Dunsch L, Petek H (2012) A multi-state single-molecule switch actuated by rotation of an encapsulated cluster within a fullerene cage. Chem Phys Lett 552:1–12
107. Park HK, Park J, Lim AKL, Anderson EH, Alivisatos AP, McEuen PL (2000) Nanomechanical oscillations in a single-C_{60} transistor. Nature 407:57–60
108. Zhao J, Zeng CG, Cheng X, Wang KD, Wang G, Yang JL, Hou JG, Zhu QS (2005) Single $C_{59}N$ molecules as a molecular rectifier. Phys Rev Lett 95:045502
109. Danilov AV, Hedegård P, Golubev DS, Bjørnholm T, Kubatkin SE (2008) Nanoelectromechanical switch operating by tunneling of an entire C_{60} molecule. Nano Lett 8:2393–2398
110. Nakaya M, Kuwahara Y, Aono M, Nakayama T (2008) Reversibility-controlled single molecular level chemical reaction in a C_{60} monolayer via ionization induced by scanning transmission microscopy. Small 4:538–541
111. Yasutake Y, Shi ZJ, Okazaki T, Shinohara H, Majima Y (2005) Single molecular orientation switching of an endohedral metallofullerene. Nano Lett 5:1057–1060
112. Neel N, Limot L, Kroger J, Berndt R (2008) Rotation of C_{60} in a single-molecule contact. Phys Rev B 77:125431
113. Bethune DS, Johnson RD, Salem JR, de Vries MS, Yannoni CS (1993) Atoms in carbon cages: the structure and properties of endohedral fullerenes. Nature 366:123–128
114. Petek H (2014) Single-molecule femtochemistry: molecular imaging at the space-time limit. ACS Nano 8:5–13
115. Huang T, Zhao J, Peng M, Popov AA, Yang SF, Dunsch L, Petek H (2011) A molecular switch based on current-driven rotation of an encapsulated cluster within a fullerene cage. Nano Lett 11:5327–5332
116. Stevenson S, Rice G, Glass T, Harich K, Cromer F, Jordan MR, Craft J, Hadju E, Bible R, Olmstead MM, Maitra K, Fisher AJ, Balch AL, Dorn HC (1999) Small-bandgap endohedral metallofullerenes in high yield and purity. Nature 401:55–57
117. Chaur MN, Melin F, Ortiz AL, Echegoyen L (2009) Chemical, electrochemical, and structural properties of endohedral metallofullerenes. Angew Chem Int Ed 48:7514–7538
118. Wang T, Wang C (2014) Endohedral metallofullerenes based on spherical I_h-C_{80} cage: molecular structures and paramagnetic properties. Acc Chem Res 47:450–458
119. Alvarez L, Pichler T, Georgi P, Schwieger T, Peisert H, Dunsch L, Hu Z, Knupfer M, Fink J, Bressler P, Mast M, Golden MS (2002) Electronic structure of pristine and intercalated $Sc_3N@C_{80}$ metallofullerene. Phys Rev B 66:035107
120. Kobayashi K, Sano Y, Nagase S (2001) Theoretical study of endohedral metallofullerenes: $Sc_{3-n}La_nN@C_{80}$ (n = 0–3). J Comput Chem 22:1353–1358
121. Heine T, Vietze K, Seifert G (2004) ^{13}C NMR fingerprint characterizes long time-scale structure of $Sc_3N@C_{80}$ endohedral fullerene. Magn Reso Chem 42:S199–S201
122. Morton JJL, Tiwari A, Dantelle G, Porfyrakis K, Ardavan A, Briggs CAD (2008) Switchable $ErSc_2N$ rotor within a C_{80} fullerene cage: an electron paramagnetic resonance and photoluminescence excitation study. Phys Rev Lett 101:013002

123. Huang T, Zhao J, Feng M, Popov AA, Yang S, Dunsch L, Petek H (2011) A Molecular switch based on current-driven rotation of an encapsulated cluster within a fullerene cage. Nano Lett 11:5327–5332
124. Huang T, Zhao J, Feng M, Popov AA, Yang S, Dunsch L, Petek H (2012) A multi-state single-molecule switch actuated by rotation of an encapsulated cluster within a fullerene cage. Frontiers article in. Chem Phys Lett 552:1–12
125. Popov AA, Dunsch L (2008) Hindered cluster rotation and ^{45}Sc hyperfine splitting constant in distonoid anion radical $Sc_3N@C_{80}-$, and spatial spin − charge separation as a general principle for anions of endohedral fullerenes with metal-localized lowest unoccupied molecular orbitals. J Am Chem Soc 130:17726–17742
126. Feng Y, Wang T, Xiang J, Gan L, Wu B, Jiang L, Wang C (2015) Tuneable dynamics of a scandium nitride cluster inside an I_h-C_{80} cage. Dalton Trans 44:2057–2061
127. Stipe BC, Rezaei MA, Ho W (1998) Inducing and viewing the rotational motion of a single molecule. Science 279:1907–1909
128. Kim Y, Motobayashi K, Frederiksen T, Ueba H, Kawai M (2015) Action spectroscopy for single-molecule reactions—experiments and theory. Prog Surf Sci 90:85–143
129. Sainoo Y, Kim Y, Okawa T, Komeda T, Shigekawa H, Kawai M (2005) Excitation of molecular vibrational modes with inelastic scanning tunneling microscopy processes: examination through action spectra of cis-2-butene on Pd(110). Phys Rev Lett 95:246102
130. Stipe BC, Rezaei MA, Ho W (1998) Coupling of vibrational excitation to the rotational motion of a single adsorbed molecule. Phys Rev Lett 81:1263–1266
131. Komeda T, Kim Y, Kawai M, Persson BNJ, Ueba H (2002) Lateral hopping of molecules induced by excitation of internal vibration mode. Science 295:2055–2058
132. Ohara M, Kim Y, Yanagisawa S, Morikawa Y, Kawai M (2008) Role of molecular orbitals near the Fermi level in the excitation of vibrational modes of a single molecule at a scanning tunneling microscope junction. Phys Rev Lett 100:136104
133. Parschau M, Passerone D, Rieder K-H, Hug HJ, Ernst K-H (2009) Switching the chirality of single adsorbate complexes. Angew Chem Int Ed 48:4065–4068
134. Ueba H, Tikhodeev SG, Persson BNJ (2010) Theory of inelastic tunneling current driven motions of single adsorbates. In: Seideman T (ed) Current-driven phenomena in nanoelectronics. Pan Stanford publishing Pte Ltd., Singapore
135. Krause M, Kuzmany H, Georgi P, Dunsch L, Vietze K, Seifert G (2001) Structure and stability of endohedral fullerene $Sc_3N@C_{80}$: a Raman, infrared, and theoretical analysis. J Chem Phys 115:6596–6605
136. Salam GP, Persson M, Palmer RE (1994) Possibility of coherent multiple excitation in atom transfer with a scanning tunneling microscope. Phys Rev B 49:10655
137. Ueba H, Persson BNJ (2007) Action spectroscopy for single-molecule motion induced by vibrational excitation with a scanning tunneling microscope. Phys Rev B 75:041403
138. Motobayashi K, Kim Y, Ueba H, Kawai M (2010) Insight into action spectroscopy for single molecule motion and reactions through inelastic electron tunneling. Phys Rev Lett 105:076101
139. Foley ET, Kam AF, Lyding JW, Avouris P (1998) Cryogenic UHV-STM study of hydrogen and deuterium desorption from Si(100). Phys Rev Lett 80:1336–1339
140. Lastapis M, Martin M, Riedel D, Hellner L, Comtet G, Dujardin G (2005) Picometer-scale electronic control of molecular dynamics inside a single molecule. Science 308:1000–1003
141. Seideman T (2005) Nonadiabatic vibronic dynamics as a tool: from surface nanochemistry to coherently driven molecular machines. Isral J Chem 45:227–237
142. Zhao J, Petek H (2014) Non-nuclear electron transport channels in hollow molecules. Phys Rev B 90:075412
143. Zhao J, Zheng Q, Petek H, Yang J (2014) Nonnuclear nearly free electron conduction channels induced by doping charge in nanotube-molecular sheet composites. J Phys Chem A 118:7255–7260

144. Zhao S, Li Z, Yang J (2014) Obtaining two-dimensional electron gas in free space without resorting to electron doping: an electride based design. J Am Chem Soc 136:13313–13318
145. Roy X, Lee C-H, Crowther AC, Schenck CL, Besara T, Lalancette RA, Siegrist T, Stephens PW, Brus LE, Kim P, Steigerwald ML, Nuckolls C (2013) Nanoscale atoms in solid-state chemistry. Science 341:157–160
146. Le Poul N, Colasson B (2015) Electrochemically and chemically induced redox processes in molecular machines. Chem Electro Chem 2:475–496

Chapter 7
Electron Spin Resonance Studies of Metallofullerenes

Taishan Wang and Chunru Wang

Abstract The electron spin resonances of metallofullerenes are helpful to disclose their geometry, electronic structures, and internal dynamic modes though analyzing the hyperfine couplings of their ESR spectra. The chapter describes the electron spin resonance and the tunable paramagnetic properties of $M@C_{82}$ (M = Sc, Y, La), $Sc_3C_2@C_{80}$, $Y_2@C_{79}N$, $TiSc_2N@C_{80}$, and others. The electron spin manipulation based on these paramagnetic species has been realized by changing temperatures and exohedral modification.

Electron transfer from the endohedral metal to outer fullerene cage makes these Endohedral metallofullerenes (EMFs) particularly stable. On the other hand, this kind of inherent electron transfer may result in an unpaired electron located on the singly occupied molecular orbitals (SOMO) of EMFs. For instance of $La@C_{82}$, the La cation usually has trivalent form and it will provide three electrons to the C_{82} cage; according to the Pauli's exclusion principle, however, one unpaired electron stays at the C_{82}^{3-}. Over the years, many EMFs with unpaired spin have been investigated and these paramagnetic species also have brought us many unique properties and potential applications.

$La@C_{82}$ is the first paramagnetic EMF studied by electron spin resonance (ESR) spectroscopy [1–3] Subsequently, the paramagnetic properties of $Sc@C_{82}$ [4], $Y@C_{82}$, [5] $Sc_3C_2@C_{80}$ [6–9] $Y_2@C_{79}N$ [10], etc., were investigated. For their ESR studies, the hyperfine coupling constants (hfcc) and *g*-factor were analyzed in detail to disclose the spin-center and kinds of metal nuclei [11]. Furthermore, the electron spin manipulation based on these paramagnetic species has been realized by changing temperatures and exohedral modification [12]. These paramagnetic species have wide applications in chemistry, physics, material, and biology, especially for quantum information progressing, magnetic switch, memory devices, single-molecule magnet (SMM), and spintronics. Herein, we introduce the electron

T. Wang · C. Wang (✉)
Laboratory of Molecular Nanostructure and Nanotechnology, Institute of Chemistry, Chinese Academy of Sciences, Beijing 100190, China
e-mail: crwang@iccas.ac.cn

A.A. Popov (ed.), *Endohedral Fullerenes: Electron Transfer and Spin*, Nanostructure Science and Technology, DOI 10.1007/978-3-319-47049-8_7

spin resonance and their tunable paramagnetic properties base on M@C_{82} (M = Sc, Y, La), Sc_3C_2@C_{80}, Y_2@$C_{79}N$, $TiSc_2N$@C_{80}, and others.

7.1 Electron Spin Resonance of M@C_{82} (M = Sc, Y, La)

In M@C_{82}(M = Sc, Y, La), the Sc, Y, La have nonzero nuclear spin (*I*), 1/2 for Y, 7/2 for Sc and La. Therefore, the spin-nucleus interaction would result in hyperfine couplings in their ESR spectrum. The ESR lines can be counted by the following equation: $2nI + 1$, where n is the number of equivalent metal nuclei. Based on this, the Sc@C_{82} and La@C_{82} both have eight lines in their ESR spectrum, whereas the Y@C_{82} has two ESR lines instead.

In ESR spectra, there are two parameters that can generally reveal the electron spin characteristics, i.e., *g*-factor and coupling constant (*a*). The *g*-factor can give information about the paramagnetic center. The hyperfine coupling constant (hfcc) is caused by the interaction between the unpaired electron and a nucleus (or nuclei). Table 7.1 lists the ESR parameters of M@C_{82}(M = Sc, Y, La). It should be noted that the Sc@C_{2v}(9)-C_{82} has a larger hfcc value (3.82 G) and a smaller *g*-factor of 1.9999 than those of other M@C_{82}. It is known that large hfc constants reflect the spin density becoming more localized. Theoretical calculations also disclosed that the La@C_{2v}(9)-C_{82} and Y@C_{2v}(9)-C_{82} has its spin localizing on the C_{82} cage. In Sc@C_{2v}(9)-C_{82}, differently, the unpaired electron mainly resides in the carbon cage and partially in the Sc nucleus, which leads to the increased hfcc value. Exactly, the spin density on the Sc site for Sc@C_{2v}(9)-C_{82} is associated with Sc(d_{yz}) orbital and this kind of *d* component gives hfcc an order of magnitude larger. The Sc(d_{yz})-contained unpaired spin may be caused by the strong hybridization between the Sc orbitals and π orbitals of fullerene cage, which is not obvious in La@C_{2v}(9)-C_{82} and Y@C_{2v}(9)-C_{82}.

The Sc(3d)-contained unpaired spin in Sc@C_{2v}(9)-C_{82} leads to its susceptible spin character. It has been reported that the ESR property of Sc@C_{2v}(9)-C_{82} exhibits great changes under different temperatures ranging from 270 to 150 K [4, 14]. Briefly, at low temperature, the intensity of the ESR signals at higher magnetic field decreases and the whole ESR spectrum exhibits paramagnetic

Table 7.1 The hfc constants (*a*) and *g*-factors of M@C_{82} (*M* = Sc, Y, La)

EMFs	*a* [G]	*g*	Temperature[K]	Solvent	Reference
La@C_{2v}(9)-C_{82}	1.2	2.0008	RT	CS_2	[11]
La@C_s(6)-C_{82}	0.83	2.0002	RT	Toluene	[11]
Y@C_{2v}(9)-C_{82}	0.49	2.0006	RT	Toluene	[5]
	0.48	2.00013	RT	CS_2	[13]
Y@C_s(6)-C_{82}	0.32	2.0001	RT	Toluene	[5]
Sc@C_{2v}(9)-C_{82}	3.82	1.9999	RT	CS_2	[14]
Sc@C_s(6)-C_{82}	1.16	2.0002	RT	CS_2	[14]

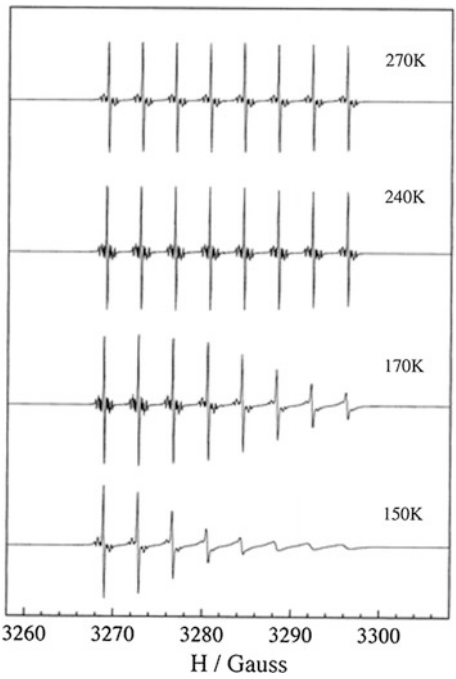

Fig. 7.1 The temperature-dependent ESR spectra of Sc@C_{2v}(9)-C_{82}. Reproduced form Ref. [14]

anisotropy (Fig. 7.1). This kind of anisotropy could be due to the insufficient rotational averaging of the g and hyperfine tensors. For metallofullerenes M@C_{82}, the endohedral metal usually has certain dynamic motion, and its motion extent is related to the environment temperature. The weakened motion of Sc nuclei would result in large dipole interaction between the d_{Sc}-electron spin and Sc nucleus, as well as anisotropic paramagnetic property for Sc@C_{2v}(9)-C_{82}. For the La@C_{2v}(9)-C_{82} and Y@C_{2v}(9)-C_{82}, however, they have smaller hfcc values and cage-based electron spin distributions. Different from the Sc@C_{2v}(9)-C_{82}, their temperature-dependent ESR spectra revealed slight anisotropic paramagnetic property under low temperature due to the delocalized unpaired spin on C_{82} cage [4].

In addition, it was revealed that the line width of Sc@C_{82} ESR spectrum in toluene and CS_2 solutions shows the dependence on a quantum number (m_1) of Sc nuclear magnetic moment under low temperatures, originating from the insufficient averaging of anisotropy of hyperfine and g tensors caused by a hydrodynamic rotation in solution [4, 14].

The chemical modification on fullerene cage have been studied to modulate the paramagnetism of La@C_{2v}(9)-$C_{82}$and Sc@C_{2v}(9)-C_{82}. The exo-adduct can influence the electronic structure due to the altered π-system of carbon cage, and consequently, their unpaired spin distributions will change. A carbine derivative isomer of La@C_{2v}(9)-C_{82}, La@C_{82}-Ad, was studied by XRD and ESR spectroscopy [15]. The X-ray analysis characterizes the isomer that the Ad moiety adds to a [6, 6]-open bond. Moreover, this La@C_{82}-Ad isomer has hfcc of 0.89 G, which is smaller than

that of pristine La@C_{2v}(9)-C_{82} (1.2 G). The similar Sc@C_{2v}(9)-C_{82} derivatives reacted with adamantylidene carbene, Sc@C_{82}-Ad, have four isomers, which have different hfcc (5.76; 3.72; 3.67; 4.14 G) that is different from that of pristine Sc@C_{2v}(9)-C_{82} (3.78 G) [16]. Notably, for one Sc@C_{82}-Ad derivative the Ad moiety also adds to a [6, 6]-open bond closest to the internal Sc metal and it has the same structure with above mentioned La@C_{82}-Ad isomer. However, this Sc@C_{82}-Ad derivative has larger hfcc of 5.76 G than that of pristine Sc@C_{2v}(9)-C_{82} (3.78 G). The increased hfcc for Sc@C_{82}-Ad isomer discloses a more Sc(d)-contained unpaired spin after chemical modification on this [6, 6] site.

The paramagnetic property of M@C_{82} has been explored to construct ordered clustering by means of host–guest chemistry. For example, a host-guest system of La@C_{82} and a cyclodimeric copper porphyrin {cyclo-$[P_{Cu}]_2$}, denoted as cyclo-$[P_{Cu}]_2 \supset$ La@C_{82}, was found with a quartet spin ground state (S = 3/2) and a ferromagnetically coupled property [17]. Interestingly, when the cyclo-$[P_{Cu}]_2 \supset$ La@C_{82} was transformed into cage-$[P_{Cu}]_2 \supset$ La@C_{82} by ring-closing olefin metathesis of its side chain olefinic termini, this compact nesting system has ferrimagnetic character with doublet spin ground state (S = 1/2).

7.2 Electron Spin Resonance of Sc_3C_2@C_{80}

For Sc_3C_2@C_{80}, the unpaired spin is localized within the internal Sc_3C_2 cluster and is primarily attributed to the π^* orbital of the C_2 moiety as well as the d_π atomic orbitals of Sc^{3+} atoms. In ESR spectrum of Sc_3C_2@C_{80}, 22 lines with relativeintensities1:3:6:10:15:21:28:36:42:46:48:48:46:42:36:28:21:15:10:6:3:1can be observed at room temperature in toluene solution with hfcc of 6.22 G and g-factor of 1.9985 coupled by the electron spin and three equivalent Sc nuclei [18].

The paramagnetic property of Sc_3C_2@C_{80} has been found to be sensible to the temperature, especially for its line width. In solution of Sc_3C_2@C_{80}, its line width value would reduce along with the decreasing in temperature. In Sc_3C_2@C_{80}, no large temperature or m_1 dependence of the line width was observed in CS_2 over the temperature range of 180–290 K and no obvious anisotropic paramagnetic property was detected even at 180 K due to the rotational Sc_3C_2 internal cluster [8]. In addition, the much larger line width (1 G) for Sc_3C_2@C_{80} can be ascribed to the slightly different three Sc nuclear spin states. The 22 lines come from the rotation of inner Sc_3C_2 cluster, and this kind of intra-molecular dynamics would average the three nuclei's environment (Table 7.2).

The chemical modification was also executed to investigate the controllable paramagnetism of Sc_3C_2@C_{80}. The exohedral adducts not only change its structures, but also influence the spin states. For a Sc_3C_2@C_{80} derivative (Sc_3C_2@C_{80}-Ad) reacted with adamantylidene carbene, it shows an ESR spectrum with the hfcc of 7.39 G (two nuclei) and 1.99 G (one nucleus) [9]. The Sc_3C_2@C_{80} fulleropyrrolidine exhibits different ESR spectrum with hfcc of 8.602 G (one nucleus) and 4.822 G (two nuclei) (Fig. 7.2) [19]. Moreover, in the Sc_3C_2@C_{80} bisfulleroid

Table 7.2 The hfc constants (*a*) and *g*-factors of $Sc_3C_2@C_{80}$

EMFs	*a* [G]	g	Temperature[K]	Solvent	Reference
$Sc_3C_2@C_{80}$	6.51	1.9985	200	CS_2	[6]
$Sc_3C_2@C_{80}$	6.22	1.9985	RT	Toluene	[18]
$Sc_3C_2@C_{80}$	6.256	2.0006	RT	*o*-DCB	[19]
$Sc_3C_2@C_{80}$ fulleropyrrolidine	8.602; 4.822; 4.822	2.0007	RT	*o*-DCB	[19]
$Sc_3C_2@C_{80}$-Ad	7.39; 7.39;1.99	1.99835	RT	CS_2	[9]
$Sc_3C_2@C_{80}$ bisfulleroid	6.73; 4.00; 4.00	–	RT	CS_2	[20]
$TiSc_2N@C_{80}$	–	1.9579	RT	Toluene	[22]
$TiY_2N@C_{80}$	–	1.9454	RT	Toluene	[23]

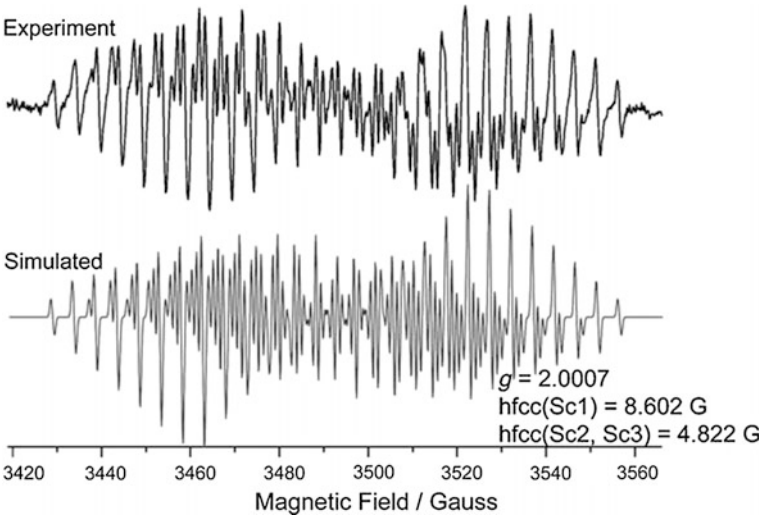

Fig. 7.2 The ESR spectrum of $Sc_3C_2@C_{80}$ fulleropyrrolidine. Reproduced from Ref. [19]

derivative two sets of hfcc can be found at 6.73 G (one nucleus) and 4.00 G (two nuclei) [20]. In addition, it can be concluded that the adduct site greatly influence the hyperfine couplings. For example, in $Sc_3C_2@C_{80}$-Ad the Ad moiety adds to a [6, 6] bond, whereas the $Sc_3C_2@C_{80}$ fulleropyrrolidine and $Sc_3C_2@C_{80}$ bisfulleroid the adducts reside at [5, 6] bond. Consequently, the $Sc_3C_2@C_{80}$-Ad has very different hfcc pattern (two nuclei with larger hfcc) from those of others (one nucleus with the largest hfcc).

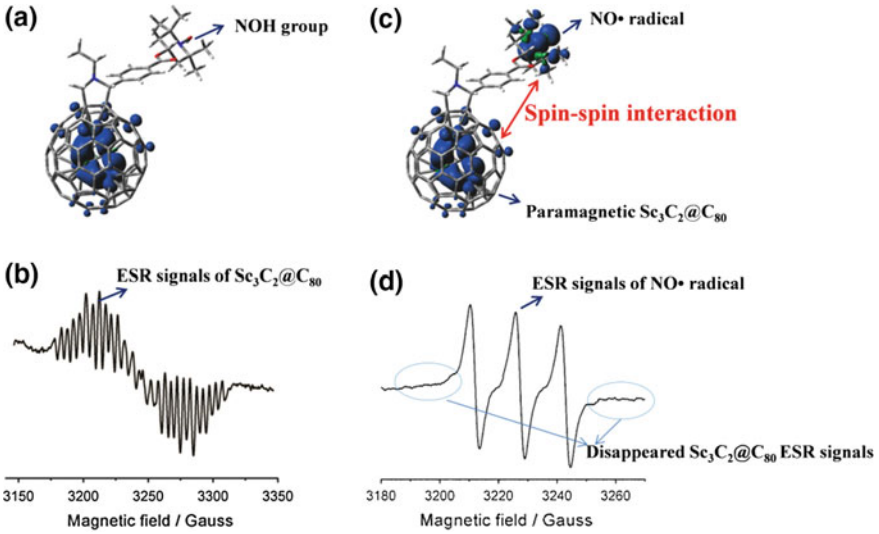

Fig. 7.3 The calculated structure of $Sc_3C_2@C_{80}$ fulleropyrrolidine with diamagnetic hydroxylamine group (**a**), and its ESR spectrum (**b**). The calculated structure of $Sc_3C_2@C_{80}$ fulleropyrrolidine with nitroxide radical group (**c**), and its ESR spectrum (**d**)

The paramagnetic properties of $Sc_3C_2@C_{80}$ can be influenced by neighboring molecular paramagnet through spin–spin interactions, realizing remote control of ESR signals for $Sc_3C_2@C_{80}$ [21]. Specifically, the nitroxide radical group was linked to $Sc_3C_2@C_{80}$ via cycloaddition with variable space length (about $1 \sim 3$ nm) between these two spin centers. Interestingly, this complex system only exhibits the ESR signals of nitroxide radical and the ESR signals of the $Sc_3C_2@C_{80}$ moiety are "switched off" (Fig. 7.3). Detailed analysis revealed that the strong dipole–dipole interactions between nitroxide radical and $Sc_3C_2@C_{80}$ in $FSc_3C_2@C_{80}PNO^{\bullet}$ reduced the spin–spin relaxation time (T_2), resulting in broadened line width (ΔH) and weakened ESR signals of $Sc_3C_2@C_{80}$ moiety.

Moreover, the ESR signals of the $Sc_3C_2@C_{80}$ moiety can be "switched on" by changing the distance between these two spin centers as well as by decreasing temperature [21]. The elongated spin–spin distance will reduce the strength of spin–spin interactions and allow the ESR signals of $Sc_3C_2@C_{80}$ moiety to come into existence again. Differently, decreasing temperature can weaken the spin–lattice interactions for this bis-spin system and then strengthen the ESR signals of $Sc_3C_2@C_{80}$ moiety. Such switchable ESR signals for metallofullerene have potential applications in quantum information processing and molecular devices.

7.3 Electron Spin Resonance of $TiM_2N@C_{80}$ and $Sc_4C_2H@C_{80}$

The $TiSc_2N@I_h$-C_{80} and $TiY_2N@I_h$-C_{80} are two novel spin-active species. The $TiSc_2N@I_h$-C_{80} exhibits broad ESR signals in toluene solution with no splitting detected at temperatures ranging from 300 to 200 K [22]. With the decrease of the temperature the gradual increase of the signal intensity were observed. For $TiY_2N@I_h$-C_{80}, a similar broad signal with a *g*-factor of 1.9579 was detected at room temperature, and this signal becomes more intense and sharper with the decrease of the measurement temperature down to 200 K [23]. These ESR results show that the $TiSc_2N@I_h$-C_{80} and $TiY_2N@I_h$-C_{80} have relatively high anisotropy of the *g*-tensor, which may be caused by the embedded electron spin in Ti^{3+} ion.

Similarly, the $Sc_4C_2H@I_h$-$C_{80}$with open-shell electronic structure also has very broad EPR signal (about 500 G) below temperature of 60 K [24]. At room temperature, no obvious EPR line was observed for $Sc_4C_2H@I_h$-C_{80} solution. When the temperature was decreased down to 60 K, an obvious EPR line was detected. The absent hyperfine coupling splitting reveals Sc(3*d*)-based unpaired spin distributions. For $TiM_2N@I_h$-C_{80} and $Sc_4C_2H@I_h$-C_{80}, this type of EPR spectra can be ascribed to the significant anisotropy of the *g* tensor, which may be caused by the embedded electron spins in $Sc^{2+}(3d^1)$ for $Sc_4C_2H@I_h$-C_{80} and $Ti^{3+}(3d^1)$ for $TiM_2N@I_h$-C_{80}, respectively.

7.4 Electron Spin Resonance of $Y_2@C_{79}N$

Endohedral azafullerene $Y_2@C_{79}N$ has an open-shell electronic structure, where an unpaired electron resides on the endohedral Y_2 dimer. $Y_2@C_{79}N$ has an ESR spectrum with three groups of hyperfine signals coupled by the unpaired spin and two equivalent Y nuclei. At 298 K, the $Y_2@C_{79}N$ exhibits three groups of signals with a 1: 2: 1 intensity ratio and further analysis revealed the hfcc of 81.8 G (two nuclei) and a *g*-factor of 1.9700 [10].

The paramagnetic property of $Y_2@C_{79}N$ has been observed to be highly sensitive to the temperature. Briefly, under low temperature of 203 K, the intensity of ESR signals at higher magnetic field begins to increase, which can be ascribed to the paramagnetic anisotropy and insufficient averaging of the paramagnetic tensors (Fig. 7.4) [25]. This kind of temperature-dependent ESR property is similar to that of above-mentioned $Sc@C_{82}$ and such paramagnetic anisotropy implies that the two Y nuclei possess a restricted motion at low temperature. As the unpaired spin locates on the internal Y_2 cluster of $Y_2@C_{79}N$, consequently, insufficient rotational averaging in resonance structure occurs. The spin property of $Y_2@C_{79}N$ is also sensitive to the exohedral modification. $Y_2@C_{79}N$ fulleropyrrolidines exhibits different ESR spectra, where two sets of hfcc for Y_2 dimmer and paramagnetic anisotropy can be found.

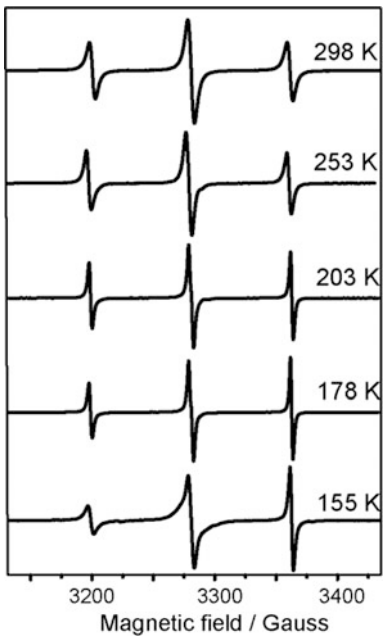

Fig. 7.4 The temperature-dependent ESR spectra of $Y_2@C_{79}N$. Reproduced from Ref. [24]

7.5 Conclusions

The electron spin resonances of metallofullerenes are helpful to disclose their geometry, electronic structures, and internal dynamic modes though analyzing the hyperfine couplings of their ESR spectra. For paramagnetic metallofullerenes, their varied properties and susceptible spin characters could be applied as molecular sensors and magnetic switch. In addition, novel molecular magnets can be designed based on these paramagnetic metallofullerenes due to their controllable spin property. It should be noted that the spin–spin interaction and spin coherence of paramagnetic metallofullerene should be further explored in order to extend their applications in quantum information progressing or memory devices.

Acknowledgements We thank the National Natural Science Foundation of China (51672281, 61227902). T. Wang particularly thanks the Youth Innovation Promotion Association of CAS.

References

1. Johnson RD, Devries MS, Salem J et al (1992) Electron-paramagnetic resonance studies of lanthanum-containing C_{82}. Nature 355(6357):239–240
2. Bethune DS, Johnson RD, Salem JR et al (1993) Atoms in carbon cages—the structure and properties of endohedral fullerenes. Nature 366(6451):123–128

3. Laasonen K, Andreoni W, Parrinello M (1992) Structural and electronic-properties of La@C_{82}. Science 258(5090):1916–1918
4. Kato T, Suzuki S, Kikuchi K et al (1993) ESR study of the electronic-structures of metallofullerenes—a Comparison between La@C_{82} and Sc@C_{82}. J Phys Chem 97 (51):13425–13428
5. Kikuchi K, Nakao Y, Suzuki S et al (1994) Characterization of the isolated Y@C_{82}. J Am Chem Soc 116(20):9367–9368
6. Shinohara H, Sato H, Ohkohchi M et al (1992) Encapsulation of a scandium trimer in C_{82}. Nature 357(6373):52–54
7. Shinohara H, Inakuma M, Hayashi N et al (1994) Spectroscopic properties of isolated Sc_3@C_{82} metallofullerene. J Phys Chem 98(35):8597–8599
8. Kato T, Bandou S, Inakuma M et al (1995) ESR study on structures and dynamics of Sc_3@C_{82}. J Phys Chem 99(3):856–858
9. Iiduka Y, Wakahara T, Nakahodo T et al (2005) Structural determination of metallofuIlerene Sc_3C_{82} revisited: a surprising finding. J Am Chem Soc 127(36):12500–12501
10. Zuo T, Xu L, Beavers CM et al (2008) M_2@C_{79}N (M = Y, Tb): isolation and characterization of stable endohedral metallofullerenes exhibiting M–M bonding interactions inside aza [80]fullerene cages. J Am Chem Soc 130(39):12992–12997
11. Shinohara H (2000) Endohedral metallofullerenes. Rep Prog Phys 63(6):843–892
12. Popov AA, Yang S, Dunsch L (2013) Endohedral fullerenes. Chem Rev 113(8):5989–6113
13. Shinohara H, Sato H, Saito Y et al (1992) Mass spectroscopic and ESR characterization of soluble yttrium-containing metallofullerenes YC_{82} and Y_2C_{82}. J Phys Chem 96(9):3571–3573
14. Inakuma M, Shinohara H (2000) Temperature-dependent EPR studies on isolated scandium metallofullerenes: Sc@C_{82}(I, II) and Sc@C_{84}. J Phys Chem B 104(32):7595–7599
15. Maeda Y, Matsunaga Y, Wakahara T et al (2004) Isolation and characterization of a carbene derivative of La@C_{82}. J Am Chem Soc 126(22):6858–6859
16. Hachiya M, Nikawa H, Mizorogi N et al (2012) Exceptional chemical properties of Sc@C_{2v}(9)-C_{82} probed with adamantylidene carbene. J Am Chem Soc 134(37):15550–15555
17. Hajjaj F, Tashiro K, Nikawa H et al (2011) Ferromagnetic spin coupling between endohedral metallofullerene La@C_{82} and a cyclodimeric copper porphyrin upon inclusion. J Am Chem Soc 133(24):9290–9292
18. Yannoni CS, Hoinkis M, Devries MS et al (1992) Scandium clusters in fullerene cages. Science 256(5060):1191–1192
19. Wang T, Wu J, Xu W et al (2010) Spin divergence induced by exohedral modification: ESR study of Sc_3C_2@C_{80} fulleropyrrolidine. Angew Chem-Int Edit Engl 49(10):1786–1789
20. Kurihara H, Iiduka Y, Rubin Y et al (2012) Unexpected formation of a Sc_3C_2@C_{80} bisfulleroid derivative. J Am Chem Soc 134(9):4092–4095
21. Wu B, Wang T, Feng Y et al (2015) Molecular magnetic switch for a metallofullerene. Nat Commun 6:6468
22. Yang S, Chen C, Popov A et al (2009) An endohedral titanium(III) in a clusterfullerene: putting a non-group-III metal nitride into the C_{80}-I_h fullerene cage. Chem Commun 6391–6393
23. Chen C, Liu F, Li S et al (2012) Titanium/yttrium mixed metal nitride clusterfullerene TiY_2N@C_{80}: synthesis, isolation, and effect of the group-III metal. Inorg Chem 51(5):3039–3045
24. Feng Y, Wang T, Wu J et al (2014) Electron-spin excitation by implanting hydrogen into metallofullerene: the synthesis and spectroscopic characterization of Sc_4C_2H@I_h-C_{80}. Chem Commun 50(81):12166–12168
25. Ma Y, Wang T, Wu J et al (2012) Susceptible electron spin adhering to an yttrium cluster inside an azafullerene $C_{79}N$. Chem Commun 48:11570–11572

Chapter 8
Electron Spin Resonance of Lanthanide EMFs

Tatsuhisa Kato

Abstract The chapter describes electron spin resonance (ESR) spectroscopic studies of lanthanide endohedral metallofullerenes. A summary of recent investigations of $La@C_{82}$, $La_2@C_{80}$, and their reduced anion and radical species is presented. Also discussed are ESR studies of lanthanide metallofullerene with high spin state, including $Eu@C_{74}$, $Eu@C_{82}$, $Gd@C_{82}$, and $Gd_2@C_{79}N$.

Fullerenes with metal(s) inside the hollow spherical carbon cages are called endohedral metallofullerenes (EMFs). On finding that fullerenes can persistently trap for atoms, researchers have been attracted by EMFs in terms of the possibilities for the free tuning of "outside chemistry" and of "inside confinement." An important question to ask is how the inside atom controls the outside chemistry of the fullerene cage, or how the topology and size of the outside cage regulate the electronic structure and dynamics of the metal(s) confined inside. Electron spin resonance (ESR) and nuclear magnetic resonance (NMR) spectroscopy were used for the investigation of EMFs initially, and they have been the most powerful methods of examining these. Compared to other methods, for example X-ray diffraction measurements, magnetic resonance spectroscopy offers a less direct method for structural determination, the ESR and NMR techniques nevertheless have advantages in the investigation of highly diluted materials. Observations across a wide temperature range are practicable, which makes it possible to probe the binding potential and to test the influence of solvents. As a result, these approaches can give information not only on the molecular tumbling motion in solution but also on the intra-molecular dynamics. Furthermore, it is possible to reduce the target fullerene using chemical or electrochemical methods in solution,

T. Kato (✉)
Institute for Liberal Arts and Sciences Kyoto University,
Yoshida-Nihonmatsu, Sakyoku, Kyoto 606-8501, Japan
e-mail: kato.tatsuhisa.6e@kyoto-u.ac.jp

A.A. Popov (ed.), *Endohedral Fullerenes: Electron Transfer and Spin*,
Nanostructure Science and Technology, DOI 10.1007/978-3-319-47049-8_8

which permits the charge redistribution under the condition of electron excess to be probed. In addition to the doublet spin state ($S = 1/2$) encased in the carbon cage of lanthanum (La) EMFs, the high spin states ($S > 1/2$) were observed for europium (Eu) and gadolinium (Gd) EMFs, depending on the surrounding carbon cage. In this review, I present a summary of recent investigations of $La@C_{82}$, $La_2@C_{80}$, and their reduced anion and radical species, and $Eu@C_{74}$, $Eu@C_{82}$, $Gd@C_{82}$, and $Gd_2@C_{79}N$.

8.1 $La@C_{82}$ Metallofullerenes

Since trace amounts of EMFs were first identified in 1991 [1], two scientific questions were raised, first whether ions were localized at a specific binding site and then second what amount of charge was transferred from the encapsulated metal ion to the cage. At an early stage in ESR spectroscopic measurements of the major isomer of $La@C_{82}$ ($La@C_{82}$-I), an answer to the latter question became clear as the data enabled the features of the electronic structure to be decoded. The ESR spectrum recorded at room temperature in CS_2 solution is shown in the upper most spectrum of Fig. 8.1. The surprisingly small isotropic hyperfine interaction (HFI) of the encapsulated La ion observed in $La@C_{82}$-I was taken as evidence for a complete charge transfer of metal valence electrons to the cage. As a result, the electronic structure of $La@C_{82}$-I was described as $La^{3+}@C_{82}^{3-}$. When the La is encapsulated inside C_{82}, three electrons transfer to the π orbital of the C_{82} cage, and a single electron is located on outer most shell of the molecule [2]. The former question, relating to the localization, was solved in the investigation of ESR line width and the ESR ^{13}C satellite lines of $La@C_{82}$-I. Considering that clear ^{13}C HFI could be observed over a wide temperature range, it was concluded that the ion is rigidly attached to the inner surface of the carbon cage. If any additional internal hopping of the ion over a different attachment site occurs, the ^{13}C HFI would be drastically influenced, and thus the ^{13}C hyperfine coupling constants (HFCC) would be modified. As a result, the widths of these ^{13}C satellites would drastically differ from those of the main components. The ESR spectrum of the $La@C_{82}$-I did not show the situation mentioned above, and then it could be concluded that no significant change occurs with respect to the binding site of the encapsulated La ion.

The progress made in isolating and the purifying EMFs by the high-performance liquid chromatography (HPLC) method expanded the investigation of the characterization of physical and chemical properties. All species of $La@C_n$ with even number n from 76 to 90 were detected as pure materials, and full separation of topological isomers of each $La@C_n$ component was attained by 2-stage HPLC separation with chlorobenzene eluent [3]. Isotropic HFCCs and g-values observed in ESR spectra of $La@C_n$ can be used for the convenient identification of the various compounds. For instance, La encapsulated in C_n cages of different topologies and sizes from those of the major isomer of $La@C_{82}$-I was observed.

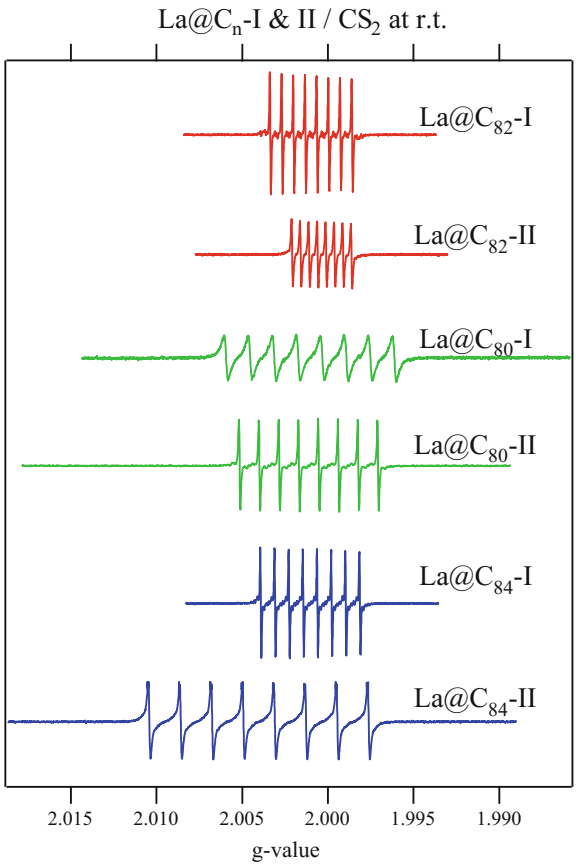

Fig. 8.1 ESR spectra of La@C_n in CS_2 solution recorded at 298 K

The spectra of La@C_n with even number n = 80–84 are shown in Fig. 8.1, with comparing their different topological isomers. However, the cage symmetry of each La@C_n has not been known except La@C_{82}-I and La@C_{82}-II, whose symmetries were determined by NMR measurements of their anion forms, as mentioned later. Nevertheless, all La@C_ns exhibited very small HFI, that is, their electronic structure can be described as $La^{3+}@C_n^{3-}$.

On the other hand line widths varied with carbon cage. For example, La@C_{80}-I and La@C_{84}-II exhibited much broader line widths, and a clear ^{13}C HFI structure was not observed. Clearly, the binding potential depends on fullerene topology and size. If the ESR spectra are observed with changing temperature, the correlation time as well as the variance of the time-modulated interactions can be deduced. It is in principle possible to distinguish between internal hopping of the ion and tumbling motions of the whole molecule with the ion rigidly attached to its position. A detailed analysis was performed [4], showing fluctuations of the electric field at the La site in combination with electron–nuclear dipole–dipole interaction.

8.2 La@C_{82} Metallofullerene Anion

NMR and ESR measurements have an advantage in the study of dilute solution compounds that can be reduced by chemical or electrochemical methods. Making full use of this possibility, the cage symmetries of La@C_{82}-I and La@C_{82}-II were determined by NMR observations of their anion form. The cage symmetry of C_{2v} was confirmed for La@C_{82}-I [5] and C_s for La@C_{82}-II [6]. By utilizing the high stability and diamagnetic nature of anion forms of EMF, ^{13}C NMR measurements became a useful method for structural determination of paramagnetic EMFs. It has also been reported that the mapping of the bond connectivity in the carbon cage of La@C_{82}-I and definitive assignment of ^{13}C NMR lines were accomplished by the 2D INADEQUATE (incredible natural abundance double quantum transfer experiment) NMR measurements [7].

8.3 La_2@C_{80} Metallofullerene

La_2@C_{80} was first reported in 1991 [8] and was subsequently found in relatively high abundance in 1995 [9]. However, an empty I_h-C_{80} fullerene without encapsulated La_2 ions has never been reported. Presumably, the empty I_h-C_{80} cage is unstable because of its open-shell electronic configuration. According to theoretical calculations [10], the I_h-C_{80} structure is stabilized by the six-electron transfer from the encapsulated La ions to the fourfold degenerate HOMO of C_{80}, suggesting an electronic structure described as $(La^{3+})_2@C_{80}^{6-}$. This theoretical explanation was confirmed by MEM/Rietveld analysis [11].

Other than C_{60}, C_{80} offers a special carbon cage in which to realize encapsulation with the highest symmetry I_h. As an example, diamagnetic La_2@C_{80} was studied by NMR in solution [12] and by MEM/Rietveld analysis of high-resolution X-ray powder diffraction data [11]. The ^{13}C and ^{139}La NMR measurements indicated that the encapsulated La_2 was not restricted to any specific binding site, thus preserving the I_h symmetry in a time average sense as seen by ^{13}C nuclei of the cage and ^{139}La inside the cage [12]. The ^{139}La NMR exhibited a single line and ^{13}C NMR showed two lines ascribed to I_h-C_{80}, indicating that the two La ions are equivalent inside the C_{80} cage, that they are confined inside the I_h cage, and that they rotate rapidly.

The MEM/Rietveld analysis clarified a novel form of confinement of La ions inside the I_h cage [11]. The MEM charge density of La atoms forms a pentagonal dodecahedron in the carbon cage preserving the I_h symmetry of the molecule. The La distribution can be considered as the average over both space and time domains, which is consistent with the NMR data. A theoretical investigation of the energetics and frequency analysis of La_2@C_{80} concluded that the D_{3d} structure is the most stable among the three (D_{2h}, D_{5d}, D_{3d}) configurations as shown in Fig. 8.4 [13]. It can be presumed that the two La ions are kept apart on the C_3 axis and hop rapidly

between pairs of apexes of the pentagonal dodecahedron, drawing out a dodecahedral trajectory in the I_h-C_{80} cage.

8.4 $La_2@C_{80}$ Metallofullerene Anion

If $La_2@C_{80}$ could be reduced by chemical or electrochemical methods, ESR measurement of reduced $La_2@C_{80}$ could be used to probe the charge redistribution in the condition of electron excess. The anion ground electric state could either be represented as $La_2^{6+}@C_{80}^{7-}$ or as $La_2^{5+}@C_{80}^{6-}$, resulting in drastic change of the La HFI. In the case of $La_2^{6+}@C_{80}^{7-}$, the small spin density on the La nuclei would give a small HFI equal to that of $La@C_{82}$, whereas $La_2^{5+}@C_{80}^{6-}$ would give a large La HFI, because of the additional spin density on La 5d or 6s orbitals. A convenient method of investigating the possible spin redistribution under reduction is therefore to probe the isotropic HFI constant of the ion.

As shown in Fig. 8.2, the $La_2@C_{80}$ anion obtained by electrochemistry exhibited ESR spectra at 180, 140, and 80 K. The spectra were spread over wide magnetic field strengths from 0 to 7000 Gauss and characterized by very large HFI. It was found that the additional electron occupied La 5d or 6s valence orbitals, and penetrated the C_{80} cage into La_2 ions. This could be called "in cage reduction." In addition, the spectra were drastically changed with decreasing temperature. It can be assumed that tumbling rotation as well as internal hopping among binding sites of La ions gave some averaging effect on the spectra with changing temperature.

The $La_2@C_{80}$ anion can be described as a spin system consisting of $S = 1/2$ coupled with two equivalent $I = 7/2$ nuclei, whose ESR spectrum can be depicted with the 15 equidistant lines by the first-order perturbation treatment in solution. However, the spectrum of the $La_2@C_{80}$ anion observed at 180 K in solution was completely different from that expected within this scheme. There are two reasons

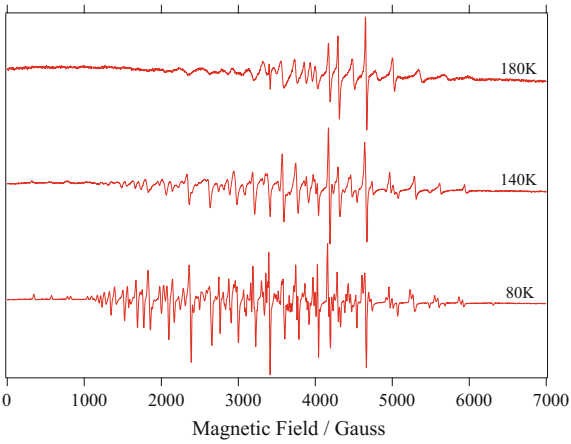

Fig. 8.2 ESR spectra of $La_2@C_{80}$ anion radical in CS_2 solution recorded at 80 K (frozen solution), 140 K (frozen solution), 180 K (solution)

for the large discrepancy: first, the inapplicability of the first-order perturbation treatment to this system because of the large La HFI. Second, there are substantial anisotropic components within the La HFI and g-tensor.

Computer simulation using the full diagonalization of the spin Hamiltonian was applied to the system. The simulation well reproduced the spectrum observed at various temperatures of 80, 140, and 180 K, as shown in Fig. 8.3. For the simulation of the frozen solution at 80 K, as shown in Fig. 8.3a, the parameters of an orthorhombic tensor, g tensor (g_x, g_y, g_z) = (1.839, 1.972, 1.835) and ^{139}La HFI tensor (A_x, A_y, A_z) = (306.5, 419.0, 311.0) Gauss, were used. The spectrum observed in frozen solution was changed with increasing temperature at 140 K, and well reproduced by the parameters of tetragonal tensors, ($g_{x=y}$, g_z) = (1.972, 1.835) and ^{139}La HFI tensor ($A_{x=y}$, A_z) = (416.0, 315.0) Gauss, as shown in Fig. 8.3b. After the solution was melted at 180 K, the isotropic parameters, g_{iso} = 1.882 and A_{iso} = 345.5/Gauss, were used for the simulation, as shown in Fig. 8.3c. The spectrum in frozen solution was changed from orthorhombic (trimetric) to tetragonal (axially symmetric) with increasing temperature. Although the magnetic field-dependent line width of the spectrum broadened the line of some transitions beyond detectability in solution at 180 K above the melting point of the solvent, the equally spaced hyperfine structures at magnetic field over 5000 Gauss never fitted the simulation unless the isotropic parameters of g_{iso} = 1.882 and A_{iso} = 345.5 Gauss were used. It was also noticeable that the two La nuclei were observed to be identical across the full range of temperature, from 4 to 298 K.

On inserting a lanthanum dimer into the I_h-C_{80} cage, I_h symmetry is reduced as shown in Fig. 8.4. For example, if the lanthanum dimer is put onto the C_2 axis of the I_h structure, the symmetry is reduced to D_{2h}. Other D_{3d} and D_{5d} symmetries are also generated in a similar way; putting a lanthanum dimer on the C_3 and C_5 axes gives D_{3d} and D_{5d} symmetries, respectively. A theoretical investigation [13] for the neutral $La_2@C_{80}$ predicted that the D_{3d} structure is the most stable among the three configurations. On the other hand it can be considered from the ESR results that the most stable configuration of the $La_2@C_{80}$ anion is D_{2h}. The ESR observations at lower temperature gave a trimetric spectrum, not an axial symmetric one, indicating that the configuration of the ground state was altered from D_{3d} to D_{2h} symmetry in the condition of electron excess.

Within the I_h-C_{80} carbon network, a C_3 axis runs through the crossing point of three adjacent hexagons, a C_2 axis through the center of the hexagon, and a C_5 through the center of the pentagon, as shown in Fig. 8.4. The I_h-C_{80} structure has fifteen equivalent C_2 axes. This means that there are fifteen equivalent wells for the D_{2h} configuration on the three-dimensional potential energy surface of the I_h-C_{80} structure. The I_h-C_{80} structure has ten C_3 axes surrounded by three neighboring C_2 axes, and six C_5 axes surrounded by five neighboring C_2 axes. At lower temperature the lanthanum dimer is restricted to one potential well among fifteen equivalent D_{2h} configurations. On increasing the temperature to above 80 K, internal hopping occurs among neighboring equivalent D_{2h} wells, which are located around the D_{3d} or C_{5d} configuration. Then thermally activated hopping results in an ESR observation of the time-averaged axially symmetric spectrum at 140 K.

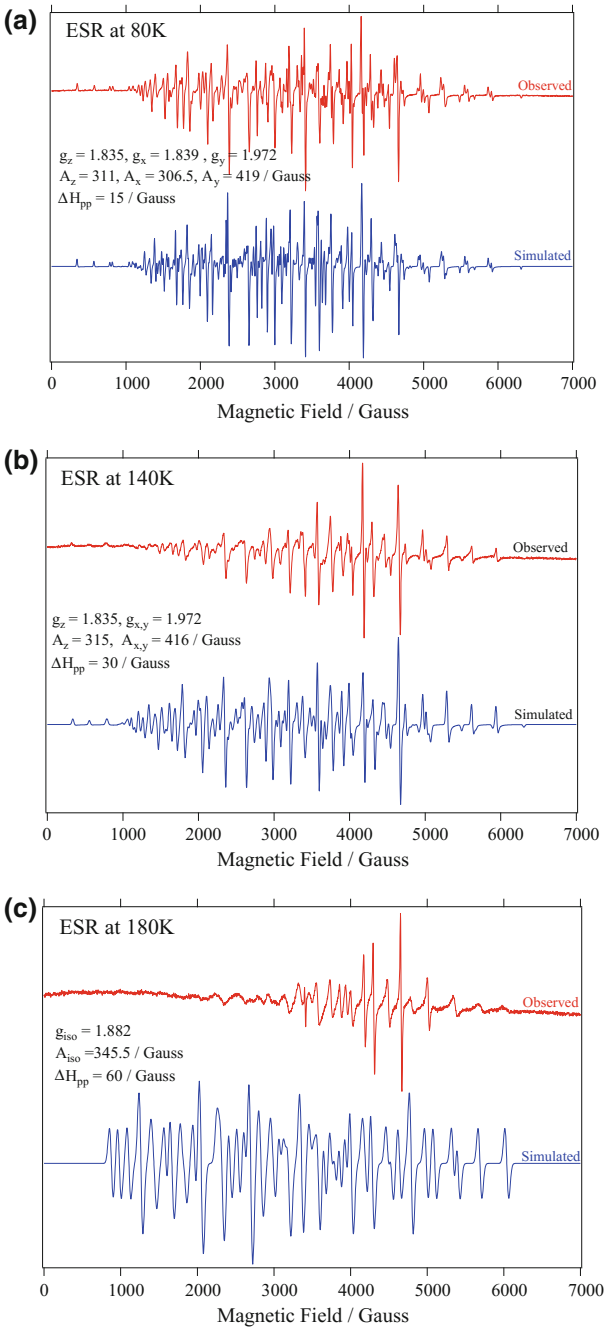

Fig. 8.3 Observed and simulated spectra of $La_2@C_{80}$ anion radical. **a** recorded at 80 K, **b** at 140 K, **c** at 180 K. The upper spectrum is observed one, the lower is simulated one using the parameters in each figure

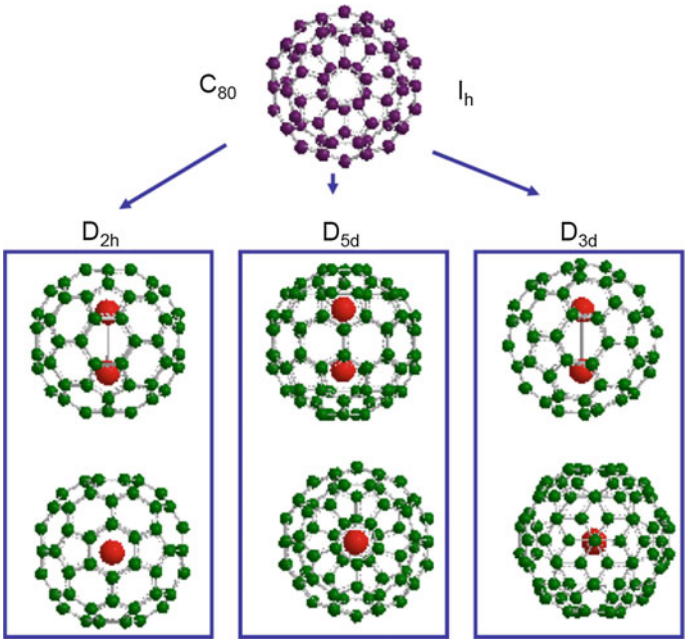

Fig. 8.4 Symmetry diagram of I_h-C_{80} cage

8.5 $La_2@C_{80}$ Radical Produced by Radical Addition

Fullerene radicals can be generated by the addition of a free radical to the fullerene surface. However, these fullerene radicals are usually very reactive and generally cannot be isolated. In contrast, $La_2@C_{80}$ reacts with 3-chloro-5,6-diphenyltriazine resulting in mono-addition of the triazinyl radical to the fullerene cages to yield a stable fullerene radical, $La_2@C_{80}$-$C_3N_3Ph_2$ [14]. The unusual stability of this radical arises from the confinement of the unpaired electron to an internal metal cluster, and it is the same situation as the $La_2@C_{80}$ anion. Accordingly, the fullerene cage protects the radical center from other reactive species.

The paramagnetic character of the resulting $La_2@C_{80}$-$C_3N_3Ph_2$ radical was confirmed by ESR measurement. As shown in Fig. 8.5, the ESR signal of $La_2@C_{80}$-$C_3N_3Ph_2$ resembles that of the $La_2@C_{80}$ anion radical. In this context, the electronic structure can be described as $(La_2)^{5+}(I_h\text{-}C_{80}\text{–}C_3N_3Ph_2)^{6-}$. The unpaired electron, formed by the radical coupling process, is not distributed on the carbon cage but is confined to the internal, La–La σ-bonding orbital. The spectrum observed in solution at 298 K was well reproduced by the simulation using the parameters: $S = 1/2$, $g = 1.899$, $A(La_1) = A(La_2) = 359$ Gauss. The simulation reveals two important observations: first, that a large spin density is associated with each La atom; and second, that each La atom has the same spin density. Although the two La atoms are found at inequivalent sites in the X-ray structure, the rotation

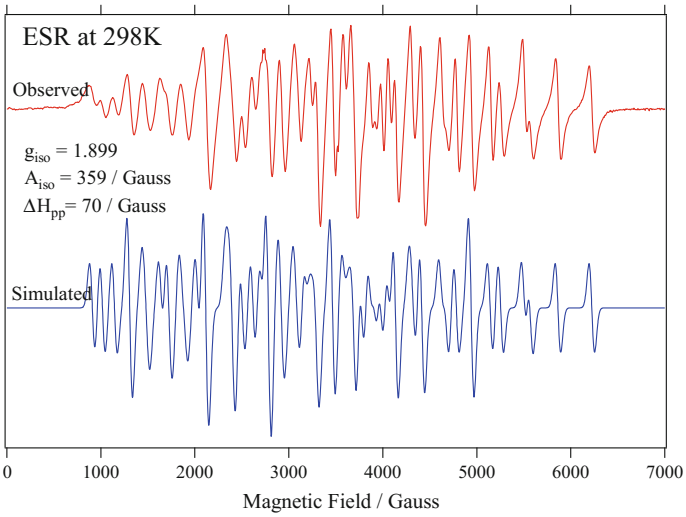

Fig. 8.5 ESR spectrum of $La_2@I_h$-C_{80} radical produced with 3-chloro-5,6-diphenyltriazine recorded at 298 K. The upper spectrum is the observed one, the lower is simulated using the parameters in the figure

of the La ions within the cage can readily average out the spin density during the timescale of ESR spectroscopy. The spectrum of the $La_2@C_{80}$-$C_3N_3Ph_2$ radical was a similar case to that of the $La_2@C_{80}$ anion at 180 K. The equally spaced hyperfine structure at the higher magnetic field only fits the simulation when the isotropic parameters of $A(La_1) = A(La_2) = 359$ Gauss are used. Although the ESR spectrum observed in solution was similar to that of the $La_2@C_{80}$ anion, a measurement gave a big contrast at lower temperature. Once the solution was frozen at lower temperature, the spectrum of the $La_2@C_{80}$-$C_3N_3Ph_2$ radical could not be observed significantly above the noise. This can be explained by the inequivalent status of the two La nuclei as shown in the X-ray measurements. ESR parameters of these two different La nuclei differ from each other, and thus the ESR peaks were split into fine lines, and their intensities were distributed over a wide range of magnetic field strength.

8.6 Lanthanide Metallofullerene with High Spin State

The other example in which the fullerene cage tunes the properties of the endohedral metal ion(s) is presented here. The relationship between the spin state and the carbon cage structure was investigated for a family of europium (Eu) EMFs, $Eu@C_{74}$ and three topological isomers of $Eu@C_{82}$. When an Eu is encapsulated in the carbon cage of $C_{74,}$ or $C_{82,}$ two electrons are transferred from the Eu atom to the

C_{74} cage, or C_{82} cage, giving the electronic state of $Eu^{2+}@C_{74}^{2-}$, or $Eu^{2+}@C_{82}^{2-}$. The encased Eu^{2+} ion has a half-filled 4f orbital, resulting in an $S = 7/2$ ground state with vanishing orbital angular moment. The spin state of the $S = 7/2$ ground state is characterized by zero-field splitting (ZFS) parameters. A combined use of a high-field ESR (W-band) spectrometer and a conventional (X-band) spectrometer was employed to determine the ZFS parameters. The $Eu@C_{74}$ and three topological isomers of $Eu@C_{82}$ exhibited characteristic spectra depending on the carbon cage structures. The observed ESR spectra were completely reproduced by computer simulations based on a spin Hamiltonian considering the ZFS term up to the forth order, as shown in Fig. 8.6 [15]. The spin Hamiltonian parameters were determined

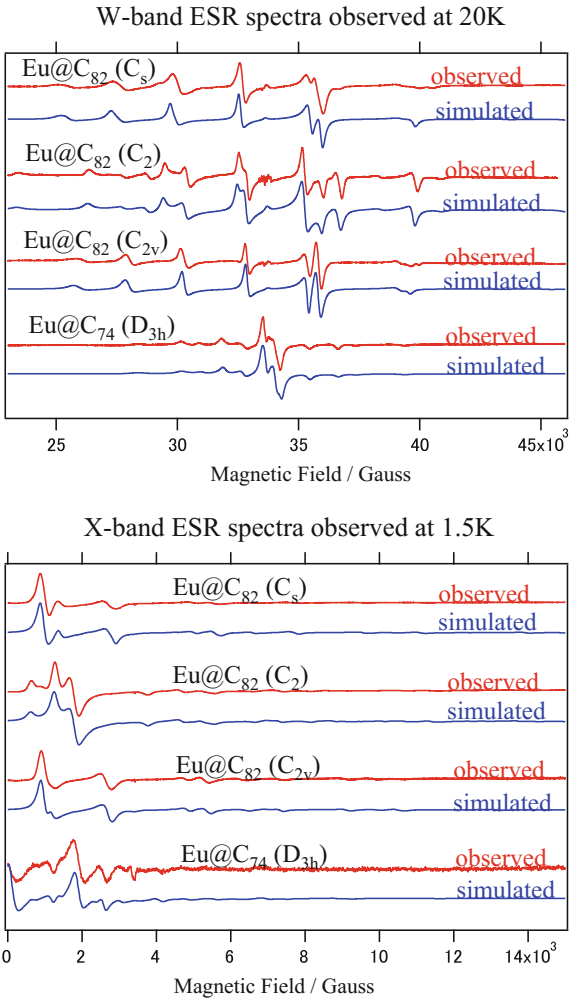

Fig. 8.6 W-band and X-band ESR spectra of $Eu@C_{82}$ (C_s), $Eu@C_{82}$ (C_2), $Eu@C_{82}$ (C_{2v}), and $Eu@C_{74}$ (D_{3h}). W-band spectra were recorded at 20 K, X-band spectra were recorded at 1.5 K. The observed spectra are lined with *red*, the simulated ones are lined with *blue*

for Eu@C_{74}, whose carbon cage symmetry is D_{3h}, and three isomers of Eu@C_{82}, having the symmetry of C_s, C_2, and C_{2v}, respectively. The spin parameters are closely related to the surrounding cage structure.

The spin state of the major isomer of Gd@C_{82} was also determined by the combination of the W-band and X-band ESR spectrometers. The ground spin state of Gd@C_{82} was characterized by an integer spin quantum number of $S = 3$. The charge transfer from the Gd atom to the C_{82} cage also characterized the electronic state of Gd@C_{82}; however, the spin state exhibited a peculiar situation. The electronic configuration of the Gd atom is [Xe] $6s^2$ $4f^7$ $5d^1$, and that the three electrons on the outer 6s and 5d orbitals are transferred to the π^* orbital of the C_{82} cage. As a result, a radical spin is formed on the C_{82} cage, playing an important role in the spin state with respect to the magnetic interaction with the $S = 7/2$ spin of Gd^{3+} ion. The total angular momentum, $S_{tot.}$, of Gd@C_{82} is given by the coupling between the radical spin ($S = 1/2$) on the C_{82} cage and the $S = 7/2$ spin on the Gd^{3+}, resulting in $S_{tot.}$=3 and $S_{tot.} = 4$ produced by the antiferromagnetic and ferromagnetic coupling, respectively. The W-band ESR spectra of Gd@C_{82} were reproduced by the $S_{tot.} = 3$ simulation spectrum combined with $S_{tot.} = 4$, as shown in Fig. 8.7. And it was concluded that the $S = 1/2$ spin on the π orbital of the C_{82} cage was coupled with the octet $S = 7/2$ spin of the Gd^{3+} ion in an antiferromagnetic manner with $J = -1.8\ cm^{-1}$ [16].

On the other hand, the ground spin state of Gd_2@$C_{79}N$ was confirmed to be assigned to a half-integer spin quantum number of $S = 15/2$ using W-band and X-band ESR measurements. The W-band measurement gave a symmetric spectrum around the intense central line as shown in the upper spectrum of Fig. 8.8. Seven peaks on both sides of the central line at equidistant intervals were observed, and a total of 15 peaks can be counted, suggesting the spin quantum number of 15/2. The

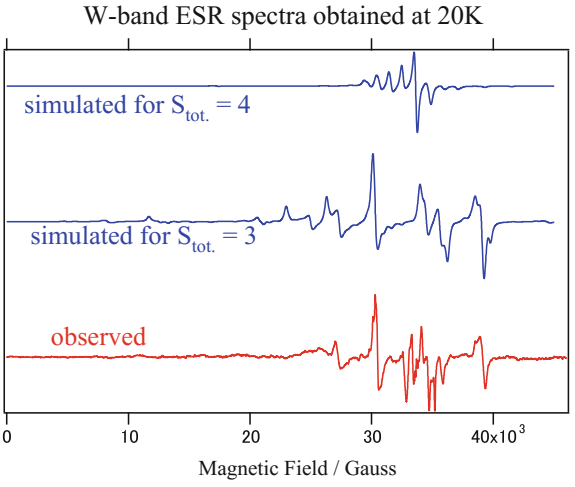

Fig. 8.7 W-band ESR spectra of the major isomer of Gd@C_{82} recorded at 20 K. The observed spectra are lined with *red*, the simulated ones are lined with *blue*, the upper most spectrum for $S_{tot.} = 4$ and the middle spectrum for $S_{tot.} = 3$

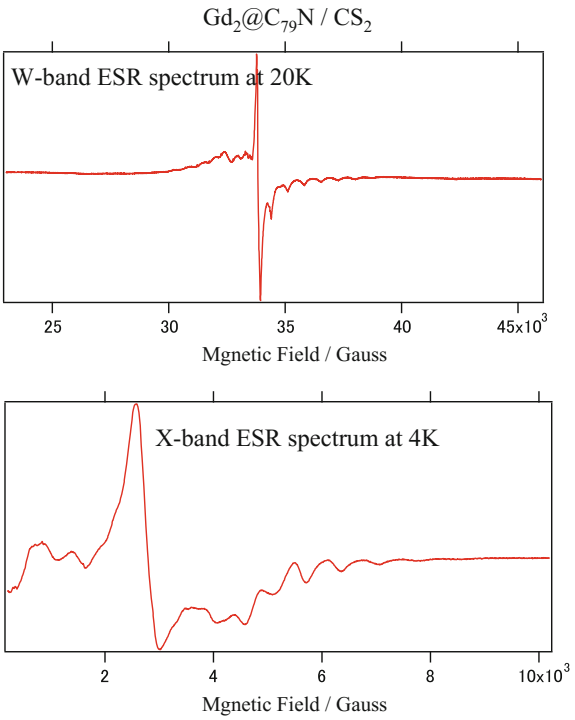

Fig. 8.8 W-band and X-band ESR spectra of $Gd_2@C_{79}N$. The W-band spectrum was recorded at 20 K, the X-band one was recorded at 4 K

$S = 1/2$ spin on the N atom of the fullerene cage and two octet $S = 7/2$ spins of two encapsulated Gds are coupled in a ferromagnetic manner with small ZFS parameters. The central line of $Gd_2@C_{79}N$ is due to the Kramer's doublet with half-integer spin quantum number of $S = 15/2$, resulting in the prominent sharp line and the weak anisotropic nature. And it was noticeable that the central ESR line was observed even at room temperature in solution in contrast with most Gd^{3+} ion environments [17].

8.7 Concluding Remarks

The results of investigations into the free tuning of "outside chemistry" and "inside confinement" have been presented for the cases of the lanthanum EMFs ($La@C_{82}$, $La_2@C_{80}$, and their reduced anion and radical species) and the EMFs with the high spin state ($Eu@C_{74}$, $Eu@C_{82}$, $Gd@C_{82}$, and $Gd_2@C_{79}N$). Some possible answers were given to the questions of how the inside atom controls the outside chemistry of the fullerene cage, and how the topology and the size of the outside cage regulate the electronic structure and dynamics of the metal(s) inside.

References

1. Chai Y, Guo T, Lin C, Haufler R, Chibante LPF, Fure J, Wang L, Alford JM, Smalley RJE (1991) Fullerenes with metals inside. J Phys Chem 95:7564–7568
2. Johnson RD, de Vries MS, Salem JR, Bthune DS, Yannoni CS (1992) Electron paramagnetic resonance studies of lanthanum-containing C_{82}. Nature 355:239–240
3. Ohkubo S, Kato T, Inakuma M, Shinohara H (2001) Separation and characterization of ESR-active lanthanum endohedral fullerenes. New Diamond Front Carbon Technol 11 (4):285–294
4. Ohkubo S, Kato T (2002) ESR parameters of series of La@C_n isomers. Appl Magn Reson 23:481–493
5. Akasaka T, Wakahara T, Nagase S, Kobayashi K, Wälchli M, Yamamoto K, Kondo M, Shirakura S, Okubo S, Maeda Y, Kato T, Kako M, Nakadaira Y, Nagahata R, Gao X, Van Caemelbecke E, Kadish KM (2000) La@C_{82} anion, an unusually stable metallofullerene. J Am Chem Soc 122:9316–9317
6. Akasaka T, Wakahara T, Nagase S, Kobayashi K, Wälchli M, Yamamoto K, Kondo M, Shirakura S, Maeda Y, Kato T, Kako M, Nakadaira Y, Gao X, Van Caemelbecke E, Kadish KM (2001) Structure determination of the La@C_{82} isomer. J Phys Chem B 105: 2971–2974
7. Tsuchiya T, Wakahara T, Maeda Y, Akasaka T, Wälchli M, Kato T, Okubo H, Mizorogi N, Kobayashi K, Nagase S (2005) 2D NMR characterization of the La@C_{82} anion. Angew Chem Int Ed 44:3282–3285
8. Alvarez MM, Gillan EG, Holezer K, Kaner RB, Min KS, Whetten RL (1991) La_2C_{80}: a soluble dimetallofullerene. J Phys Chem 95:10561–10563
9. Suzuki T, Maruyama Y, Kato T, Kikuchi K, Nakao Y, Ahiba Y, Kobayashi K, Nagase S (1995) Electrochemistry and Ab intio study of the dimetallofullerene La_2@C_{80}. Anew Chem Int Ed 34(10):1094–1096
10. Kobayashi K, Nagase S, Akasaka K (1995) A theoretical study of C_{80} and La_2@C_{80}. Chem Phys Lett 245:230–236
11. Nishibori E, Takata M, Sakata M, Taninaka A, Shinohara H (2001) Pentagonal-dodecahedral La_2 charge density in [80-I_h] fullerene: La_2@C_{80}. Angew Chem Int Ed 40(16):2998–2999
12. Akasaka T, Nagase S, Kobayashi K, Wälchli M, Yamamoto K, Funasaka H, Kako M, Hoshino T, Erata T (1997) ^{13}C and ^{139}La NMR studies of La_2@C_{80}: first evidence for circular motion of metal atoms in endohedral dimetallofullerenes. Angew Chem Int Ed 36(15): 1643–1645
13. Shimotani H, Ito T, Iwasa Y, Taninaka A, Shinohara H, Nishibori E, Takata M, Sakata M (2004) Quantum Chemical Study on the Configurations of Encapsulated Metal Ions and the Molecular Vibration Modes in Endohedral Dimetallofullerene La_2@C_{80}. J Am Chem Soc 126:364–369
14. Yamada M, Kurihara H, Suzuki M, Saito M, Slanina Z, Uhlik F, Aizawa T, Kato T, Olmstead MM, Balch AL, Maeda Y, Nagase S, Lu X, Akasaka T (2015) Hiding and recovering electrons in a dimetallic endohedral fullerene: air-stable products from radical additions. J Am Chem Soc 137:232–238
15. Matsuoka H, Ozawa N, Kodama T, Nishikawa H, Ikemoto I, Kikuchi K, Furukawa K, Sato K, Shiomi D, Takui T, Kato T (2004) Multifrequency EPR study of metallofullerenes: Eu@C_{82} and Eu@C_{74}. J Phys Chem B 108:13972–13976
16. Furukawa K, Okubo S, Kato H, Shinohara H, Kato T (2003) High-field/ high-frequency ESR study of Gd@C_{82}-I. J Phys Chem A 107:10933–10937
17. Fu W, Zhang J, Fuhrer T, Champion H, Furukawa K, Kato T, Mahaney EJ, Burke GB, Williams AK, Walker K, Dixon C, Ge J, Shu C, Harich K, Dorn CH (2011) Gd_2@C_{79}N: isolation, charaterization, and monoadduct formation of a very stable heterofullerene with a magnetic spin state of S = 15/2. J Am Chem Soc 133:9741–9750

Chapter 9
Ion Radicals of Endohedral Metallofullerenes Studied by EPR Spectroscopy

Alexey A. Popov

Abstract This chapter describes EPR spectroscopic studies of the charged states of dimetallofullerenes, carbide clusterfullerenes, nitride clusterfullerenes, and their derivatives, as well as oxide clusterfullerene $Sc_4O_2@C_{80}$ and cyano-clusterfullerene $Sc_3CN@C_{80}$. Spin density distribution in the cation and anion radicals resemble HOMO and LUMO of the neutral molecules. Therefore, EPR spectroscopic studies of the ion radicals of endohedral metallofullerenes provide important information on the electronic structure of pristine molecule. The size of the metal-based hyperfine coupling constants in the ion radicals reveals the extent at which the spin density is localized on the endohedral species or on the fullerene cage. Besides, EPR spectra of ion radicals can provide information on the internal dynamics of the cluster. In particular, freezing rotation of the Sc_3N cluster in the derivative of $Sc_3N@C_{80}$ is revealed via EPR spectra of their anion radicals.

9.1 Introduction

To be eligible for EPR spectroscopic studies, endohedral metallofullerenes (EMFs) should be paramagnetic. Therefore, the EMFs studied by EPR spectroscopy can be classified into two groups: (i) EMFs, which are paramagnetic in their pristine states, and (ii) diamagnetic EMFs, which are transformed into paramagnetic forms via either chemical or electrochemical redox reactions. The first group was already discussed in Chaps. 7 and 8, whereas here we will focus on the ion radicals of EMFs.

Electrochemical studies of endohedral metallofullerenes (EMFs) described in detail in Chap. 2 showed that EMFs can exhibit two different mechanisms of redox processes: fullerene-based reduction or oxidation or a cluster-based process. The second type (dubbed as *endohedral electron transfer*) is particular interesting as it

A.A. Popov (✉)
Leibniz Institute for Solid State and Materials Research,
Helmholtzstraße 20, 01069 Dresden, Germany
e-mail: a.popov@ifw-dresden.de

A.A. Popov (ed.), *Endohedral Fullerenes: Electron Transfer and Spin*,
Nanostructure Science and Technology, DOI 10.1007/978-3-319-47049-8_9

can create unusual spin and valence states of endohedral metal clusters. As the spin density distribution in the cation and anion radicals resemble HOMO and LUMO of the neutral molecule, EPR spectroscopic studies of the ion radicals provide important information on the electronic structure of pristine EMFs. Localization of the spin density on endohedral species can be revealed via large metal-based hyperfine coupling (hfc) constants, and hence EPR studies provide a direct spectroscopic evidence of the endohedral (*in cavea*) or fullerene-based mechanism of the electron transfer. Stable radicals have been successfully generated by chemical or electrochemical electron transfer reactions for several types of EMFs, including dimetallofullerenes, carbide clusterfullerenes, nitride clusterfullerenes and their derivatives, as well as oxide clusterfullerene $Sc_4O_2@C_{80}$ and cyano-clusterfullerene $Sc_3CN@C_{80}$.

9.2 Dimetallofullerenes and Carbide Clusterfullerenes

As discussed in Chap. 2, HOMO or LUMO of dimetallofullerenes (di-EMFs) formed by trivalent lanthanides is the metal–metal bonding orbital. Hence, single-electron reduction or oxidation of such di-EMFs can give radical ions with metal-metal bonding single-occupied MO (SOMO). When metals are Sc, Y, or La, the nature of the corresponding ion radical can be verified by EPR spectroscopy via analysis of the hyperfine structure. It has been already discussed in Chap. 8 that reaction of $La_2@C_{80}$, which has metal-based LUMO, with potassium in THF results in the anion radical with rich hyperfine structure originating from the huge $a(^{139}La)$ coupling constant. This proves that the La–La bonding MO is the LUMO in the pristine $La_2@C_{80}$ and this orbital is populated by a single electron in the anion [1]. Similar ESR spectra were reported for the electrochemically generated anions of pyrrolidine adducts of $La_2@C_{80}$ [2].

In 2013, Wang et al. [3] reported EPR spectroscopic study of the radical anion of $Y_2@C_{82}$-C_s(6) generated by the reduction of the EMF by metallic potassium in THF. The spectrum exhibited a hyperfine structure produced by two equivalent Y atoms with the $a(^{89}Y)$ constant of 34.3 G (Fig. 9.1a). DFT calculations showed that in contrast to carbide clusterfullerene with the same carbon cage (see below), the spin density in the radical anion of $Y_2@C_{82}^-$ is primarily localized between two Y atoms, and hence the *hfc* constant is almost two order of magnitude larger than in $Y_2C_2@C_{82}^-$. This finding is rather confusing because DFT calculations of the pristine molecule predict that it has Y–Y bonding HOMO, not the LUMO. Presumably, Y–Y bonding orbital in $Y_2@C_{82}$ is mixing well with the cage-based MOs, hence giving large contribution both to the HOMO and LUMO of the molecule.

Electrochemical studies and DFT calculations of $Sc_2@C_{82}$-C_{3v}(8) revealed that the HOMO of the molecule is Sc–Sc bonding MO, and hence large spin density on Sc ions can be expected in the cation radical [4, 5]. Indeed, EPR study of the cation formed via oxidation of $Sc_2@C_{82}$ by tris(4-bromophenyl) aminium

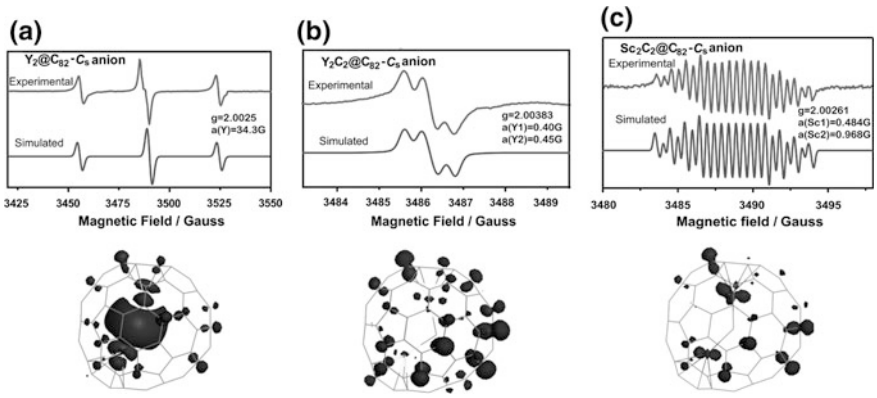

Fig. 9.1 Experimental and simulated EPR spectra (*top row*) and spin density distribution (*bottom row*) of anion radicals $Y_2@C_{82}^-$ (**a**), $Y_2C_2@C_{82}^-$ (**b**), and $Sc_2C_2@C_{82}^-$ (**c**). Reproduced with permission from [3]

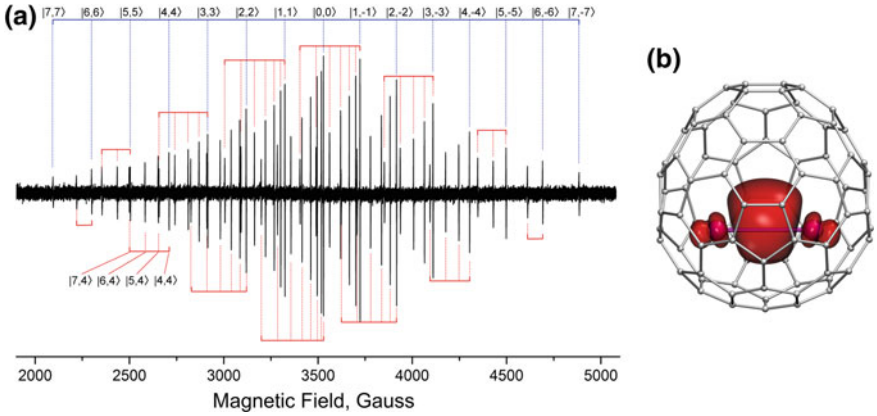

Fig. 9.2 **a** EPR of the cation radical $Sc_2@C_{82}^+$. Assignment of the peaks to $|I,m_I>$ states is shown in *blue* and *red lines*. *Blue lines* denote the state with $I = |m_I|$, *red lines* show groups with identical m_I values and $I \geq |m_I|$. **b** Spin density distribution in $Sc_2@C_{82}^+$

hexachloroantimonate revealed a complex hyperfine structure spanning the range of 2800 G (Fig. 9.2a), whereas DFT calculation predicted localization of spin density between two Sc atoms (Fig. 9.2b).

The complex spectral pattern observed for the molecule having only two equivalent Sc ions requires a more detailed explanation. Sc has nuclear spin $I = 7/2$, and the "dimer" with equivalent Sc atoms has a total spin of $I = I_1 + I_2$, which spans integer values form 0 to 7. In the first order of perturbation theory, position of resonance lines in EPR spectrum is dependent only on the projection of the total momentum, m_I:

$$B = B_0 - am_I, \tag{9.1}$$

where B is the field of the resonance signal, and a is a hyperfine coupling constant. In this situation, the Sc_2 dimer is expected to have 15 resonances in the EPR spectrum corresponding to $m_I = 0, \pm 1, \ldots \pm 7$. However, experimental spectrum of $Sc_2@C_{82}^+$ shown in Fig. 9.2a is more complex and has as many as 64 lines. The reason for the splitting of resonances is that it is necessary to consider higher terms of the perturbation theory expansion when the *hfc* constant is large. Already in the second order, resonance positions are determined not only by m_I but also by the total momentum I itself:

$$B = B_0 - am_I - \frac{a^2}{2B_0}[I(I+1) - m_I^2] + \ldots \tag{9.2}$$

As a result, up to 64 lines can be expected in the spectrum of the Sc dimer when hyperfine constant a is sufficiently large, as it happens in $Sc_2@C_{82}^+$. Figure 9.2a shows assignment of all observed lines and indicates positions expected in the first order (blue lines) and their splitting in the higher orders of perturbation theory according to different values (red lines). Despite the complex hyperfine pattern, position of all peaks can be well reproduced with a single $a(^{45}Sc)$ value of 199.2 G and a g-factor of 1.994. The $a(^{45}Sc)$ constant in $Sc_2@C_{82}^+$ is the largest among all Sc-based EMF radicals and is one of the largest among all Sc-based radicals in general. As the measurements were performed in solution at room temperature, the constant is isotropic and can be used to estimate the contribution of s-atomic orbitals of Sc to the spin density (and hence to the Sc–Sc bonding orbital). ScO radical with $a(^{45}Sc)$ value of 630 G is known to be pure Sc-4 s^1 system [6]. Taking it as a reference, the contribution of Sc atomic s-orbitals to the spin density is determined as 32%, in reasonable agreement with the shape and orbital composition of the spin density calculated by DFT (Fig. 9.2b).

Carbide clusterfullerenes $M_2C_2@C_{82}$, at least those with the C_{82} cage, might be seen as close relatives of dimetallofullerenes $M_2@C_{82}$ due to the same charge transfer between the cluster and the cage. However, the internal structure of the cluster is changed dramatically by introduction of the C_2 unit. Metal–metal bonding MO is not present any more, and cluster-based orbitals are often shifted away from the frontier MO levels, resulting in the large contribution of the fullerene cage to the spin density in ion radicals.

Carbide clusterfullerene $Sc_3C_2@C_{80}$-I_h(7) is well known for its paramagnetism (see Chap. 7), but majority of carbide clusterfullerenes is represented by diamagnetic compounds of $M_2C_2@C_{2n}$ composition (Chap. 1). Anion radicals of three of them, $Sc_2C_2@C_{72}$-C_s(10528), $Sc_2C_2@C_{82}$-C_s(6), and $Y_2C_2@C_{82}$-C_s(6), have been generated in solution by reaction with potassium in THF and then studied by EPR spectroscopy. $Sc_2C_2@C_{72}$ has two equivalent Sc ions, and the EPR spectrum of its anion radical has 15 equidistant lines with the hyperfine constant of 0.77 G (Fig. 9.3) [7]. In contrast to the $Sc_2@C_{82}^+$ discussed above, spin density in the

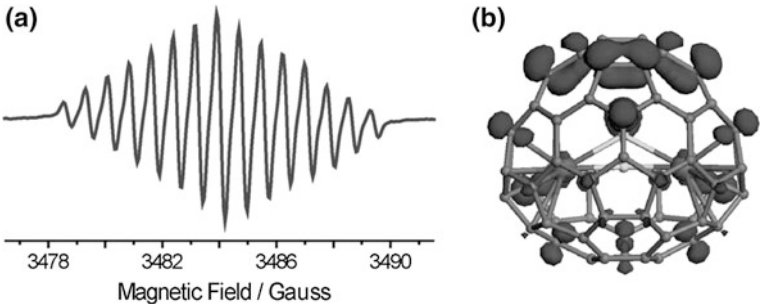

Fig. 9.3 **a** EPR spectrum of the anion radical $Sc_2C_2@C_{72}^-$. **b** Spin density distribution in $Sc_2C_2@C_{72}^-$. Reproduced with permission from [7]

$Sc_2C_2@C_{72}^-$ is predominantly localized on the carbon cage, hence the small $a(^{45}Sc)$ and the absence of second-order effects in the hyperfine structure. Radical anions of $M_2C_2@C_{82}$-$C_s(6)$ (M = Sc, Y) exhibited a more complex hyperfine structure with nonequivalent metal atoms (Fig. 9.1), showing that the M_2C_2 cluster is not rotating inside the $C_s(6)$ cage at room temperature [3]. Small hfc values ($a(^{45}Sc)$ = 0.48, 0.97; $a(^{89}Y)$ = 0.40, 0.45) agree with DFT calculations predicting that the spin density in these anion radicals is mainly localized on the carbon cage (Fig. 9.1). Note that for another isomer of $Sc_2C_2@C_{82}$, with $C_{3v}(8)$ cage, DFT predicts a cluster-localized LUMO (see Fig. 2.5 in Chap. 2), but corresponding anion radical has not been studied yet.

9.3 Nitride Clusterfullerenes and Their Derivatives

Nitride clusterfullerenes (NCFs) have rich electrochemistry, but majority of compounds show irreversible reduction in cyclic voltammetry, indicating that anion radicals undergo a follow-up processes (presumably a dimerization [8], see Chap. 2). Only two non-derivatized NCFs studied so far, $Sc_3N@C_{80}$ and $Sc_3N@C_{68}$, produced anion radicals with measurable EPR spectra. Although oxidation of NCFs seems to be more reversible, EPR spectrum of the cation radical could be obtained only for $Sc_3N@C_{68}$ [9].

Weak coupling of an unpaired electron to nuclear spins of three equivalent Sc atoms produces a first-order hyperfine structure with 22 lines. Electrochemical oxidation of $Sc_3N@C_{68}$ with in situ measurement of the EPR spectra gave a 22-line spectrum with the $a(^{45}Sc)$ constant of 1.28 G (Fig. 9.4a) [9]. The value is rather small and indicates that the spin density is localized on the cage with only a small contribution from Sc atoms (Fig. 9.4b). Electrochemical generation of the anion radical in identical condition gave a spectrum with a similar hyperfine pattern and $a(^{45}Sc)$ value of 1.75 G (Fig. 9.4c), but intensity of the peaks was an order of magnitude lower than that for the cation radical [10]. Substantial decrease of the

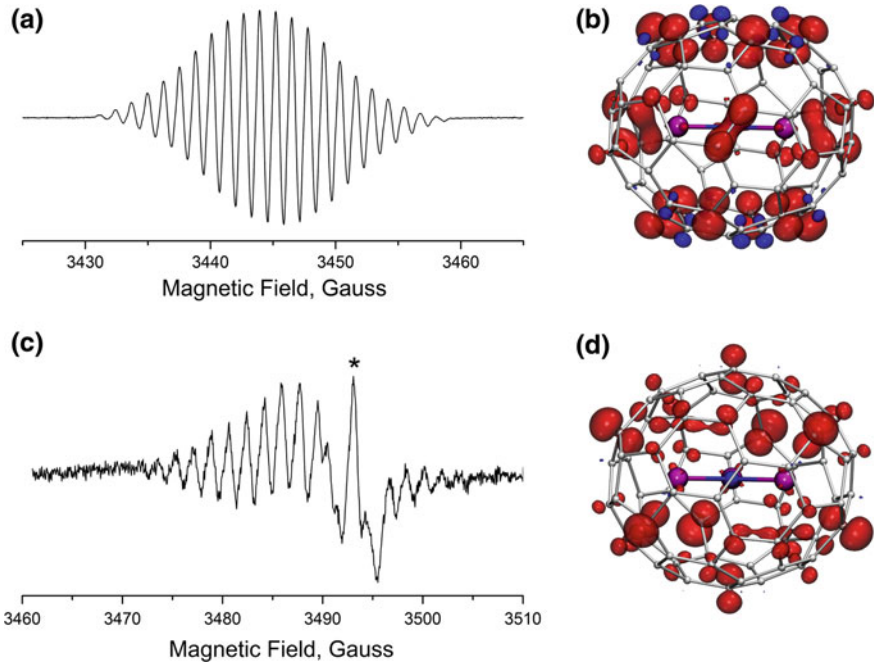

Fig. 9.4 **a** EPR spectrum of the cation radical $Sc_3N@C_{68}^+$. **b** Spin density distribution in $Sc_3N@C_{68}^+$. **c** EPR spectrum of the anion radical $Sc_3N@C_{68}^-$. **d** Spin density distribution in $Sc_3N@C_{68}^-$. Reproduced with permission from [10]

EPR intensity for the anion radical was explained by the possible dimerization of the anion radical.

Anion radical of $Sc_3N@C_{80}^-$ was obtained by reaction with potassium in THF [11], by electrolysis [12], or by reduction with cobaltocene [13]. Despite pronounced tendency to dimerize [8], the anon radical still afforded well-resolved EPR spectra (Fig. 9.5a). The pattern of 22 lines is well distinguishable, but the spectrum has additional features due to the second-order effects caused by a large $a(^{45}Sc)$ value of 55.6 G. Due to the large hfc value, the spectrum spans the range of ca 1100 G. DFT calculations prove that the spin density in the anion radical is predominantly localized on Sc atoms (Fig. 9.5b). Both computational and experimental studies showed that in the highly isotropic environment of the icosahedral I_h-symmetric carbon cage, the Sc_3N cluster rotates almost freely on the nanosecond timescale [14–17], and the free rotation of the cluster is presumably preserved in the anionic state [18].

EPR spectroscopy confirms that anion radicals of $Sc_3N@C_{68}$ and $Sc_3N@C_{80}$ are formed in the result of the cage-based and the cluster-based reduction processes, respectively. In the former, the LUMO is localized on the fullerene cage, whereas in the latter it is mostly localized on the cluster. Spin density distribution in anion

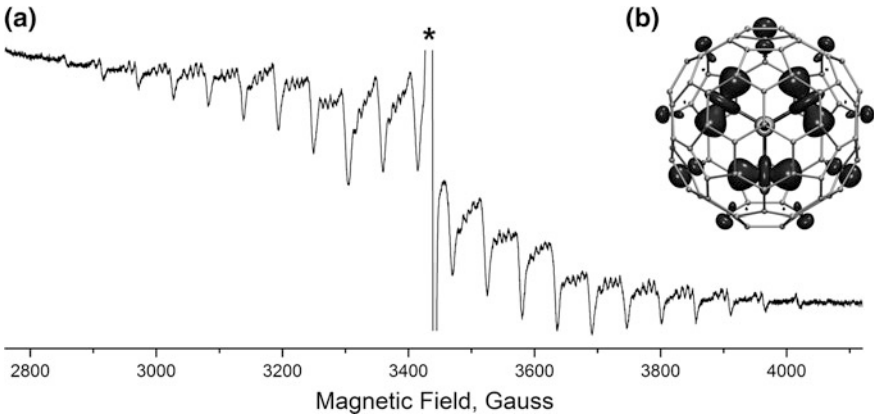

Fig. 9.5 **a** EPR spectrum of anion radical $Sc_3N@C_{80}^-$ obtained by reaction of $Sc_3N@C_{80}$ with cobaltocene in *o*-dichlorobenzene solution; adapted from [13]. **b** Spin density distribution in the lowest energy conformer of $Sc_3N@C_{80}^-$

Table 9.1 ^{45}Sc hyperfine coupling constants in the ion radicals of Sc-based nitride clusterfullerenes

Compound	Charge	$a(^{45}Sc)$, G	g-factor	References
$Sc_3N@C_{68}$	+1	3 × 1.28	2.0010	[9]
$Sc_3N@C_{68}$	−1	3 × 1.75	2.0032	[10]
$Sc_3N@C_{80}$	−1	3 × 55.6	1.9992	[11]
[5,6]-pyrrolidino	−1	9.6, 2 × 33.4	1.9972	[19]
[5,6]-benzo	−1	9.1, 2 × 33.3	1.9982	[21]
[6,6]-benzyl	−1	~0.6, 2 × 47.9	1.9971	[21]
$Sc_3N@C_{80}(CF_3)_2$	−1	2 × 9.34, 10.7	1.9958	[13]
$Sc_3N@C_{80}(CF_3)_2$	−3	2 × 10.8, 49.2	2.0006	[13]
$Sc_3N@C_{80}(CF_3)_{10}$	−1	~0.6, 11.1, 21.5	2.0009	[22]
$Sc_3N@C_{80}(CF_3)_{12}$	−1	~0.6, 7.4, 8.1	2.0023	[22]

radicals resembles LUMOs of these molecules, which can be clearly seen from the values of the hyperfine coupling constants.

The extended π-systems of fullerenes are subject to exohedral modifications via cycloadditions or radical additions (e.g., of CF_3 groups). Chemical functionalization of the carbon cages typically changes the fullerene π-system (since some sp^2 carbon atoms change their hybridization state to sp^3) and thus affects the frontier MO energies and electrochemistry. The decrease of the symmetry of the π-system in the derivative also makes the endohedral environment less isotropic than in the pristine $Sc_3N@C_{80}$-I_h molecule. Therefore, even small modifications of the π-system can affect the dynamics and electronic properties of the endohedral cluster. EPR spectra of the anion can be used to clarify how derivatization affects LUMO distribution and internal dynamic of the cluster (Table 9.1).

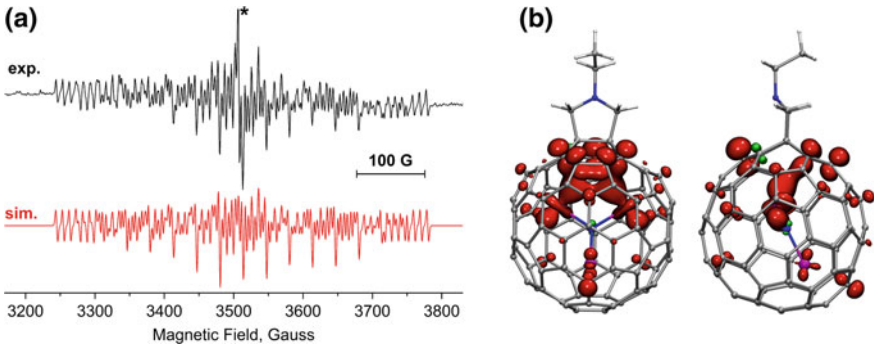

Fig. 9.6 **a** Experimental (exp.) and simulated (sim.) EPR spectra of the anion radical of the [5,6] $Sc_3N@C_{80}$-pyrrolidino cycloadduct. **b** Spin density distribution in the anion radical. Reproduced with permission from [19]

Assuming that the cluster rotates freely and rapidly, $Sc_3N@C_{80}$-I_h exhibits only two types of C–C bonds, denoted as [5,6] and [6,6], i.e., pentagon/hexagon and hexagon/hexagon edges. Cycloadditions across [5,6]-bonds are usually thermodynamically preferred. Pyrrolidino adduct of $Sc_3N@C_{80}$ is a typical example of [5,6]-cycloadduct. The compound exhibits reversible reduction behavior and hence affords a stable anion [19]. Figure 9.6a shows the EPR spectrum of the anion radical obtained by reduction of [5,6]-pyrrolidino $Sc_3N@C_{80}$ with potassium in THF solution. The spectrum is extended over 535 G and has complex hyperfine pattern, which can be well reproduced by considering two equivalent Sc atoms with $a(^{45}Sc)$ constants of 33.4 G and one Sc with the hfc constant of 9.6 G. Extended DFT calculations showed that cycloaddition indeed hinders rotation of the cluster inside the functionalized fullerene, especially in the anionic state. In the lowest energy conformer, two Sc atoms are coordinated to the fullerene near the cycloadduct, whereas the third atom is facing the opposite site of the cage. In agreement with experimental results, calculations also showed that the Sc atoms located near the cycloaddition site have larger *hfc* values and spin population than the third atom (Fig. 9.6b).

Unlike many other cycloaddition reactions to $Sc_3N@C_{80}$ favoring either [5,6]-closed or [6,6]-open adducts, the benzyne addition to $Sc_3N@C_{80}$ affords both [5,6] and [6,6]-closed monocycloadducts [20]. Electrochemical studies of the [5,6] and [6,6]-benzo-cycloadducts of $Sc_3N@C_{80}$ showed that both addition modes stabilize the LUMO and shift the first reduction potential from −1.26 V (versus the $Fe(Cp)_2^{+/0}$ redox couple) in pristine $Sc_3N@C_{80}$ to −1.11 V for the [5,6]-adduct and to −1.08 V for the [6,6]-adduct. Reversible reduction behavior of the adducts in electrochemical studies shows that their anion radicals are fairly stable at room temperature in solution. Figure 9.7 shows the EPR spectra of the isomeric anion radicals obtained by reaction of the cycloadducts with cobaltocene [21]. Both compounds exhibit Sc-based hyperfine structure extended over more than 500 G. Despite very similar molecular structures, the ^{45}Sc hyperfine patterns of the two

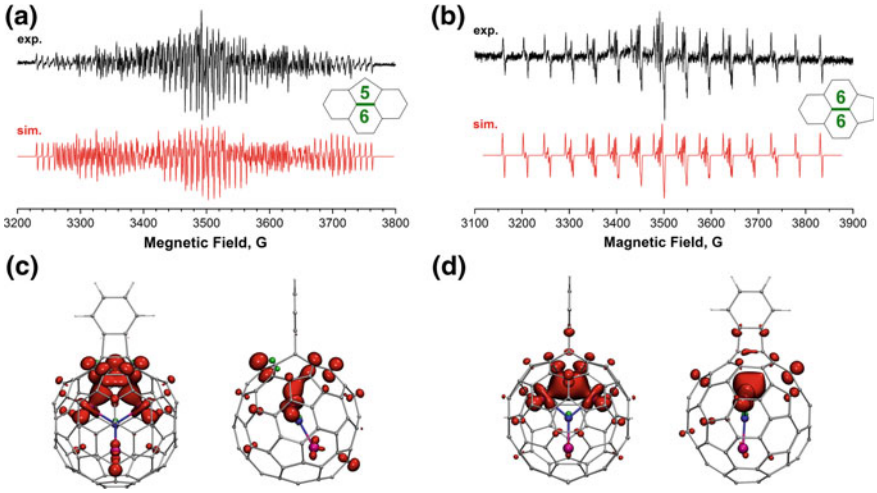

Fig. 9.7 (**a**,**b**) Experimental (exp.) and simulated (sim.) EPR spectra of anion radicals of [5,6] (**a**) and [6,6] (**b**) $Sc_3N@C_{80}$-benzoadducts; *thick green lines* in the *insets* show cycloaddition sites ([5,6] and [6,6] C–C bonds). (**c**,**d**) Spin density distribution in anion radicals of [5,6] (**c**) and [6,6] (**d**) $Sc_3N@C_{80}$-benzoadducts; each molecule is shown in two projections. Reproduced with permission from [21]

isomers are remarkably different. In the [5,6]-benzoadduct, one Sc has hfcc of 9.1 G, and two others and equivalent with the $a(^{45}Sc)$ constant of 33.3 G. This spectrum is very similar to that of the [5,6]-pyrrolidino adduct discussed above. The hyperfine structure for the anion radical of the [6,6]-isomer is simpler and corresponds to the coupling of the unpaired electron spin to two equivalent Sc nuclei with $a(^{45}Sc)$ values of 47.9 G. The *hfc* constant of the third Sc atom was estimated as 0.6 G, but could not be precisely determined because it is smaller than the line width of 1.3 G. Large *hfc* values point to the predominant localization of the spin density on the Sc_3N cluster similar to the pristine $Sc_3N@C_{80}$, but cycloadducts have inhomogeneous spin density distribution between the Sc atoms, indicating that the cluster rotation is frozen, at least on the EPR timescale.

DFT calculations revealed that in the anionic state each cycloadduct has one preferable orientation of the endohedral cluster shown in Fig. 9.7 together with the spin density distribution. For both structures, calculations show that two Sc atoms coordinate fullerene cage near the cycloadduct; those Sc atoms have large hfc constant. The third Sc atom is located at the opposite site of the fullerene cage and has small spin population. The net spin populations for [5,6] and [6,6]-benzoadducts are 0.51 and 0.64, respectively, which is smaller than 0.80 predicted for the anion radical of $Sc_3N@C_{80}$ at the same level of theory.

Radical addition of CF_3 groups to $Sc_3N@C_{80}$ affords a series of $Sc_3N@C_{80}(CF_3)_x$ derivatives with x ranging from 2 to 16. For three of them,

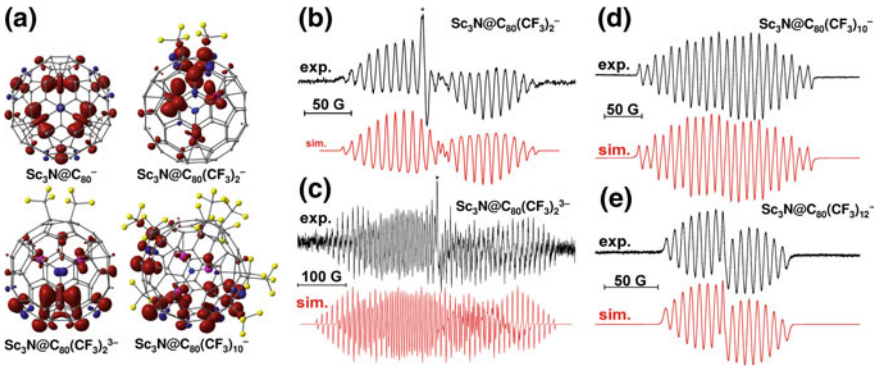

Fig. 9.8 **a** Spin density distribution in anion radicals $Sc_3N@C_{80}^-$, $Sc_3N@C_{80}(CF_3)_2^-$, $Sc_3N@C_{80}(CF_3)_2^{3-}$, and $Sc_3N@C_{80}(CF_3)_{10}^-$. **b–e**) Experimental (exp.) and simulated (sim.) EPR spectra of $Sc_3N@C_{80}(CF_3)_2^-$ (**b**), $Sc_3N@C_{80}(CF_3)_2^{3-}$ (**c**), $Sc_3N@C_{80}(CF_3)_{10}^-$ (**d**), and $Sc_3N@C_{80}(CF_3)_{12}^-$ (**e**). Reproduced with permission from [23]

$Sc_3N@C_{80}(CF_3)_2$, $Sc_3N@C_{80}(CF_3)_{10}$, and $Sc_3N@C_{80}(CF_3)_{12}$, ion radicals could be obtained in solution and studied by EPR spectroscopy. In cyclic voltammetry study $Sc_3N@C_{80}(CF_3)_2$ exhibits two single-electron oxidation and three single-electron reduction steps, all reversible at low scan rates. High stability of the charge states of $Sc_3N@C_{80}(CF_3)_2$ in solution enabled in situ ESR spectroscopic characterization of the electrochemically generated cation, anion, and trianion radicals; stable anion radical was also obtained chemically by reaction with cobaltocene [13]. Unlike the cation radical, which shows only a single-line EPR spectrum with ^{13}C satellites, anion and trianion exhibited a rich ^{45}Sc hyperfine structure in their EPR spectra with $a(^{45}Sc)$ values of 2 × 9.34, and 10.7 G in $Sc_3N@C_{80}(CF_3)_2^-$, and 2 × 10.8, and 49.2 G in $Sc_3N@C_{80}(CF_3)_2^{3-}$ (Fig. 9.8). The $a(^{45}Sc)$ values show that exohedral addition of two CF_3 groups to $Sc_3N@C_{80}$ hinders the rotation of the Sc_3N cluster and mixes fullerene and cluster states in the frontier orbitals of the derivative so that the overall cluster contribution to the spin density is reduced. The cage contribution to the LUMO is further enhanced with the increase of the number of CF_3 groups as can be deduced from the hyperfine coupling constants of the radical anions $Sc_3N@C_{80}(CF_3)_{10}^-$ with $a(^{45}Sc)$ values 0.6, 11.1, 21.5 G, and $Sc_3N@C_{80}(CF_3)_{12}^-$ with $a(^{45}Sc)$ values 0.6, 7.4, and 8.1 G (Fig. 9.8) [22]. DFT calculations also show a gradual decrease of the net spin population of the Sc_3N cluster to 42% in $Sc_3N@C_{80}(CF_3)_2^-$, to 13% in $Sc_3N@C_{80}(CF_3)_{10}^-$, and 11% in $Sc_3N@C_{80}(CF_3)_{12}^-$ (Fig. 9.8).

Aside from $Sc_3N@C_{68}$, $Sc_3N@C_{80}$, and its derivatives, stable anion radicals suitable for the EPR spectroscopic study could be obtained for [5,6]-pyrrolidine cycloadduct $Y_3N@C_{80}(C_4H_9N)$. The pristine $Y_3N@C_{80}$ is reduced irreversibly and attempts to study its anion radical by EPR spectroscopy failed. However, [5,6]-cycloaddition resulted in the compound with reversible reduction behavior,

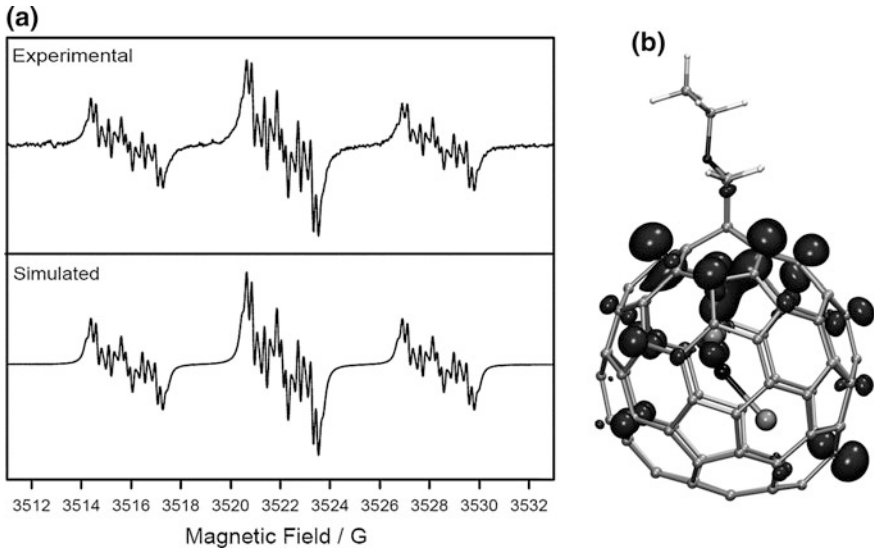

Fig. 9.9 **a** Experimental and simulated EPR spectra of the anion radical of [5,6]-$Y_3N@C_{80}(C_4H_9N)^-$; Reproduced with permission from [24]. **b** Spin density distribution in [5,6]-$Y_3N@C_{80}(C_4H_9N)^-$

and its anion radical could be obtained by reduction with potassium in THF [24]. EPR spectrum of $Y_3N@C_{80}(C_4H_9N)^-$ shown in Fig. 9.9 exhibits rich hyperfine structure assigned to Y atom with $a(^{89}Y)$ constants of 2×6.26, and 1.35 G. Besides, measurable hfc constants were detected for one nitrogen atom with $a(^{14}N) = 0.51$ G and two pairs of equivalent hydrogens with $a(^1H)$ values of 2×0.19 and 2×0.21 G. X-ray diffraction studies and DFT calculations show that similar to the Sc_3N adducts, two Y atoms with larger hfc values are coordinated close to the cycloaddition site. DFT computations have shown that the net spin population of the nitride cluster in $Y_3N@C_{80}(C_4H_9N)^-$ is 18% [25], which is smaller than for the Sc_3N cluster in an analogous adduct.

To summarize, EPR spectroscopic studies of anion radicals of NCF derivatives reveal an important information on the electronic structure and dynamics of the cluster in these molecules. In comparison to the freely moving Sc_3N cluster in the pristine $Sc_3N@C_{80}^-$, all derivatives exhibit fixed cluster positions, inhomogeneous spin density distributions, and large variations of the *hfc* values within the Sc_3N or Y_3N cluster. Exohedral derivatization significantly reduces the net spin population on the Sc atoms in the cluster, and this effect is markedly dependent on the regiochemistry of the adduct site on the fullerene cage. The high structural specificity of the ESR spectroscopic data makes it a valuable tool for the study of cluster structure and dynamics in EMF compounds and their derivatives.

9.4 Other Clusterfullerenes

Oxide clusterfullerene $Sc_4O_2@C_{80}$-I_h(7) has rather peculiar electronic structure with two pairs of Sc atoms in a different valence state. The atoms bonded to two oxygens have a formal state of Sc^{III}, whereas those bonded to only one oxygen have a formal state of Sc^{II} and form a Sc^{II}–Sc^{II} bond. Both HOMO and LUMO of the molecule were predicted to be localized on the endohedral cluster [26]. Reversible redox behavior of the compound in both cathodic and anodic ranges showed that cation and anion radicals were sufficiently stable and could be studied in situ by EPR spectroscopy during electrolysis in o-dichlorobenzene solution [27]. Complex hyperfine patterns of the radicals (Fig. 9.10) were simulated by considering two pairs of equivalent Sc atoms, albeit with substantially different hfc constants. The $a(^{45}Sc)$ values of 2 × 2.6 and 2 × 27.4 G in the anion, 2 × 150.4 and 2 × 19.0 G in the cation were assigned to Sc^{II} and Sc^{III} atoms, respectively, with the help of

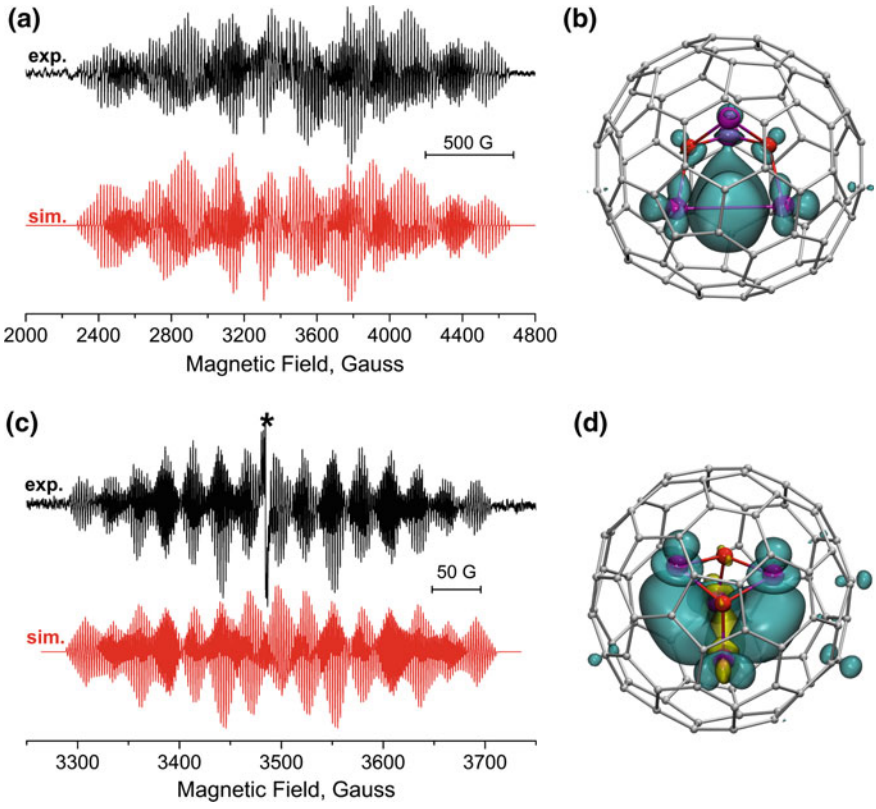

Fig. 9.10 **a** Experimental (exp.) and simulated (sim.) EPR spectra of cation radical $Sc_4O_2@C_{80}^+$; **b** Spin density distribution in $Sc_4O_2@C_{80}^+$; **c** Experimental (exp.) and simulated (sim.) EPR spectra of anion radical $Sc_4O_2@C_{80}^-$; **d** Spin density distribution in $Sc_4O_2@C_{80}^-$. Reproduced with permission from [26]

extended DFT calculations and molecular dynamics simulations. Spin density in both species is localized on the Sc_4O_2 cluster (Fig. 9.10b,d), leading to large *hfc* values and second-order features in the hyperfine structure. Particularly large *hfc* constant of the Sc^{II} atoms in the cation radical, 150.4 G, is explained by the Sc–Sc bonding nature of the HOMO in $Sc_4O_2@C_{80}$. This orbital resembles the HOMO of $Sc_2@C_{82}$, which also has large *hfc* value (199.2 G) in the cationic state (see above). Thus, EPR spectroscopy confirmed that $Sc_4O_2@C_{80}$ has redox-active endohedral cluster both in reduction and oxidation processes.

$Sc_3CN@C_{80}$-I_h is another clusterfullerene with stable anion radical. Electrochemical reduction potential of the compound is positively shifted versus the value expected for the cage-based process. Likewise, DFT calculation predicts cluster-based LUMO for $Sc_3CN@C_{80}$ indicating that the first reduction should be localized on the Sc_3CN cluster [28]. Reduction of $Sc_3CN@C_{80}$ with potassium produced an anion radical whose spectrum consisted of 36 lines (Fig. 9.11a). Simulation showed that the spectrum can be well fitted by the pair of equivalent Sc atoms with the $a(^{45}Sc)$ value of 3.89 G and the third Sc atom with the *hfc* constant of 1.95 G [29]. The hyperfine splitting due to the endohedral nitrogen could not be detected. Different values for Sc atoms indicate that the CN unit is not rotating inside the cluster on the ESR timescale (note that the compound also exhibits two peaks in the ^{45}Sc NMR). This is different from the situation in $Sc_3C_2@C_{80}$, in which C_2 unit is rotating at room temperature. DFT calculations predict that the spin density in the anion radical is mainly localized on the endohedral cluster (Fig. 9.11b).

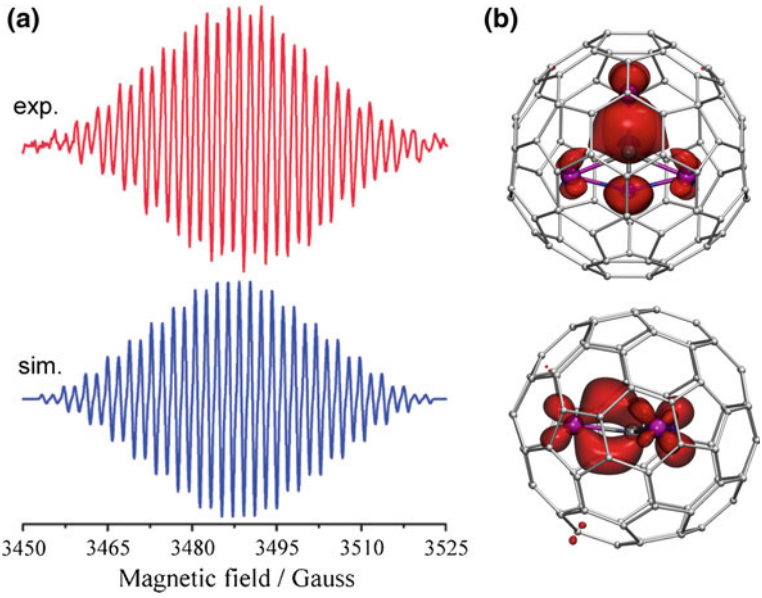

Fig. 9.11 **a** Experimental (exp.) and simulated (sim.) EPR spectra of the anion radical $Sc_3CN@C_{80}^-$; Reproduced with permission from [29]. **b** DFT-calculated spin density distribution in $Sc_3CN@C_{80}^-$; the molecule is shown in two projections

However, the $a(^{45}Sc)$ constants in $Sc_3CN@C_{80}^-$ are relatively small when compared to $Sc_3N@C_{80}^-$ which also has endohedrally localized spin density. The reason of such a deviation is in predominant localization of the spin density on the CN unit, rather than on Sc atoms as in the nitride clusterfullerene. Calculations also predict that the $a(^{45}Sc)$ constants are in fact negative and hence result from the large spin polarization on Sc centers. Remarkably, single-crystal X-ray diffraction applied for the structure elucidation of $Sc_3N@C_{80}$ could not distinguish C and N atoms in the CN group, and hence it is not clear which of the atoms adopts a central position in the cluster. Computations of *hfc* constants with C-centered and N-centered conformations of the anion radical showed that thermodynamically more stable C-centered conformation fits experimental data much better [29].

9.5 Concluding Remarks

EPR spectroscopy is found to be a particular convenient and informative spectroscopic technique for the study of the charged states of endohedral metallofullerenes. The hyperfine structure observed in the spectra of La-, Y-, and particular Sc-based EMFs provides a wealth of information on the electronic structure of the EMFs molecules and their internal dynamics. Metal–metal bonding in dimetallofullerenes and $Sc_4O_2@C_{80}$ is well presented in EPR spectra via huge coupling constants when single-occupied metal–metal bonding orbital is formed. Modulation of the size of the $a(^{45}Sc)$ constant in anion radicals of $Sc_3N@C_{80}$ by its chemical derivatization clearly shows how the LUMO is shifting from the cluster in the pristine molecule to the fullerene cage in the derivatives. Inhomogeneity of the fullerene π-system in the adducts also hinders rotation of the cluster, which lifts degeneracy of $a(^{45}Sc)$ *hfc* constants and leads to complex hyperfine patterns.

References

1. Kato T (2007) Metal dimer and trimer within spherical carbon cage. J Mol Struct 838(1–3): 84–88
2. Yamada M, Okamura M, Sato S et al (2009) Two regioisomers of endohedral pyrrolidinodimetallofullerenes $M_2@I_h$-$C_{80}(CH_2)_2NTrt$ (M = La, Ce; Trt = trityl): control of metal atom positions by addition positions. Chem-Eur J 15(40):10533–10542
3. Ma Y, Wang T, Wu J et al (2013) Electron spin manipulation via encaged cluster: differing anion radicals of $Y_2@C_{82}$-C_s, $Y_2C_2@C_{82}$-C_s, and $Sc_2C_2@C_{82}$-C_s. J Phys Chem Lett 4(3): 464–467
4. Kurihara H, Lu X, Iiduka Y et al (2012) $Sc_2@C_{3v}(8)$-C_{82} *vs.* $Sc_2C_2@C_{3v}(8)$-C_{82}: drastic effect of C_2 capture on the redox properties of scandium metallofullerenes. Chem Commun 48:1290–1292
5. Popov AA, Avdoshenko SM, Pendás AM et al (2012) Bonding between strongly repulsive metal atoms: an oxymoron made real in a confined space of endohedral metallofullerenes. Chem Commun 48:8031–8050

6. Weltner W, McLeod D, Kasai PH (1967) ESR and optical spectroscopy of ScO, YO, and LaO in neon and argon matrices; establishment of their ground electronic states. J Chem Phys 46(8):3172–3184
7. Feng Y, Wang T, Wu J et al (2013) Structural and electronic studies of metal carbide clusterfullerene $Sc_2C_2@C_s$-C_{72}. Nanoscale 5(15):6704–6707
8. Konarev DV, Zorina LV, Khasanov SS et al (2016) A crystalline anionic complex of scandium nitride endometallofullerene: experimental observation of single-bonded $(Sc_3N@I_h\text{-}C_{80}^{-})_2$ dimers. Chem Commun 52:10763–10766
9. Yang SF, Rapta P, Dunsch L (2007) The spin state of a charged non-IPR fullerene: the stable radical cation of $Sc_3N@C_{68}$. Chem Commun 2:189–191
10. Rapta P, Popov AA, Yang SF et al (2008) The charged states of $Sc_3N@C_{68}$: an in situ spectroelectrochemical study of the radical cation and radical anion of a non-IPR fullerene. J Phys Chem A 112:5858–5865
11. Jakes P, Dinse KP (2001) Chemically induced spin transfer to an encased molecular cluster: an EPR study of $Sc_3N@C_{80}$ radical anions. J Am Chem Soc 123(36):8854–8855
12. Elliott B, Yu L, Echegoyen L (2005) A simple isomeric separation of D_{5h} and I_h $Sc_3N@C_{80}$ by selective chemical oxidation. J Am Chem Soc 127(31):10885–10888
13. Popov AA, Shustova NB, Svitova AL et al (2010) Redox-tuning endohedral fullerene spin states: from the dication to the trianion radical of $Sc_3N@C_{80}(CF_3)_2$ in five reversible single-electron steps. Chem-Eur J 16(16):4721–4724
14. Popov AA, Chen C, Yang S et al (2010) Spin-flow vibrational spectroscopy of molecules with flexible spin density: electrochemistry, ESR, cluster and spin dynamics, and bonding in $TiSc_2N@C_{80}$. ACS Nano 4(8):4857–4871
15. Popov AA, Dunsch L (2008) Hindered cluster rotation and ^{45}Sc hyperfine splitting constant in distonoid anion radical $Sc_3N@C_{80}$, and spatial spin charge separation as a general principle for anions of endohedral fullerenes with metal-localized lowest unoccupied molecular orbitals. J Am Chem Soc 130(52):17726–17742
16. Stevenson S, Rice G, Glass T et al (1999) Small-bandgap endohedral metallofullerenes in high yield and purity. Nature 401(6748):55–57
17. Heine T, Vietze K, Seifert G (2004) ^{13}C NMR fingerprint characterizes long time-scale structure of $Sc_3N@C_{80}$ endohedral fullerene. Magn Reson Chem 42:S199–S201
18. Popov AA, Dunsch L (2011) Charge controlled changes in the cluster and spin dynamics of $Sc_3N@C_{80}(CF_3)_2$: the flexible spin density distribution and its impact on ESR spectra. Phys Chem Chem Phys 13(19):8977–8984
19. Elliott B, Pykhova AD, Rivera J et al (2013) Spin density and cluster dynamics in $Sc_3N@C_{80}^{-}$ upon [5, 6] exohedral functionalization: an ESR and DFT study. J Phys Chem C 117(5):2344–2348
20. Li F-F, Pinzon JR, Mercado BQ et al (2011) [2 + 2] cycloaddition reaction to $Sc_3N@I_h$-C_{80}. The formation of very stable [5,6]- and [6,6]-adducts. J Am Chem Soc 133(5):1563–1571
21. Popov AA, Pykhova AD, Ioffe IN et al (2014) Anion radicals of isomeric [5, 6] and [6] Benzoadducts of $Sc_3N@C_{80}$: remarkable differences in endohedral cluster spin density and dynamics. J Am Chem Soc 136(38):13436–13441
22. Shustova NB, Peryshkov DV, Kuvychko IV et al (2011) Poly(perfluoroalkylation) of metallic nitride fullerenes reveals addition-pattern guidelines: synthesis and characterization of a family of $Sc_3N@C_{80}(CF_3)_n$ (n = 2-16) and their radical anions. J Am Chem Soc 133(8): 2672–2690
23. Popov AA, Dunsch L (2011) Electrochemistry in Cavea: endohedral redox reactions of encaged species in fullerenes. J Phys Chem Lett 2(7):786–794
24. Echegoyen L, Chancellor CJ, Cardona CM et al (2006) X-ray crystallographic and EPR spectroscopic characterization of a pyrrolidine adduct of $Y_3N@C_{80}$. Chem Commun 25:2653–2655
25. Valencia R, Rodriguez-Fortea A, Clotet A et al (2009) Electronic structure and redox properties of metal nitride endohedral fullerenes $M_3N@C_{2n}$ (M = Sc, Y, La, and Gd; 2n = 80, 84, 88, 92, 96). Chem-Eur J 15(41):10997–11009

26. Valencia R, Rodriguez-Fortea A, Stevenson S et al (2009) Electronic structures of scandium oxide endohedral metallofullerenes, $Sc_4(\mu_3\text{-}O)_n@I_h\text{-}C_{80}$ (n = 2, 3). Inorg Chem 48:5957–5961
27. Popov AA, Chen N, Pinzón JR et al (2012) Redox-active scandium oxide cluster inside a fullerene cage: spectroscopic, voltammetric, electron spin resonance spectroelectrochemical, and extended density functional theory study of $Sc_4O_2@C_{80}$ and its ion radicals. J Am Chem Soc 134(48):19607–19618
28. Wang T-S, Feng L, Wu J-Y et al (2010) Planar quinary cluster inside a fullerene cage: synthesis and structural characterizations of $Sc_3NC@C_{80}\text{-}I_h$. J Am Chem Soc 132(46):16362–16364
29. Feng Y, Wang T, Wu J-Y et al (2013) Spin-active metallofullerene stabilized by the core of NC moiety. Chem Commun 49:2148–2150

Chapter 10
Nuclear Magnetic Resonance Spectroscopy of Endohedral Metallofullerenes with Paramagnetic Metal Ions: Structure Elucidation and Magnetic Anisotropy

Alexey A. Popov

Abstract Paramagnetic NMR spectroscopy of EMFs with paramagnetic metal ions can deliver information on the structural and magnetic properties of EMFs. For a series of Ce-EMFs, analysis of the temperature dependence of chemical shifts in NMR spectra proved that the main contribution to the paramagnetic shifts is the dipolar "pseudocontact" term. As this term includes geometric parameters of the molecule, position and dynamics of endohedral metal atoms can be deduced from variable-temperature NMR spectra. For lanthanide-based nitride clusterfullerenes, pNMR provide information on the sign and size of the magnetic anisotropy of lanthanide ions. The influence of the cluster geometry on the paramagnetic chemical shifts is then discussed for $HoM_2N@C_{80}$ (M = Sc, Y, Lu) nitride clusterfullerenes.

10.1 Introduction

Nuclear magnetic resonance (NMR) spectroscopy is a popular method of the structure determination of fullerenes along with single-crystal X-ray diffraction (see Chap. 1). The vast majority of NMR spectroscopic studies of EMFs were dedicated to the determination of the cage structures by ^{13}C NMR spectroscopy in solution. Usually, such studies require that the fullerene is diamagnetic—then NMR lines are relatively narrow and the chemical shifts are characteristic and reflect the chemical environment. Many metallofullerenes, especially monometallofullerenes, are paramagnetic due to the odd number of electrons transferred from metal atom(s) to the carbon cage. NMR studies of such EMFs require their reduction or oxidation to the stable diamagnetic form. For instance, the structure of $La@C_{82}$-C_{2v}(9) was

A.A. Popov (✉)
Leibniz Institute for Solid State and Materials Research,
Helmholtzstraße 20, 01069 Dresden, Germany
e-mail: a.popov@ifw-dresden.de

A.A. Popov (ed.), *Endohedral Fullerenes: Electron Transfer and Spin*,
Nanostructure Science and Technology, DOI 10.1007/978-3-319-47049-8_10

determined by measuring ^{13}C NMR spectrum of its anion (Fig. 10.1). But even when the carbon cage in an EMF molecule is diamagnetic (i.e., the formal charge of the cage is even), the metal ions inside can be intrinsically paramagnetic, such as it is typical for many rare-earth metals in 2+ and 3+ valence states. In the presence of endohedral paramagnetic centers, the lines in ^{13}C NMR spectra are strongly broadened, often to such an extent that the measurement of NMR spectra becomes impossible. However, in certain cases, NMR spectra of paramagnetic EMFs still can be obtained. Similar to La@C_{82}-C_{2v}, ^{13}C NMR spectra of Ce@C_{82}^- [1, 2] and Pr@C_{82}^- [3] were successfully measured and gave the basis for their structure elucidation (for Ce@C_{82}^-, 2D INADEQUATE spectra were also obtained, see Fig. 10.1b). Likewise, three isomers of Tm@C_{82} were among the first paramagnetic EMFs characterized by ^{13}C NMR [4] (Fig. 10.2). Figures 10.1 and 10.2 show that the range of chemical shifts of paramagnetic EMFs is much broader than in diamagnetic molecules (compare to La@C_{82}^- in Fig. 10.1), which complicates the search of the fullerene signals. Besides, positions of ^{13}C NMR signals of paramagnetic compounds exhibit pronounced temperature dependence, as illustrated in Fig. 10.2b for one of the isomers of Tm@C_{82}. Despite intrinsic difficulties associated with measurements and interpretation of NMR spectra of paramagnetic EMFs (denoted as pNMR hereafter), the method has become quite popular since early 2000s. In particular, Ce-based EMFs and their derivatives, but also a number of nitride clusterfullerenes with different lanthanides have been studied by pNMR techniques. In comparison to conventional NMR, pNMR not only allows determination of the carbon cage symmetry, but also can give an additional information on the position and dynamics of endohedral metal atoms as well as on their magnetic properties.

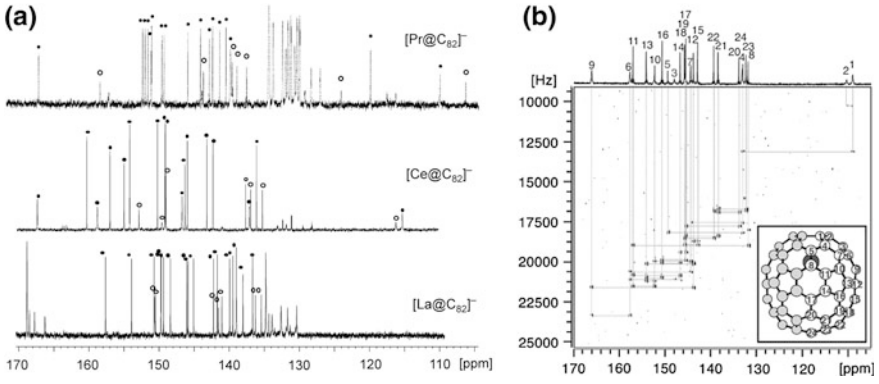

Fig. 10.1 **a** ^{13}C NMR spectra of [M@C_{82}-C_{2v}(9)]$^-$ anions (M = La, Ce, Pr). Signals of fullerenes are marked with *closed* and *open circles* (for double and single intensity peaks, respectively). Note that C_{2v}(9) cage has 24 ^{13}C NMR signals, of them 17 with double and 7 with single intensity. The spectra are reproduced with permission from [3] and [1]. **b** Two-dimensional INADEQUATE NMR spectrum of [Ce@C_{82}-C_{2v}(9)]$^-$ at 288 K. Reproduced with permission from [2]

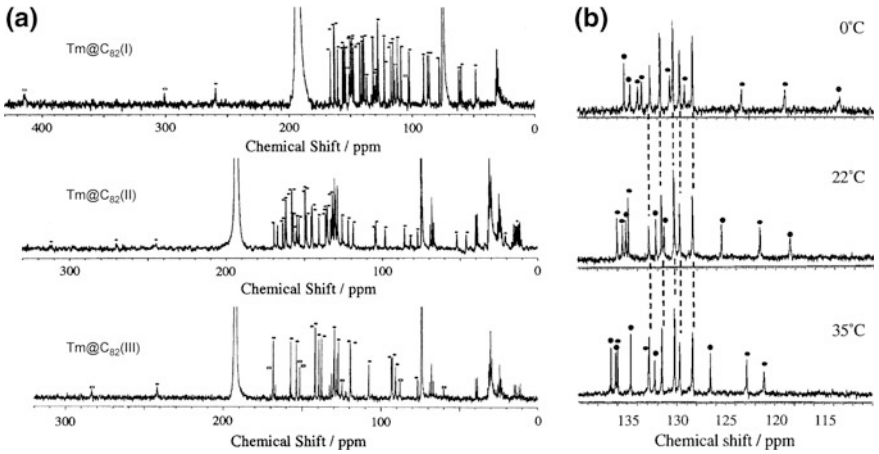

Fig. 10.2 **a** ^{13}C NMR spectra of three isomers of Tm@C_{82}; peaks marked with *circles* are assigned to EMF signals. **b** ^{13}C NMR spectra of Tm@C_{82}(II) measured at different temperatures (only limited range is shown). Reproduced with permission from [4]

The chemical shift of a nuclei in a paramagnetic compound can be described as a sum of diamagnetic and paramagnetic terms, $\delta^{\text{exp}} = \delta^{\text{dia}} + \delta^{\text{para}}$. In due turn, the paramagnetic shift has two major contributions, Fermi contact δ^{fc} and pseudo-contact δ^{pc} [5–7]. The contact shift results from the interaction between the nuclear spin of atoms of interest (such as ^{1}H, ^{13}C or ^{45}Sc) and the spin-polarized electron density of the molecule (in particular in the region close to the nuclei of interest). As such, the contact shift is proportional to the hyperfine coupling constant $A/\hbar$ weighed with the expectation value of the spin operator $\langle S_z \rangle$ of the lanthanide

$$\delta_i^{\text{fc}} = \langle S_z \rangle_{\text{Ln}} \frac{A}{\hbar} \frac{\mu_B}{3kT\gamma_I}, \tag{10.1}$$

where μ_B is the Bohr magneton, γ_I is the gyromagnetic ratio of the measured nucleus, and $\langle S_z \rangle$ values are tabulated for each lanthanide.

The pseudocontact shift is caused by dipolar through-space interactions of the nuclear and electronic magnetic dipoles. In a molecule containing single lanthanide ion, the pseudocontact shift of an i-th atom can be computed as

$$\delta_i^{\text{pc}} = \frac{1}{12\pi R_i^3} \left(\left(3\cos^2\theta_i - 1\right) \left(\chi_{zz}^{\text{Ln}} - \frac{\chi_{xx}^{\text{Ln}} + \chi_{yy}^{\text{Ln}}}{2} \right) + \frac{3}{2} \left(\chi_{xx}^{\text{Ln}} - \chi_{yy}^{\text{Ln}} \right) \sin^2\theta_i \cos 2\varphi_i \right), \tag{10.2}$$

where $\chi_{\alpha\alpha}^{\text{Ln}}$ are components of the magnetic susceptibility tensor of the lanthanide, whereas R_i, θ_i, and φ_i are polar coordinates of the i-th atom in the coordinate system centered on the lanthanide ion. That is, R_i is a distance between the atom of

interest and the lanthanide ion, and θ_i is an angle between quantization axis z and the vector connecting the lanthanide ion and the i-th atom. For the uniaxial ligand field, $\chi_{xx}^{Ln} = \chi_{yy}^{Ln}$, and Eq. 10.1a is reduced to

$$\delta_i^{pc} = \frac{(3\cos^2\theta_i - 1)}{12\pi R_i^3}\left(\chi_{zz}^{Ln} - \frac{\chi_{xx}^{Ln} + \chi_{yy}^{Ln}}{2}\right) \tag{10.3}$$

As can be seen from Eq. 10.2, the pseudocontact shift contains information on the molecular structure and on the magnetic anisotropy of the paramagnetic center. Paramagnetic NMR is therefore a popular structure elucidation tool for metal complexes, polymers, or biomolecules [6–10]. At the same time, it has also been used to determine or verify crystal-field splitting parameters in lanthanide complexes [11–16]. Since structural information and magnetic anisotropy parameters are contained only in the pseudocontact term, it is necessary to separate its contribution to the experimentally measured paramagnetic chemical shift from the contact shift contribution [17].

10.2 Paramagnetic NMR of Ce-EMFs: Temperature Dependence and Metal Position

In Bleaney theory of paramagnetic NMR, Fermi contact shift scales as T^{-1}, whereas pseudocontact shift has T^{-2} dependence, so that the temperature dependence of the experimental chemical shift can be written down as follows:

$$\delta_i^{para}(T) = \delta_i^{dia} + c_i^{fc}T^{-1} + c_i^{pc}T^{-2}, \tag{10.4}$$

where c_i^{fc} and c_i^{pc} are characteristic constants for each nuclei in the molecule. Therefore, the temperature dependence of the measured chemical shifts can show which of the contributions is dominating. For that, experimental chemical shift can be fitted to the equations $\delta_i^{para}(T) = \delta_i^{dia} + c_i^{fc}T^{-1}$ or $\delta_i^{para}(T) = \delta_i^{dia} + c_i^{pc}T^{-2}$ and then extrapolated to $T^{-1} = 0$ or $T^{-2} = 0$ limits, respectively. Extrapolation gives the estimation of diamagnetic shift δ_i^{dia}, which can be then compared to the experimental chemical shift of the diamagnetic analog (for Ce-EMFs, isostructural La-EMFs provide good estimation of diamagnetic values). Figure 10.3 illustrates the use of such analysis for $Ce_2@C_{78}$-D_{3h}(5) [18]. 8 ^{13}C NMR signals of the symmetric cage were measured in the 283–303 K range and then extrapolated to $T^{-1} = 0$ (Fig. 10.3b) or $T^{-2} = 0$ (Fig. 10.3c). Estimation of δ_i^{dia} values using equation $\delta_i^{para}(T) = \delta_i^{dia} + c_i^{fc}T^{-1}$ gives the values far away from the chemical shifts of $La_2@C_{78}$-D_{3h}(5) (especially for the signal 8), whereas good agreement is obtained for the equation $\delta_i^{para}(T) = \delta_i^{dia} + c_i^{pc}T^{-2}$. Thus, paramagnetic shift in $Ce_2@C_{78}$ is dominated by the pseudocontact term, which agrees well with the

strongly localized, "buried" nature of unpaired $4f^1$ electron in Ce^{3+} ions. The same conclusion was obtained from the temperature dependence of the chemical shifts in other Ce-EMFs and their derivatives [1, 2, 18–23].

The dominance of the pseudocontact shift in Ce-EMFs allows determination of the relative position of paramagnetic metal ions and different cage carbon atoms from the temperature dependence of the chemical shifts. Assuming uniaxial anisotropy of lanthanide and taking into account Eq. 10.3, the c_i^{pc} constants can be computed as

$$c_i^{pc} = \frac{C}{T^2} \sum_j \frac{\left(3\cos^2\theta_{ij} - 1\right)}{R_{ij}^3}, \tag{10.5}$$

where C is a Bleaney factor (tabulated parameter for each lanthanide), and index j runs over all Ce atoms in the molecule. Figure 10.4a shows how θ_{ij} angles and R_{ij} radii are defined in $Ce_2@C_{78}$, and histograms in Figs. 10.4b and 10.4c compare c_i^{pc} values determined experimentally from the temperature dependence to those computed using Eq. 10.4 with DFT-optimized structure of $La_2@C_{78}$ for geometry parameters (Fig. 10.4d). Large c_i^{pc} value for atom 8 corresponds well to the computed value for the atoms labeled H (Fig. 10.4d), which are located on the poles coordinated to Ce atoms. This pattern proves that metal atoms in $Ce_2@C_{78}$ are coordinated to two particular hexagons and are not circulating over the whole

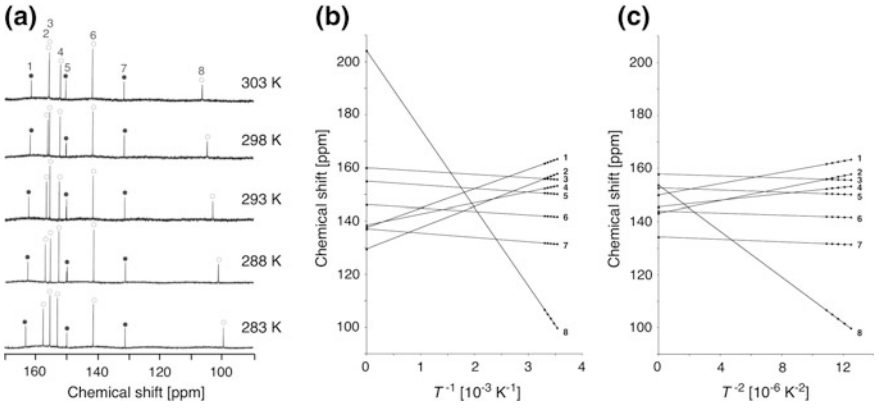

Fig. 10.3 **a** ^{13}C NMR spectra of $Ce_2@C_{78}$-$D_{3h}(5)$ in CS_2 at 283–303 K. The relative integrated intensity ratio of the *lines* marked with an *open circle* and a *solid circle* is 2:1. **b** Line fitting plot of experimental chemical shifts using eq. $\delta_i^{para}(T) = \delta_i^{dia} + c_i^{fc}T^{-1}$; estimated δ_i^{dia} values are far from chemical shifts in $La_2@C_{78}$; **c** Line fitting plot of experimental chemical shifts using eq. $\delta_i^{para}(T) = \delta_i^{dia} + c_i^{pc}T^{-2}$; estimated δ_i^{dia} values are close to chemical shifts in $La_2@C_{78}$. Reproduced with permission from [18]

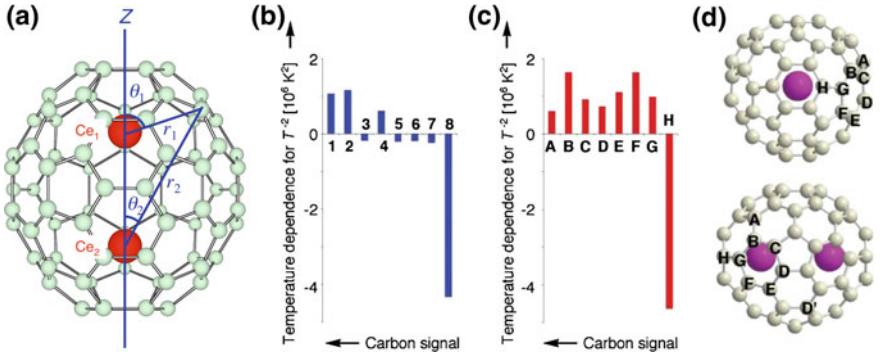

Fig. 10.4 **a** Molecular structure of $Ce_2@C_{78}$-$D_{3h}(5)$ showing how θ_{ij} angles and R_{ij} radii are defined. **b** experimental c_i^{pc} values; numbers correspond to peaks in Fig. 10.3a. **c** c_i^{pc} values computed using Eq. 10.5, letters correspond to atom labeling shown in (**d**). Reproduced with permission from [18]

molecule. In a similar fashion, conclusions on localized nature of Ce atoms were obtained in variable-temperature NMR studies of $[Ce@C_{82}]^-$-$C_{2v}(9)$ [1, 2], non-IPR $Ce_2@C_{72}$-$D_2(10611)$ [21], or a bis-silylated adduct of $Ce_2@C_{80}$-$I_h(7)$ [24]. On the contrary, uniformly small c_i^{pc} values of $Ce_2@C_{80}$-$I_h(7)$ [24] and $CeM_2N@C_{80}$-$I_h(7)$ (M = Sc, Y, Lu) [23, 25] agree well with the three-dimensional rotation of Ce_2 and $CeLu_2N$ clusters inside the icosahedral C_{80} cage. For $Ce_2@C_{80}$-$D_{5h}(6)$, two-dimensional circulation of Ce atoms along a band of ten hexagons was found [20].

Dipolar magnetic field generated by endohedral Ce atoms can reach out rather far outside the carbon cage and produce sensible chemical shifts in the exohedrally attached organic groups in chemical derivatives of Ce-EMFs. It opens a possibility of ^1H pNMR studies of the derivatives, which can also provide an information on the position and dynamics of endohedral Ce ions [18, 19, 24, 26]. Figure 10.5 shows ^1H NMR spectra of one of the $CH_2C_6H_3(CH_3)_2$ (3,5-dimethyl-benzyl) monoadducts to $Ce@C_{82}$ [27]. Temperature dependence of the chemical shifts of protons in the derivative can be well established (types of protons in the molecule are shown in Fig. 10.5b). Reliable prediction of the pseudocontact shift requires correct choice of the main anisotropy axis, which is not obvious, especially for derivatives of monometallofullerenes. Figure 10.5d compared experimental data to the results of computations with different choices of the axis orientation (shown in Fig. 10.5c). The axis orientation chosen along the local electric field in the molecule (predicted by the DFT calculations) gives good agreement to experimental data. When correct axis orientation is determined, endohedral Ce ions can be used as local probes for location of given atoms via their chemical shifts.

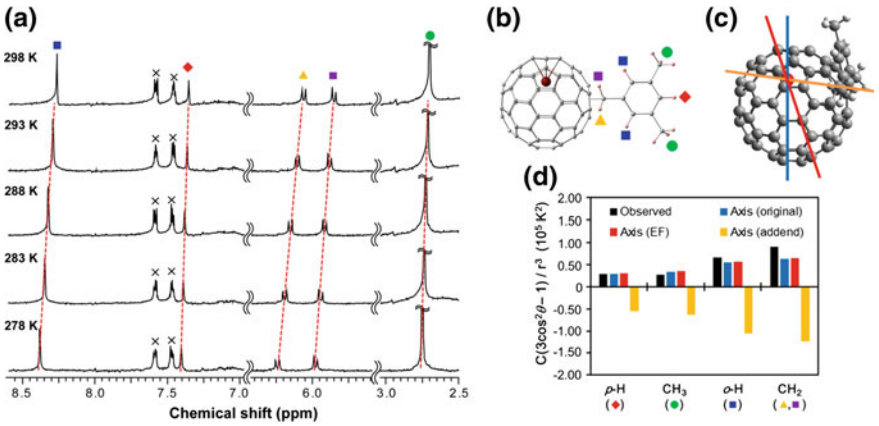

Fig. 10.5 **a** ^{1}H NMR spectra of Ce@C_{82}-$CH_2C_6H_3(CH_3)_2$ monoadduct at 278–298 K; peaks marked with *colored* symbols are assigned to the compound. **b** Schematic molecular structure of the adduct showing labeling of protons used in (**a**). **c** Different choices of the magnetic anisotropy axis in Ce@C_{82}-$CH_2C_6H_3(CH_3)_2$ (*blue*—as in original Ce@C_{82}; *red*—computed from electrostatic modeling; *yellow*—the line connecting Ce and position of the addend). **d** c_i^{pc} values, obtained from experimental data (*black*) and calculated using different orientations of anisotropy axes. Reproduced with permission from [27]

10.3 Magnetic Anisotropy of Lanthanide Ions in Nitride Clusterfullerenes

In the view of single molecule magnetism discovered for $DySc_2N@C_{80}$ nitride clusterfullerenes [28] (see Chap. 11 for a detailed overview), understanding magnetic anisotropy of lanthanide ions in nitride clusterfullerenes is necessary for a design of even stronger EMF-based molecular magnets. Solution NMR studies can provide complimentary information on the magnetic anisotropy of lanthanide ions for the temperatures not well accessible by direct magnetization measurements.

A systematic pNMR study of $MSc_2N@C_{80}$-I_h(7) compounds with all lanthanides forming nitride clusterfullerenes (M = Y, La, Ce, Pr, Nd, Gd, Tb, Dy, Ho, Er, Tm, Lu) was reported in [29]. Figure 10.6 shows ^{13}C NMR and ^{45}Sc NMR spectra of these EMFs. At room temperature, fast rotation of the MSc_2N cluster inside the symmetric C_{80}-I_h carbon cage averages carbon signals, leaving only two ^{13}C NMR peaks with a 3:1 intensity ratio corresponding to 60 carbon atoms at the pentagon–hexagon–hexagon junctions (PHHJ) and 20 atoms at the triple hexagon junctions (THJ, see Fig. 10.6a). Thanks to the simple two-line spectrum of the C_{80} carbon cage, ^{13}C signals of paramagnetic $MSc_2N@C_{80}$ molecules (denoted as **1M** hereafter) are detectable even when they are severely broadened as in **1Tb** or **1Dy**. In **1Ce**, **1Pr**, **1Nd**, **1Tb**, **1Dy**, and **1Ho** the ^{13}C signals are shifted upfield with respect to the diamagnetic values. The magnitude of the paramagnetic shift varies from few ppm in **1Ce**, **1Pr**, and **1Nd** to tens of ppm in **1Tb**, **1Dy**, and **1Ho**

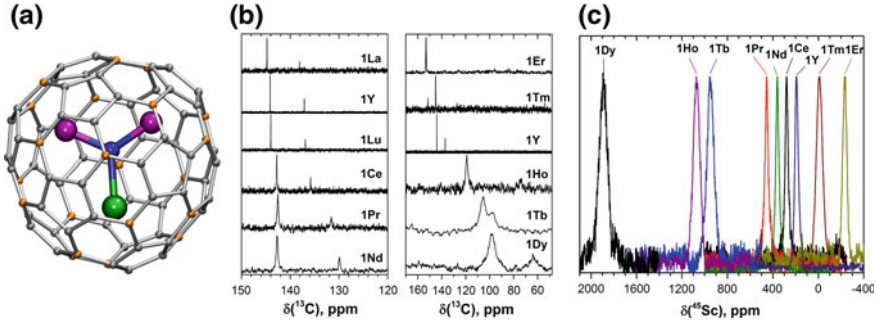

Fig. 10.6 **a** Molecular structure of $MSc_2N@C_{80}$-I_h; lanthanide (M) is colored *green*, Sc is *magenta*, *N* is *blue*; carbon atoms are *grey* (PHHJ) or *orange* (THJ). **b** ^{13}C NMR spectra of $MSc_2N@C_{80}$ molecules at 288 K (note different scale in two panels); **c** ^{45}Sc NMR spectra of $MSc_2N@C_{80}$ molecules. Reproduced with permission from [29]

(Fig. 10.6b). In **1Er** and **1Tm** the lanthanide-induced shift is downfield. The PHHJ and THJ ^{13}C signals of **1Er** are coinciding near the room temperature and appear at 153.2 ppm, but can be resolved at higher or lower temperatures. In **1Tm**, the stronger lanthanide-induced shift of the THJ signal pushes it to a lower field than that of the PHHJ (in all other **1M** compounds the PHHJ signal appears at lower field than that of the THJ carbons).

In ^{45}Sc NMR spectra, all $MSc_2N@C_{80}$ compounds exhibit one relatively broad peak (Fig. 10.6c). The ^{45}Sc chemical shifts of the diamagnetic **1La** and **1Lu** are 198 and 200 ppm, respectively, whereas in paramagnetic **1M** molecules the ^{45}Sc signal position spans the range from −233 ppm in **1Er** to 1892 ppm in **1Dy**. The peak width varies from 30 to 40 ppm for the diamagnetic **1Lu** and **1La** and paramagnetic **1Ce**, **1Pr**, **1Nd,** and **1Er,** to ca 70–80 ppm for the **1Tb**, **1Dy**, **1Ho**, and **1Tm**.

Direction of the lanthanide-induced paramagnetic shift is determined by a magnetic anisotropy of the lanthanide ion, and hence experimental NMR data give information at least on the sign of the anisotropy, if the paramagnetic shift is dominated by pseudocontact term. In contrast to Ce-EMFs discussed in the previous section, the use of temperature dependence of the chemical shifts and fitting it to reduced forms of Eq. 10.4 did not yield reasonable values. The localized "buried" nature of the 4f electrons in lanthanides implies that the contact contribution to the paramagnetic shift should be rather small. Typically, the values become negligible when the nucleus of interest is separated by more than four bonds from the lanthanide ion. However, in the **1M** molecules both Sc and carbon atoms are located rather close to the lanthanide, and hence the contact term cannot be fully ignored. Calculations of spin-density distribution in **1Gd** clearly demonstrate nonzero spin density on atoms close to Gd (Fig. 10.7a). Besides, Bleaney's theory has certain assumptions (ligand field splitting is less than thermal energy, truncation of the expansion of the magnetic susceptibility in reciprocal temperature series is

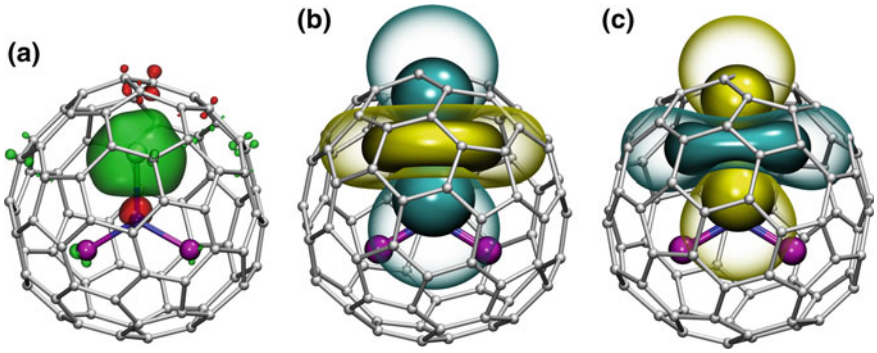

Fig. 10.7 **a** DFT-computed spin density distribution in $GdSc_2N@C_{80}$ (*green* (+) and *red* (−)). **b** Pseudocontact shift isosurface in $DySc_2N@C_{80}$ at 288 K computed using point charge model, solid/transparent surfaces correspond to ± 6000/± 1500 ppm. **c** The same as (**b**) but for $ErSc_2N@C_{80}$, solid/transparent surfaces correspond to ± 2000/± 500 ppm. Reproduced with permission from [29]

limited to T^{-2}), which are not fulfilled for lanthanide complexes with large anisotropy, such as $MSc_2N@C_{80}$ molecules.

Nevertheless, availability of NMR data on the wholes series of lanthanides allowed estimation of the contact term in $MSc_2N@C_{80}$ using Reilley's method and more sophisticated approaches using two or three nuclei at once [29]. Besides, contact term can be estimated using Eq. 10.1 and DFT-computed hyperfine coupling constants for **1Gd** (it can be assumed that $A/\hbar$ are the same for all lanthanides, and hence the values computed for Gd can be used for other compounds). Analysis of the ^{13}C chemical shifts of $MSc_2N@C_{80}$ compounds using these approaches showed that although pseudocontact shift is larger than the contact shift, the latter can be quite significant. For instance, for the PHHJ carbons, δ^{fc} values can be as high as 36% for **1Ho**. Furthermore, for **1Ce**, **1Pr**, **1Nd**, **1Er**, and **1Tm** the sign of δ^{fc} and δ^{pc} is opposite, and hence resulting values of paramagnetic shift are not fully reflecting magnetic anisotropy. For THJ carbons, the relative contribution of the contact term is reduced, but still remains high. On the contrary, for the ^{45}Sc chemical shifts the contact term contribution is below 10%, and ^{45}Sc NMR (Fig. 10.6c) appears more suitable for the analysis of magnetic anisotropy of lanthanide ions in nitride clusterfullerenes.

Magnetic susceptibility in Eq. 10.2 is determined by the thermal population of m_J levels of a lanthanide ion split by a ligand field. When these levels are known, direct estimation of the magnetic susceptibility tensor at different temperatures is possible using Van Vleck formulae, and therefore pseudocontact chemical shifts can be computed using Eqs. 10.2 or 10.3. In [29], ligand field and splitting of m_J levels in each **1M** molecule were computed using the point charge model and Bader atomic charges. Figure 10.8a shows the energy levels obtained in those calculations. The central nitrogen atom gives the main contribution to the ligand field in nitride clusterfullerenes because of its large negative charge (Bader charge −1.7) and close distance to the lanthanide ion. Two Sc ions produce the second largest

contribution after the nitride ion. Their positive charges (Bader charge of ca +1.7) reduce the effect of the nitride ion (e.g., in **1Dy** the ligand field splitting is reduced by ca 35% when Sc contribution is "turned on") and introduce a deviation from the uniaxial symmetry. The charges of carbon atoms are much smaller than those of N and Sc (below −0.1), and hence only few carbons close to the lanthanide ion have nonnegligible contribution to the ligand field [30]. Thus, the ligand field experienced by lanthanide ions in **1M** molecules has roughly a uniaxial character induced by a large negative point charge of the nitride ion, which results in rather simple ligand field splitting pattern despite the low molecular symmetry.

The ground magnetic state of the ions with oblate shape of the 4f electron density (Ce, Pr, Nd, Tb, Dy, Ho) has the largest J_z value (5/2 in **1Ce**, 4 in **1Pr**, 9/2 in **1Nd**, 6 in **1Tb**, 15/2 in **1Dy**, and 8 in **1Ho**), and the energy of the other m_J states is gradually increasing with the decrease of $|m_J|$. The splitting in $MSc_2N@C_{80}$ molecules is very large: the smallest overall splitting, 571 cm^{-1}, is found in **1Ho**, whereas the largest ligand field splitting is reaching 1915 cm^{-1} in **1Ce**. The gaps between the ground state and the first excited states are so large that even near room temperature the ground magnetic state with the largest J_z projection has the dominant contribution to the magnetic properties. The ligand field splitting pattern in **1Er** and **1Tm** is completely different because of the prolate shape of the 4f electron density of these lanthanides. The ground state for these lanthanides has the lowest J_z projection ($m_J = \pm 1/2$ in **1Er** and $m_J = 0$ in **1Tm**). The energy is increasing with the increase of the $|m_J|$ values, and the density of states is higher in the low-energy part of the spectrum. As a result, the room-temperature magnetic properties of **1Er** and **1Tm** result from the contribution of several m_J states. Thus, lanthanide with oblate and prolate shapes of 4f density has different sign of magnetic anisotropy and

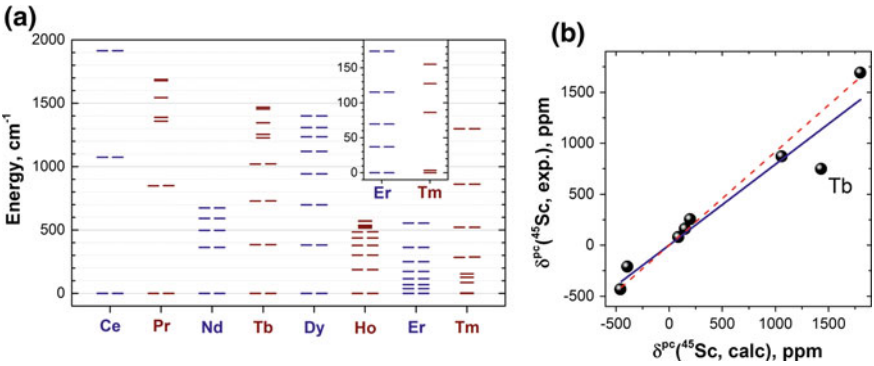

Fig. 10.8 **a** Ligand field splitting of the m_J levels in $MSc_2N@C_{80}$ molecules computed using point charge model. The *inset* shows low-energy levels in $ErSc_2N@C_{80}$ and $TmSc_2N@C_{80}$. Each degenerate ± m_J level of Kramers ions (Ce, Nd, Dy, Er) and quasi-degenerate (within 3 cm^{-1}) levels of non-Kramers ions are shown as *double lines*. **b** Comparison between experimental and computed ^{45}Sc pseudocontact chemical shifts. *Solid line* is a linear fit for a complete set of data ($R^2 = 0.94$), whereas *dashed line* is obtained for fitting without $TmSc_2N@C_{80}$ and $TbSc_2N@C_{80}$. Reproduced with permission from [29]

hence different direction of paramagnetic shift. Figure 10.7b illustrates this situation by visualizing δ^{pc} isosurfaces for **1Dy** and **1Er** computed with point charge model and Eq. 10.2. The difference is also well seen in the ^{45}Sc NMR spectra of **1M** molecules (Fig. 10.6a) as the signals of **1Er** and **1Tm** are shifted upfield versus **1Y**, whereas the signals of other **1M** molecules are shifted downfield.

The use of pNMR data goes beyond determination of the sign of anisotropy. Comparison between experimental and computed δ^{pc} values can be used then to evaluate reliability of the computed ligand field splitting levels or even to determine ligand field parameters. Figure 10.8b shows such comparison for ^{45}Sc chemical shifts in the $MSc_2N@C_{80}$ series. Experimental and computed values exhibit remarkably good agreement expect for the data for **1Tb**, whose chemical shift is significantly overestimated by theory. This may point to the limitation of the point charge model used in [29] to computed ligand field. Nonetheless, since δ^{pc} shift in ^{45}Sc NMR spectra are close to the total paramagnetic shifts, ^{45}Sc NMR spectra of paramagnetic mixed-metal nitride clusterfullerenes can be used straightforwardly for semi-quantitative analysis of the size of the magnetic anisotropy of the endohedral lanthanide ions.

10.4 Paramagnetic NMR of $HoM_2N@C_{80}$ and $Ho_2MN@C_{80}$-I_h (M = Sc, Y, Lu)

Since nitride ion in the close vicinity of the endohedral lanthanide ions is the main cause of the magnetic anisotropy of nitride clusterfullerenes, variation of the metal–nitrogen bond lengths is expected to change magnetic anisotropy of the lanthanide. In [30], possible influence of the change of the cluster geometry parameters on magnetism was studied by pNMR for a series of Ho-based nitride clusterfullerenes, $HoM_2N@C_{80}$-I_h and $Ho_2MN@C_{80}$-I_h NCFs (M = Sc, Y, Lu).

Figure 10.9 shows 125 MHz ^{13}C NMR spectra of $HoM_2N@C_{80}$ and $Ho_2MN@C_{80}$ series measured at 300 K in CS_2 solution. Whereas diamagnetic $Lu_3N@C_{80}$-I_h (still present in the $HoLu_2M@C_{80}$-I_h sample) exhibits two sharp ^{13}C signals at 144.3 and 137.6 ppm (Fig. 10.9a), replacement of one diamagnetic metal atom in $M_3N@C_{80}$-I_h with Ho dramatically changes ^{13}C NMR spectra. The spectral lines are substantially broadened and shifted to higher field due to the presence of paramagnetic Ho^{3+} ions. PHHJ signals are found at 119 ppm (M = Sc), 107 ppm (M = Lu), and 101 ppm (M = Y), whereas tentative positions of THJ signals are determined as 74 ppm (Sc), 66 ppm (Lu), and 76 ppm (Y). Surprisingly, paramagnetic shift δ^{para} depends strongly on the diamagnetic metal. For PHHJ signals, the shift increases systematically with the size of M^{3+} ion. When the second Ho ion is introduced into the nitride cluster, paramagnetic shifts are further increased.

Equation 10.3 shows that dependence of the ^{13}C paramagnetic shift on the radius of M^{3+} ions can be caused either by variation of the magnetic anisotropy of the Ho^{3+} ion, or by variation of the molecular geometry and hence $cos^2\theta$ and/or R.

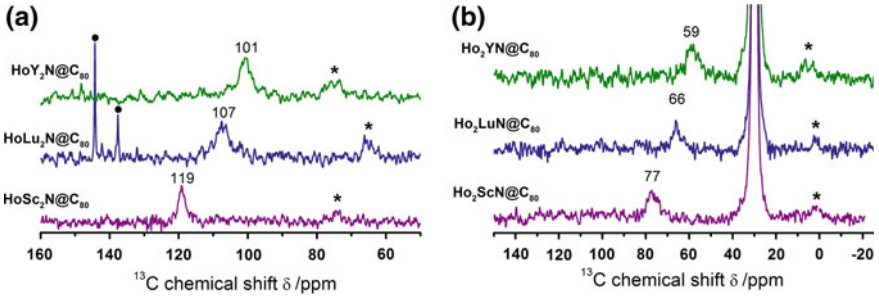

Fig. 10.9 ^{13}C NMR spectra of $HoM_2N@C_{80}$-I_h (**a**) and $Ho_2M@C_{80}$-I_h (**b**) (M = Sc, Y, or Lu) measured in CS_2 solution at 300 K. PHHJ signals are marked with their chemical shifts, prospective THJ signals are marked with *asterisks*, and signals of $Lu_3N@C_{80}$ present in the $HoLu_2N@C_{80}$ sample are marked with *dots*. A strong signal near 30 ppm in (**b**) is due to the deuterated acetone. Reproduced with permission from [30]

Note that because of the cluster rotation, measured chemical shifts are averaged over all carbon atoms and hence the geometrical factor includes not only atomic coordinates in the energy minimum, but also the influence of the cluster size on its dynamics inside the cage.

Low-temperature XMCD measurements did not reveal any measurable differences in the ground magnetic state of Ho ions in different fullerenes. However, NMR measurement is performed at room temperature, where the influence of excited states may become significant, which requires the analysis of the ligand field splitting. Ionic radii of diamagnetic metal ions are increasing from Sc^{3+} (0.745 Å) to Lu^{3+} (0.86 Å) to Y^{3+} (0.90 Å) [31]. As a result, the Ho–N distances are decreasing from 2.163 Å in $HoSc_2N@C_{80}$ to 2.067 Å in $HoY_2N@C_{80}$. Point charge calculations showed that the decrease of the Ho–N distance resulted in the increase of the ligand field splitting by ca 20%. For instance, in $HoY_2N@C_{80}$ the first excited state with $|m_J| = 7$ is at 232 cm^{-1}, which is 46 cm^{-1} higher than the energy of the first excited state in $HoSc_2N@C_{80}$ (186 cm^{-1}). As a result, computations of the magnetic susceptibility tensor using the Van Vleck formulae showed that the $\Delta\chi$ value ($\Delta\chi = \chi_{\parallel} - \chi_{\perp}$) for $HoY_2N@C_{80}$ is 19% higher than that in $HoSc_2N@C_{80}$ at 300 K. Though considerable, this difference cannot fully account for the 70% difference in paramagnetic shifts between $HoSc_2N@C_{80}$ and $HoY_2N@C_{80}$. Therefore, the structural factor has even higher impact on the paramagnetic shifts. Indeed, computations of the structural factor either using a static model (e.g., simply averaging over all carbon atoms for DFT-optimized structures), or using a dynamic approach (averaging the factors in molecular dynamics trajectory) confirmed that the structural factor is considerably different in $HoSc_2N@C_{80}$ and $HoY_2N@C_{80}$. Thus, even seemingly subtle variations of the coordination of Ho^{3+} to the fullerene cage results in a considerable change of the paramagnetic contribution to the chemical shifts of cage carbons.

10.5 Concluding Remarks

NMR spectroscopy of EMFs with paramagnetic metal ions have contributed considerably towards better understanding of molecular structure, internal dynamics, and magnetic properties of EMFs. It appears especially useful for Ce-containing EMFs since in such molecules the contribution of contact term is rather small, whereas lanthanide-induced broadening of NMR lines is still not very strong. Yet, EMFs with other lanthanides can be also successfully studied by this technique. In particular, the whole row of lanthanide-containing nitride clusterfullerenes $MSc_2N@C_{80}$ has been studied in detail. Distinguishing between contact and pseudocontact terms still remains a problem for a majority of lanthanides, but once it is solved—paramagnetic NMR gives a wealth of information on magnetic anisotropy and relative position of endohedral lanthanide ions.

References

1. Wakahara T, Kobayashi J, Yamada M et al (2004) Characterization of $Ce@C_{82}$ and its anion. J Am Chem Soc 126(15):4883–4887
2. Yamada M, Wakahara T, Lian Y et al (2006) Analysis of lanthanide-induced NMR shifts of the $Ce@C_{82}$ anion. J Am Chem Soc 128(5):1400–1401
3. Wakahara T, Okubo S, Kondo M et al (2002) Ionization and structural determination of the major isomer of $Pr@C_{82}$. Chem Phys Lett 360(3–4):235–239
4. Kodama T, Ozawa N, Miyake Y et al (2002) Structural study of three isomers of $Tm@C_{82}$ by ^{13}C NMR spectroscopy. J Am Chem Soc 124(7):1452–1455
5. Bertini I, Luchinat C, Parigi G (2001) Solution NMR of paramagnetic molecules. Application to metallobiomolecules and models. Elseviser Science B. V, Amsterdam
6. Peters JA, Huskens J, Raber DJ (1996) Lanthanide induced shifts and relaxation rate enhancements. Prog Nucl Magn Reson Spectrosc 28(3–4):283–350
7. Liu W-M, Overhand M, Ubbink M (2014) The application of paramagnetic lanthanoid ions in NMR spectroscopy on proteins. Coord Chem Rev 273–274:2–12
8. Bertini I, Luchinat C, Parigi G (2002) Magnetic susceptibility in paramagnetic NMR. Prog Nucl Magn Reson Spectrosc 40(3):249–273
9. Koehler J, Meiler J (2011) Expanding the utility of NMR restraints with paramagnetic compounds: background and practical aspects. Prog Nucl Magn Reson Spectrosc 59(4):360–389
10. Piguet C, Geraldes CFGC (2003) Paramagnetic NMR lanthanide induced shifts for extracting solution structures. In: Gschneidner KA, Bünzli J-CG, Pecharsky VK (eds) Handbook on the physics and chemistry of rare earths, vol 33. Elsevier, Amsterdam, pp 353–463
11. Damjanovic M, Katoh K, Yamashita M et al (2013) Combined NMR analysis of huge residual dipolar couplings and pseudocontact shifts in terbium(III)-phthalocyaninato single molecule magnets. J Am Chem Soc 135(38):14349–14358
12. Ishikawa N, Iino T, Kaizu Y (2002) Determination of ligand-field parameters and f-electronic structures of hetero-dinuclear phthalocyanine complexes with a diamagnetic yttrium(III) and a paramagnetic trivalent lanthanide ion. J Phys Chem A 106(41):9543–9550
13. Bertini I, Janik MBL, Lee Y-M et al (2001) Magnetic susceptibility tensor anisotropies for a lanthanide ion series in a fixed protein matrix. J Am Chem Soc 123(18):4181–4188

14. Hiller M, Maier M, Wadepohl H et al (2016) Paramagnetic NMR analysis of substituted biscyclooctatetraene lanthanide complexes. Organometallics 35(11):1916–1922
15. Damjanović M, Morita T, Katoh K et al (2015) Ligand π-radical interaction with f-shell unpaired electrons in phthalocyaninato-lanthanoid single-molecule magnets: a solution NMR spectroscopic and DFT study. Chem-Eur J 21(41):14421–14432
16. Castro G, Regueiro-Figueroa M, Esteban-Gómez D et al (2016) Magnetic anisotropies in rhombic lanthanide(III) complexes do not conform to Bleaney's theory. Inorg Chem 55 (7):3490–3497
17. Reilley CN, Good BW, Desreux JF (1975) Structure-independent method for dissecting contact and dipolar nuclear magnetic resonance shifts in lanthanide complexes and its use in structure determination. Anal Chem 47(13):2110–2116
18. Yamada M, Wakahara T, Tsuchiya T et al (2008) Location of the metal atoms in $Ce_2@C_{78}$ and its bis-silylated derivative. Chem Commun 558–560
19. Takano Y, Aoyagi M, Yamada M et al (2009) Anisotropic magnetic behavior of anionic $Ce@C_{82}$ carbene adducts. J Am Chem Soc 131:9340–9346
20. Yamada M, Mizorogi N, Tsuchiya T et al (2009) Synthesis and characterization of the D_{5h} isomer of the endohedral dimetallofullerene $Ce_2@C_{80}$: two-dimensional circulation of encapsulated metal atoms inside a fullerene cage. Chem-Eur J 15:9486–9493
21. Yamada M, Wakahara T, Tsuchiya T et al (2008) Spectroscopic and theoretical study of endohedral dimetallofullerene having a non-IPR fullerene cage: $Ce_2@C_{72}$. J Phys Chem A 112:7627–7631
22. Wang XL, Zuo TM, Olmstead MM et al (2006) Preparation and structure of $CeSc_2N@C_{80}$: an icosahedral carbon cage enclosing an acentric $CeSc_2N$ unit with buried f electron spin. J Am Chem Soc 128(27):8884–8889
23. Zhang L, Popov AA, Yang S et al (2010) An endohedral redox system in a fullerene cage: the Ce based mixed cluster fullerene $Lu_2CeN@C_{80}$. Phys Chem Chem Phys 12:7840–7847
24. Yamada M, Nakahodo T, Wakahara T et al (2005) Positional control of encapsulated atoms inside a fullerene cage by exohedral addition. J Am Chem Soc 127(42):14570–14571
25. Zhang Y, Schiemenz S, Popov AA et al (2013) Strain-driven endohedral redox couple Ce^{IV}/Ce^{III} in nitride clusterfullerenes $CeM_2N@C_{80}$ (M = Sc, Y, Lu). J Phys Chem Lett 4:2404–2409
26. Guldi DM, Feng L, Radhakrishnan SG et al (2010) A molecular $Ce_2@I_h$-C_{80} switch-unprecedented oxidative pathway in photoinduced charge transfer reactivity. J Am Chem Soc 132(26):9078–9086
27. Takano Y, Tashita R, Suzuki M et al (2016) Molecular location sensing approach by anisotropic magnetism of an endohedral metallofullerene. J Am Chem Soc 138(25):8000–8006
28. Westerström R, Dreiser J, Piamonteze C et al (2012) An endohedral single-molecule magnet with long relaxation times: $DySc_2N@C_{80}$. J Am Chem Soc 134(24):9840–9843
29. Zhang Y, Krylov D, Rosenkranz M et al (2015) Magnetic anisotropy of endohedral lanthanide ions: paramagnetic NMR study of $MSc_2N@C_{80}$-I_h with M running through the whole 4f Row. Chem Sci 6:2328–2341
30. Zhang Y, Krylov D, Schiemenz S et al (2014) Cluster-size dependent internal dynamics and magnetic anisotropy of Ho ions in $HoM_2N@C_{80}$ and $Ho_2MN@C_{80}$ families (M = Sc, Lu, Y). Nanoscale 6:11431–11438
31. Shannon R (1976) Revised effective ionic radii and systematic studies of interatomic distances in halides and chalcogenides. Acta Crystallogr Sect A 32(5):751–767

Chapter 11
Magnetic Properties of C_{80} Endofullerenes

Rasmus Westerström and Thomas Greber

Abstract This chapter summarizes the investigations of the endohedral metallofullerenes (EMFs) with a C_{80} carbon shell in view of their magnetic properties, where the recently discovered single-molecule magnetism in dysprosium based species are highlighted.

11.1 Paramagnets

C_{80} is not an abundant species in the fullerene synthesis with the Krätschmer–Huffman method [1]. This can be rationalized with the electronic structure of C_{80} cages, where the highest molecular orbital (HOMO) is not full. However, as it was shown theoretically, C_{80}^{6-} molecules have a large HOMO-LUMO gap and thus predicted to be stable [2]. Some years later the discovery of $Sc_3N@C_{80}$ [3] realized this prediction, since the Sc_3N endohedral unit transfers six electrons to the C_{80} cage. Importantly, it was realized that scandium may be substituted with other trivalent rare earth ions. The 14 rare earth (R) (including promethium) that are trivalent in the Krätschmer–Huffman plasma result in 560 possible endohedral trimetal nitride clusters, where the majority (540) are paramagnetic. Of course, this number increases significantly if additional endohedral compositions are considered, such as the very recently discovered magnetic carbide clusters [4, 5]. We deal here with 4f electron paramagnetism inside a diamagnetic C_{80} cluster. The 4f shell is localized deep inside the corresponding atom and, depending on the filling it can carry large angular momentum and spin that results in magnetic moments of up to 10 μ_B. Importantly, the corresponding anisotropy or deviation from spherical symmetry of the charge distribution indicates the lifting of the Hund ground state

T. Greber (✉)
Physik-Institut, University of Zürich, Zürich, Switzerland
e-mail: greber@physik.uzh.ch

R. Westerström
Synchrotron Radiation Research, Department of Physics,
Lund University, 188 221 00, Lund, Sweden

A.A. Popov (ed.), *Endohedral Fullerenes: Electron Transfer and Spin*,
Nanostructure Science and Technology, DOI 10.1007/978-3-319-47049-8_11

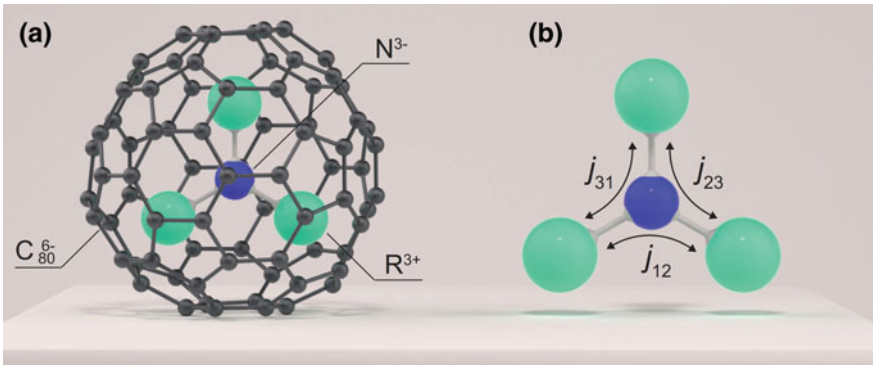

Fig. 11.1 **a** Ball-and stick-model of $R_3N@C_{80}$; R = Rare earth. **b** Model of the endohedral $R_3^{3+}N^{3-}$ unit and the corresponding couplings $j_{i,k}$ that are partly mediated across the N^{3-} ion. From Ref. [19]

degeneracy, a prerequisite for single-molecule magnets [6]. Figure 11.1a displays a model of the $R_3N@C_{80}$ molecule, where the most abundant isomer with icosahedral I_h symmetry is shown. In Fig. 11.1b, the endohedral unit with the possible magnetic interactions that are mediated by the central N^{3-} ion and the magnetic dipole field the two neighbours are shown. The magnetization is ruled by dipolar and exchange interaction between the different constituents. The dipolar interaction is rather strong: Given a distance of 0.35 nm between two magnetic moments of 10 μ_B we get a maximum dipole–dipole interaction of 0.25 meV corresponding to an effective temperature of 3 K. Furthermore, the central N^{3-} ion imposes a ligand field that lifts the Hund ground state degeneracy, orients the anisotropic 4f shell and enables magnetic order.

The gadolinium ($4f^7$) and diamagnetic atoms containing molecules $Gd_nD_{3-n}N@C_{80}$ $n \in \{1, 2, 3\}$, D being diamagnetic D$\in$ {Sc,Y,La,Lu} are closest to an ideal paramagnet, where the magnetic moments follow an external field. This is due to the isotropic 4f charge distribution in the half filled 4f shell of Gd^{3+} and has also practical implications that make $Gd_3N@C_{80}$ a candidate contrast agent for magnetic resonance imaging (MRI) applications [7]. Electron spin resonance experiments on $Gd_3N@C_{80}$ indicate that it can be described as 3 weakly coupled gadolinium ions with a half-filled 4f shell of spin 7/2 [8]. The systematic study on the magnetism of the series $GdnSc_{3-n}N@C_{80}$ $n \in \{1, 2, 3\}$ showed that the magnetisation curve of $n = 1$ fits to a Brillouin function with spin 7/2, while for $n = 2$ and $n = 3$ the data may not be fitted with a Brillouin function, which indicates interaction between different magnetic moments [9]. In the same publication it was also shown by diluting the molecules with non-paramagnetic $Lu_3N@C_{80}$ that the intermolecular interaction is larger than the intramolecular interaction.

Erbium ($4f^{11}$) containing C_{80} fullerenes are investigated also in view of the optical sensitivity of the 4f shell and the possibility of optical switching of the

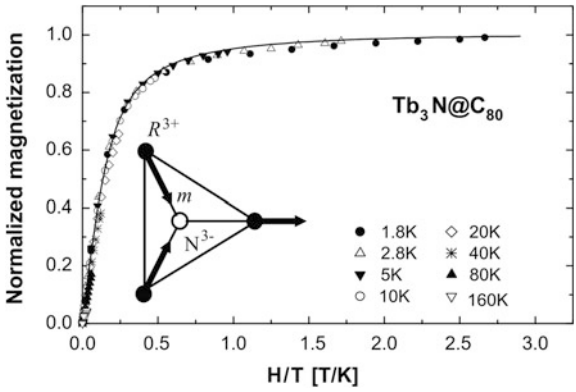

Fig. 11.2 Magnetization M (H/T) of $Tb_3N@C_{80}$ (*symbols*) normalized to saturation. *H* is the external magnetic field μ_0B. The *solid line* is a Brillouin function. *Inset* proposed configuration of the individual rare earth magnetic moments m (*arrows*) in the (R_3N) cluster. From Ref. [12]

magnetization. Between 2 and 300 K the magnetisation of $ErSc_2N@C_{80}$ scales well with the field temperature quotient H/T as it is the case for a Brillouin function, where the J_z levels are degenerate in zero field. It was also shown that for $n = 2$ and $n = 3$ the magnetization does not scale with n [10]. In today's understanding, the poor fit to the parameters expected from the Er $^4I_{15/2}$ Hund ground state suggests the importance of the ligand fields and the n-dependence indicates intramolecular interaction. Though, the anisotropy of the Er 4f shell is not particularly strong, and the N^{3-} ligand field does not promote a high J_z ground state that is favorable for single-molecule magnets.

The case of thulium ($4f^{12}$) showed paramagnetsim that could, for the case of $Tm_3N@C_{80}$, not be saturated in a field of 7 T at 1.8 K [11]. This points to a zero field ground state with low magnetic moment, the details of which still remain to be explored.

The Dresden group focused on ions with large 4f shell anisotropy and a concomitant J_z ground state with large magnetic moment: $Tb_3N@C_{80}$ and $Ho_3N@C_{80}$ [12, 13]. In Fig. 11.2 the magnetic susceptibility of $Tb_3N@C_{80}$ is shown as a function of the H-field/temperature quotient *H/T*. From the apparent paramagnetism a magnetic saturation moment of 18 μ_B per molecule was inferred. This is about a factor of 0.7 smaller than the moment that would be expected from three free Tb^{3+} ions. From these results, noncollinear magnetism was inferred: It was proposed that the ligand field forces the magnetic moments along two possible orientations, parallel or antiparallel to the Tb–N bond. In an external magnetic field, the moments assume the orientation where the projection of the moment is parallel to the external field. These results are important because they indicate that the ground state of Tb_3N and Ho_3N inside C_{80} can be described with a pseudospin model, i.e., with a Hamiltonian where the magnetic interaction is reduced to magnetic moments with two possible orientations. However, at this stage no indications of magnetic interaction between the pseudospins of Tb or Ho were inferred.

11.2 Single-Molecule Magnets

Single-molecule magnets like the famous manganese (Mn_{12}) compound [14] are molecules containing paramagnetic species that maintains their magnetization for milliseconds or longer [15]. In 2004 Ishikawa et al. [16] reported on the discovery of mononuclear lanthanide complexes exhibiting long magnetization relaxation times at high temperatures. This new category of magnets at the single-molecular level was realized with a single Tb^{3+} ion in a phthalocyanine double-decker configuration. For the case of the endofullerenes, it was shown later that the dysprosium-based trimetal nitride endofullerenes, also realize single-ion magnetism, though with much longer spin relaxation times. Furthermore, the use of the trimetal endofullerenes allows to study the interaction between two or three lanthanide 4f ions in an atomically precise environment.

11.2.1 Endohedral Single-Ion Magnets

The metal-nitride-cluster fullerenes (NCFs) encapsulate clusters containing three rare earth ions at the corners of a triangle with a central nitrogen ion, see Fig. 11.1. The rare earth metals adopt a trivalent state, whereas the nitrogen ion and the carbon cage have a closed shell configuration with a formal charge of −3 and −6 respectively. The $R_3N@C_{80}$ molecule is thus diamagnetic unless the endohedral cluster contains lanthanide species with a partially filled 4f shell. The magnetic moment of the system is for this reason solely determined by the spin and orbital momentum of the encapsulated paramagnetic rare earth ions. Still, the surrounding diamagnetic and ionic ligands have a decisive influence on the magnetic properties of the system, as was put forward by Wolf et al. [13]. The concomitant ligand field lifts the degeneracy of the ground state and enables single-molecule magnetism.

Now we consider a LnD_2N cluster containing one paramagnetic lanthanide ion (Ln^{3+}), and diamagnetic species (D^{3+} and N^{3-}). For a free paramagnetic ion, the Hund ground state for the partially filled 4f shell is degenerate in the absence of an external electric or magnetic field. The situation is considerably different for the endohedral cluster where electrostatic interactions with the surrounding ligands, especially the central nitrogen ion, lead to a lifting of the 2J + 1 degeneracy. This means that certain J_z 's become the ground state J_g that is degenerate for $J_g \neq 0$. For the general case the ground state is twofold degenerate $+J_g$, where $+J_g$ has due to time reversal symmetry opposite magnetization to $\pm J_g$. The two states $\pm J_g$ are separated by an energy barrier that limits magnetization reversal by quantum tunneling and thermal excitation. Therefore the ligand field restricts the orientation of the magnetic moment, where the interactions with the N^{3-} ion result in a magnetic anisotropy (easy) axis that must be oriented along the lanthanide–nitrogen bond if the ground state J_g corresponds to the largest possible J_z. Otherwise spin reorientation may occur.

In contrast an isotropic system, where the moment is free to align with an external H field, here the moments orient in the ligand field, and we deal with noncollinear magnetism.

At low temperatures, the ground state doublet determines the magnetic properties of the endohedral lanthanide ion. At zero magnetic field the two components $\pm J_g$ are populated with equal probability, and the system does not exhibit a net magnetization. Applying an external magnetic field lifts the degeneracy of the doublets. The J_g with a parallel component of projected moment along the field direction becomes energetically favorable and by that more populated. The magnetisation adopts an equilibrium value determined by the corresponding Zeeman splitting and temperature of the system. The two components of the ground state doublet are separated by an energy barrier much larger than the Zeeman energy. At low temperatures the thermal energy of the system is not large enough to 'instantaneously' establish equilibrium and kinetics become important. Reaching the equilibrium magnetization is associated with a relaxation time τ, which depends on the temperature and the J_g reversal energy barrier. Consequently, at low temperatures the 4f moment displays a slow response to external magnetic field changes. If the relaxation rate is slow compared to the measurement time, the system exhibits magnetic hysteresis. At small external fields, the hyperfine coupling and the dipole interactions lead to a small splitting of the ground state doublets. Such a lifting of the degeneracy of the ground state doublet allows the magnetization to shortcut the reversal energy barrier and to reverse the magnetization by quantum tunneling of the magnetization (QTM).

11.2.1.1 $DySc_2N@C_{80}$

$DySc_2N@C_{80}$ was the first endohedral metallofullerene where single-molecule magnet behavior was observed, as evidenced by the detection of hysteresis [17]. This discovery was facilitated by the easy accessibility of a circular dichroism beamline. In comparison to the standard tool of superconducting quantum interference device (SQUID) magnetometry, x-ray circular dichroism is sensitive to samples that may be several orders of magnitude smaller than those used for SQUID magnetometry. The drawbacks of the x-ray based methods, as compared to SQUID magnetometry, is price, cryogenic control, and the unavoidable fact that the x-rays and the concomitant secondary electrons demagnetize the molecules [18]. The magnetism of the $DySc_2N@C_{80}$ endofullerene is governed by the spin and orbital momentum of the Dy 4f electrons. X-ray absorption spectroscopy (XAS) provides a tool for probing the magnetism of the system by resonantly exciting 3d $\rightarrow$ 4f transitions, i.e., the $M_{4,5}$ edge. Figure 11.3a displays XAS data recorded from a powder sample of $DySc_2N@C_{80}$ using right (I^+) and left (I^-) polarized x-rays. The polarization dependent absorption is directly related to the unbalance in the spin and orbital momentum of the 4f valence electrons relative to the applied magnetic field and the angular momentum of the x-ray photons. The difference in absorption between the two polarizations provides the x-ray magnetic

circular dichroism (XMCD) spectrum that reflects the spin an orbital magnetic moment of the absorbing Dy ion. By applying a sum rule analysis to the XAS data a powder averaged magnetic moment of the endohedral Dy^{3+} ions of 4.4 μ_B is determined. The extracted value is comparable to that of 4.7 μ_B as obtained with a pseudospin analysis of SQUID data, which indicated a J_z = 15/2 ground state [19, 21, 22]. Figure 11.3b shows an element-specific magnetization curve obtained by recording the maximum XMCD signal at the Dy M_5 edge as a function of the applied magnetic field. The observed hysteresis is a direct indication that the rate at which the magnetization of the single dysprosium ions relaxes to its equilibrium value is slow compared to the measurement time (μ_0dH/dt = 1 T/min). The element specificity of XAS provides the magnetic properties of the individual Dy ions and is related to nonelement sensitive characterization techniques such as SQUID magnetometry. Figure 11.3c displays magnetization curve recorded at 2 K for $DySc_2N@C_{80}$ using SQUID magnetometry. The good agreement with the XMCD data demonstrates that the magnetic moments measured by the SQUID can be attributed to the endohedral dysprosium ions. The deviation between the two data sets is a consequence of x-ray induced demagnetization [18] and temperature calibration.

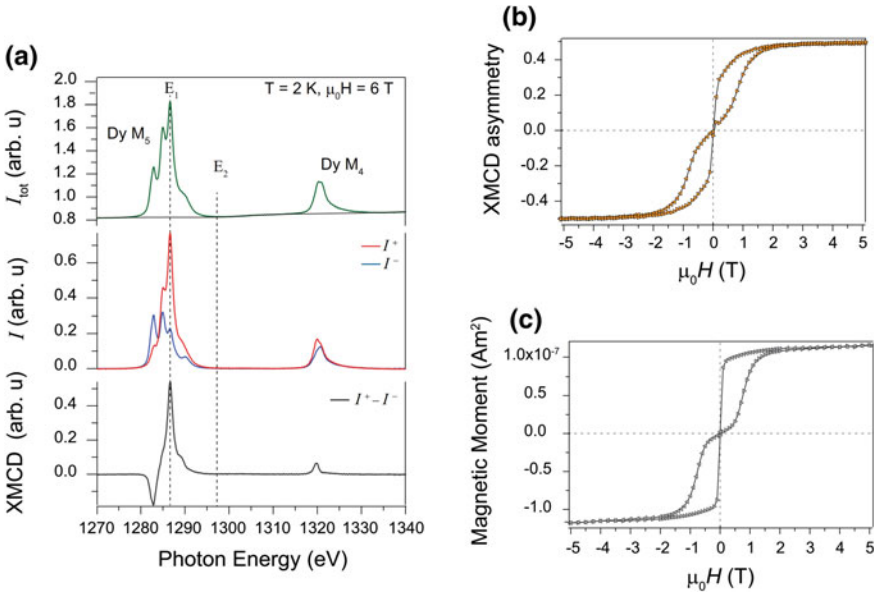

Fig. 11.3 **a** *Top panel* Sum of the x-ray absorption spectra of both x-ray helicities *Itot* recorded at the Dy $M_{4,5}$ edge at 6 T. *Center panel* Polarization dependent x-ray absorption spectra after subtraction of the background, I^+ (*red*) and I^- (*blue*). *Bottom panel* Magnetic circular-dichroism XMCD (I^+–I^-). **b–c** Magnetization curves recorded at 2 K by XMCD (**b**) and SQUID magnetometry (**c**). The element-specific magnetization curve in (**b**) was constructed from the asymmetry $[(I^+_{E_1} - I^+_{E_2}) - (I^-_{E_1} - I^-_{E_2})]/[(I^+_{E_1} - I^+_{E_2}) + (I^-_{E_1} - I^-_{E_2})]$, where E_1 and E_2 are the photon energies in panel (**a**). Adopted from [17]

11.2.1.2 $HoSc_2N@C_{80}$

$HoSc_2N@C_{80}$ also displays single-molecule magnet behavior [20]. Alternating current (ac) susceptibility measurements reveal that this molecule exhibits compared to $DySc_2N@C_{80}$ much faster relaxation of the magnetization. In a small applied magnetic field it was found to be in the order of milliseconds or more than five orders of magnitude faster than for $DySc_2N@C_{80}$. The equilibrium magnetic properties of $HoSc_2N@C_{80}$ indicate as well strong magnetic anisotropy. Figure 11.4 shows the measured magnetization curve of a powder sample, and the corresponding magnetization lifetimes. From the observed magnetization in a powder sample a magnetic moment of 9.15 μ_B was inferred, which is close to a $J_z = 8$ ground state with a LandŽ g factor of 5/4. Both Dy^{3+} and Ho^{3+} have a significant anisotropy in the N^{3-} ligand field and the largest J_z of 15/2 and 8, respectively, assume the ground states, and they have similar thermal demagnetisation barriers [17, 20]. The reason for the large differences in magnetization relaxation times between $HoSc_2N@C_{80}$ and $DySc_2N@C_{80}$ must lie in the nature of the Dy $4f^9$, and the Ho $4f^{10}$ ions, since the two molecules may be considered to be otherwise isostructural. Hyper-fine interaction between the 4f electrons and the nuclear spins may also not explain the strong effect: Dysprosium has four different stable isotopes with different nuclear spins and holmium has one stable isotope with spin 7/2. However, Dy^{3+} ($4f^9$) is a Kramers ion, with an odd number of electrons and a degenerate ground state in zero field and this must be an effective protection by symmetry for the decay of the magnetization via quantum tunneling of the magnetization [20].

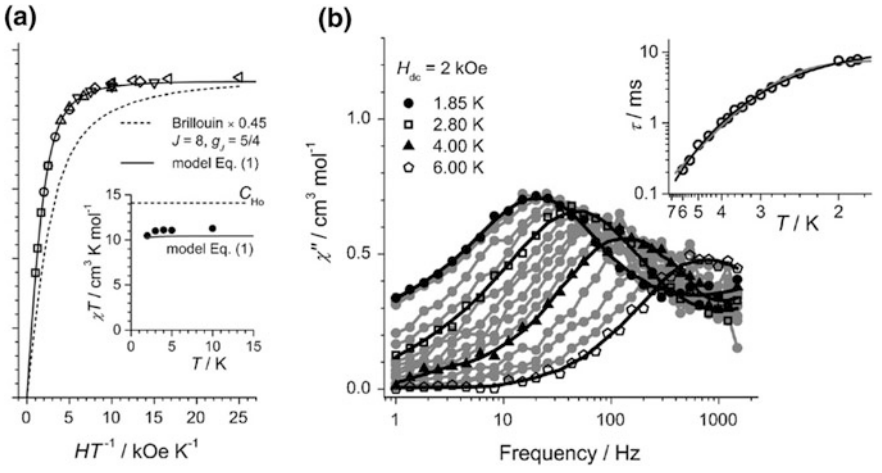

Fig. 11.4 $HoSc_2N@C_{80}$: **a** magnetization curves of $HoSc_2N@C_{80}$ sample. Clearly, the data do not fit a Brillouin function as expected from an isotropic $^5I_8$ Hund ground state of Ho^{3+}. This indicates strong magnetic anisotropy. **b** Alternating current (ac) susceptibility measurements, where the imaginary part χ indicates single-molecule magnetism. The Arrhenius plot in the *inset* indicates for temperatures below 2 K magnetization tunneling times in the order of 8 ms. Adopted from [20]

11.2.2 Polynuclear Endohedral Single-Molecule Magnets

Figure 11.5 displays magnetization curves from the complete dysprosium–scandium endofullerene series $Dy_nSc_{3-n}N@C_{80}$ ($n \in \{1, 2, 3\}$ recorded at 2 K using SQUID magnetometry. As in the case of the single-ion complex $n = 1$, an x-ray absorption characterization was performed for $n = 2$ and $n = 3$ using XMCD to confirm that the detected magnetism of the sample originates from the endohedral Dy ions. The significant difference in the shape of the detected hystereses demonstrates how strongly the endohedral moments interact. Noticeably, there is large remanence for $n = 2$, as compared to a sharp drop in the magnetization at low fields for $n = 1$ and a narrow hysteresis with vanishing zero-field magnetization for $n = 3$. The distinct shape and zero-field behavior is a direct consequence of the magnetic interaction between the endohedral dysprosium ions for $n \in \{2, 3\}$.

The zero-field behavior can be understood by recalling that the n moments of the ground state multiplets are strongly anisotropic and align with the Dy–N ligand field. Under this condition, the magnetic interactions in the ground state are described by a noncollinear Ising model with n pseudospins that can take two orientations, parallel or antiparallel to the corresponding Dy–N axis. The pseudospin picture leads to 2^n magnetic configurations, divided into $2^{(n-1)}$ doublets, where in zero field each doublet consists of two degenerate and time reversal symmetric states with opposite magnetization, see Fig. 11.5b. In the case of $n = 1$,

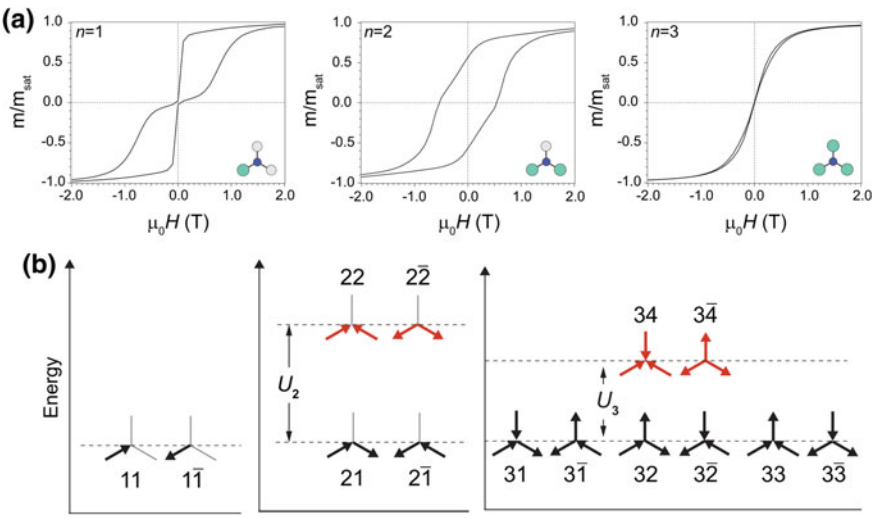

Fig. 11.5 **a** Hysteresis curves for **1–3** recorded using SQUID magnetometry at 2 K with a field sweep rate of 0.8 mTs^{-1}. **b** Ground state magnetic structure for $Dy_nSc_{3-n}N@C_{80}$ based on 2^{n-1} ferromagnetically coupled time reversal symmetric doublets (n, ±d) for $n = 1$–3, where d is the doublet index. The energies U_2 and U_3 are the exchange and dipole barriers for 2 and 3, respectively. Adopted from [19]

no intramolecular interaction occurs. At zero field, the magnetic moment tunnels through the barrier that separates the two states of opposite magnetization. The efficient demagnetization through quantum tunneling of the magnetization (QTM) is clearly seen in the abrupt jump in the magnetization when approaching $\mu_0 H = 0$ T.

11.2.2.1 $Dy_2ScN@C_{80}$

When adding a second Dy ion to the endohedral cluster, the exchange and dipolar coupling of the two moments results in two non-degenerate doublets; a ferromagnetically coupled and an antiferromagnetically coupled one (see Fig. 11.5b).

While the dipolar coupling, which for the given endohedral geometry of an equilateral triangle with 0.36 nm sides and a 10 μ_B moment is in the order of 0.4 meV, is always ferromagnetic, the exchange may be ferromagnetic or antiferromagnetic. The net coupling strength may be extracted from the magnetization curves and turns out to be 1 meV and ferromagnetic [19]. In contrast to the single-ion complex ($n = 1$), no single-tunneling path connects the two time reversal symmetric ground states. This explains the remanence: A magnetization reversal in the di-dysprosium case requires a simultaneous tunneling of the magnetic moments on both dysprosium sites, or crossing of the exchange and dipole barrier of 1 meV that separates the two ground states [19]. Consequently, at low temperatures the system exhibits a blocking of the magnetization that in turn leads to a stabilization of the zero-field magnetization.

As opposed to a ferromagnet, the remanent magnetization in the present case the decay with a time dependent rate τ (see Fig. 11.6a). The nonlinear decay reveals the presence of (at least) two relaxation mechanisms, which has been ascribed to different hyperfine interaction of different Dy isotopes intermolecular [17]. The decay rates for the slower process are displayed in Fig. 11.6b, where a 100 s blocking temperature of about 3.6 K is determined [23]. This 100 s blocking temperature has been determined from the slowest decay constant, and this procedure might not be applicable for other molecules, where extrapolation of the slowest decay channel indicates an initial weight of less than 10% [23]. However, this is among the highest blocking temperatures reported for single-molecule magnets [24–26].

The relaxation times exhibit two temperature regimes, as indicated by the two straight lines. Down to 2 K the relaxation times do not display a temperature independent region, as observed for quantum tunneling of a single moment for $n = 1$. The absence of a quantum tunneling regime is a consequence of the exchange and dipolar coupling of the two moments, where a single- tunneling event is associated with this effective exchange energy. By fitting a sum of two Arrhenius equations to the data, the two energy barriers can be extracted with energies 0.73 and 4.3 meV respectively. The lower barrier ($T < 4$ K) corresponds to the energy gap between the two doublets (Fig. 11.5b). The extracted value of 0.73 meV is in good agreement with the value of 1 meV as determined by a pseudospin analysis of the magnetization curves at 6 K [19]. The second barrier (4.3 meV) is related to

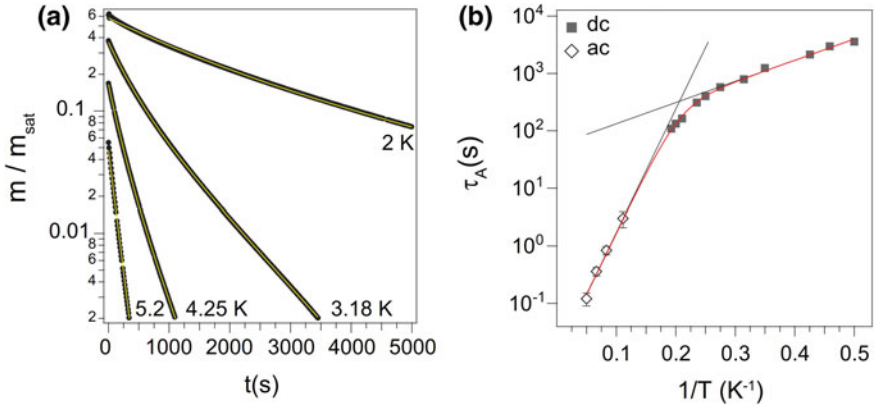

Fig. 11.6 **a** Zero-field relaxation curves for **2** after saturation at $\mu_0 H = 7$ T. *m*sat is the magnetization at 7 T. The *line* corresponds to a fit of a double- ($T < 4.5$ K) and a single- ($T > 4.5$ K) exponential. **b** Corresponding relaxation times for the slower process τA as a function of inverse temperature. *Open symbols* are ac susceptibility results. The *red line* is the best fit of a sum of two Arrhenius equations. Adopted from [19]

relaxation via higher lying excited states. It is worth to be noted that the prefactors of the Arrhenius kinetics are very large compared as to other dysprosium-based SMMs [17, 19].

11.2.2.2 Endohedral SMM's Without Central Nitrogen: $Dy_2TiC@C_{80}$ and $Dy_2TiC_2@C_{80}$

Only recently it was demonstrated that C_{80}-based single-molecule magnets without a central nitrogen ion exist [5]. Figure 11.7 shows magnetic hysteresis for two different isomers of $Dy_2TiC@C_{80}$ and $Dy_2TiC_2@C_{80}$ [5]. The stability of the remnant magnetization can be quantified by determining the temperature at which the zero-field magnetization relaxation time is 100 s, the so-called 100 s blocking temperature (TB100) [23]. For $Dy_2TiC@C_{80}$-I_h T_{B100} is 1.7 K as compared to $T_{B100} = 3.6$ K for $Dy_2ScN@NC_{80}$. The higher T_{B100} value for the nitride cluster-fullerene indicates that the nitride ion in the endohedral cluster is advantageous for longer remanence times. The second isomer $Dy_2TiC@C_{80}$ II has very similar magnetic properties, which indicates that the coordination of the endohedral unit with respect to the cage is of less importance for the magnetism. On the other hand the experimental results assert the central role of the central atom in the endohedral cluster, i.e., nitrogen or carbon. This is further emphasized by the significantly different remanence of $Dy_2TiC_2@C_{80}$ where two carbon atoms share the center.

This new handle for tailoring endohedral fullerenes may not be underestimated, since the isolation of $Dy_2TiC@C_{80}$-I_h is much simpler that that of $Dy_2ScN@C_{80}$-I_h, and it can be expected that the change of the central ionic unit will give new insight on the superexchange mechanism that couples the two Dy ions.

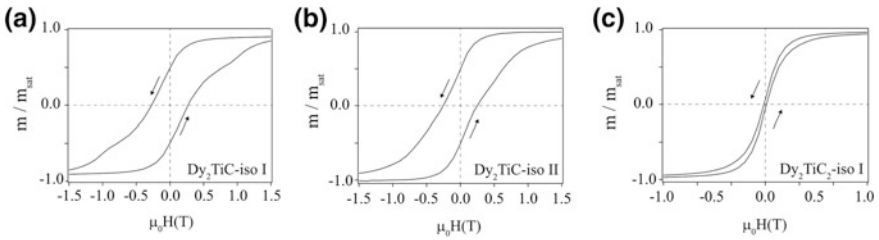

Fig. 11.7 Hysteresis curves for three different TiC-based C_{80} endohedral single-molecule magnets recorded at 1.8 K with a field sweep rate of 5 mT s^{-1}. **a** $Dy_2TiC@C_{80}$ isomer I, **b** $Dy_2TiC@C_{80}$ isomer II **c** $Dy_2TiC_2@C_{80}$, note the different scale of the magnetic field. Adopted from [5]

11.2.2.3 $Dy_3N@C_{80}$

The narrow hysteresis and vanishing zero-field magnetization for $n = 3$ makes it the softest single-molecule magnet of the three. The poor bistability of the three dysprosium moments can be understood by considering a situation where the endohedral ions sit on the corners of an equilateral triangle. The fact that the system exhibits a paramagnetic response to the external field indicates that the three moments are ferromagnetically coupled. For any given pair of ferromagnetically coupled moments, the energy of the system is independent of the orientation of the third, leading to a sixfold degenerate ground state (Fig. 11.5b). This situation is analogous to the textbook case of magnetic (geometric) frustration in an antiferromagnetically coupled isotropic system, where three spins cannot be pairwise antialigned. As in the case of the single-ion complex, there is a single-tunneling path connecting the different ground state configurations, thereby allowing for an efficient demagnetization of the system. Magnetic frustration may thus play a crucial role in the suppression of magnetic blocking in single-molecule magnets.

11.2.3 Endohedral Single-Molecule Magnets on Surfaces

The magnetic bistability and the quantum nature of the molecular spin, make SMMs promising systems for application in spintronics, quantum computing, and high-density storage [27, 28]. A fundamental prerequisite for engineering molecule-based devices is that the magnetic anisotropy and bistability remain unchanged as the molecules are deposited onto substrates or integrated into different device architectures. Creating a stable macrospin in an assembly of nanomagnets will additionally require an ordering of the molecules by, e.g., self-assembly on different surfaces. Deposition of SMMs on reactive surfaces, such as ferromagnetic metals relies on in situ preparation under ultra high vacuum (UHV). In contrast to most SMMs, the endofullerenes discussed in this chapter are particularly stable, survive sublimation and may be easily imaged and manipulated with scanning probes [29–32]. The carbon cage protects the encapsulated magnetic ions from environmental effects.

The structure of $Dy_3N@C_{80}$ on Cu(111) has been studied in great detail by means of scanning tunneling microscopy and resonant x-ray photoelectron diffraction [32]. Figure 11.8 shows a scanning tunneling (STM) image of a monolayer of $Dy_3N@C_{80}$ on Cu(111). While it was not possible to look inside the C_{80} cages with STM, resonant x-ray photoelectron diffraction revealed a preferential orientation of the endohedral clusters parallel to the Cu(111) surface.

As it is shown in the following section, x-ray absorption experiments provide direct insights into the arrangement of the endohedral clusters. The anisotropic charge distribution in the 4f shell allows for the determination of its preferential orientation by comparison of x-ray absorption at different angles, and the corresponding dichroism provides magnetic information. Angle-scanned x-ray absorption spectroscopy (XAS) is thus providing a tool for determining the structural and magnetic anisotropies of highly diluted systems deposited onto surfaces [33]. Figure 11.9a shows the x-ray absorption spectrum from a low coverage of $Dy_2ScN@C_{80}$ on a Rh(111) surface as a function of the angle between the surface normal and the x-ray beam. The density of molecules on the surface is half of a single-molecule thick film (0.5 ML). The angle dependence of the Dy multiplet spectra is a direct fingerprint of an anisotropic 4f orbital charge distribution due to a preferential orientation of the Dy bonds in the system. This effect would not be present for an isotropic distribution of the encaged Dy_2ScN units and, for this reason, indicates an ordering of the endohedral cluster with respect to the surface. The direction of the Dy–N bonds can be determined by comparing the experimental spectra with multiplet calculations performed with the x-ray beam and an external magnetic field applied parallel (I_z), and perpendicular (I_x) to the Dy–N bond. In the present case is the resemblance between the calculated (I_x) spectrum and data measured at normal incidence ($\theta = 0$) in Fig. 11.9b indicates that the endohedral units adopt an orientation parallel to the surface.

Whereas the angle dependence of XAS provides structural information on the system, the corresponding XMCD spectra probe the magnetic anisotropy.

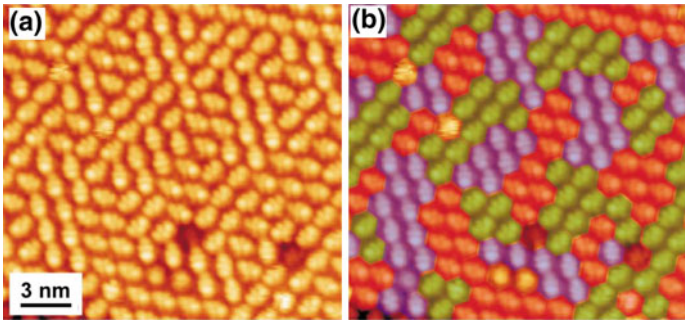

Fig. 11.8 **a** Low temperature scanning tunneling microscopy zoom into a monolayer of $Dy_3N@C_{80}$ on Cu(111). The data show intramolecular orientation and indicate different very small domains (see color coding in the *right panel*). From Ref. [32]

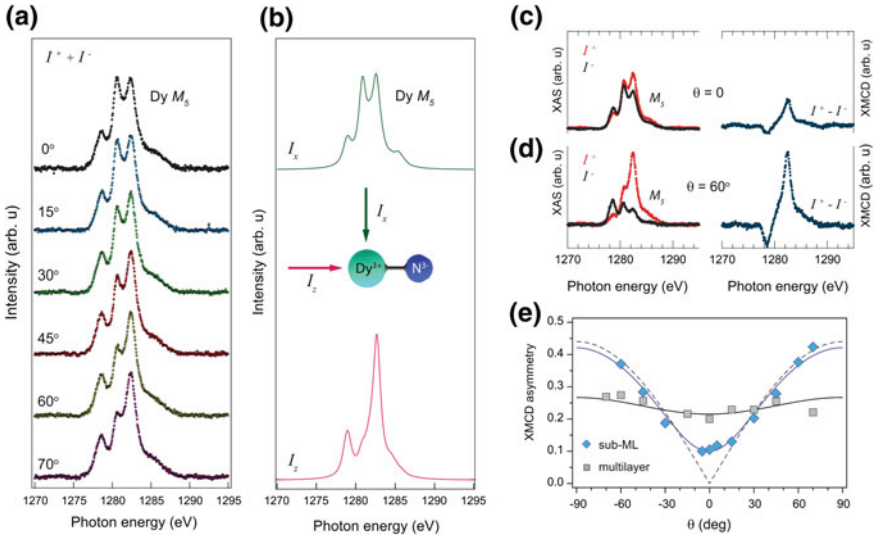

Fig. 11.9 **a** X-ray absorption spectroscopy (XAS) data measured at the Dy M_5 edge from a sub-ML of $Dy_2ScN@C_{80}$/Rh(111) $T \approx 4$ K, $\mu_0 H = 6.5$ T. Each data set is normalized to the integrated intensity. **b** Calculated absorption with the x-ray beam and external field oriented parallel *Iz,* and perpendicular *Ix*, to the magnetic easy axis (Dy–N bond). **c** Polarization dependent XAS spectra (*left panel*), and the corresponding XMCD spectra (*right panel*), measured at an incidence angle of $\theta = 0°$ **c** and $\theta = 60°$ **d**. **e** Angle dependence of the integrated XMCD signal normalized to the integrated XAS over the Dy M_5 edge. The *dashed line* corresponds to the expected angle dependence for magnetic moments oriented parallel to the surface, whereas the *blue line* takes into account a Gaussian distribution, centered in the surface plane and with a standard deviation of 16°. Adopted from [33]

The magnitude of the XMCD signal is determined by the projection of the magnetic moment of the absorbing dysprosium ion onto the direction of the impinging x-rays [33]. For an isotropic system, where the magnetic moments are either randomly distributed or aligned to the external magnetic field, the XMCD signal is independent of the incidence angle. For the sub-ML system, a significant angle dependence is observed (Fig. 11.9c–d) which indicates a macroscopic magnetic anisotropy. The magnetic anisotropy can be further quantified by measuring the XMCD signal for several incidence angles. The angle dependence in Fig. 11.9e demonstrates that the dysprosium moments are indeed predominantly oriented parallel to the surface, with a small out-of-plane fraction inferred by the nonvanishing dichroism at normal incidence. The magnetic ordering is directly related to the strong axial anisotropy of the individual Dy ions and the preferred adsorption geometry of the endohedral cluster imposed by the surface. Also shown in Fig. 11.9e is the corresponding measurement on a system with seven times more molecules (3.5 ML). The weak angular anisotropy is attributed to the residual influence of the surface indicating that the endofullerenes above the first molecular layer do not interact as strongly with the substrate. The multilayer data are thus representative for the bulk phase.

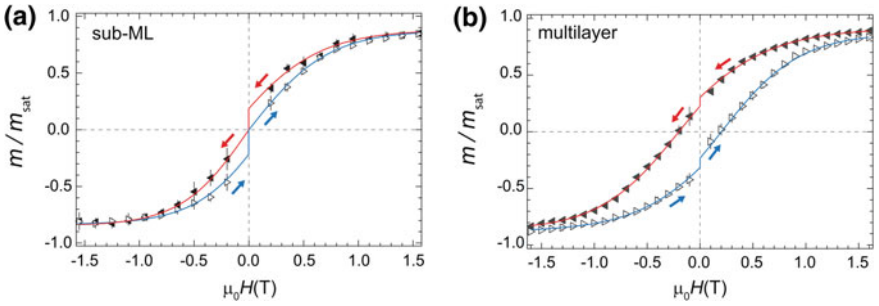

Fig. 11.10 Hysteresis curves measured from a multilayer and a sub-ML of $Dy_2ScN@C_{80}$ on Rh (111) at a magnetic field sweep rate of 2 T/min and a sample temperature of $\sim$4 K. The x-ray flux was 5×10^{10} photons/mm^2/s. The data were recorded with the x-ray beam and the magnetic field at an incidence angle of $\theta = 60°$. The magnetization curves correspond to the average of several independent measurements, where the error bars are the standard deviation at each external magnetic field setting. The *arrows* indicate the ramping direction of the magnetic field, the lines are guides to the eye, and *m*sat is the saturated value at $\pm$6.5 T. The drop in magnetization at zero field is a consequence of the time of 30 s it takes for the magnet to switch polarity. Adopted from [33]

For a fixed temperature and magnetic field sweep rate, the opening of the hysteresis can be taken as a measure of the relaxation times in the system. Comparing the magnetization curves for the two systems thus allows the determination of the influence of the metal substrate. Figure 11.10 shows element specific magnetization curves from the Dy M_5 edge at a field sweep rate of 2 T/min with the x-rays and the magnetic field at an angle of 60° with respect to the surface normal. For bulk samples of $Dy_2ScN@C_{80}$, a significant remanence and coercive field are found (Fig. 11.5a). This is also observed in the multilayer system, where the drop in magnetization at zero field is attributed to the delay of 30 s when changing the polarity of the magnet. From the 25% decrease in magnetization during these 30 s, we derive a remanence relaxation time of 110 s in the multilayer system. Compared to bulk samples measured "in the dark" with SQUID (Fig. 11.6b), this is about four times faster and mainly related to the x-ray induced demagnetization [18].

The much narrower hysteresis for the sub-ML indicates that the magnetic bistability is modified by the proximity of the rhodium surface. From the ratio of the hysteresis openings for the two systems, we obtain a four times faster relaxation rate in the sub-ML and a remanence time under x-ray irradiation at 4 K of about 30 s.

References

1. Kroto HW, Heath JR, O'Brien SC et al (1985) C_{60}—Buckminsterfullerene. Nature 318 (6042):162–163
2. Nakao K, Kurita N, Fujita M (1994) Ab-initio molecular-orbital calculation for C_{70} and seven isomers of C_{80}. Phys Rev B 49(16):11415–11420
3. Stevenson S, Rice G, Glass T et al (1999) Small-bandgap endohedral metallofullerenes in high yield and purity. Nature 401(6748):55–57

4. Svitova AL, Ghiassi K, Schlesier C et al (2014) Endohedral fullerene with μ_3-carbido ligand and titanium-carbon double bond stabilized inside a carbon cage. Nat Commun 5:3568
5. Junghans K, Schlesier C, Kostanyan A et al (2015) Methane as a selectivity booster in the arc-discharge synthesis of endohedral fullerenes: selective synthesis of the single-molecule magnet $Dy_2TiC@C_{80}$ and Its congener $Dy_2TiC_2@C_{80}$. Angew Chem-Int Edit Engl 54(45): 13411–13415
6. Rinehart JD, Long JR (2011) Exploiting single-ion anisotropy in the design of f-element single-molecule magnets. Chem Sci 2(11):2078–2085
7. Shu C, Corwin FD, Zhang J et al (2009) Facile preparation of a new gadofullerene-based magnetic resonance imaging contrast agent with high 1H relaxivity. Bioconjugate Chem 20(6): 1186–1193
8. Náfrádi B, Antal Á, Pásztor Á et al (2012) Molecular and spin dynamics in the paramagnetic endohedral fullerene $Gd_3N@C_{80}$. J Phys Chem Lett 3:3291–3296
9. Svitova AL, Krupskaya Y, Samoylova N et al (2014) Magnetic moments and exchange coupling in nitride clusterfullerenes $Gd_xSc_{3-x}N@C_{80}$ (x = 1-3). Dalton Trans 43:7387–7390
10. Tiwari A, Dantelle G, Porfyrakis K et al (2008) Magnetic properties of $ErSc_2N@C_{80}$, $Er_2ScN@C_{80}$ and $Er_3N@C_{80}$ fullerenes. Chem Phys Lett 466:155–158
11. Zuo T, Olmstead MM, Beavers CM et al (2008) Preparation and structural characterization of the I_h and the D_{5h} isomers of the endohedral fullerenes $Tm_3N@C_{80}$: icosahedral C_{80} cage encapsulation of a trimetallic nitride magnetic cluster with three uncoupled Tm^{3+} Ions. Inorg Chem 47(12):5234–5244
12. Wolf M, Muller KH, Eckert D et al (2005) Magnetic moments in $Ho_3N@C_{80}$ and $Tb_3N@C_{80}$. J Magn Magn Mater 290:290–293
13. Wolf M, Muller KH, Skourski Y et al (2005) Magnetic moments of the endohedral cluster fullerenes $Ho_3N@C_{80}$ and $Tb_3N@C_{80}$: the role of ligand fields. Angew Chem-Int Edit 44(21):3306–3309
14. Sessoli R, Gatteschi D, Caneschi A et al (1993) Magnetic bistability in a metal-ion cluster. Nature 365(6442):141–143
15. Gatteschi D, Sessoli R, Villain J (2006) Molecular nanomagnets. Oxford University Press, New York
16. Ishikawa N, Sugita M, Ishikawa T et al (2003) Lanthanide double-decker complexes functioning as magnets at the single-molecular level. J Am Chem Soc 125:8694–8695
17. Westerström R, Dreiser J, Piamonteze C et al (2012) An endohedral single-molecule magnet with long relaxation times: $DySc_2N@C_{80}$. J Am Chem Soc 134(24):9840–9843
18. Dreiser J, Westerström R, Piamonteze C et al (2014) X-ray induced demagnetization of single-molecule magnets. Appl Phys Lett 105(3):032411
19. Westerström R, Dreiser J, Piamonteze C et al (2014) Tunneling, remanence, and frustration in dysprosium-based endohedral single-molecule magnets. Phys Rev B 89(6):060406
20. Dreiser J, Westerström R, Zhang Y et al (2014) The metallofullerene field-induced single-ion magnet $HoSc_2N@C_{80}$. Chem-Eur J 20(42):13536–13540
21. Vieru V, Ungur L, Chibotaru LF (2013) Key role of frustration in suppression of magnetization blocking in single-molecule magnets. J Phys Chem Lett 4(21):3565–3569
22. Cimpoesu F, Dragoe N, Ramanantoanina H et al (2014) The theoretical account of the ligand field bonding regime and magnetic anisotropy in the $DySc_2N@C_{80}$ single ion magnet endohedral fullerene. Phys Chem Chem Phys 16:11337–11348
23. Westerström R, Popov A, Greber T (2015) An operational definition of the 100 second blocking temperature T_{B100} for single molecule magnets. arXiv:150603657
24. Rinehart JD, Fang M, Evans WJ et al (2011) Strong exchange and magnetic blocking in N_2^{3-}-radical-bridged lanthanide complexes. Nat Chem 3(7):538–542
25. Rinehart JD, Fang M, Evans WJ et al (2011) A N_2^{3-} radical-bridged terbium complex exhibiting magnetic Hysteresis at 14 K. J Am Chem Soc 133(36):14236–14239
26. Le Roy JJ, Ungur L, Korobkov I et al (2014) Coupling strategies to enhance single-molecule magnet properties of erbium-cyclooctatetraenyl complexes. J Am Chem Soc 136(22):8003–8010

27. Leuenberger MN, Loss D (2001) Quantum computing in molecular magnets. Nature 410(6830):789–793
28. Bogani L, Wernsdorfer W (2008) Molecular spintronics using single-molecule magnets. Nat Mater 7(3):179–186
29. Butcher MJ, Nolan JW, Hunt MRC et al (2003) Adsorption and manipulation of endohedral and higher fullerenes on Si(100)-2x1. Phys Rev B 67(12):125413
30. Huang T, Zhao J, Feng M et al (2012) A multi-state single-molecule switch actuated by rotation of an encapsulated cluster within a fullerene cage. Chem Phys Lett 552:1–12
31. Yasutake Y, Shi ZJ, Okazaki T et al (2005) Single molecular orientation switching of an endohedral metallofullerene. Nano Lett 5(6):1057–1060
32. Treier M, Ruffieux P, Fasel R et al (2009) Looking inside an endohedral fullerene: inter- and intramolecular ordering of $Dy_3N@C_{80}$ (I_h) on Cu(111). Phys Rev B 80:081403
33. Westerström R, Uldry A-C, Stania R et al (2015) Surface aligned magnetic moments and hysteresis of an endohedral single-molecule magnet on a metal. Phys Rev Lett 114:087201

Chapter 12
Nonmetallic Endofullerenes and the Endohedral Environment: Structure, Dynamics, and Spin Chemistry

Ronald G. Lawler

Abstract Over the past two decades, nonmetallic endohedral fullerenes containing most of the noble gases and several small molecules have been prepared from C_{60} and a few other closed- and open-cage fullerenes and isolated in sufficient quantities and purity to be characterized by a variety of spectroscopic and other physical methods. Of particular interest has been determining the effects of encapsulation on the properties both of the cage and of the trapped atom or molecule. Nuclear magnetic resonance, which is independent of the optical properties of the fullerene or the medium, and often insensitive to impurities, has revealed many details of the structure and dynamics of the intracage environment. Low-temperature infrared spectroscopy at both long and short wavelengths, inelastic neutron scattering (INS), and low-temperature solid-state NMR have been used to study the coupled translation–rotation of H_2 and H_2O molecules trapped in C_{60}. Special attention has been paid to detecting, enriching, and monitoring the stability of the *para* and *ortho* nuclear spin–rotational isomers of H_2 and H_2O in the endohedral environment with a view toward using the fullerene cage as a "bottle" for storing or releasing the isomers in condensed media under controlled conditions.

12.1 Introduction

The study of atoms and molecules in confined spaces has a long history. It includes small chemical species trapped in clathrates [1], in frozen rare gases [2] or other inert matrices or inert solvents [3], and has now been extended into the burgeoning field of supramolecular chemistry [4, 5].

Fullerene molecules represent the most recent entry into the field of guest–host chemistry involving atoms and small molecules. Interest in hydrogen storage,

R.G. Lawler (✉)
Department of Chemistry, Brown University, Providence, RI 02912, USA
e-mail: ronald_lawler@brown.edu

A.A. Popov (ed.), *Endohedral Fullerenes: Electron Transfer and Spin*,
Nanostructure Science and Technology, DOI 10.1007/978-3-319-47049-8_12

for example, has led to studies of molecular hydrogen trapped in a crystalline C_{60} matrix [6]. Most notable, however, has been the rapid development of studies of atoms and small molecules encapsulated in fullerene cages or partially opened structures formed by chemically modifying the now readily available C_{60} and C_{70} fullerides.

This chapter will deal with examples of nonmetals trapped in fullerene cages. The emphasis will be on reviewing the progress that has been made in determining the extent to which encapsulation modifies the properties of both the trapped species and the cage. Special attention will be paid to the role that nuclear, electron, and rotational spin effects have been revealed by a variety of spectroscopic methods.

In general, host–guest interactions may be either strong or weak. In the former category are hydrogen-bonded molecules or organometallic coordination complexes. Although hydrogen bonding does not seem to play a role in the endofullerenes studied to date, the majority of endohedral metallofullerenes might be described as "inside-out" coordination complexes. In contrast, this chapter will deal only with the properties of endofullerenes in which the interaction between host and guest is due primarily to van der Waals forces or other weak interactions. As we will see, in most examples, the effect of the encapsulated atom or molecule on the properties of the host, or "cage", is small but detectable. Subtle changes in the properties of guest molecules also occur and in many cases may be measured with impressive precision, primarily because of the high resolution of the some of the techniques that can now be applied to atoms and small molecules in condensed phases.

Coverage will be confined to endofullerenes that have been prepared in large enough quantities and sufficient purity to be investigated by techniques applicable to liquid solutions or the solid phase. It should be noted, however, that in many cases, the existence of an endofullerene was shown by mass spectrometry before its successful isolation or synthesis in macroscopic amounts; and there are others, like $N_2@C_{60}$ and $N_2@C_{70}$ that seem to have been separated by chromatography but for which little other information is yet available [7, 8]. There is, however, indirect evidence that N_2 can be incorporated into an open-fullerene [9].

A list of weakly interacting endohedral species so far studied includes the noble gases, atomic nitrogen and phosphorus, several small molecules, most notably H_2 and H_2O, and, for completeness, muonium, for which some evidence exists for a weak perturbation by encapsulation. The most studied hosts have been C_{60} and C_{70}. These, as well as elemental carbon, have been the starting materials for producing many of the atomic and endohedral metallofullerenes by a variety of energetic techniques that bring the atom and cage together rather violently. This method has not been successful, however, for the synthesis of useful amounts of molecular endofullerenes because the conditions required tend to destroy the molecular precursors. Fortunately, the advent of the "molecular surgery" approach [10] to endofullerene syntheses has now made available an array of open-fullerene hosts with varying sizes of openings into which it has now proven possible to insert and study spectroscopically CO, CH_4, NH_3, and HF. Noted only briefly in later sections

are a variety of derivatives of endofullerenes prepared by methods developed earlier for functionalizing the empty fullerene cages. Also not explicitly discussed are a few examples of single atoms trapped in the higher fullerenes that have played such a large role in the development of endohedral metallofullerene chemistry.

The presentation is organized according to the type of measurement that has been employed to characterize the series of nonmetallic endofullerenes.

12.2 Effects of Guests on Host Cage Properties and Guest/Host Communication

12.2.1 Separation of Filled and Unfilled Fullerenes

The most common evidence that an endo molecule is able to affect the properties of the cage is the ability to separate the filled and empty cages by chromatography or other techniques [7, 8, 11–17]. The mechanism for transmission of the intracage interaction to the outside of the cage probably involves either slight alteration of the electron distribution on the surface of the cage [18] or, in the case of dipolar or highly polarizable guests like H_2O or xenon, possibly direct interaction with the external medium through the wall of the cage.

12.2.2 Equilibrium and Rate Effects

A detailed study [18] of the equilibration of Xe@C_{60} and He@C_{60} with 9,10-dimethylanthrancene to form the Diels–Alder adduct was carried out using ^{129}Xe and ^{3}He NMR to monitor the relative amounts of adduct and free endofullerene. Assuming the trapped He has a negligible effect on the equilibrium constant, the results showed that adding Xe to C_{60} increases both ΔH and ΔS for the reaction, making the addition reaction less exothermic but with a smaller entropy loss. This was interpreted as an indication that the Xe atom changes the electronic structure of the cage by "pushing the fullerene electrons outward". The conclusion is supported by SCF and MP2 calculations.

There seems so far to have been no report comparing the chemical reactivity of H_2@C_{60} or H_2O@C_{60} with C_{60} other than qualitative observations that the product yields and isomer distributions from reactions of both molecular endofullerenes are similar to those obtained from pristine C_{60} [16, 19, 20]. However, the equilibrium between dimethylanthracene and C_{70} encapsulating one and two H_2 molecules has been studied [21]. A small difference in equilibrium constant between H_2@C_{70} and $(H_2)_2$@C_{70} was attributed to an increase in the electron density on the surface of the cage by pressure in the more crowded interior of the doubly occupied endofullerene.

Several reports deal with rates and equilibria involving processes involving atoms or molecules within the cage or between the cage interior and the outside medium. The rate and equilibrium constant for exchange of water between the interior of an open-fullerene and the surrounding solvent has been found to correlate with the polarity of the solvent [22]. As expected, increasing solvent polarity favors external water. Water exchange between the solvent and the space within an open-fullerene may also be detected by rapid deuterium exchange with added D_2O or saturation transfer between NMR peaks of the two sites by selective irradiation [23].

An early measurement [24] of He escape rates from an open-fullerene were measured by monitoring the intensity of the ^{3}He NMR signal from the endofullerene relative to an added $^3He@C_{60}$ standard. The activation energy barrier agreed very well with *ab initio* calculations but the activation entropy for escape was unexpectedly negative. The negative entropy for the rate of escape was attributed to constriction of the He atom relative to the interior as it passed the orifice of the open cage. Measurements of H_2 escape rate using ^{1}H NMR were made for H_2 in an open-fullerene [25] and a negative entropy of activation also observed.

Exit rates of encapsulated H_2 from a series of open-fullerenes with variable size openings have been measured by monitoring the loss of the NMR peak from encapsulated H_2 [26]. It is found that the rate increases linearly with the area of the opening. The rate and equilibrium constant for escape of He from one of the open-fullerenes were measured by ^{3}He NMR [27]. The activation energy for He escape is substantially lower than that for H_2. The equilibrium constant is found to be nearly independent of temperature, consistent with a low enthalpy change upon encapsulation predicted by theory [28]. The qualitative interpretation of this result is that the energy of the helium atom is about the same in the solvent and in the fullerene host even though the barrier to escape is substantial.

The successful incorporation of two endofullerene species in the larger cages [25, 29] raises the question of the rate of intracage exchange of the two species. It is found that two H_2 molecules in an open-fullerene derived from C_{70} occupy magnetically nonequivalent sites [25]. The NMR peaks, however, exhibit line broadening and coalescence as the temperature is raised to room temperature. The exchange process occurs with activation enthalpy and entropy of ca 8 kcal/mol and −6 cal/mol-K, respectively. The asymmetric C_{70} cage produced by Diels–Alder addition of 9,10-dimethylanthracene to $(H_2)_2@C_{70}$, that should also have nonequivalent H_2 sites, exhibits only a single H_2 peak at room temperature or above. Low temperature measurements were not reported. Similarly, the ^{3}He spectrum of an asymmetric cage derived from $(He)_2@C_{70}$ exhibits only a single peak at room temperature [29]. The barrier to exchange between the sites was estimated as 4.5 kcal/mol.

The parent doubly occupied fullerenes, $(He)_2@C_{70}$ and $(H_2)_2@C_{70}$, also exhibit only a single peak under all conditions studied. This is consistent with calculations [30] for $(H_2)_{2@}C_{70}$ that indicate a preferred structure with the H_2 molecules occupying symmetrically equivalent sites with H–H bonds perpendicular to the long axis of the C_{70} and having a "crossed" mutual orientation.

12.2.3 Electrochemistry

In marked contrast to the endohedral metallofullerenes, the presence of entrapped H_2 or H_2O has only a minor effect on the electrochemical properties of the cage. For $H_2@C_{60}$, it is found that the endofullerene becomes progressively more difficult to reduce than empty C_{60} as electrons are added to the cage. The differences reach 0.15 eV at the stage of hexa-anion formation. This is attributed to an electron repulsion effect of the endohedral hydrogen on the π-electrons of the cage [16].

Cyclic voltammetry of $H_2O@C_{60}$ yielded an irreversible oxidation curve and four quasi-reversible reduction curves that were indistinguishable from those of empty C_{60} under the same conditions. Higher reduction potentials were not explored [17].

Electrochemical reduction of pure samples of the noble gas endofullerenes seems not to have been reported so far. Charge exchange experiments on $Ar@C_{60}$, however, led to the conclusion [12] that the energy required to produce $Ar@C_{60}^+$ lies between 7.53 and 7.8 eV, a range that includes the 7.65 eV ionization potential of C_{60} [31]. The authors note that this contrasts, for example, with the significantly lower ionization potential of 6.3 eV for $La@C_{60}$.

12.2.4 Photochemistry

12.2.4.1 UV/Vis

All of the atoms and small molecules that have been encapsulated in C_{60} or other closed fullerenes are transparent in the UV/Vis region. Any changes in spectrum therefore are a result of perturbations of the electronic structure of the cage. In the most definite example of such a perturbation, it is found that the lowest excited singlet state of $Kr@C_{60}$ is shifted to lower energy relative to C_{60} by 45 cm^{-1} with negligible change in intensity. This is interpreted as an indication of a weak interaction of Kr with the cage but retention of I_h symmetry in the endofullerene [13]. On the other hand, it has been noted that the UV/Vis spectrum of $H_2@C_{60}$ is "the same as that of empty C_{60}" [16].

12.2.4.2 Triplet Lifetime

Another indication that the π-electrons of the fullerene cage may be perturbed by a guest is the lifetime of an electronically excited state. It is found, for example, that the triplet decay rate of the C_{60} host is accelerated by 12% at 77 K by encapsulated Kr [13]. This is attributed to an "endohedral heavy atom effect" by the krypton atom. More dramatically, the triplet decay rate is accelerated by a factor of 22 in

$N@C_{60}$ [32, 33]. On the other hand, it was found that the triplet lifetimes of C_{60}, $H_2@C_{60}$ and $D_2@C_{60}$ do not differ significantly [34].

12.2.4.3 $^1O_2$ Sensitization

Despite the absence of a significant effect of guest H_2 or D_2 on the triplet lifetime of C_{60}, it was discovered that the endofullerenes catalyze the conversion of singlet oxygen to the ground state triplet more efficiently than empty C_{60} [34]. Furthermore, the quenching rate of $H_2@C_{60}$ exceeds that of $D_2@C_{60}$ by a factor of three and both endofullerenes are significantly more effective quenchers than H_2 or D_2 in solution or the gas phase. It was suggested that the enhanced effect relative to free hydrogen may arise from formation of an exciplex between the fullerene and $^1O_2$. The isotope effect is consistent with vibrationally assisted intersystem crossing that is made more effective by the higher frequency motion associated with encapsulated H_2 relative to D_2.

12.2.5 Mechanical Properties—Negative Thermal Expansion Coefficients

The effect of an endohedral species on the lattice parameters of solid C_{60} is of interest because of the superconductivity observed for doped C60 [35]. This has prompted an EXAFS study at the Ar K-edge in $Ar@C_{60}$ to probe the change in cage diameter with temperature [36]. It is found that the average Ar-C distance *decreases* with temperature. This finding is discussed within the context of other compounds which exhibit negative thermal expansion. It is suggested that "buckling" of the C_{60} surface produced by small shifts in average bond distances may produce the effect. Far infrared spectroscopy was used to compare changes in cage vibrational frequencies with temperature in $Kr@C_{60}$ and pristine C_{60} [37]. Small, but significant, changes are observed and interpreted to suggest "a modest guest–host interaction and a slight modification of the encapsulant/cage interaction".

12.2.6 X-ray Diffraction

The structures of a few nonmetallic endofullerenes have been determined by diffraction methods. Most notable is the detection [38] of the encapsulated He atom in the complex $He@C_{60}{\cdot}(NiOEP)_2$. This is claimed to be the first report of the observation of a helium atom using single-crystal X-ray analysis. It followed the successful location of Kr in a 9% filled sample of $Kr@C_{60}{\cdot}(NiOEP)_2$ [39]. The position was also found using EXAFS at the Kr K-edge on a 99% pure sample [40].

In both cases, the Kr-C distance was found to be similar to the sum of the Kr and C van der Waals radii leading to the conclusion that the Kr atom is tightly confined within the cage. The electron density of a rotationally disordered $Ar@C_{60}$ sample was calculated from powder X-ray patterns assuming a spherical electron density for the C_{60} cage [41].

The H_2O molecule encapsulated in the analogous complex $H_2O@C_{60}{\cdot}(NiOEP)_2$ was easily located by X-ray diffraction [17]. Detection of H_2 by X-ray diffraction seems so far to be limited to an open-fullerene synthetic intermediate [42], where the H_2 molecule is shown to be embedded well down inside the π-electron system of the cage.

As expected, in all of examples of C_{60} guests, the encapsulated atom or molecule was unambiguously located at the center of the C_{60} cage. It should be noted, however, that molecular dynamics simulations of radial distributions of noble gases in C_{60} [43] find that in all cases the most probable position is away from the center. This suggests that X-ray diffraction or other techniques so far used to probe the location of the endo species are detecting spatial or time averages.

12.2.7 Vibrational Spectra

It has been noted that the frequencies of four IR active modes of C_{60} and $H_2O@C_{60}$ are identical to within a fraction of a wavenumber [17]. A detailed study of the IR and Raman spectra of $Ar@C_{60}$ and $Kr@C_{60}$, however, found significant shifts to both higher and lower frequencies, the shifts increasing in magnitude with the size of the endo atom [44]. The results were analyzed in terms of a model invoking subtle changes in van der Waals and vibronic interactions. They were in good agreement with ab initio numerical experiments with DFT and MP2 procedures. In contrast, an earlier IR measurement on $Kr@C_{60}$ [13] found a positive shift of the three detected IR active modes. No explanation was given.

A shift to higher frequency by 1 cm^{-1} in one of the cage vibrations was observed in the IR of a sample of $H_2@C_{60}$ taken at room temperature [16]. This was interpreted as evidence for a slight repulsive interaction between the cage and the inner molecule.

The allowed infrared transitions of $H_2O@C_{60}$ in the frequency range near the symmetric and asymmetric stretching modes of the H_2O molecule do not overlap with cage vibrational frequencies and should in principle be observable. Nevertheless they are reported to be too weak to observe in ordinary samples [17]. It has been suggested that the transition intensities are weakened by the shielding effect of the H_2O dipole by the carbon cage [45]. Calculations based on instantaneous vibrational analysis predict a shift of the symmetric stretch to higher frequency but little or no shift of the frequency of the asymmetric stretch [45].

Attempts to observe the H–H stretching frequency directly in Raman spectra have so far failed for $H_2@C_{60}$ because of interference from the strong fluorescence of the C_{60} cage [16].

Table 12.1 Change in ^{13}C chemical shift of C_{60} carbon of endofullerenes relative to empty cage

Endo species	$\Delta\delta$ (ppm)	vdW radius (Å)[a]	Lit. ref. for $\Delta\delta$
He	+0.02	1.40	[152]
Ar	+0.17	1.88	[35]
Kr	+0.39	2.02	[13]
Xe	+0.95	2.16	[14]
H_2	+0.078[c]	1.74[b]	[15]
H_2O	+0.11	1.96[b]	[17]
N atom	+0.07[d]	1.55	[32]

[a]van der Waals radii from Bondi [153]. [b]Radius of longest axis, estimated using the Bondi procedure [153]. [c]Somewhat smaller shifts are observed for the carbons in C_{70} containing one or two H_2 molecules [21]. [d]Theoretical estimate. The ^{13}C peak of $N@C_{60}$ is undetectable due to broadening by electron paramagnetism

12.2.8 ^{13}C NMR Chemical Shifts of Cage Carbons

One of the most consistent pieces of evidence for intracage interactions is the consistent small changes in the chemical shift of ^{13}C nuclei in C_{60} and C_{70}. These are summarized for C_{60} in Table 12.1. Values for *endo* H_2, H_2O and a calculated value for the nitrogen atom are also included. A systematic upfield increase in chemical shift is observed as the size of the endohedral noble gas atom is increased. Theory supports the origin of the effect as arising from small distortions of the electron distribution of the carbon lattice [46].

12.2.9 Radical and Triplet State Interactions

There are two reports of the observation of a small hyperfine coupling between the hydrogen molecule and the unpaired electrons on a fullerene cage [47, 48].

ENDOR spectra of H_2 trapped in the radical anion of a derivative of $H_2@C_{60}$ with a fused five-membered ring were compared with the spectra of the empty fullerene radical anion [47]. Detailed comparison of spectra taken over a range of temperatures yielded an isotropic hyperfine coupling of 0.1 MHz and the components of an anisotropic hyperfine tensor. DFT calculations of the hyperfine parameters were in good agreement with experiment. It was also found that at low temperature, the splitting of the ENDOR signal disappeared. This was interpreted to demonstrate electron spin catalysis of the conversion between the *para* ($I = 0$) and *ortho* ($I = 1$) spin states of H_2 which favors the nonmagnetic $I = 0$ state at low temperature. The *ortho–para* conversion time was estimated to be no longer than one hour at 100 K.

Electron spin echo and ENDOR measurements [48] on the excited triplet state of $H_2@C_{60}$ at 20 K yielded values for the proton hyperfine tensor consistent with an elongated cage. The observed values agreed well with the results of density functional theory calculations. Under the conditions used to detect the triplet state, only molecules in the *ortho* ($I = 1$) nuclear spin state could be observed. The spin decoherence time, T_2, of the encapsulated *ortho*-H_2 was measured to be 440 μs at 20 K, a value that corresponds to a nuclear spin relaxation rate ca. 1000 times faster than the related spin-lattice relaxation for H_2 in ground state C_{60} at the same temperature [49]. This is consistent with relaxation enhancement due to dipolar coupling of H_2 nuclei to the unpaired electrons on the surface of the cage.

12.3 NMR Chemical Shift Probes of Internal Magnetic Fields and Aromaticity in the Fullerene Cage

12.3.1 ^{3}He NMR, Aromaticity, and Ring Currents

The first fullerene paper [50] predicted that the three-dimensional aromaticity of the C_{60} cage might give rise to interesting ring current effects that could be probed by chemical shift perturbations in the NMR of nuclei in a guest atom or molecule. In the case of ^{3}He, this proved to be spectacularly successful, in large part because of the early efforts of Martin Saunders and his colleagues at Yale University. The NMR of ^{3}He in $He@C_{60}$ was the first to be studied with sufficiently high resolution to be able to probe the internal field in the fullerene cage [51]. The observed upfield shift of 6 ppm relative to external ^{3}He in the same medium has been the subject of numerous qualitative and quantitative theoretical studies [52–56]. It was shown early that the effect may be explained via the interplay of opposing "ring currents" within the π-system of the cage. It was predicted that the five- and six-membered rings should produce shielding (downfield) and deshielding (upfield) effects, respectively [52, 53]. Despite the larger effect expected to be produced by a five-membered ring, the larger number of six-membered rings in C_{60} (20, compared to 12) produces a net deshielding effect [54]. This explanation is also consistent with the observation that even larger deshielding occurs with ^{3}He in C_{70}, where the relative numbers of six and five members are even larger (25 vs. 12). The model has also been shown to be consistent with the observation that endohedral chemical shifts of ^{3}He observed in the higher symmetrical fullerenes [57–59] are in between those for C_{60} and C_{70}. Even larger shifts are predicted, but so far not observed, for ^{3}He in smaller fullerenes [54].

12.3.2 ^{3}He in Derivatives, Other Closed Fullerenes, and Open-Fullerenes

The extraordinary sensitivity of the ^{3}He chemical shift to the structure of the surrounding π-system has made it a very useful structural label for a variety of closed fullerene derivatives and open-fullerene capsules [60]. The structures of three most commonly used open-fullerenes are shown in Fig. 12.1 and the NMR chemical shifts of nuclei in the endohedral atoms or molecules are given in Table 12.2. It is notable that in most cases, the disruption of the C_{60} π-system by addition of structures or opening of the ring produces additional shielding. This is qualitatively consistent with an increase in the ratio of six- to five-membered ring currents. Similar effects have now been observed using ^{1}H NMR to distinguish isomers in mixtures of derivatives of $H_2@C_{60}$ [61, 62] and $H_2O@C_{60}$ [20].

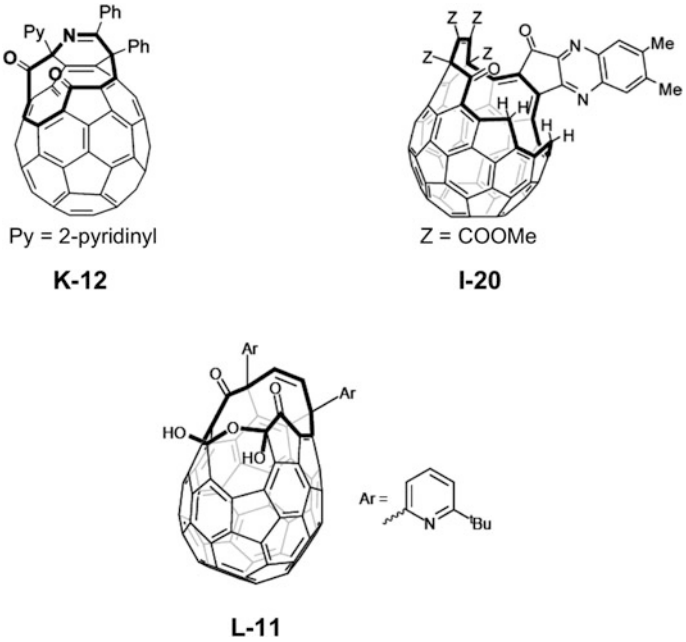

Fig. 12.1 Open-fullerene structures referred to in Table 12.2. The *label number* refers to the number of atoms in the orifice of the cage opening. *Letters* refer to the research group that originally synthesized the structure: *K* "Komatsu" [55], *I* "Iwamatsu" [23], *L* "Levitt" [144]

Table 12.2 Chemical shift changes of nuclei in encapsulated atoms and molecules

Endo species	Fullerene	$\Delta\delta$(ppm)[a]	Lit. ref.
^{3}He	C_{60}	−6.36	[151]
$^{1}H_2$	C_{60}	−5.98 [−8.63][b]	[15]
$^{1}H_2O$	C_{60}	−6.20 [−8.19][b]	[17]
^{129}Xe	C_{60}	−8.89[c] [−16.4][d]	[14, 18]
$^{7}Li+$	C_{60}	−10.5[e]	[147]
$^{1}H_2$	K-12	−10.23	[15]
$^{1}H_4C$	I-20	−12.5	[148]
$^{1}H_3N$	I-20	−12.8	[149]
$^{1}H_2O$	I-20	−12.9 [−14.8][b]	[23]
^{1}HF	L-11	−11.5[b]	[144]
$^{13}CH_4$	I-20	−18.3	[148]
^{13}CO	I-20	−10.0	[150]
$^{14}NH_3$	I-20	−21.1	[149]
$H^{19}F$	L-11	−2.55[e]	[144]
^{3}He	C_{60}^{6-}-C_{60}	−42.4[f]	[63]
N	C_{60}^{6-}-C_{60}	-35.1[g]	[67]
^{3}He	C_{70}^{6-}-C_{70}	+37.1[f]	[63]
N	C_{70}^{6-}-C_{70}	+41.0[g]	[67]

[a]Unless otherwise indicated, the shift is relative to a nucleus in the atom or molecule dissolved in the same solvent. [b]Relative to the gas phase [145]. [c]Relative to ^{129}Xe in C_6D_6 solvent [14]. [d]Relative to ^{129}Xe in 3:1 o-$C_6H_4Cl_2$:C_6D_6. [18]. [e][Li@C_{60}]$_9$$SbCl_6$); relative to LiCl in D_2O [147]. [e]Calculated relative to gaseous HF monomer that is estimated to be −221.36 ppm relative to CCl_3F liquid [146]. [f]Chemical shift difference of the *endo* atom occurring when the fullerene cage accepts six electrons. [g]Relative g-factor shift in EPR of the quartet state of the encapsulated N atom upon addition of six electrons

12.3.3 Anions

It has proven possible to add varying numbers of electrons to endofullerenes of C_{60} and a few other fullerene cages under conditions where high-resolution magnetic resonance measurements can be carried out [59]. The hexa-anions He@C_{60}^{6-} and He@C_{70}^{6-} were among the first to be studied [63] and were shown to exhibit, respectively, enormously enhanced deshielding and shielding of ^{3}He. The hexa-anions are diamagnetic closed shell π-systems in which the lowest energy antibonding orbitals are fully occupied. The hexa-anions of several higher fullerenes containing endohedral ^{3}He have also been prepared [59].

To date, the only fullerene anion reported with endohedral hydrogen is the di-anion H_2@C_{60}^{2-} [64]. A very large downfield shift of 27.8 ppm relative to H_2@C_{60} is observed. This is attributed to a reversal of the ring currents in the five- and six-membered rings of the fullerene. It is supported by ab initio calculations, assuming that the lowest energy state of H_2@C_{60}^{2-} is the singlet state. This is

consistent with EPR measurements that indicate a ground state singlet, but a detectable low-lying triplet state, for C_{60}^{2-} [65].

12.3.4 Other Endo Nuclei: ^{129}Xe, ^{1}H, ^{13}C, ^{14}N, ^{19}F, N-Atom

The upfield shifts observed for encapsulated H_2 have now been measured for protons in $H_2@C_{60}$, $H_2@C_{70}$ and a number of H_2 encapsulating fullerene derivatives and open-fullerenes and anions [20, 66]. $H_2O@C_{60}$ and its derivatives also exhibit similar upfield shifts [20]. Cage-induced shifts of protons and other nuclei in several small molecules in the I-20 open-fullerene now include trapped CH_4, NH_3, CO, and HF, although the cages have not yet been closed. The chemical shifts are tabulated in Table 12.2. Also included is a comparison between the chemical shift change for endohedral ^{3}He and the g-factor shift of N atom in C_{60} and C_{70} when six electrons are added to the cage to produce the diamagnetic hexa-anion [67]. Theoretical predictions of ^{129}Xe chemical shifts in $Xe@C_{60}$ have been published [68, 69].

12.3.5 Magnetic Resonance of Open-Shell Endohedral Species

The noble gases and all of the endohedral molecules studied so far are closed shell systems. Three nonmetallic endofullerenes with open-shells having unpaired electrons, however, are known and give detectable magnetic resonance spectra: $N@C_{60}$ [70], $P@C_{60}$ [71] and muonium@C_{60} [72]. $N@C_{60}$ and $P@C_{60}$ exhibit large increases in hyperfine coupling between the unpaired electrons and the nucleus relative to the free atoms. This is attributed to admixture of excited states that acquire orbital angular momentum by interaction with the cage. The effect is substantially larger for P than for N. On the other hand, the hyperfine interaction between the unpaired electron and the positive muon (analogous to a proton) is decreased by a few percent in the C_{60} cage relative to free muonium [72]. It is pointed out that the decrease is similar to that observed for hydrogen atoms trapped in van der Waals media such as solid argon and krypton [73] but the hydrogen atom shifts are larger than the shifts for muonium itself in those media.

12.3.6 Two Atoms and Molecules in C_{60}, C_{70}

The only direct evidence for occupation of C_{60} by more than one He atom comes from the NMR peak attributed to the diamagnetic hexa-anion $(He)_2@C_{60}^{6-}$ that is

shifted slightly from that of $He@C_{60}^{6-}$ [74]. A very large downfield shift of ^{3}He is observed in both ions, qualitatively because the ring currents in the five- and six-membered rings change direction [59, 63]. Two H_2 molecules have been successfully added to C_{70} and small changes in chemical shift are observed relative to $H_2@C_{70,}$ presumably because double occupancy forces the hydrogen molecules away from the center of the cage [21].

It was also shown to be possible to incorporate a helium atom and a nitrogen atom in the same C_{60} or C_{70} cage [38]. The EPR lines are significantly broadened, presumably by collisions with the endohedral He atom. A small increase in the ^{14}N hyperfine splitting occurs as the interior space becomes more confining as a consequence of increased s-character in the electron density at the nucleus.

12.4 Cryogenic Spectroscopy Probes of the Lower Energy States of Small Caged Molecules

The previous sections of this chapter were concerned primarily with properties of endofullerenes that are qualitatively independent of whether the caged species is an atom or molecule. The primary concern was delineating the ways that a weakly interacting trapped species may modify to some extent the properties of the cage. Notable effects on the endo species were limited to those properties, most prominently chemical shift changes, that serve as a probe of the electronic structure of the cage. In fact, apart from NMR, or in the case of $N@C_{60}$ and $P@C_{60}$, EPR, the trapped atoms studied so far are transparent to the wavelengths usually employed for spectroscopic characterization.

The successful preparation of useful quantities of $H_2@C_{60}$. $H_2@C_{70}$, $H_2O@C_{60}$ and several of their open and closed derivatives raises the possibility of probing in much more detail the state of encapsulated species. In particular, this has led in the last decade to extensive studies of the low-lying rotational energy levels of small molecules using spectroscopy at cryogenic temperatures. To date, the investigation has been carried out almost exclusively by a remarkable international collaboration among five research groups, each with its own focus: Cryogenic NMR with Magic Angle Spinning (Malcolm Levitt, Southampton University, UK); Low temperature mid- and far-infrared spectroscopy (MIR & FIR) (Toomas Room, National Institute of Chemical Physics and Biosphysics, Estonia); and Low temperature Inelastic Neutron Scattering (INS) (Anthony Horsewill, University of Nottingham, UK). Sufficient amounts of high quality samples for these studies were prepared by the research group of Nicholas Turro, Columbia University, USA, in conjunction with their investigations of the spin chemistry of small molecule endofullerenes, using precursors provided by Yasujiro Murata, Kyoto University, Japan, who, along with Koichi Komatsu, pioneered the “molecular surgery” approach to endofullerene

synthesis. A sixth group (Zlatko Bačić, New York University, USA) provided theoretical support for the low-temperature spectroscopy investigations.

Detailed descriptions and summaries of these studies have been published [75–78]. The combined efforts of this collaboration formed the basis for a symposium organized under the auspices of The Royal Society held on March 15–16, 2012. Papers from the conference have been published [79]. The presentation below will provide some background on the techniques and summarize the most important results, with particular attention to the characterization of the structure and dynamics of H_2 and H_2O in C_{60}. The original papers and reviews may be consulted for the details of experimental methods, data analysis, and interpretation of the results.

12.4.1 Translation and Rotation of H_2 and H_2O

The new feature that endohedral molecules bring to the study of the intracage environment is the interplay between translational and rotational motions of the trapped species. Although the parameters needed to describe the rotations of small molecules like H_2 and H_2O in isolation are well known, there remains uncertainty about how freely molecules rotate in the constrained intracage environment. Proper description of the translational motion of caged molecules, on the other hand, requires an understanding of the forces acting between the molecule and the cage. Being able to directly observe transitions due to changes in intracage translational motion provides rigorous tests of the various theories of cage molecule force fields. The additional possibility of translation–rotation interaction may be understood as follows.

It is well known that the quantized rotational energy of a small molecule is inversely proportional to its moment of inertia (in the general case, a tensor), *I*. *I* in turn is proportional to the mass and bond distances in the molecule, i.e., the molecular size. Thus, the rotational energies, and energies of transitions between them, are largest *when molecules are light and small.* Similarly, the quantized translational energy of a particle in a box, i.e., cage, is inversely proportional to its mass and the dimension of the cage, i.e., translation energies are largest when *particles are light and the box is small*. Consequently, when molecular and cage dimensions are comparable, some energy levels for translation and rotation may have values close enough that small perturbations may mix the states, i.e.. lead to translation–rotation (T–R) coupling.

The extensive studies of spectroscopy at low temperatures performed on $H_2@C_{60}$ and $H_2O@C_{60}$ and a few other small molecule endofullerenes may be understood as elaborations of the above oversimplified picture. Some of the results of these measurements are presented below.

12.4.2 Mid IR (MIR)

Four papers [80–83] from the Estonian group report measurements of MIR absorption by $H_2@C_{60}$ and its isotopologues, $HD@C_{60}$ and $D_2@C_{60}$ in the H–H stretching frequency region 4000–5000 cm^{-1}. It might at first appear surprising that endohedral H_2 should exhibit any absorption of radiation in this region, since the stretching transition of a homonuclear diatomic molecule is forbidden [84]. Indeed, as expected, no IR absorption was noted in this region in the first reports of the $H_2@C_{60}$ synthesis [15], due in part to the inherent weakness of the transition but also to broadening by unresolved rotational and translational fine structure.

Infrared absorption by $H_2@C_{60}$ in this region has been observed at 6 K with good sensitivity and a resolution of at least 0.3 cm^{-1} [80]. The narrow lines lead to resolution of an array of fine structure and greatly improved sensitivity. The sensitivity is also improved relative to free H_2 by a transient dipole moment induced by motion of the molecule within the surrounding cage.

Analysis of the rich translation–rotation structure on the vibration transition has yielded important information about the structure and dynamics of the endo H_2 molecule. In particular it is found that:

(i) Detailed analysis of the spectrum yielded a shift of −90 cm^{-1} for the pure H–H vibration relative to the free H_2 molecule. It was shown that this is consistent with a predominantly attractive interaction between H and the carbons of the fullerene cage that slightly stretches the H–H bond.

(ii) The resolution was sufficient to resolve structure due to the *ortho* ($I = 1$) and *para* ($I = 0$) nuclear spin isomers of H_2 [84]. In free H_2, the *para* isomer is thermodynamically more stable than the *ortho* by ca. 120 cm^{-1}, which corresponds to a temperature of ca. 170 K. At higher temperatures, an equilibrium mixture of ca. 3:1 statistically favors the *ortho* form, but at 6 K, the temperature of the IR measurements, an equilibrium sample would be essentially pure *para*. Nevertheless the ratio measured in samples cooled from room temperature to 6 K exhibit the high temperature ratio. It is therefore concluded that *ortho–para* conversion in the sample must be very slow. The spectral assignments were aided by this property of the caged H_2. It was possible to employ a sample enriched in the *para* form at Columbia University and shipped cold by air from New York to Tallinn, Estonia before equilibration occurred [81]!

(iii) The transition frequencies are fit well by a model for H_2 in C_{60} consisting of a vibrating rotor moving in a spherical translational potential. The intensities are explained by a translational-motion-induced dipole moment.

(iv) A few of the lines exhibited further splittings of the order of 1 cm^{-1}. It was noted that this could arise from crystal field effects or motion of the C_{60} cage within the solid matrix. This is consistent with small splittings of rotational levels inferred from very low-temperature heat capacity measurements on solid $H_2@C_{60}$ [85].

(v) Measurements on H_2, HD and D_2 in C_{60} [82, 83] made it possible to refine the parameters describing the model used to fit the spectroscopic data. In addition to a consistent decrease in vibration frequency, encapsulation slightly decreased the rotational constant, consistent with a small increase in H–H bond length.

(vi) The potential used to describe translational motion of H_2 is principally harmonic but has a small quartic component. The harmonic frequency for translational oscillations in the vibrational ground state is found [81] to be $4x10^{12}$ s^{-1} corresponding to a potential energy contribution of 138 cm^{-1}. This is similar in magnitude to the rotational constant of 60 cm^{-1} and is consistent with confinement of the H_2 particle in a space similar to size of the molecule. The translational oscillations of H_2 in C_{60} may therefore be considered to occur on the timescale of less than a picosecond.

12.4.3 Far IR (FIR)

The C_{60} cage has no vibrations below 300 cm^{-1} [86], the region where rotational (and in the case of the endofullerenes, translational) transitions of the endohedral species should occur. Such transitions are, however, forbidden in homonuclear diatomic molecules and cannot be observed for $H_2@C_{60}$. On the other hand, the pure rotation spectrum of H_2O, a polar molecule, encapsulated in C_{60} is readily observed in solid samples at cryogenic temperatures [77]. It is found that the three lowest-energy allowed rotational transitions are within experimental error the same as in gaseous H_2O. Unlike the case of $H_2@C_{60}$ there is no clear indication of translation–rotation coupling.

12.4.4 Inelastic Neutron Scattering (INS)

The information available from infrared and Raman spectroscopies, though essential to modern structure determination, is limited by electric dipole selection rules imposed by the fact that the species detected is the photon. As we have seen above, in the case of the H_2 and other molecules with high symmetry, this property places some restrictions on the intensities of vibration and rotation transitions.

A special limitation occurs for H_2 and H_2O and similar molecules with symmetrically equivalent protons. In these molecules, the rotational state description must be replaced by nuclear spin–rotation states that possess the symmetry properties upon interchange of odd-spin particles such as ^1H that are needed to satisfy the requirements of Fermi–Dirac statistics. Analogous requirements hold for equivalent nuclei with even-spin, such as ^2H, that obey Bose–Einstein statistics

[87]. As a result, as has been mentioned in passing with regard to MIR spectra, H_2 and H_2O molecules come in two forms: *para* ($I = 0$) and *ortho* ($I = 1$) spin isomers. Under some conditions, these forms act as distinct chemical species and, in the case of H_2, may even be separated by chromatography [88]. Of particular significance is the fact that a transition between the isomers requires simultaneous change of the rotational and nuclear spin states. Such transitions using photons are highly forbidden.

Both the electric dipole and spin symmetry selection rules are ameliorated when it becomes possible to excite transitions involving nuclear motion or nuclear spins using neutrons. In this case the operable force is the strong force, not electromagnetism. It is manifested by the scattering of neutrons by nuclei in the sample and is particularly strong for protons. Strong force encounters are also able to change the spin of an individual proton thereby breaking the symmetry of a set of otherwise equivalent nuclei. In the case of H_2 and H_2O, this leads to observation of transitions between *para* and *ortho* states, as well as transitions within a single form, that involve nuclear motion. If the energy lost, or gained, by a neutron during an encounter can be measured, spectroscopy results. This experimental technique is known as inelastic neutron scattering (INS).

Six papers [77, 89–93] from the group based in Nottingham describe INS investigations carried out at CERN on $H_2@C_{60}$, $H_2O@C_{60}$ and H_2 in an open-fullerene at cryogenic temperatures. The results complement the IR investigations of similar samples in that the frequencies of *para–ortho* transitions are detected and the resolution in some cases is somewhat better than observed in the infrared. The observation of energy *gain* transitions, analogous to anti-Stokes lines in Raman spectroscopy, gives rise to temperature-dependent features that provide additional information about the translation–rotation manifold of the endo molecules. The result is both an extension and refinement of the parameters measured by MIR and FIR.

The principal results obtained by INS are summarized below. Individual papers may be consulted for experimental details and methods of analysis.

(i) Where the same translation–rotation transitions were observed by both IR and INS the agreement in energy is good. In the case of $H_2@C_{60}$, where only MIR spectra are observable, the IR spectrum combines information from the ground and first vibrational states. INS at low temperature, on the other hand, provides information about the lowest vibrational state exclusively.

(ii) Measurements on $H_2@C_{60}$ were extended down to 1.6 K in order to probe the region where heat capacity effects indicated a possible level splitting due to crystal field effects [85]. Although small shifts in energy with temperature consistent with such an effect were observed, the results were considered inconclusive due to questions about sample purity.

(iii) Small splittings of the lowest energy translational transition in the INS of $H_2@C_{60}$ exhibit strong variations in intensity. It is suggested that developments in the theory of INS [94] should make it possible to extract

information from the intensity distribution about the translation–rotation wave function that is not available by other methods.

(iv) In $H_2O@C_{60}$, the transition between the lowest *para* and *ortho* states exhibits a small but significant splitting. This is interpreted as a lifting of the degeneracy of the *ortho* state by crystal packing forces, cage distortion or interaction between endofullerene molecules. The splitting was too small to be observed in the FIR of the *ortho* form. The splitting in $H_2O@C_{60}$ is substantially larger than the perturbation of the lowest state in $H_2@C_{60}$ suggested by IR and heat capacity measurements. It is suggested that the greater sensitivity of the energy of encapsulated H_2O to the surrounding environment is due to its polar character.

(v) As with IR, INS serves as a very effective probe of the relative populations of *ortho*- and *para*-H_2O in the solid at low temperatures.

12.4.5 Theoretical Modeling of Endohedral Translational and Rotational Energies

The possibility of the availability of spectroscopic probes of the translation and rotational environment of small molecules in closed fullerenes has stimulated a vigorous theoretical effort to describe such effects and provide guidance to analysis of the experimental data.

The most extensive investigation has been a series of papers from the group of Zlatko Bačić at New York University dealing with H_2 and its isotopologues encapsulated in C_{60}, C_{70} and an open-fullerene [95–101]. These were carried out as part of the international endofullerene collaboration. The calculations are 5-D quantum calculations employing a Lennard–Jones potential between the H atoms and each of the carbon atoms in the cage. The ordering and degeneracies of the calculated T–R energy levels agree well with those inferred spectroscopically assuming a spherical potential. The most recent development has been refining the analysis of INS intensities and the discovery of a previously unknown selection rule for INS [94].

The NYU calculations refine the methodology employed by Cross who was the first to attempt to describe the interplay of translation and rotation of molecules trapped in C_{60} [102, 103]. The first paper was published before $H_2@C_{60}$ was prepared. More recent theoretical studies have extended the quantum calculations to fullerene cages [43, 104] and single-walled nanotubes [105], clathrates [106–109] and interstitial sites in solid C_{60} [110]. A recent publication theorizes about the properties and dynamics of a water molecule in $H_2O@C_{60}$ but stops short of calculating explicit translation–rotation energies that might be compared with emerging spectroscopic data [111].

It should also be noted that nonlinear vibrational dynamics of neon in C_{60} were simulated using molecular dynamics methods [112] before the isolation of any of

the noble gas fullerenes. Ne@C_{60} has not yet been isolated in macroscopic amounts despite the observation of both Ne@C_{60} and Ne_2@C_{60} by mass spectrometry [113, 114]. It is predicted that Ne@C_{60} should be stable toward loss of Ne [115]. It has also been shown indirectly that Ne may enter an open-fullerene [9].

12.4.6 Cryogenic Magic Angle Spinning Nuclear Magnetic Resonance (MASNMR)

The first low-temperature spectroscopic study carried out on H_2 in fullerene was a solid-state NMR measurement on H_2 in an open-fullerene [116, 117]. The goal was to explore the possibility of anisotropic interactions experienced by endohedral H_2 and also to obtain an estimate of the correlation time for H_2 rotation. Neither property is accessible for H_2 using other methods. The work built on an earlier study of H_2 trapped in interstitial sites in solid C_{60} [118, 119].

An additional property of NMR that has proven of value in conjunction with other spectroscopic methods is its ability to characterize and quantify the *ortho*-forms of H_2 or H_2O in a sample. The *para* (I = 0) isomer is NMR silent. This has served as the preferred method from monitoring the rate of *ortho–para* conversion in H_2O in C_{60} [120] and has also confirmed the splitting of the lowest rotational energy level of *ortho*-H_2O@C_{60} [77].

Seven papers on the solid-state NMR of H_2 and H_2O in endofullerenes have so far been published by the Southampton group. The principal results relating to the environment in the fullerene cage are as follows:

(i) Analysis of the relaxation time of H_2 in an open-fullerene leads to the conclusion that there is substantial cross-relaxation between the endohedral H_2 and exohedral protons on the rim of the open cage. It is pointed out that there may be useful applications of this method of communication between the inside and out of the cage.

(ii) The dependence of solid-state NMR on the orientation of the molecule containing the observed nucleus makes it a very sensitive probe of rotation both of the endohedral molecule and the cage itself [121]. The use of magic angle spinning increases the resolution so that subtle aspects of the motion are revealed. For example, the increasing anisotropy of the average rotation of H_2 as the cage is made more asymmetric going from C_{60} to open and bridged structures is readily revealed by an increase in the residual dipolar splitting of the resonance peak. A small residual dipolar coupling observed in H_2@C_{60} is explained by weak interaction between H_2 molecules in adjacent C_{60} cages [121]. Solid state ^{1}H NMR of H_2@C_{70} has employed the dipolar coupling of H_2 to probe cooperative alignment of the C_{70} cages in the crystal lattice at low temperature. It is pointed out that this illustrates that H_2 in an asymmetric internal environment may serve as a “spy” to report the orientation of the host molecule [122].

(iii) ^{13}C NMR spectra and relaxation times indicate a phase transition in solid $H_2@C_{60}$ that occurs at a temperature about 30 K lower than observed for empty C_{60}. ^{13}C relaxation below the transition temperature is stated to be "driven in part by infrequent large amplitude rotational jumps" [121].

(iv) Residual dipolar coupling is also observed at low temperature in $H_2O@C_{60}$ [123]. The best explanation for the effect was considered to be static distortion of the C_{60} cage by the polar H_2O molecule.

(v) In a masterful study, solid-state NMR has been used to measure the rate of *ortho–para* conversion of H_2O encapsulated in C_{60} over a range of temperatures [120]. It is found that the conversion exhibits second-order kinetics. A plausible mechanism for the conversion is suggested to be coupling of electric dipole moments of H_2O molecules in adjacent cages. The perturbed rotational angular momentum could then act indirectly on the nuclear spins via the nuclear spin–rotation interaction. Experiments to test the hypothesis would include employing samples diluted with empty C_{60}.

12.5 Nuclear Spin Relaxation Probes of the Dynamics of Small-Caged Molecules

12.5.1 ^1H Relaxation Times in $H_2@C_{60}$ and $H_2O@C_{60}$

In the title of a paper [102] published 5 years before the successful synthesis of $H_2@C_{60}$, R.J. Cross posed the question "Does H_2 Rotate Freely Inside Fullerenes?". He proposed a simple model for the interaction of H_2 with the carbon cage that was consistent with rapid collisions of H_2 with the cage wall and rapid changes in rotational state due to changing torque on the H_2 molecule. Shortly after samples of $H_2@C_{60}$ became available, this conclusion was tested by measuring the ^1H spin relaxation time of H_2 in C_{60} in comparison with the T_1 for H_2 dissolved in the same medium [124]. The results were refined by comparison with HD in the same sample [125] and extended to $H_2O@C_{60}$ [126, 127].

The goal of the T_1 measurements was estimation of the correlation time for molecular reorientation, associated with the nuclear spin dipole–dipole interaction, τ_{dip}, and for changes in rotational angular momentum associated with the nuclear spin–rotation interaction, τ_{sr}. It was possible to separate the effects for encapsulated H_2 and H_2O in two ways:

(a) The dipole–dipole interaction, and to a smaller extent the spin–rotation interaction, change in predictable ways when deuterium is substituted for one of the hydrogens [126] in H_2 and H_2O. If one assumes that the reorientation and rotational angular momentum correlation times are about the same for the two isotopologues, T_1 measurements on HD and H_2 allow calculation of the two correlation times. It is interesting that one of the first reports of encapsulated H_2

and HD in an open-fullerene [24] noted that the ^{1}H NMR linewidth for H_2 was significantly broader than that for HD. This was interpreted, correctly, as arising from a reduction in the dipolar contribution to relaxation of HD and proposed that "rotation is somewhat impeded by the cage".

(b) The dipole–dipole and spin–rotation mechanisms exhibit opposite dependencies on temperature and viscosity. The dipolar correlation time is lengthened as the sample is cooled because reorientation slows down. For the usual values of τ_{dip}, this leads to an increase in relaxation rate, i.e., decrease in T_1 as the temperature is lowered. The spin–rotation interaction, on the other hand, becomes more effective at higher temperatures because the population of rotational states with larger angular momentum increases.

One or both of these methods were used to obtain estimates of the reorientation and rotational angular momentum changes in encapsulated H_2 and H_2O in C_{60} and some derivatives [124–127]. The details are presented in the publications. The most significant results are as follows:

(i) H_2 reorients itself and undergoes changes in rotational motion about 10 times more slowly than gaseous H_2 dissolved in the same solvent. Both reorientation and angular momentum change occur on the timescale of a few picoseconds in C_{60}. This is much faster than rotation of the C_{60} cage in the solvent but much slower than the "free rotation" rate of H_2 which is in the range of 0.01 picosecond. The picture of H_2 rotation being uncoupled from the motion of the C_{60} cage is supported by the lack of sensitivity of T_1 to solvent viscosity which changes the reorientation rate of the cage. From the standpoint of the endohedral H_2, the fullerene cage is essentially static. This is also supported by the observation that the T_1 of endohedral H_2 in solid C_{60} and solutions of C_{60} are nearly the same at the same temperature [121, 124].

(ii) Reorientation of H_2 in C_{60} is somewhat faster than angular momentum change at the same temperature. This is consistent with a picture of H_2 as a rotating "gyroscope" whose direction of rotation is changed by collisions with the wall faster than changes of the rotation rate [124, 125].

(iii) For $H_2O@C_{60}$, it is found that the τ_{sr} is nearly the same as for H_2 in C_{60} indicating that wall collisions have about the same effectiveness in changing the rotational angular momentum [126]. The reorientation correlation time, τ_{dip}, for H_2O, however, is more than tenfold longer than τ_{sr} and is nearly the same as the reorientation rate of the C_{60} cage in the solvent. This conjures up a picture of a spinning H_2O molecule sticking to the wall of the cage on the multi-picosecond timescale, but subject to forces that change the spin rate, i.e., rotational angular momentum, but not the direction of the rotational axes.

(iv) It is found that increasing the dielectric constant of the solvent by more than a factor of three produces a negligible change in the T_1 of $H_2O@C_{60}$. This would indicate that the endohedral water molecule is sufficiently isolated

from the surrounding solvent that its motion is not detectably affected by interaction of the electric dipole with the surrounding medium [126].

12.5.2 Relaxation of Endomolecules by External Paramagnets

NMR relaxation times have been used as a probe of the magnetic interaction of endohedral H_2 and H_2O with the external magnetic field arising from paramagnetic relaxation reagents or attached paramagnets. The mechanism of relaxation involves the electron-nuclear dipole–dipole interaction modulated by molecular encounters between the fullerene and an added paramagnet in solution, or rotation of a fullerene cage with a covalently attached stable radical. It should be pointed out that there was implicit recognition of the likelihood of relaxation through the fullerene wall in early measurements of ^{3}He trapped in fullerenes [51]. A "relaxation reagent", $Cr(acac)_3$, was added to the samples before ^{3}He NMR measurements in anticipation that the expectedly long T_1 of ^{3}He would be shortened by addition of the paramagnet and make possible faster data acquisition. It apparently worked.

12.5.2.1 Intermolecular Relaxation Reagents

The first paper intended to explore paramagnet relaxation of a trapped fullerene species measured the effects on the T_1's of $H_2@C_{60}$, H_2 and added C_6H_6 in the same solvent that were produced by adding nitroxide radicals or biradicals [128]. The bimolecular contribution to T_1 was analyzed using a standard outer sphere point dipole diffusion model for paramagnets in solution. Later reports [129, 130] compared the effects of the same paramagnet on H_2 and H_2O in C_{60} and a series of open-fullerenes. The principal results were as follows:

(i) The parameter of interest in analyzing the bimolecular contribution to T_1 was the effective distance between the unpaired electron(s) in the paramagnet and the observed nucleus [128]. This was compared with reasonable estimates of the distance expected on the basis of molecular models. A distance smaller than expected would correspond to more effective relaxation than expected and vice versa. The bimolecular contribution to T_1 was also measured for ^{1}H in dissolved H_2 and added benzene as non-fullerene controls. Measurement of T_1 for ^{13}C in the C_{60} cage provided information about the magnetic interaction with the surface of the cage.
Values of the distance derived from T_1 measurements on dissolved H_2, $^{13}C_{60}$ and C_6H_6 were within the range expected using the diffusion model. In the case of the endohedral protons of H_2, however, the derived distance would have required that the paramagnet reside within the cage! In terms of the

bimolecular contribution to T_1, H_2 in C_{60} is relaxed five times more effectively by an external paramagnet than is H_2 in solution. A large part of this arises from the slower diffusion of the C_{60} cage which increases the lifetime of the radical/molecule contact pair. It was suggested that the remaining effect may be due to a small hyperfine interaction between the nitroxide unpaired electron and the endohedral H_2 induced in the cage and transmitted to the guest molecule. It is not clear, however, why this effect would not also have enhanced the ^{13}C T_1 of the fullerene cage.

(ii) The bimolecular contribution to T_1 from added nitroxide was also compared for H_2 and H_2O in C_{60} and in each of the two closely related open-fullerenes [130]. It is found that the bimolecular contributions were nearly identical for four of the six endofullerenes. One of the outliers was $H_2@C_{60}$ which was discussed above. The other was H_2O in an open cage that, unlike the counterpart containing H_2, had two OH groups attached to the rim of the opening. It was suggested that the OH groups might stabilize a hydrogen-bonded complex with the nitroxide thereby increasing the effectiveness of the relaxation.

(iii) Bimolecular relaxation induced by a series of transition metal complexes was measured for H_2 in C_{60} and in an open-fullerene and for H_2O on a related open-fullerene. It was found that the effect of the added complexes was virtually identical for all three fullerenes. An excellent correlation was found between the relaxation time and the square of the magnetic moment of the complex as expected from the classical diffusion model [129].

12.5.2.2 Intramolecular Attached Nitroxides

Intermolecular relaxation occurs at the whim of random encounters between the relaxant and the nucleus of interest. Theoretical interpretation depends to a major extent on the model used for dynamic processes in liquids. In an attempt to provide firmer theoretical basis for evaluation of paramagnetic effects on endofullerene species a series of cages with nitroxide radicals attached by bridges or tethers was synthesized [62, 66, 130–133]. The paramagnet contribution to T_1 was determined simply by subtracting the relaxation rate measured for the corresponding diamagnetic hydroxylamine precursor of the nitroxide. The results were analyzed by a simple point dipole model involving rotation of the labeled endofullerene with a fixed distance between the unpaired electron and the endo nucleus. Details are available in the published papers. The principal results were as follows:

(i) As expected from theory, a remarkably good correlation was found between the relaxation rate and the inverse sixth power of the distance estimated from molecular modeling for six nitroxide labeled derivatives of C_{60} [131].

(ii) Small peptide chains were inserted as spacers between the nitroxide and the fullerene cage [133]. The assumed inverse sixth power dependence of the relaxation rate on distance was used to reveal that one of the peptide chains is

more flexible, i.e., can access conformations that put the nitroxide closer to the *endo* H_2, than the other.

(iii) Density functional theory calculations were carried out on the bridged and tethered nitroxide derivatives [132]. The dipole–dipole mechanism assumed in previous work was confirmed and relaxation time estimates based on a more realistic model of rotational diffusion of the modified fullerene cage agreed well with the observed values.

12.6 Nuclear Spin Isomers of Symmetric Caged Molecules

The subtle effects of nuclear spin symmetry on transitions between the rotational states of H_2 and H_2O were discussed above in connection with the analysis of IR, INS, and NMR of *para* and *ortho* forms of the endohedral molecules in $H_2@C_{60}$ and $H_2O@C_{60}$. The rates of *para–ortho* transitions also provide an extremely sensitive test of the way that small molecules are affected by the environment. The results of studies designed to probe *para–ortho* conversion in endofullerenes using paramagnetic catalysts are presented below. Another goal was to develop methods by which high concentrations of one of the isomers may be produced and stored inside the fullerene cage for practical purposes [134, 135]. The subject has been recently reviewed [136].

12.6.1 Mechanism of Nuclear Spin Isomer Conversion

The simplest process that induces transitions between the $I = 0$ (*para*) and $I = 1$ (*ortho*) nuclear spin states is analogous to nuclear spin relaxation. What is required is a symmetry breaking interaction that produces a difference between the, usually transient, magnetic fields experienced by the two otherwise equivalent nuclei. The first quantitative treatment of the theory was presented by Wigner in 1933 [137]. The Wigner theory was later cast in the formalism of relaxation theory for the special case of transient magnetic fields induced by bimolecular encounters by paramagnet catalysts in solution [138]. The main qualitative features of this mechanism are:

(i) As in relaxation theory, the process arises from simple time-dependent perturbation theory applied to the quantum nuclear spin-molecular rotation system. In this model, transition probabilities are proportional to the square of the perturbation. In the case of magnetic catalysis, the rate of the process depends on the square of the magnetic moment of an added paramagnet. This is similar to the effects on spin-lattice relaxation of added inter- or intramolecular paramagnetic catalysts reported for encapsulated H_2 and H_2O [129, 131].

(ii) The Wigner theory and later elaborations of it usually assume that the dominant perturbation of the nuclear spin system is the dipole–dipole interaction with the paramagnet. This interaction varies as the inverse third power of the distance between the nuclear and electron magnetic moment. For a second-order perturbation, this predicts variation of the rate as the inverse sixth power of the distance, as observed, for example, in the studies of relaxation in endofullerenes with attached paramagnets [62, 66, 130–133]. Unlike spin relaxation, however, catalysis of *para–ortho* conversion should vary as the inverse eight-power of the distance. This arises because the perturbation inducing the conversion is the *gradient* of the magnetic field experienced by the nuclei, which, for the dipole–dipole interaction is proportional to the *inverse fourth power* of the distance.

12.6.2 *Methodology for Measuring* para–ortho *Conversion Rates*

Measurement of the conversion rate requires first, a method for producing a nonequilibrium concentration of the spin isomers and second, a method of monitoring the concentration of one or both of the isomers as the sample returns to equilibrium. In the case of the conversion rate reported for $H_2O@C_{60}$ [120], the first requirement was met by cooling the sample at a sufficiently low temperature to produce an excess of the *para* isomer. The cooling time was determined by the natural conversion rate. The second requirement was met by measuring the time dependence of the solid-state NMR signal from *ortho*-H_2O as the sample returned to equilibrium at a desired temperature. The times involved were on the order of one day or less. Low-temperature IR and NMR of $H_2O@C_{60}$ also were able to detect changes in the concentrations of the isomers as a function of temperature [77, 120].

The strategy of cooling the sample to enrich the *para* isomer is not feasible in the case of H_2. The uncatalyzed rate of conversion is on the order of months or years [80, 81, 139]. A magnetic catalyst must therefore be employed to achieve low-temperature equilibration and the catalyst removed in a short time compared to the conversion rate. For H_2, this is usually accomplished by flowing the gas through a powdered catalyst that contains magnetic sites [87]. For H_2 in solid C_{60} or other fullerenes, new methods had to be developed. It has already been mentioned that the conversion of H_2 at low temperature could also be revealed through changes in the splitting pattern of the ENDOR signal of H_2 in the radical anion of a bridged fullerene [47] and in the triplet state [48] of $H_2@C_{60}$ arising from catalysis of *ortho–para* conversion by the paramagnetic cage. Conversion seems to take place in the solid paramagnetic bridged fullerene at 100 K [47] but not in the triplet state of $H_2@C_{60}$ at 20 K [48].

Three different methods for enriching $H_2@C_{60}$ in the *para* isomer have been developed:

(i) *Cooling a sample of the fullerene in liquid $^3O_2$ and rapidly boiling off the O_2 after low-temperature equilibration is achieved.* Dispersal of the fullerene in a zeolite matrix was necessary to promote complete contact with the liquid O_2 catalyst. The enriched trapped H_2 could then be rapidly extracted from the zeolite before conversion could take place [81, 139, 140].

(ii) *Attaching a functional group to the fullerene cage that can be converted to a paramagnet capable of producing a magnetic field gradient across the trapped H_2 molecule*. Following low-temperature equilibration, the catalytic group must be rapidly back-converted to the nonmagnetic form. This method has been termed "a magnetic switch" [141]. The most effective group has been a hydroxylamine that may be converted reversibly into a nitroxide catalyst [133, 141, 142].

(iii) *Low-temperature photoexcitation of a fullerene contained trapped H_2 to give the paramagnetic triplet state.* Rapid decay of the triplet and reexcitation of the endofullerene lead to equilibration of the sample at low temperature and trapping of the nonequilibrium concentration of the *para* form after photoexcitation is stopped. This has been termed a "photochemical on-off switch" for *ortho–para* conversion [140].

The *para–ortho* conversion rate of the *para*-H_2 enriched samples produced by any of the three methods was determined by monitoring the ^1H NMR spectrum of the trapped H_2 using the nonoverlapping spectrum of HD in the same fullerene as an internal standard. Lacking the necessary symmetry properties, HD does not possess nuclear spin–rotation isomers and serves as a tracer for the total amount of fullerene in the sample.

Using the above methods, the following results were obtained. Details will be found in the references.

(i) The predicted inverse eighth power dependence of the conversion rate on distance was confirmed using the same series of tethered endohedral H_2 nitroxides that was employed in the T_1 studies [142]. This confirms the dipolar mechanism for catalysis.

(ii) Using a modification of the Wigner theory for the case of a rotating H_2 molecule at a fixed distance from the catalyst, it was calculated that the correlation time for modulation of the dipolar interaction is approximately 2×10^{-12} s at room temperature [142]. This is similar to the correlation times for angular momentum change and reorientation of H_2 in C_{60} deduced from T_1 measurements [124, 125].

(iii) Nitroxides were used as bimolecular catalysts for *para-ortho* conversion in $H_2@C_{60}$ [136, 139] and the conversion rate compared with that for dissolved H_2 under the same conditions [143]. The bimolecular conversion rate for free H_2 is ca. 100 times faster than for H_2 encapsulated in the fullerene. This is consistent with the cage preventing a close approach of catalyst to the

trapped H_2. It also confirms the effectiveness of the fullerene cage as a "bottle" for storing H_2 enriched in one of the spin isomers. Possible applications of this effect are discussed in a review [136].

(iv) Bimolecular conversion rates with a nitroxide catalyst were compared for $H_2@C_{60}$ and H_2 encapsulated in three open-fullerenes [136]. Only small differences were observed, H_2 in the open-fullerenes being slightly more accessible to catalysis than in $H_2@C_{60}$.

(v) The rate constant for spin relaxation, T_1^{-1}, induced by paramagnets for H_2 in fullerene cages is about *one million* times faster than the rate constant for *para–ortho* conversion of the same H_2 molecule, regardless of whether the catalysis is inter- or intramolecular [142]. This might seem surprising, given that both processes arise from the same dipole–dipole magnetic interaction. The conversion process is, however, slowed down because it depends on the gradient of fluctuating field, not the average value. The inverse eighth power compared to inverse sixth power dependence on distance means that for the same amount of catalysis conversion requires that the catalyst be closer to H_2. Another significant factor is the large *ortho–para* energy gap that the dipolar perturbation must drive for conversion to occur compared to the energy gap for nuclear spin relaxation of the electron-nuclear spin system. The former is of the order of 100 cm^{-1} or more, the rotational energy difference between the ortho and para states. Nuclear relaxation catalysis, on the other hand, under a wide range of conditions, is dominated by transitions that flip only the nuclear spin. Depending on the magnetic field, the corresponding energy gap can be orders of magnitude smaller than rotational energy difference. Together the two effects explain why fullerene cages show significant potential as magnetically shielding microbottles for storing H_2 (or D_2 or T_2) enriched in one of the spin isomers. Possible applications of enriched samples have been discussed elsewhere [136].

12.7 Summary and Future Directions

What we know about the interior environment of a closed fullerene as seen by a small atom or molecule based on the (techniques and observations) used so far might be summarized as follows:

(i) The cage dimensions change very little on encapsulation, but the electrons are perturbed and may be pushed to the outside of the cage as the size of the endo species increases (X-ray diffraction, reactivity, chromatographic separation, IR)

(ii) A small *endo* species experiences a translational potential that is flat near the center, but increases rapidly near the surface, and has nearly spherical symmetry in C_{60}. (INS, IR and NMR measures of T–R energy spectra, 5-D quantum calculations)

(iii) The interior surface of the cage is sufficiently "sticky" to inhibit somewhat the rotational motion of the *endo* molecule (NMR relaxation, molecular dynamics calculations)
(iv) The interior species is able to communicate magnetically with the outside world ($^1O_2$ sensitization, intra- and intermolecular paramagnet induced relaxation, *ortho–para* conversion magnetic catalysis)
(v) The fullerene may act as a weak Faraday cage (IR of $H_2O@C_{60}$, H_2O *ortho–para* conversion, ^1H relaxation insensitive to solvent polarity).

Although the body of work itemized above is substantial, considerable additional progress may be anticipated in the near future. Much could be accomplished by extending the methods and techniques already developed to new endofullerenes. The molecular surgery approach is especially promising as a way of producing useful quantities of a variety of guest/host fullerene molecules. The main requirements will be matching the orifice size to the desired endohedral species and discovering, by trial and error or calculation and design, the proper balance between encapsulation equilibrium and relative cage closure and escape rates.

Assuming that the barriers to preparation will continue to be lowered, where might future investigations of nonmetallic endofullerenes lead? A few possibilities come to mind.

(i) Efforts to close the C_{60} cage on a few atoms and small molecules of the right size will build on past efforts. These include encapsulating HF, CO, and producing sufficient quantities of $Ne@C_{60}$ and $N_2@C_{60}$ to characterize spectroscopically. Incorporation of N_2 leads to the possibility of studying the properties of the *ortho* and *para* isomers of $^{15}N_2$ or $^{14}N_2$. Encapsulating O_2 might prove a challenge but offers intriguing possibilities for studied endohedral magnetism. Successfully producing endohedral $^1O_2$, by sensitization via the cage, might even give rise to the formation of an *endohedral* dioxirane! And, of course, attempts to isolate and characterize (endo) $H@C_{60}$ will continue.
(ii) Closed cages incorporating larger molecules, such as CH_4 and NH_3, or even SF_6 or CH_3F, may require extending the molecular surgery approach to larger cages. A good start has been made with C_{70} and some open-fullerenes and might be extended to the higher closed fullerenes if sufficient quantities become available. All of the above examples would be good candidates for extending nuclear spin isomer studies beyond diatomic molecules, although SF_6, because of its large moment of inertia, would provide challenges for directly probing rotational levels.
(iii) Multiple occupancy of C_{70} or higher fullerenes with H_2, H_2O, and N_2 allow the possibility of isolating clusters of small molecules for structural and dynamic studies using condensed phase techniques at high temperatures.
(iv) Given the intense absorption of radiation over much of the UV/Vis wavelength range by the π-electrons of the fullerene cage, carrying out photochemistry on small endohedral molecules is likely to be challenging since the cage is also a radiation shield! It is more likely that the π-systems of

formaldehyde, ethylene or acetylene, for example, all of which might well fit inside C_{70}, might be better excited by energy transfer from the outside of the cage. Excitation of trapped I_2 or CH_3I might also generate potentially reactive radical species.

(v) A number of measurements could be extended to small molecule endofullerenes which have already been prepared. For example, *ortho–para* conversion rates in $D_2@C_{60}$ and $D_2O@C_{60}$ would provide a stringent test of the extent to which these rates depend on the size of the nuclear moment and T–R energy levels. The effect of the nuclear quadrupole moment, a probe of electric field gradient, could also be evaluated in D_2, D_2O, $H_2^{17}O$, and $^{14}NH_3$ through nuclear relaxation times and comparison with the free molecules in the same medium or the gas phase. Similarly, low-temperature spectroscopy of CH_4 and NH_3 and their isotopologues, which have already been trapped in an open-fullerene, would extent studies of T–R coupling and nuclear spin statistics to spin systems with different symmetry.

There are sure to be many surprises and unforeseen applications waiting as the field of endofullerene science moves out of its adolescent phase.

Acknowledgements It was a pleasure and a privilege to be part of the worldwide endofullerene collaboration established by Professor Nicholas Turro of Columbia University. The work there, until his untimely death in 2012, spanned nearly the entire period of small-molecule endofullerene research up to the present. This review is dedicated to his memory.

References

1. Strobel TA, Sloan ED, Koh CA (2009) Raman spectroscopic studies of hydrogen clathrate hydrates. J Chem Phys 130:014506
2. Michaut X, Vasserot A-M, Abouaf-Marguin L (2004) Temperature and time effects on the rovibrational structure of fundamentals of H_2O trapped in solid argon: hindered rotation and the RTC satellite. Vibrat Spectros 34:83–93
3. Chen Z, Lin Y-Y, Strauss HL (2000) Raman spectra of D_2 in water and ice. J Phys Chem B 104:3274–3279
4. Rudkevich DM, Leontiev AV (2004) Molecular encapsulation of gases. Aust J Chem 57:713–722
5. Brotin T, Dutasta J-P (2009) Cryptophanes and their complexes-present and future. Chem Rev 109:88–130
6. Fitzgerald SA, Churchill HOH, Korngut PM et al (2006) Low-temperature infrared spectroscopy of H_2 in crystalline C_{60}. Phys Rev B 73:155409
7. Suetsuna T, Dragoe N, Harneit W et al (2002) Separation of $N_2@C_{60}$ and $N@C_{60}$. Chem Eur J 8:5080–5083
8. Ito S, Shimotani H, Takagi H et al (2008) On the synthesis conditions of N and N_2 endohedral fullerenes. Fullerenes Nanotubes Carbon Nanostruct 16:206–213
9. Stanisky CM, Cross RJ, Saunders M (2009) Putting atoms and molecules into chemically opened fullerenes. J Am Chem Soc 131:3392–3395
10. Murata M, Murata Y, Komatsu K (2008) Surgery of fullerenes. Chem Commun 46: 6083–6094

11. Saunders M, Khong A, Shimshi R (1996) Chromatographic fractionation of fullerenes containing noble gas atoms. Chem Phys Lett 248:127–128
12. DiCamillo BA, Hettich RL, Guiochon G et al (1996) Enrichment and characterization of a noble gas fullerene: Ar@C_{60}. J Phys Chem 100:9197–9201
13. Yamamoto K, Saunders M, Khong A et al (1999) Isolation and spectral properties of Kr@C_{60}, a stable van der Waals molecule. J Am Chem Soc 121:1591–1596
14. Syamala MS, Cross RJ, Saunders M (2002) ^{129}Xe NMR spectrum of xenon inside C_{60}. J Am Chem Soc 124:6216–6219
15. Komatsu K, Murata M, Murata Y (2005) Encapsulation of molecular hydrogen in fullerene C_{60} by organic synthesis. Science 307:238–240
16. Murata M, Murata Y, Komatsu K (2006) Synthesis and properties of endohedral C_{60} encapsulating molecular hydrogen. J Am Chem Soc 128:8024–8033
17. Kurotobi K, Murata Y (2011) A single molecule of water encapsulated in fullerene C_{60}. Science 333:613–616
18. Frunzi M, Cross RJ, Saunders M (2007) Effect of xenon on fullerene reactions. J Am Chem Soc 129:13343–13346
19. Matsuo Y, Isobe H, Tanaka T et al (2005) Organic and organometallic derivatives of dihydrogen-encapsulated [60] fullerene. J Am Chem Soc 127:17148–17149
20. Li Y, Lei X, Lawler RG et al (2012) Synthesis, isomer count, and nuclear spin relaxation of H_2O@open-C_{60} nitroxide derivatives. Org Lett 14:3822–3825
21. Murata M, Maeda S, Morinaka Y et al (2008) Synthesis and reaction of fullerene C_{70} encapsulating two molecules of H_2. J Am Chem Soc 130:15800–15801
22. Frunzi M, Baldwin AM, Shibata N et al (2011) Kinetics and solvent-dependent thermodynamics of water capture by a fullerene-based hydrophobic nanocavity. J Phys Chem A 115:735–740
23. Iwamatsu S-I, Uozaki T, Kobayashi K et al (2004) A bowl-shaped fullerene encapsulates a water into the cage. J Am Chem Soc 126:2668–2669
24. Rubin Y, Jarrosson T, Wang G-W et al (2001) Insertion of helium and molecular hydrogen through the orifice of an open fullerene. Angew Chem Int Ed 40:1543–1546
25. Murata Y, Maeda S, Murata M et al (2008) Encapsulation and dynamic behavior of two H_2 molecules in an open-cage C_{70}. J Am Chem Soc 130:6702–6703
26. Chuang S-C, Murata Y, Murata M et al (2007) An orifice-size index for open-cage fullerenes. J Org Chem 72:6447–6453
27. Stanisky CM, Cross RJ, Saunders M et al (2005) Helium entry and escape through a chemically opened window in a fullerene. J Am Chem Soc 127:299–302
28. Patchovski Thiel: Patchovskii S, Thiel W (1997) Equilibrium yield for helium incorporation into buckminsterfullerene; quantum-chemical evaluation. J Chem Phys 106:1796–1799
29. Khong A, Jiménez-Vázquez HA, Saunders M et al (1998) An NMR study of He_2 inside C_{70}. J Am Chem Soc 120:6380–6383
30. Sebastianelli F, Xu M, Bačić Z (2010) Hydrogen molecules inside fullerene C_{70}: quantum dynamics, energetics, maximum occupancy, and comparison with C_{60}. J Am Chem Soc 132:9826–9832
31. Zimmerman JA, Eyler JR, Bach SBH et al (1991) "Magic number" carbon clusters: ionization potentials and selective reactivity. J Chem Phys 94:3556–3562
32. Nikawa H, Araki Y, Slanina Z et al (2010) The effect of atomic nitrogen on the C_{60} cage. Chem Commun 46:631–633
33. Wakahara T, Matsunaga Y, Katayama A (2003) A comparison of the photochemical reactivity of N@C_{60} and C_{60}: photolysis with disilirane. Chem Commun 2003:2940–2941
34. López-Gejo J, Martí AA, Ruzzi M et al (2007) Can H_2 inside C_{60} communicate with the outside world? J Am Chem Soc 129:14554–14555
35. Takeda A, Yokoyama Y, Ito S et al (2006) Superconductivity of doped Ar@C_{60}. Chem Commun 2006:912–914
36. Dragoe N, Flank AM, Lagarde P et al (2011) Molecular thermal contraction of the Ar@C_{60} endohedral fullerene. Phys Rev B 84:155448

37. Brown S, Cao J, Musfeldt JL et al (2006) Search for microscopic evidence for molecular level negative thermal expansion in fullerenes. Phys Rev B 73:125446
38. Morinaka Y, Sato S, Wakamiya A et al (2013) X-ray observation of a helium atom and placing a nitrogen atom inside He@C_{60} and He@C_{70}. Nature Commun 4:1554
39. Lee M, Suetsuna T et al (2002) Crystallographic characterization of Kr@C_{60} in (0.09Kr@C_{60}/)0.91C_{60})·{Ni^{II}(OEP)}·2C_6H_6. Chem Commun 2002:1352–1353
40. Ito S, Takeda T, Yokoyama et al (2004) Kr extended X-ray absorption fine structure study of endohedral Kr@C_{60}. J Phys Chem B 108:3191–3195
41. Sawa H, Kakiuchi T, Wakabayashi Y et al (2007) Direct observation of a gas molecule (H_2, Ar) swallowed by C_{60}. AIP Conf Proc 879:1419–1422
42. Sawa H, Wakabayashi Y, Murata Y et al (2005) Floating single hydrogen molecule in an open-cage fullerene. Angew Chem Int Ed 44:1981–1983
43. Even W, Smith J, Roth MW (2005) Molecular dynamics simulations of noble gases encapsulated in C_{60} fullerene. Mol Simul 31:207–213
44. Cimpoesu F, Ito S, Shimotani et al (2011) Vibrational properties of noble gas endohedral fullerenes. Phy Chem Chem Phys 13:9609–9615
45. Yagi K, Watanabe D (2009) Infrared spectra of water molecule encapsulated inside fullerene studied by instantaneous vibrational analysis. Int J Quantum Chem 109:2080–2090
46. Bühl M, Patchovskii S, Thiel W (1997) Interaction energies and NMR chemical shifts of noble gases in C_{60}. Chem Phys Lett 275:14–18
47. Zoleo A, Lawler RG, Lei X et al (2012) ENDOR evidence of electron-H_2 interaction in a fulleride embedding H_2. J Am Chem Soc 134:12881–12884
48. Filifou V, Mamone S, Simmons S et al (2013) Probing the C_{60} triplet state coupling to nuclear spins inside and out. Phil Trans R SocA 371:20120475
49. Carravetta M, Danquigny A, Mamone S et al (2007) Solid-state NMR of endohedral hydrogen-fullerene complexes. Phys Chem Chem Phys 9:4879–4894
50. Kroto HW, Heath JR, O'Brien SC et al (1985) C_{60}: Buckminsterfullerene. Nature 318:162–163
51. Saunders M, Jiménez-Vázquez Cross RJ et al (1994) Probing the interior of fullerenes by 3He NMR spectroscopy of endohedral 3He@C60 and 3He@C70. Nature 367:256–258
52. Pasquarello A, Schlüter M, Haddon RC (1992) Ring currents in icosahedral C_{60}. Science 257:1660–1661
53. Pasquarello A, Schlüter M, Haddon RC (1993) Ring currents in topologically complex molecules: application to C_{60}, C_{70}, and their hexa-anions. Phys Rev A 47:1783–1789
54. Bühl M (1998) The relation between endohedral chemical shifts and local aromaticities in fullerenes. Chem Eur J 4:734–739
55. Kleinpeter E, Klod S, Koch A (2008) Endohedral and external through-space shieldings of the fullerenes C_{50}, C_{60}, C_{60}^{6-}, C_{70}, C_{70}^{6-}—Visualization of (anti) aromaticity and their effects on the chemical shifts of encapsulated nuclei. J Org Chem 73:1498–1507
56. Bühl M, Thiel W, Jiao H et al (1994) Helium and lithium NMR chemical shifts of endofullerene compounds: an *ab initio* study. J Am Chem Soc 116:6005–6006
57. Saunders M, Jiménez-Vázquez HA, Cross RJ et al (1995) Analysis of isomers of the higher fullerenes by 3He NMR spectroscopy. J Am Chem Soc 117:9305–9308
58. Saunders M, Cross RJ, Jiménez-Vázquez HA et al (1996) Noble gas atoms inside fullerenes. Science 271:1693–1697
59. Sternfeld T, Saunders M, Cross RJ et al (2003) The inside story of fullerene anions: a ^{3}He NMR aromaticity probe. Angew Chem 115:3244–3247
60. Saunders M, Jiménez-Vázquez HA, Bangerter BW et al (1994) ^{3}He NMR: a powerful new tool for following fullerene chemistry. J Am Chem Soc 116:3621–3622
61. Murata M, Ochi Y, Kitagawa T et al (2008) NMR studies of monofunctionalized fullerene cation and anion encapsulationg a H_2 molecule. Chem Asian J 3:1336–1342
62. Li Y, Lei X, Lawler RG et al (2011) Synthesis and characterization of bispyrrolidine derivatives of H_2@C_{60}: differentiation of isomers using ^{1}H NMR spectroscopy of endohedral H_2. Chem Commun 47:2282–2284

63. Shabtai E, Weitz A, Haddon RC et al (1998) ^{3}He NMR of He@C_{60}^{6-} and He@C_{70}^{6-}. New records for the most shielded and the most deshielded ^{3}He inside a fullerene. J Am Chem Soc 120:6389–6393
64. Murata M, Ochi Y, Tanabe F et al (2008) Internal magnetic fields of dianions of fullerene C_{60} and its cage-opened derivatives studied with encapsulated H_2 as an NMR probe. Angew Chem Int Ed 47:2039–2041
65. Trulove PC, Carlin RT, Eaton GR et al (1995) Determination of the singlet-triplet energy separation for C_{60}^{2-} in DMSO by Electron Paramagnetic Resonance. J Am Chem Soc 117:6265–6272
66. NJT947: Li Y, Lei X, Lawler RG et al (2011) Indirect ^{1}H NMR characterization of H_2@C_{60} nitroxide derivatives and their nuclear spin relaxation. Chem Commun 47:12527–12529
67. Pietzak B, Weidinger A, Dinse K-P et al (2002) Group V endohedral fullerenes: N@C_{60}, N@C_{70}, and P@C_{60}. In: Akasaka T, Nagase S (eds) Endofullerenes: a new family of carbon clusters. Kluwer Academic Publishers, Doordrecht, pp 13–65
68. Sears DN, Jameson CJ (2003) Calculation of the ^{129}Xe chemical shift in Xe@C_{60}. J Chem Phys 118:9987–9989
69. Straka M, Lantto P, Vaara J (2008) Toward calculations of the ^{129}Xe chemical shift in Xe@C_{60} at experimental conditions: relativity, correlation, and dynamics. J Phys Chem A 112:2658–2668
70. Murphy TA, Pawlik T, Weidinger A et al (1996) Observation of atomlike nitrogen in nitrogen-implanted solid C_{60}. Phys Rev Lett 77:1075–1078
71. Knapp C, Weiden N, Käss H et al (1998) Electron paramagnetic resonance study of atomic phosphorus encapsulated in [60]fullerene. Mol Phys 95:999–1004
72. Kiefl RF, Duty TL, Schneider JW et al (1992) Evidence for endohedral muonium in K_xC_{60} and consequences for electronic structure. Phys Rev Lett 69:2005–2008
73. Kiefl RF, Warren JB, Marshall GM et al (1981) Muonium in the condensed phases of Ar, Kr, and Xe. J Chem Phys 74:308–313
74. Sternfeld T, Hoffman RE, Saunders M et al (2002) Two helium atoms inside fullerenes: probing the internal magnetic field in C_{60}^{6-} and C_{70}^{6-}. J Am Chem Soc 124:8786–8787
75. Turro NJ, Chen JY-C, Sartori E et al (2010) The spin chemistry and magnetic resonance of H_2@C_{60}. From the Pauli Principle to trapping a long lived nuclear excited spin state inside a buckyball. Acc Chem Res 43:225–345
76. Mamone S, Chen JY-C, Bhattacharyya et al (2011) Theory and spectroscopy of an incarcerated quantum rotor: The infrared spectroscopy, inelastic neutron scattering and nuclear magnetic resonance of H_2@C_{60} at cryogenic temperature. Coord Chem Rev 255:938–948
77. Beduz C, Carravetta M, Chen JY-C et al (2012) Quantum rotation of *ortho* and *para*-water encapsulated in a fullerene cage. PNAS 109:12894–12898
78. Levitt MH (2013) Spectroscopy of light-molecule endofullerenes. Phil Trans R Soc A 371:20120429
79. Levitt MH, Horsewill AJ (eds) (2013) Nanolaboratories: physics and chemistry of small-molecule endofullerenes. Phil Trans R Soc A 371(1998)
80. Mamone S, Ge Min, Hüvonen D et al (2009) Rotor in a cage: infrared spectroscopy of an endohedral hydrogen-fullerene complex. J Chem Phys 130:081103
81. Ge M, Nagel U, Hüvonen D et al (2011) Interaction potential and infrared absorption of endohedral H_2 in C_{60}. J Chem Phys 134:054507
82. Ge M, Nagel U, Hüvonen D et al (2011) Infrared spectroscopy of endohedral HD and D_2 in C_{60}. J Chem Phys 135:114511
83. Rõõm T, Peedu L, Ge M et al (2013) Infrared spectroscopy of small-molecule fullerenes. Phil Trans R Soc A 371:20110631
84. Herzberg G (1950) Molecular spectra and molecular structure I. Spectra of diatomic molecules, 2nd edn. Van Nostrand, Princeton
85. Kohama Y, Rachi T, Jing J et al (2009) Rotational sublevels of an ortho-hydrogen molecule encapsulated in an isotropic C_{60} cage. Phys Rev Lett 103:073001

86. Schettino V, Pagliai M, Ciabini L et al (2001) The vibrational spectrum of fullrene C_{60}. J Phys Chem A 105:11192–11196
87. Farkas A (1935) Orthohydrogen, parahydrogen and heavy hydrogen. Cambridge University Press, London
88. Chen JY-C, Li Y, Frunzi M et al (2013) Nuclear spin isomers of guest molecules in $H_2@C_{60}$, $H_2O@C_{60}$ and other fullerenes. Phil Trans R Soc A 371:20110628
89. Horsewill AJ, Panesar KS, Rols S et al (2009) Quantum translator-rotator: Inelastic neutron scattering of dihydrogen molecule trapped inside anisotropic fullerene cages. Phy Rev Lett 102:013001
90. Horsewill AJ, Rols S, Johnson MR et al (2010) Inelastic neutron scattering of a quantum translator-rotator in a closed fullerene cage: Isotope effects and translation-rotation coupling in H_2C_{60} and $HD@C_{60}$. Phys Rev B 82:081410(R)
91. Horsewill AJ, Goh K, Rols S et al (2013) Quantum rotation and translation of hydrogen molecules encapsulated inside C_{60}: temperature dependence of inelastic neutron scattering spectra. Phil Trans R Soc A 371:20110627
92. Horsewill AJ, Panear KS, Rols S (2012) Inelastic neutron scattering investigations of the quantum molecular dynamics of a H_2 molecule entrapped inside a fullerene cage. Phys Rev B 85:205440
93. Goh KSK, Jiménez-Ruiz M, Johnson MR et al (2014) Symmetry-breaking in the endofullerene $H_2O@C_{60}$ revealed in the quantum dynamics of *ortho* and *para*-water: a neutron scattering investigation. Phys Chem Chem Phys 16:21330–21339
94. Xu M, Jiménez-Ruiz M, Johnson MR et al (2014) Confirming a predicted selection rule in inelastic neutron scattering spectroscopy: the quantum translator-rotator H_2 entrapped inside C_{60}. Phys Rev Lett 113:123001
95. Xu M, Sebastianelli F, Bačić Z (2008) Quantum dynamics of coupled translational and rotational motions of H_2 inside C_{60}. J Chem Phys 128:011101
96. Xu M, Sebastianelli F, Bačić Z et al (2008) H_2, HD, and D_2 inside C_{60}: coupled translation–rotation eigenstates of the endohedral molecules from quantum five-dimensional calculations. J Chem Phys 129:064313
97. Xu M, Sebastianelli F, Gibbons BR et al (2009) Coupled translation-rotation eigenstates of H_2 in C_{60} and C_{70} on the spectroscopically optimized interaction potential: effects of cage anisotropy on the energy level structure and assignments. J Chem Phys 130:224306
98. Sebastianelli F, Xu M, Bačić Z et al (2010) Hydrogen molecules inside fullerene C70: quantum dynamics, energetics, maximum occupancy, and comparison with C_{60}. J Am Chem Soc 132:9826–9832
99. Ye S, Xu M, Bačić Z et al (2010) Quantum dynamics of a hydrogen molecule inside an anisotropic open-cage fullerene: coupled translation-rotation eigenstates and comparison with inelastic neutron scattering spectroscopy. J Phys Chem A 114:9936–9947
100. Xu M, Ye S, Powers A et al (2013) Inelastic neutron scattering spectrum of $H_2@C_{60}$ and its temperature dependence decoded using rigorous quantum calculations and a new selection rule. J Chem Phys 139:064309
101. Xu M, Ye S, Lawler R et al (2013) HD in C_{60}: theoretical prediction of the inelastic neutron scattering spectrum and its temperature dependence. Phil Trans R Soc A 371:20110630
102. Cross RJ (2001) Does H_2 rotate freely inside fullerenes? J Phys Chem A 105:6943–6944
103. Cross RJ (2008) Vibration-rotation spectroscopy of molecules trapped inside C_{60}. J Phys Chem A 112:7152–7156
104. Felker PM (2013) Near-orbital/configuration-interaction study of coupled translation-rotation states in $(H_2)_2@C_{70}$. J Chem Phys 138:044309
105. Mondelo-Martell M, Huarte-Larranago F (2015) 5D quantum dynamics of the $H_2@SWT$ system: quantitative study of the rotational-translational coupling. J Chem Phys 142:084304
106. Sebastianelli F, Xu M, Kanan DK et al (2007) One and two hydrogen molecules in the large cage of the structure II clathrate hydrate: quantum translation-rotation dynamics close to the cage wall. J Phys Chem A 111:6115–6121

107. Sebastianelli R, Xu M, Bacic Z (2008) Quantum dynamics of small H_2 and D_2 clusters in the large cage of structure II clathrate hydrate: energetics, occupancy, and vibrationally averaged cluster structures. J Chem Phys 129:244706
108. Felker PM (2013) Fully quantal calculation of H_2 translation-rotation in $(H_2)_4@5^{12}6^4$ clathrate inclusion compounds. J Chem Phys 138:174306
109. Felker PM (2014) Fully quantal calculation of H_2 translation-rotation states in the $(p\text{-}H_2)_2@5^{12}6^4$ clathrate hydrate inclusion compound. J Chem Phys 141:184305
110. Ye S, Xu M, FitzGerald S et al (2013) H_2 in solid C_{60}: coupled translation-rotation eigenstates in the octahedral site from quantum five-dimensional calculations. J Chem Phys 138:244707
111. Farimani AB, Wu Y, Aluru NR (2013) Rotational motion of a single water molecule in a buckyball. Phys Chem Chem Phys 15:17993–18000
112. Bug ALR, Wilson A, Voth GA (1992) Nuclear vibrational dynamics of a neon atom in C_{60}. J Phys Chem 96:7864–7869
113. Saunders M, Jiménez-Vázquez H, Cross RJ et al (1993) Stable compounds of helium and neon: $He@C_{60}$ and $Ne@C_{60}$. Science 259:1428–1430
114. Laskin J, Peres T, Lifshitz C et al (1998) An artificial molecule of Ne_2 inside C_{70}. Chem Phys Lett 285:7–9
115. Jiménez-Vázquez HA, Cross RJ (1996) Equilibrium constants for noble-gas fullerene compounds. J Chem Phys 104:5589–5593
116. Carravetta M, Murata Y, Murata M et al (2004) Solid-state NMR spectroscopy of molecular hydrogen trapped inside an open-cage fullerene. J Am Chem Soc 126:4092–4093
117. Carravetta M, Johannessen OG, Levitt MH (2006) Cryogenic NMR spectroscopy of endohedral hydrogen-fullerene complexes. J Chem Phys 124:104507
118. Tomaselli M, Meier BH (2001) Rotational-state selective nuclear magnetic resonance spectra of hydrogen in a molecular trap. J Chem Phys 115:11017–11020
119. Tomaselli M (2003) Dynamics of diatomic molecules confined in a chemical trap I. Nuclear magnetic resonance experiments on hydrogen in solid C_{60}. Mol Phys 101:3029–3051
120. Mamone S, Consistrè M, Carignani E et al (2014) Nuclear spin conversion of water inside fullerene cages detected by low-temperature nuclear magnetic resonance. J Chem Phys 140:194306
121. Carravetta M, Danquigny A, Mamone S et al (2007) Solid-state NMR of endohedral hydrogen-fullerene complexes. Phys Chem Chem Phys 9:4879–4894
122. Mamone S, Consistrè M, Heinmaa I et al (2013) Nuclear magnetic resonance of hydrogen molecules trapped inside C_{70} fullerene cages. Chem Phys Chem 14:3121–3130
123. Consistrè M, Mamone S, Denning M et al (2013) Anisotropic nuclear spin interactions in $H_2O@C_{60}$ determined by solid-state NMR. Phil Trans R Soc A 371:20120102
124. Sartori E, Ruzzi M, Turro NJ et al (2006) Nuclear relaxation of H_2 and $H_2@C_{60}$ in organic solvents. J Am Chem Soc 128:14752–14753
125. Chen JY-C, Martí AA, Turro NJ et al (2010) Comparative NMR properties of H_2 and HD in toluene-d_8 and in H_2/HD@C_{60}. J Phys Chem B 114:14689–14695
126. Li Y, Chen JY-C, Lei X et al (2012) Comparison of nuclear spin relaxation of $H_2O@C_{60}$ and $H_2@C_{60}$ and their nitroxide derivatives. J Phys Chem Lett 3:1165–1168
127. Chen JY-C (2011) Spin chemistry of guest@host systems: $H_2@C_{60}$ and nitroxide@octa acid. Dissertation, Columbia University
128. Sartori E, Ruzzi M, Turro NJ et al (2008) Paramagnet enhanced nuclear relaxation of H_2 in organic solvents and $H_2@C_{60}$. J Am Chem Soc 130:2221–2225
129. Frunzi M, Lei X, Murata Y et al (2010) Magnetic interaction of solution-state paramagnets with encapsulated H_2O and H_2. J Phys Chem Lett 1:1420–1422
130. Li Y, Lei X, Chen JY-C et al (2013) Paramagnet enhanced nuclear spin relaxation in $H_2O@open\text{-}C_{60}$ and $H_2@open\text{-}C_{60}$. Org Lett 15:4746–4749
131. Li Y, Lei X, Lawler RG et al (2010) Distance-dependent paramagnet-enhanced nuclear spin relaxation of $H_2@C_{60}$ derivatives covalently linked to a nitroxide radical. J Phys Chem Lett 1:2135–2138

132. Rastrelli F, Frezzato D, Lawler RG et al (2013) Predicting the paramagnet-enhanced NMR relaxation of H_2 encapsulated in endofullerene nitroxides by density-functional theory calculations. Phil Trans R Soc A 371:20110634
133. Garbuio L, Li Y, Antonello S et al (2014) Interaction of $H_2@C_{60}$ and nitroxide through conformationally constrained peptide bridges. Photochem Photobiol 90:439–447
134. Lloyd LS, Asghar A, Burns MJ et al (2014) Hyperpolarizatoin through reversible interactions with *para*hydrogen. Catal Sci Technol 4:3544–3554
135. Graafen D, Ebert S, Neudert O et al (2014) ^{1}H NMR spectroscopy and MR imaging with hyperpolarized substances. Ann Rept NMR Spectros 82:167–215
136. Chen JY-C, Li Y, Frunzi M et al (2013) Nuclear spin isomers of guest molecules in $H_2@C_{60}$, $H_2O@C_{60}$ and other fullerenes. Phil Trans R Soc A 371:20110628
137. Wigner E (1933) Über die paramagnetische umwandlung von para-orthowasserstoff III. Zeit fur Physik Chem B 23:28–32
138. Atkins PW, Clugston MJ (1974) Ortho-para hydrogen conversion in paramagnetic solutions. Mol Phys 27:1619–1631
139. Li Y, Chen JY-C, Lei X et al (2012) Comparison of nuclear spin relaxation of $H_2O@C_{60}$ and $H_2@C_{60}$ and their nitroxide derivatives. J Phys Chem Lett 3:1165–1168
140. Frunzi M, Jockusch S, Chen JY-C et al (2011) A photochemical on-off switch for tuning the equilibrium mixture of H_2 nuclear spin isomers as a function of temperature. J Am Chem Soc 133:14232–14235
141. Li Y, Lei X, Jockusch S et al (2010) A magnetic switch for spin-catalyzed interconversion of nuclear spin isomers. J Am Chem Soc 132:4042–4043
142. Li Y, Lei X, Lawler RG et al (2011) Distance-dependent para-H_2 to ortho-H_2 conversion in $H_2@C_{60}$ derivatives covalently linked to a nitroxide radical. J Phys Chem Lett 2:741–744
143. Sartori E, Ruzzi M, Lawler RG et al (2008) Nitroxide paramagnet-induced *para-ortho* conversion and nuclear spin relaxation of H_2 in organic solvents. J Am Chem Soc 130:12752–12756
144. Krachmalnicoff A, Bounds R, Mamone S et al (2015) Synthesis and characterisation of an open-cage fullerene encapsulating hydrogen fluoride. Chem Commun 51:4993–4996
145. Garbacz P, Jackowski K, Makulski W et al (2012) Nuclear magnetic shielding for hydrogen in selected isolated molecules. J Phys Chem A 116:11896–11904
146. Hindermann DK, Cornwell CD (1968) Fluorine and proton NMR study of gaseous hydrogen fluoride. J Chem Phys 48:2017–2025
147. Aoyagi S, Nishibori E, Sawa H (2010) A layered ionic crystal of polar $Li@C_{60}$ superatoms. Nat Chem 2:678–683
148. Whitener KE Jr, Cross RJ, Saunders M et al (2009) Methane in an open-cage [60] fullerene. J Am Chem Soc 131:6338–6339
149. Whitener KE Jr, Frunzi M, Iwamatsu S-I et al (2008) Putting ammonia into a chemically opened fullerene. J Am Chem Soc 130:13996–13999
150. Iwamatsu S-I, Stanisky CM, Cross RJ et al (2006) Carbon monoxide inside an open-cage fullerene. Angew Chem Int Ed 45:5337–5340
151. Smith AB III, Strongin RM, Brard L et al (1994) Synthesis and 3He NMR studies of C_{60} and C_{70} epoxide, cyclopropane, and annulene derivatives containing endohedral helium. J Am Chem Soc 116:10831–10832
152. Morinaka Y, Tanabe F, Murata M et al (2010) Rational synthesis, enrichment, and ^{13}C NMR spectra of endohedral C_{60} and C_{70} encapsulating a helium atom. Chem Commun 46:4532–4534
153. Bondi A (1964) van der Waals volumes and radii. J Phys Chem 68:441–451

Chapter 13
Preparation and Chemistry of $N@C_{60}$

Shen Zhou and Kyriakos Porfyrakis

Abstract Endohedral fullerene $N@C_{60}$, which is formed by C_{60} plus an atomic nitrogen located in the centre of the fullerene cage, has attracted interest, due to its exotic properties, such as exceptionally long spin relaxation time. Its preparation and chemical functionalization are discussed in this chapter; those are the most important topics in $N@C_{60}$ field, as preparation directly affects the availability of this new material, and chemical functionalization enables us to control and tune its properties. Herein, we will firstly introduce different synthesis, purification, and characterization methods of $N@C_{60}$, then move on to $N@C_{60}$ stability. At the end, a variety of $N@C_{60}$-related chemical reactions are reviewed, with emphasis on how the properties of the molecule change after functionalization.

13.1 $N@C_{60}$ Production

13.1.1 Synthesis

There are several techniques applied for the synthesis of $N@C_{60}$. Extreme conditions are commonly used for all of these methods, because the formation of an atomic nitrogen encapsulated in fullerene cage from nitrogen gas and pristine fullerene is a nonthermodynamically favourable process. Nevertheless, once the molecule is formed, the fullerene cage isolates and stabilizes the nitrogen radical, so the products synthesized can be collected and stored. The ratio of $N@C_{60}$ to C_{60} resulting from different methods of synthesis has been reported to range from 1:100,000 to 1:100.

The first method, ion implantation using a commercial ion source, is adopted from the original way that Murphy and co-workers firstly synthesized $N@C_{60}$ in 1996 [1].

S. Zhou · K. Porfyrakis (✉)
Department of Materials Science, University of Oxford, Oxford OX1 3PH, UK
e-mail: kyriakos.porfyrakis@materials.ox.ac.uk

A.A. Popov (ed.), *Endohedral Fullerenes: Electron Transfer and Spin*,
Nanostructure Science and Technology, DOI 10.1007/978-3-319-47049-8_13

Figure 13.1 illustrates the optimized experiment setup. An effusion cell is applied to sublime C_{60} and to gradually build up a C_{60} film on a cooled target. The rate of fullerene sublimation is recorded by a thickness monitor, so that a feedback control on the heating power can be applied to obtain a constant deposition rate on the cooling target. While the C_{60} film is growing, nitrogen ions generated by a commercial, low-energy, ion source are bombarding the surface of the C_{60} film. Benefiting from the *in situ* formation of film and continuous nitrogen bombardment, the productively of this method is scalable up to grams of crude products per run, while the yield ($N@C_{60}/C_{60}$) is *c.a.* 10^{-4} in concentration.

$C_{59}N$ has been reported as a by-product of this method, by Abe [2]. According to their research focused on the effect of the beam energy, the synthesis of $N@C_{60}$ requires ion energy larger than 20 eV, while $C_{59}N$ will be synthesized when the energy is between 40 and 50 eV. Therefore, beam energy is an important parameter that controls $N@C_{60}$ production. Experimental optimization suggested 40 eV to be the most efficient condition for increased yield of $N@C_{60}$ [3]. Compared with ordinary ion implantation technology, such a low beam energy limits the beam current and subsequently the yield. Therefore, it seems that the main experimental barrier to improving the yield further with this method is having an ion source with a large beam current density at low beam energy range.

The second method "glow discharge" is designed for a lower cost experiment setup (Fig. 13.2). By utilizing the collision between N_2 and fullerene in high temperature, $N@C_{60}$ was synthesized with a yield from 5 to 15 ppm [4, 5]. Owing to the inefficient dissociation process of N_2, not only atomic N but also N_2 were found to be encapsulated into the fullerene cage. In addition to that, the harsh reaction conditions, such as 650 °C and 850 V, are beyond the stability of $N@C_{60}$, thus the production yield of this method remains lower in comparison to the others.

As the third method, a radio frequency capacitively coupled plasma system was introduced to the synthesis of $N@C_{60}$ in 2002 [6, 7]. The N^+ ions are created by a

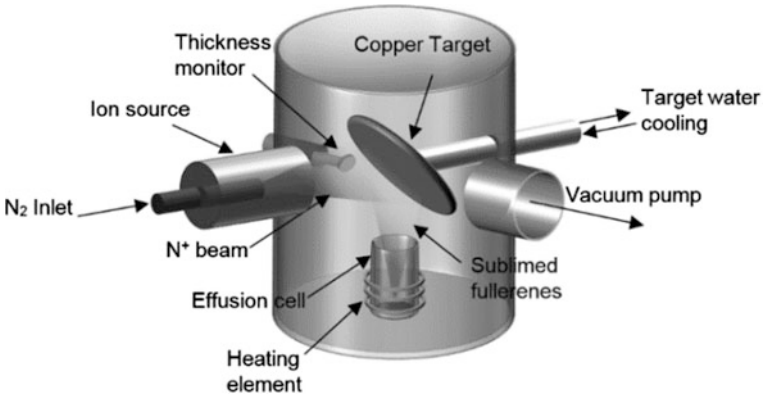

Fig. 13.1 Experimental setup of a nitrogen implantation apparatus using a commercial ion source

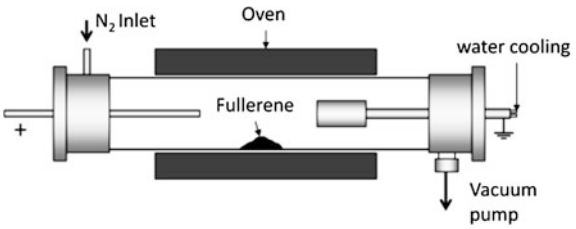

Fig. 13.2 Schematic view of a glow discharge reactor

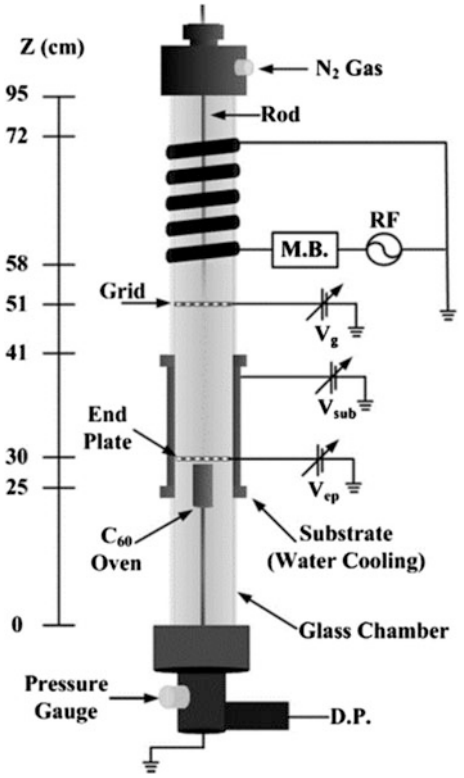

Fig. 13.3 Schematic view of nitrogen implantation apparatus with RF plasma (reprinted from Ref. [11], copyright AIP Publishing LLC)

13.56 MHz plasma generator from N_2 gas, and finally collide and react with C_{60} evaporated from an effusion cell (Fig. 13.3). With intensive work on yield optimisation on tuning parameters like pressure, grid voltage, beam energy, and oven temperature, the purity of the crude product were improved from 200 ppm to 0.83% [8–11]. Therefore, this technique have its amazing advantage in directly synthesis spin-enriched N@C_{60}/C_{60} mixtures. However, with only 1–5% of the final product being soluble, the productivity of this method is limited by the significant polymerization of C_{60} during the synthesis procedure. Besides, the scalability of this method is a remaining problem to tackle.

13.1.2 Purification

Since every method of synthesis of $N@C_{60}$ offers a mixture of $N@C_{60}$ and C_{60}, separating $N@C_{60}$ from C_{60} is an important topic. To date, the only successful method for purification of $N@C_{60}$ is preparative HPLC (High-Pressure Liquid Chromatography). $N@C_{60}$ and C_{60} have almost identical chemical and physical properties. HPLC uses small differences in their molecular weight and polarizability to separate the two species.

Different HPLC columns have been applied to the enrichment of $N@C_{60}$, such as PBB [12, 13], Buckyprep [3, 14–16] and PYE [12, 15, 17]. The ratio between retention times of $N@C_{60}$ and C_{60} in these columns were reported to be 1.027 [12] 1.037 [16] and 1.007 [12], respectively. In terms of the separation mechanism, Buckyprep and PYE column, which are functionalized with pyrene groups, mainly utilize the larger dispersion force resulting from the higher molecular weight of $N@C_{60}$ than C_{60}. On the other hand, it has been reported that the PBB column (functionalized with the large, electronegative element bromine) can incorporate the larger polarizability of $N@C_{60}$ together with the difference in molecular weight as a means of separation [12]. Considering the limited content of $N@C_{60}$ in the crude mixture, the separation is normally performed with multiple stages. At the beginning of the separation, a large quantity of mixture needs to be processed while the eluting peak of $N@C_{60}$ is not detectable. Conservatively collecting the second half fraction of C_{60} peak can quickly enrich the spin in a large scale. When the mixture is enriched to a good extent to resolve the eluting curve of $N@C_{60}$, recycling the mixture enables a complete separation between C_{60} and $N@C_{60}$. Figure 13.4 and Fig. 13.5 show the HPLC chart using PBB and Buckyprep, respectively. They are respectively in the initial stage (Fig. 13.4) and the final stage (Fig. 13.5) of the purification.

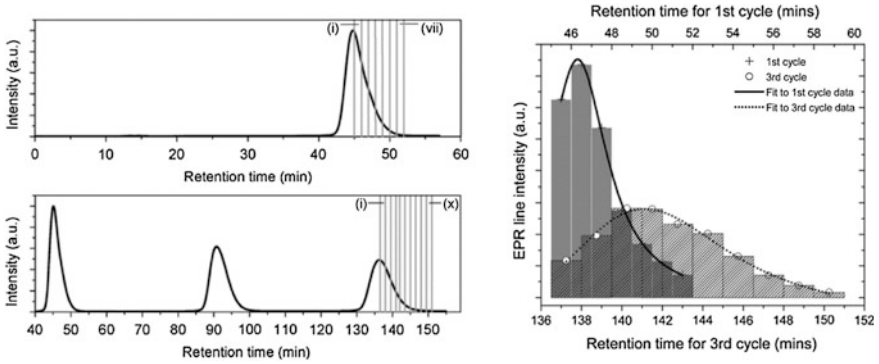

Fig. 13.4 Non-recycling and Recycling HPLC chart of the spin enrichment of the crude mixture of $N@C_{60}/C_{60}$ (column: 15 PBB 100 × 500 mm, eluent: toluene 300 ml/min) (*left*). EPR signal mapping of eluting fractions in different retention times, which reconstructs the eluting curve of $N@C_{60}$ (*right*) (reprinted from Ref. [13])

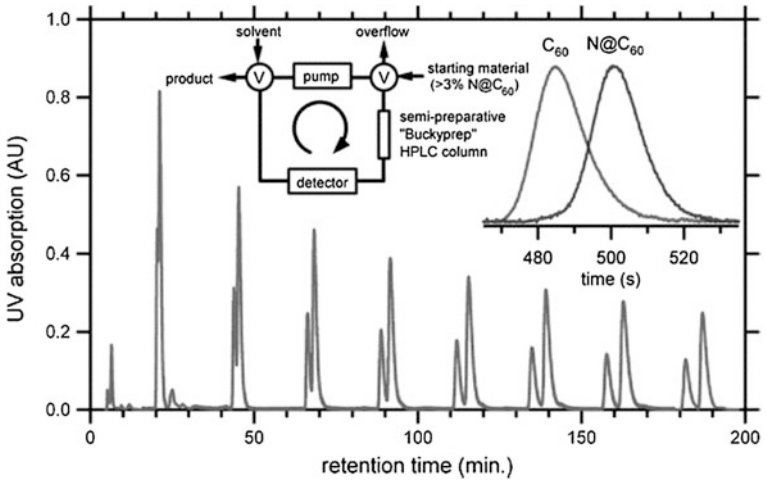

Fig. 13.5 Recycling HPLC chart for separating C_{60} and N@C_{60} in the final stage with well enriched mixture (column: Buckyprep 10 × 250 mm, eluent: toluene/hexane, 4:1, 3 ml/min). *Inset* The setup of recycling HPLC, and analytical HPLC of the pure substances (column: Buckyprep 4.6 × 250 mm, eluent: toluene, 1 ml/min) (reprinted from Ref. [16])

In order to avoid misassignment of the HPLC peak of the product, the fingerprint of the EPR signal of N@C_{60} (discussed in Sect. 13.1.3) is a better criterion to indicate the elution of N@C_{60}, during the entire purification procedure. By-products like N_2@C_{60}, $C_{60}O$ also elute in similar retention times depending on the column used.

13.1.3 Characterization

A vast array of techniques has been used to characterize N@C_{60}, but its electron paramagnetic properties are the most characteristic ones. Among different ways of measuring its spin signal, X-band CW-EPR is the most commonly used method. Due to the three unpaired electrons in the 2p orbital of the nitrogen, N@C_{60} is a paramagnetic spin system similar to atomic nitrogen. Its spin Hamiltonian can be written as $\widehat{H} = \frac{\mu_B}{\hbar} B_0^T g \widehat{S} + \widehat{S}^T A \widehat{I}$ in high field limitation, where μ_B the Bohr magnetron, B_0 is the external field, g is the g-factor of the electron spin, and $\boldsymbol{A}$ is the hyperfine interaction tensor. Figure 13.6 demonstrates the energy level diagrams and the allowed transitions for ^{14}N@C_{60} and ^{15}N@C_{60} in high field, respectively. In both situations, the energy levels firstly split to four levels caused by Zeeman effect, and each energy level divides to various hyperfine energy levels depending on the nuclear spin of the nitrogen atom. Due to the triple degeneration of the transitions, there will be three EPR lines for ^{14}N@C_{60} and two for ^{15}N@C_{60} in the

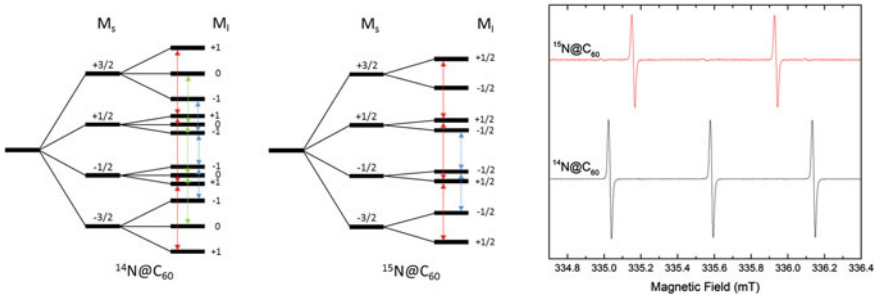

Fig. 13.6 Energy level diagrams and the allowed transitions for $^{14}N@C_{60}$ (*left*) and $^{15}N@C_{60}$ (*middle*) in high field, and the X-band CW-EPR spectra of $^{15}N@C_{60}$ and $^{14}N@C_{60}$ in toluene solution at room temperature (*right*)

X-band CW-EPR spectra. If high resolution measurement is applied, second-order hyperfine coupling from the nitrogen nuclear spin and hyperfine coupling from the ^{13}C on fullerene cage (shown in Fig. 13.7) will also be detected [18, 19] (the spectrum was taken with $^{14}N@C_{60}$ sample. In following content, N represents the most natural abundant ^{14}N isotope, unless specified). The most unique property of the EPR signal of $N@C_{60}$ is its long relaxation time [20, 21]. The relaxation time consist of spin-lattice relaxation time (T_1) and spin–spin relaxation time (T_2). T_2 = 250 μs which is the longest spin–spin relaxation time for a molecular radical was observed from $N@C_{60}$ in CS_2 solution at 170 K [20].

Apart from the electron spin properties, mass spectroscopy and UV/Vis absorption spectroscopy were also applied to characterize $N@C_{60}$. Demonstrated in Fig. 13.8, the most well-resolved mass spectrum of $N@C_{60}$ was taken by MALDI-TOF technique, with 1, 1, 4, 4-tetraphenyl-1, 3-butadiene being the matrix [22]. The mass spectrum showed a similar isotropic distribution to that of C_{60}, and the additional mass charge ratio of 14 is due to the presence of the incarcerated nitrogen atom. Different UV/Vis absorption spectra of $N@C_{60}$ have been reported in the literature. While the completely indistinguishable optical properties of $N@C_{60}$ and C_{60} have being reported (Fig. 13.9 left), we previously reported that the absorption features of C_{60} in 440–640 nm region are greatly diminished in the spectrum of $N@C_{60}$ (Fig. 13.9 right). The latter further supported the diminishment to the suppressing effect of the nitrogen atom to Herzberg–Teller vibronic interactions which enable these transitions in a C_{60} molecule. Despite the argument of the absorption features in 440–640 nm, the unchanged absorption onset and the unchanged forbidden character of the transition between the quartet and doublet state of the nitrogen atom that confirmed by both studies suggested the lack of interaction between the nitrogen atom and the cage.

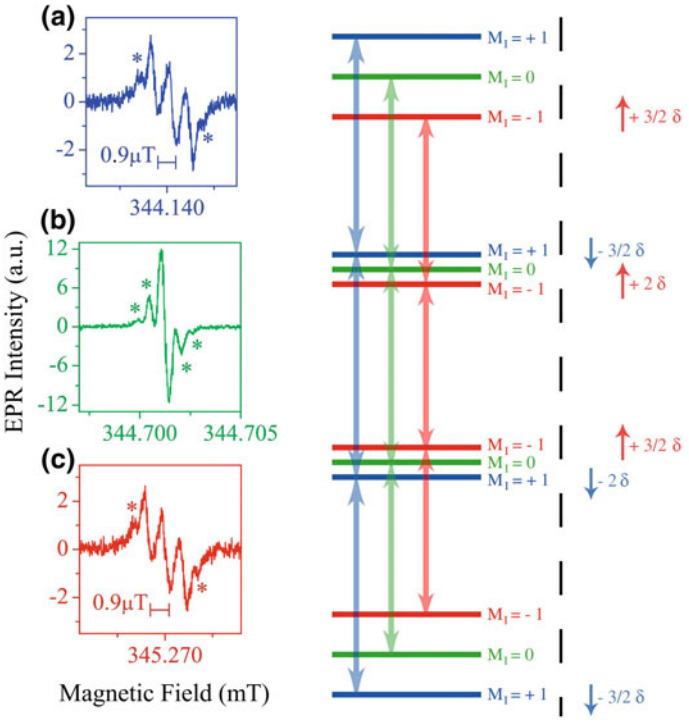

Fig. 13.7 Zoom-in EPR signals (*left*) of $^{14}N@C_{60}$ left peak (**a**), middle peak (**b**) and right peak (**c**) showing details of the line-shape structure caused by the second-order hyperfine corrections and hyperfine coupling due to the ^{13}C on the fullerene cage (marked with *asterisk*). The second-order corrections to the energy levels of $^{14}N@C_{60}$, $\delta = a^2/(\gamma_e B_0)$ (*right*) (reprinted from Ref. [19])

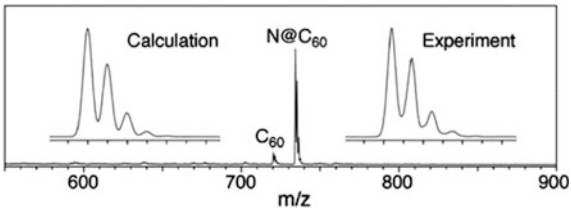

Fig. 13.8 MALDI-TOF mass spectrum of a mixture of $N@C_{60}/C_{60}$ (8:2) with 1,1,4,4-tetraphenyl-1,3-butadiene (reprinted from Ref. [22])

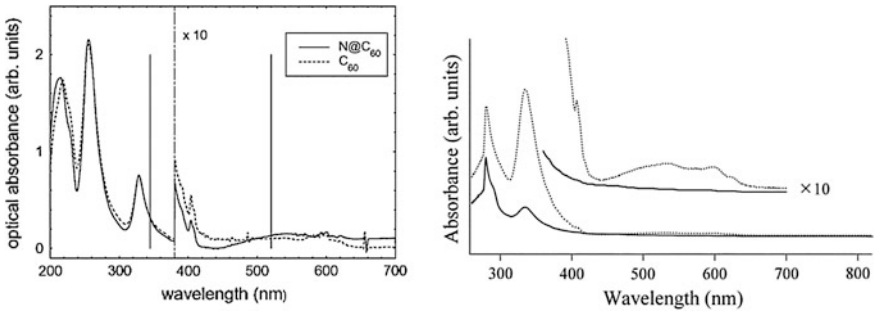

Fig. 13.9 The rather controversial UV/Vis spectrum of N@C_{60} dissolved in Hexane, taken by different researchers (*left*) [14], (*right*) [12] (reprinted from Refs. [12, 14])

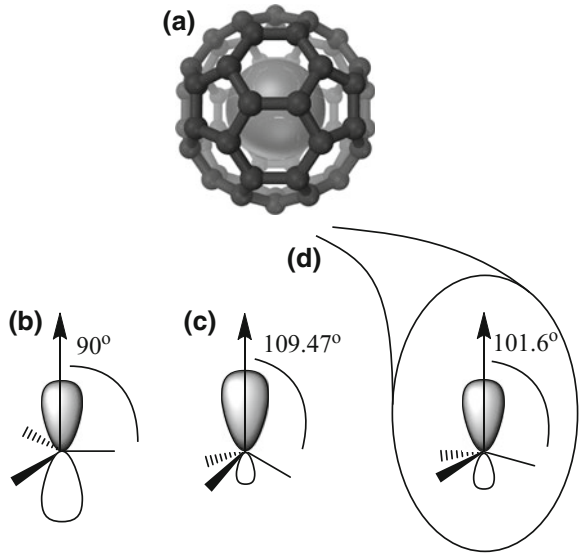

Fig. 13.10 **a** The molecular model of N@C_{60}, **b** ideally planar sp^2-hybridized carbon atom (e.g. in C_2H_4 and graphene) , **c** ideally tetrahedral sp^3-hybridized carbon atom (e.g. in CH_4), and (d) the non-planar sp^2-hybridized carbon atom in C_{60}

13.2 Stability of N@C_{60}

As we mentioned in the synthesis section, the formation of N@C_{60} is not an energetically favourable procedure. The main reason behind the successful encapsulating lays in the relative chemical inertness of the inner surface of C_{60} molecule. Although all carbons on the cage are sp^2, their bond angles are more close to those in a sp^3 carbon (comparisons are shown in Fig. 13.10b–d) [23]. The resulting strain is not only the fundamental driving force for different exohedral chemical functionalizations [23, 24], but also makes the inner surface of C_{60} molecule inert. Because an endohedral chemical bond request a pyramidalization of the sp^2 carbon towards the cage centre, which would further enhance bond strain.

Despite of the inertness of the inner surface of the fullerene cage, which kinetically prevents the nitrogen atom from escaping at ordinary ambient conditions, the product can decompose, if the energy barrier of the decomposition can be overcome. Different reaction conditions during the functionalization procedure might offer the required energy. Therefore, it is worth reviewing the stability issue of the novel molecule, before moving on to its chemical functionalization.

13.2.1 Thermal Stability

According to thermal annealing experiments on N@C_{60} powder, it has been reported that the main signal decay occurs around 500 K, with a 20% pre-decay happened around 440 K [25]. The spin signal of N@C_{60} was completely quenched after 520 K. The lost signal could not be recovered by cooling down the temperature afterward, which implies the endohedral fullerene system decomposed during the heating procedure. It is worth mentioning that a pre-decay was found to be independent from the major decay stage, suggesting there were two different species in N@C_{60} powder sample decomposing at different temperature. Without experimental confirmation, potential isomers or the influence of ^{13}C on the fullerene cage were proposed to explain the two independent stages of decomposition. Overall, compared with those of other group-V endohedral fullerenes, such as N@C_{70}, P@C_{60}, the thermal stability of N@C_{60} is the best, but it is still lower than those of other endohedral fullerenes like He@C_{60} [26] and endohedral metallofullerenes [27]. Therefore, high temperature needs to be avoided during storage and functionalization of N@C_{60}.

The mechanism of thermal decomposition was studied by density functional calculations [25, 28]. Figure 13.11 compares the calculated formation enthalpies of individual states during three optimized decomposition procedures, which are through a [5, 6] bond (a), through a [6, 6] bond (b), and through a carbon atom (c). The *x*-axis represents the distance from the nitrogen atom to the centre of the fullerene cage. The penetration of the nitrogen atom through a [6, 6] bond having the lowest the energy barrier (41 kcal/mol) would be the dominant decomposition mechanism, while the penetration through a [5, 6] bond (energy barrier 49 kcal/mol) offers an alternative mechanism. On the contrary, the penetration around a carbon atom or the centre of a pentagon/hexagon (not shown in Fig. 13.11) are energetically not allowed. The energy barrier of *c.a.* 40 kcal mol^{-1} could well explain the low decomposition temperature of N@C_{60} based on the Arrhenius equation. Nevertheless, since all calculations were based on the endohedral nitrogen atom in its doublet state ($S = 1/2$), the spin-forbidden transition from the quartet ground state ($S = 3/2$) to a doublet state might be difficult to take place. Starting from quartet state instead, the higher energy barrier and the evolution of the formation enthalpies during the penetration through a [6, 6] bond are compared with those of doublet state in Fig. 13.12.

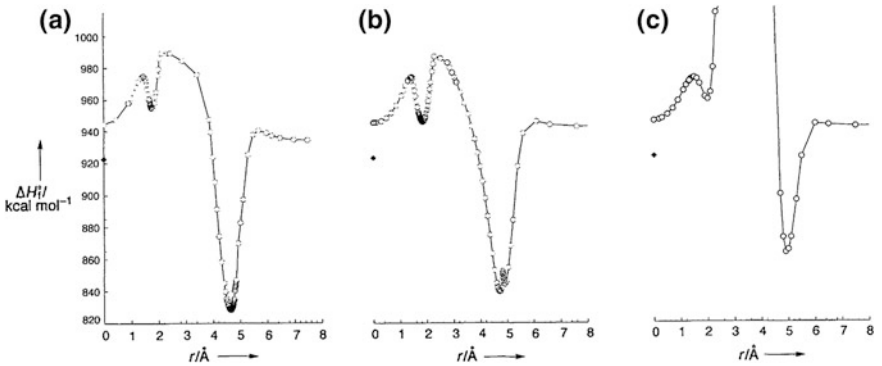

Fig. 13.11 Calculated formation enthalpies of individual states during three optimized decomposition procedures, which are through a [5, 6] bond (**a**), through a [6, 6] bond (**b**) and around a carbon atom (**c**). All calculations were performed for N in its doublet state, and the energy of quartet state is labelled with lozenge (reprinted from Ref. [28])

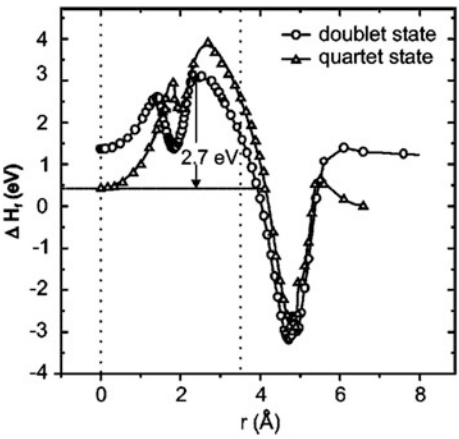

Fig. 13.12 Evaluation of the formation enthalpies via the [6, 6] bond decomposition mechanism, starting from a doublet N and quartet N, respectively, (reprinted from Ref. [25])

13.2.2 Chemical Stability

$N@C_{60}$ has been reported to be unstable when it is exposed to Lewis base such as DBU at room temperature [29]. Figure 13.13 demonstrates the significant spin quenching phenomenon after adding DBU to $N@C_{60}$. The well-resolved spin signal of $N@C_{60}$ first got suppressed by a broad spin signal of the fullerene anion after adding DBU. Neutralizing the fullerene anion with acid could not recover the spin signal. Therefore, this research proved that exposure to DBU will destabilize the endohedral system, which is this particularly important during the chemical functionalization of $N@C_{60}$.

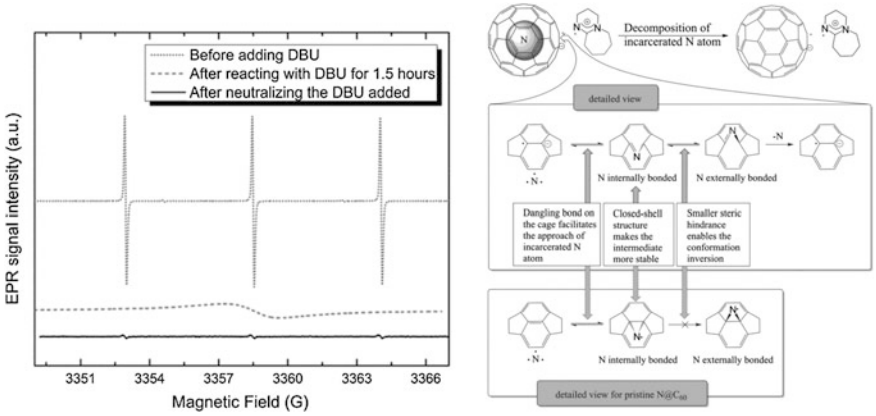

Fig. 13.13 The significant spin quenching phenomenon after adding DBU to N@C_{60}, and the proposed decomposition pathway for N@C_{60}^- compared with pristine N@C_{60} (reprinted from Ref. [29])

The cause of the instability was proposed to be the decomposition of the fullerene anion formed after interaction with a Lewis base such as DBU. During the nitrogen penetration through a [6, 6] bond which has been proved to be the most energetically favourable procedure for the decomposition of pristine N@C_{60}, there are three main reasons why the fullerene anion can further decrease the energy barrier. First, the presence of negative charge and dangling bond on the cage facilitates the approach of the incarcerated nitrogen atom. Secondly, the intermediate state during the penetration is a closed-shell structure, which lowers the kinetic barrier significantly. Finally, the conformation inversion procedure also has less steric hindrance.

13.2.3 Photo Stability

It has been reported that N@C_{60} is light-sensitive [30, 31], and the half-life time for N@C_{60} in degassed CS_2 exposed to ambient light at room temperature was measured to be 4951 minuses. The interaction mechanism between N@C_{60} and light has not been completely understood, but excluding light irradiation is highly recommend during storage and functionalization of N@C_{60}.

Fullerenes were shown to have a long triplet excitation states after being irradiated by laser [32], and the presence of the nitrogen atom inside the cage affects the life time of the fullerene triplet. As Fig. 13.14 shows, although the transient absorption at 750 nm does not vary from N@C_{60} to C_{60} samples, the life time of the absorbance in N@C_{60} ($t_{1/2}$ = 2.3 μs) is significantly decreased compared with that of pristine C_{60} ($t_{1/2}$ = 51 μs), which means the life time the fullerene triplet is shorter in N@C_{60} [22]. Therefore, the encapsulated nitrogen participates somehow

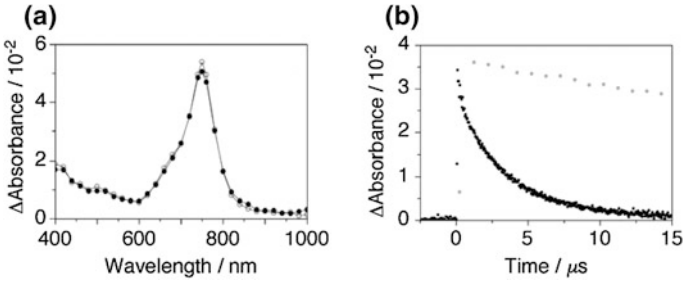

Fig. 13.14 Transient absorption spectrum obtained by 532 nm laser light photolysis of N@C_{60} (*filled circles*) and C_{60} (*open circles*) in Ar-saturated toluene at room temperature at 1000 ns after 532 nm laser irradiation. **b** Decay profiles of the triplet state of N@C_{60} (*filled circles*) and C_{60} (*open circles*) at 750 nm in deaerated toluene at room temperature (reprinted from Ref. [22])

to the decay of the fullerene triplet. Nevertheless, the photo stability of N@C_{60} may not be necessarily related to the triplet excitation state. On the contrary, when toluene is used as the solvent, previous research showed that photo-induced decomposition is realized via local heating created by direct photon absorption and energy exchange with the surrounding solvent molecules [26, 27].

13.2.4 High-Pressure Stability

Apart from the photo stability study, N@C_{60} solution samples have been shown to be high-pressure resistant by a up to 0.8 GPa annealing experiment [33]. More interestingly, although rapid thermal decomposition happening at around 480 K cannot be stopped by applying high-pressure, the high-pressure treatment could suppress the gradual thermal decomposition in the intermediate temperature range (up to at least 400 K). Since a lot of fullerene reaction requires heating in this temperature range, introducing high-pressure might improve the spin retention ratio after the reaction.

13.3 Chemistry of N@C_{60}

Compared with other electron spin systems, N@C_{60} is particularly intriguing due to the significant possibilities for functionalization on the fullerene cage. Due to the minor interaction between the incarcerated nitrogen atom and the fullerene cage, N@C_{60} resembles C_{60} in chemical reactivity. Therefore, a number of chemical modifications were developed by transferring the reaction conditions from well-known C_{60} reactions. On the other hand, several non-covalent

functionalizations of N@C_{60} have also been reported. With the development of these functionalization methods, the electron spin of N@C_{60} becomes tuneable and controllable in a molecular level.

13.3.1 Prato Reaction and Its Application to the N@C_{60} System

Prato reaction is a type of [3 + 2] pericyclic addition reaction between fullerene and azomethine ylides, which were first reported by M. Prato in 1993 [34]. As Fig. 13.15 shows, the azomethine ylides are first generated from α-animoacid and aldehyde/ketone through a decarboxylation route, then added on the fullerene cage, mainly on a [6, 6] bond.

The regioselectivity and mechanism of Prato reaction has been studied at the B3LYP/6-31G(d, p)//AM1 level [35]. The research explained the predomination of closed [6, 6] fullerenopyrazoline in the product, and proposed that the 1, 3 dipolar addition proceeds by a concerted mechanism rather than any stepwise mechanism.

The main advantage of applying a Prato reaction is the abundant choice of aldehydes/ketones. Thereby, it is the most widely reported chemical functionalization method for N@C_{60}, despite the reaction need for heating at around 110 °C, which goes against the low thermal stability of N@C_{60}.

To date, five variant mono pyrrolidine derivatives of N@C_{60} listed in Fig. 13.16 have been reported [31, 36–38]. The synthetic conditions of these derivatives are directly adopted from the reaction conditions for pristine fullerene, namely, refluxing the solution of N@C_{60}, amino acid and the proper aldehydes (formaldehyde for A, 3,4-dibenzyloxybenzaldehyde for B, 4-nitrobenzaldehyde for C, 1-pyrenecarboxaldehyde for *D* and a porphyrin-aldehyde for *E*) for 2 h. A quantitative study on the spin retention ratio before and after the reaction for derivative C is reported to be *c.a.* 73%, which means the reaction conditions during a Prato reaction is to some extend commensurate to the limited stability of N@C_{60}.

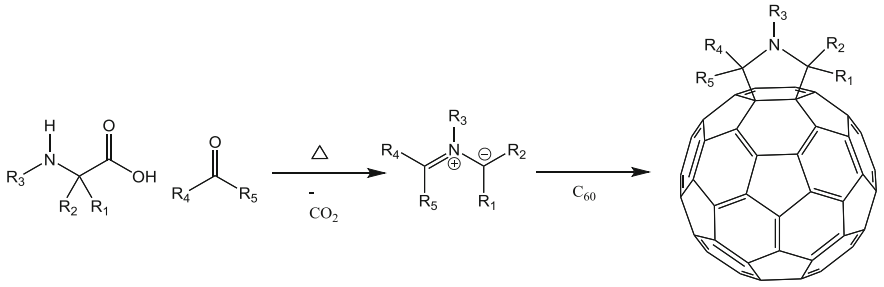

Fig. 13.15 In-situ formation of azomethine ylides, and its reaction with C_{60}

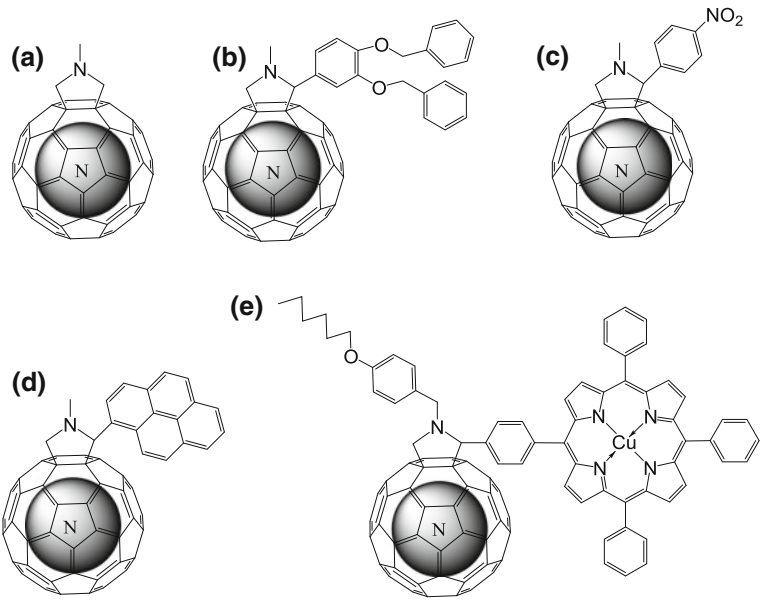

Fig. 13.16 Five variant monopyrrolidine derivatives of N@C_{60} reported in the literature **a**, **b** [36], **c** [37], **d** [31], **e** [38]

The EPR signal of derivatives of **A**, **B**, **C**, and **D** (Fig. 13.17) are relatively similar to each other, as the addends have EPR signal very similar to pristine N@C_{60} in liquid solution. The presence of the addends disturbs the symmetric cage only slightly, which consequently removes the degeneration of different EPR transitions in the $S = 3/2$ spin system. Named zero-field splitting effect (ZFS), this phenomenon will lead to a set of side peaks in the EPR spectra, which appear in all N@C_{60} functionalization experiments. We will extensively introduce this phenomenon in Sect. 13.3.5. Apart from the rise of the ZFS signal, only derivative C was found to have a significant change to the isotropy of the hyperfine constant, as the triplet peaks of hyperfine coupling became considerably unequal [37]. Although it is difficult to quantitatively prove the hyperfine coupling maintained its isotropy after the functionalization, it is thought that the significant increasing of the middle peak might be artificially introduced by an unknown impurity formed during the chemical functionalization reaction, as similar impurity signal overlapping with the middle peak has been reported previously with different derivatives [36, 39, 40]. The spin multiplicity of the impurity signal has been determined by pulsed EPR nutation experiments to be ½, which is different from that N@C_{60}.

The fifth mono pyrrolidine derivative of N@C_{60} is a hetro spin dyad **E**, which contains both a nitrogen spin encapsulated in the cage and a copper spin coordinated by TPP [38]. Unexpectedly, the dyad showed EPR spectra containing only features of the CuTPP moiety without the triplet signal of N@C_{60}. Different from spin decomposition which forbids the recovery of the nitrogen spin signal, the

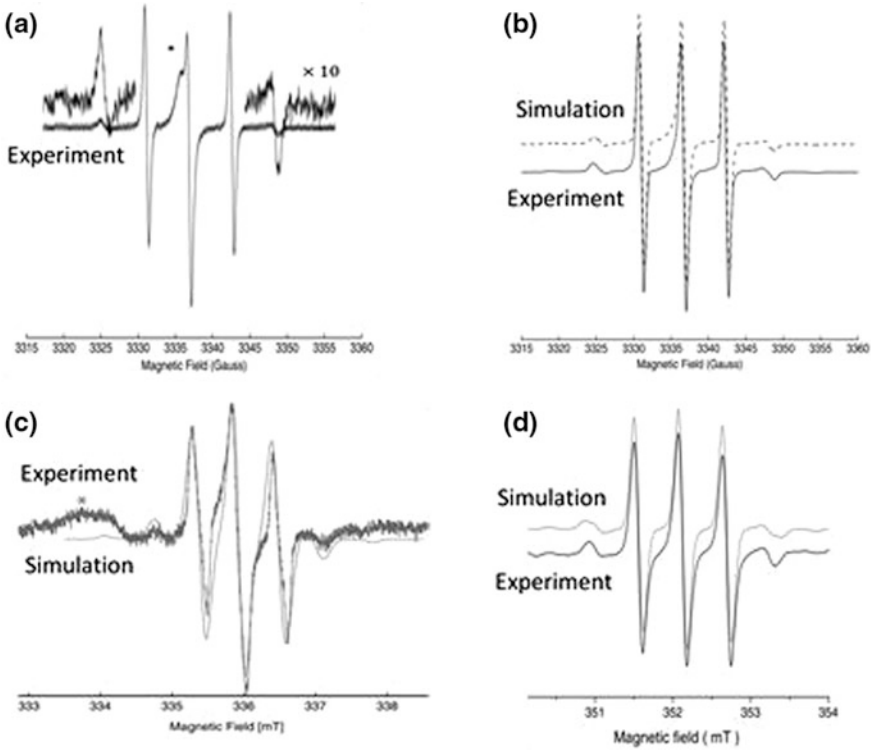

Fig. 13.17 The EPR spectra **a**, **b** [36], **c** [37] and **d** [31] of mono pyrrolidine derivatives **A**, **B**, **C** and **D** of N@C_{60}, respectively (reprinted from Refs. [31, 36, 37])

absence of nitrogen signal is caused by a suppressing effect of CuTPP spin over the N@C_{60} spin. The suppressing effect could be confirmed by demetalation experiment which recovered the nitrogen spin by converting CuTPP moiety to H_2TPP moiety (Fig. 13.18). The physical cause of the signal-suppressing phenomenon was then analyzed to be a strong intramolecular dipolar coupling effect.

N@C_{60}, due to its exceptional spin properties, is an ideal molecule for quantum information processing (QIP), where quantum information can be encoded on the nuclear and electron spins of the molecule. These quantum bits (or qubits) must be linked together in order for scalable QIP to become reality. Hence the Prato reaction was successfully applied to link N@C_{60} dimers, which shed light for the first time on assembling spin qubits at a molecular level. Figure 13.19 demonstrates the synthesis scheme. Since N@C_{60} and C_{60} are chemically indistinguishable in the reaction mixture, the ratio between N@C_{60} and C_{60} will directly affect the ratio among three different products. When 1% N@C_{60}/C_{60} was applied, the half-filled dimer was the dominant spin-active product, whereas, the double-filled dimer became significant if more than 50% N@C_{60}/C_{60} was applied. In the half-filled dimer, the additional fullerene cage contained no spin, thus its spin properties

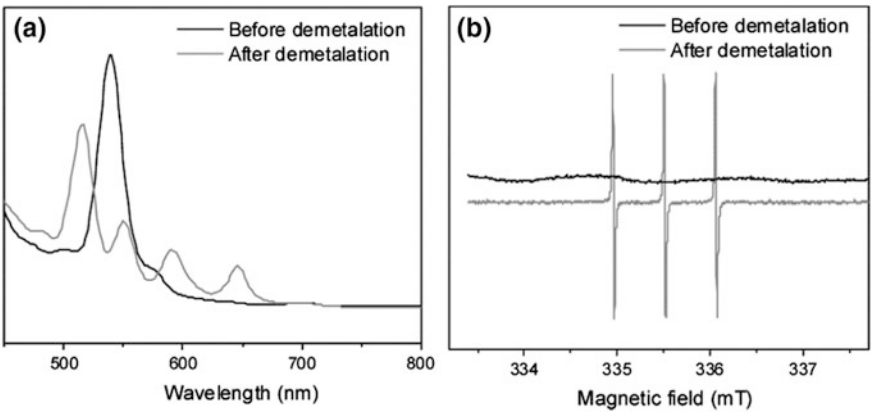

Fig. 13.18 The comparison of UV/Vis and EPR spectra for derivative E before and after demetalation (reprinted from Ref. [38])

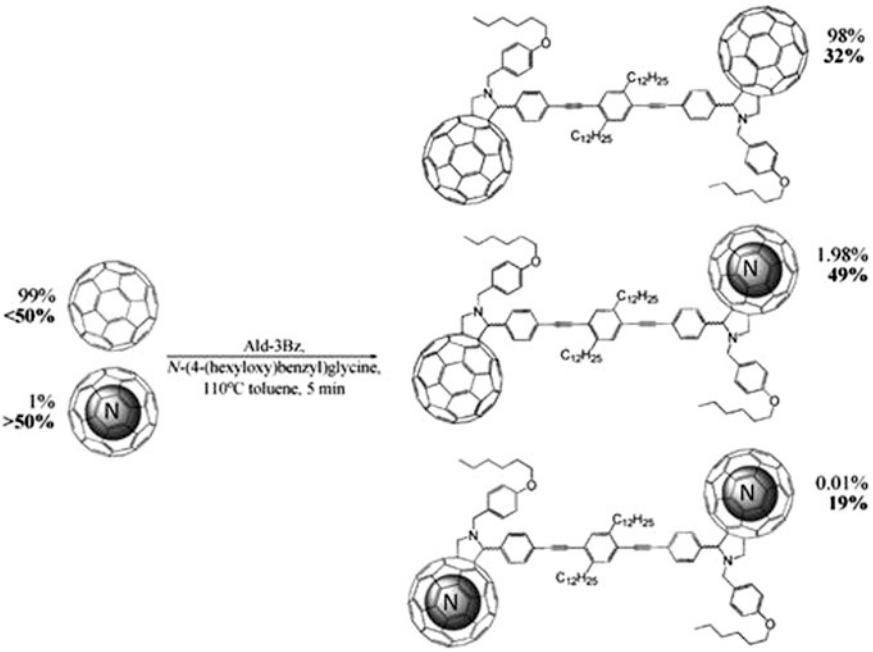

Fig. 13.19 The reaction scheme for chemically assembling two N@C_{60} molecules to form a dimer. The ratio of N@C_{60}/C_{60} affects the distribution of the products. Two sets of reactions starting from 1 and 50% of N@C_{60}/C_{60} mixture were labelled by non-bold and bold numbers, respectively (reprinted from Ref. [41])

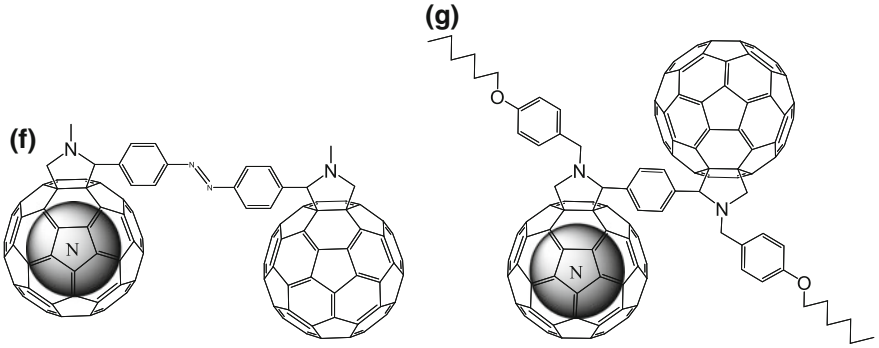

Fig. 13.20 Two half-filled N@C_{60} dimers having the properties of tuning the distance between two fullerenes (**F**) [42] and selectively linking different endohedral spins (**G**) [43]

remained similar to other mono Prato adducts. In the double-filled dimer, however, two spin qubits were chemically assembled together and spin interactions such as dipolar coupling were observed.

Since obtaining pure N@C_{60} is time consuming and expensive, most N@C_{60} dimers reported so far are half-filled dimers. Figure 13.20 demonstrates two half-filled dimers. Instead of focusing on the spin interactions, these dimers revealed different structural novelty, which can also be applied to a double-filled dimer. For dimer **F**, the photoisomerization of the azobenzene moiety has been reported, and the distance between the two fullerenes can be tuned by light irradiation. This azobenzene bridge will enable a spin distance control in a double-filled dimer, which is essential to tuning the spin coupling strength. For dimer **G**, a stepwise method was developed to introduce two fullerenes into the structure one-by-one, which enables the synthesis of an asymmetric dimer such as ^{14}N@C_{60}-^{15}N@C_{60}. Having different spins in adjacent qubits will facilitate global addressing in QIP implementations.

13.3.2 Bingel Reaction and Its Application in the N@C_{60} System

The Bingel reaction is a type of nucleophilic addition reaction introducing a cyclopropane on the fullerene cage, first introduced by Bingel in 1993 [44]. Similar to the regioselectivity of Prato reaction, the Bingel reaction can attach numerous cyclopropane adducts to the [6, 6] bond. There are two proposed mechanisms depending on the reagents and conditions (Fig. 13.21).

Benefiting from the mild, room temperature conditions, Bingel reaction was the first method of chemical functionalization introduced to N@C_{60} [4, 47, 48]. Demonstrated in Fig. 13.22, early research claimed that the incarcerated atom will

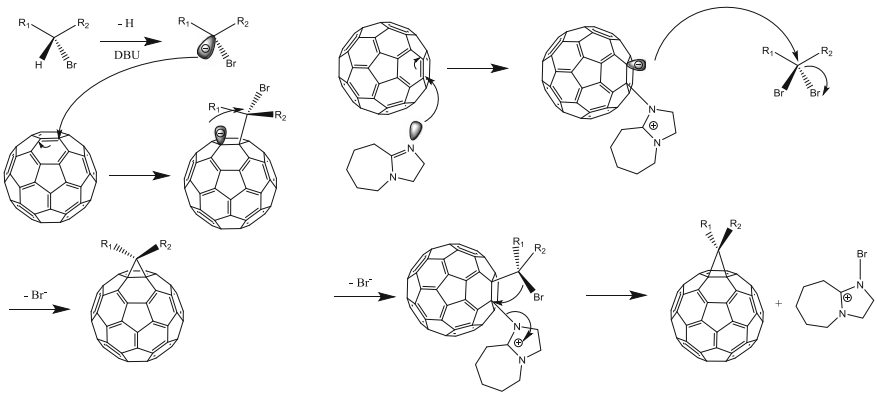

Fig. 13.21 The addition/elimination mechanism of Bingel reaction starting from the malonate, proposed by Diederich [45] (*left*), and an alternative mechanism of Bingel reaction starting from the fullerene proposed by Hirsch [46] (*right*)

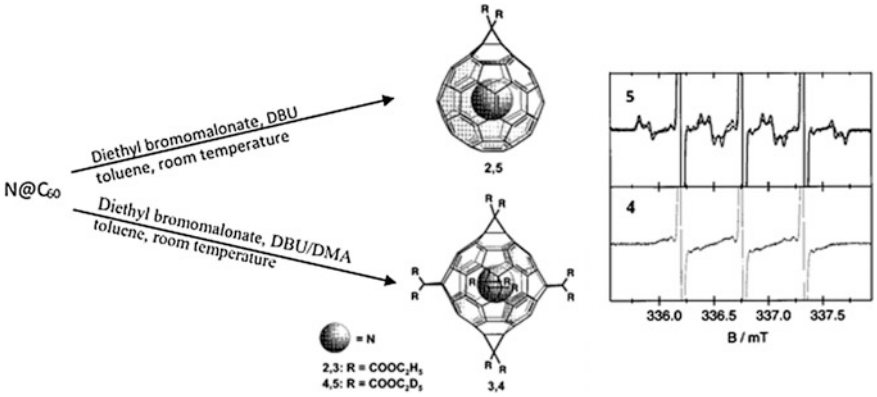

Fig. 13.22 Synthesis of mono- and hexaaddcut of $N@C_{60}$ *via* Bingel reaction (*left*), and the EPR signal of two deuterated Bingel reaction derivatives of $N@C_{60}$ (*right*). The *solid line* in the EPR signal of derivative **5** is the simulation result, assuming the zero-field splitting parameters being D = 9.15 MHz and E = 0.45 MHz (reprinted from Ref. [47])

not be influenced during the entire reaction. The EPR signal of the resulting Bingel reaction derivatives of $N@C_{60}$ were also studied. Similar to an ordinary Prato reaction derivative, the functionalization with mono addend mainly causes a ZFS effect, while the g-factor and hyperfine coupling constant were found to be almost unchanged. However, the symmetric hexa-adduct shows no ZFS peaks.

Despite the success of applying the Bingel reaction to $N@C_{60}$ in the early days, a more recent report revealed a significant spin decay after applying an *in situ* Bingel reaction to $N@C_{60}$ system (shown in Fig. 13.23) [49].

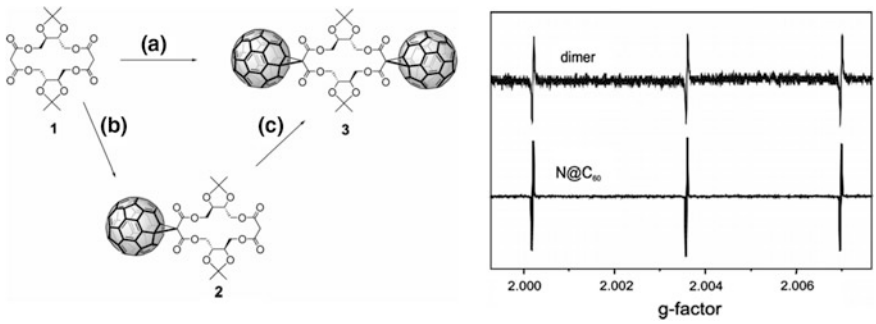

Fig. 13.23 Synthesis of a bisfullerene (*left*), and the significant EPR signal decrease after the *in situ* Bingel reaction (*right*). Reagents and conditions: **a** C_{60},I_2,P_1-*t*Bu, toluene, 1 h, 18%; **b** C_{60}, I_2,P_1-*t*Bu, toluene, 1 h, 41%; **c** C_{60},I_2,P_1-*t*Bu, toluene, 1 h, 44% (reprinted from Ref. [49])

The conflicting result can be partially explained by the chemical stability of N@C_{60} reviewed in Sect. 13.2.2. When mono-bromomalonate is used for the Bingel reaction with stoichiometric catalyst base, the stronger acidity of the mono-bromomalonate prevents the direct interaction between fullerene and DBU. Therefore, the Lewis base induced spin decay will not take place. However, in an *in situ* Bingel reaction, the delay of the formation of bromomalonate from malonate and the brominating agent, leaves N@C_{60} sufficient time to get attacked by the catalyst base, which will lead to decomposition. In addition, the two different reaction mechanisms during the Bingel reaction could explain the difference in spin retention ratio, as well. Because bis-bromomalonate is the dominant product of the bromination under a base, and the resulting bis-bromomalonate will react with N@C_{60} via the second Bingel reaction mechanism shown in Fig. 13.21 on the right. Starting with direct interaction between the fullerene and DBU, the second Bingel reaction mechanism will also lead to decomposition.

Having understood the potential cause of the decomposition of the endohedral structure, a quantitative study on the spin retention ratio proposed the best reaction conditions for the Bingel reaction [29]. Shown in Fig. 13.24, by using 0.5‰ diluted DBU in stoichiometric ratio, up to 94% of the spin signal can be retained during the Bingel reaction. Taking account the limited stability of N@C_{60}, this reaction scheme offers a better method for chemical functionalization of N@C_{60} than the most popular Prato reaction. Meanwhile, the importance of carefully controlling the reaction conditions was also studied. In contract to the high spin retention ratio with diluted DBU, both excess and undiluted DBU lead to significant decompositions during a Bingel reaction.

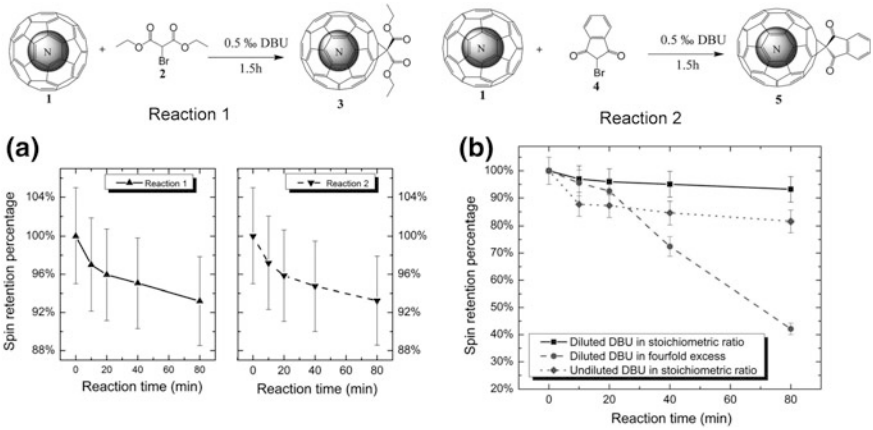

Fig. 13.24 The high spin retention ratio of reaction 1 and reaction 2 in controlled reaction conditions (**a**), comparison of the spin retention ratio of reaction 1 in different reaction conditions (**b**) (reprinted from Ref. [29])

13.3.3 Other N@C_{60}-Related Reactions

Apart from the Prato and Bingel reactions, other N@C_{60}-related reactions have been reported (shown in Fig. 13.25), but more obstacles are needed to be overcome for these chemical functionalization methods.

Two Diels–Alder reactions with N@C_{60} have been reported [36]. The reaction yield and the spin retention ratio were found to be suitable for the endohedral system. However, the draw back lays in the retro reaction of a D–A reaction. It may cause decomposition of adducts, as well as undesired transitions between different adduct isomers. In addition, compared with the Prato reaction, the less availability of dienes than that of the precursors of azomethine ylides leads to difficulty into preparing reagents for the designed molecular structure.

A photochemical reaction has been utilized to link a disilirane onto the N@C_{60} [50], but a sharp decrease of spin signal was observed in the product. Apart from the lower photochemical reactivity of N@C_{60} that the authors attribute it to, the decomposition of N@C_{60} may also contribute to the loss of the spin signal.

Direct dimerization of N@C_{60} was performed by Dinse in 2001 [39], and it was claimed that no spins were lost by utilizing a mechano-chemical method [51]. Nevertheless, the poor thermal stability [52] of C_{120} itself seriously limits the feasibility of synthesizing measurable amount of directly bonded N@C_{60}–N@C_{60}.

The N@C_{60} oxide has also been studied [40]. Although pure product can be separated and characterized by HPLC and EPR, respectively, the oxide of N@C_{60} was found to be thermally unstable. A new, broad spin signal is gradually replacing the spin signal of N@C_{60} during its heating at 100 °C. Dimerization and polymerization of N@C_{60}O at this temperature were proposed to be the reason of the

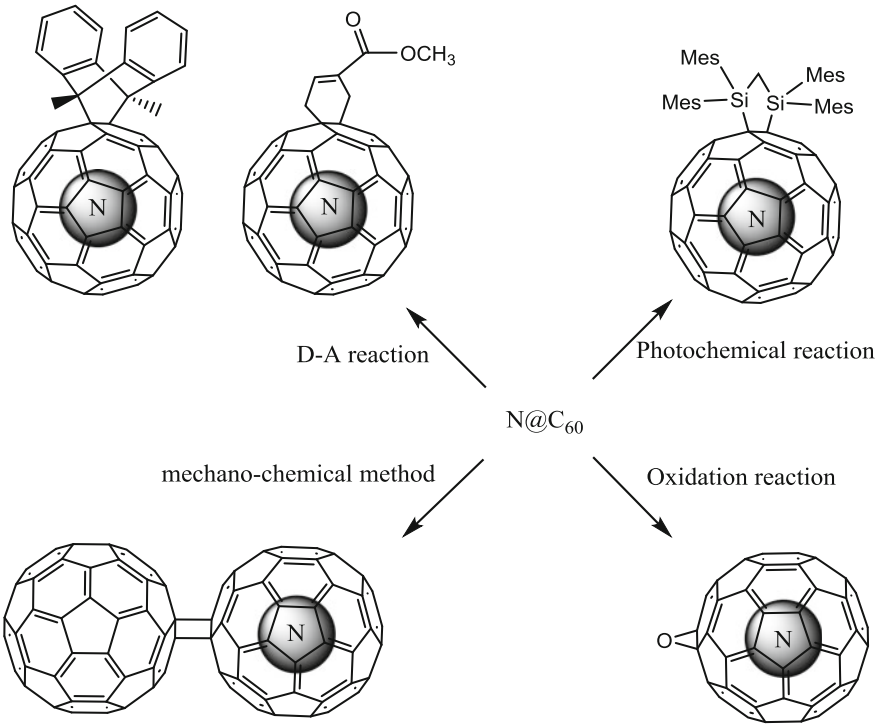

Fig. 13.25 Other reactions that have been reported with N@C_{60}. Diels–Alder reaction products [36], photochemical reaction product [50], mechano-chemical dimerization product [39] and oxide [40] of N@C_{60}

instability, as the intermediate state of the dimerization and polymerization might facilitate the decomposition.

Of course, the above reactions are not the only ones that can be tried with N@C_{60}. Indeed, due to the low availability of N@C_{60}, there are still a number of popular fullerene chemistry reactions, such as the diazo reaction that has not been applied to N@C_{60} yet.

13.3.4 Non-covalent Functionalization of N@C_{60}

Apart from the covalent functionalization of N@C_{60} which mainly focuses on the fine tuning of the molecular structure of N@C_{60} derivatives, several non-covalent functionalizations of N@C_{60}, such as peapod molecules and co-crystallizations, have also been reported. These non-covalent functionalization methods are usually focused on supramolecular assemblies of N@C_{60}.

The peapod-like molecule where fullerenes are encapsulated in single-walled nanotubes (SWNTs) was first analyzed by HRTEM in 1998 [53]. Since low temperature treatments such as the refluxing solvent method [54] and the supercritical fluid method [55] were developed to encapsulate fullerenes into single-walled nanotubes, $N@C_{60}$@SWCNT was synthesized by refluxing a mixture of pre-treated SWNTs, $N@C_{60}$ and n-hexane at 69 °C for 2 h, followed by removing residual solvent and non-encapsulated fullerenes with heat and sonication, respectively, [54]. The peapod structure assembling $N@C_{60}$ together offers a promising way to perfectly align $N@C_{60}$ molecules in one-dimension. Nevertheless there are two remaining drawbacks to be overcome for this no-covalent functionalization method, according to the relevant EPR study (Fig. 13.26). First, the spin retention was too low after treatment. Second, the spin signal of SWNTs itself could suppress strongly or interfere with the signal of $N@C_{60}$.

While the $N@C_{60}$ peapod molecule achieved the alignment of $N@C_{60}$ in one-dimension, co-crystallized $N@C_{60}$·BrPOT managed to built up a three-dimensional architecture of these molecular qubits [56]. Two crystal structures were obtained when a solution of a mixture of $N@C_{60}$ and 2,4,6-tris-(4-bromophenoxy)-1,3,5-triazine (BrPOT) was slowly cooled down from 100 °C to room temperature in toluene. While the fullerenes are only partially ordered in the hexagonal structure, they are fully ordered in the rhombohedral structure. As revealed by single-crystal XRD measurements, the fullerenes are located on a centre of symmetry forming a slightly distorted cubic closed packed structure (the Wykoff position 6a, 0 0 z). Each fullerene sits in an individual pocket formed by BrPOT molecules (Fig. 13.27 left). While the molecules were aligned, such $N@C_{60}$ containing crystal also offered a perfect alignment of electron spins, which was characterized by the sharp ZFS peaks, as well as the angle-dependent EPR signal (Fig. 13.27 right).

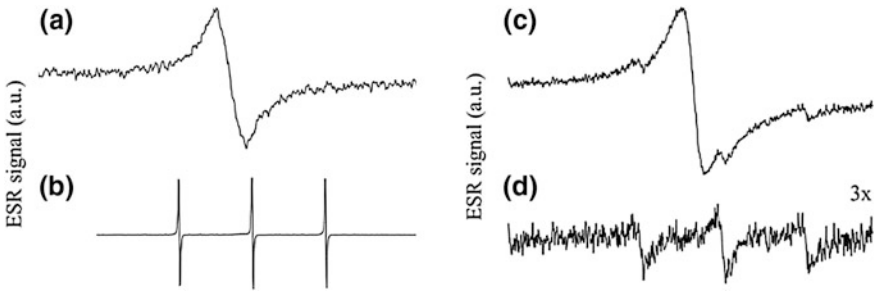

Fig. 13.26 The room temperature EPR spectra of **a** pristine SWNTs, **b** crystalline $N@C_{60}/C_{60}$, **c** $(N@C_{60}/C_{60})$@SWCNT and **d** the triplet component of (**c**). The ratio of $N@C_{60}$:C_{60} is 1–10 ppm (reprinted from Ref. [54])

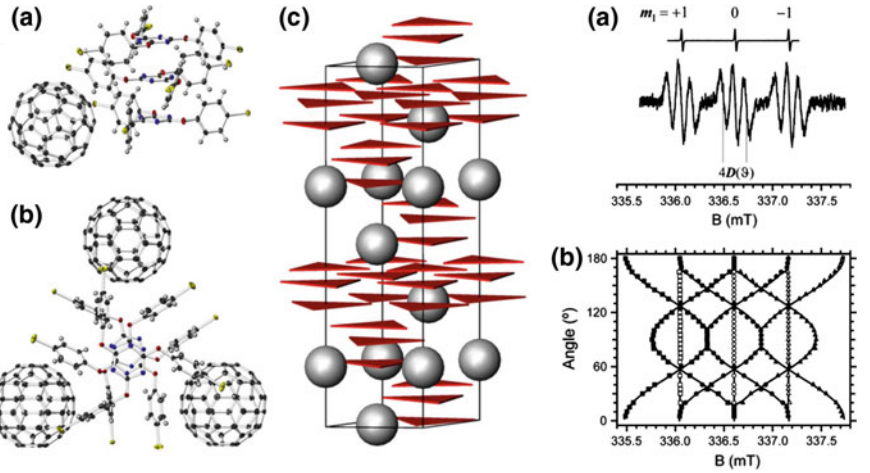

Fig. 13.27 Views of the rhombohedral structure of N@C_{60}·BrPOT (*left*): **a** side view of the essential building block; **b** top view of this building block; **c** unit cell including BrPOT molecules (red triangles) of adjacent cells. The EPR characterization of the co-crystalline (*right*) **a** EPR spectra of N@C_{60} in solid C_{60} (upper trace), and of rhombohedral N@C_{60}·BrPOT (*lower trace*), oriented at 47°. **b** Angular dependence of EPR line positions. Symbols: $m_I = +1$ (*squares*), 0 (*circles*), and −1 (*triangles*). *Open* and *closed* symbols denote m_S = (1/2, −1/2) and (±1/2, ±3/2) transitions, respectively (reprinted from Ref. [56])

13.3.5 Zero-Field Splitting in N@C_{60} Derivatives

As we discussed in Sect. 13.1.3, there are nine allowed transitions for ^{14}N@C_{60} and six allowed transitions for ^{15}N@C_{60}, and all of these transitions are triply degenerated because of the symmetry of C_{60} cage. Therefore, three and two sharp lines are shown in the CW-EPR spectra of ^{14}N@C_{60} and ^{15}N@C_{60}, respectively. Once the symmetry of the cage is reduced, the degeneracy of the −3/2-to-1/2, −1/2-to-+1/2 and +1/2-to-+3/2 transitions is removed, thus additional peaks are expected in the spectrum. Figure 13.28 demonstrated the change of the energy levels after breaking the symmetry of N@C_{60}. The energy level splitting occurs even at zero magnetic field, so the phenomenon is called zero-field splitting (ZFS), and it could appear in any $S > ½$ system. The splitting D_{eff} is an angle-dependent parameter determined by a traceless second-order tensor **D**, which could be expressed as a diagonal matrix in its eigenframe with elements being $D_{xx} = -1/3D + E, \mathrm{D}_{yy} = -1/3D - E$ and $\mathrm{D}_{zz} = 2/3D$, where D and E are the ZFS parameters representing the axial and non-axial components of the tensor. Due to the angle dependence of D_{eff}, the energy of −3/2-to-1/2 and +1/2-to-+3/2 transitions are also different in angles. Therefore, sharp signal of these transitions could only be obtain when the molecules are aligned in the same direction (such as in a single-crystal sample). Otherwise, broad ZFS peaks will be obtained in powder and frozen-solution sample

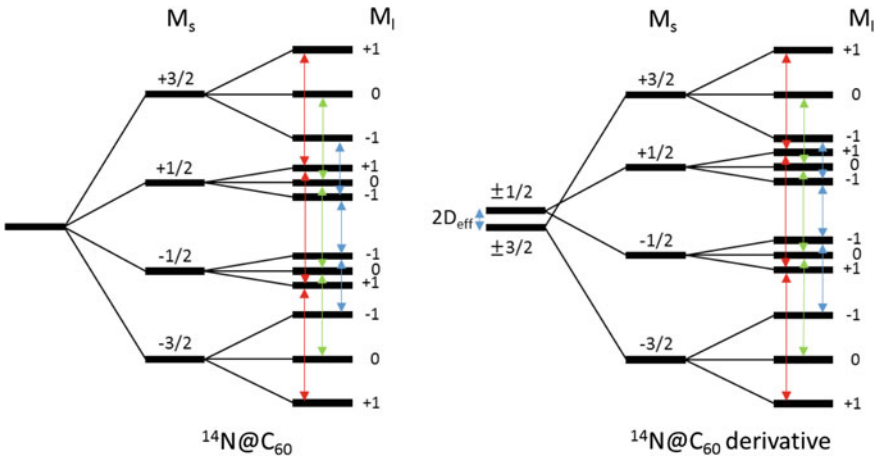

Fig. 13.28 The influence of the zero-field splitting effect to energy levels after breaking the symmetry of N@C_{60} with functional groups

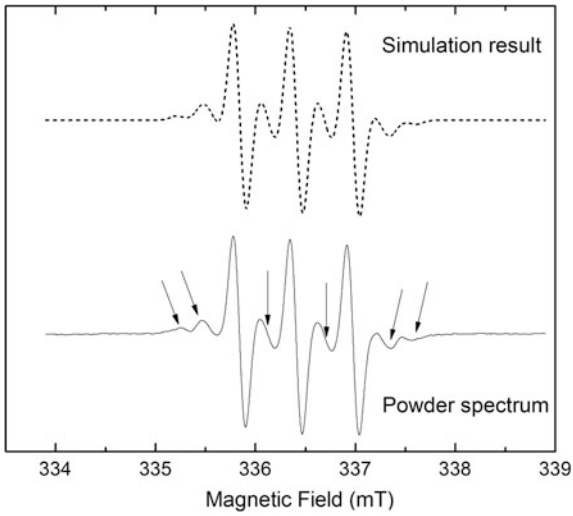

Fig. 13.29 Frozen-solution CW-EPR spectrum and the simulation result for a Bingel reaction product of ^{14}N@C_{60}. The additional peaks due to zero-field spitting are shown (indicated by *arrows*)

(Fig. 13.29), and no ZFS peaks could be detected in fast tumbling samples (such as in a liquid solution).

Considering the low crystallinity of fullerenes, powder spectra of N@C_{60} sample are commonly used to characterize the ZFS effect, and simulation with software, such as Easyspin [57], is used to extract the ZFS parameters of D and E from the broad ZFS peaks. Table 13.1 lists different N@C_{60} derivatives and their simulated ZFS parameters. A clear relationship between the axial parameter D and the addend could be found in a way that the stronger the distortion in the direction of the

Table 13.1 Different simulated zero-field splitting parameters reported in the literature

Derivative type	Ring size of the addend	[*D*, *E*]/MHz
Prato reaction product	5	[16.4, 0.4] [36], [17.2, 0.6] [36], [14.19, 0.74] [41], [16.75, 0.93] [31], [14.6, 0.56] [43], [16.1, 0.7] [42], [17.0, 0.8] [37]
Bingel reaction product	3	[8.4, 0.36] [29], [8.9, 0.57] [29], [9.15, 0.45] [47], [8.6, 0.45] [49]
Dimerization product	4	[14, 0.56] [39]
Oxidization product	3	[6.6, 0.5] [40]
Diels–Alder reaction product	6	[16.2, 0.4] [36]

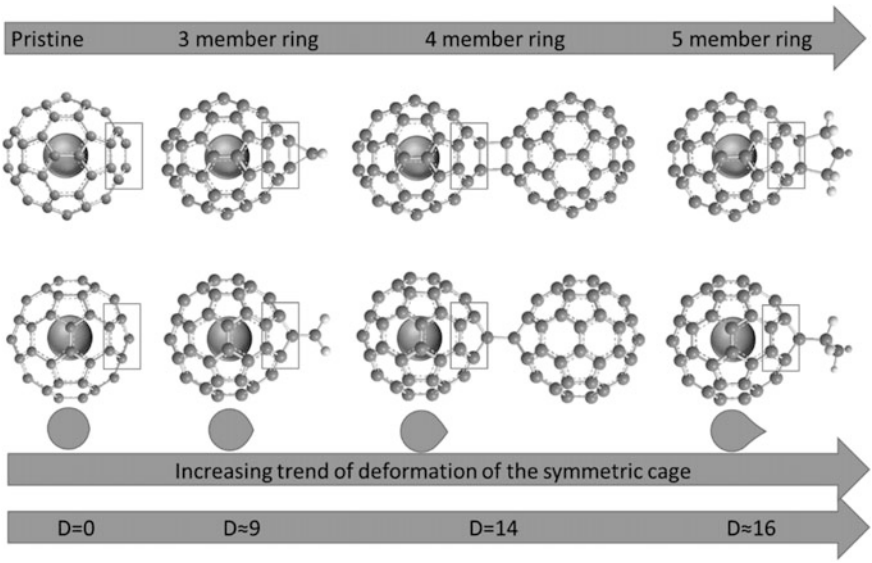

Fig. 13.30 The consistent trend of the distortion in the direction of the principal axis of the molecular symmetry and the axial parameter *D*, which suggests the axial component of the ZFS tensor is parallel to the symmetry axis of the molecule

principal axis of the molecular symmetry is, the larger value for the axial parameter *D* will be (Fig. 13.30). Therefore, we could further suggest that the axial component of the ZFS tensor is parallel to the symmetry axis of the molecule. On the other hand, the direction of the non-axial component *E* is difficult to determine, due to its small value and insignificant difference of the molecule in the plane perpendicular to its symmetry axis.

The ZFS effect in $N@C_{60}$ derivative is an important criterion to prove the successful functionalization of $N@C_{60}$, as other conventional technology, such as NMR, MS and UV/Vis are neither applicable nor sensitive enough. In addition, the ZFS effect also enables one to tune the energy levels as well as the spin signal. On the other hand, ZFS was proposed to be the dominant relaxation mechanism in solution for $N@C_{60}$ derivatives [37]. Therefore, the chemical modification of the fullerene cage is found to decrease the spin relaxation and correlation time of the endohedral spin. Nevertheless, it is worth noting that not all $N@C_{60}$ derivatives have a ZFS effect. As the ZFS is the result of symmetry breaking, if the new $N@C_{60}$ derivative still retains high symmetry, the EPR transitions of the derivative will still be triply degenerate. The only reported high symmetry derivatives of $N@C_{60}$ are hexaadducts: $N@C_{66}(COOC_2D_5)_{12}$, $N@C_{66}(COOC_2H_5)_{12}$ with T_h symmetry [47]. As expected, no ZFS peaks were detected in the EPR spectra for either samples. Compared to monoadduct, the absence of the ZFS effect raises the T_1 and T_2 relaxation times by a factor of two. Therefore, when long T_1 and T_2 are needed in applications like quantum information processing, a multiply substituted $N@C_{60}$ derivative could remove the disadvantage of lower relaxation time introduced by covalent functionalization.

13.3.6 Stability of $N@C_{60}$ Derivatives

We have already seen that there are several factors that affect the stability of $N@C_{60}$. The question arises "what happens with the stability of $N@C_{60}$ derivatives?" Thermal stability of Bingel reaction products of $N@C_{60}$ [25] and photostability of Prato reaction product of $N@C_{60}$ [31] have been studied separately.

As Fig. 13.31 shows, the functionalization of cyclopropane on fullerene cage slightly improves the thermal stability of the endohedral system [25]. By applying an Arrhenius plot to the decay rates, the activation energy of mono-malonates and

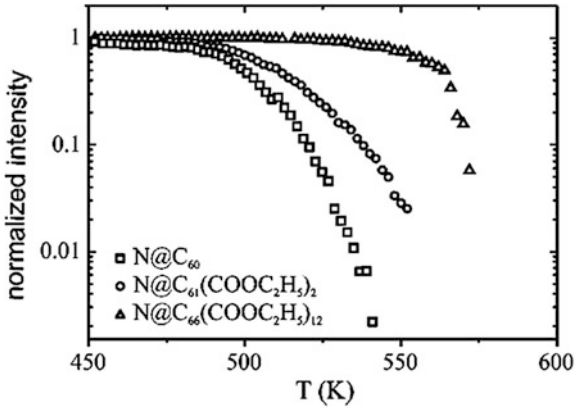

Fig. 13.31 The evolution of the intensity of the spin signal for the monoadduct and hexaadduct of $N@C_{60}$ in comparison with that of $N@C_{60}$. The heating rate was 2 K in 82 s (reprinted from Ref. [25])

hexamalonates of N@C_{60} were calculated to be 1.6 and 1.8 eV, which are higher than that of pristine N@C_{60} (1.57 eV). It is certainly intriguing that the malonate derivatives of N@C_{60} are more thermally robust than pristine N@C_{60}. More research is needed to identify the reasons for this behaviour.

In contract to the higher thermal stability of Bingel reaction products, Prato reaction products of N@C_{60} showed lower photo stability, as demonstrated in Fig. 13.32. While the pristine N@C_{60} has got a half-life time of 4951 min in the tested conditions, the half-life time decreased to 280 and 266 min for derivative 1 and derivative 2, respectively. It is worth noting that the difference of the functional groups in the addends does not lead to significant variation to the photo-stability, even though the derivatives show different optical absorptions. This means the effect of a peripheral optically active pyrenyl group on photo-induced decay is negligible, and one could further deduce that the decomposition mainly relates to the pyrrolidine ring on the cage, as it is the main cause of distortion of the structure of pristine N@C_{60}.

Since the photo stability study above was performed in toluene solution, where the decomposition mainly takes place via a local heating mechanism (discussed in Sect. 13.2.3), the photo stability discussed in the Prato reaction product was fundamentally related to the thermal stability of it. Therefore, the two different types of stability are to some extent comparable, which suggests a stabilization effect for the cyclopropane addend and the opposite effect for the pyrrolidine addend.

The decomposition behaviour of the endohedral system was theoretically explained by a density functional theory (DFT) study, shown in Fig. 13.33 [58]. By comparing the decomposition pathway and the energy profile through the functionalized [6, 6] bond, the presence of pyrrolidine plays a catalytic role, whereas the presence of cyclopropane hinders the decomposition. Therefore, it was shown that the Bingel and Prato N@C_{60} derivatives show opposite behaviour.

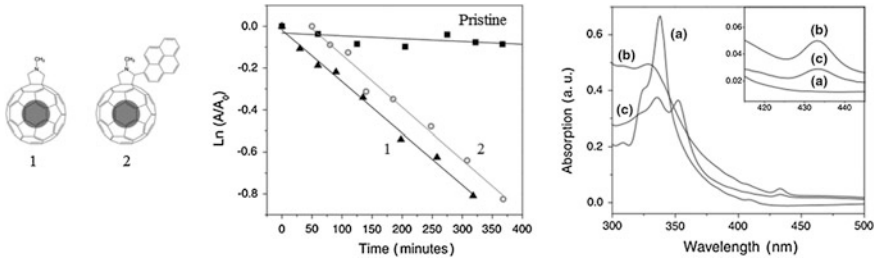

Fig. 13.32 The molecular structure of N@C_{60} derivative **1** and **2** (*left*), their photo stability compared with that of pristine N@C_{60} (*middle*), and the UV/Vis absorption spectra (*right*) of **a** mixture of pyrene and C_{60} (molar ratio 1/1), **b** derivative **1**, **c** derivative **2** (reprinted from Ref. [31])

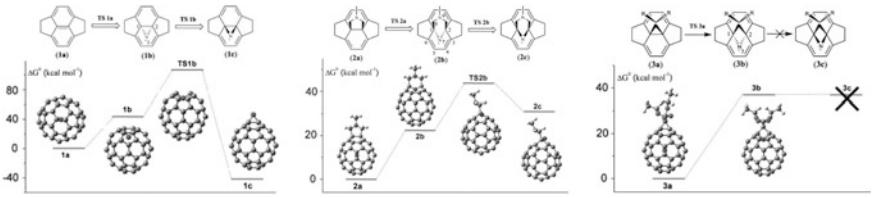

Fig. 13.33 The decomposition pathways and the computed energy profile for pristine N@C_{60} through a [6, 6] bond (*left*), pyrrolidine derivative of N@C_{60} through the functionalized [6, 6] bond (*middle*) and cyclopropane derivative of N@C_{60} through the functionalized [6, 6] bond (*right*) (reprinted from Ref. [58])

13.4 Summary

In this chapter, we delved into the synthesis, properties and chemistry of N@C_{60}, one of the most remarkable endohedral fullerenes, where a very reactive atom like nitrogen gets incarcerated in a fullerene cage (C_{60} is the most common case, but C_{70} is also possible). This fullerene gives the unprecedented possibility for manipulating, moving around or even building larger structures made of "free" nitrogen atoms.

We have described the most common methods for synthesizing N@C_{60}. Regarding its synthesis, the main challenge that still needs to be addressed is the production of material with high enough purity and in macroscopic amounts.

Due to nitrogen's reactive nature the stability of N@C_{60} is an important issue. Here, however, a lot of the challenges can be overcome. By storing N@C_{60} in solution at ambient temperature and protected from light exposure, it is possible to keep active samples for months or even years without significant decay.

The extremely long lifetimes of both its electron and nuclear spins, make N@C_{60} quite useful for exotic applications such as quantum computing. To its advantage, we can use the well-developed C_{60} chemistry in order to produce scalable structures of N@C_{60} derivatives. We have outlined the major synthetic routes that have been applied to date (both covalent and non-covalent in nature).

We have also detailed the electronic properties of N@C_{60} and its derivatives (mainly using the EPR array of techniques) and shown ways of how to tune the lifetimes, align the molecules and generally apply exquisite control on their electronic signature.

Research in N@C_{60} and similar endohedral nitrogen molecules has advanced considerably in the last 20 years. A lot of challenges have been addressed and a lot of progress has been achieved. Without doubt, more work is necessary for real applications involving N@C_{60} to become reality; however, we are today a lot closer than where we were even 5 years ago.

References

1. Murphy TA, Pawlik T, Weidinger A et al (1996) Observation of atomlike nitrogen in nitrogen-implanted solid C_{60}. Phys Rev Lett 77(6):1075–1078
2. Abe S, Sato G, Kaneko T et al (2006) Effects of ion energy control on production of nitrogen-C_{60} compounds by ion implantation. Jpn J Appl Phys Part 1 Regul Pap Brief Commun Rev Pap 45(10B):8340–8343
3. Weidinger A, Waiblinger M, Pietzak B et al (1998) Atomic nitrogen in C60: N@C60. Appl Phys A-Mater Sci Process 66(3):287–292
4. Pietzak B, Waiblinger M, Murphy TA et al (1997) Buckminsterfullerene C_{60}: a chemical Faraday cage for atomic nitrogen. Chem Phys Lett 279(5–6):259–263
5. Ito S, Shimotani H, Takagi H et al (2008) On the synthesis conditions of N and N_2 endohedral fullerenes. Fullerenes Nanotubes Carbon Nanostruct 16(3):206–213
6. Huang H, Ata M, Ramm M (2002) $^{14}N@C_{60}$ formation in a nitrogen rf-plasma. Chem Commun 18:2076–2077
7. Ata M, Huang HJ, Akasaka T (2004) Nitrogen radio frequency plasma processing of fullerenes. J Phys Chem B 108(15):4640–4646
8. Kaneko T, Abe S, Ishida H et al (2007) An electron cyclotron resonance plasma configuration for increasing the efficiency in the yield of nitrogen endohedral fullerenes. Phys Plasmas 14 (11):110705
9. Miyanaga S, Kaneko T, Ishida H et al (2010) Synthesis evaluation of nitrogen atom encapsulated fullerenes by optical emission spectra in nitrogen plasmas. Thin Solid Films 518 (13):3509–3512
10. Cho SC, Kaneko T, Ishida H et al (2012) Highly efficient synthesis of nitrogen-atom endohedral fullerene by controlling plasma ion behaviors. Appl Phys Express 5(2):026202
11. Cho SC, Kaneko T, Ishida H et al (2015) Nitrogen-atom endohedral fullerene synthesis with high efficiency by controlling plasma-ion irradiation energy and C_{60} internal energy. J Appl Phys 117(12):123301
12. Kanai M, Porfyrakis K, Briggs AD et al (2004) Purification by HPLC and the UV/Vis absorption spectra of the nitrogen-containing incar-fullerenes *i*NC_{60}, and *i*NC_{70}. Chem Commun 2:210–211
13. Plant SR, Porfyrakis K (2014) Using electron paramagnetic resonance to map N@C_{60} during high throughput processing. Analyst 139(18):4519–4524
14. Jakes P, Dinse KP, Meyer C et al (2003) Purification and optical spectroscopy of N@C_{60}. Phys Chem Chem Phys 5(19):4080–4083
15. Suetsuna T, Dragoe N, Harneit W et al (2002) Separation of N_2@C_{60} and N@C_{60}. Chem-Eur J 8(22):5079–5083
16. Harneit W, Huebener K, Naydenov B et al (2007) N@C_{60} quantum bit engineering. Phys Status Solidi B 244(11):3879–3884
17. Wakahara T, Matsunaga Y, Katayama A et al (2003) A comparison of the photochemical reactivity of N@C_{60} and C_{60}: photolysis with disilirane. Chem Commun 23:2940–2941
18. Morton JJL, Tyryshkin AM, Ardavan A et al (2005) A new mechanism for electron spin echo envelope modulation. J Chem Phys 122(17):174504
19. Benjamin SC, Ardavan A, Andrew G et al (2006) Towards a fullerene-based quantum computer. J Phys-Condes Matter 18(21):S867–S883
20. Morton JJL, Tyryshkin AM, Ardavan A et al (2006) Electron spin relaxation of N@C_{60} in CS2. J Chem Phys 124(1):14508
21. Morton JJL, Tyryshkin AM, Ardavan A et al (2007) Environmental effects on electron spin relaxation in N@C_{60}. Phys Rev B 76(8):085418
22. Nikawa H, Araki Y, Slanina Z et al (2010) The effect of atomic nitrogen on the C_{60} cage. Chem Commun 46(4):631–633
23. Lu X, Chen ZF (2005) Curved Pi-conjugation, aromaticity, and the related chemistry of small fullerenes (<C_{60}) and single-walled carbon nanotubes. Chem Rev 105(10):3643–3696

24. Haddon RC (1993) Chemistry of the fullerenes—the manifestation of strain in a class of continuous aromatic-molecules. Science 261(5128):1545–1550
25. Waiblinger M, Lips K, Harneit W et al (2001) Thermal stability of the endohedral fullerenes N@C_{60}, N@C_{70}, and P@C_{60} (vol B 63, art. no. 045421, 2001). Phys Rev B 6415(15):159901
26. Shimshi R, Khong A, JimenezVazquez HA et al (1996) Release of noble gas atoms from inside fullerenes. Tetrahedron 52(14):5143–5148
27. Krause M, Kuzmany H, Georgi P et al (2001) Structure and stability of endohedral fullerene Sc_3N@C_{80}: a Raman, infrared, and theoretical analysis. J Chem Phys 115(14):6596–6605
28. Mauser H, Hommes N, Clark T et al (1997) Stabilization of atomic nitrogen inside C_{60}. Angew Chem-Int Edit 36(24):2835–2838
29. Zhou S, Rasovic I, Briggs GAD et al (2015) Synthesis of the first completely spin-compatible N@C_{60} cyclopropane derivatives by carefully tuning the DBU base catalyst. Chem Commun 51(33):7096–7099
30. Farrington BJ, Hingston TJ, Briggs GA et al (2011) Photostability of N@C_{60} in common solvents. ECS Trans 35(25):113–117
31. Liu G, Khlobystov AN, Ardavan A et al (2011) Photochemical stability of N@C_{60} and its pyrrolidine derivatives. Chem Phys Lett 508(4–6):187–190
32. Fraelich MR, Weisman RB (1993) Triplete States of C_{60} and C_{70} in solution: long intrinsic lifetimes and energy pooling. J Phys Chem 97(43):11145–11147
33. Iwasiewicz-Wabnig A, Porfyrakis K, Briggs GAD et al (2009) Investigations of N@C_{60} and N@C_{70} stability under high pressure and high temperature conditions. Phys Status Solidi B 246(11–12):2767–2770
34. Maggini M, Scorrano G, Prato M (1993) Addition of azomethine ylides to C_{60}—synthesis, characterization, and functionalization of fullerene pyrrolidines. J Am Chem Soc 115 (21):9798–9799
35. Kavitha K, Venuvanalingam P (2005) Open versus closed 1,3-dipolar additions of C_{60}: a theoretical investigation on their mechanism and regioselectivity. J Org Chem 70(14):5426–5435
36. Franco L, Ceola S, Corvaja C et al (2006) Synthesis and magnetic properties of N@C_{60} derivatives. Chem Phys Lett 422(1–3):100–105
37. Zhang JY, Morton JJL, Sambrook MR et al (2006) The effects of a pyrrolidine functional group on the magnetic properties of N@C_{60}. Chem Phys Lett 432(4–6):523–527
38. Liu G, Khlobystov AN, Charalambidis G et al (2012) N@C_{60}–porphyrin: a dyad of two radical centers. J Am Chem Soc 134(4):1938–1941
39. Goedde B, Waiblinger M, Jakes P et al (2001) 'Nitrogen doped' C_{60} dimers (N@C_{60}-C_{60}). Chem Phys Lett 334(1–3):12–17
40. Jones MAG, Britz DA, Morton JJL et al (2006) Synthesis and reactivity of N@C_{60}O. Phys Chem Chem Phys 8(17):2083–2088
41. Farrington BJ, Jevric M, Rance GA et al (2012) Chemistry at the nanoscale: synthesis of an N@C_{60}–N@C_{60} endohedral fullerene dimer. Angew Chem-Int Edit Engl 51(15):3587–3590
42. Zhang J, Porfyrakis K, Morton JJL et al (2008) Photoisomerization of a fullerene dimer. J Phys Chem C 112(8):2802–2804
43. Plant SR, Jevric M, Morton JJL et al (2013) A two-step approach to the synthesis of N@C60 fullerene dimers for molecular qubits. Chem Sci 4(7):2971–2975
44. Bingel C (1993) Cyclopropylation of fullerenes. Chem Ber-Recl 126(8):1957–1959
45. Diederich F, Isaacs L, Philp D (1994) Syntheses, structures, and properties of methanofullerenes. Chem Soc Rev 23(4):243–255
46. Hörmann F, Hirsch A (2013) Giant fullerene polyelectrolytes composed of C_{60} building blocks with an octahedral addition pattern and discovery of a new cyclopropanation reaction involving dibromomalonates. Chem-Eur J 19(9):3188–3197
47. Dietel E, Hirsch A, Pietzak B et al (1999) Atomic nitrogen encapsulated in fullerenes: effects of cage variations. J Am Chem Soc 121(11):2432–2437
48. Lips K, Waiblinger M, Pietzak B et al (2000) Atomic nitrogen encapsulated in fullerenes: realization of a chemical Faraday cage. Phys Status Solidi A-Appl Res 177(1):81–91

49. Hörmann F, Hirsch A, Porfyrakis K et al (2011) Synthesis and magnetic properties of a nitrogen-containing fullerene dimer. Eur J Org Chem 2011 (1):117–121
50. Wakahara T, Kato T, Ki Miyazawa et al (2012) $N@C_{60}$ as a structural probe for fullerene nanomaterials. Carbon 50(4):1709–1712
51. Komatsu K, Wang GW, Murata Y et al (1998) Mechanochemical synthesis and characterization of the fullerene dimer C_{120}. J Org Chem 63(25):9358–9366
52. Zhang JY, Porfyrakis K, Sambrook MR et al (2006) Determination of the thermal stability of the fullerene dimers C_{120}, $C_{120}O$, and $C_{120}O_2$. J Phys Chem B 110(34):16979–16981
53. Smith BW, Monthioux M, Luzzi DE (1998) Encapsulated C_{60} in carbon nanotubes. Nature 396(6709):323–324
54. Simon F, Kuzmany H, Rauf H et al (2004) Low temperature fullerene encapsulation in single wall carbon nanotubes: synthesis of $N@C_{60}$@SWCNT. Chem Phys Lett 383(3–4):362–367
55. Khlobystov AN, Britz DA, Wang JW et al (2004) Low temperature assembly of fullerene arrays in single-walled carbon nanotubes using supercritical fluids. J Mater Chem 14 (19):2852–2857
56. Naydenov B, Spudat C, Harneit W et al (2006) Ordered inclusion of endohedral fullerenes $N@C_{60}$ and $P@C_{60}$ in a crystalline matrix. Chem Phys Lett 424(4–6):327–332
57. Stoll S, Schweiger A (2006) EasySpin, a comprehensive software package for spectral simulation and analysis in EPR. J Magn Reson 178(1):42–55
58. Liu G, Khlobystov AN, Briggs GAD et al (2012) Catalytic and non-catalytic roles of pendant groups in the decomposition of $N@C_{60}$: a DFT investigation. Chem Commun 48(42):5148–5150

Chapter 14
Spin Quantum Computing with Endohedral Fullerenes

Wolfgang Harneit

Abstract This chapter reviews the present state of the art in using the endohedral fullerenes $N@C_{60}$ and $P@C_{60}$ as qubits in a spin quantum computer. After a brief introduction to spin quantum computing (Sect. 14.1), we first discuss (Sect. 14.2) the rich spin structure of these endohedral fullerenes and specific theoretical proposals for architectures and operation models leading to a scalable quantum computer. We then briefly discuss (Sect. 14.3) those aspects of materials science that are needed to realize the proposed architectures. The central part of this chapter (Sect. 14.4) is a review of quantum operations and entanglement realized with endohedral fullerenes. Finally, we review (Sect. 14.5) efforts to realize single spin detection of endohedral fullerenes and conclude (Sect. 14.6) with a brief outlook on outstanding problems to be solved for obtaining a scalable quantum register.

14.1 Introduction to Spin Quantum Computing

More than 20 years after its inception [1, 2], the idea of using quantum information to outperform classical computers remains an inspiring and challenging goal for the experimentalist [3]. Even in 2016, it is still unclear which of the numerous hardware concepts offers the most viable route to a large or even medium-scale implementation, i.e., a quantum processor using significantly more than a handful of quantum bits.

We take the opportunity to review here the present state of the art in using endohedral fullerenes for building a quantum computer. We will concentrate on $N@C_{60}$ and $P@C_{60}$ with their well-known favorable spin properties since they have been most studied in the quantum-computing context. The related systems of metallofullerenes [4] and other molecular atom cages like silsesquioxanes [5] are largely disregarded here, although recent studies indicate that they may also have some favorable properties for quantum information science [6–9].

W. Harneit (✉)
Fachbereich Physik, Universität Osnabrück, Osnabrück, Germany
e-mail: wolfgang.harneit@uos.de

A.A. Popov (ed.), *Endohedral Fullerenes: Electron Transfer and Spin*,
Nanostructure Science and Technology, DOI 10.1007/978-3-319-47049-8_14

After a brief introduction to solid-state spin quantum computing (Sect. 14.1), we start with fundamental considerations about the system architecture for a scalable fullerene-based quantum register element (Sect. 14.2), outline the main developments in endohedral fullerene materials science relevant for realizing such a register (Sect. 14.3), review experimental implementations of quantum operations in endohedral fullerene ensembles (Sect. 14.4), illustrate the ongoing quest to realize an efficient single-spin read-out for these materials (Sect. 14.5), and conclude with a very brief outlook on further experimental challenges and opportunities (Sect. 14.6).

14.1.1 Nuclear Spin Qubits in Liquids

Spins can be considered as 'natural qubits' since they are often two-level systems that interact little with their environment and behave quantum mechanically even in large ensembles. Nuclear magnetic resonance on molecules dissolved in liquids (liquid-NMR) allows characterizing all nuclear spins in the molecule, including their mutual spin–spin couplings, with very high precision. This facilitates the realization of even complex quantum algorithms using only molecular design.

In the early days of quantum computing (QC), NMR as a mature technique was thus at the forefront of establishing that the theoretical foundations of quantum information science were sound [10]. And it has demonstrated many of the key algorithms like prime factoring [11]. Liquid-NMR continues to drive the development of advanced QC concepts [12].

Several limitations to the liquid-NMR approach for large-scale applications have been pointed out early on [13], which all have their fundamental origin in the small amount of energy separating the $|0\rangle$ and $|1\rangle$ qubit states. The nuclear Zeeman splitting of a proton in an ordinary laboratory magnetic field of $B_0 = 10$ T corresponds to $\Delta E = 1.8$ μeV, which is far below the thermal energy of $k_B T = 26$ meV at room temperature. This leads (a) to small thermal spin polarization (3×10^{-5} in the considered case; 0.5% at $T = 2$ K) and (b) to inefficient direct detection of the low-energy electromagnetic radiation associated with Zeeman transitions, confining liquid-NMR to the use of very large ensembles ($>10^{15}$) of identical spin systems at room temperature.

Using electron spins instead of nuclear spins can overcome some of the mentioned limitations, since the Zeeman energies are about a factor of 10^3 higher. Electron spins also interact more strongly with the environment and are thus easier to read out. On the other hand, electrons have shorter spin lifetimes and must be carefully shielded.

14.1.2 Solid-State Spin Qubits

The scaling problems of the liquid-NMR approach can be overcome by going to solid-state spin systems, as was illustrated in the seminal proposal of B.E. Kane for a silicon-based computer [14]. The key ideas of Kane's paper have guided many

solid-state spin proposals and it is worthwhile summarizing them here: (a) nuclear spins are realized by impurity atoms brought into a perfectly crystalline and diamagnetic matrix, ensuring minimal interaction with the environment; (b) the impurity atom simultaneously acts as electron donor and thus has an associated electron wave function including spin; (c) the electron wave function is spatially confined but can be manipulated by gate electrodes. With these ingredients, the electron spin can act as a 'gateway' or 'bus' to the nuclear spin, allowing (d) addressing, manipulating, and reading out individual qubits, and (e) controlling the nearest neighbor qubit–qubit interaction.

The single-spin read-out capability immediately offers a way to produce high-spin polarization on demand, since an individual qubit can be read out repeatedly until its wave function has collapsed to a desired Eigenstate (e.g., $|0\rangle$). The interaction control, proposed originally as gate-induced spatial modulation of the electron–electron exchange interaction between neighboring qubits, represents a highly desirable element that simplifies certain quantum operations, but even 'always-on' interactions like dipolar spin–spin coupling suffice for universal quantum computing [15].

The silicon quantum computer concept is still being actively investigated today. Being technically extremely challenging, first convincing and thus highly exciting results were obtained only in the last few years. For example, very long spin coherence times and precise quantum operations involving a Kane-type qubit were recently reported [16–18]. Two-qubit operations are however still in their infancy due to difficulties in fabricating larger quantum registers with sufficient control over each qubit.

An alternative solid-state spin qubit that has recently attracted a lot of attention is the nitrogen-vacancy center (NVC) in diamond. The NVC provides single-spin optical readout even at room temperature [19, 20]. This has lead to a fascinating and fast development of single-spin quantum control and to proposals for its use as a quantum bit [21].

Large-scale computer architectures will require deterministic fabrication of qubits. Kane's proposal and proposals for NVC quantum computers are typical top-down approaches, which start with a macroscopic crystalline substrate and end up with almost atomic-precision fabrication of spin qubits (dopant atoms in silicon or color centers in diamond), which is hard to achieve by ion implantation. This is even more challenging for the NV center in diamond since (a) fabrication technologies for diamond are less mature than for silicon and (b) the formation of NVC color centers is a two-step process requiring (i) N ion implantation and vacancy creation, and (ii) recombination of both defects to produce a NV center [22].

The single-spin readout capability of the NVC however makes it an excellent readout system for other spins, including qubits in spin-based QC proposals. Already, advances in quantum control of singly addressed NVCs have allowed to detect and control larger and larger portions of the 'dark' spin environment, ending up with current trends to map out the 3D electron spin environment using a single NVC [23] and to realize even single-molecule NMR based on NVC detection [24].

14.1.3 Paramagnetic Endohedral Fullerenes

In this review, we will concentrate on $N@C_{60}$ and $P@C_{60}$, which we call *paramagnetic* or *pnictide* endohedral fullerenes (PEFs). In the quantum-computing context, PEFs are officially classified as 'impurity spin' systems in similarity with Kane's Si:P proposal or with the alternative nitrogen-vacancy center (NVC) in diamond (see Sect. 14.1.2).

In contrast to solid-state spin qubits based on dopant atoms or color centers, molecular spin systems provide a bottom-up route to large-scale quantum register fabrication [25, 26]. In a first stage, identical molecular qubits can be fabricated (incidentally also by ion implantation for PEFs) and purified chemically, and only later assembled in almost arbitrarily complex architectures using chemical engineering approaches [27]. This decoupling of qubit creation and assembly is a potentially big advantage for device architecture and scalability and one of the main drivers for using PEFs as a QC resource.

14.2 System Architecture and Computing Models

We review basic approaches on how the central processing unit of a PEF-based quantum computer could be constructed. We start (Sect. 14.2.1) by identifying possible qubits in the multilevel spin system and point out some important consequences of the high-spin character of the electron spin. In Sect. 14.2.2, we discuss the nature of spin–spin interactions in PEFs and the resulting central architecture of a one-dimensional quantum register.

14.2.1 Qubits in the Multilevel Electron–Nuclear Spin System

Pnictide endohedral fullerenes consist of a fullerene cage with a paramagnetic atom of IUPAC group 15 (pnictides), which is freely suspended in the cage center by dispersive van der Waals forces [28]. This constitutes a highly shielded symmetric spin system with long coherence times, favorable for spin quantum computing. The fullerene cage acts as a robust handle to the fragile atom, conferring thermodynamic and chemical stability and hence some flexibility in designing devices.

In $N@C_{60}$ (Refs. [29, 30]) and $P@C_{60}$ (Refs. [31, 32]), the encapsulated atom has a half-filled p shell and hence a total electron spin $S = 3/2$ with Zeeman sublevels characterized by the quantum number $m_S = \pm 1/2,\ \pm 3/2$. Pnictide atoms also have a nuclear spin $I = 1/2$ (^{15}N, ^{31}P) or $I = 1$ (^{14}N) with corresponding quantum number m_I. The effective spin Hamiltonian of an isolated PEF molecule is given to first order by

$$H_0(B_l)/h = \nu_S(B_l)S_z - \nu_I(B_l)I_z + AS_zI_z + D\left(S_z^2 - 5/4\right), \quad (1)$$

where $\nu_{S,I}(B_l) = g_{e,n}\beta_{e,n}B_l/(2\pi)$ are the Larmor frequencies at effective local magnetic field B_l, $g_{e,n}$ are the isotropic g-factors and $\beta_{e,n}$ the magnetons for electron and nucleus, respectively. Note that g-factors, and hence Larmor frequencies, are signed quantities. The scalars A and D are frequencies characterizing isotropic hyperfine interaction *(hfi)* between electron and nuclear spin and axial zero-field interaction *(zfi)*, which is characteristic for high-spin systems and originates from dipolar interaction between the three constituent electrons [25]. Parameters for the most important PEF molecules are summarized in Table 14.1.

Electron and nuclear spins can be discussed as independent resources; in a magnetic field larger than ~20 mT (i.e., for $g_e\beta_e B_l \gg A$), they have well-defined quantum numbers that can be used to characterize a PEF spin eigenstate as $|m_S, m_I\rangle$. Spin control is achieved by driving allowed transitions, either in the microwave (MW) range for electron spin resonance (ESR, $\Delta m_S = \pm 1$, $\Delta m_I = 0$) or in the radio-frequency (RF) range for nuclear magnetic resonance (NMR, $\Delta m_S = 0, \Delta m_I = \pm 1$).

First-order hyperfine coupling (A) splits the electron spin resonance $(|\Delta m_S| = 1)$ into as many equidistant lines as there are nuclear spin states $(2I + 1 = 2$ or $3)$. These lines are still triply degenerate in the absence of zero-field interaction $(D = 0)$. The degeneracy is lifted for $D \neq 0$, leading to $(2I + 1) \times (2S)$ selectively addressable ESR lines (see Fig. 14.1). Similarly, there are $(2I) \times (2S + 1)$ NMR resonances with a first-order splitting in m_S and a first-order degeneracy in m_I for the $I = 1$ system $^{14}N@C_{60}$, lifted only by the second-order hyperfine interaction. Second-order *hfi* can lead to other effects in high-resolution spectroscopy (see Sect. 14.4.1 for its use in qubit characterization) but is otherwise less relevant for quantum computing due to its small size.

A total number of eight (^{15}N, ^{31}P) or twelve (^{14}N) Zeeman sublevels result from the static Hamiltonian (see Fig. 14.1). Up to three qubits ($2^3 = 8$) may thus be defined and entangled [33], and even four qubits would be possible in the $S = 3/2$, $I = 3/2$ spin system of the (not yet experimentally reported) $As@C_{60}$ analogue [34]. The four levels of the high $S = 3/2$ electron spin can in principle be used to encode either two qubits [33, 35] or a *ququart* (a four-level generalization of the two-level qubit), which is useful in some quantum-computing schemes and has been studied for analogous $I = 3/2$ nuclear spins in the NMR domain [36, 37]. In both cases, however, transition-selective addressing is mandatory, requiring a finite

Table 14.1 Typical parameters for the PEF spin Hamiltonian (Eq. 1)

Quantity	Multiplier	$^{14}N@C_{60}$	$^{15}N@C_{60}$	$^{31}P@C_{60}$
ν_S	$\times(B_l/T)$	28000		
ν_I	$\times(B_l/T)$	3.08	−4.32	17.25
A		15.8	22.2	138.5
D		0–30	0–30	0–127

The Larmor frequencies $\nu_{S,I}$ depend on the effective local magnetic field B_l while D depends on the local symmetry (see Sect. 14.3.3); $D = 0$ for 'bare' C_{60} in an isotropic environment. All values are given in MHz

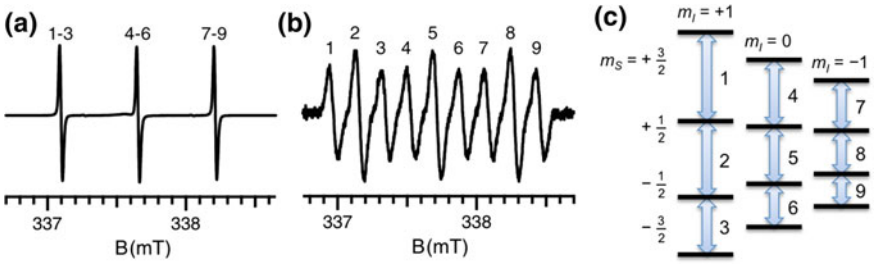

Fig. 14.1 Electron spin resonance (ESR) spectra of $^{14}N@C_{60}$ diluted in C_{60}. **a** Polycrystalline powder sample; **b** sample in anisotropic crystalline host matrix (Br-POT); **c** energy levels and allowed ESR transitions. Adapted with permission from Ref. [38] (© 2007 WILEY-VCH Verlag GmbH & Co. KGaA, Weinheim)

'quadrupolar' splitting Hamiltonian of the form QI_Z^2. In the PEF Hamiltonian, this corresponds to nonzero D in the *zfi*-term, which leads to a lifting of the ESR transition degeneracy (see Fig. 14.1).

The *zfi* term is intimately linked to the shape of the total electron wave function of the encapsulated atom, which is in turn strongly influenced by the fullerene cage. It is absent for *effective* high cage symmetries such as occur for low-symmetry fullerenes dissolved in liquids due to rapid tumbling or for 'bare' (i.e., chemically unmodified) C_{60} cages even in a crystalline environment at room temperature, where the molecules rotate freely. Ways to change *zfi* size and orientation will be discussed in more detail in Sect. 14.3.3. Here, we note that the presence or absence of *zfi* has notable consequences on the way that all four sublevels of the electron spin can be addressed and hence used for quantum information.

The nuclear spin can be seen as an independent qubit, which is even better shielded from the environment than the electron spin. The nuclear spin has much longer relaxation and coherence times, but manipulating it with resonant RF pulses is also much slower. Section 14.4 will show that there is a net gain for quantum computation; the gain in coherence time is larger than the loss in control speed. Therefore, the nuclear spin has been considered as the primary logical qubit in several theoretical proposals, with the electron spin serving as a 'gateway' or 'bus' only [39–41].

14.2.2 Spin–Spin Interactions and the Linear Qubit Register

Experimental studies on the concentration dependence of ESR line broadening [42] and theoretical calculations [30] show that the exchange interaction between two endohedrals is negligible, leaving magnetic dipole interaction as the only strong coupling. For two adjacent endohedrals at a typical [43] center-to-center distance of 1.0 nm, the magnetic dipole interaction between electron spins can be as large as $\sim$50 MHz. This dipolar coupling between electron spins scales as r^{-3} with the

fullerene distance r, is anisotropic, and is not confined to nearest neighbours since it acts 'through space'. Any disorder in the spatial arrangement of fullerenes may therefore be a considerable source of decoherence.

This suggests that a one-dimensional arrangement of spins in a *linear qubit register* will provide the highest degree of interaction control, and this arrangement has been at the focus of theoretical proposals for endohedral fullerenes (Fig. 14.2) [25, 26, 35, 39–41, 44–46]. A linear chain also provides a simple means to make every qubit addressable when a magnetic field gradient is applied along the chain direction [39]. Taking z as the direction of the external magnetic field B_0, as the chain direction, and as the direction of the (constant) gradient ∇B_G, the local magnetic field $B_l(z) = B_0 + z\nabla B_G$ changes as a function of z and hence so do the resonance frequencies $\nu_{S,I}$. This leads to the total spin Hamiltonian of a linear chain of N identical PEF molecules

$$H_N = \sum_{j \le N} H_0\big(B_l(z_j)\big) + h \sum_{j<k} D_{jk}\big(|z_j - z_k|\big) S_{Zj} S_{Zk}, \tag{2}$$

where $D_{jk}(r) = (51.9\,\mathrm{MHz}) \times (r/\mathrm{nm})^{-3}$ and $H_0(B)$ is given by Eq. (1) with $B_l(z) = B_0(1 + \Delta(z - z_0))$ and $\Delta = (\nabla B_G)/B_0$.

The always-on nature of dipolar coupling between electron spins is an undesirable feature for quantum-computing. Dipolar interaction in the chain extends to more distant fullerenes, leading to a highly structured ESR spectrum for each qubit in the chain; individual addressing is nevertheless still possible if the electron spins are kept in a highly polarized state (see Fig. 14.3). Furthermore, dipolar coupling continually drives a state-dependent evolution of the electron spins, making them useless as memory qubits or requiring continuous active decoupling by microwave pulses [15].

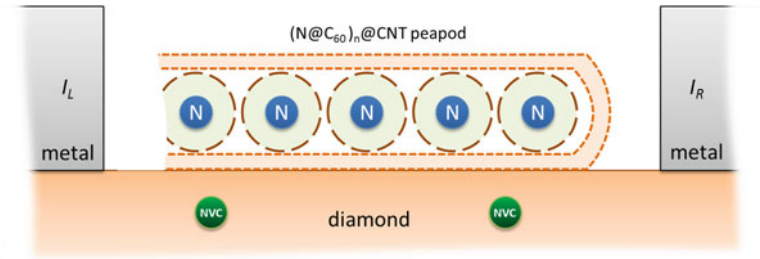

Fig. 14.2 Sketch of a linear spin-chain quantum register with optical readout. $N@C_{60}$ or $P@C_{60}$ electron–nuclear spin qubits are lined up inside a carbon nanotube (CNT), which is placed on top of a diamond substrate with shallow nitrogen-vacancy centers (NVC). A current is driven through nearby metal electrodes, producing a magnetic field gradient that enables addressing of individual fullerene or NVC spins with MW or RF pulses. Thus, controlled quantum operations between fullerene spins coupled by magnetic dipole interaction can be performed. Initial and final spin states are prepared and read out optically via spin–spin coupling to the NVC readout qubits

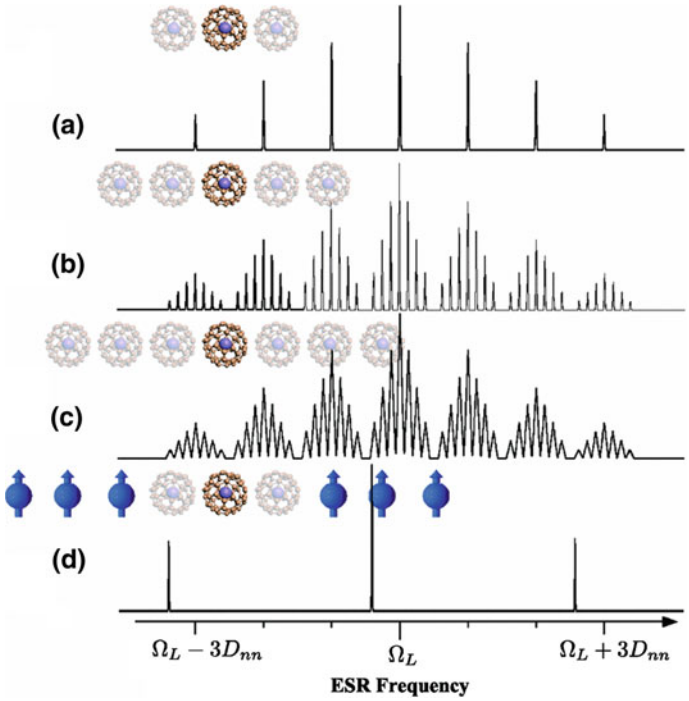

Fig. 14.3 PEF electron spin transition frequencies as a function of chain length. **a** Nearest neighbors only; **b** two and **c** three neighbors on each side; **d** infinite chain where all but the nearest neighbors are polarized (i.e., in the 'passive' ground state). Reprinted with permission from Ref. [45] (© 2010 American Physical Society)

The solution is to take the nuclear spins as primary logical qubits. The combination of an electron–nuclear spin system at each fullerene site then turns out to provide an elegant way to control qubit–qubit interaction [40, 41, 45]. Direct dipolar coupling between nuclear spins of adjacent fullerenes is negligible (<10 kHz) and may be selectively enhanced using the electron spin as a 'bus' or 'auxiliary' qubit. Several strategies have been proposed [35, 45, 47] for 'swapping' quantum information between the logical nuclear spins and the bus electron spins that are otherwise kept in a polarized ground state. Logical two-qubit operations then proceed by swapping out nuclear qubit states onto the electron spins, engineering electron-spin-only quantum operations, and 'swapping back' the information onto the nuclei.

Even with traditional approaches to create an electron–nuclear swap operation, which takes up most of the gating time, thousands of fullerene qubits may be made to function in a single-quantum register [41]. Furthermore, Morton et al. have shown [48] that nuclear phase gates may be realized much more rapidly (see Sect. 14.4.2), potentially increasing this number. Finally, there have been proposals to build a quantum network out of several independent linear chains by entangling them at a distance [45, 49].

14.3 Materials Science Aspects

Having identified the linear spin chain as the basic architecture for most QC concepts, we now discuss materials science aspects specific to the QC application of endohedral fullerenes. Broader reviews of PEF materials science can be found in several reviews; we recommend a book chapter by B. Pietzak et al. on early work [50] and the chapter of K. Porfyrakis in this book [51] (see Chap. 13) for more recent work.

14.3.1 Synthesis, Purification, Stability

PEF molecules are produced by low-energy ion implantation, which affords a mixture of 'empty' and 'filled' fullerenes with a filling ratio or efficiency $\epsilon = X(\mathrm{N@C_{60}})/X(\mathrm{C_{60}} + \mathrm{N@C_{60}}) \leq 10^{-4}$. The filling ratio is then increased up to unity by multistep HPLC purification. This protocol is quite precise and yields near 100% purity [52]; yet it is extremely laborious. The low overall synthesis yield still constitutes one of the major obstacles in quantum-computing research. A significant observation is that chemical derivatives (or 'adducts') of $\mathrm{N@C_{60}}$ can be separated from their 'empty' $\mathrm{C_{60}}$ counterparts using the same HPLC methods [53]. This allows using larger sample amounts during a possibly low-yield chemical adduct synthesis while enriching the endohedral fraction *of the product* during a post-synthesis HPLC workup step.

The thermal, chemical, and optical stability of PEF complexes have been investigated several times [54]. Thermal decomposition sets in above 130–150 °C; the thermal stability is thus sufficient for safe handling at room temperature and even allows chemical reactions to occur under reflux in toluene. It can be increased by encapsulation into carbon nanotubes [55]. The situation is less clear for the optical stability; recent studies indicate that while properly cooled PEF molecules are not harmed by high-power optical irradiation, insufficient cooling may induce thermal instability [56]. This may have caused confusion in some optical stability investigations.

14.3.2 Integration in Solid-State Architectures

A solid-state quantum computer needs complex and precise spatial arrangements of fullerenes. The moderate thermal stability of PEF molecules implies that one cannot use vacuum sublimation for thin-film deposition or other high-temperature processes, such as crystal growth or encapsulation into carbon nanotubes driven by thermal diffusion. Hence alternative 'cold' deposition [38, 58, 59] and encapsulation [60, 61] methods have been developed for PEFs, with potential applications for other thermolabile molecules.

Given these preparation methods, self-assembly of fullerenes is then possible as has been investigated in numerous studies. Here, we arbitrarily quote recent (sublimation-based) studies of self-assembly on surfaces, where even 2D architectures are possible [62, 63]. In 3D matrices, ordering may include chain-like or at least one-dimensional motifs such as in liquid crystals [64–66] or in pore-forming organic compounds [38, 67, 68].

Finally, the possibly best defined and most highly ordered linear arrangement proceeds by encapsulation into carbon nanotubes (CNTs) [60, 61]. The electronic and optical properties of CNTs make this particularly attractive as it could permit electrical readout [26, 45] or distant entanglement schemes in hybrid architectures [49, 69, 70].

14.3.3 Control of the Zero-Field Splitting

The zero-field interaction (*zfi*) is essential for several QC proposals (see Sect. 14.2) since it allows transition-selective addressing of all spin sublevels. It is important to note that the *zfi* is anisotropic and reflects the molecular symmetry, hence not only the size of D has to be controlled but also its orientation.

For highly symmetric systems (spherical or cubic), D is exactly zero. The same holds for fast orientational averaging, as occurs in liquid samples and even in polycrystalline C_{60} samples at room temperature. Small D values are observable at lower temperatures in solid PEF samples: $N@C_{60}$-doped C_{60} powder [71], $P@C_{60}$-doped powder [72], $N@C_{60}$-doped C_{60} crystals [73]. The D values are distributed in both amplitude and orientation, resulting in featureless and broad ESR lines. Nevertheless, valuable spectroscopic information can be gleaned even in this situation using the *nutation* behavior specific to $S = 3/2$ systems (see Sect. 14.4.2).

Larger D values can be engineered using either covalent or non-covalent chemical functionalization. Covalent modifications have been investigated since the early days: Dietel et al. have shown the first mono-adducts characterized by D values of around 10 MHz, and regio-selective attachment of up to six addends of $N@C_{60}$, affording a nearly cubic hexakis adduct [74]. Franco et al. [75] have systematically varied addends in mono-adducts and investigated their effect on D. First fullerene dimers were reported by Goedde et al. [76] and many contributions were made by the Porfyrakis group [53, 57, 77, 78]. Covalent functionalization leads to D values of up to 15 MHz for $N@C_{60}$ (comparable to the hyperfine interaction), but the resulting EPR spectra are usually broad and of little use for quantum information due to random orientation of the molecular axes induced by the covalent addends. This can in principle be avoided if stiff addends are used and if the adducts are grafted or self-assembled on a geometrically ordering substrate such as a flat surface or a carbon nanotube.

Non-covalent interactions of fullerenes in molecular environments provide an alternate route towards useful zero-field effects [27]. The basic idea here is that the pseudo-aromatic fullerene cage may act as a transducer for symmetry-lowering π–π

interactions with the environment. This is already obvious from the finite D values observed [71] in polycrystalline samples of 'bare' (unmodified) endohedral fullerenes (vide supra), which is due to C_{60}–C_{60} interaction. If the environment is highly ordered, this may lead to induced order of the fullerenes.

Several groups investigated interactions with molecular recognition systems that wrap around the fullerene [75, 79, 80]. While leading to zero-field interaction D of similar size as due to covalent C_{60} chemistry, these systems are also difficult to orient. Surprisingly, partial orientation of the near-spherical C_{60} fullerenes was found in liquid crystals [64, 65], but the D values were rather small and significant residual disorder was found.

Inclusion of endohedrals in pore-forming organic crystals (halo-phenoxy-triazines like Br-POT [81]) has shown the best *zfi* control so far [67, 82]. Inclusion of fullerenes in *cylindrical* Br-POT pores leads to partial orientation with significant disorder due to co-included solvent molecules and is thus similar to the liquid crystal case. Somewhat surprisingly, a second mode of co-crystallization was found that leads to the formation of a highly oriented arrangement of individual host-guest 'pockets' for fullerenes. This structure induces near-perfect rotational order for the fullerenes as well as considerable D values exceeding those obtained by covalent functionalization. This system was therefore used to realize two-qubit gates (see Sect. 14.4.3).

Inducing orientational order is also vital for investigations of 'all-endohedral' PEF dimers containing pnictide spins in both monomers because it would allow control over the dipolar spin–spin interaction, which is necessary for realizing controlled two-qubit interactions (see Sect. 14.4.4). Similar orientation approaches using other matrices such as zeolites or metalorganic frameworks have yet to be explored systematically.

14.4 Quantum Operations and Entanglement

We give a short overview over key experiments on quantum operations in magnetically dilute ensembles of group-V endohedrals, which illustrate some of the theoretical proposals outlined in Sect. 14.2. Starting with spin relaxation and coherence times, we review 1-qubit operations for electron and nuclear spin, and intra-fullerene electron-nuclear two-qubit operations such as coherent state transfer and entanglement. We end with a discussion of the status for inter-fullerene two-qubit operations.

14.4.1 Spin Relaxation and Coherence

In the coupled electron–nuclear spin system of PEFs, the electron spin–lattice relaxation time T_{1e} is of fundamental interest. T_{1e} dominates electron spin coherence T_{2e} at room temperature [83] and nuclear spin coherence T_{2n} at low temperature

[84]. The mechanisms inducing spontaneous spin flips and hence T_{1e} relaxation are quite sensitive to the environment of the fullerenes [85].

In liquids, collisional processes may distort the fullerene and hence modulate terms in its spin Hamiltonian, most notably the zero-field interaction (*zfi*). Indeed, chemically modified N@C_{60} molecules with a permanent *zfi* show accelerated relaxation in liquids, whereas *g*-factor and hyperfine interaction are quite insensitive to symmetry-lowering distortions of the fullerene cage [74]. The *zfi*-based collisional relaxation model was also invoked to explain the faster relaxation [26] in the P@C_{60} molecule, which also shows [67, 72] larger matrix-induced *zfi* than N@C_{60} does [71, 82].

As an alternative to the collisional T_{1e} model, an Orbach process was proposed [83, 85] to explain relaxation above $T > 150$ K, essentially based on the temperature dependence of T_{1e} and T_{2e} in frozen solution and powder samples. The Orbach process describes relaxation via low-lying excited states outside the usual spin ground-state manifold. These states were identified with molecular vibrations. Differences of $T_{1e}(T)$ in frozen solutions of toluene and CS_2 were attributed to the excitation of different molecular vibrations of the C_{60} cage [85], but direct evidence for the suppression of the lowest energy $H_g(1)$ 'squashing' mode of C_{60} in frozen toluene solutions is lacking. Furthermore, the $H_g(1)$ mode [86] is clearly symmetry-breaking for the confinement potential of the trapped atom (thus capable of inducing a transient *zfi*), whereas the $A_g(1)$ 'breathing' mode (invoked to explain the toluene data [85]) could only modulate the isotropic hyperfine interaction, which is not sufficient to establish thermodynamic equilibrium in the spin system [87]. Therefore, the direct identification of Orbach energies with molecular vibration energies remains questionable. Finally, there must be further mechanisms determining T_{1e} below about $T = 150$ K, which remain to be identified.

Electron spin dephasing T_{2e} and relaxation T_{1e} have the same temperature dependence near room temperature. There is a systematic difference between 'inner' ($m_S = 1/2 \leftrightarrow -1/2$) and 'outer' ($\pm 1/2 \leftrightarrow \pm 3/2$) transitions, $T_{2e}^o = (2/3)T_{2e}^i = (4/9)T_{1e}$ [83], which could be measured independently due to a rare echo modulation effect occurring in ^{14}N@C_{60} [88]. At temperatures lower than about $T = 100$ K, T_{2e} is independent of temperature in powder samples while T_{1e} still rapidly grows. Several studies [84, 85] show that T_{2e}^o may be much shorter than T_{2e}^i for N@C_{60}, but interestingly this is not the case for P@C_{60} with its much larger zero-field and hyperfine interactions [68, 89, 90].

At low temperatures, the dominant T_{2e} dephasing mechanism can be attributed to uncontrolled dipolar interaction between different endohedral spins [84, 90]. This can be remedied by achieving better coupling control, as should be possible in a linear spin chain (see Sect. 14.2.2). Preliminary studies of P@C_{60} at high endohedral spin dilution show that dephasing by impurity nuclear spins then takes over, leading to a lower limit of the achievable $T_{2e} \geq 3.9$ ms at $T = 5$ K [90].

The nuclear relaxation times are much harder to access, but specialized experiments provided the estimates $T_{2n} = 135$ ms (measured at $T = 10$ K using a coherence transfer method [84]) and $T_{1n} \approx 12$ hours (measured at $T = 4.2$ K in a

Table 14.2 Highest reported spin relaxation times for PEF powder samples at $\boldsymbol{T} = 4.2 - 10\,\mathrm{K}$

	T_{1n}	T_{2n}	T_{1e}	T_{2e}
Time/ms	4×10^7	135	1300	3.9
PEF type	$^{14}N@C_{60}$	$^{15}N@C_{60}$	$^{31}P@C_{60}$	$^{31}P@C_{60}$
Reference	[91]	[84]	[89]	[90]

T_1 spin-lattice relaxation, T_2 spin–spin relaxation (coherence) for electron (e) and nuclear (n) spin

dynamic nuclear polarization experiment [91]). The 'best' PEF relaxation data published to date for $4.2\,\mathrm{K} \leq T \leq 10\,\mathrm{K}$ and $B_0 \approx 0.35\,\mathrm{T}$ are gathered in Table 14.2. These data show that there is room for improvement in materials purification since they do not meet the standard assumption for clean material, which is that T_{2e} and T_{2n} should reach T_{1e} at low temperatures.

14.4.2 Qubit Addressing and Single-Qubit Operations

Single-qubit rotations can be achieved by microwave (MW) irradiation for the electron spin or by radio-frequency (RF) irradiation for the nuclear spin. The electron spin nutation behavior is more complicated for the $S = 3/2$ spin system than for $S = 1/2$ spins [72]. In general, $S = 3/2$ spin operators have to be used for a complete description. For vanishing zero-field interaction, the isolated electron spin 'classically' behaves exactly as a $S = 1/2$ system, e.g., a π pulse of the same length exactly inverts the sublevel populations for $S = 1/2$ or $S = 3/2$. For superpositions or coherences, such as those produced by $\pi/2$ pulses, one has to distinguish between 'inner' (involving only $|m_S| = 1/2$ levels) and 'outer' (involving $|m_S| = 1/2$ and $3/2$ levels) coherences [84]. Both will be excited for turning angles other than multiples of π.

If there is interaction with other spins, e.g., hyperfine interaction with the nucleus or dipolar interaction with neighboring electron spins, the different coherences lead to new effects due to conditional phase evolution. For the hyperfine case, for example, the phase evolution will depend on both quantum numbers, m_S and m_I [88]. Such effects can in principle be used to engineer desired phase evolutions across a spin chain, but the full theory quickly becomes opaque. Therefore, the standard operating model for a fullerene-based linear-chain quantum register is to use only π pulses on the electron spins and avoiding electron-spin coherences as much as possible [40, 41, 45].

The situation is conceptually simpler if there is a finite *zfi*, since transition-selective ESR and NMR pulses then give access to the full Hilbert space. This means that qubits can be arbitrarily defined, and that single MW or RF pulses can be treated as if they applied to a 'fictitious' $S = 1/2$ spin. Examples for using

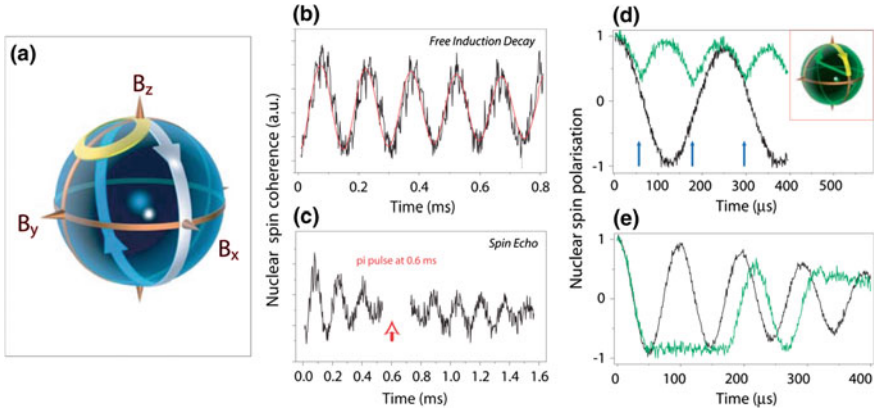

Fig. 14.4 Fast nuclear phase gate using a driven electron spin. **a** Effect of applying resonant (*white*) or detuned (*yellow*) microwave pulses on the electron spin magnetization. **b** Free induction decay, and **c** spin echo of the nuclear spin indicate that the nuclear coherence time T_{2n} is limited only by the electron spin T_{1e}. **d, e** *Black*: unperturbed Rabi oscillations between the two nuclear spin states of the ^{15}N atom; *green*: nuclear spin evolution under the influence of bang–bang decoupling pulses. Adapted with permission from Ref. [92] (© 2006 WILEY-VCH Verlag GmbH & Co. KGaA, Weinheim)

this addressing mode can be found in the works of Meyer et al. [72] and of Naydenov et al. [68].

In practical experiments, electron-spin rotations with non-selective MW excitation can suffer from a number of 'imperfections' leading to gate errors. Morton et al. have used PEFs to study ways to quantify such errors [93] and to suppress them by applying methods known from NMR, such as BB1 composite pulses [94].

Since the nuclear spin has far superior relaxation and coherence times (see Sect. 14.4.1), it is considered the primary 'logic' qubit in the endohedral spin system [39]. RF pulses to manipulate it are however far slower than the MW pulses used to manipulate the electron spin, potentially limiting the number of logical operations. Morton et al. have shown [48, 92] that in the coupled spin system, the electron can be used as an auxiliary resource to dramatically speed up nuclear spin manipulation [95]. In essence, driving an electron spin transition connected to the nuclear spin can create arbitrary changes of the nuclear phase with high precision, but at the time scale of the electron spin Rabi frequency ('bang-bang' pulse duration $\sim$100 ns, see Fig. 14.4). The resulting fast nuclear phase gates may help to make quantum computing with endohedrals universal in the sense that a sufficient number of logical operations can be performed with integrated error correction [96]. First work demonstrating how to integrate error correction with quantum operations on endohedral fullerene qubits can be found in the coherence transfer experiment [84] discussed in the next section.

14.4.3 Electron-Nuclear Two-Qubit Operations

The spin structure of PEFs has been used to explore the feasibility of entanglement and coherence transfer between electron spins and nuclear spins. Most experiments were performed on $^{15}N@C_{60}$ molecules diluted in a polycrystalline C_{60} matrix and hence used non-selective addressing [48, 84, 97, 98]. One study [68] used transition-selective addressing of magnetically dilute $P@C_{60}$:C_{60} encapsulated in a molecular matrix [67], which provides a high degree of orientational order and hence a clear *zfi* structure.

In the work of Mehring et al. [97, 98], the 'outer' electron spin states of [15] N with $|m_S| = 3/2$ were used while the 'inner' $|\pm 1/2\rangle$ states were disregarded (see Fig. 14.5). Electron-nuclear pseudo-entanglement was demonstrated and quantified via quantum state tomography. Very high fidelities ($F > 0.99$) for state preparation were found in these experiments, both for pseudo-pure and pseudo-entangled states [98]. The prefix 'pseudo' indicates that at the relatively high temperature of $T = 50$ K (chosen for the experimental reason of otherwise too large T_{1e} values), the density matrix is still separable and hence 'pseudo-entangled'. A calculation shows that real entanglement can be created below about $T = 7.5$ K at W-band conditions ($B_0 = 3.5$ T, $f_{MW} = 95$ GHz), which is realistically achievable [97].

Despite the good fidelity of state preparation, the lifetime of the entangled state turned out to be limited to ~ 0.2 µs while the single-quantum coherence time was much higher ($T_{2e} \sim 3$ µs). In a follow-up experiment [68], selective addressing was used to explore entanglement between two arbitrarily defined qubits in $P@C_{60}$ (one electron spin level pair with $m_I = 1/2$ and $m_S = \pm 1/2$ and the other with $m_I = -1/2$ and $m_S = -1/2, -3/2$). State preparation was again found to be of very high fidelity, but the resulting lifetime of the entangled state was even shorter. Both papers attributed entangled-state decoherence to unresolved *zfi*, but detailed investigations in this direction have yet to be carried out, e.g., by comparing with entanglement involving only $m_S = \pm 1/2$ states, or using 'quadrupolar' quantum state tomography [99].

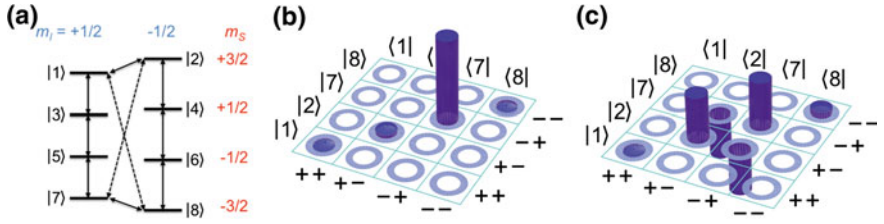

Fig. 14.5 Electron–nuclear pseudo-entanglement. **a** Energy levels of $^{15}N@C_{60}$ and **b, c** quantum state tomography. **b** Experimentally determined density matrices of the pseudo-pure state $|\mathbf{7}\rangle = |m_S = -3/2, m_I = +1/2\rangle \equiv |-+\rangle$, $\rho_7 = |\mathbf{7}\rangle\langle\mathbf{7}|$, and **c** of the pseudo-entangled Bell state $\Psi_{27}^{-} = (|\mathbf{2}\rangle - |\mathbf{7}\rangle)/\sqrt{2} \equiv (|+-\rangle - |-+\rangle)/\sqrt{2}$. Reprinted with permission from Ref. [97] (© 2004 American Physical Society)

An essential ingredient of the linear chain register (Sect. 14.2.2) is to 'swap' spin quantum information between 'logical' nuclear and 'bus' electron spin qubits. An experiment demonstrating this type of coherence transfer was realized in dilute $^{15}N@C_{60}$ powder by Brown et al. [84]. This experiment operated only on $m_S = \pm 1/2$ states and disregarded the $|\pm 3/2\rangle$ states due to their poor coherence properties. The experiment itself used a straightforward transfer sequence from electron spin coherence to nuclear spin coherence, dispensing with pseudo-pure state creation (Fig. 14.6). On the other hand, a judicious choice of refocusing pulses was interspersed to maximize gate fidelity. A two-way (back-and-forth) gate fidelity of $F = 0.89$ was obtained that could be increased to $F = 0.93$ using the previously optimized [94] BB1 electron spin operation pulses.

14.4.4 Towards Electron-Electron Two-Qubit Operations

Studies of two-qubit operations or entanglement between electron spins localized on neighboring endohedral fullerenes are still lacking. In the first proposals [25, 27], chemical dimers were proposed as a likely route towards such studies, but this approach has proved to be harder than anticipated. The main reason is the low overall synthesis yield of endohedral fullerenes, which makes chemical coupling reactions hard to realize.

Although C_{60} dimers can be easily produced and 'half-endohedral' dimers have been demonstrated using various approaches [76, 77], all coupling reactions bear the inherent danger of spin loss. The Porfyrakis group has studied this problem in some detail; recent achievements include nearly lossless Bingel reactions [57] as

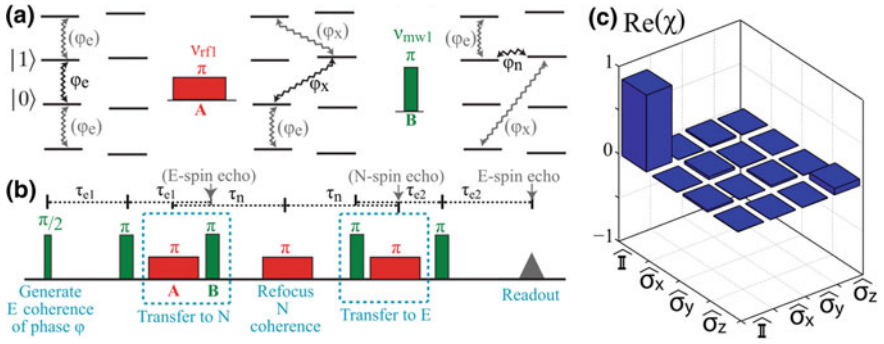

Fig. 14.6 Transfer of a qubit state from the electron spin to the nuclear spin of $^{15}N@C_{60}$ (diluted in C_{60}) within the $m_S = \pm 1/2$ subspace. **a** Coherences are depicted by *wiggly lines*; 'unwanted' coherences generated by the initial $\pi/2$ pulse on the $S = 3/2$ electron spin are shown in *gray*. **b** The full two-way transfer sequence. **c** Quantum process tomography matrix χ for the two-way transfer, yielding a fidelity $F = 0.88$. Reprinted with permission from Ref. [84] (© 2011 American Physical Society)

well as more sophisticated dimer coupling schemes [77] that take into account the limitations of low-yield endohedral synthesis. A doubly endohedral dimer was already reported [78] but its spin properties could only be investigated in a disordered solid-state sample. Since the Hilbert space of a $(^{14}N@C_{60})_2$ dimer has dimension 144, highly ordered samples (see Sect. 14.3.3) are needed for further progress.

An alternative route towards controlled fullerene–fullerene coupling is given by non-covalent encapsulation in matrices such as carbon nanotubes (see Sect. 14.3.2), with the added benefit of a natural linear orientation [60, 61]. To investigate such samples however requires that a single-spin read-out be found.

14.5 The Single-Qubit Read-Out Challenge

There is a great fundamental and practical need for finding single-spin readout methods compatible with endohedral fullerenes. This will allow using solid-state architectures based on individual spin chains rather than big ensembles of fullerenes or fullerene dimers. Spin chains (see Sect. 14.2.2) bring advantages in interaction control, desirable both for reduced error rates (suppression of uncontrolled dipolar interactions, see Sect. 14.4.1) and for making quantum-computing universal through local interaction gating. Even quantum cellular automaton (QCA) architectures with only global interaction control [35] would benefit. Moreover, a strong (projective) read-out allows for efficient qubit state preparation and polarization, enabling more elaborate quantum protocols. In the following, we first review the limits of traditional 'inductive' microwave detection, which has recently progressed almost to single-spin detection. The remaining sections describe indirect electrical and optical detection of PEF spins that exploit quantum-mechanical selection rules.

14.5.1 Microwave Detection in Micro-Resonators and Superconducting Cavities

The sensitivity of 'normal' electron spin resonance (ESR) is limited by polarization issues in the same manner as NMR is (see Sect. 14.1.2). The electron spin Zeeman energy is $\sim 10^3$ times larger than for nuclei, so that thermal electron spin polarization can surpass 50% at realistic conditions (W-band, conventional helium cryostat).

The sensitivity of commercial spectrometers is in the region of $10^9 \text{spins}/\sqrt{\text{Hz}}$; it can be enhanced substantially using micro-resonators or superconducting microwave cavities. Experiments with $N@C_{60}$ in micro-resonators [100, 101] showed a spin sensitivity of roughly $1.8 \times 10^4 \,\text{spins}/\sqrt{\text{Hz}}$ at room temperature, and

calculations extrapolating from this result showed that single-spin sensitivity can be reached at low temperatures with optimized resonator structures. The latest development demonstrated a spin sensitivity of $6.7 \times 10^3 \text{spins}/\sqrt{\text{Hz}}$ for phosphorus in silicon at 10 K [102], implying that an overnight measurement has indeed single-spin sensitivity. Using superconducting amplifiers and microwave structures, Bienfait et al. reported a spin sensitivity of $1.7 \times 10^3 \text{spins}/\sqrt{\text{Hz}}$ for Bi donors implanted in silicon [103], which is a further improvement by a factor of 4.

A major advantage of using non-superconducting micro-resonators is that high magnetic fields and gradient-imaging methods can be used (see Fig. 14.7). With proper design, ESR imaging may reach spatial resolutions down to 1 nm. A thorough discussion of this kind of technical issues can be found in the work of Blank et al. [100].

Although single-spin ESR sensitivity seems within reach for the near future, the current measurement times are still prohibitive for routine work. Furthermore, inductive spin measurements are 'weak' and not projective, so that this approach will likely not be part of a final quantum computer; rather, the imaging capabilities of the micro-resonator approach may turn out to be an extremely valuable tool in developing extended solid-state spin systems.

14.5.2 Electrical Detection

Electrical detection of spin states in electronic devices is possible using spin selection rules governing carrier transport or carrier recombination (see Fig. 14.8). In the transport approach, a current is driven through a single endohedral molecule [104], and Pauli blocking is used to infer the Zeeman state of the coupled system consisting of a charged fullerene cage and the endohedral atom. The second detection approach, known as *electrically detected magnetic resonance* (EDMR),

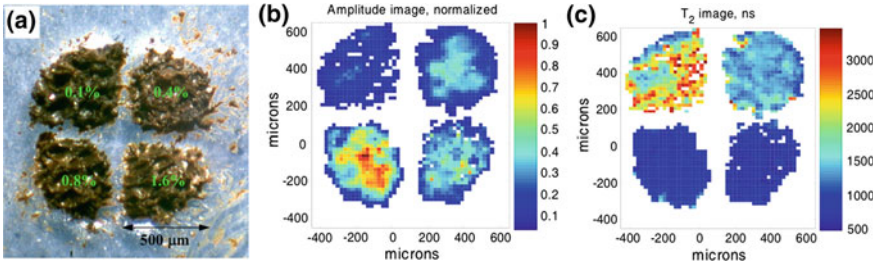

Fig. 14.7 High-sensitivity imaging of N@C_{60} in a micro-resonator. ESR images of a heterogeneous sample made of C_{60}:N@C_{60} powder with four different N@C_{60} enrichment levels of 0.1, 0.4, 0.8, 1.6%. **a** Optical image showing powder heaps in a 4-quadrant pattern. **b** ESR amplitude image, **c** ESR T_{2e} image. Reproduced with permission from Ref. [100] (© 2009 the PCCP Owner Societies)

uses spin-dependent recombination of charge carriers in C_{60} thin films [105] or C_{60} microcrystals [106].

Direct detection of spin levels in a single-molecule transistor (SMT) device using $N@C_{60}$ was demonstrated by Grose et al. [104] and reproduced independently by Roch et al. [107]. Devices were fabricated by adsorbing almost pure $N@C_{60}$ molecules onto an initially continuous Pt or Au wire, which was deposited on top of an oxidized Al gate electrode. The wire was then broken using electro-migration to form a nanometre-scale gap. Differential conductance measurements at $T \approx 100$ mK as a function of magnetic field B_0 showed a transition from a $S = 2$ to a $S = 1$ spin state for the singly charged $N@C_{60}$, i.e., from ferromagnetic to antiferromagnetic coupling between the endohedral $S = 3/2$ and the C_{60} cage $S = 1/2$ spin (see Fig. 14.9).

Large exchange couplings of several Tesla (>0.1 meV) between the endohedral atom and electrons on the C_{60} cage were determined, but the exact value varied considerably from sample to sample. These variations indicate that the physical situation may be more complex than the simple picture of isotropically coupled endohedral and cage spin. In particular, the anisotropic distribution of charges on the cage, which oscillates between one and two electrons in the experiments, may strongly influence the magnetic coupling.

The reported measurements constitute single-molecule quantum state measurements, but they are quasi-static and only report the spin's ground state so far. For use in quantum computation, they should be combined with fast gating [108] and microwave manipulation of the electron spin [109] as has been shown for other solid-state spin qubits, and possibly with spin-filtering contacts [110]. These techniques are already very challenging *per se* and it turns out that reproducible device fabrication is even harder for single-molecular devices than for top-down fabricated qubits such as GaAs quantum dots.

Indirect electrical spin detection via carrier pair recombination is known as EDMR. This technique naturally includes coherent spin control with MW pulses,

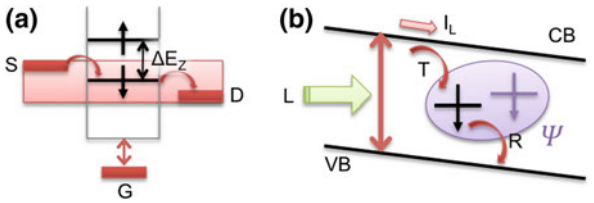

Fig. 14.8 Electrical spin detection schemes. **a** Spin-dependent quantum transport through a single molecule. Energy levels (*black*) defined by the molecular electronic structure—including Zeeman splitting ΔE_Z—can be shifted with a gate (G) in and out of the bias window (*shaded area*) defined by source (S) and drain (D) potential difference V_{SD}. **(b)** Spin-dependent photocurrent (SDPC) in a semiconductor. Illumination with light (L) creates carriers in conduction (CB) and valence band (VB), which can be trapped (T) in localized states (*black*), e.g., as self-localized polarons. The spin state $\boldsymbol{\Psi}$ may prevent or accelerate recombination (R) of the trapped carrier, influencing the macroscopic photocurrent I_L through the device

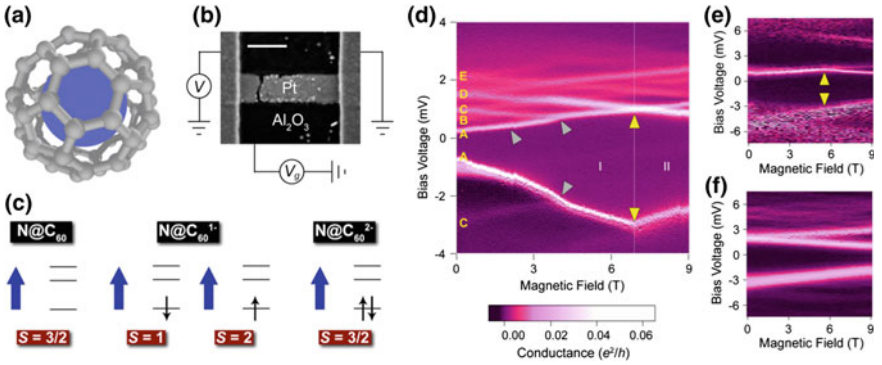

Fig. 14.9 Spin states in N@C_{60} single-molecule transistor devices. **a** Sketch of the N@C_{60} molecule. **b** Scanning electron microscopy image of a sample at room temperature following electro-migration (scale bar: 200 nm). **c** Spin states in N@C_{60} and its anions; *blue arrows*: endohedral spin S_N, *black arrows*: spin S_e of electron(s) in lowest unoccupied orbitals; possible values for total spin $S_q = S_N \pm S_e$ depends on charge state $q = 0, 1, 2$. **d** Differential conductance dI/dV for N@C_{60} SMT device 1 as a function of bias voltage V and applied magnetic field B, at constant gate voltage $V_g = -891$ mV on the positive side of the degeneracy point. In region I, the ground-state transition $(q+1) \rightarrow q$ corresponds to decreasing spin, $S_{Z,q+1} - S_{Z,q} < 0$, while in region II $S_{Z,q+1} - S_{Z,q} > 0$. **e** Same as (**d**) for N@C_{60} SMT device 2. **f** Same for a C_{60} SMT device. No change in slope is observed for the ground-state peaks of C_{60}. Adapted from Ref. [104] (© 2008 Nature Publishing Group)

making it a good platform for quantum-computing studies. Pulsed EDMR has been applied to the Kane silicon qubit at low temperatures [111]. Studies on pure C_{60} thin film devices found spin pair states with lifetimes in the microsecond range even at room temperature [105], which is particularly attractive for keeping measurement times short. A sensitivity in the range of $\sim 10^3$ detected elementary charges was reached in these experiments, but EDMR is capable of even higher sensitivity [112]. The results obtained for 'empty' C_{60} were used to predict the EDMR spectrum for dipole-coupled N@C_{60} molecules (see Fig. 14.10a, b) [105], and several groups tried to measure corresponding spectra.

The experimental realization of an EDMR-based read-out has taken a long time due to the necessary development of 'cold' processing methods compatible with the limited thermal stability of PEFs (see Sect. 14.3.1 and Sect. 14.3.2). Using a table-top cw ESR spectrometer with fast sample-changeover times [106], we have recently accelerated and improved our sample development. Figure 14.10c shows a room temperature cw ESR spectrum of N@C_{60}-doped microcrystals on a grid electrode. The spectral features are rather more complicated than the naïve prediction from 2007, which neglected the anisotropy and distance dependence of dipolar coupling. The observed spectrum is compatible with simulations of an ensemble of strongly dipolar-coupled spin pairs consisting each of one $(S = 3/2,\ I = 1)$ N@C_{60} and one $(S = 1/2,\ I = 0)$ $C_{60}^{\bullet +}$ radical molecule. The

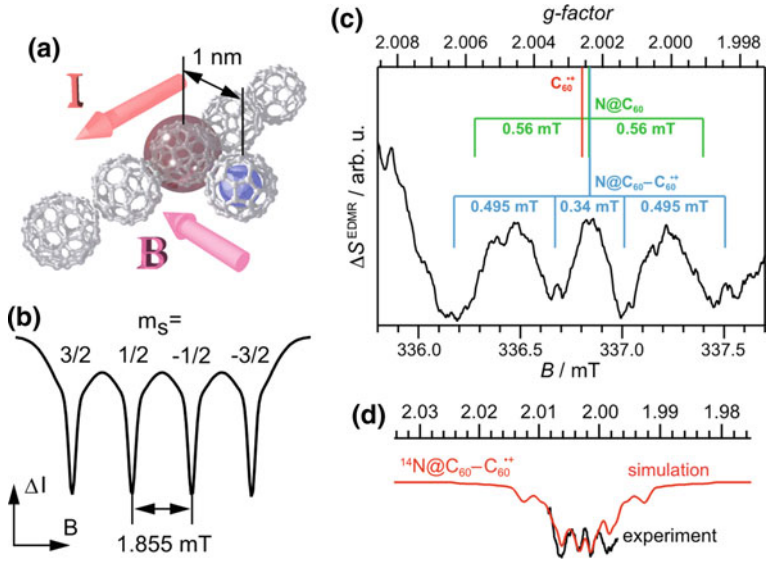

Fig. 14.10 EDMR detection of endohedral fullerene spins. **a** Scheme for the EDMR readout of N@C_{60} electron spin states by nearby fullerenes. The localized C_{60} spin involved in spin-dependent transitions, marked by a surrounding sphere, is dipole-coupled to an adjacent N@C_{60} molecule. **b** Simulated integrated cw-EDMR spectrum expected for the $(S(N@C_{60}) = 3/2,\ S'(C_{60}) = 1/2)$ spin pair with scalar coupling strength $J = 52$ MHz (orientation dependence neglected). Reprinted with permission from Ref. [105] (© 2007 American Physical Society). **c** Observed integrated cw-EDMR difference spectrum (average of two samples) constructed by subtraction of a broad resonance due to uncoupled cationic $C_{60}^{\bullet+}$ radicals. Line positions of constituent $C_{60}^{\bullet+}$ (measured by EDMR) and N@C_{60} (by ESR) are indicated. The spectrum can be qualitatively simulated with a powder average of dipolar-coupled $(S = 3/2,\ S' = 1/2)$ spin pairs with average $J_D = 30-35$ MHz, corresponding to a distance $d = 1.1-1.2$ nm. Adapted from Ref. [113]

pairs are assumed to have a random orientation but a fixed average distance of 1.1–1.2 nm, yielding an average dipolar coupling constant of 30–35 MHz.

These preliminary results are encouraging for further studies using pulsed EDMR at variable temperatures. They need to be extended with pulsed excitation and detection in order to assess coupling strength and relaxation times more quantitatively; the rather narrow EDMR line widths (<0.2 mT) indicate that the good spin properties of N@C_{60} are retained to some degree in these experiments. It will be interesting to see how far EDMR sensitivity can be pushed by advanced device design. A yet unsolved problem is how to gain control over the dipolar coupling orientation. Carbon nanotube encapsulation of dimers would allow this, but CNT EDMR has yet to be demonstrated.

14.5.3 Optical Detection

Optical spin detection uses similar selection rules as electrical detection. In optics, the detection efficiency is boosted by the large photon energy and furthermore provides a way for fast spin polarization. In specific systems with paramagnetic ground states, single-spin sensitivity can be reached at room temperature. These properties have made the nitrogen-vacancy center (NVC) in diamond [19] popular as a highly controllable single-spin quantum bit [21].

Fullerenes have optical transitions that can be used in a similar way, but usually they have a diamagnetic ground state. The controllable spin thus exists only for several microseconds in a metastable state reached by inter-system crossing and is not particularly suited as a logical quantum bit. Nevertheless, transient spin states can be used for spin state read-out [114], especially if their creation is accompanied by optical spin polarization. Of particular interest are paramagnetic endohedral fullerenes containing transition metal ions, like $Er_3N@C_{80}$, which have spin-dependent luminescence at low temperature [6].

Unfortunately, $N@C_{60}$ offers no direct optical access to the spin since the nitrogen atom is extremely well decoupled from the carbon cage, leading to independent energy levels; the first allowed transition of the nitrogen atom is in the deep ultraviolet (>10 eV). Therefore, coupling to readout systems is needed. Since NVCs have the proven potential for detecting weakly coupled electron spins with single-spin sensitivity [115, 116], we have started investigating this system as a read-out.

Spin–spin coupling experiments were performed by depositing enriched $N@C_{60}$:C_{60} mixtures from solution onto diamond surfaces implanted with shallow NVCs. First studies using cw-ODMR remained inconclusive [117], i.e., the coupling was not large enough for a detectable line splitting. Pulsed ODMR measurements of similar samples (see Fig. 14.11) showed Rabi oscillations of coupled 'dark' electron spins. It is difficult to quantify the number of coupled spins from these experiments that suffered from a rather low spin coherence time of the NVC readout qubit (<1 μs) [118]. Thus, a full characterization of the dark spins was not possible and coherent coupling control has yet to be demonstrated.

A current topic of research is hence to increase the spin coherence times of NVCs shallow enough to sense external spins deposited onto the surface. We found that NV centers in nano-diamonds (diameter <25 nm) are useful for realizing small quantum algorithms at room temperature [119] and for sensing small magnetic fields in their environment [120]. NVCs in nano-diamonds however still show shorter relaxation times than NVCs in bulk diamond. Coherence can be prolonged using decoupling pulses [118, 121]. Recent efforts to optimize NVC for external spin sensing have led to an intense scrutiny of the diamond surface. Since scanning tunneling microscopy (STM) cannot be used with ease on insulating surfaces, we have employed atomic-resolution non-contact-AFM [122]. In conjunction with photoelectron spectroscopy, this has helped us set up protocols to reproducibly prepare ultra-clean diamond surfaces [123]. The latest developments in NVC

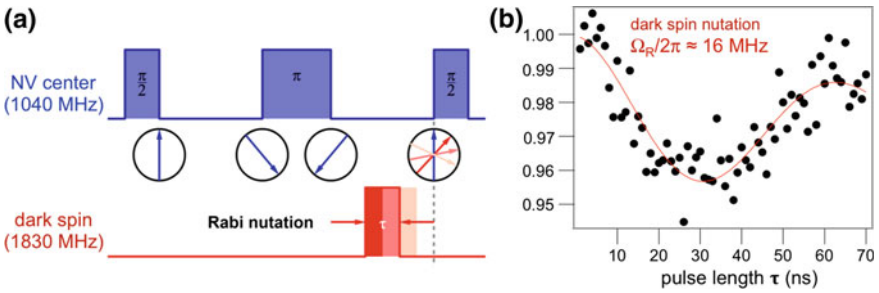

Fig. 14.11 ODMR detection of *dark spins* near a single nitrogen-vacancy center in diamond. **a** Pulse scheme for indirect detection of optically inactive (‘*dark*’) spins by a single NVC. An optically detected spin echo is performed on the NVC, while nearby *dark spins* are driven with microwave pulses. This results in perturbed echo formation and hence diminished luminescence at resonance. **b** Rabi nutation of one or several *dark spins*, presumed to be $N@C_{60}$, as detected by the modulated echo intensity of a single NVC. Adapted from Ref. [118]

research show that high-resolution mapping of external spins is possible [23, 121], indicating that the nitrogen-vacancy center can indeed be used as a quantum state detector.

14.6 Summary and Outlook

Ensemble experiments on pnictide endohedral fullerenes have confirmed the potential of this class of molecules for quantum information. In order to progress from this potential to actual devices, a number of challenges have to be overcome.

First and foremost, the synthesis route must be simplified and made efficiently scalable since the scarcity of pure endohedral material has hindered progress in this field considerably. The low overall yield (see Sect. 14.3.1) can be improved at two stages: (a) the ion implantation yield of 3×10^{-4} should be raised at least into the percent range; (b) multistep HPLC must be avoided by finding better stationary phases, possibly based on molecular recognition.

The second major milestone is the demonstration of a fast and strong read-out at convenient experimental conditions (moderate temperatures, no vacuum, etc.). This may be achieved either via electrical or optical detection. The EDMR route has to be extended down to the single-spin level, which requires developments in device architecture. The most promising approach is optical detection via nitrogen-vacancy centers in diamond or similar detection systems. Recent investigations on the stability of $N@C_{60}$ fullerenes [56] show that the combined optical and thermal load has to be somewhat reduced to enable long-term stability.

With this milestone, spin polarization and large-scale operation in one-dimensional chains will become possible. Such systems can be prepared by the methods indicated in Sect. 14.3, immediately leading to thousands of molecular

qubits lined up for experiments. Their investigation will enable a realistic assessment of the ultimate system scaling size for a PEF-based quantum register. Finally, integration of medium-scale quantum registers into hybrid quantum systems [124] will be of interest.

References

1. Feynman RP (1982) Simulating physics with computers. Int J Theor Phys 21:467–488
2. Deutsch D (1985) Quantum theory, the church-turing principle and the universal quantum computer. Proc R Soc A Math Phys Eng Sci 400:97–117
3. Ladd TD et al (2010) Quantum computers. Nature 464:45–53
4. Popov AA, Yang S, Dunsch L (2013) Endohedral fullerenes. Chem Rev 113:5989–6113
5. Paech M, Stoesser R (2000) In: Auner N, Weis J (eds) Organosilicon Chemistry IV: From Molecules to Materials. Wiley-VCH Verlag GmbH, Germany, pp 521–525. doi:10.1002/9783527619917.ch87
6. Jones MAG, Morton JJL, Taylor RA, Ardavan A, Briggs GAD (2006) PL, magneto-PL and PLE of the trimetallic nitride template fullerene $Er_3N@C_{80}$. Phys status solidi 243:3037–3041
7. Brown RM et al (2010) Electron spin coherence in metallofullerenes: Y, Sc, and $La@C_{82}$. Phys Rev B 82:33410
8. Schoenfeld RS, Harneit W, Paech M (2006) Pulsed and cw EPR studies on hydrogen atoms encaged in octasilsesquioxane molecules. Phys status solidi 243:3008–3012
9. Mitrikas G, Efthimiadou EK, Kordas G (2014) Extending the electron spin coherence time of atomic hydrogen by dynamical decoupling. Phys Chem Chem Phys 16:2378–2383
10. Cory DG et al (2000) NMR based quantum information processing: achievements and prospects. Fortschritte der Phys 48:875–907
11. Vandersypen LMK et al (2001) Experimental realization of Shor's quantum factoring algorithm using nuclear magnetic resonance. Nature 414:883–887
12. Lu D et al (2015) In: Takui T, Hanson G, Berliner L (eds) Electron Spin Resonance (ESR) Based Quantum Computing. Springer, New York at http://arxiv.org/abs/1501.01353, http://link.springer.com/chapter/10.1007/978-1-4939-3658-8_7
13. Jones JA (2000) NMR quantum computation: a critical evaluation. Fortschritte der Phys 48:909–924
14. Kane BE (1998) A silicon-based nuclear spin quantum computer. Nature 393:133–137
15. Ladd TD et al (2002) All-silicon quantum computer. Phys Rev Lett 89:17901
16. Laucht A et al (2015) Electrically controlling single-spin qubits in a continuous microwave field. Sci Adv 1:e1500022–e1500022
17. Pla JJ et al (2012) A single-atom electron spin qubit in silicon. Nature 489:541–545
18. Pla JJ et al (2013) High-fidelity readout and control of a nuclear spin qubit in silicon. Nature 496:334–338
19. Gruber A et al (1997) Scanning confocal optical microscopy and magnetic resonance on single defect centers. Science 276:2012–2014
20. Jelezko F et al (2004) Observation of coherent oscillation of a single nuclear spin and realization of a two-qubit conditional quantum gate. Phys Rev Lett 93:130501
21. Childress L, Hanson R (2013) Diamond NV centers for quantum computing and quantum networks. MRS Bull 38:134–138
22. Orwa JO et al (2010) Fabrication of single optical centres in diamond—a review. J Lumin 130:1646–1654
23. Grinolds MS et al (2014) Subnanometre resolution in three-dimensional magnetic resonance imaging of individual dark spins. Nat Nanotechnol 9:279–284

24. Bhallamudi VP, Hammel PC (2015) Nitrogen–vacancy centres: nanoscale MRI. Nat Nanotechnol 10:104–106
25. Harneit W (2002) Fullerene-based electron-spin quantum computer. Phys Rev A 65:32322
26. Ardavan A et al (2003) Nanoscale solid-state quantum computing. Philos Trans R Soc A 361:1473–1485
27. Meyer C, Harneit W, Weidinger A, Lips K (2002) Experimental steps towards the realisation of a fullerene quantum computer. Phys status solidi 233:462–466
28. Vinit, Sujith SV, Ramachandran CN (2016) Spin-spin coupling in nitrogen atom encapsulated C_{60}, C_{59} N, and their respective dimers. J Phys Chem A 120:6990–6997
29. Almeida Murphy T et al (1996) Observation of atom like nitrogen in nitrogen-implanted solid C_{60}. Phys Rev Lett 77:1075–1078
30. Greer JC (2000) The atomic nature of endohedrally encapsulated nitrogen N@C_{60} studied by density functional and Hartree-Fock methods. Chem Phys Lett 326:567–572
31. Knapp C et al (1998) Electron paramagnetic resonance study of atomic phosphorus encapsulated in [60]fullerene. Mol Phys 95:999–1004
32. Larsson JA, Greer JC, Harneit W, Weidinger A (2002) Phosphorous trapped within buckminsterfullerene. J Chem Phys 116:7849
33. Gün A, Gençten A (2011) Three-qubit quantum entanglement for SI (S = 3/2, I = 1/2) spin system. Int J Quantum Inf 9:1635–1642
34. Gün A, Çakmak S, Gençten A (2013) Construction of four-qubit quantum entanglement for SI (S = 3/2, I = 3/2) spin system. Quantum Inf Process 12:205–215
35. Twamley J (2003) Quantum-cellular-automata quantum computing with endohedral fullerenes. Phys Rev A 67:52318
36. Teles J et al (2012) Quantum information processing by nuclear magnetic resonance on quadrupolar nuclei. Philos Trans R Soc A 370:4770–4793
37. Gedik Z et al (2015) Computational speed-up with a single qudit. Sci Rep 5:14671
38. Harneit W, Huebener K, Naydenov B, Schaefer S, Scheloske M (2007) N@C_{60} quantum bit engineering. Phys status solidi 244:3879–3884
39. Suter D, Lim K (2002) Scalable architecture for spin-based quantum computers with a single type of gate. Phys Rev A 65:52309
40. Ju C, Suter D, Du J (2007) Two-qubit gates between noninteracting qubits in endohedral-fullerene-based quantum computation. Phys Rev A 75:12318
41. Ju C, Suter D, Du J (2011) An endohedral fullerene-based nuclear spin quantum computer. Phys Lett A 375:1441–1444
42. Waiblinger M et al (2000) Magnetic interaction in diluted N@C_{60}. AIP Conference Proceedings 544:195–198(AIP)
43. Heiney PA et al (1991) Orientational ordering transition in solid C_{60}. Phys Rev Lett 66:2911–2914
44. Harneit W, Meyer C, Weidinger A, Suter D, Twamley J (2002) Architectures for a spin quantum computer based on endohedral fullerenes. Phys status solidi 233:453–461
45. Yang WL, Xu ZY, Wei H, Feng M, Suter D (2010) Quantum-information-processing architecture with endohedral fullerenes in a carbon nanotube. Phys Rev A 81:32303
46. Kamenev DI, Berman GP, Tsifrinovich VI (2006) Creation of entanglement in a scalable spin quantum computer with long-range dipole-dipole interaction between qubits. Phys Rev A 73:62336
47. Feng M, Twamley J (2004) Selective pulse implementation of two-qubit gates for spin-3/2-based fullerene quantum-information processing. Phys Rev A 70:32318
48. Morton JJL et al (2006) Bang–bang control of fullerene qubits using ultrafast phase gates. Nat Phys 2:40–43
49. Hu YM, Yang WL, Feng M, Du JF (2009) Distributed quantum-information processing with fullerene-caged electron spins in distant nanotubes. Phys Rev A 80:22322
50. Pietzak B, Weidinger A, Dinse K-P, Hirsch A (2002) In: Akasaka T, Nagase S (eds) Endofullerenes: a new family of carbon clusters. Springer, Netherlands, pp 13–65. doi:10.1007/978-94-015-9938-2_2

51. Porfyrakis K (2016) In: Popov AA (ed) Endohedral fullerenes: electron transfer and spin. Springer, Verlag
52. Jakes P, Dinse K-P, Meyer C, Harneit W, Weidinger A (2003) Purification and optical spectroscopy of N@C_{60}. Phys Chem Chem Phys 5:4080
53. Zhang J et al (2006) The effects of a pyrrolidine functional group on the magnetic properties of N@C_{60}. Chem Phys Lett 432:523–527
54. Waiblinger M et al (2001) Corrected article: thermal stability of the endohedral fullerenes N@C_{60}, N@C_{70}, and P@C_{60}. Phys Rev B 64:159901
55. Tóth S et al (2008) Enhanced thermal stability and spin-lattice relaxation rate of N@C_{60} inside carbon nanotubes. Phys Rev B 77:214409
56. Eckardt M, Wieczorek R, Harneit W (2015) Stability of C_{60} and N@C_{60} under thermal and optical exposure. Carbon N Y 95:601–607
57. Zhou S, Rašović I, Briggs GAD, Porfyrakis K (2015) Synthesis of the first completely spin-compatible N@C_{60} cyclopropane derivatives by carefully tuning the DBU base catalyst. Chem Commun 51:7096–7099
58. Pong W-T, Durkan C, Li H, Harneit W (2006) Strategies for the deposition of free radical organic molecules for scanning-probe microscopy experiments. J Scanning Probe Microsc 1:55–62
59. Červenka J, Flipse CFJ (2010) Fullerene monolayer formation by spray coating. Nanotechnology 21:65302
60. Simon F et al (2004) Low temperature fullerene encapsulation in single wall carbon nanotubes: synthesis of N@C_{60}@SWCNT. Chem Phys Lett 383:362–367
61. Khlobystov AN et al (2004) Low temperature assembly of fullerene arrays in single-walled carbon nanotubes using supercritical fluids. J Mater Chem 14:2852
62. Diaconescu B et al (2009) Molecular self-assembly of functionalized fullerenes on a metal surface. Phys Rev Lett 102:56102
63. Deak DS, Silly F, Porfyrakis K, Castell MR (2006) Template ordered open-grid arrays of paired endohedral fullerenes. J Am Chem Soc 128:13976–13977
64. Jakes P et al (2002) Electron paramagnetic resonance investigation of endohedral fullerenes N@C_{60} and N@C_{70} in a liquid crystal. J Magn Reson 156:303–308
65. Meyer C et al (2002) Alignment of the endohedral fullerenes N@C_{60} and N@C_{70} in a liquid crystal matrix. Phys Rev A 65:61201
66. Liu G et al (2013) Alignment of N@C_{60} derivatives in a liquid crystal matrix. J Phys Chem B 117:5925–5931
67. Naydenov B et al (2006) Ordered inclusion of endohedral fullerenes N@C_{60} and P@C_{60} in a crystalline matrix. Chem Phys Lett 424:327–332
68. Naydenov B, Mende J, Harneit W, Mehring M (2008) Entanglement in P@C_{60} encapsulated in a solid state matrix. Phys status solidi 245:2002–2005
69. Rabl P et al (2010) A quantum spin transducer based on nanoelectromechanical resonator arrays. Nat Phys 6:602–608
70. Borneman TW, Granade CE, Cory DG (2012) Parallel information transfer in a multinode quantum information processor. Phys Rev Lett 108:140502
71. Dinse K-P, Käß H, Knapp C, Weiden N (2000) EPR investigation of atoms in chemical traps. Carbon N Y 38:1635–1640
72. Meyer C, Harneit W, Naydenov B, Lips K, Weidinger A (2004) N@C_{60} and P@C_{60} as quantum bits. Appl Magn Reson 27:123–132
73. Wakahara T, Kato T, Miyazawa K, Harneit W (2012) N@C_{60} as a structural probe for fullerene nanomaterials. Carbon N Y 50:1709–1712
74. Dietel E et al (1999) Atomic nitrogen encapsulated in fullerenes: effects of cage variations. J Am Chem Soc 121:2432–2437
75. Franco L et al (2006) Synthesis and magnetic properties of N@C_{60} derivatives. Chem Phys Lett 422:100–105
76. Goedde B et al (2001) 'Nitrogen doped' C_{60} dimers (N@C_{60}–C_{60}). Chem Phys Lett 334:12–17

77. Plant SR et al (2013) A two-step approach to the synthesis of N@C_{60} fullerene dimers for molecular qubits. Chem. Sci. 4:2971
78. Farrington BJ et al (2012) Chemistry at the nanoscale: synthesis of an N@C_{60}-N@C_{60} endohedral fullerene dimer. Angew Chemie 124:3647–3650
79. Yang J et al (2012) Probing the zero-field splitting in the ordered N@C_{60} in buckycatcher $C_{60}H_{28}$ studied by EPR spectroscopy. Phys Lett A 376:1748–1751
80. Gil-Ramírez G et al (2010) A cyclic porphyrin trimer as a receptor for fullerenes. Org Lett 12:3544–3547
81. Couderc G, Hulliger J (2010) Channel forming organic crystals: guest alignment and properties. Chem Soc Rev 39:1545
82. Naydenov B et al (2006) N@C_{60} and N@C_{70} oriented in a single-crystalline matrix. Phys status solidi 243:2995–2998
83. Morton JJL et al (2006) Electron spin relaxation of N@C_{60} in CS_2. J Chem Phys 124:14508
84. Brown RM et al (2011) Coherent state transfer between an electron and nuclear spin in ^{15}N@C_{60}. Phys Rev Lett 106:110504
85. Morton JJL et al (2007) Environmental effects on electron spin relaxation in N@C_{60}. Phys Rev B 76:85418
86. Menéndez J, Page JB (2000) Light scattering in solids VIII. In: Cardona M, Güntherodt G (eds) Topics in applied physics, vol 76. Spinger, Berlin, Heidelberg, pp 27–95
87. Knorr SB (2002) ESR studies of the electronic properties of fullerenes and their compounds (in German). PhD thesis. Universitaet Stuttgart, Germany
88. Morton JJL et al (2005) A new mechanism for electron spin echo envelope modulation. J Chem Phys 122:174504
89. Meyer C (2003) Endohedral fullerenes for quantum computing. PhD thesis. Freie Universitaet Berlin, Germany
90. Naydenov B (2006) Encapsulation of endohedral fullerenes for quantum computing. PhD thesis. Freie Universitaet, Berlin
91. Morley GW et al (2007) Efficient dynamic nuclear polarization at high magnetic fields. Phys Rev Lett 98:220501
92. Morton JJL et al (2006) The N@C_{60} nuclear spin qubit: bang-bang decoupling and ultrafast phase gates. Phys status solidi 243:3028–3031
93. Morton JJL et al (2005) Measuring errors in single-qubit rotations by pulsed electron paramagnetic resonance. Phys Rev A 71:12332
94. Morton JJL et al (2005) High fidelity single qubit operations using pulsed electron paramagnetic resonance. Phys Rev Lett 95:200501
95. Simmons S, Wu H, Morton JJL (2012) Controlling and exploiting phases in multi-spin systems using electron spin resonance and nuclear magnetic resonance. Philos Trans R Soc A Math Phys Eng Sci 370:4794–4809
96. Zhang J, Souza AM, Brandao FD, Suter D (2014) Protected quantum computing: interleaving gate operations with dynamical decoupling sequences. Phys Rev Lett 112:50502
97. Mehring M, Scherer W, Weidinger A (2004) Pseudoentanglement of spin states in the multilevel ^{15}N@C_{60} System. Phys Rev Lett 93:206603
98. Scherer W, Mehring M (2008) Entangled electron and nuclear spin states in ^{15}N@C_{60}: density matrix tomography. J Chem Phys 128:52305
99. Auccaise R et al (2008) A study of the relaxation dynamics in a quadrupolar NMR system using quantum state tomography. J Magn Reson 192:17–26
100. Blank A, Suhovoy E, Halevy R, Shtirberg L, Harneit W (2009) ESR imaging in solid phase down to sub-micron resolution: methodology and applications. Phys Chem Chem Phys 11:6689
101. Blank A, Talmon Y, Shklyar M, Shtirberg L, Harneit W (2008) Direct measurement of diffusion in liquid phase by electron spin resonance. Chem Phys Lett 465:147–152
102. Artzi Y, Twig Y, Blank A (2015) Induction-detection electron spin resonance with spin sensitivity of a few tens of spins. Appl Phys Lett 106:84104

103. Bienfait A et al (2015) Reaching the quantum limit of sensitivity in electron spin resonance. Nat Nanotechnol 11:253–257
104. Grose JE et al (2008) Tunnelling spectra of individual magnetic endofullerene molecules. Nat Mater 7:884–889
105. Harneit W et al (2007) Room temperature electrical detection of spin coherence in C_{60}. Phys Rev Lett 98:216601
106. Eckardt M, Behrends J, Münter D, Harneit W (2015) Compact electrically detected magnetic resonance setup. AIP Adv 5:47139
107. Roch N et al (2011) Cotunneling through a magnetic single-molecule transistor based on $N@C_{60}$. Phys Rev B 83:81407
108. Elzerman JM et al (2004) Single-shot read-out of an individual electron spin in a quantum dot. Nature 430:431–435
109. Petta JR et al (2005) Coherent Manipulation of Coupled Electron spins in semiconductor quantum dots. Science 309:2180–2184
110. Feng M, Twamley J (2004) Readout scheme of the fullerene-based quantum computer by a single-electron transistor. Phys Rev A 70:30303
111. McCamey DR, Van Tol J, Morley GW, Boehme C (2010) Electronic spin storage in an electrically readable nuclear spin memory with a lifetime >100 seconds. Science 330:1652–1656
112. McCamey DR et al (2006) Electrically detected magnetic resonance in ion-implanted Si: P nanostructures. Appl Phys Lett 89:182115
113. Eckardt M (2016) Electrically detected magnetic resonance on fullerene-based organic semiconductor devices and microcrystals. PhD thesis. Johannes Gutenberg-Universitaet Mainz, Germany
114. Filidou V et al (2012) Ultrafast entangling gates between nuclear spins using photoexcited triplet states. Nat Phys 8:596–600
115. Grotz B et al (2011) Sensing external spins with nitrogen-vacancy diamond. New J Phys 13:55004
116. Gaebel T et al (2006) Room-temperature coherent coupling of single spins in diamond. Nat Phys 2:408–413
117. Huebener K, Schoenfeld RS, Kniepert J, Oelmueller C, Harneit W (2008) ODMR of NV centers in nano-diamonds covered with $N@C_{60}$. Phys status solidi 245:2013–2017
118. Schoenfeld RS (2011) Optical readout of single spins for quantum computing and magnetic sensing. PhD thesis. Freie Universitaet, Berlin
119. Shi F et al (2010) Room-temperature implementation of the deutsch-jozsa algorithm with a single electronic spin in diamond. Phys Rev Lett 105:40504
120. Schoenfeld RS, Harneit W (2011) Real time magnetic field sensing and imaging using a single spin in diamond. Phys Rev Lett 106:30802
121. Romach Y et al (2015) Spectroscopy of surface-induced noise using shallow spins in diamond. Phys Rev Lett 114:17601
122. Nimmrich M et al (2010) Atomic-resolution imaging of clean and hydrogen-terminated C (100) − (2 × 1) diamond surfaces using noncontact AFM. Phys Rev B 81:201403
123. Dyachenko O et al (2015) A diamond (100) surface with perfect phase purity. Chem Phys Lett 640:72–76
124. Morton JJL, Lovett BW (2011) Hybrid solid-state qubits: the powerful role of electron spins. Annu Rev Condens Matter Phys 2:189–212

Index

A.A. Popov (ed.), *Endohedral Fullerenes: Electron Transfer and Spin*,
Nanostructure Science and Technology, DOI 10.1007/978-3-319-47049-8